THÈSE

Pour obtenir le grade de

DOCTEUR DE L'UNIVERSITÉ GRENOBLE ALPES

École doctorale : STEP - Sciences de la Terre de l'Environnement et des Planètes
Spécialité : Sciences de la Terre et de l'Environnement
Unité de recherche : Institut des Sciences de la Terre

Déformation crustale associée au cycle sismique dans les Andes Centrales à partir de séries temporelles géodésiques InSAR et GNSS

Crustal Deformation Associated with the Seismic Cycle in the Central Andes from InSAR and GNSS Geodetic Time Series

Présentée par :

Bertrand LOVERY

Direction de thèse :

Anne SOCQUET PHYSICIEN, UNIVERSITE GRENOBLE ALPES	Directrice de thèse
Mohamed CHLIEH IRD	Co-directeur de thèse
Mathilde RADIGUET Physicienne Adjointe, UNIVERSITE GRENOBLE ALPES	Co-directrice de thèse
Marie-Pierre DOIN DIRECTRICE DE RECHERCHE, CNRS	Co-encadrante de thèse

Rapporteurs :

Sabrina METZGER
SENIOR SCIENTIST, Helmholtz-Zentrum Potsdam
Romain JOLIVET
PROFESSEUR DES UNIVERSITES, ENS Paris

Thèse soutenue publiquement le **8 décembre 2025**, devant le jury composé de :

Laurence AUDIN, DIRECTRICE DE RECHERCHE, IRD délégation Sud-Est	Présidente
Anne SOCQUET, PHYSICIENNE, Université Grenoble Alpes	Directrice de thèse
Mathilde RADIGUET DE LA BASTAIE, PHYSICIENNE ADJOINTE, Université Grenoble Alpes	Co-directrice de thèse
Sabrina METZGER, SENIOR SCIENTIST, Helmholtz-Zentrum Potsdam	Rapporteure
Romain JOLIVET, PROFESSEUR DES UNIVERSITES, ENS Paris	Rapporteur
Shaoyang LI, ASSOCIATE PROFESSOR, Chinese Academy of Sciences	Examinateur

Invités :

Marie-Pierre Doin
DIRECTRICE DE RECHERCHE, ISTerre
Mohamed Chlieh
CHARGE DE RECHERCHE, ISTerre

The road to hell is paved with works-in-progress.
Philip Roth

Remerciements

Je remercie mes encadrants, qui m'ont accordé leur confiance et qui m'ont donné les moyens de mener cette thèse à son terme : Anne Socquet, son énergie et sa hauteur de vue ; Mohamed Chlieh, sa connaissance approfondie de la littérature et ses bons mots ; Marie-Pierre Doin, son expertise remarquable en InSAR et sa rigueur irréprochable ; ainsi que Mathilde Radiguet, sa fine compréhension des enjeux de modélisation et son enthousiasme.

Bien entendu, je remercie mes rapporteurs, Sabrina Metzger et Romain Jolivet, pour leur lecture experte et attentive, ainsi que pour les commentaires détaillés et constructifs qu'ils m'ont transmis. Mes remerciements vont également aux examinateurs, Laurence Audin et Shaoyang Li, qui ont aimablement accepté de prendre le temps d'assister à ma soutenance.

Je tiens également à remercier les membres de mon CSI, Virginie Pinel et Félix Perosanz, pour le temps qu'ils m'ont consacré et le soutien qu'ils m'ont apporté.

En outre, je remercie mes collègues et amis d'ISTerre, qui ont contribué à la discussion scientifique et qui ont rendu ces années plus agréables. La liste n'est pas exhaustive, je ne citerai que quelques noms parmi d'autres : Amine, Anuar, Arthur, Audrey, Bénédicte, Bryan, Caroline, Diego, Erwan, Fabien, Franck, Giuseppe, Hang, Heming, Hugo, Isabelle, Jannes, Juan Carlos, Juliette, Léa, Léo, Marc, Mirko, Pierre, Renata, Shan, Tristan, Yuji, Zaccaria…

Enfin, mes remerciements vont naturellement à ma famille, notamment mes parents, qui m'ont toujours soutenu au cours de ce long cheminement. Ainsi qu'à mes amis de longue date, qui se reconnaîtront, et à mes enseignants qui m'ont donné le goût de la démarche scientifique.

Résumé

Les zones de subduction sont des lieux d'expression d'une forte activité sismique, au sein desquelles la majorité des grands séismes se produisent. La déformation de la plaque supérieure au cours du cycle sismique peut-être mesurée au moyen de techniques géodésiques, permettant d'estimer le glissement sur l'interface ou a contrario le degré de blocage de l'interface pendant la phase intersismique. Les Andes centrales constituent un lieu d'un intérêt notable en ce qui concerne l'étude des processus physiques impliqués par la subduction. En effet, des événements sismiques d'importance s'y produisent relativement fréquemment, avec pas moins de quatre séismes de magnitude supérieure à huit au cours des trois dernières décennies : les séismes d'Antofagasta en 1995 (Mw8.0), d'Arequipa en 2001 (Mw8.4), de Pisco en 2007 (Mw8.0) et d'Iquique en 2014 (Mw8.1). En outre, des hétérogénéités structurales, telles que les rides océaniques de Nazca ou de Perdida, semblent segmenter les ruptures sismiques le long de la fosse Pérou-Chili. Estimer le potentiel sismogénique des Andes centrales, notamment au Sud Pérou où la quantité de données géodésiques disponibles a considérablement augmenté au cours des dernières années, est par conséquent un enjeu primordial.

Suite à notre analyse de séries temporelles GNSS inédites, nous proposons un modèle de couplage intersismique du Sud Pérou avec une résolution jusqu'alors inégalée. Ce modèle témoigne d'une forte hétérogénéité, avec un fort couplage au large des villes de Lima, Atico et Ilo, et un faible couplage au niveau des points d'entrée en subduction de la ride de Nazca et de la zone de fracture de Nazca sous le continent Sud-Américain. A partir de ce modèle, nous avons mené une analyse de budget de moment afin d'estimer la magnitude maximale que le segment Sud Pérou pourrait héberger, ainsi que le temps de récurrence associé. Les résultats indiquent la possibilité d'un séisme de magnitude 8.4 à 9.0, associé à un temps de récurrence de 100 et 900 ans respectivement.

En complément de cette première étude, nous avons souhaité exploiter les déplacements postsismiques consécutifs au séisme d'Arequipa de 2001, que l'on observe sur des séries temporelles GNSS au Sud Pérou. En effet, il est rare de disposer d'un enregistrement de 24 ans de déplacement postsismique. Cela constitue une opportunité remarquable de contraindre la structure et la rhéologie de la subduction au Sud Pérou, pour laquelle peu de modèles sont disponibles. Nous avons pour cela développé un modèle par éléments finis de la subduction au Sud Pérou, permettant de modéliser les déplacements à la surface du continent associés à la relaxation viscoélastique de l'asthénosphère. Des résultats satisfaisants ont été obtenus en appliquant une viscoélasticité newtonienne de Burgers au sein de l'asthénosphère, avec une viscosité de Maxwell $\eta_M = 9 \cdot 10^{18}$ Pa·s et une viscosité de Kelvin $\eta_K = 5 \cdot 10^{18}$ Pa·s. Il ressort également de cette analyse l'existence d'un coin mantélique froid et élastique au Sud Pérou, appelé *cold-nose*.

Enfin, nous avons tiré profit du traitement InSAR massif proposé par le service FLATSIM dans le cadre du pôle de données et services FormaTerre, afin de cartographier finement la déformation de surface horizontale et verticale à l'échelle des Andes centrales. Dans cet objectif, nous avons étudié la contribution de processus non-tectoniques à la variabilité des rampes de phase des acquisitions InSAR, notamment les marées océaniques et terrestres, ainsi que le délai affectant la propagation des ondes électromagnétiques au sein de l'ionosphère. Nous avons référencé les cartes de vitesse InSAR à partir des vitesses mesurées par le réseau GNSS, ainsi que décomposé le signal InSAR en cartes de vitesses horizontale et verticale, permettant de mesurer le signal de déformation associé aux différents processus géophysiques à l'œuvre dans les Andes centrales : blocage intersismique, déformation co-sismique et post-sismique associées à des séismes de subduction ou crustaux, volcanisme, et glissements de terrain. La résolution spatiale offerte par l'InSAR, notamment sur la composante verticale, nous a permis d'affiner les modèles de couplage intersismique et de quantifier le déplacement au travers de systèmes de failles importants, au niveau de la Cordillère Blanche et de Cuzco, qui ont été proposés comme limites d'une microplaque appelée *sliver* péruvien.

Mots clefs: Subduction, cycle sismique, GNSS, InSAR, couplage intersismique, post-sismique, méthode aux éléments finis, relaxation viscoélastique, Andes centrales, Pérou, Chili

Abstract

Subduction zones are theaters of high seismic activity, where most major earthquakes occur. The deformation of the upper plate during the seismic cycle can be measured using geodetic techniques, allowing to estimate the slip on the interface or, conversely, the degree of locking on the interface during the interseismic phase. The Central Andes are a place of considerable interest for the study of the physical processes involved in subduction. Indeed, it hosts significant seismic events relatively frequently, with four earthquakes of magnitude greater than eight in the last three decades: the Antofagasta earthquake in 1995 (Mw8.0), the Arequipa earthquake in 2001 (Mw8.4), the Pisco earthquake in 2007 (Mw8.0), and the Iquique earthquake in 2014 (Mw8.1). In addition, structural heterogeneities, such as the Nazca and Perdida oceanic ridges, appear to segment seismic ruptures along the Peru-Chile trench. Estimating the seismogenic potential of the Central Andes, particularly in Southern Peru, where the amount of geodetic data available has increased considerably in recent years, is therefore a key issue.

Following our analysis of unpublished GNSS time series, we propose an interseismic coupling model for Southern Peru with unprecedented resolution. This model shows significant heterogeneity, with high coupling off the coast of Lima, Atico, and Ilo, and weaker coupling where the Nazca Ridge and Nazca Fracture Zone subduct beneath the South American continent. Based on this model, we conducted a moment budget analysis to estimate the maximum magnitude earthquake that the South Peru segment could host, as well as the associated recurrence time. The results indicate the possibility of an earthquake with a magnitude of 8.4 to 9.0, associated with a recurrence time of 100 and 900 years, respectively.

To complement this initial study, we wanted to exploit the post-seismic displacements following the 2001 Arequipa earthquake, which can be observed in GNSS time series in Southern Peru. Indeed, it is rare to have access to 24 years of post-seismic displacement records. This provides a remarkable opportunity to constrain the structure and rheology of subduction in Southern Peru, for which few models are available. To this end, we developed a finite element method model of the subduction in Southern Peru, allowing us to model the displacements on the continental surface associated with the viscoelastic relaxation of the asthenosphere. Satisfactory results were obtained by applying a Newtonian Burgers viscoelasticity within the asthenosphere, with a Maxwell viscosity $\eta_M = 9 \cdot 10^{18}$ Pa·s and a Kelvin viscosity $\eta_K = 5 \cdot 10^{18}$ Pa·s. This analysis also reveals the existence of a cold, elastic mantle wedge in Southern Peru, known as the *cold-nose*.

Finally, we took advantage of the massive InSAR processing offered by the FLATSIM service as part of the FormaTerre data and services center to map horizontal and vertical surface deformation in detail across the Central Andes. In this purpose, we studied the contribution of non-tectonic processes to the variability of phase ramps in InSAR acquisitions, in particular ocean tide loading and solid Earth tides, as well as the delay affecting the propagation of electromagnetic waves within the ionosphere. We referenced the InSAR velocity maps using velocities measured by the GNSS network and decomposed the InSAR signal into horizontal and vertical velocity maps, enabling us to measure the deformation signal associated with the various geophysical processes at work in the Central Andes: interseismic locking, co-seismic and post-seismic deformation associated with subduction or crustal earthquakes, volcanism, and landslides. The spatial resolution offered by InSAR, particularly on the vertical component, allowed us to refine interseismic coupling models and quantify displacement through major fault systems in the Cordillera Blanca and Cuzco, which have been proposed as the boundary of a microplate called the Peruvian *sliver*.

Keywords: Subduction, seismic cycle, GNSS, InSAR, interseismic coupling, postseismic, finite element method, viscoelastic relaxation, Central Andes, Peru, Chile

Contents

1 Introduction **2**

2 State of the art **10**
2.1 The seismic cycle at subduction zones . . . 10
2.1.1 Subduction in a nutshell . . . 10
2.1.2 Overview of the seismic cycle . . . 13
2.1.3 The interseismic coupling . . . 15
2.1.4 Mechanics and rheology of subduction zones . . . 22
2.2 The Peru-Chile subduction . . . 39
2.2.1 Seismotectonic activity . . . 39
2.2.2 Kinematic and active deformation of the Peru-Chile subduction . . . 42
2.2.3 Oceanic structures . . . 46
2.2.4 Review of interseismic coupling models in Central Andes . . . 47

3 Data and methods **73**
3.1 Geodetic techniques . . . 73
3.1.1 Overview . . . 73
3.1.2 The GNSS technique . . . 79
3.1.3 The InSAR technique . . . 93
3.2 Technical aspects of the seismic cycle modeling . . . 124
3.2.1 The inverse problem . . . 124
3.2.2 Modeling the subduction by Finite Element Method . . . 128
3.2.3 Defining Burgers rheology in PyLith . . . 131

4 Heterogeneous Locking and Earthquake Potential on the South Peru Megathrust from Dense GNSS Network **134**
4.1 Manuscript . . . 136
4.2 Supplements . . . 176

5 Viscoelastic Relaxation Following the 2001 Mw8.4 Arequipa Earthquake and Its Impact on the Interseismic Coupling of the South Peru Megathrust **202**
5.1 Manuscript . . . 204
5.2 Supplements . . . 231

6 Modeling non-tectonic signals in InSAR phase ramps **267**
6.1 Manuscript . . . 268
6.2 Supplements . . . 287

7 Large Scale InSAR and GNSS Timeseries Analysis over the Central Andes **312**

8 Conclusions and outlook **348**

References **353**

List of Figures **383**

9 Annexes **401**



Vicuñas in the highlands of the Lucanas Province (South Peru), on the way back after servicing GNSS sites in November 2024.

Chapter 1

Introduction

Earthquakes are one of the most threatening natural phenomena due to the huge amount of energy they can release in a few seconds. To get a rough idea, the 2011 Mw9.1 Tohoku earthquake that occurred offshore Japan released an energy of 200 petajoules ($2{\cdot}10^{17}$ J), which is equivalent to 45 megatons of TNT, causing significant damage to humans and their infrastructures. In addition, an earthquake nucleating near the trench can generate a destructive tsunami with consequences more disastrous than the earthquake itself. For example, the 40-meter high tsunami following the 2011 Tohoku earthquake was the cause of about 95% of the 20,000 casualties (Ishigaki et al., 2013; Mori et al., 2011). Subduction zones are especially affected by great earthquakes: out of the 17 earthquakes with moment magnitude Mw > 8.5 recorded since 1900, 16 occurred in subduction. And because of the offshore and near-trench location of the ruptures, the tsunami risk is also a major issue.

The ultimate goal of predicting earthquakes may not yet be accessible to humankind (Allègre et al., 1982; Kanamori, 2003; Ridzwan and Yusoff, 2023; Sornette and Sammis, 1995), however, there is information and knowledge that can be gathered to help living with earthquakes. Estimating the seismic potential of an area helps to assess the hazard to populations and better define which measures can be implemented to mitigate the risk, such as building earthquake-resistant infrastructures, assessing the required height of seawalls, or training the population how to behave. This PhD thesis aspires to be a step toward a better estimate of seismic potential, and more generally to contribute to the knowledge of the physical processes at work on subduction zones.

Since the beginning of the 20th century, earthquakes are reported in seismic catalogs at a world-wide scale and their magnitude is estimated using seismometers. For older events, qualitative information is available in places with written records, allowing to identify areas that were affected by large earthquakes over the last centuries and to have a rough estimate of their magnitude based on the damage. Thanks to advances in paleoseismology, it is even possible to report some earthquakes and tsunamis

that have occurred several millennia ago by identifying geological evidences created by active faults motion and geological deposits (Grant Ludwig, 2015; Klinger, 2022). This backlog shows that some segments of a given subduction can host great and large earthquakes, while others are only affected by moderate and small seismicity. For instance, several earthquakes of magnitude 8 to 9.5 have been reported on the Peru-Chile subduction from 11°S to 46°S, along the coasts of Chile and Central to South Peru, while no earthquake above magnitude 7.8 has ever been reported in North Peru from 2°S to 11°S (Dorbath et al., 1990; Villegas-Lanza et al., 2016). On the Nankai trench (Japan), the Southern segment in front of Kyushu and Shikoku islands appears to be less affected by earthquakes above magnitude 8 than the Northern segments (Mogi, 1981). It is now widely recognized that this heterogeneity in the seismic potential is spatially correlated to the degree of locking on the plate interface, quantified by the interseismic coupling (Chlieh et al., 2008; Konca et al., 2008; Loveless and Meade, 2011; Métois et al., 2016). This can be understood by considering that when a fault segment is locked, mechanical energy is accumulating over time as the down-going plate is pulling the overriding plate. At some point, the system reaches a certain threshold, the accumulated energy is released during an earthquake where the overriding plate starts to slip in the opposite direction as during the interseismic (elastic rebound theory proposed by Reid, 1910). On the other hand, if there is no locking at the fault interface (known as *creeping* areas), no elastic deformation is built and no mechanical energy is accumulating to generate an earthquake. Therefore, providing accurate interseismic coupling models is a key issue to quantify the seismic potential on a subduction.

Interseismic coupling models can be used in conjunction with seismic catalogs to estimate the maximum magnitude earthquake that a given fault segment could host, and its associated recurrence time. The basic idea behind this method, known as moment budget analysis (Avouac, 2015), is to balance the moment accumulated through interseismic loading (known from interseismic coupling models) with the moment released by earthquakes (known from seismic catalogs) in order to constrain frequency-magnitude relationships on the maximum magnitude earthquake. These analyses, however, depend on the accuracy of the seismic catalogs (completeness, estimation of the magnitudes) and the accuracy of the interseismic coupling models (spatial distribution and amplitude of the locking on the interface). Also, they require some assumptions on the amount of aseismic slip, resulting from afterslip (Marone et al., 1991) or slow-slip events (Hirose et al., 1999; Radiguet et al., 2011; Schwartz and Rokosky, 2007; Socquet et al., 2017), during the seismic cycle.

Interseismic coupling models are derived from geodetic observations by measuring the surface displacement on the overriding plate during the so-called interseismic period. Geodetic observations present an interesting complementarity to seismological observations, since they provide information on the building of seismic potential

that may not have been recorded yet in seismic catalogs. For instance, if an asperity is fully locked for 200 years no seismicity may appears in the seismic catalogs (that are typically 50 to 120 years old) while the deformation of the overriding plate can be recorded if there are geodetic measurements in the vicinity. Geodetic observations are however limited by their spatial distribution. Typically, few measurements are available close to the trench at subduction zones since seafloor observations are very rare due to the difficulty to acquire such measurements, which means that the resolution in the shallowest part of the subduction is often lacking despite its importance for assessing tsunami risk. Even on the continent, measurements are often tens of kilometers apart and not distributed evenly. Also, observations are limited by their temporal coverage. Space geodetic observations span one to three decades at best, which means that we do not get a full vision of the seismic cycle. It is therefore difficult to assess if the observed velocity is representative of the actual interseismic velocity on a longer timescale. They can be contaminated by various processes related to the seismic cycle, such as postseismic deformation or slow-slip events, and non-tectonic processes such as landslides, volcanic deformation, or hydrological loading. Studies on the postseismic deformation following great megathrust events such as the 1960 Mw9.5 Valdivia earthquake in Chile showed that they can produce broad surface displacement more than 70 years after the earthquake due to the viscoelastic relaxation of the asthenosphere (Hu et al., 2004; K. Wang et al., 2007).

Geodetic time series have therefore to be corrected from all signals that are affecting the estimation of the interseismic velocities. While it is possible to correct for the coseismic and postseismic displacements related to an earthquake happening within the time period of the acquisition using a trajectory model, things can become more complicated when the event started prior to the acquisition period. In this case, using a trajectory model is not possible and it requires to develop a model of the actual physical process, such as the time evolution of the postseismic deformation following a large earthquake.

Using a realistic geometry of the slab interface is also fundamental to correctly map the interseismic coupling. Early interseismic coupling models were considering simple geometries with rectangular faults, which is not representative of what we know from the shape of the slab interface at many subduction zones (Bürgmann et al., 2005; Chlieh et al., 2011; Manaker et al., 2008). Indeed, slab models using seismicity and seismic tomography data show relatively strong variations in the dipping angle of the slab both in the along-dip and along-strike directions for several subduction zones, such as the Peru-Chile subduction, Nankai, or Cascadia (Hayes et al., 2018; W. P. Schellart, 2011). Using an inadequate geometry can lead to an incorrect localization of asperities, or a bad estimation of the amplitude of locking if the depth of the interface is wrong.

We know from the analysis of postseismic deformation and thermal models that the asthenosphere can behave viscoelastically (Chanard et al., 2018; Cohen and Kramer,

1984; Lambert and Barbot, 2016; S. Li et al., 2017; Pollitz, 2019; Wada and Wang, 2009; K. Wang et al., 2012). Still, many interseismic coupling models rely on a pure elastic behavior. S. Li et al., 2015 and K. Wang et al., 2012 showed that this assumption may lead to an overestimation of the locking depth and an inadequate estimation of the coupling magnitude, especially in the far field. Performing such viscoelastic models requires appropriate assumptions on the structure and rheology of the subduction, including the thickness of the continental and oceanic lithospheres, or the viscosity of the asthenosphere. Various rheological laws have been proposed to model the relaxation of the asthenosphere at subduction zones, with Newtonian (Boulze et al., 2022; Klein et al., 2016; S. Li et al., 2018; Pollitz, 2005; K. Wang et al., 2012) or non-Newtonian (Barbot, 2018; Muto et al., 2019; Peña et al., 2020) formulations. Since there is no strong consensus on these parameters, additional tests on new subduction segments and earthquakes are required. It is also an opportunity to test structural features proposed by authors in the recent years, notably the inclusion of an elastic stagnant and cold mantle wedge known as *cold-nose* (Luo and Wang, 2021; Sun and Wang, 2015; Wada and Wang, 2009), while maintaining a sensible degree of complexity that can be constrained by the available data.

In addition to viscoelastic behavior, we know from active tectonics that the overriding plate is accumulating some permanent deformation on a long timescale (Baize et al., 2020; Dewey and Lamb, 1992; Matsu'ura, 2015). However, we do not know at which phase of the seismic cycle this plastic deformation occurs and through which mechanisms (Jolivet et al., 2020; Kosari et al., 2024; Saillard et al., 2009; K. Wang et al., 2012). Some authors proposed that long-term uplift at the coast is arising from uplift during the interseismic period that is not completely canceled-out by the subsidence associated with the coseismic phase, due to plastic deformation (Saillard et al., 2017; Saillard et al., 2011; Song and Simons, 2003; Van Dinther et al., 2013). Conversely, Melnick, 2016 proposed that the long-term uplift of the coast in North Chile is caused by intermediate-depth earthquakes, similar to the 2007 Mw7.7 Tocopilla earthquake. In the case of a plastic deformation occurring during the interseismic phase, the permanent deformation is controlled by the degree of locking and the depth of maximum locking (Béjar-Pizarro et al., 2013; Rousset et al., 2016; Saillard et al., 2017). Viscoelasticity in the asthenosphere could also play a role in controlling the plastic deformation of the upper plate by altering the applied stress on the lithosphere (Beuchert and Podladchikov, 2010; Duretz et al., 2021; S. Li et al., 2015; Shi et al., 2020; K. Wang et al., 2012). This aspect may be particularly fundamental for areas where subsidence is observed during both coseismic and interseismic periods, while long-term permanent uplift is observed, such as in Japan (Matsu'ura et al., 2014; Nishimura, 2014; Uchida and Bürgmann, 2021). Postseismic uplift in the coastal domain has been observed following the 2011 Mw9.1 Tohoku earthquake, which could partially explain the long-term uplift (Hashima and Sato, 2017; Nishimura, 2014). Answering these questions

related to permanent deformation requires dense geodetic measurements, that are progressively becoming available thanks to the deployment of denser GNSS (Global Navigation Satellite System) networks and the rise of remote sensing techniques, notably InSAR (Interferometric Synthetic Aperture Radar) that allows a dense mapping of the surface deformation with a high sensitivity to vertical displacements.

This PhD thesis is focused on the Central Andes (~8°S to ~26°S), which is an area with a history of strong seismicity (Figure 1.1). It hosted three earthquakes of magnitude Mw > 8.0 since the beginning of the millennium, that left traces in the geodetic measurements: the 2001 Mw8.4 Arequipa, the 2007 Mw8.0 Pisco, and the 2014 Mw8.1 Iquique earthquakes. Historical seismicity reports potentially even greater events, with an earthquake magnitude of about 8.8 in 1868 rupturing the South Peru segment (Dorbath et al., 1990). The 2001 Arequipa earthquake is especially interesting due to the long postseismic record of 24 years available, that was only studied on the first twelve years (Hergert and Heidbach, 2006; Perfettini et al., 2005; Sun et al., 2018). It represents an opportunity to study long-term viscoelastic relaxation of the asthenosphere and to assess the impact of past earthquakes on the interseismic coupling. In addition, it provides constraints to assess an appropriate rheology of the subduction zone. This information is for the moment lacking for Peru, and it can be used to develop a viscoelastic interseismic coupling model for South Peru. Central Andes also have the advantage of having a relatively short trench-to-coast distance of about 100 to 200 km, compared to some other subductions like Japan or Sumatra (about 300 km), allowing to better constrain the locking degree in the shallow part. The high relief of the Andes (up to 6,768 meters in the White Cordillera) is a testimony of significant plastic deformation of the overriding plate. The relatively smooth profile of the trench is only altered by the Arica bend, where the Andes are particularly thick (more than 1,000 km). This segment is characterized by a high crustal thickness of 70 km and a substantial volcanic activity, which may suggest a weaker rheology due to the incoming heat flow. The slab geometry is then experiencing a transition from steep to flat in the direction of the Nazca ridge (North-west), which may induce a different sensitivity to viscoelastic effects due to the variation of viscoelastic thickness. Several bathymetric features are subducting below the South America continent in South Peru (the Nazca ridge and the Nazca Fracture Zone) and North Chile (the Perdida, Sala y Gomez, and Copiapo ridges). These features have been reported as acting as more or less strong barriers against seismic rupture propagation (Kaneko et al., 2010; Métois et al., 2016; Robinson et al., 2006; Villegas-Lanza et al., 2016), and assessing the along-strike coupling variation associated with their subduction can provide information on their effect on the mechanical behavior of the interface.

While some subductions, especially Nankai, the Japan trench, or Cascadia, are well instrumented since several decades, the instrumentation in Central Andes developed

more recently. In South Peru, tens of continuous and survey GNSS sites have been installed during the last 15 years, significantly increasing the density of observation compared to previous geodetic studies in the area (Bevis et al., 2001; Chlieh et al., 2011; Gagnon et al., 2005; Norabuena et al., 1998; Villegas-Lanza et al., 2016). In addition, we benefit from the InSAR time series processed from Sentinel-1 acquisitions spanning the 2015 to 2021 period in the framework of the FLATSIM Central Andes project (FormaTerre, 2020), allowing the possibility of using InSAR time series for large-scale tectonic applications. This last point requires to reference the InSAR data in a stable reference frame in order to extract meaningful interseismic velocities.

Some previous geodetic studies in Central Andes introduced additional blocks, known as *slivers* or *third plate*, for which the authors apply a rigid block motion that improved the fit to the observations. In South Peru Villegas-Lanza et al., 2016 defined a Peruvian sliver with a South-east motion of about 5 mm/yr relative to the continent, while in North Chile Métois et al., 2013 and Métois et al., 2016 applied a 5 to 8 mm/yr North-east motion to an Andean sliver. While introducing these slivers was driven by a better fit of their interseismic models to the observed GNSS velocities, the actual boundaries of these blocks are relatively unclear and the amplitude and direction of their motion are not constrained by strong geological evidences. In North Chile, S. Li et al., 2015 and Yáñez-Cuadra et al., 2022 showed that the Andean sliver is not required by the data if they account for viscoelasticity or internal deformation respectively.

Identifying sliver motions and assessing the partitioning of the deformation in the upper plate require dense mapping of the surface deformation, notably on the vertical component. Such measurements are currently lacking for Central Andes, especially in Peru. To overcome this issue, we use GNSS and InSAR time series, that are complementary: GNSS provides displacements on the three (East, North, Up) components with a dense temporal resolution and an absolute referencing, while InSAR brings a higher spatial resolution at the cost of a lower temporal resolution and a unidirectional measurement that needs to be referenced. We apply the appropriate corrections on these datasets and we extract the signals of interest: coseismic, postseismic, or interseismic deformation. We then invert interseismic velocities to estimate interseismic coupling distributions. Several studies have already been conducted on modeling the interseismic coupling in Central Andes (e.g., Chlieh et al., 2011; S. Li et al., 2015; Métois et al., 2016; Villegas-Lanza et al., 2016) but they are often restricted to either the Peruvian or the Chilean side, so there is no unified model at the scale of the Central Andes. They were also limited to the geodetic data available at their time, which is evolving relatively fast. In addition, they sometimes use some assumptions that may need to be reconsidered, such as simple geometries, pure elastic rheology, or rigid block motions. Some authors, such as S. Li et al., 2015 or M. Moreno et al., 2011 showed that some additional physical processes may need to be considered, notably viscoelasticity, in order

to account for the rheology of the medium and past earthquakes. In this perspective, we developed a finite element method (FEM) model of the subduction in order to model the viscoelastic relaxation following the 2001 Mw8.4 Arequipa earthquake, and to account for more realistic structure and rheology of the subduction zone.

In Chapter 2 *State of the art* we discuss the fundamental concepts, the regional context, and the existing interseismic coupling models, while in Chapter 3 *Data and methods* we detail the geodetic methods (GNSS and InSAR) that we used in this PhD, as well as the technical modeling aspects. A first article, published in *Journal of Geophysical Research: Solid Earth*, constitutes the Chapter 4. It includes a new interseismic coupling model for South Peru from dense interseismic GNSS measurements and a moment budget analysis in order to assess the maximum magnitude earthquake in South Peru with its associated recurrence time. Some additional materials are provided, notably coseismic and afterslip models for the 2014 Mw8.1 Iquique earthquake. Chapter 5 is a second article, published in *Geophysical Research Letters*, focused on modeling the viscoelastic relaxation following the 2001 Mw8.4 Arequipa earthquake. The FEM model of the subduction is constrained by GNSS timeseries, allowing to correct the interseismic coupling model for the postseismic displacements associated with the Arequipa earthquake. It also provides information on the structure and rheology of the subduction zone in South Peru. Viscoelastic Green's functions are also computed to have a full viscoelastic interseismic coupling model. In Chapter 6, a modeling work on the non-tectonic signals in the InSAR phase ramps is described (ocean tide loading, solid earth tides, and ionospheric phase delay). Note that some of the results have been carried out to a study from Marconato et al., for which I am part of the authorship, submitted to *Geophysical Research Letters*. A last article, in preparation, is part of Chapter 7. It is aimed at using the GNSS and InSAR datasets in a joint inversion of interseismic coupling at the scale of Central and South Peru, with a viscoelastic rheology. It also provides a portfolio of geophysical events observed on long InSAR time series (volcanic deformation, earthquakes, active crustal faults, and landslides). The observed displacements across major crustal faults, the Cuzco fault system and the Cordillera Blanca, are discussed in relation with the Peruvian sliver. Finally, the Chapter 8 distills the main results of this work and indicates some outlook.

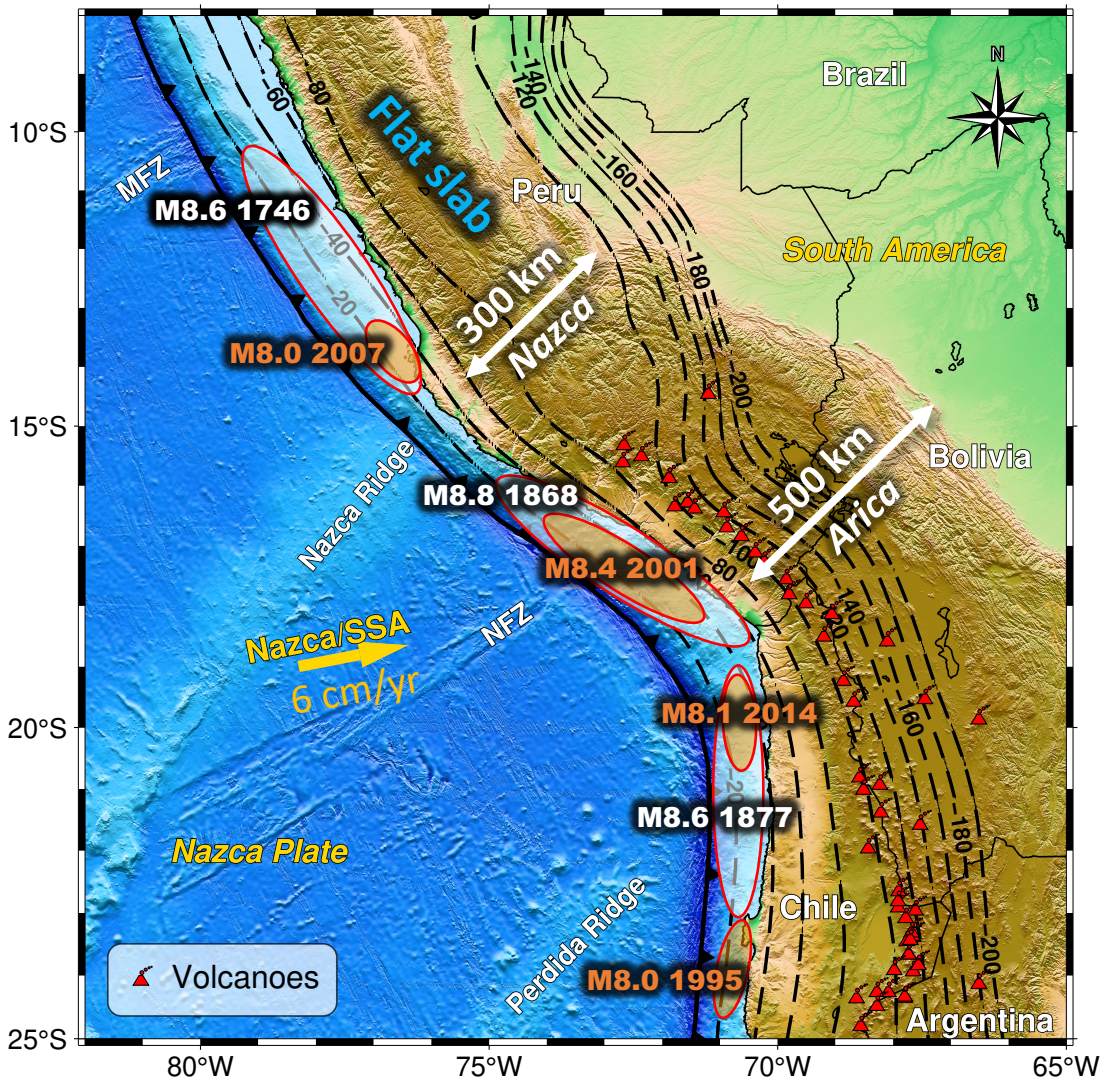

Figure 1.1: Basic seismotectonic context in Central Andes. Major earthquake ruptures (M≥ 8) since 1868 along the Peru-Chile trench (M. E. Beck, 1998; S. L. Beck and Ruff, 1989; Dorbath et al., 1990; Silgado, 1978; Villegas-Lanza et al., 2016) are reported by white (historical) or orange (recent, 1995 or later) ellipses. Volcanoes are reported in red, and major oceanic features in white. Slab contours are depicted by black dashed lines from the Slab2 model every 20 km (Hayes et al., 2018). The Andes are wider in the vicinity of the Arica bend (500 km or more), in the dipping slab area, while they are thinner (about 300 km in the Nazca region) in the flat slab area.

Chapter 2

State of the art

2.1 The seismic cycle at subduction zones

2.1.1 Subduction in a nutshell

The concept of subduction was formalized in the third quarter of the twentieth century, with the first use of the word *subduction* in 1951 by the Swiss geologist André Amstutz in order to explain the formation of the Alps (Amstutz, 1955), inspired by the work from Alfred Rittmann who introduced the notion of sub-crustal creep to explain the distribution of volcanoes around the Pacific (Rittman, 1951). Subduction is one of the mechanisms involved in plate tectonics, where a *tectonic plate* made of the rigid outer shell of the Earth, referred as lithosphere (typically in the order of 50 to 100 km thick), is sinking progressively below another tectonic plate at a rate ranging from a few mm/yr to several cm/yr (Figure 2.1). Although Alfred Wegener first published his theory of continental drift in 1912 (Wegener, 1912), it took half a century for this idea to be widely accepted by the geological and geophysical communities. It can involve either continental or oceanic plates. In the case of a subduction between a continental and an oceanic plate, the latter being denser is sinking below the continent. The downgoing plate is often referred as the *slab*. In compressional tectonic settings, the strain produced by the subduction process is building relief, such as the Andes. Subduction also causes geophysical processes threatening the populations, including volcanism caused by the subducting plate dehydration, and earthquakes caused by the accumulation of mechanical energy over time.

Most of the great earthquakes (with a moment magnitude Mw$\geq$ 8.5) occur at oceanic subduction zones because of the large surface of rupture they offer. Out of the 17 great earthquakes recorded between 1900 and 2025 (Figure 2.3), only the 1950 Mw8.6 Assam-Tibet earthquake occurred at a continental collision (Coudurier-Curveur et al., 2020),

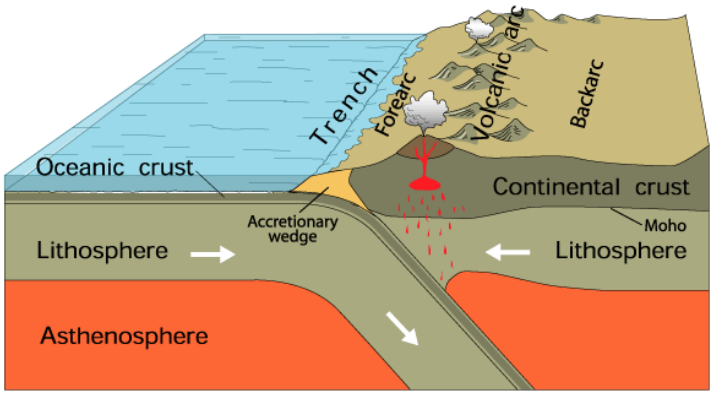

Figure 2.1: Schematic view of an ocean-continent subduction (from the United States Geological Survey). This illustration is representative of the Peru-Chile subduction, however readers should be aware that the shape of the subducting slab or the width of the mountain range can differ. Also, not all subductions have a volcanic arc.

and the 2012 Mw8.6 earthquake off the West coast of Northern Sumatra occurred as strike-slip faulting within the Indo-Australia oceanic lithosphere (Meng et al., 2012). The Pacific Ring of Fire is hosting several active subduction zones, including the Peru-Chile trench, the Middle America trench (offshore of Mexico and Central America), the Aleutian trench (offshore of Alaska), the Japanese subduction system, or the Java trench (Indonesia). Other subduction zones include the Makran trench (Iran to Pakistan), or the Hellenic subduction zone in the Mediterranean Sea (Figure 2.2). In addition, most active subductions are oceanic subductions, meaning that there is a risk of tsunami, which is a major threat to the large populations living in the vicinity of these subduction zones. For instance, the 2011 Mw9.1 Tohoku earthquake in Japan triggered a powerful tsunami, with waves reaching heights of up to 40 meters (Hooper et al., 2013).

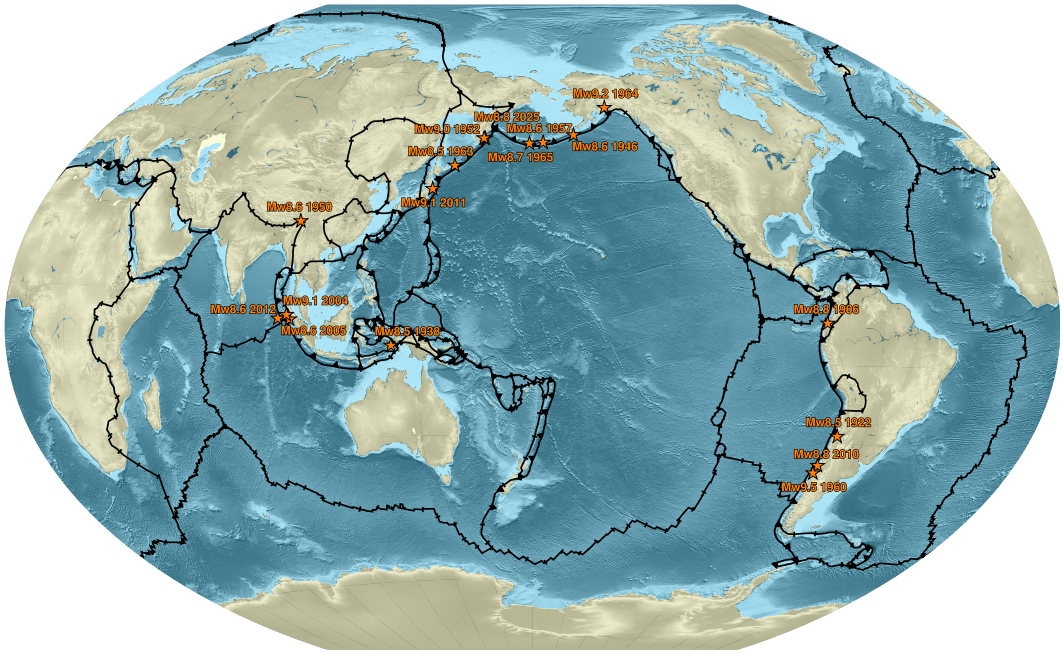

Figure 2.2: All Mw≥ 8.5 earthquakes in the world since 1900. Out of 17 events, 16 nucleated at a subduction. Plates boundaries from Bird, 2003 are reported by black lines.

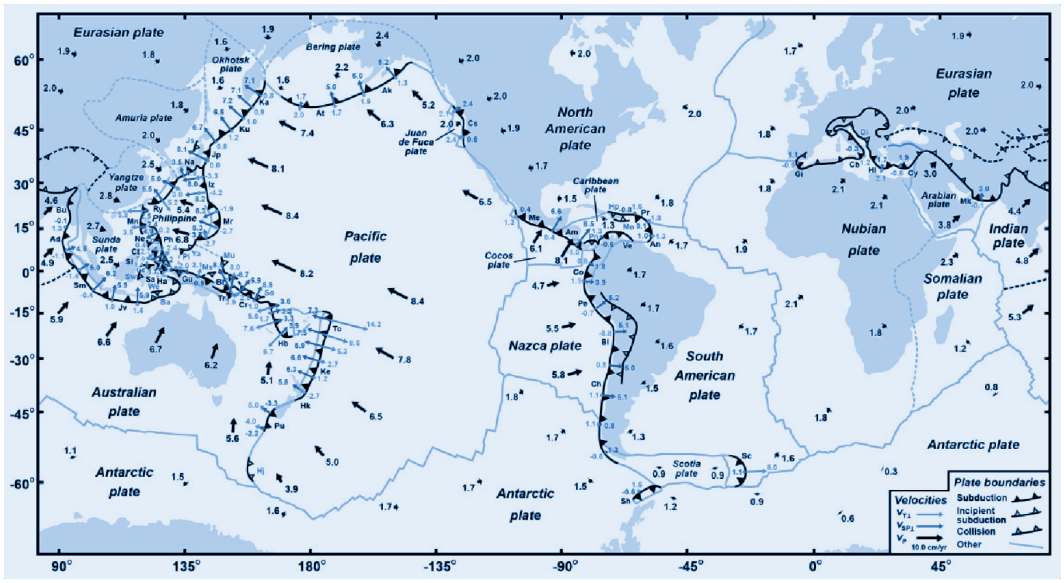

Figure 2.3: Main tectonic plates, with their boundaries: subductions, incipient subductions, and collisions (modified from W. Schellart, 2023). Geodetic plate motion model from Kreemer et al., 2014 are reported by black vectors. Trench-normal subducting plate velocities v_{SP} are reported by dark blue vectors, while trench velocities v_T are reported by light blue vectors. The velocities are expressed in the Indo-Atlantic reference frame from O'Neill et al., 2005.

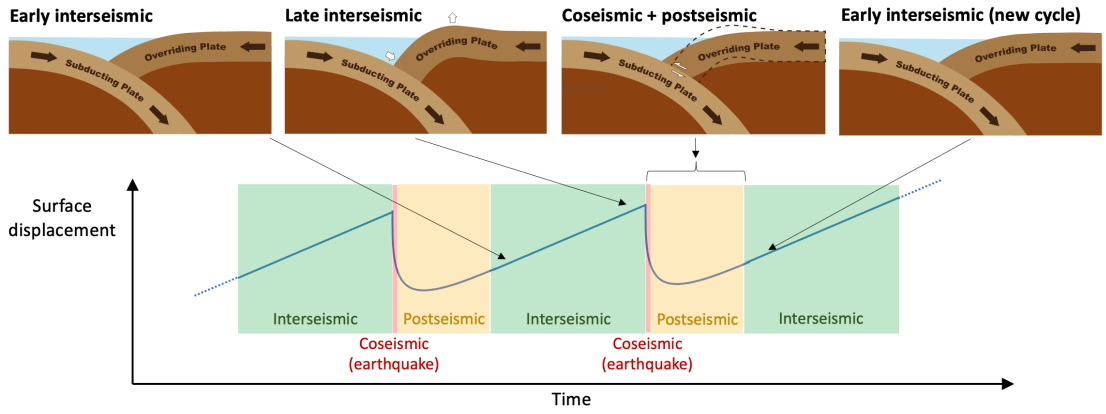

Figure 2.4: Schematic view of the seismic cycle for a single recurring earthquake, neglecting slow slip events and other earthquakes. The surface displacements on the overriding plate in a given direction plate are expressed along time, while an exaggerated view of the plate deformation is shown at several phases of the cycle.

2.1.2 Overview of the seismic cycle

In a context of subduction, both plates are accumulating strain and mechanical energy. If the plate convergence velocity is constant over time (e.g., about 6 cm/yr in Central Andes), which is an adequate assumption on a time scale of a few decades (DeMets et al., 2010), the deformation of the Earth surface on the overriding plate is linear in time. This surface velocity is proportional to the plate convergence velocity and to the degree of locking on the interface (often referred as *interseismic coupling*). We refer to this phase as the *interseismic* phase (Figure 2.4), as it corresponds to the secular phase between earthquakes.

At some point, we reach a certain threshold where the plate interface is not accommodating strain anymore and is starting to slip in the opposite direction to its interseismic phase, which generates an earthquake with seismic waves propagating away from the plate interface (fault). This phase is referred as the *coseismic* phase and is typically lasting a few seconds to a few minutes.

Then, the *postseismic* phase starts, with the overriding plate motion still in the same direction as the coseismic phase, but with a slower velocity decaying over time. When the postseismic phase ends, the overriding plate motion resumes to its interseismic velocity, and a new interseismic phase begins. Three physical processes are involved during the postseismic phase: the afterslip, the viscoelastic relaxation, and the poroelastic rebound. The afterslip consists of aseismic slip on the fault, consecutive to the coseismic slip, and is usually modeled as a logarithmic decay (Marone et al., 1991). Note that the same law is ruling the distribution of aftershocks (smaller earthquakes

following the mainshock in the vicinity of its rupture) over time (Ōmori, 1894). Afterslip is a medium-term process, typically lasting months to years. The viscoelastic relaxation of the asthenosphere, underlying the lithosphere down to about 700 km, is the response of the medium to the stress transfer caused by the earthquake. It is often modeled by a Newtonian (i.e., linear) viscosity law, the simplest being a Maxwell body which is an elastic spring attached to a viscous damper. This is a long-term process, that can last several decades (K. Wang et al., 2007). The poroelastic rebound is caused by fluid circulation after the earthquake, consecutive to a change in the pore pressure gradient in the rocks surrounding the rupture area. A metaphorical image would be to squeeze a sponge full of water (this corresponds to the coseismic period) in order to let the water come out of the sponge, then we put it back into water: the sponge is absorbing water and is inflating again (this corresponds to the postseismic phase). It is a short-term process, typically lasting a few days to a few months (Peltzer et al., 1996).

While the postseismic and interseismic phases appear sharply demarcated on our sketch, it is actually non-trivial to discriminate them in the observations. The pretended *interseismic* velocity that we may record with geodetic techniques can potentially be contaminated by long-lasting postseismic signal. One may argue that checking the linearity of the signal is sufficient to ensure that the postseismic phase is over, but it is important to keep in mind that the observations often do not allow to get the full picture, as they are limited in time and do not cover a full seismic cycle. For instance in the Central Andes, it is pretty rare to have more than ten years of data on a GNSS time series, and often with some discontinuities due to operational challenges. This shade is a fundamental aspect of this PhD thesis, and has been explored in Chapter 5 by modeling the viscoelastic relaxation, which is the main contribution to long-lasting postseismic signal.

Also, we considered here a characteristic earthquake cycle scenario, where we always have the same area rupturing after the same time window, with the same coseismic offset. Nature is of course more complex, various magnitude earthquakes can nucleate at various locations on the plate interface and aperiodically, leading to more complex signals (Figure 2.5). Furthermore, the observation of aseismic transient slip events on various subduction zones, known as slow slip events (SSE), complicates this basic vision (Hirose et al., 1999; Radiguet et al., 2011; Schwartz and Rokosky, 2007; Socquet et al., 2017).

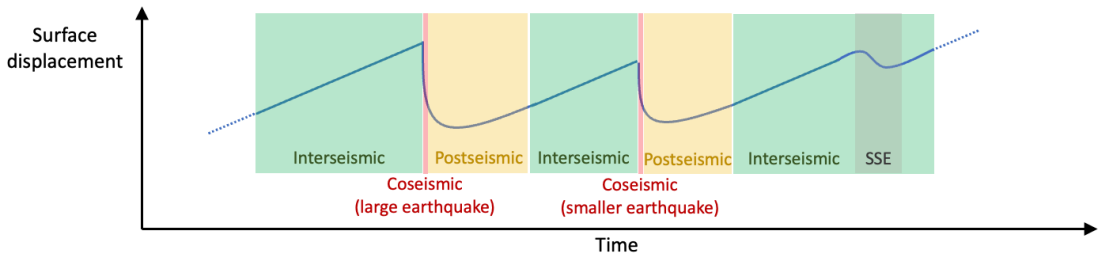

Figure 2.5: More realistic view of the seismic cycle, with earthquakes of various magnitudes and slow slip events (SSE). The surface displacements on the overriding plate in a given direction plate are expressed along time.

2.1.3 The interseismic coupling

Conceptual definition

The interseismic coupling χ_i, a.k.a. *locking* or simply *coupling* in this manuscript, is defined as

$$\chi_i = 1 - \frac{V_{slip}}{V_{convergence}} \tag{2.1}$$

with V_{slip} the slip velocity on the subduction interface during the interseismic phase and $V_{convergence}$ the relative plate convergence velocity. We can assess V_{slip} by inverting the surface velocities obtained from geodetic measurements such as GNSS or InSAR, while $V_{convergence}$ can be estimated from GNSS or DORIS (Doppler Orbitography by Radiopositioning Integrated on Satellite) measurements (c.f. section *Geodetic techniques* in Chapter 3) at a larger scale (Kendrick et al., 2003). Interseismic coupling quantifies how locked the plate interface is, from a fully creeping ($\chi_i = 0$) to a fully locked ($\chi_i = 1$) regime (Figure 2.6).

The higher is the coupling, the higher is the mechanical energy accumulating over time. Intuitively, we can expect areas with a higher coupling to be associated with a higher risk of hosting a large earthquake, as this energy accumulating will have to be released at some point, either by sudden slip on the interface or by rupturing the surrounding medium. Actually, a good correlation between interseismic coupling distributions and seismic ruptures is often observed (Chlieh et al., 2011; Kaneko et al., 2010; Loveless and Meade, 2011; Métois et al., 2016). Predicting earthquakes is a subject of great interest that has not been accomplished to date (Allègre et al., 1982; Kanamori, 2003; Ridzwan and Yusoff, 2023; Sornette and Sammis, 1995), however assessing interseismic coupling on a given region gives an indication on the severity of the seismic risk.

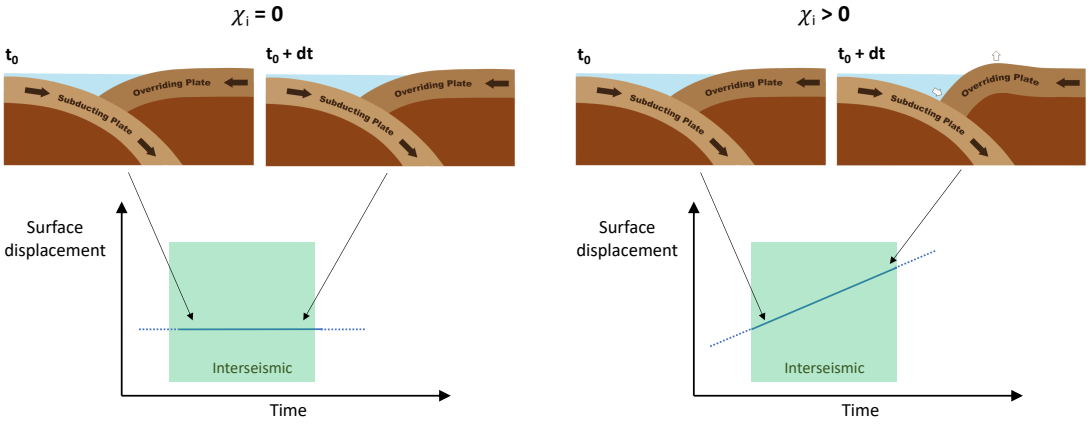

Figure 2.6: Schematic view of a subduction segment with zero coupling (left) or non-zero coupling (right). When $\chi_i = 0$ there is no friction between the two plates and no deformation is observed, while when $\chi_i > 0$ we observe a progressive deformation of the overriding plate over time.

The increase in the density of geodetic measurements, notably GNSS sites, significantly improved the accuracy of interseismic coupling models. These models show that the spatial distribution of interseismic coupling on a given slab interface can be very heterogeneous, with variations both in the along-dip and the along-strike directions.

The along-strike variations are constrained by the geodetic measurements, showing significant variations both in the horizontal and vertical velocities at several subduction zones: Chile (Béjar-Pizarro et al., 2013; S. Li et al., 2015; Métois et al., 2016; M. Moreno et al., 2011, Figure 2.7), Peru (Chlieh et al., 2011; Nocquet et al., 2014; Villegas-Lanza et al., 2016), North-East Japan (Nishimura et al., 2004; Suwa et al., 2006), Nankai (Yokota et al., 2016), Sumatra (Chlieh et al., 2008), or Cascadia (S. Michel et al., 2019). This along-strike segmentation is linked to variations in the mechanical properties of the megathrust interface, leading to a velocity weakening behavior in highly coupled areas and a velocity strengthening behavior in low coupled areas (Kaneko et al., 2010; C. H. Scholz, 1998). Variations in the normal stress on the interface could also play a role in the along-strike segmentation of coupling (Kaneko et al., 2010; Wallace et al., 2012). These two aspects may explain why changes in the interseismic coupling have been observed where oceanic structures are subducting (Chlieh et al., 2008; Chlieh et al., 2011; Molina et al., 2021; M. Moreno et al., 2011; Philibosian and Meltzner, 2020; C. H. Scholz and Campos, 2012; Villegas-Lanza et al., 2016), as oceanic structures introduce some heterogeneity in the material composition, fractures, hydration, or pressure variations on the overriding plate. A correlation between interseismic coupling, basal friction, and positive gravity anomaly has been proposed by some authors (Bassett and

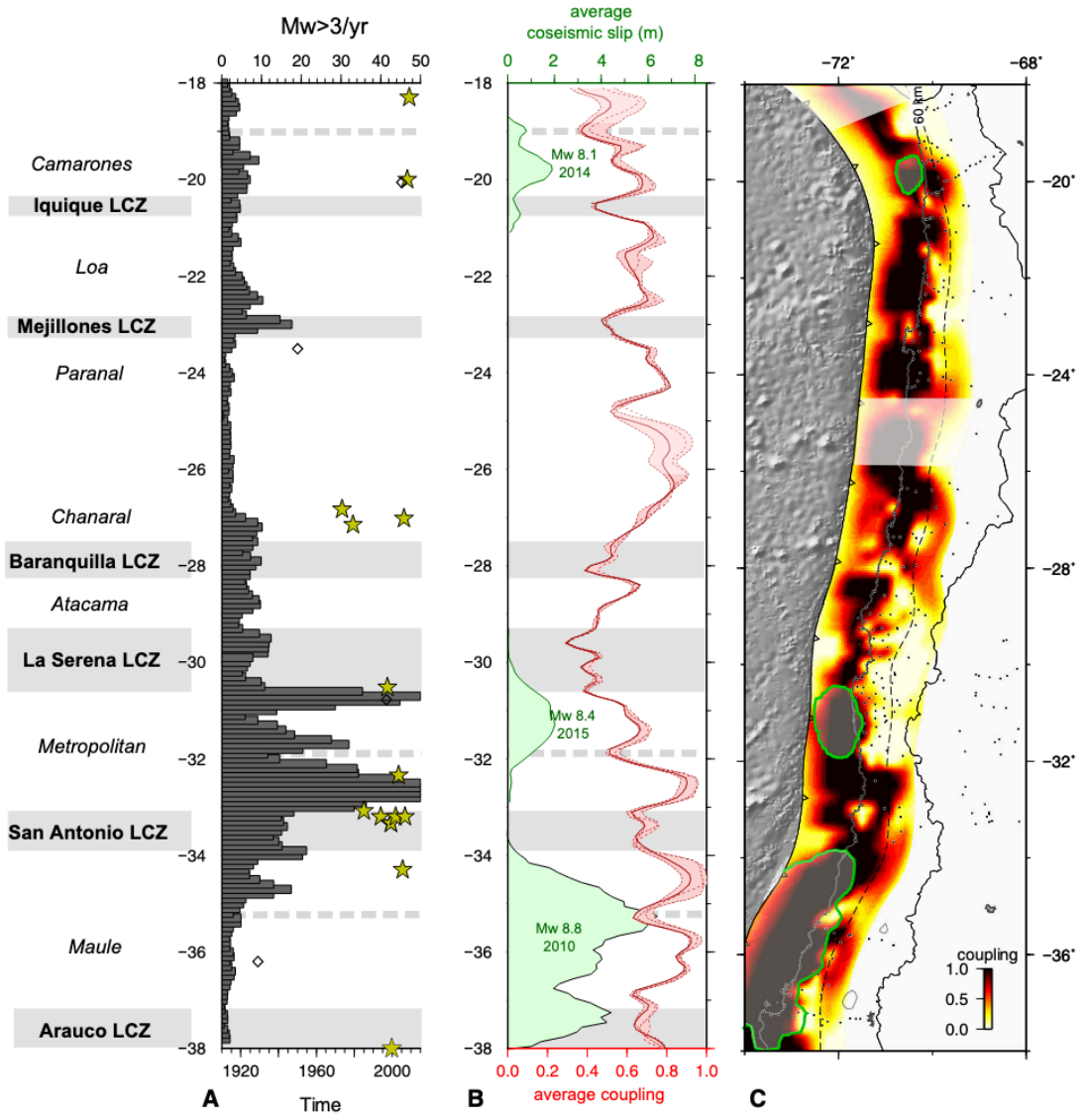

Figure 2.7: Figure from Métois et al., 2016 showing heterogeneous coupling on the Chile subduction. LCZ stands for *low coupling zone*. The histogram on panel *A* depicts the rate of Mw>3 earthquakes from the CSN seismic catalog during the interseismic period. Yellow stars indicate swarm-like sequences. Diamonds indicate significant intraplate earthquakes. Panel *B* is showing the variations of coupling, averaged along-dip, and the slip distributions for the Maule, Iquique, and Illapel earthquakes. Finally, panel *C* is showing the coupling distribution with the rupture areas of the Maule, Iquique, and Illapel earthquakes. Note that some areas, highlighted by white rectangles, lack resolution. Overall, coupling is varying significantly along strike and along dip. We observe lowered coupling where some oceanic features are subducting: the Iquique, the Mejillones, the Baranquilla, and the San Antonio ridges. Seismic ruptures overlap quite well with highly locked patches.

Watts, 2015; Bürgmann et al., 2005; Molina et al., 2021; Song and Simons, 2003).

Along-dip variations in the coupling distribution are constrained by the gradients of geodetic measurements. This allows to determine relatively well the down-dip limit of the coupling, however it is more difficult to constrain the up-dip limit near the trench without seafloor measurements. Thermal modeling can also help to define the width of the seismogenic zone that typically extents from the isotherms 100°C to about 350°C (Currie et al., 2002; Gutscher et al., 2013; Hyndman et al., 1997; Völker et al., 2011).

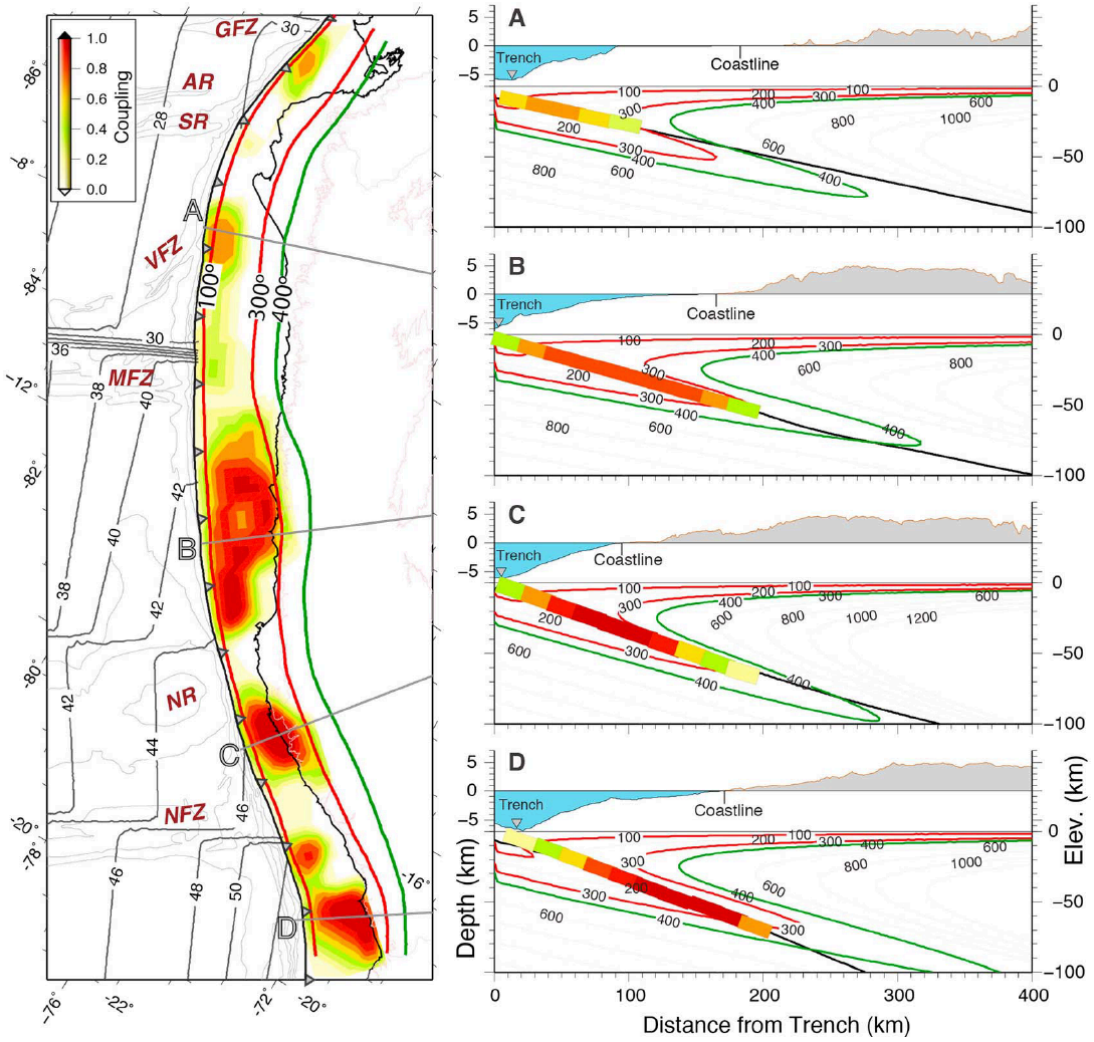

Figure 2.8: Figure from Villegas-Lanza et al., 2016 showing the thermal structure of the Peruvian megathrust. On the map is reported the age of the seafloor ranging from 20 to 55 Ma. In this study, the locking is mostly located between the isotherms 100°C and 300°C.

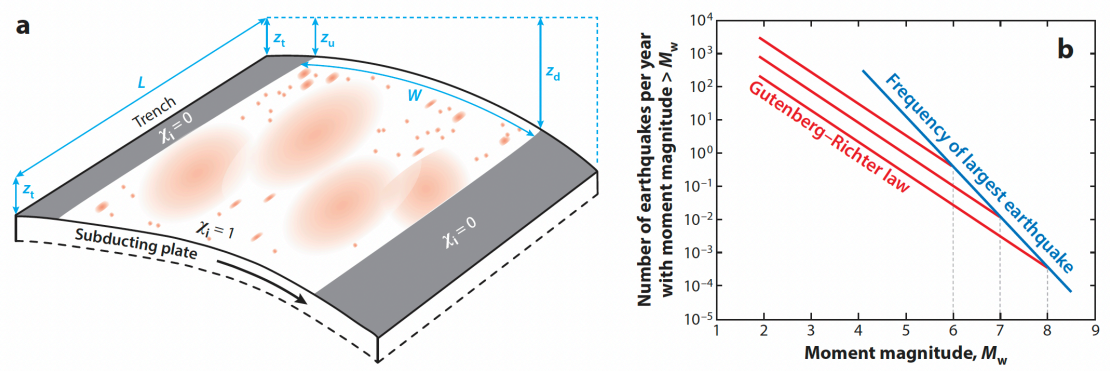

Figure 2.9: Figure from Avouac, 2015 illustrating the moment budget assessment using the interseismic coupling χ_i.

Linking interseismic coupling to seismic potential

The interseismic coupling can be used to assess the seismic potential of a subduction zone, as we performed in Chapter 4 by using a methodology similar to Avouac, 2015. As illustrated on Figure 2.9, the first step is to compute the annual moment deficit rate $\dot{M}_0$ associated with a coupling model over a specific portion of the subducting megathrust:

$$\dot{M}_0 = \int_{megathrust} \mu V \chi_i dS \tag{2.2}$$

with μ the shear modulus that is estimated from the Earth models of density and seismic wave velocity such as PREM (Preliminary Reference Earth Model, Dziewonski and Anderson, 1981), V the plate convergence velocity, and χ_i the interseismic coupling.

The moment deficit rate is then balanced with the seismicity in the area, by considering a robust seismic catalog with homogeneous magnitudes such as the ones provided by the International Seismological Center (ISC) (Willemann and Storchak, 2001 or the global Centroid-Moment-Tensor (gCMT) (Dziewonski et al., 1981; Ekström et al., 2012), that are characterized by the b-value of their Gutenberg-Richter law (Gutenberg and Richter, 1949). The mean recurrence time $T(M_{max})$ of the associated earthquake potential is thus defined as:

$$T(M_{max}) = \frac{1}{\left(1 - \frac{2b}{3}\right)\alpha} \frac{M_{max}}{\dot{M}_0} \tag{2.3}$$

with b the b-value and α the ratio of seismic events over all transient events:

$$\alpha = \frac{M_0^{seismic}}{M_0^{seismic} + M_0^{aseismic}} \tag{2.4}$$

The aseismic moment $M_0^{aseismic}$ includes afterslip and slow slip events occurring over one full seismic cycle.

Actually, it arises from this methodology that the earthquake potential is controlled by five main parameters:

- The average interseismic coupling, which is dependent of the geodetic data and all the assumptions that are made to model it, notably on the slab geometry, the rheology, or the inversion parameters.
- The plate convergence velocity V, that is known from geodetic measurements at continental scale. These models may show some variations depending on the technological advances in geodetic techniques, however they are most likely accurate within 10% (Jarrin et al., 2023; Kendrick et al., 2003).
- The b-value of the seismic catalogs, which may vary quite significantly from one catalog to another. For instance, on the South Peru segment the b-value of the gCMT catalog is about 0.7 while it is about 1.0 for the Peruvian Instituto Geofísico del Perú (IGP) catalog. These discrepancies may result from different instrumentation and methodologies to compute the magnitudes into an homogeneous scale.
- The fraction of transient slip that is seismic α, which is difficult to estimate accurately as we may not capture all the transient aseismic events during the seismic cycle.
- The shear modulus μ, which is often estimated from global models that may not be perfectly representative of a specific area.

As all these parameters are subject to some uncertainties, it can be wise to consider a range of possible values for each parameter in order to explore the distribution of earthquake potential (cf. Chapter 4 for more details). In our analysis for South Peru, the b-value appeared to be the largest factor of uncertainty so we recommend considering several seismic catalogs for the analysis.

2.1.4 Mechanics and rheology of subduction zones

Structure of subduction zones

As indicated on Figure 2.1, each tectonic plate involved in the subduction process can be divided into two main layers: the lithosphere on top and the asthenosphere below. The lithosphere is composed of the crust and the shallow part of the mantle, referred as lithospheric mantle. It is relatively rigid and it behaves elastically at the timescale we study, up to thousands years (K. Wang et al., 2012). On the other hand, the weaker asthenosphere exhibits a viscoelastic behavior, and is able to enter a convection cycle. One should not confuse the lithosphere which is a layer only defined by its physical properties with the crust that is defined by its chemical properties. Note that oceanic and continental lithospheres are not equivalent, both in term of thickness and constitution, and the same goes for the oceanic and continental asthenospheres. The oceanic lithosphere is mostly made of dense mafic material (i.e., silicates with a high content of magnesium and iron) such as olivine and peridotite. Its estimated thickness can vary quite a lot from a subduction zone to another, and even along its travel direction, with values ranging from 30 to 140 km (Boulze et al., 2025; M. P. Doin and Fleitout, 1996; S. Li et al., 2015; McKenzie et al., 2005). The continental lithosphere thickness is also expected to vary significantly, from 30 to 280 km on cratons (S. Li et al., 2015; McKenzie et al., 2005; Steinberger and Becker, 2018), and it is less dense than the oceanic one. The lower boundary of the asthenosphere, both on continental and oceanic side, is not well defined but it is expected to extend down several hundreds kilometers (Karato, 2012). It is important to note that the heat flux beneath volcanic arcs tends to weaken the crust in its lowest part and to partially melt it, leading to a viscoelastic behavior (Itoh et al., 2019; Luo and Wang, 2021). Hence, the apparent elastic thickness beneath the volcanic arc at subduction zones is reduced, from about 60-70 km to 20-30 km in Central Andes (Giambiagi et al., 2022; Tassara and Echaurren, 2012; Tassara et al., 2006).

The viscoelastic properties of the mantle have been identified thanks to the vertical surface displacements associated with the significant ice melting following the end of the last glacial period (115,000 to 11,700 years ago), known as post-glacial rebound. This phenomenon has been observed mostly in polar regions (e.g., Canada, Alaska, Scandinavia, or Antarctica) and led some authors to estimate roughly the viscosity in the lower mantle to about 10^{21} Pa·s (Eddington, 1928; Hubbert, 1937, 1945). More recent studies report lower viscosity below the crust, in the order of 10^{18} to 10^{20} Pa·s (Crawford et al., 2018; Le Breton et al., 2010; Sigmundsson, 1991). As a general trend, the viscosity in the upper mantle is expected to be lower than in the lower mantle, in order for the convective mechanism to supply the adequate heat flow (Phipps Morgan et al., 1995; Rabinowicz et al., 1980). This zone of low viscosity in the upper mantle is associated to a decrease in the velocity of the seismic waves from about 30 to 250

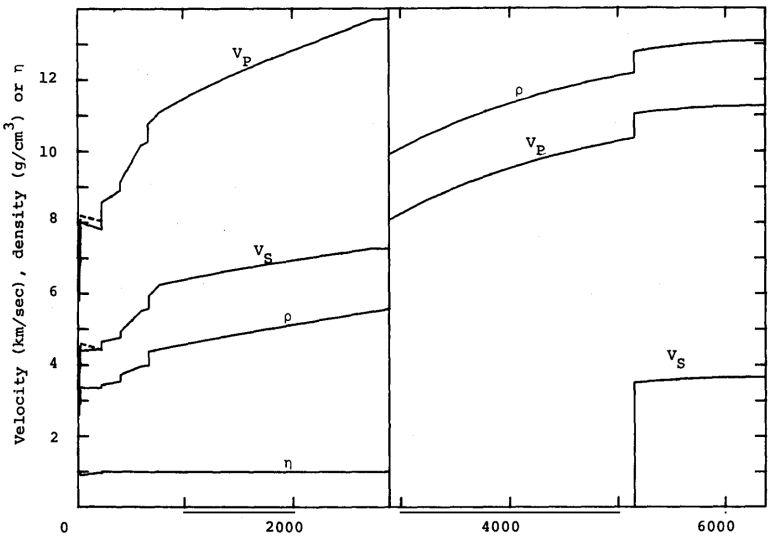

Figure 2.10: Figure from Dziewonski and Anderson, 1981 showing seismic P-wave (V_P) and S-wave (V_S) velocities according to depth. Both V_P and V_S are increasing with depth in the mantle (down to about 3,000 km), except in the low velocity zone (lower mantle, about 30 to 250 km). Then, V_P is dropping when crossing the core-mantle boundary (about 3,000 km) and V_S disappears since there is no shear in a liquid like the outer core.

km deep (Figure 2.10), known as *low velocity zone* (Dziewonski and Anderson, 1981; Gutenberg, 1926).

Note that while the structure on a sketch appears as well defined layers with sharp discontinuities, the reality may be more complex. By studying 17 subduction zones (including Nankai, Sumatra, Cascadia, Northern and South-Central Chile) Wada et al., 2008 and Wada and Wang, 2009 showed that the two plates are viscously coupled beyond a depth known as *decoupling depth* at about 70-80 km, and that the interface between the two tends to broaden with depth. The asthenosphere dynamics is then driven both by the coupling with the subducting lithosphere, and by the convection that primary controls the heat flow in the viscously coupled part (Figure 2.11). The heat flow in the shallow part, atop the decoupling depth, is on the other hand mainly controlled by the subducting slab. Subsequently, the forearc is colder and stagnant, we refer to this zone as the *cold nose*. They also report that the volcanic arc is located atop a ~100-km depth on the interface, corresponding to a melting point at 1,200°C, and that it is a constant on most subduction zones.

The rheological contrast between the cold nose and the hotter arc and back-arc is important to model the earthquake cycle: the cold nose behaves elastically while the arc and back-arc exhibit viscoelastic behavior. Luo and Wang, 2021 concluded that an elastic cold nose is required to explain the secondary zone of postseismic uplift observed after several large earthquakes (e.g., the 1960 Mw9.5 Valdivia, 2010 Mw8.8

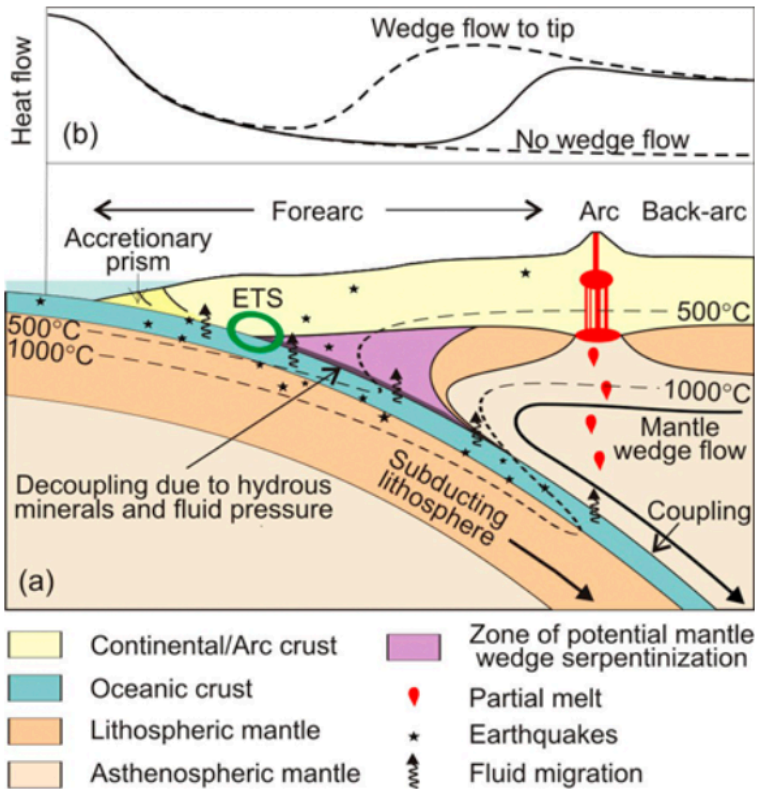

Figure 2.11: Figure from Wada and Wang, 2009 illustrating a typical oceanic-continental subduction. The stagnant forearc, a.k.a. *cold nose*, is indicated in purple. The volcanic arc is located atop the melting point at a depth of about 100 km on the interface. Episodic slip and tremors have been observed in Cascadia and Nankai around the area indicated by the green circle.

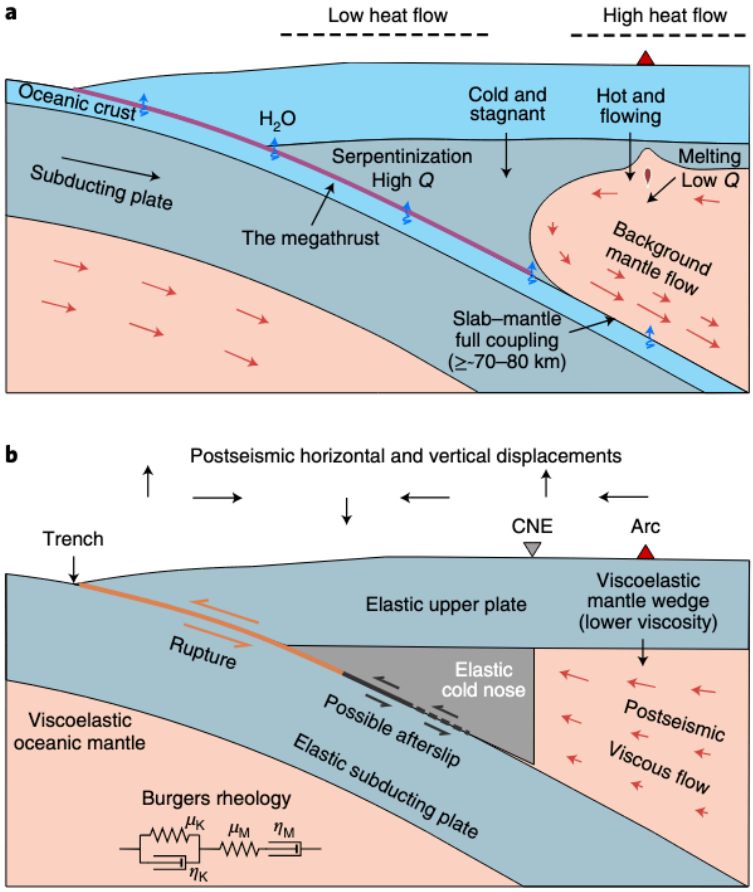

Figure 2.12: Figure from Luo and Wang, 2021 illustrating the thermal (a) and rheological (b) structures of subduction zones. The cold nose is elastic, as well as the continental and oceanic lithospheres, while the continental and oceanic asthenosphere are viscoelastic (Burgers rheology).

Maule, or 2011 Mw9.1 Tohoku earthquakes) without introducing unrealistic features such as a very deep coseismic slip or a very thick lithosphere in the volcanic arc (Figure 2.12). They also showed that the along-dip location of the cold nose edge controls the location of the maximum postseismic uplift, which is located atop the cold nose edge (Figure 2.13). The existence of an elastic cold nose on most subduction zones, notably along the Peru-Chile subduction, is also supported by positive velocity anomalies in the fore-arc (Gao, Tilmann, et al., 2021).

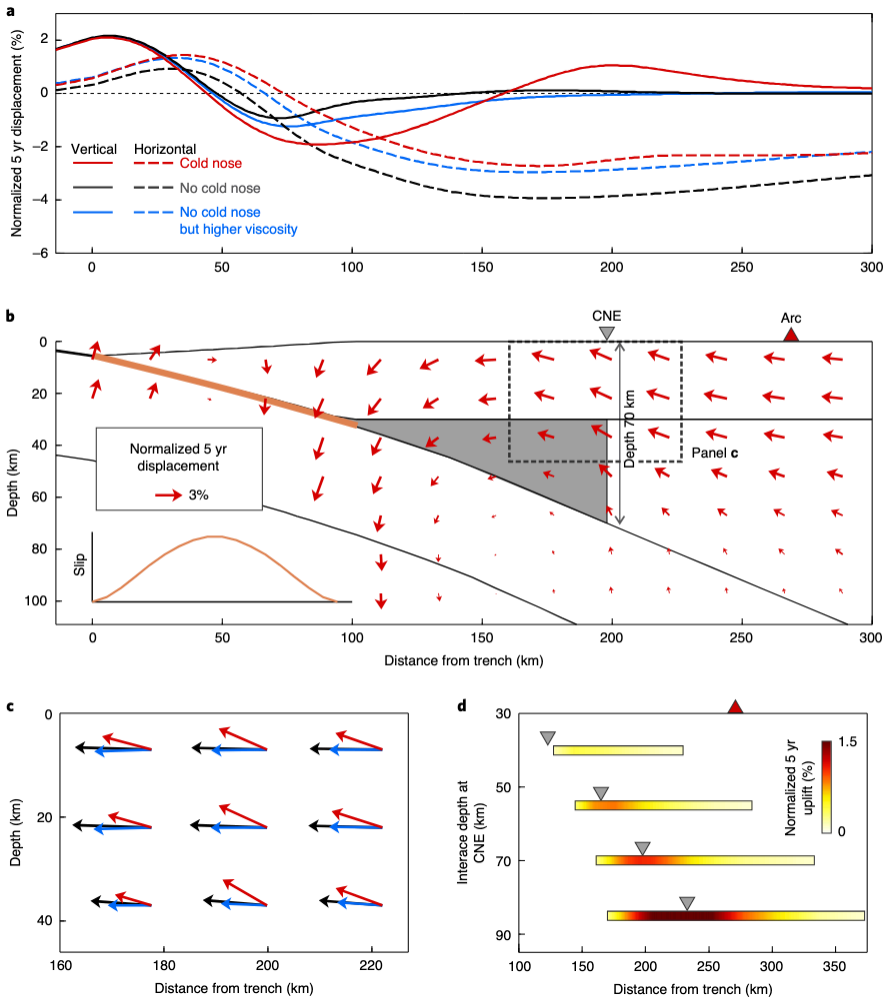

Figure 2.13: Figure from Luo and Wang, 2021 showing 2-D models of postseismic deformation to emphasis the importance of the cold nose. On panel (a) are shown vertical (solid lines) and horizontal (dashed lines) postseismic displacements at five years. A model without cold nose is shown in black, a model with higher viscosity in blue, and a model with an elastic cold nose in red. The elastic cold nose is required to generate uplift atop the cold nose edge. The structure with the elastic cold nose is reported on panel (b). On panel (c) are reported the three models of panel (a) on the area delimited by dashed lines on panel (b). Panel (d) shows the effect of the cold nose edge depth on the uplift.

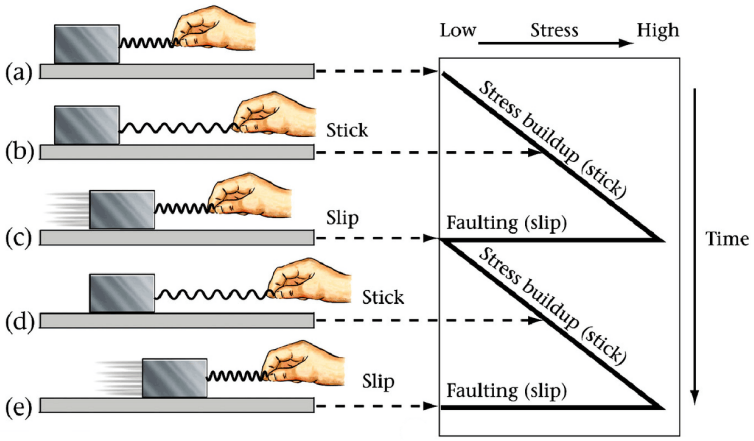

Figure 2.14: Figure from Punjab Engineering College illustrating stick-slip behavior.

On the frictional behavior of the megathrust interface

Previously, we introduced the observation that large earthquakes nucleate on some parts of the subduction, while other areas may be less prone to host them. While this observed seismic segmentation has to be taken with caution, due to the limited historical catalogs, it appears to be constrained by some geological markers such as the seafloor bathymetry of the subducting plate. Indeed, we observed that some oceanic ridges and fracture zones appear to behave as barriers against the propagation of large seismic ruptures (Kaneko et al., 2010; Philibosian and Meltzner, 2020).

The area where earthquakes can nucleate and propagate is referred as the *seismogenic zone*. At a macroscopic scale, it can be delimited along dip with up-dip and down-dip limits, and along strike. The seismogenic behavior of the interface is determined by its frictional properties, that need to allow the accumulation of mechanical energy over time (loading during the interseismic period) and the propagation of the rupture. It can be described by a stick-slip frictional law (Byerlee and Brace, 1968; Ida, 1975). As illustrated on Figure 2.14, stick-slip behavior can be described with a spring attached to a solid body lying on a table. We start with a system at rest (a) where no force is applied on the spring and the body is steady. Then we pull progressively on the spring (b), and at a certain threshold that is controlled by the static friction coefficient μ_s, the body starts to slip (c), until the kinetic friction overcomes the force applied by the string (d). The same cycle can repeat again and again, and by analogy the *stick* phases of this cycle (b and d) correspond to the interseismic phase of the earthquake cycle, while the *slip* phases (c and e) correspond to the coseismic phase. Note that once the body is moving, the motion is controlled by kinetic friction μ_k, and the kinetic friction coefficient being usually lower than the static friction coefficient, the force required to maintain motion is lower than the force required to initiate the motion.

As reported in C. H. Scholz, 1998, some additional complexity has been introduced over the years to describe earthquake tribology, following empirical observations (Dieterich, 1972; C. Scholz et al., 1972; Stesky et al., 1974):

- The static friction coefficient μ_s is not a constant for a given rupture area. Actually, if the interface is loaded in static contact for a time t, μ_s is increasing logarithmically with t.
- The kinetic friction is logarithmically dependent to the sliding velocity V. This dependence can be positive or negative, depending on the rock nature and the pressure-temperature conditions.
- If an abrupt change of sliding velocity happens, the kinetic friction coefficient μ_k is going to reach its new value after a characteristic slip distance L.

These observations have been included within the so-called rate-and-state friction law, notably in its Dieterich-Ruina formulation, also known as the *slowness law* (Dieterich, 1978; Ruina, 1983):

$$\tau = \left[\mu_0 + \alpha.log\left(\frac{V}{V_0}\right) + \beta.log\left(\frac{V_0\theta}{L}\right)\right]\bar{\sigma} \tag{2.5}$$

with τ the shear stress and $\bar{\sigma}$ the effective normal stress, defined as the applied normal stress minus the pore pressure. The slip velocity V has a reference value V_0, at which the steady-state friction is equal to μ_0. α and β are material-dependent coefficients. θ is a state variable evolving according to:

$$\dot{\theta} = 1 - \frac{\theta V}{L} \tag{2.6}$$

At steady state, the fiction law can be simplified as:

$$\tau = \left[\mu_0 + (\alpha - \beta)log\left(\frac{V}{V_0}\right)\right]\bar{\sigma} \tag{2.7}$$

The velocity-dependence of steady-state friction is then defined by the $(\alpha - \beta)$ parameter:

$$\alpha - \beta = \frac{\partial \mu_{ss}}{\partial\left[log(V)\right]} \tag{2.8}$$

with μ_{ss} the steady-state friction coefficient.

Two cases arise:

- $(\alpha - \beta) \geq 0$ corresponds to a velocity-strengthening regime, that is fundamentally stable. Earthquakes cannot nucleate in these areas, and any rupture will be stopped.
- While $(\alpha - \beta) < 0$ corresponds to a velocity-weakening regime, that can lead to instabilities. Unstable sliding occurs if the effective normal stress $\bar{\sigma}$ reaches the critical value $\bar{\sigma}_c$:

$$\bar{\sigma}_c = -\frac{kL}{\alpha - \beta} \tag{2.9}$$

  - If $\bar{\sigma} < \bar{\sigma}_c$, sliding is stable under pseudo-static loading, and it can become unstable if experiencing a high-enough velocity jump. Earthquakes cannot nucleate here but they may propagate.
  - While if $\bar{\sigma} \geq \bar{\sigma}_c$, sliding is always unstable. Earthquakes can nucleate and propagate under this regime.

To summarize, earthquake nucleate and propagate in the areas of the plate interface that exhibit rate-weakening behavior, while afterslip can happen in areas exhibiting rate-strengthening behavior (Perfettini et al., 2010). We can have a more microscopic approach and consider that the seismogenic zones that we observe, typically tens to hundreds kilometers large, are composed of smaller rate-strengthening and rate-weakening asperities. An area is then seismogenic if the density and the connectivity between the small rate-weakening areas is enabling rupture propagation (Avouac, 2015).

Beyond the concept of seismogenic zone, some authors have proposed a more refined classification of frictional environments on the subduction interface, such as Yamanaka and Kikuchi, 2004 or Lay et al., 2012. The latter propose four distinct rupture domains (A,B, C, and D), extending along-dip from the trench to the down-dip edge of the seismogenic zone:

- From the trench to 15 km deep, domain A can exhibit aseismic behavior or host tsunami earthquakes with large coseismic displacements and a slow rupture expansion due to the presence of sediments and fluids. The 1960 Mw7.6 and 1996 Mw7.5 tsunami earthquakes in Northern Peru have probably ruptured this domain.
- From 15 to ~35 km deep, domain B hosts large earthquakes, generating a large displacement on a wide area. For instance, the 2001 Mw8.4 Arequipa, 2007 Mw8.0 Pisco, or 2014 Mw8.1 Iquique earthquakes have nucleated and propagated mostly in this domain.

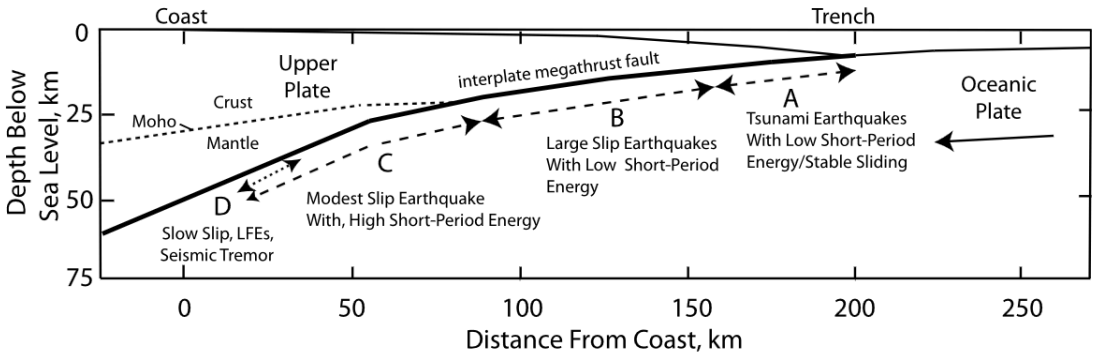

Figure 2.15: Figure from Lay et al., 2012 indicating the four rupture domains they define (A, B, C, and D) on a megathrust. Note that it is here scaled for the subduction Northeast of Honshu.

- From ~35 to 55 km deep, domain C hosts smaller earthquakes on isolated patches. The 1996 Mw7.7 Nazca earthquake in South Peru or the 2007 Mw7.7 Tocopilla earthquake in Central-North Chile are examples of such earthquakes. Note that domain C earthquakes tend to have their energy dissipated in more coherent short-period bursts than domain B earthquakes.
- On relatively young subductions (e.g., Cascadia, South-West Japan, or Chile) with moderate dip, low-frequency earthquakes, tremors, and slow-slip events occur in domain D from ~30 to ~45 km deep. It is considered a transitional region between seismic and aseismic zones.

The down-dip limit of the seismogenic zone is often constrained by thermal models (Peacock, 1996; Penniston-Dorland et al., 2015; Syracuse et al., 2010; van Keken and Wilson, 2023) and laboratory experiments showing that rocks with a high quartz content have a ductile behavior above 350°C, which should prevent locking and seismic behavior (Kanaya and Hirth, 2018; Oleskevich et al., 1999; Tse and Rice, 1986). In Peru and Chile the 350°C isotherm is expected to be located at a depth of about 60 km (Villegas-Lanza et al., 2016, Figure 2.8). Assessing the interseismic coupling can help to refine the delimitation of the seismogenic zone, both along-dip and along-strike.

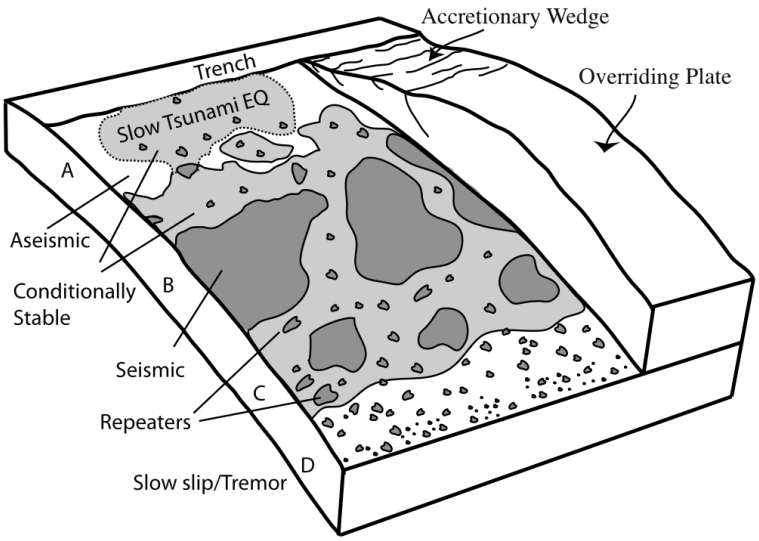

Figure 2.16: Figure from Lay et al., 2012 showing a 3-D representation of the A,B,C, and D rupture domains. Areas of unstable frictional behavior are drawn in dark gray and labeled as *seismic*, while *aseismic* regions are in white. Medium gray indicate regions that exhibit stable sliding, except when adjacent seismic patch rupture. Slow-slip events and seismic tremors can happen in domain D.

Accounting for viscoelasticity

The earthquake cycle is often modeled in a pure elastic medium, including the coseismic phase (Chlieh et al., 2011; Fialko et al., 2005; Hashimoto et al., 2010; Jara et al., 2018), the postseismic phase with the afterslip (Chlieh et al., 2007; Marone et al., 1991; Tissandier et al., 2023), and the interseismic phase (Métois et al., 2016; Nocquet et al., 2014; Savage and Thatcher, 1992; Villegas-Lanza et al., 2016). While this assumption is perfectly valid to model for the coseismic phase, as it is a short-term process lasting seconds to minutes, it is more questionable for the postseismic and interseismic phases which are more long-term processes. For postseismic, we discussed that two other processes are actually involved in addition to afterslip: poroelastic rebound and viscoelastic relaxation of the asthenosphere. The later being a key to understand postseismic displacements over a long timescale of several decades (Barbot and Fialko, 2010; Klein et al., 2016; Sun and Wang, 2015; K. Wang et al., 2007). While for interseismic, several studies showed that viscoelasticity could play an important role for assessing the locking on the plate interface (S. Li et al., 2020; S. Li et al., 2015; Pollitz et al., 2010; K. Wang et al., 2001; K. Wang et al., 2012). Accounting for viscoelastic relaxation when computing interseismic coupling models tends to reduce the locking depth and to discard the need of additional rigid block motion from a sliver (S. Li et al., 2015). In order to understand how we model viscoelasticity, let's define some basic

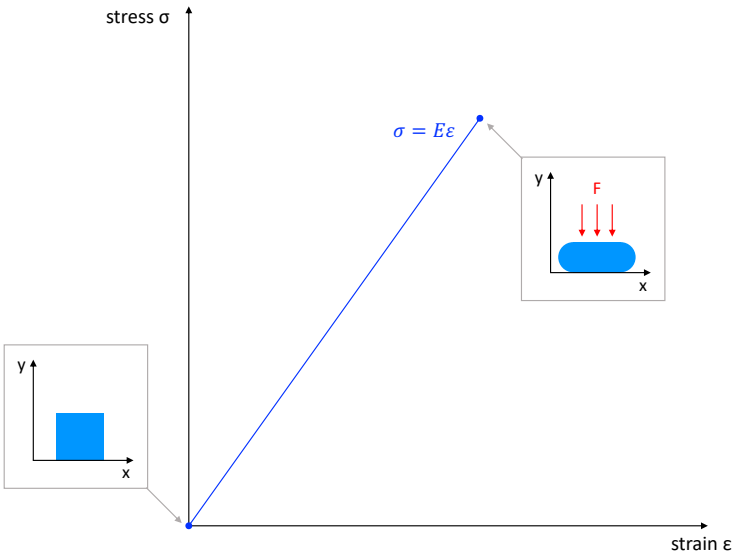

Figure 2.17: Linear elasticity on a strain vs. stress diagram when applying an axial compressive force F on an object.

notions of continuum mechanics.

Elasticity is defined as the regime where we have a linear relationship between the stress σ and the strain ε, given by the Hooke's law:

$$\sigma = E\varepsilon \tag{2.10}$$

For tension or axial compression, stress and strain are linked by the Young's modulus (a.k.a. elastic modulus) E and the deformation is reversible, meaning that when the applied force is released the object returns to its original shape without any persistent deformation (Figure 2.17). Typical values for E are 50 MPa for rubber, 10 GPa for wood, 68 GPa for aluminum, 200 GPa for steel, or 1 TPa for diamond.

We experience elastic deformation in our everyday life when pulling on a rubber band or inflating a tire. Most materials, like rubber, shows transversal elongation when applying longitudinal compression and vice versa. Transversal ($d\varepsilon_{trans}$) and longitudinal ($d\varepsilon_{long}$) deformations are linked by the Poisson's ratio ν:

$$\nu = -\frac{d\varepsilon_{trans}}{d\varepsilon_{long}} \tag{2.11}$$

Most materials have a Poisson's ratio between 0 and 0.5, typical values include 0.15 for concrete, 0.3 for sand and steel, and 0.5 for rubber. Interestingly, some materials

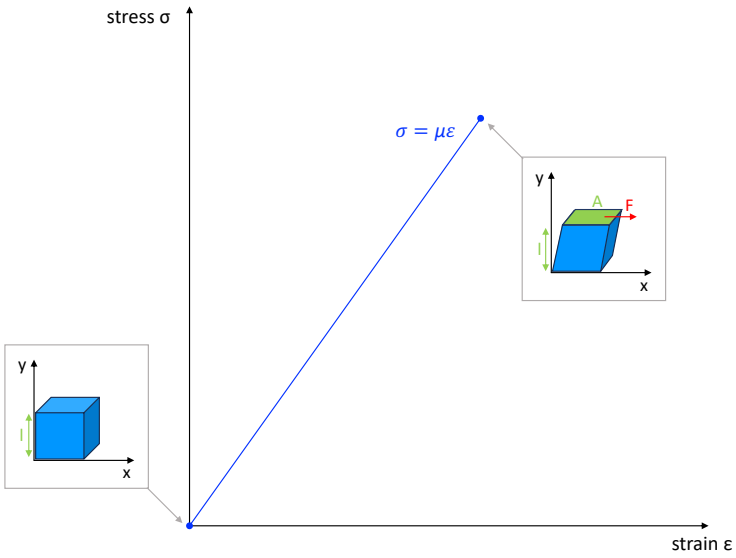

Figure 2.18: Linear elasticity on a strain vs. stress diagram when applying a shear force F on an object.

exhibit a negative Poisson's ratio, referred as *auxetic* materials, including some forms of graphene or carbon in diamond-like phases (Goldstein et al., 2014).

Young's modulus and Poisson's ratio are enough to describe simple elastic problems with uniaxial compression or tension, but for more general applications we need to introduce the shear modulus μ and the bulk modulus K. The shear modulus μ (a.k.a. rigidity) indicates the response to shear stress (Figure 2.18). For a transverse force F applied on an object of length l over an area A and generating a transverse displacement Δx, it is defined as:

$$\mu = \frac{Fl}{A\Delta x} \tag{2.12}$$

Typical values of μ are 600 kPa for rubber, 4 GPa for wood, 24 GPa for granite, 25 GPa for aluminum, 80 GPa for steel, or 480 GPa for diamond. For isotropic material, it is linked to Young's modulus and Poisson's ratio by the following relation:

$$\mu = \frac{E}{2(1+\nu)} \tag{2.13}$$

Knowing the density ρ, both Young's modulus E and shear modulus μ can be obtained from the seismic P-wave and S-wave velocities respectively:

$$E = \rho v_p^2 \tag{2.14}$$

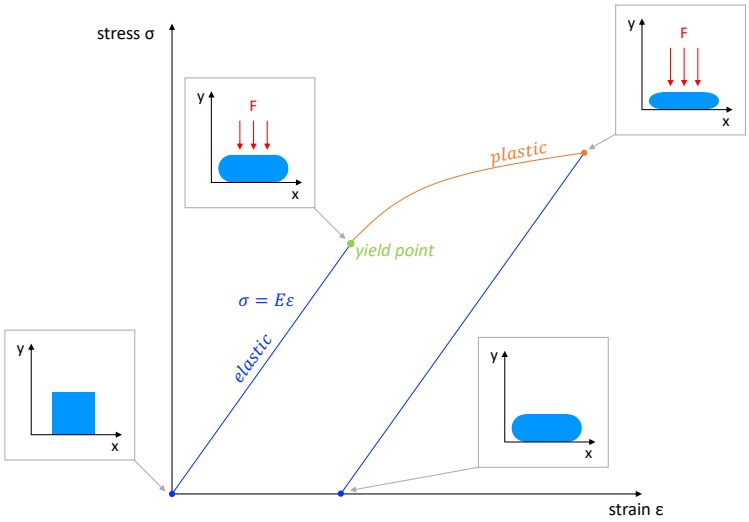

Figure 2.19: Strain vs. stress diagram when applying an axial compressive force F on an object. First, the object deforms elastically, but past a certain threshold known as the yield point, it enters the plastic deformation regime. Permanent deformation is acquired in the plastic regime, meaning that the object will not return to its initial shape after releasing the stress.

$$\mu = \rho v_s^2 \tag{2.15}$$

The bulk modulus K quantifies the resistance of a material to bulk compression. For an object of volume V subject to a pressure P, it is defined as:

$$K = -V\frac{dP}{dV} \tag{2.16}$$

Typical values for bulk modulus are 2 GPa for rubber, 50 GPa for granite, 160 GPa for steel, or 443 GPa for diamond. It is linked to Young's modulus E and Poisson's ratio ν by the following relation:

$$K = \frac{E}{3(1-2\nu)} \tag{2.17}$$

Let's come back to our simple axial compression example. If we continue to apply stress up to a certain threshold, known as the yield point, the deformation regime will switch from linear elasticity to plasticity (Figure 2.19). In this case, permanent deformation is acquired by the material. If we release the stress, hysteresis appears on the stress vs. diagram and the object will not return to its initial shape.

The lithosphere tends to be considered as mainly elastic (Pollitz, 2019; Tesauro et al., 2012) but it can undergo some plastic deformation, leading to the building of relief. The

asthenosphere on the other hand has been identified as a viscoelastic medium (Chanard et al., 2018; Cohen, 1979; Pollitz, 2019; Savage and Prescott, 1978). A viscoelastic material exhibits both elastic and viscous characteristics, meaning that it behaves to some extent like a fluid. Compared to a purely elastic material, a viscoelastic material has a delayed response to external changes, with time-dependent strain. Viscoelastic materials in our everyday life include ketchup, polymers because of their long atomic molecules, fresh concrete, or wood on longer timescales (several decades). Compared to elastic materials, viscoelastic materials are characterized by an additional physical quantity that is the viscosity, quantifying the resistance to a change in the shape or movement of the material seen as a fluid. Viscosity can vary with thermodynamical conditions (pressure, temperature) and the deformation rate. It means that the same material can behave elastically or viscoelastically depending on the conditions. For instance, olivine at atmospheric pressure has a viscosity in the order of 10^{24} Pa·s at room temperature, while it can go down to 10^{19} Pa·s above 1,000°C (Kohlstedt and Hansen, 2015). To be more specific, viscosity can refer to two different quantities in textbooks: *dynamic* viscosity and *kinematic viscosity*, the later being simply the ratio of dynamic viscosity over density. In this manuscript, like in most Earth science papers, we refer to *viscosity* as the dynamic viscosity. When the viscosity of a material is independent of strain rate, it is considered a *Newtonian fluid*. We also refer to *linear viscosity*. They follow Newton's law of viscosity for a laminar flow in the x-direction (Landau and Lifshitz, 2013):

$$\tau_{xy} = \mu \frac{dv_x}{dy} \tag{2.18}$$

with τ_{xy} the shear stress in the x and y components, μ the dynamic viscosity, and v_x the flow velocity. In usual pressure-temperature conditions, gases and most liquids including water, alcohol, or engine oil can be considered Newtonians. Non-Newtonians fluids include honey, ketchup, or magma. The non-Newtonian behavior of ketchup is quite easy to observe: ketchup is flowing significantly easier after shaking the bottle. Note that some fluids, known as *superfluids*, can have a zero viscosity meaning that they flow without losing any kinetic energy. This behavior occurs when forming a Bose-Einstein condensate (Cohen-Tannoudji et al., 2018). Consequently, superfluid transition is observed at very low temperature and is easier to observe on bosonic elements, for instance it occurs at 2.491 mK for helium-3 (fermions) and 2.17 K for helium-4 (bosons). Asthenosperic materials are not going to behave as superfluids, however there may be some debate about their Newtonian or non-Newtonian behavior. Numerous studies about postseismic relaxation considered them as Newtonian (Hu et al., 2004; Klein et al., 2016; S. Li et al., 2020; Sun and Wang, 2015), while some others considered them as non-Newtonian (Barbot, 2018; Muto et al., 2019; Peña et al., 2020). We chose to stick to linear viscosity in this PhD as it is not evident that the added complexity of a non-linear viscosity is required. Actually, the studies using a non-linear

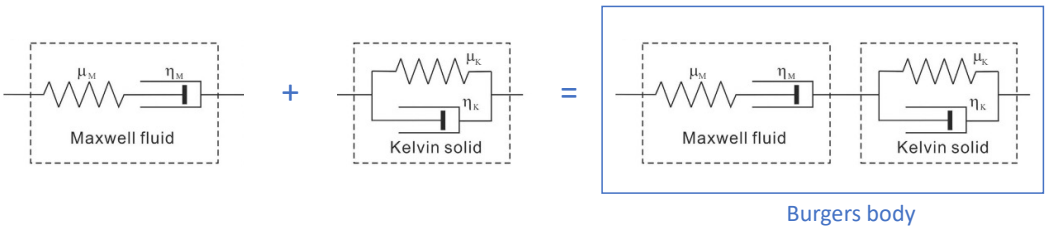

Figure 2.20: Maxwell, Kelvin-Voigt, and Burgers viscoelastic models. By attaching a Maxwell fluid to a Kevin-Voigt solid, we form a Burgers body.

law of viscosity (power law) do not show that the medium is physically behaving as a non-Newtonian fluid, but that the power law is fitting their surface displacement time series. The study from Boulze et al., 2022 perform an extensive analysis of the post-seismic relaxation following three large earthquakes in Chile (Maule, Illapel, and Iquique) and they found a better fit with a linear *Burgers* rheology than a power law rheology.

Viscoelastic materials can be described with springs to model the elastic response and dampers to model the viscous response. By combining springs and dampers we can form more or less complex models, the three most common models for modeling linear viscosity being the *Maxwell*, *Kelvin-Voigt*, and *Burgers* models (Figure 2.20).

A Maxwell model is simply a spring (shear modulus μ_M, Young's modulus E_M) attached in series to a damper (viscosity η_M). Quick elastic deformation is accommodated by the spring, while the damper is producing a long-term viscous flow (Figure 2.21). It was introduced by James Clerk Maxwell in 1867 to describe the dynamics of gases (Maxwell, 1867). The characteristic Maxwell relaxation time τ_M is given by:

$$\tau_M = \frac{\eta_M}{\mu_M} \tag{2.19}$$

Stress σ and strain ε are linked by the equation

$$\frac{\dot{\sigma}}{E_M} + \frac{\sigma}{\eta_M} = \dot{\varepsilon} \tag{2.20}$$

The Maxwell model is adequate to describe long-term relaxation in the asthenosphere.

Then, the Kelvin-Voigt model is a spring (shear modulus μ_K, Young's modulus E_K) and a damper (viscosity η_K) in parallel. This setup is similar to a car suspension, the damper smoothing fast deformation rates. The final deformation is the same as for an elastic body, but spread in time. It was introduced in 1865 by Lord Kelvin (a.k.a.

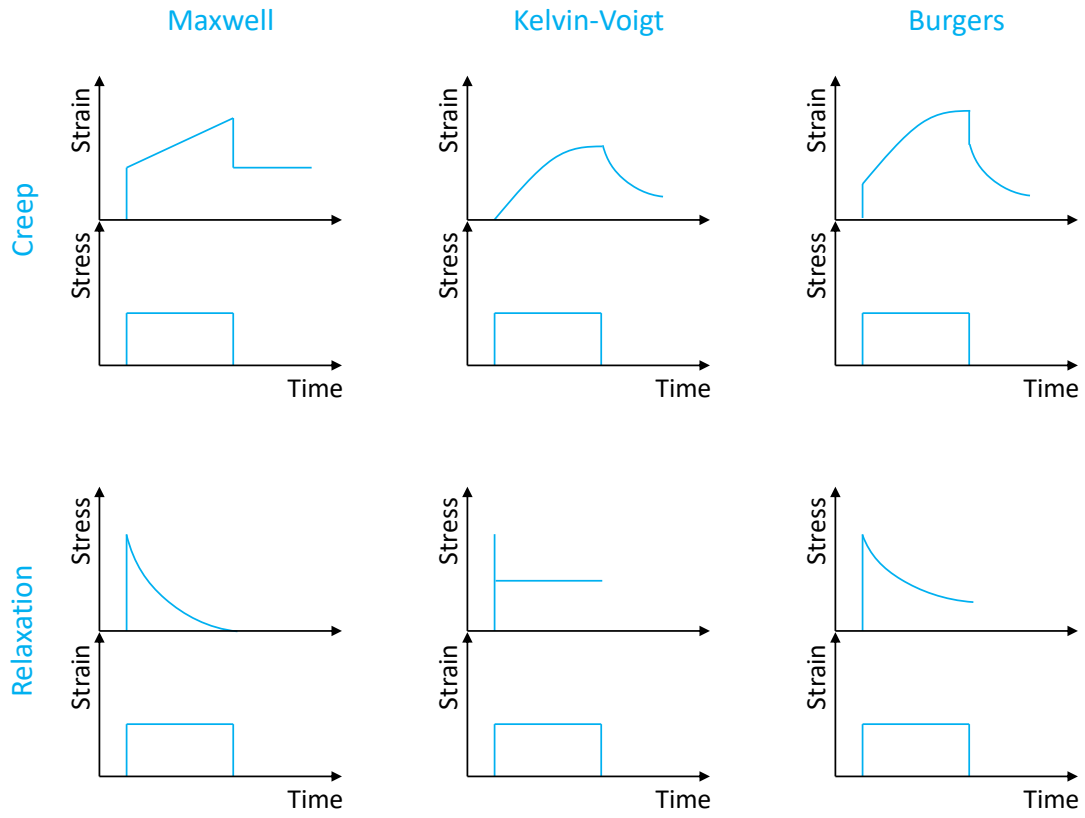

Figure 2.21: Stress and strain evolution along time during creep or relaxation, for Maxwell, Kelvin-Voigt, and Burgers viscoelastic models.

William Thomson) and by Woldemar Voigt in 1890 to study the viscoelasticity of metals (Thomson, 1865; Voigt, 1890). The characteristic Kelvin relaxation time τ_K is given by:

$$\tau_K = \frac{\eta_K}{\mu_K} \tag{2.21}$$

Stress σ and strain ε are linked by the equation

$$\sigma = E_K \varepsilon + \eta_K \dot{\varepsilon} \tag{2.22}$$

By joining a Maxwell solid and a Kelvin-Voigt solid, we obtain a Burgers body. This model, introduced by Johannes Martinus Burgers (Burgers, 1935), is characterized by a bi-viscous rheology with two characteristic times: the one from the Kelvin-Voigt solid and the one from the Maxwell fluid. Stress σ and strain ε are linked by the equation

$$\sigma + \left(\frac{\eta_K}{E_K} + \frac{\eta_M}{E_K} + \frac{\eta_M}{E_M}\right)\dot{\sigma} + \frac{\eta_K \eta_M}{E_K E_M}\ddot{\sigma} = \eta_M \dot{\varepsilon} + \frac{\eta_K \eta_M}{E_K}\ddot{\varepsilon} \tag{2.23}$$

Burgers rheology is widely used to model the relaxation in the asthenosphere, allowing to fit both long-term displacements like a Maxwell model, and shorter-term deformation (Boulze et al., 2022; Klein et al., 2016; S. Li and Chen, 2024; S. Li et al., 2018; Sun and Wang, 2015; K. Wang et al., 2012). The two relaxation times account for the heterogeneity inside the asthenosphere, due to small-scale convection.

2.2 The Peru-Chile subduction

The Peru-Chile trench is usually defined as being about 6,000 km long, extending from Ecuador to Patagonia. The most active tectonic area is ranging from Central Peru (~10°S) to the triple junction with the Antarctic plate in South Chile (~47°S). Multiple great megathrust earthquakes have been measured, or reported for the older ones, all along this segment, including the 1960 Mw9.5 Valdivia earthquake which is considered as the largest earthquake ever reported on Earth. The Andes are a testimony of the past and present activity of the subduction, indicating anelastic deformation in the upper plate, with elevation reaching 6,961 m at the Aconcagua peak in Argentina (~32°S) and exceeding 6,000 m in several places in Peru and Chile. They extend on about 8,900 km, from Venezuela to Chile, with an average elevation of ~4,000 m. On the opposite, the trench is going down to 8,065 m below the sea level offshore of Antofagasta (~23°S), making it the deepest trench in the South Pacific ocean. In addition to intense seismic activity, the subduction also triggers volcanic activity in the Andes, notably over the Andean Central Volcanic Belt (15°S to 30°S) which hosts 44 active and potentially active stratovolcanoes (Aguilera et al., 2022) such as the Sabancaya volcano at 70 km from the Arequipa city in South Peru, or the Lascar volcano in North Chile, that both showed signs of activity in the recent years (Boixart et al., 2020; Gaete et al., 2020; Machacca et al., 2023; MacQueen et al., 2020). In the frame of this PhD thesis, we focus on the Central Andes (especially from 8°S to 26°S), encompassing Central and South Peru from Trujillo to the Arica bend, as well as North Chile down to the Copiapo ridge. In this area, the coast of Peru and Chile is located about 100 to 200 km away from the Peru-Chile trench, which marks the point where the oceanic Nazca plate starts to subduct beneath the South America continent, at a velocity of about 6 cm/yr (Jarrin et al., 2023; Kendrick et al., 2003).

2.2.1 Seismotectonic activity

Eighteen earthquakes with a magnitude Mw $\geq$ 8 have been recorded in Peru and Chile since 1900 (Figure 2.22): 6 in Peru (mostly South of 10°S) and 12 in Chile (from 19.6°S to 38.1°S). In Peru, five out of the six earthquakes are megathrust events, rupturing the slab interface in Central and South Peru (South of 10°S): the 1940 Mw8.2 Huacho, 1942 Mw8.1, 1966 Mw8.1 Paramonga, 2001 Mw8.4 Arequipa, and 2007 Mw8.0 Pisco earthquakes (M. E. Beck, 1998; Dorbath et al., 1990; Villegas-Lanza et al., 2016). Special attention will be paid to the 2001 Mw8.4 Arequipa earthquake in this thesis, since strong coseismic and long-lasting postseismic displacements have been recorded in GNSS data (Sun et al., 2018; Villegas-Lanza et al., 2016). On June 23 2001 it ruptured the South Peru segment on about 300 km, within the same area that ruptured during the Mw~8.8 1868 earthquake on a longer segment from the Nazca Ridge to the Arica

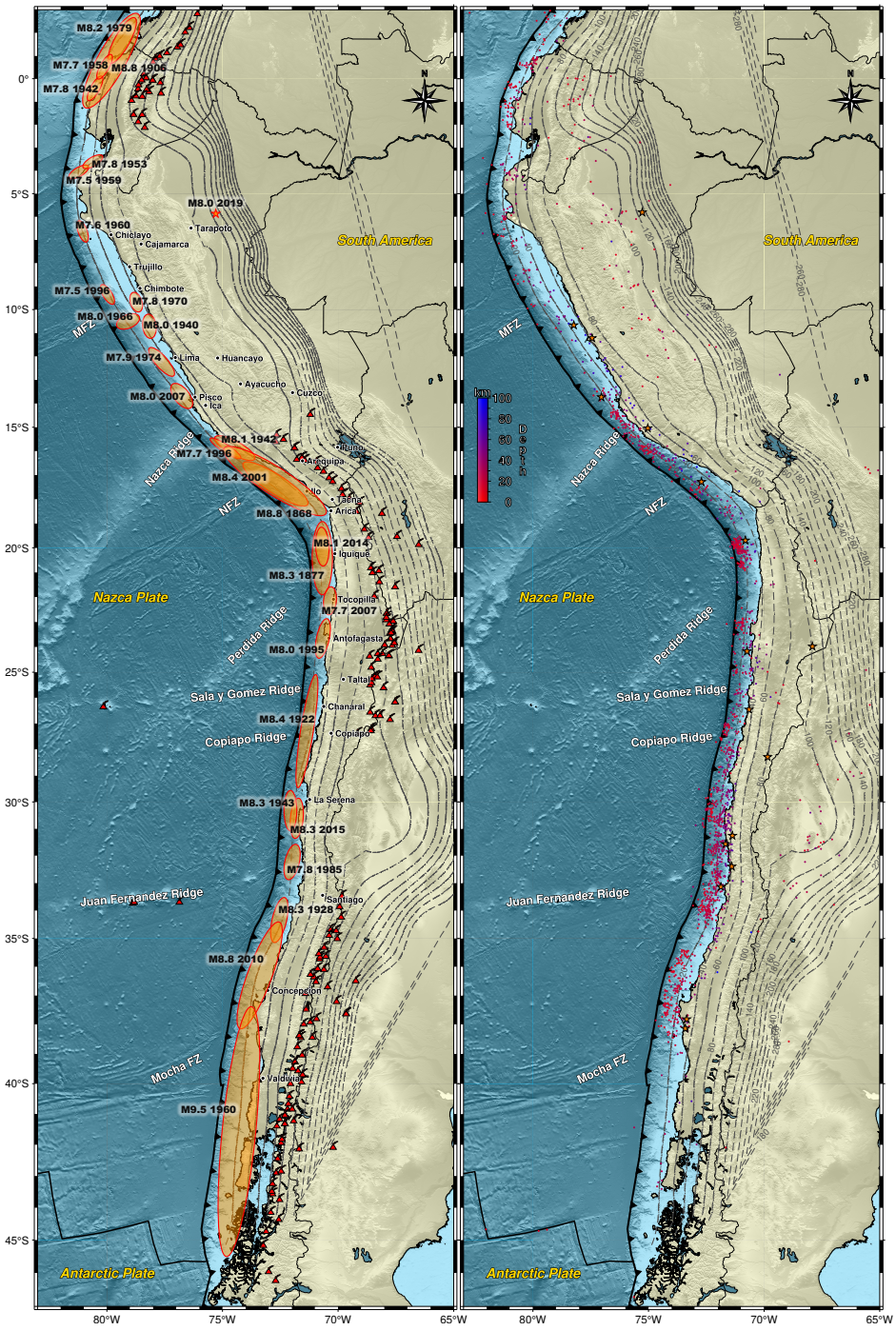

Figure 2.22: *Left:* Major earthquake ruptures (M≥ 7.5) since 1868 along the Peru-Chile trench (M. E. Beck, 1998; S. L. Beck and Ruff, 1989; Dorbath et al., 1990; Silgado, 1978; Villegas-Lanza et al., 2016). Volcanoes are reported in red, major cities in black, and major oceanic features in white. Slab contours are depicted by gray dashed lines from the Slab2 model every 20 km (Hayes et al., 2018). *Right:* Thrust seismicity from gCMT (Dziewonski and Anderson, 1981; Ekström et al., 2012) since 1976, down to 100 km deep, and color-coded by depth. The magnitude of completeness is about 5.2. Plotting thrust events only should be more representative of the plate interface seismicity than plotting all mechanisms, however not all events are on the interface. The seismicity tends to be higher where large earthquakes happened during the observation period because of the aftershock and foreshocks sequences, this is clearly observed for the 2014 Mw8.1 Iquique earthquake. Still, two gaps of seismicity are observed in Chile: one from 21°S to 23°S, and one from 34.5°S to 35.5°S. In Peru, less seismicity is observed in the Northern part.

bend, and it generated a 7 to 8 m tsunami reaching the coast of Camaná (Tavera et al., 2006). It was followed on June 23 by a Mw7.7 aftershock. The sixth earthquake, Mw8.0 in 2019, was not located on the subduction interface, instead it ruptured a normal fault at about 130 km deep (Vallée et al., 2023) in the Northern part of Peru.

In Chile, the most notable event was the 1960 Mw9.5 Valdivia earthquake, that is considered the largest earthquake ever recorded (Barrientos and Ward, 1990; M. S. Moreno et al., 2009). It ruptured the subduction interface on May 22 on about 1,000 km in Southern Chile. The 10-minute rupture was followed by a 25-meter tsunami reaching the coast of Chile, including the city of Valdivia. Even Hawaii, located 10,000 km from the epicenter, was severely affected by 10-m waves. The mainshock was preceded by a Mw8.1 foreshock the day before. North of the 1960 rupture, the Mw8.8 Maule earthquake nucleated in 2010 (M. Moreno et al., 2010). On the Central Chile segment, the Mw8.3 Illapel earthquake ruptured in 2015 at about 200 km North of Santiago (Klein et al., 2017). While the Northern Chile segment hosted the Mw8.0 Antofagasta earthquake in 1995 (Delouis et al., 1997) and the Mw8.1 Iquique earthquake in 2014 (Schurr et al., 2014).

Several segments along the Peru-Chile subduction are often referred to as *seismic gaps* in the literature (Alvarez-Vargas et al., 2025; Delouis et al., 2009; González-Alfaro et al., 2018; León et al., 2019; Lorito et al., 2011; Métois et al., 2013; Ruegg et al., 2009; Yáñez-Cuadra et al., 2022). The definition of seismic gap may vary, for instance Mogi, 1979 discriminates seismic gaps into two types: the first type is defined as segments that have not experienced a large seismic rupture since several decades, the second type is a gap in the smaller seismicity between the occurrence of large earthquakes. When not specified, authors tend to refer to the first type of seismic gap (McCann et al., 1979; Nishenko, 1991), including the seismic gaps identified on the Peru-Chile subduction. In any case, a seismic gap is an area that may be prone to host a a very large earthquake in the future because of the amount of energy accumulating and not released since a long time. Three seismic gaps are identified in Chile:

- The North Chile seismic gap from 20°S to 23°S, South of the 2014 Iquique rupture (Delouis et al., 2009; González-Alfaro et al., 2018; León et al., 2019; Métois et al., 2013). This segment ruptured in 1877 through a M~8.5 earthquake and is mostly locked since (Chlieh et al., 2011; Jolivet et al., 2020; S. Li et al., 2015; Métois et al., 2013; Métois et al., 2016). It is associated to a high tsunami risk (Comte and Pardo, 1991; León et al., 2019).

- The Atacama seismic gap from 25°S to 30°S (M. E. Beck, 1998; Yáñez-Cuadra et al., 2022) ruptured in 1922 in a Mw~8.5 earthquake. It is also associated to a high tsunami risk. This segment appears to be highly locked (Klein et al., 2018; Métois et al., 2012; Métois et al., 2016; Yáñez-Cuadra et al., 2022), with some

creep where the Salas & Gomez and Copiapo ridges are subducting (Klein et al., 2018; Yáñez-Cuadra et al., 2022). Note that historical records on this segment are limited, due to little colonial settlement prior to the 1830s in the Atacama region (Comte and Pardo, 1991).

- The Concepción-Constitución seismic gap from 35°S to 37°S (Alvarez-Vargas et al., 2025; Campos et al., 2002; Lorito et al., 2011; Ruegg et al., 2009) ruptured in 1835 through a M~8.5 earthquake and appeared to be locked since (Métois et al., 2016; M. Moreno et al., 2011). In 2010 it ruptured again during the 2010 Mw8.8 Maule earthquake.

The Central Peru segment, from the Mendana fracture zone (10.5°S) to the Nazca ridge (15°S) can also be considered a seismic gap, as it has not rupture completely since the 1746 M~8.6 earthquake. However, it ruptured partially during the the 1940 Mw8.1, 1974 Mw7.9, 1996 Mw8.0, and 2007 Mw8.0 earthquakes, leading to an energy release on all its length.

On Figure 2.22 is reported the thrust seismicity from the gCMT seismic catalog (Dziewonski and Anderson, 1981; Ekström et al., 2012) since 1976, down to 100 km deep. We observe two gaps in Chile, that correspond to the second type of seismic gap described by Mogi, 1979: one from 21°S to 23°S in the North Chile seismic gap South of the 2014 Iquique rupture, and one between 34.5°S and 35.5°S. It appears to be also a decrease in seismicity offshore of the Arica bend, and a significantly lower interface seismicity North of the Nazca ridge on all the Central and North Peru segments. Interestingly, while the interface seismicity is lowered, inland crustal thrust seismicity appears North of the Nazca ridge. It may indicate a change in the compressive regime of the upper plate, constrained by the subduction of the Nazca ridge.

2.2.2 Kinematic and active deformation of the Peru-Chile subduction

The Peru-Chile trench is relatively straight on its Chilean segment and could be roughly approximated as a North-South line. But as soon as we reach the Arica bend, crossing the border with Peru, the trench tilts toward a North-West to South-East orientation and is kind of convex over Peru when seen from the ocean. The obliquity, relative to the trench-perpendicular vector, is ranging from about 20° in Chile to about 40° in South Peru.

While we consider the convergence velocity between the Nazca and South America plates to be quite uniform along the trench, from about 57 mm/yr in Northern Peru to about 68 mm/yr in Chile (Kendrick et al., 2003; Villegas-Lanza et al., 2016), additional rigid block motions (slivers) have been introduced by several authors to better explain

the displacements recorded by geodetic measurements (Figure 2.24). For instance, a *North Andean Sliver* has been introduced by Nocquet et al., 2014 in Ecuador with a ~7.5 mm/yr East-northeast velocity. Nocquet et al., 2014 and Villegas-Lanza et al., 2016 introduced a *Peruvian Sliver*, divided into a Western part with a ~5 mm/yr South-East velocity and an Eastern part with a ~3 mm/yr North-East velocity, separated by crustal faults such as the Cordillera Blanca and the Cuzco fault system. In Chile, Métois et al., 2016 applied an *Andean sliver* with a North-East velocity ranging from about 8 mm/yr in North Chile to about 5 mm/yr in the Maule region, delimited on its Eastern side by the Andean fold-thrust belt, and consistent with the shortening observed by Brooks et al., 2003 in the Bolivian Subandean. However, some authors show that it may possible to discard the use of slivers when accounting for internal deformation (Yáñez-Cuadra et al., 2022) or viscoelasticity (S. Li et al., 2015). In any case, it appears from the overlapping of the Peruvian and Andean slivers (Figure 2.24) and their inconsistent velocities that these slivers cannot explain entirely the deformation at the scale of the Central Andes, notably in the vicinity of the Arica bend where a change from counterclockwise (Peru) to clockwise (Chile) rotation has to be accommodated (Arriagada et al., 2008; M. E. Beck, 2004; Métois et al., 2016).

It is interesting to note that the Andes are very wide in North Chile and South Peru (more than 1,000 km wide), while they are getting thinner southward and northward (Figure 2.23). It is in this area that the Altiplano is located, with more than 4,000 meters highlands. It means that the widest area is located in the vicinity of the Arica bend, where the trench direction is changing drastically, and where we have a dipping slab. It corresponds also to the Central Volcanic Zone, which is characterized by a high crustal thickness of 70 km. In Peru, North of the Nazca Fracture Zone subduction (~17°S) the slab starts to flatten between 80 and 100 km depths (Figure 2.22), this is referred as the Peruvian flat slab. The same phenomenon is observed in Chile but more progressively: the more we go southward of the Arica bend, the more the slab flattens between 80 and 100 km depths. It is between 28°S and 32°S that the slab is the flattest, in the Area referred as the Pampean flat slab, which is characterized by an absence of volcanism (Ramos et al., 2002).

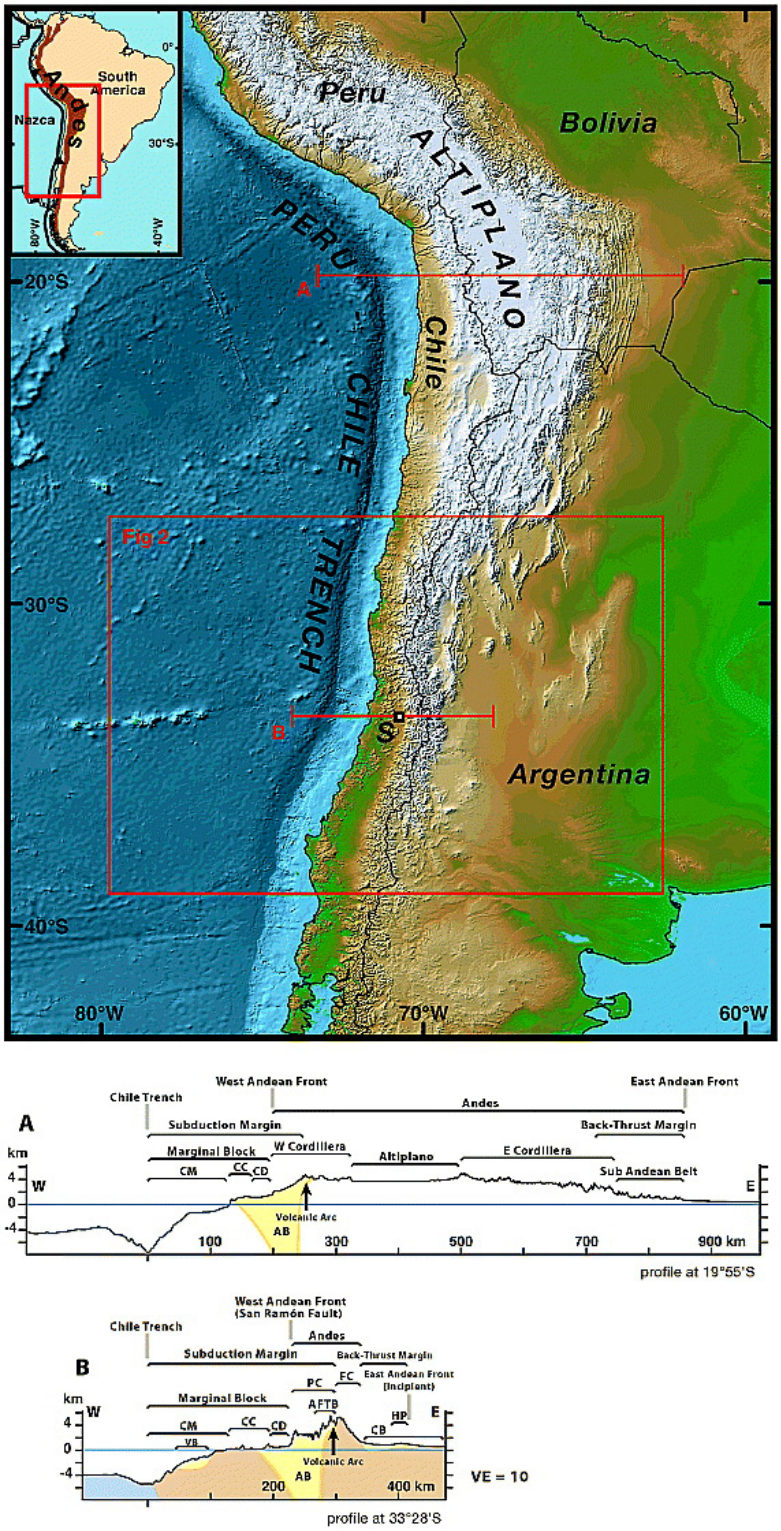

Figure 2.23: Figure from Armijo et al., 2010 showing the topography and the main tectonic features at two profiles: one in Northern Chile at 20°S (profile A), and one in Central Chile close at the latitude of Santiago (33°S, profile B). Profile A corresponds to an area where the Andes are very wide compared to profile B. Triassic and pre-Triassic continental basement are colored in brown, post-Triassic basins in yellow, and oceanic crust in blue on the profiles.

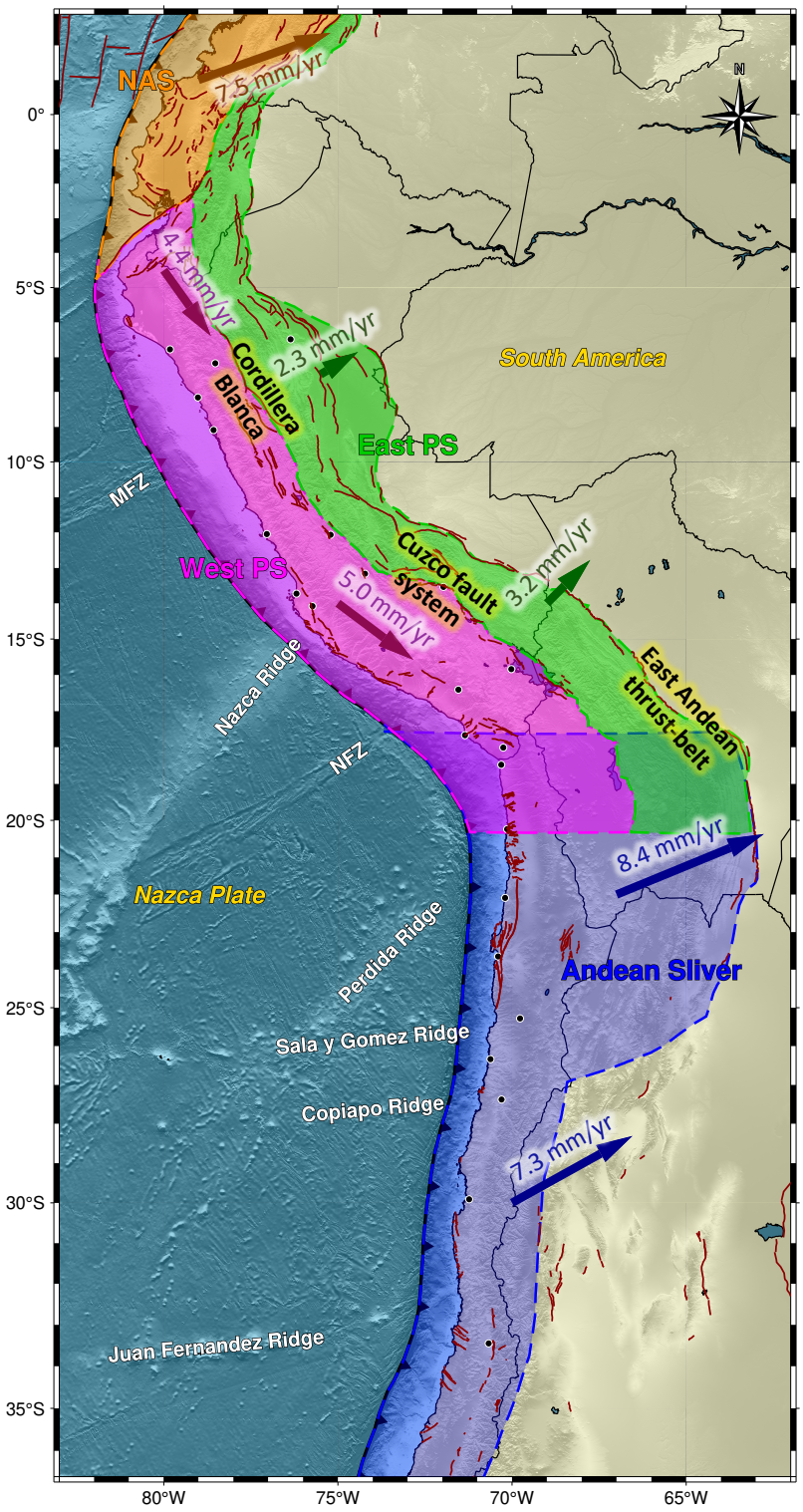

Figure 2.24: Main continental slivers used in geodetic studies over the Peru-Chile trench, with their respective velocities relative to South America: North Andean sliver (NAS, orange) from Nocquet et al., 2014, Western (magenta) and Eastern (green) Peruvian slivers (PS) from Villegas-Lanza et al., 2016, and Andean sliver (royal blue) from Métois et al., 2016. Main active faults are reported as red lines from the GEM Active Faults Database (Styron and Pagani, 2020) and the Chilean Database of Active Faults (Maldonado et al., 2021). The Eastern boundaries of the Eastern PS and Andean sliver are following the East Andean thrust-belt. Note that the Peruvian slivers were defined in a study focused on Peru, while the Andean sliver was defined for Chile, so their South and North boundaries respectively are defined arbitrary. When considering the whole Central Andes, none of these solutions are fully satisfying.

2.2.3 Oceanic structures

Several oceanic features are being subducted on the Peru-Chile trench, affecting the geometry of the slab, the topography, the earthquake ruptures segmentation, and the interseismic coupling distribution (Molina et al., 2021; Philibosian and Meltzner, 2020; Saillard et al., 2017).

In Peru, seven main bathymetric structures can the identified, from North to South: The Grijalva, Alvarado, and Sarmiento ridges, the Virú and Mendaña fracture zones, the Nazca ridge, and the Nazca fracture zone (NFZ). Here we are especially interested by the Nazca ridge and the NFZ. The Nazca Ridge is composed of thick (~18 km) basaltic ocean crust (Woods and Okal, 1994) and is about 200 km wide, with a 1,500-metre extra height on the bathymetry. The high buoyancy of the ridge has led to the flattening of the subduction in Central Peru (Gutscher et al., 2000). It is also believed to be the cause of the Pisco forearc sedimentary basin uplifting (Ochoa et al., 2021). The Nazca ridge is acting as a strong seismic barrier, stopping the rupture of several large earthquakes, including the 2007 Mw8.0 Pisco, the 1996 Mw7.7, or the 1942 Mw8.2 earthquakes (Dorbath et al., 1990; Philibosian and Meltzner, 2020; Villegas-Lanza et al., 2016). Actually, no earthquake has been known to have crossed the Nazca ridge. The ridge is also a persistent low-coupling area on the interseismic coupling distributions (Chlieh et al., 2011; Villegas-Lanza et al., 2016). Similar features of lower coupling and capabilities to slow earthquake ruptures have also been observed for the NFZ, to a lesser extent (Villegas-Lanza et al., 2016). The NFZ is believed to have slowed down the rupture of the 2001 Mw8.4 Arequipa earthquake (Robinson et al., 2006).

In Chile, several oceanic ridges are also subducting: the Iquique, Perdida, Sala y Gomez, Copiapo, and Juan Fernandez ridges. The Juan Fernandez ridge subduction (~32-33°S) is often used to explain the Pampean flat slab (Gao, Yuan, et al., 2021; Gutscher et al., 2000; von Huene et al., 1997). Several of these bathymetric features have also been reported as seismic barriers and areas of lower coupling, notably the Iquique and Juan Fernandez ridges (Métois et al., 2016; Molina et al., 2021; M. Moreno et al., 2011; Philibosian and Meltzner, 2020).

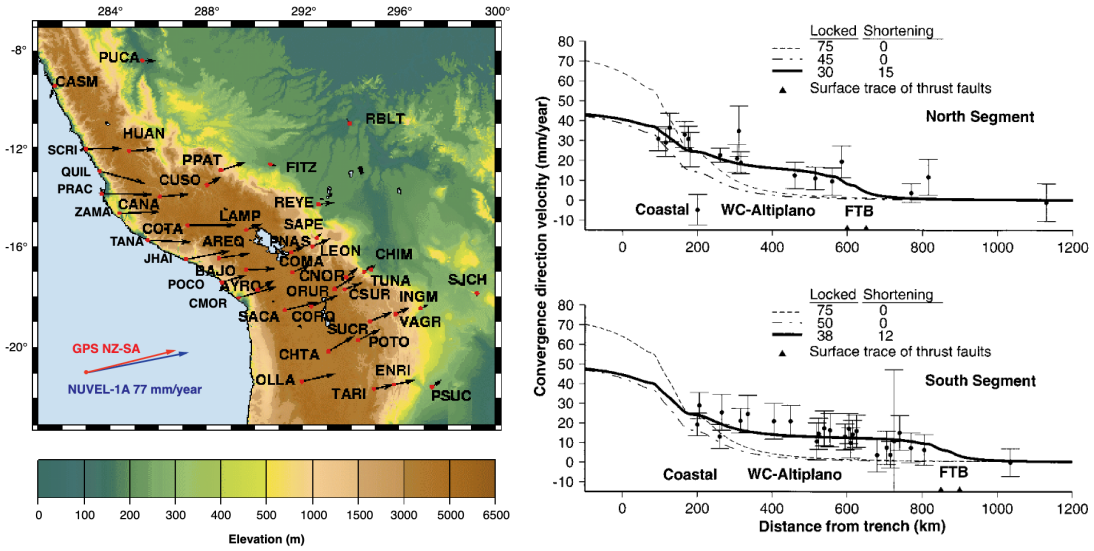

Figure 2.25: Figures from Norabuena et al., 1998 showing the GNSS network they used (left) with the crustal deformation model they proposed (right).

2.2.4 Review of interseismic coupling models in Central Andes

Since the development of GNSS measurements in the 1990's, several models of interseismic coupling have been published for the Peru-Chile trench, essentially considering an elastic rheology. In this section we review some of the interseismic coupling models proposed across Central Andes, in Central to South Peru and North Chile.

Elastic models

Norabuena et al., 1998 used 43 GNSS sites from 8°S to 22°S, including one permanent GNSS site and 42 survey sites measured in 1994 and 1996 in the frame of the SNAPP project (Figure 2.25). They proposed a simple model with a 50% locking down to a 20-km depth with a 12 mm/yr crustal shortening.

Using a similar dataset, Bevis et al., 2001 proposed a model with a near 100% locking between 10 and 50-km depth, with a 5-6 mm/yr shortening.

Following the seafloor geodesy acquisitions conducted in 2001 and 2003 offshore of Central Peru, Gagnon et al., 2005 concluded that the locking is very high on the shallow part, from 2 to 40 depth (Figure 2.26). This may explain why the area is prone to host tsunami-earthquakes, like the 1996 Mw7.7 Nazca earthquake (Satake and Tanioka, 1999). However this study does not enable to capture lateral variations in the shallow

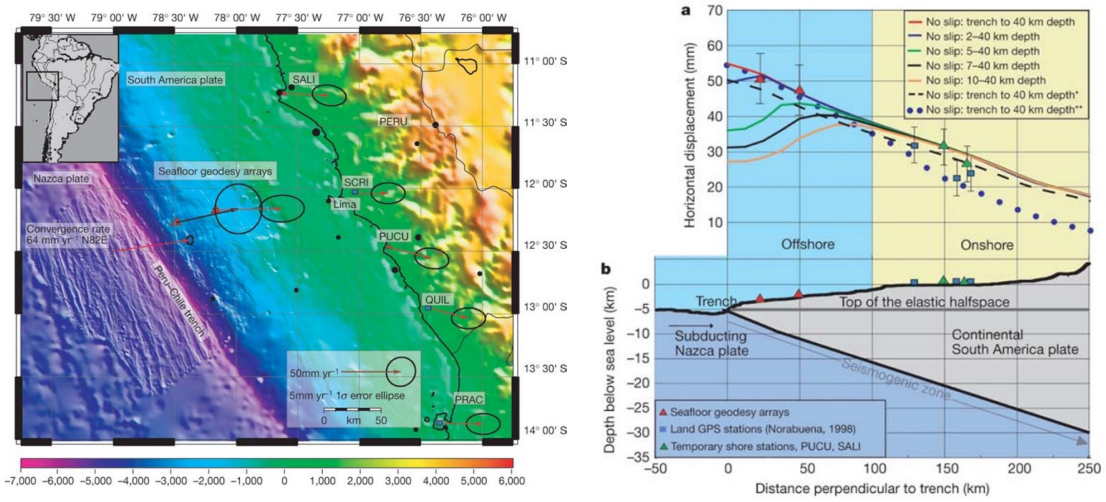

Figure 2.26: Figures from Gagnon et al., 2005 showing the location of the seafloor geodesy arrays (left) and the various surface deformation models they propose with various locking depths. There data required shallow locking close to the trench.

locking, as the seafloor measurements were all performed at a similar latitude (about 12.2°S).

The analysis from Chlieh et al., 2011 combined the survey GNSS measurements from Norabuena et al., 1998 with the ones from Gagnon et al., 2005 and additional GNSS measurements in North Chile, bringing the total number of observation sites to 87 (Figure 2.27). In addition, they use an InSAR ERS (European Remote Sensing satellite) interferogram mapping the deformation in North Chile between 1995 and 1999. By inverting these data, they propose an heterogeneous coupling distribution in Peru with two locked asperities offshore of Lima and Pisco, between the Nazca ridge and the NFZ, and between the NFZ and the Arica bend. Low coupling is observed where the Nazca ridge and the NFZ are subducting. The coupling distribution they propose in North Chile is more homogeneous, with a very high locking from the Arica bend to Antofagasta (where the model stopped), from the trench to a 50-km depth.

Using 100 GNSS sites from Bogota to Lima, Nocquet et al., 2014 showed that the coupling in North Peru (North of 10.5°S) is very low, with sub-millimeter annual velocities at the surface (Figure 2.28). It seems that the coupling is decreasing significantly when crossing the Mendana fracture zone: from a value of about 0.8 South of the ridge, it drops to zero North of the ridge. Still, some relatively large earthquakes have been observed on the North Peru subduction: a Mw7.6 in 1960 and a Mw7.5 in 1996. This observation may seem contradictory with the absence of apparent locking in the area, however it may be explained by shallow locking (less than 10 km deep) not observed at GNSS sites as they are too far from the trench. It is consolidated by the fact that

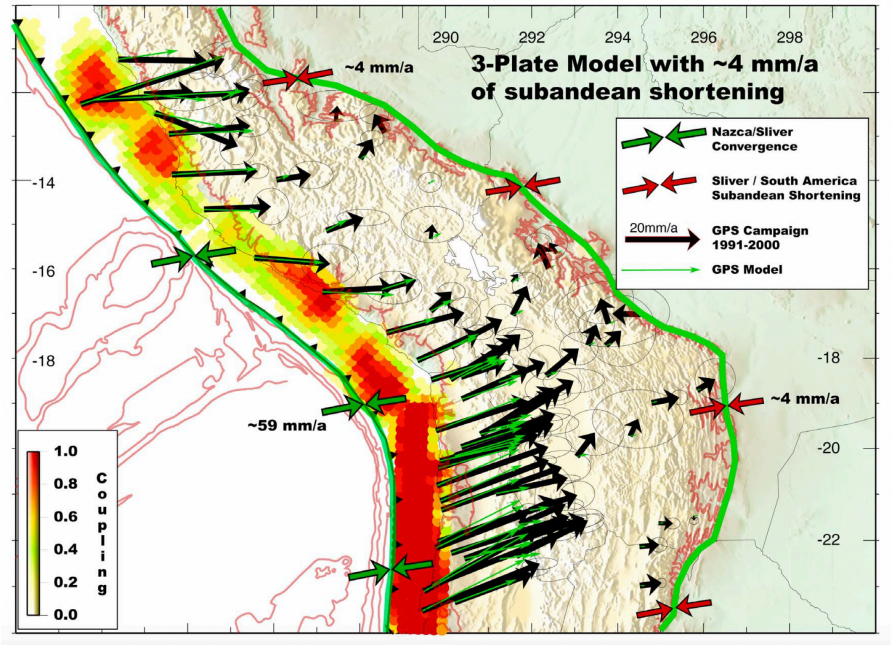

Figure 2.27: Figure from Chlieh et al., 2011 showing their interseismic coupling model for Central-South Peru and North Chile, with 4 mm/yr of Subandean shortening. The coupling is very high and almost uniform on the Chilean segment, while it is highly heterogeneous in Peru, with low coupling where the Nazca ridge and NFZ are subducting. However, it should be noted that the data are significantly sparser in Peru.

the 1960 and 1996 earthquakes generated tsunamis, which is often associated with a shallow rupture.

Following this 2014 study, Villegas-Lanza et al., 2016 analyzed over 100 GNSS sites over the whole Peru on the 2008-2013 period to compute a new coupling model for the Peru subduction. They first compute a coupling model with a simple two-plate model (Figure 2.29). Similar to Nocquet et al., 2014, they observe very low coupling on the North Peru segment, but with small locked asperities. In Central Peru the locking is quite high (>0.8), as well as in South Peru with two locked asperities: one between the Nazca ridge and the NFZ, and one between the NFZ and the Arica bend.

Interestingly, the residuals from the inversion of the GNSS velocities are mainly oriented toward the South-East quarter, which means that there is a systematic trend that was not accounted for. From this observation, they propose another model with a three-plate geometry: a rigid sliver (named Peruvian Sliver, PS) has been added between the Nazca and South America plates, for which the ~5 mm/yr South-East motion has been assessed from the residuals of the former inversion (Figures 2.30 and 2.31).

The coupling distribution remains relatively similar to the two-plate model in pattern, but with less coupling overall (Figure 2.30). The residuals are now uniformly distributed in direction, and most of them are below 2 mm/yr, meaning that the fit was improved and that the systematic trend was removed.

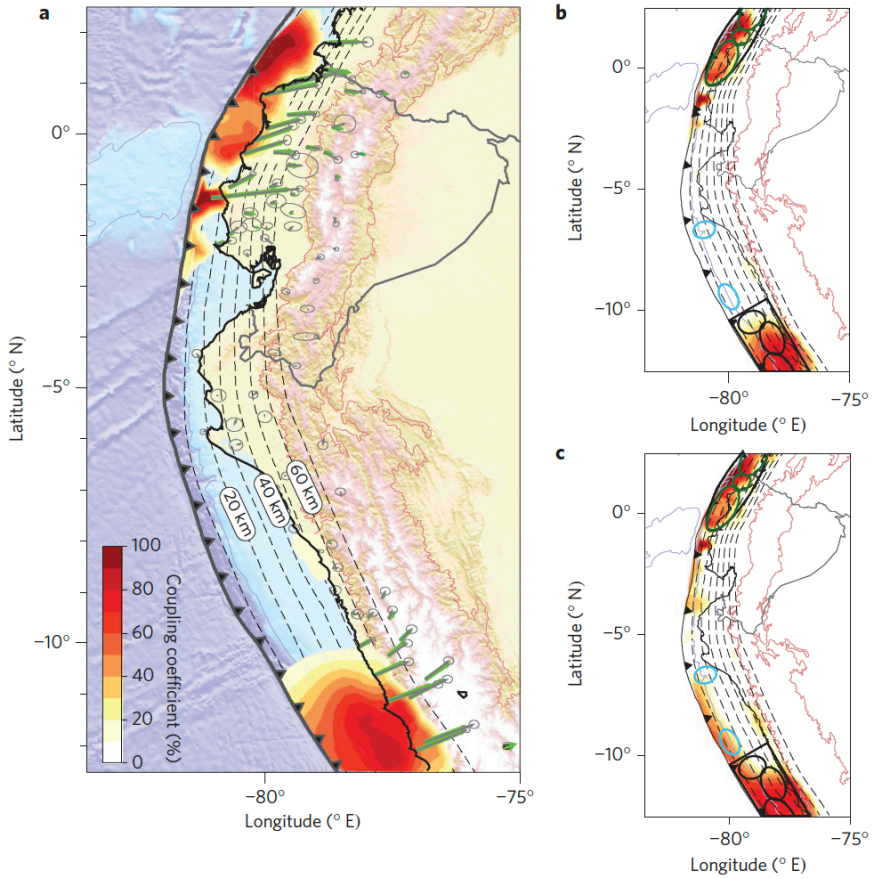

Figure 2.28: Figure from Nocquet et al., 2014 showing the coupling distribution in Northern Peru. The model on panel *a* shows full creeping from 3°S to 10°S, while the model on panel *c* shows shallow coupling close to the trench. This difference results from the different slip priors in the inversion: creeping slip prior (zero coupling) for panel *a* and locked slip prior for panel c. The slip prior has an impact in the areas with poor resolution, notably close to the trench because of the remoteness of the GNSS sites (no offshore GNSS). Finally, panel *b* shows the same model as panel *a* with some coseismic ruptures, including the 1960 Mw7.6 and 1996 Mw7.5 tsunami earthquakes in North Peru (blue contours).

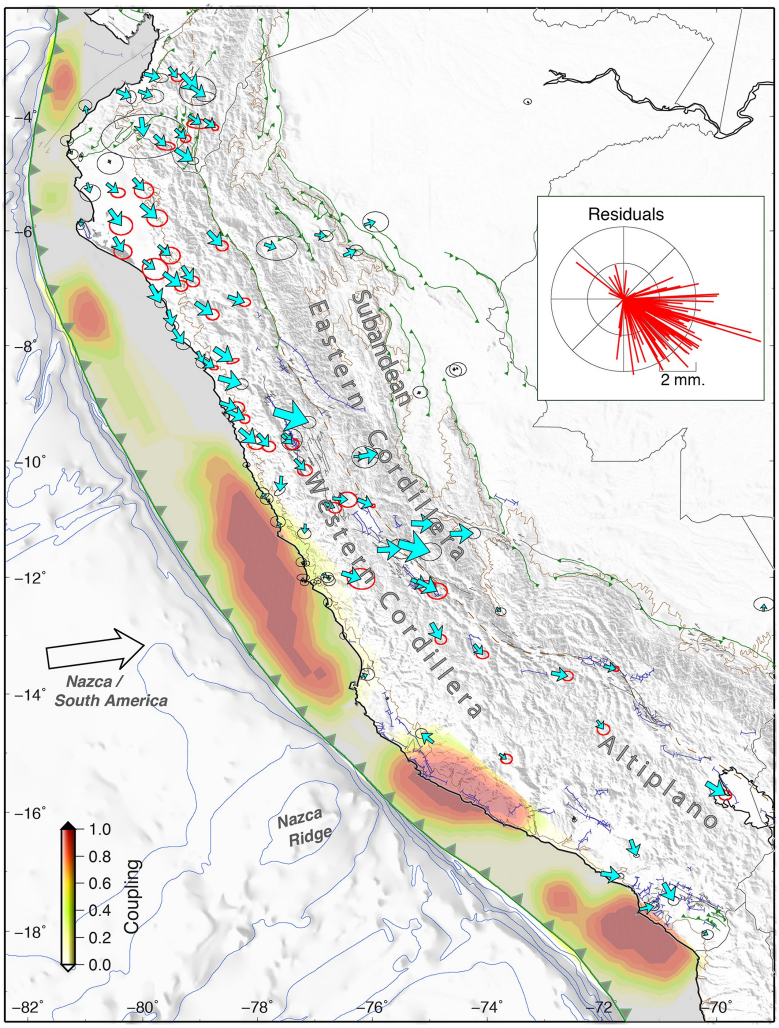

Figure 2.29: Figure from Villegas-Lanza et al., 2016 showing their coupling distribution from the inversion of over 100 GNSS sites in Peru, with a two-plate model. Residuals from the inversion are depicted by the blue arrows, and are also reported on the rose. They are relatively high and most of them are oriented in the South-East quarter.

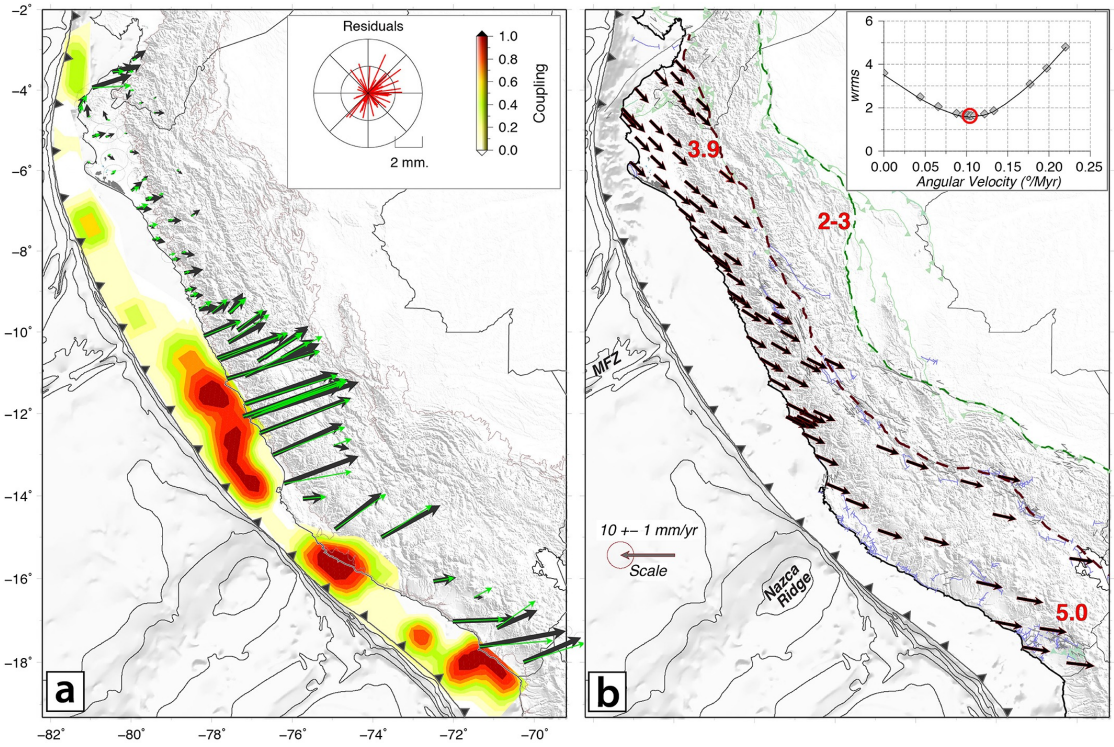

Figure 2.30: Figure from Villegas-Lanza et al., 2016 showing the coupling distribution with the three-plate model (panel *a*), accounting for a sliver motion. The observed and predicted interseismic GNSS displacements are displayed as black and green vectors respectively. The residuals on the rose are now uniformly distributed in direction, and most of them are below 2 mm/yr. On panel *b* is shown the predicted displacement of the sliver.

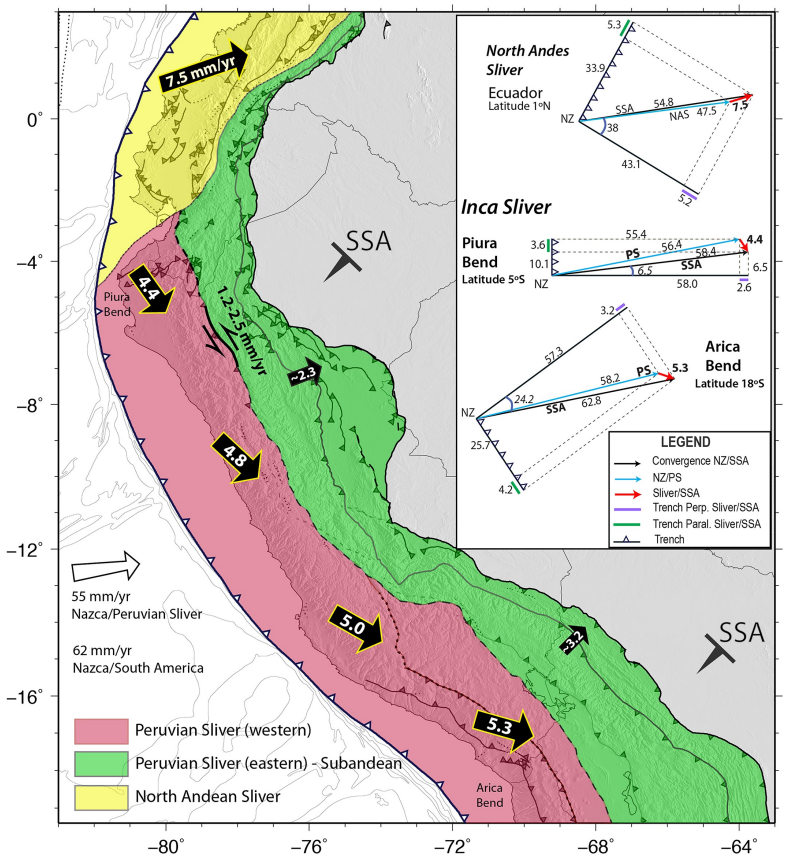

Figure 2.31: Figure from Villegas-Lanza et al., 2016 indicating the continental slivers involved in the partitioning of the deformation on the Peruvian margin: the North Andean Sliver (NAS) from Nocquet et al., 2014, the Peruvian Sliver (PS), and the Eastern Cordillera - Subandean region. Velocities are expressed in the SSA reference frame, in mm/yr.

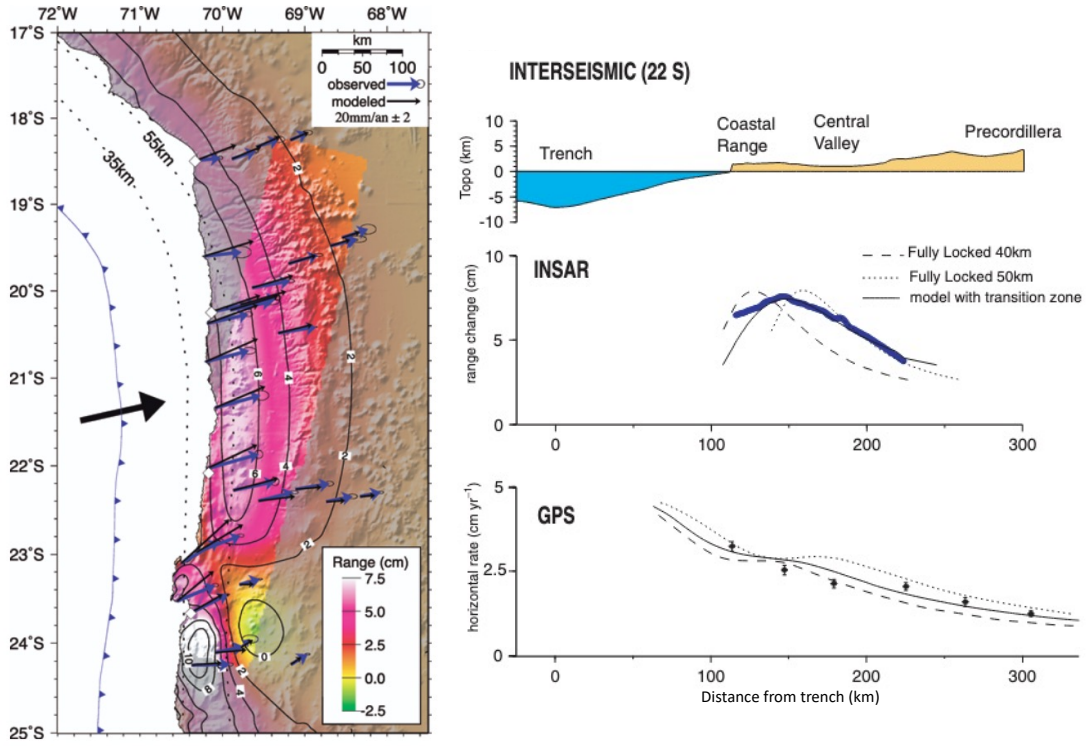

Figure 2.32: Figure modified from Chlieh et al., 2004 showing the fit of the interseismic model to the GNSS and InSAR data. On the left panel, dotted lines indicate the 35 (boundary between full locking and the transition zone) and 55 (boundary between the transition zone and the creeping zone) km isodepth contours. On the right panel the fit to InSAR and GNSS data along a profile at 22°S.

Let's now look at the interseismic coupling models that have been proposed on the Chilean part of the subduction, notably from 18°S to 28°S.

Chlieh et al., 2004 was one of the first studies to perform an analysis of interseismic velocities at the scale of North Chile (18°S to 25°S). They used five years of GNSS measurements (1996 to 2001), including 26 survey sites and 2 continuous stations installed in 1995 and located in the vicinity of the Iquique city (Figure 2.32). In addition, they used two ERS interferograms spanning on 3 years each (1996 to 1999). They were able to fit these data with a relatively simple model of coupling: full locking down to 35 km, a transition zone from 35 to 55 km, and no coupling deeper than 55 km.

Métois and collaborators released an interseismic coupling model on a large portion of the Chile subduction (18°S to 38°S) from GNSS measurements spanning on the 2004-2012 period through four articles. Métois et al., 2012 focused on the 24°S to 38°S segment, while Métois et al., 2013 focused on the North Chile seismic gap from 18°S to 24°S, and Métois et al., 2014 added new measurements in the Atacama region (25°S to

29°S). They added some complexity by considering an Andean sliver motion (Brooks et al., 2003; Vigny et al., 2009), leading to a three-plate model.

They estimated in Métois et al., 2014 an Euler pole of 39.2°S ±2, 61.5°W ±2, −0.25°/Myr ±0.1 from the residuals for a two-plate inversion, corresponding to a Northeast block motion of about 5 mm/yr with a 2 mm/yr gradient from North to South (Figure 2.24). Their arguments for justifying the introduction of this sliver, apart from the structural elements indicating the presence of some thrust faults in the Subandean region (Brooks et al., 2003; Ramos et al., 1986; Vigny et al., 2009), are a better fit to the horizontal displacements in the far field and to the vertical displacements in general. While the first point is effectively shown by their results (Figures 2.33 and 2.35), the second point is more questionable (Figure 2.34). Vertical displacements are not significantly better fit with the three-plate plate, as only the near range sites on profile *a* and the sites of profile *b* appear to be better fit but with still a significant misfit.

Finally, they wrapped up everything in Métois et al., 2016 in order to have a unified coupling model from 18°S to 38°S, and sticking to a three-plate model. The dataset includes 396 horizontal velocities and 70 vertical velocities, allowing a dense mapping of the deformation in Chile (Figure 2.36). Still, some weaknesses remain in the instrumentation, notably with a more than 150-km gap along-strike in the Taltal area (~25°S). The coupling distribution they obtain is highly heterogeneous (Figure 2.37), with some locking all along the subduction but with varying depth and width. Several areas of lower coupling are observed where oceanic features are subducting: the Iquique, the Mejillones, the Baranquilla, and the San Antonio low coupling zones. Deeper coupling (more than 40 km depth) appears to be limited between 28°S and 32°S which corresponds to the Pampean flat slab. They also observe a convincing overlap between the coseismic ruptures of the 2010 Mw8.8 Maule, 2014 Mw8.1 Iquique, and 2015 Mw8.4 Illapel earthquakes, and the areas of high coupling (>0.8).

The study from Klein et al., 2018 plugs the gap in the Taltal region, by analyzing 20 sGNSS sites measured at least three times between 2012 and 2018 (Figure 2.38). They propose an interseismic coupling model from 21.5°S to 28.5°S showing a low-coupling anomaly where the Salas & Gomez ridge is subducting (~25°S). Interestingly, the sliver motion proposed by Métois et al., 2014 was not able to fit the GNSS velocities in the Taltal region, which require an additional block motion of about 8 mm/yr, suggesting that a single rigid Andean sliver may be too simplistic. In this way, several authors have explored the possibility of continuous internal deformation instead of a rigid block motion, that we are going to discuss in the next paragraphs.

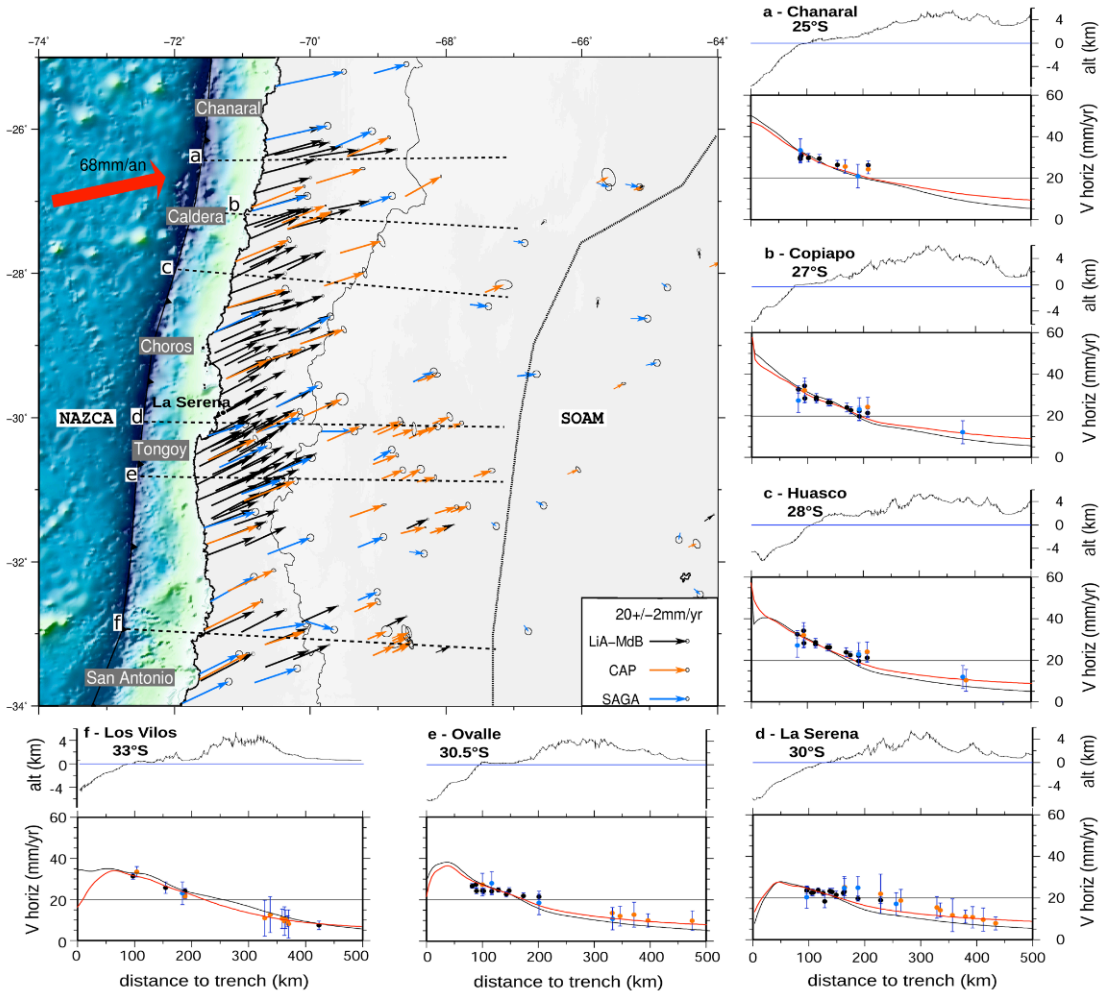

Figure 2.33: Figure from Métois et al., 2014 showing their observed interseismic velocities (black vectors) on a map, along with two previously published datasets (CAP in orange and SAGA in blue), in the SSA reference frame. The Eastern boundary of the Andean sliver is indicated by the black dotted line. Six profiles are plotted (panels *a* to *f*) to show the agreement between the GNSS velocities (dots) and the deformation model with a two-plate (black line) or three-plate model (orange line). The three-plate model fits better the sites in the far range, although it is more difficult to state for the Northern profiles due to the sparsity of the data.

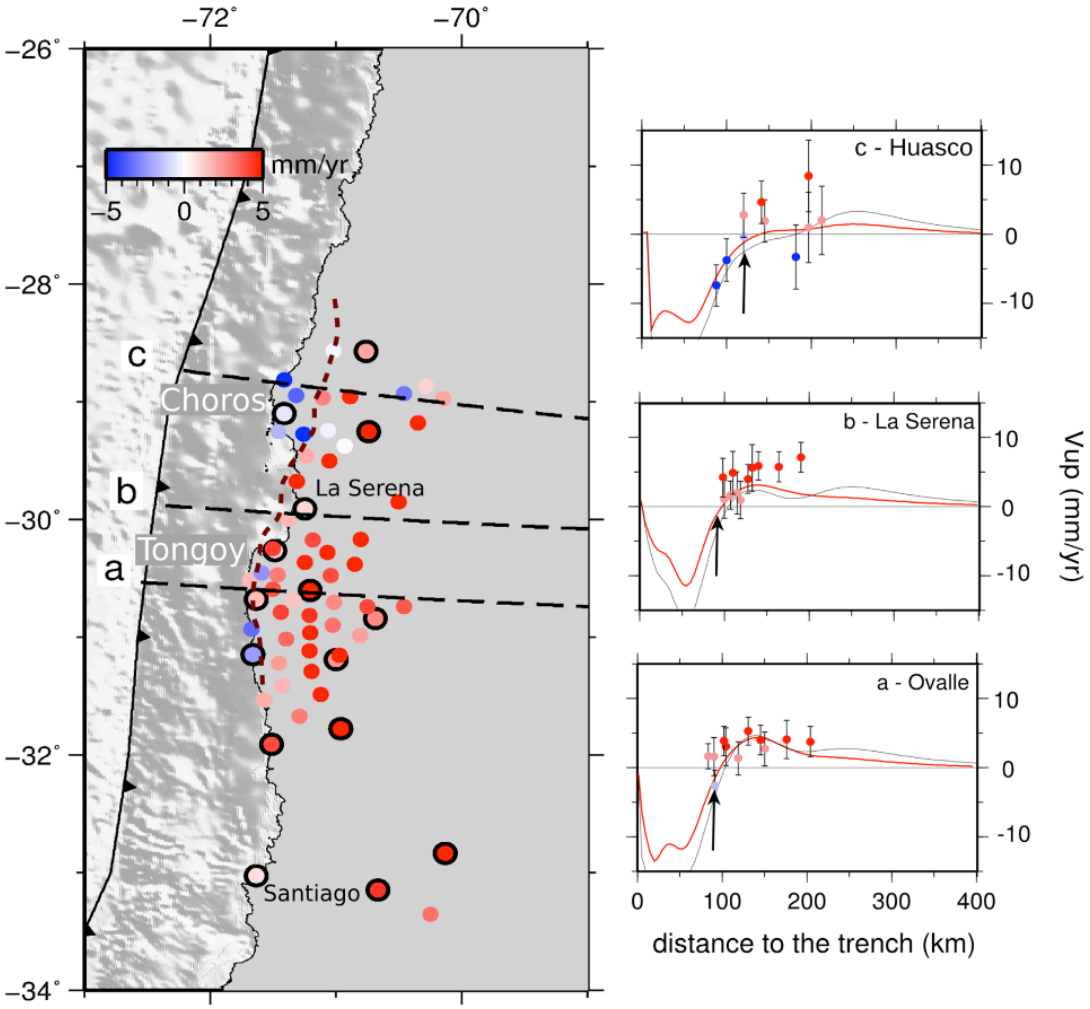

Figure 2.34: Figure from Métois et al., 2014 reporting the observed vertical GNSS velocities. Subsidence is indicated in blue while uplift is in red. cGNSS stations are surrounded by a black contour. Three profiles (a, b, c) are shown with the two-plate model in black and the three-plate model in red. The authors argue that the three-plate model fits better the vertical displacements, which is somewhat questionable. Actually, only the near range sites on profile *a* and the and the sites of profile *b* appear to be better fit but with still a significant misfit.

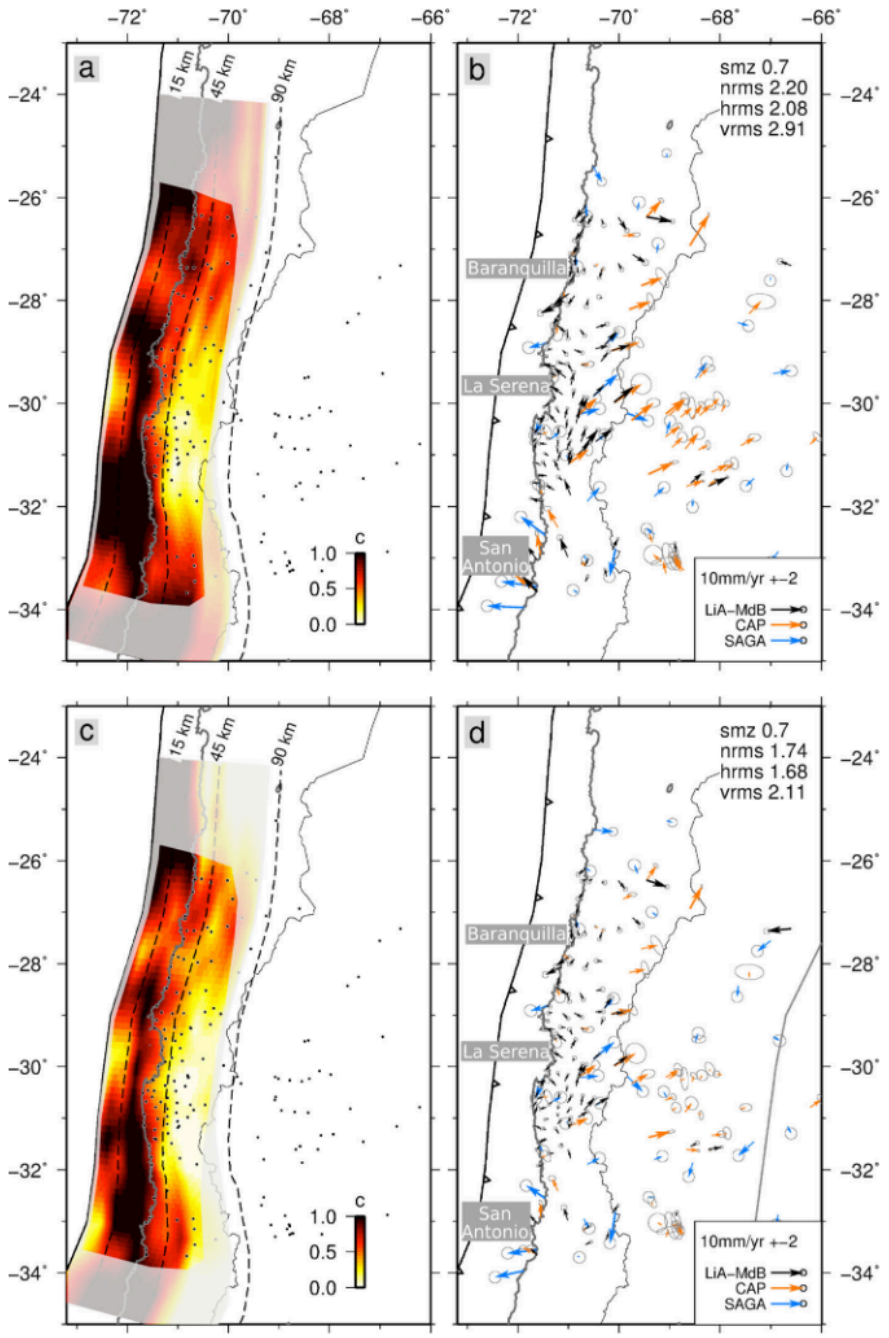

Figure 2.35: Figure from Métois et al., 2014 showing the interseismic coupling distributions for a two-plate (a) or a three-plate (c) model, with their associated residuals on panels (b) and (d) respectively. Areas with low resolution are indicated in gray. Overall, most of the residuals appear to be lowered by adding the third plate, as well as the average coupling.

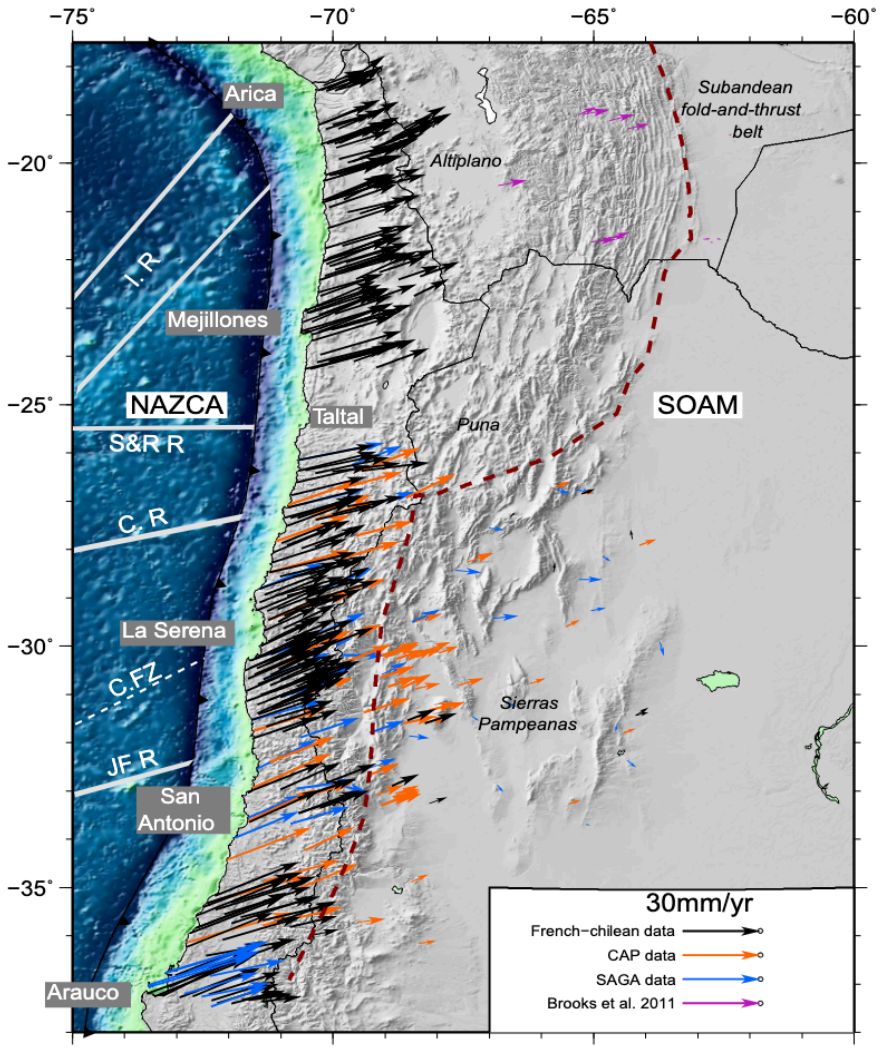

Figure 2.36: Figure from Métois et al., 2016 showing the horizontal interseismic velocities in the SSA reference frame. Data processed by the authors (in black) are complemented with other velocity fields (CAP, SAGA, and Brooks et al., 2011) for a total of 396 sites. Note that a major gap remains in the Taltal area.

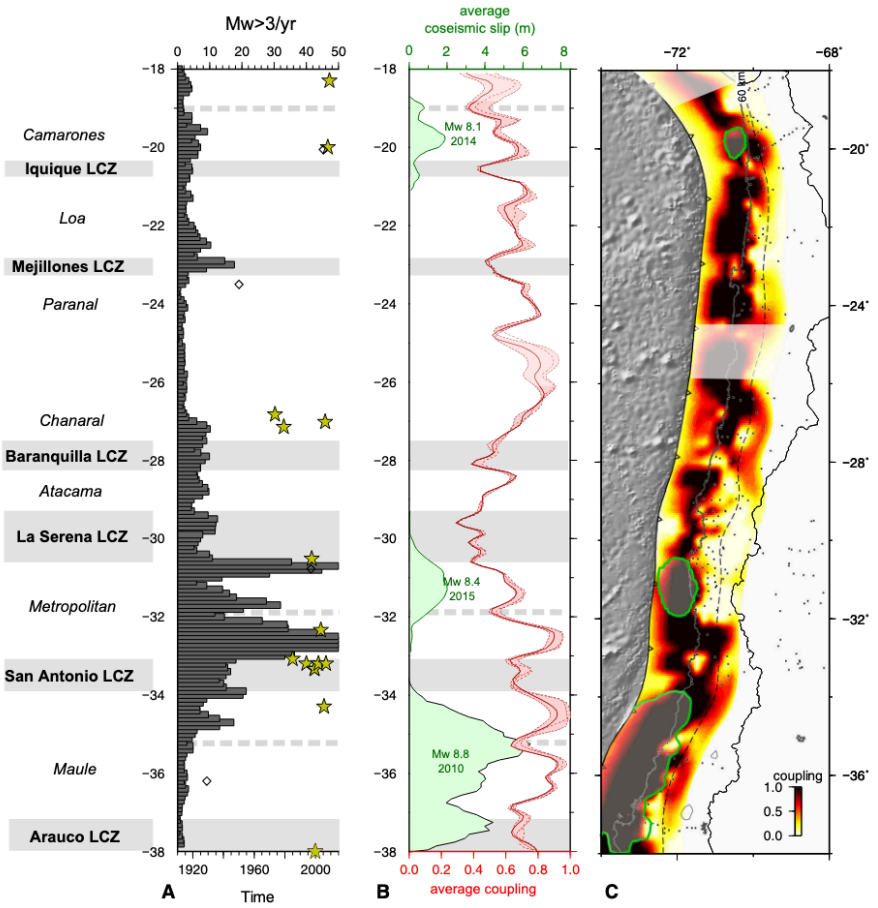

Figure 2.37: Figure from Métois et al., 2016 showing heterogeneous coupling on the Chile subduction. The histogram on panel *A* depicts the rate of Mw>3 earthquakes from the CSN seismic catalog during the interseismic period. Yellow stars indicate swarm-like sequences. Diamonds indicate significant intraplate earthquakes. Panel *B* is showing the variations of coupling, averaged along-dip, and the slip distributions for the Maule, Iquique, and Illapel earthquakes. Finally, panel *C* is showing the coupling distribution with the rupture areas of the Maule, Iquique, and Illapel earthquakes. Note that some areas, highlighted by white rectangles, lack resolution. Overall, coupling is varying significantly along strike and along dip. We observe lowered coupling where some oceanic features are subducting: the Iquique, the Mejillones, the Baranquilla, and the San Antonio ridges. Seismic ruptures overlap quite well with highly locked patches.

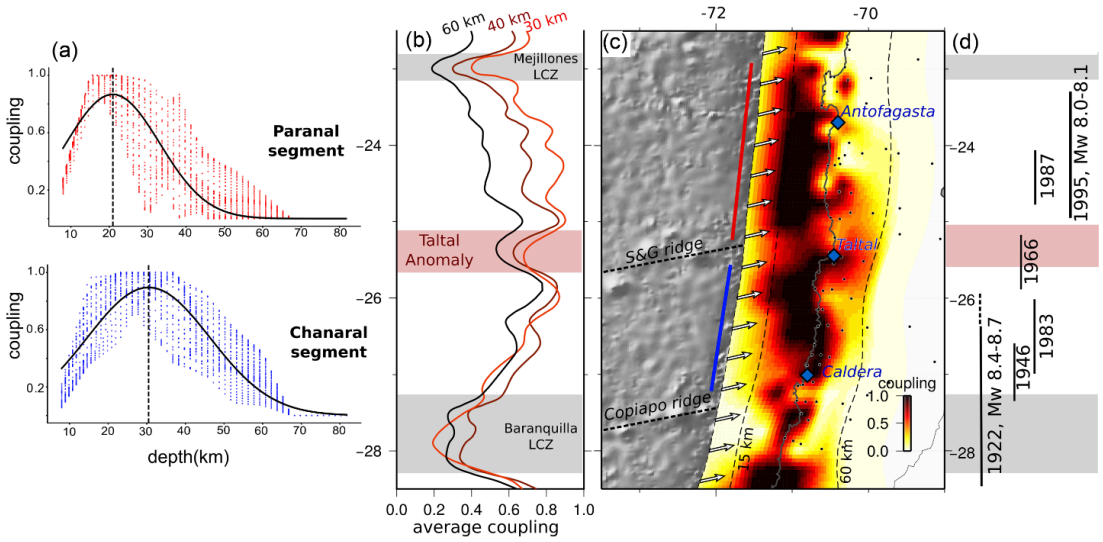

Figure 2.38: Figure from Klein et al., 2018 showing their best coupling model (c), with along strike variations (b) when integrated down to 30 (red), 40 (dark red), or 60 (black) km. We observe a low-coupling anomaly where the Salas & Gomez ridge is subducting. Major earthquake ruptures are reported on panel (d). Variations of coupling along deep averaged on two segments are reported on panel (a). It shows that on the Northern segment (red) the depth of maximum locking is about 20 km, while it is about 30 km on the Southern segment.

Deformation of the upper plate

On a segment from 23°S to 30°S, Yáñez-Cuadra et al., 2022 showed that the sliver motion can be discarded by accounting for internal deformation (Figure 2.39). They also use a conventional linear least-square inversion in an elastic half-space, but with the adjunction of a *regional motion model* which is basically a linear gradient of surface deformation intended to model a progressive internal deformation.

The internal deformation they simulate has the effect of generating a shallower locking distribution, most of the coupling being located between the trench and a 30-km depth. The along strike segmentation is quite similar to the results from Métois et al., 2016 and Klein et al., 2018, except that they do not recover the Taltal low-coupling anomaly from Klein et al., 2018. Otherwise, they observe a decrease in coupling where the Barranquilla and La Serena ridges are subducting. The authors conclude that a rigid sliver motion was not required when accounting for internal deformation, and that the extensional strain rate they observe in the direction of the plate convergence is compatible with what is expected for fore-arc extensional tectonics (Cortés-Aranda et al., 2021; González L. et al., 2006).

Jolivet et al., 2020 are interested in quantifying permanent plastic deformation in Northern Chile (18°S - 24°S). They start from the observation that the coastal domain along subduction zones is affected by long-term (10^5 - 10^6 years) vertical displacement, notably in Chile (Regard et al., 2010; Saillard et al., 2009) or in Japan (Matsu'ura, 2015), meaning that the deformation during the seismic cycle is not purely elastic. The rate of this persistent vertical deformation is expected to be about ten times lower than the typical interseismic vertical deformation rate, in the order of tenth of millimeters per year versus millimeters per year (Béjar-Pizarro et al., 2013; Jolivet and Simons, 2018; Melnick, 2016; Regard et al., 2010). The authors would like to assess what fraction of this permanent deformation is acquired during the coseismic or the interseismic phase of the seismic cycle. They inverted the GNSS displacements from Métois et al., 2016 and InSAR Envisat time series over the 2003-2010 period to model the interseismic coupling (Figure 2.40). Note that modeling the coupling was not the main objective of this paper, as they use it more to compute interseismic vertical displacement rates, but it is still interesting to see if adding InSAR data can change the coupling segmentation compared to Métois et al., 2016 (keeping in mind that the inversion method is different).

It appears that the along-strike segmentation is quite similar to Métois et al., 2016, with low coupling where the Iquique and Mejillones ridges are subducting, except that low coupling is now observed North of the Iquique earthquake rupture (~20°S). This later point may be explained by the fact that Jolivet et al., 2020 allowed their coupling model to go as low as 80 km depth, leading to some very deep coupling between 60 and 80 km deep, notably in the Northern part. In addition, the resolution close to the trench in the Northern part (North of 20°S) is low due to increasing distance from the

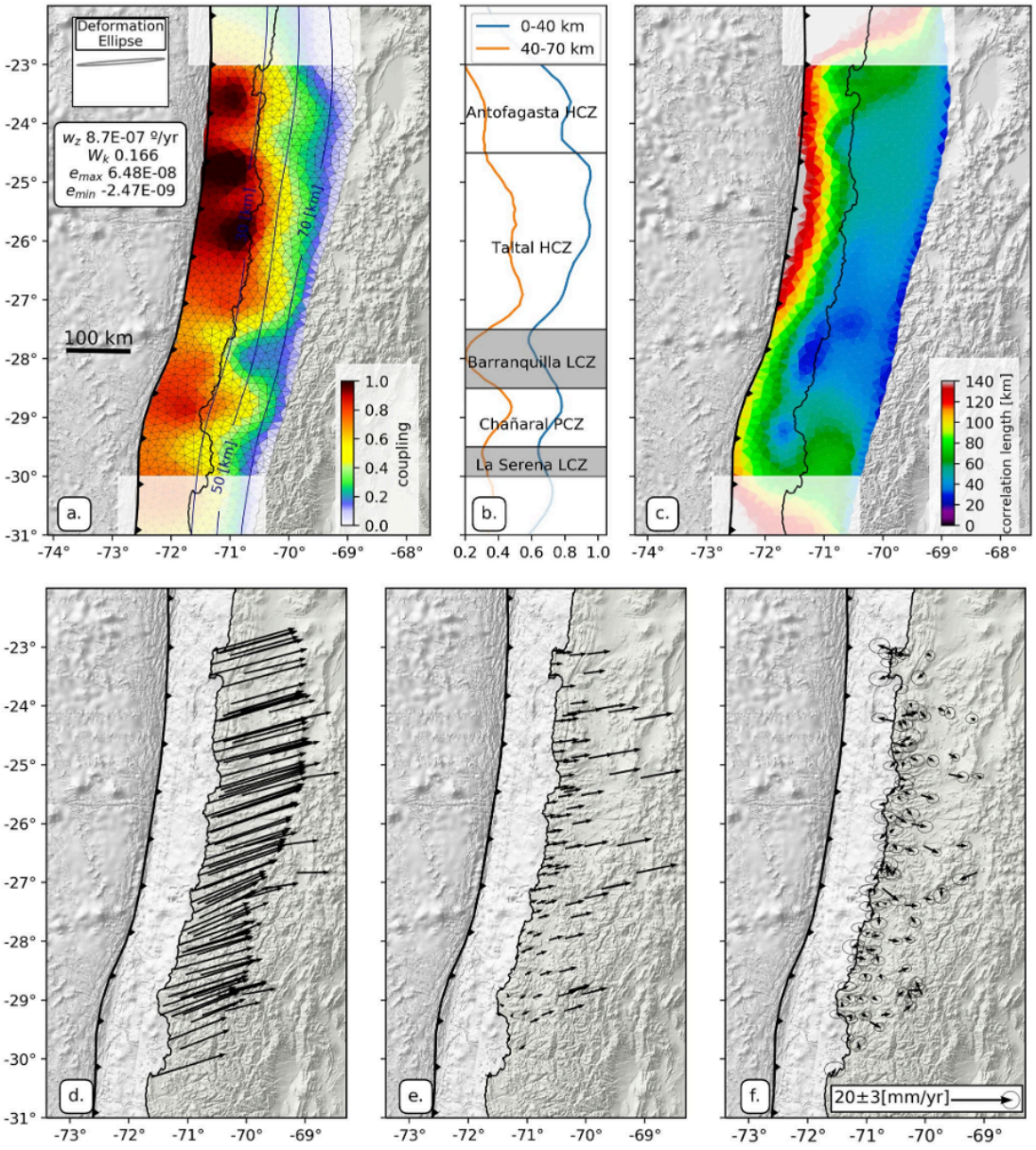

Figure 2.39: Figure from Yáñez-Cuadra et al., 2022 showing their interseismic coupling distribution (a) with its along-strike variations (b) integrated between 0 and 40 km (blue) or between 40 and 70 km (orange). Panel (c) shows posterior coupling correction lengths. Panel (d) shows the modeled surface velocities for their interseismic coupling model and panel (e) the regional motion model. Finally, panel (f) shows the residuals.

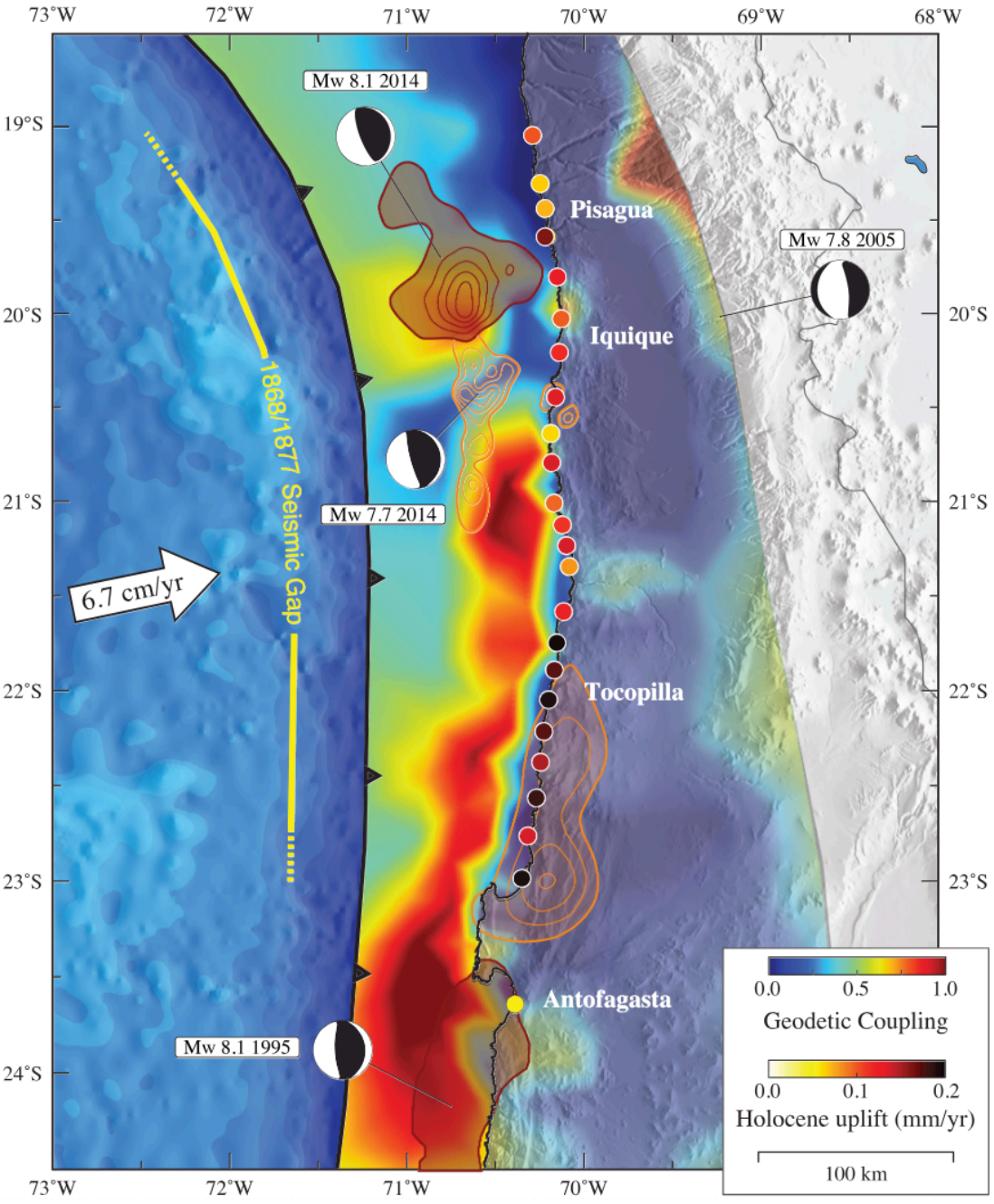

Figure 2.40: Figure from Jolivet et al., 2020 showing the coupling distribution they obtained by inverting interseismic GNSS velocities from Métois et al., 2016 and Envisat InSAR time series. The colored discs indicate the holocene uplift rates from Melnick, 2016.

trench to the coast.

They compared the uplift rates from their coupling model to the Holocene uplift rates from Melnick, 2016 and they concluded that about 4 to 8% of the interseismic deformation is not canceled-out by coseismic and postseismic deformation, leading to permanent deformation over the seismic cycle.

Viscoelastic models

M. Moreno et al., 2011 modeled the coupling on the South-Central Chile segment (36° to 46°S). They used GNSS data from 42 survey sites measured between 2002 and 2009, and 12 continuous stations recording on the ~2005 to ~2010 period (Figure 2.41). The velocities obtained from these sites have been combined with 86 velocities spanning the 1994-2005 period published in Klotz et al., 2001, Ruegg et al., 2009, and K. Wang et al., 2007.

Since this area is affected by the postseismic displacements following the great 1960 Mw9.5 Valdivia earthquake that are expected to last at least 70 years (Hu et al., 2004; K. Wang et al., 2007), the authors developed a more refined modeling strategy to assess the interseismic coupling: they simulate the viscoelastic relaxation associated with the 1960 earthquake using a finite element method (FEM) model for various viscosity values (continental mantle viscosity between $1{\cdot}10^{19}$ and $6{\cdot}10^{19}$ Pa·s), and they compute viscoelastic Green's functions in order to model the interseismic coupling. The resulting coupling distribution corrected from the postseismic viscoelastic relaxation shows some heterogeneity (Figure 2.42), but overall it is highly locked. Lower coupling is observed at about 39°S, which may be related to the subduction of the Valdivia fracture zone. Furthermore, a large gap of coupling is observed at about 46°S where the Chile ridge is subducting. However, we should keep in mind that the less coupled areas may also result from a lack of resolution because of the sparsity of the GNSS network in some places, notably in the South. In addition, the authors are able to provide information on the rheology of the subduction zone on this segment. They propose segmented optimal continental viscosity: $4{\cdot}10^{19}$ Pa·s North of 42°S, $3.5{\cdot}10^{19}$ Pa·s from 42°S to 44°S, and $3{\cdot}10^{19}$ Pa·s South of 44°S. They indicate that this decreasing gradient of velocity toward the South is in agreement with the heat flow increase resulting from the subduction of a younger oceanic plate in the South. Still, this is important to note that this gradient in optimal viscosity is relatively small and that other parameters could influence it, notably the viscosity of the oceanic plate that was taken uniform ($1{\cdot}10^{20}$ Pa·s) while it could also vary along strike due to the age gradient.

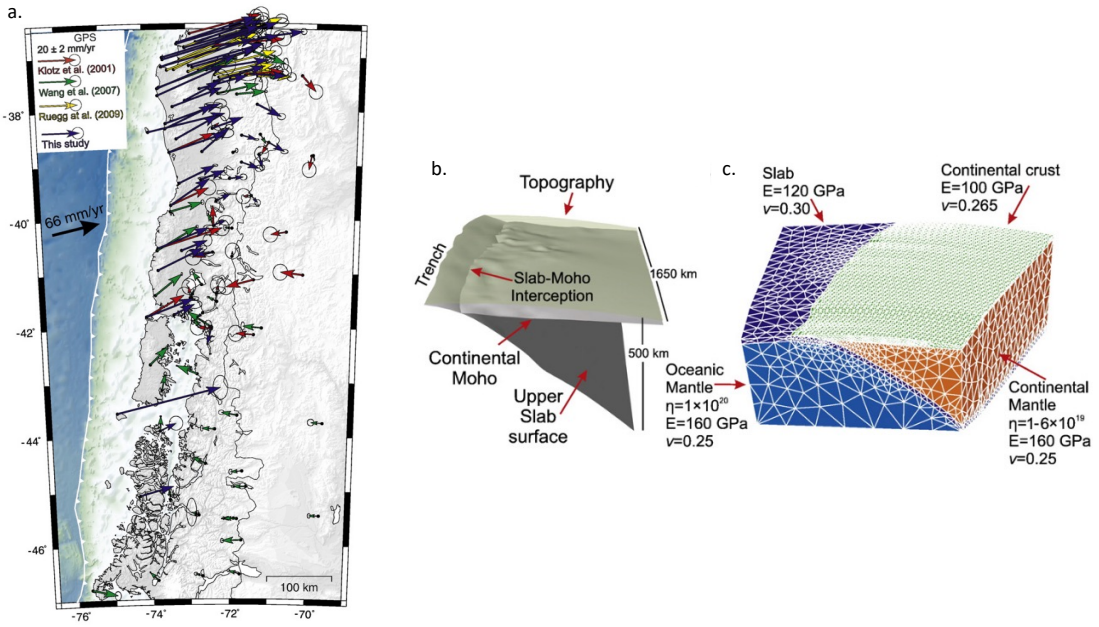

Figure 2.41: Figure modified from M. Moreno et al., 2011 showing on panel *a* the GNSS velocities in the SSA reference frame. On panel *b* is shown the structure of the FEM model they use, with the Young's modulus E, the Poisson's ratio ν, and the viscosity η (for viscoelastic blocks only). Four blocks are defined: slab and continental crust (elastic), oceanic and continental mantle (viscoelastic).

S. Li et al., 2015 developed 2-D and 3-D FEM models of the Chilean subduction to explore the effects of viscoelastic relaxation of the asthenosphere on the coupling.

They focused on North Chile from 18°S to 25°S and build four-block models of the subduction (Figure 2.43): elastic oceanic and continental plates, and viscoelastic oceanic (viscosity of $1{\cdot}10^{20}$ Pa·s, rigidity of 64 GPa) and continental (viscosity of $4{\cdot}10^{19}$ Pa·s, rigidity of 64 GPa) mantles. Forward models show that larger horizontal displacement are observed with viscoelasticity, especially in the far-field (Figure 2.44). In addition, viscoelasticity increases the amplitude of uplift and subsidence, and generates secondary zones of uplift and subsidence. Then, they compute viscoelastic Green's functions in order to invert the GNSS velocities in a viscoelastic medium. The resulting coupling distribution shows shallower locking and lower misfit compared to the inversion in a pure elastic medium (Figures 2.45 and 2.46). These observations led the authors to warn about the tendency of elastic models to overestimate the locking depth. This study also shows that a sliver motion is not required to fit the observed surface displacement, since viscoelasticity is able to explain the far-field displacements that were not fitted by pure elastic models. Finally, they also report a very good correlation of their viscoelastic interseismic coupling distribution with the rupture of the

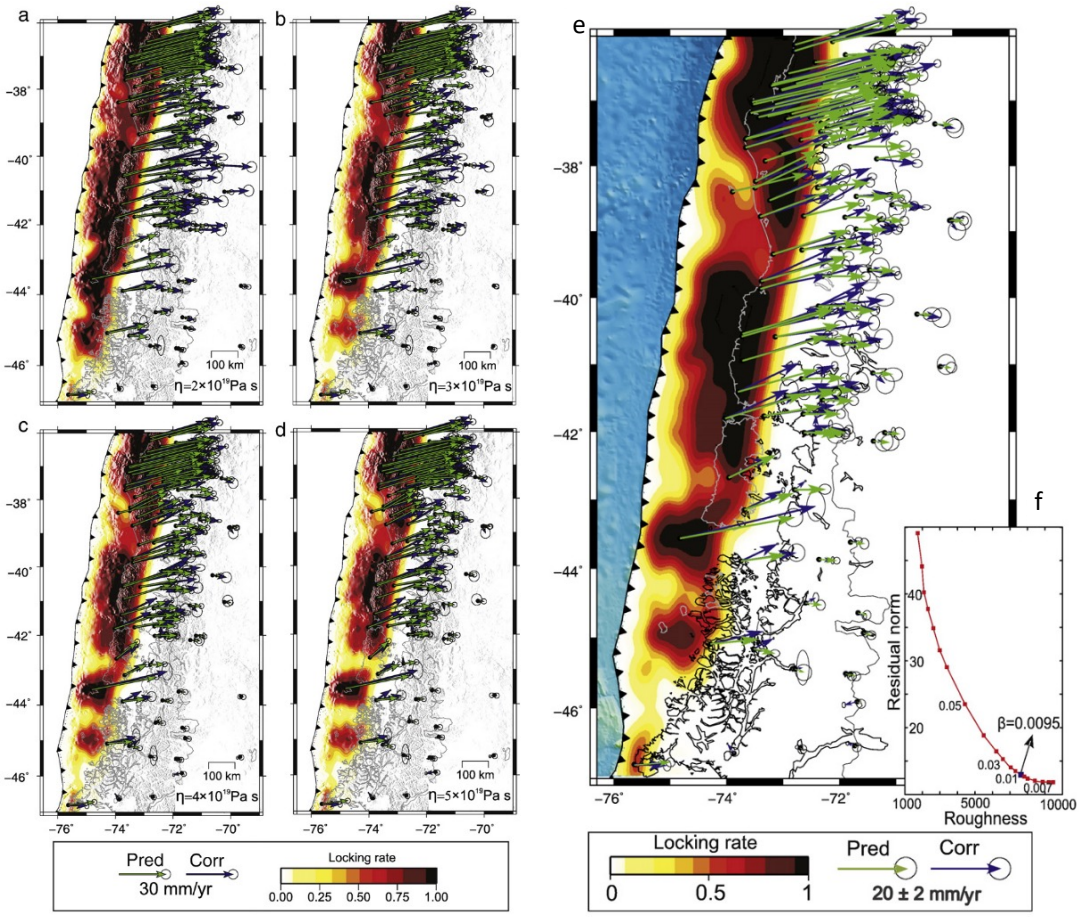

Figure 2.42: Figure modified from M. Moreno et al., 2011 showing on panels *a* to *d* the coupling distributions for a range of uniform continental mantle viscosity from 2 to $5{\cdot}10^{19}$ Pa·s. We observe that the more viscous is the rheology, the smaller is the coupling because of the smaller postseismic displacements to correct. On panel *e* is shown their best model of coupling, with a viscosity ranging from $3{\cdot}10^{19}$ Pa·s in the South to $4{\cdot}10^{19}$ Pa·s in the North. On panel *f* is plotted the tradeoff curve for the smoothing parameter.

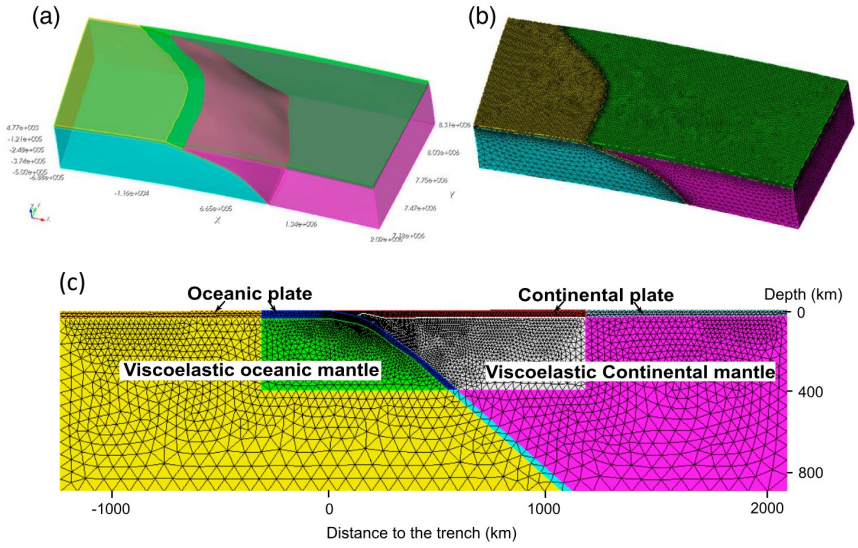

Figure 2.43: Figure modified from S. Li et al., 2015 showing the structure of their FEM subduction model (a). They shaped their model from the slab contours and continental moho. The meshing is shown on panel (b), with finer cells close to the slab and upper surface. Four blocks are defined (c): elastic oceanic and continental plates, and viscoelastic oceanic and continental mantles.

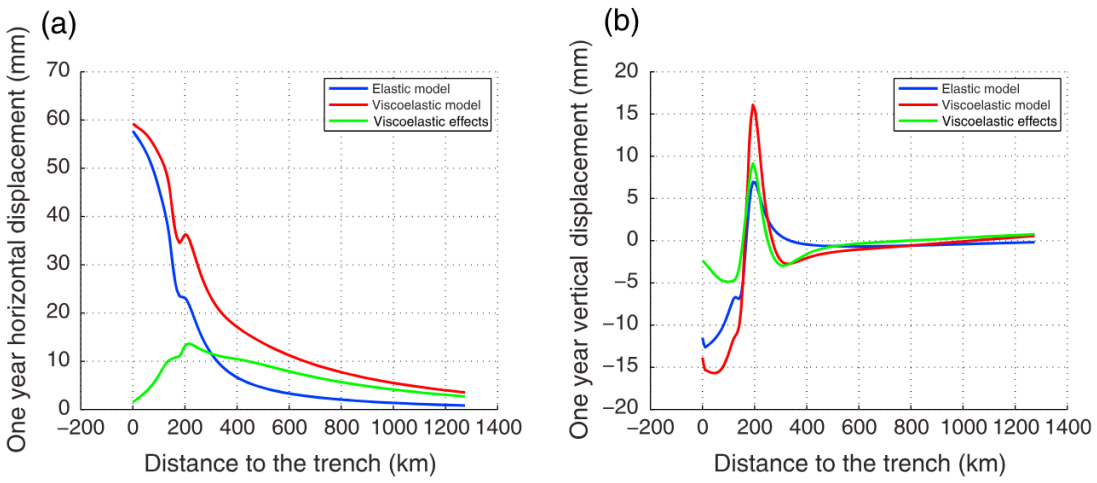

Figure 2.44: Figure from S. Li et al., 2015 illustrating the viscoelastic effects on the horizontal (a) and vertical (b) surface deformation. The elastic and viscoelastic interseismic models are depicted by the blue and red lines respectively, while the green line shows the difference between the two and so the viscoelastic effects. Larger horizontal displacements, especially in the inland region are observed with viscoelastic rheology. The subsidence and uplift peaks are also larger with viscoelasticity, and a second zone of subsidence as well as a second zone of uplift in the far-field appear.

2014 Mw8.1 Iquique earthquake.

To summarize, this overview of interseismic coupling models in Peru and Chile shows that while the Peru-Chile subduction has been studied extensively, notably the Central Andes, there is still room for improvement and clarification. First, the geodetic measurements were lacking completeness both spatially and temporally, especially in South Peru. In addition, earlier studies have been performed with simple geometries, while we now benefit from more accurate models of the slab geometry (Hayes et al., 2018). Later studies (Jolivet et al., 2020; S. Li et al., 2015; Métois et al., 2016; Villegas-Lanza et al., 2016; Yáñez-Cuadra et al., 2022) also show that some clarification is required regarding the necessity of rigid slivers. Finally, additional work is required to account for past earthquakes, notably the 2001 Mw8.4 Arequipa and 2014 Mw8.1 Iquique earthquakes, and for a more realistic rheology, especially in South Peru. All these aspects constitute a step toward a unified interseismic coupling model at the scale of the Central Andes.

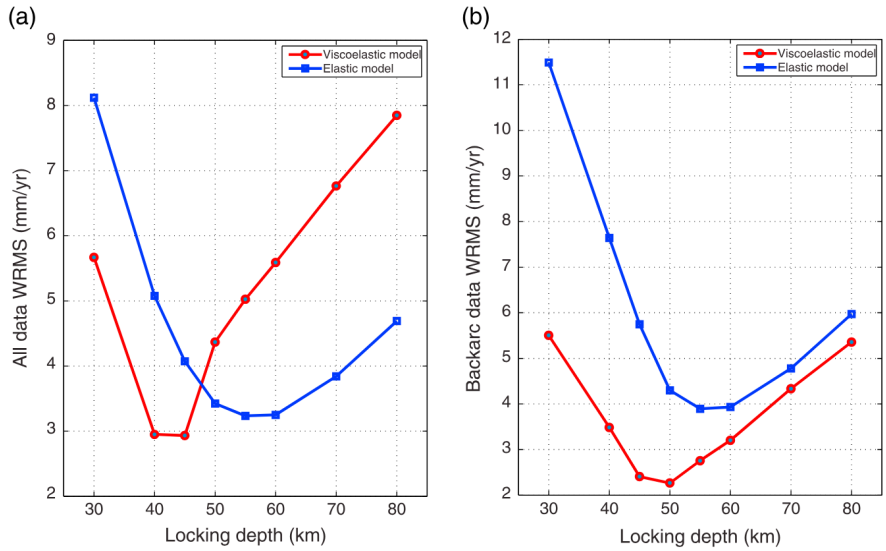

Figure 2.45: Figure from S. Li et al., 2015 showing a comparison of the misfit curves from forward elastic (blue) and viscoelastic (red) models, on all the sites (a) or restricted to the back-arc (b). The WRMS misfit values are computed from the horizontal GNSS observations. We observe that the misfit is lowered by introducing viscoelasticity, especially in the back-arc. In addition, the optimal locking depth is lowered from about 55 to 42 km.

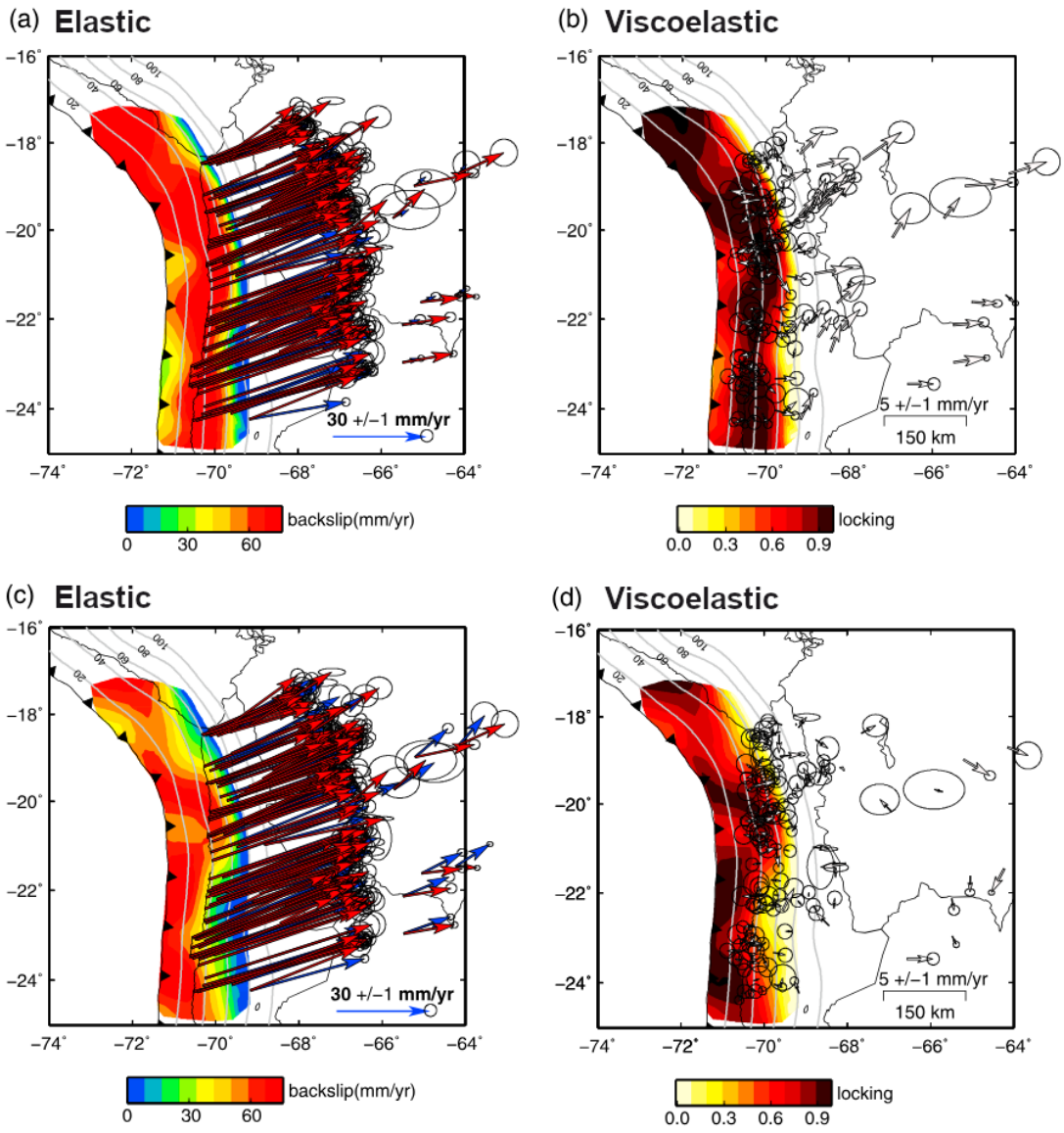

Figure 2.46: Figure modified from S. Li et al., 2015 showing the slip distribution and interseismic coupling distributions they obtained with an elastic (a, c) or viscoelastic (b, d) model. Observed and modeled horizontal velocities are depicted by the red and blue vectors respectively on panels (a) and (c). Residuals are indicated by the black vectors on panels (b) and (d). We observe a shallower locking depth, as well as lowered residuals with viscoelasticity.

Chapter 3

Data and methods

3.1 Geodetic techniques

3.1.1 Overview

Various geodetic techniques have been developed to quantify the Earth surface displacements, either on the horizontal or vertical components, in a relative or absolute reference frame. These surface displacements can be related to the seismic cycle (e.g., coseismic, postseismic, and interseismic displacements) or to other processes such as landslides, volcanic deformation, or hydrological loading. Four geodetic techniques are mainly used in this purpose: Global Navigation Satellite System (GNSS), radar interferometry (InSAR), optical correlation, and tiltmeters.

GNSS is satellite-based geopositioning of fixed receivers on the ground (Figure 3.1). It is used to monitor ground deformation since the 1990's and it allows to recover East, North, and vertical components of displacement, although the vertical component tends to be less reliable than the horizontal ones. The recording can be continuous in time, with daily acquisitions or even higher rates, if a station is permanently installed (cGNSS). One can also measure a given points more or less periodically with a temporary setup, which is referred as survey GNSS (sGNSS). In this latter case, we typically install the GNSS receivers for a few days during a survey, and we repeat the surveys at a typical interval of one to three years.

There is also a reversed configuration where the transmitters are on the ground and the receivers are airborne, that is used by the French system DORIS (Doppler Orbitography and Radiopositioning Integrated by Satellite) operated by the CNES (Figure 3.2). There are 60 ground stations that use the Doppler effect (frequency shift of a signal depending of its velocity and travel direction) to locate satellites that have an onboard

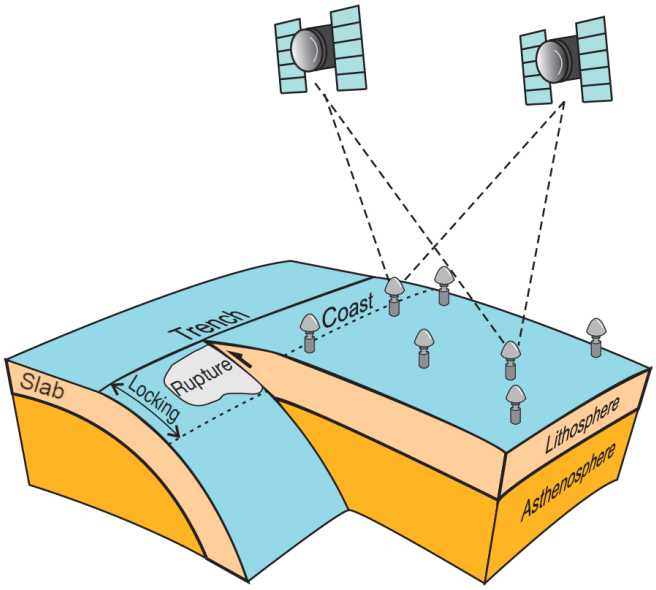

Figure 3.1: Measuring Earth surface displacements with GNSS on the overriding plate at a subduction zone (modified from K. Wang et al., 2012).

DORIS receiver. This system was launched in 1990 but is not as commonly used as conventional GNSS, still it is efficient to compute accurate satellite orbits and some ground monitoring studies have been performed using DORIS (Soudarin and Crétaux, 2006).

Radar interferometry (InSAR) uses active radar measurements to estimate the distance between the antenna and the ground: an electromagnetic radar pulse is sent toward the Earth surface and is backscattered to the antenna (Figure 3.3). The radar can be embedded on a car, an airborne vehicle (plane, drone, or even the Space Shuttle), or a satellite. The monitoring of the seismic cycle is done using satellite-based InSAR measurements in order to cover a large area with frequent acquisitions. The main advantage compared to GNSS is a better spatial coverage: modern radar satellites can monitor areas several hundred kilometers wide with a resolution (size of the pixel on the ground) in the order of 10 to 100 meters. Whereas GNSS measurements are limited by the distribution of GNSS sites on the ground with often tens of kilometers between the stations, which can go down to a few kilometers on some very dense networks such as in Japan or some parts of the United States, and some areas may not be instrumented at all. However, InSAR has two significant drawbacks compared to GNSS: the density of acquisition in time is limited by the repeat pass of the satellite which is typically several days to several weeks, and it only measures the displacement in the line-of-sight of the satellite instead of the three (East, North, Up) components

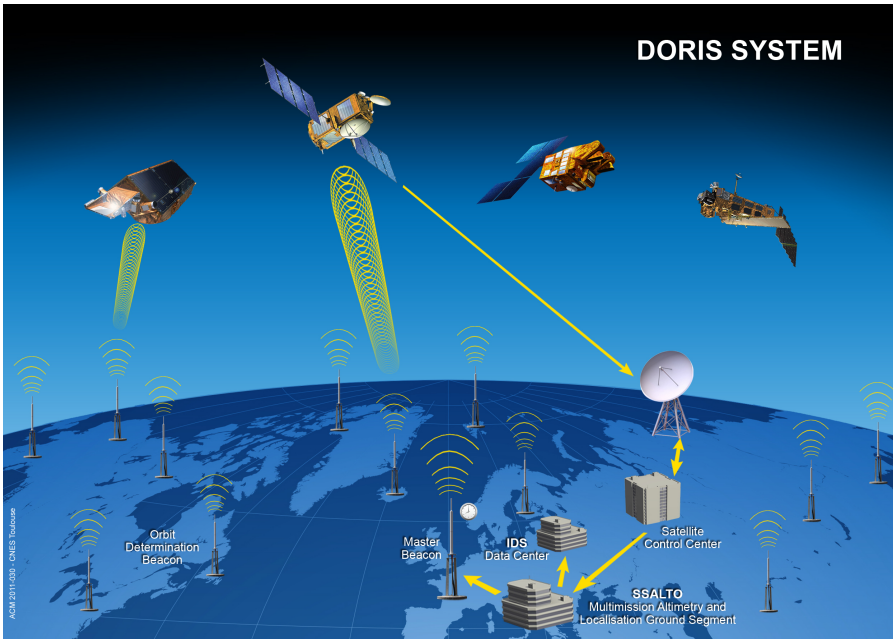

Figure 3.2: Figure from the CNES showing the basic acquisition scheme of DORIS. Transmitters on the ground are communicating with receivers onboard of satellites. A control center is continuously monitoring the network.

although it is sometimes possible to recover horizontal and vertical components with some assumptions.

Optical correlation is a method based on optical images which is tracking the displacements of pixels in time (Figure 3.4). With at least two images of the same area at two different epochs, optical correlation is able to quantify of how many pixels a feature has moved using an automated software, sometimes based on machine learning (Montagnon et al., 2024). Like for InSAR, the acquisitions can be performed from any camera on board of a vehicle, including satellites. It means that the density of acquisition in time is also limited by the repeat pass. But unlike InSAR, optical methods measure horizontal displacements (and vertical displacements to some extent) instead of line-of-sight displacements. This method is often used for small features such as landslides, or to monitor displacements on a strike-slip fault where one can measure the relative offset between the two fault sides. One of the limitations of optical correlation is that one needs a reference on the image to quantify displacements of a given feature, restraining large scale applications. Also, despite it is possible to have sub-pixel tracking with an accuracy of about 1/10 pixel (Skakun et al., 2017), optical methods are still limited to measuring large offsets of at least 10 cm. Finally, acquisitions cannot be performed when there are clouds or insufficient lighting. Overall, this technique is not suitable to measure postseismic or interseismic displacements at

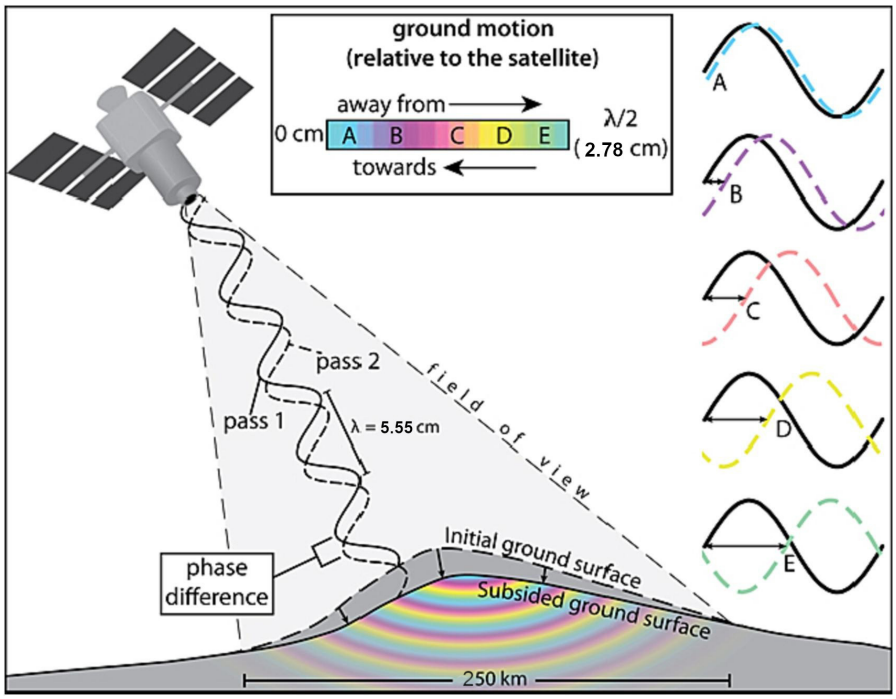

Figure 3.3: Application of InSAR to measure ground deformation (Modified from B. Zhang et al., 2022). An electromagnetic wave is sent toward the ground by the radar equipment onboard of the satellite, and the back-scattered signal is received. By measuring the phase shift between successive passes, one can compute the displacement in the line-of-sight. For Sentinel-1 satellites, the wavelength is 5.55 cm and the swath width is 250 km.



Figure 3.4: Figure from Xiwei et al., 2025 showing Sentinel-2 optical acquisitions before (a) and after (b) the 2025 Mw7.7 Myanmar earthquake. By pixel tracking they measured an horizontal offset of more than 4 meters, that can easily be seen on the road profiles. Note the difference in colors between the two acquisitions, probably due to different weather conditions.

a large scale.

Tiltmeters measure inclination on one or two axes. Various technologies have been used over the years, from purely mechanical to microelectromechanical units or hydraulic systems (Figure 3.5). They were widely used before the spread of GNSS, and are still commonly used today for monitoring volcanoes or landslides. Tiltmeters have also been used for tectonic applications, especially long-base hydraulic tiltmeters (tens to hundreds meters long), due to their ability to capture variations at a high sampling rate. They are used in complement to GNSS because of their different sensitivity to the distance d to the source of strain ($1/d^3$ vs. $1/d^2$ for GNSS, Boudin et al., 2022).

Note that some additional geodetic technics exist, such as satellite laser ranging (SLR) which uses a laser beam to measure the distance to a satellite, very-long-baseline interferometry (VLBI) that computes the distance between several telescopes receiving the same radio wave from an astronomical radio source (e.g., a quasar or a neutron star), or strainmeters which measure directly the deformation of an underground body (for

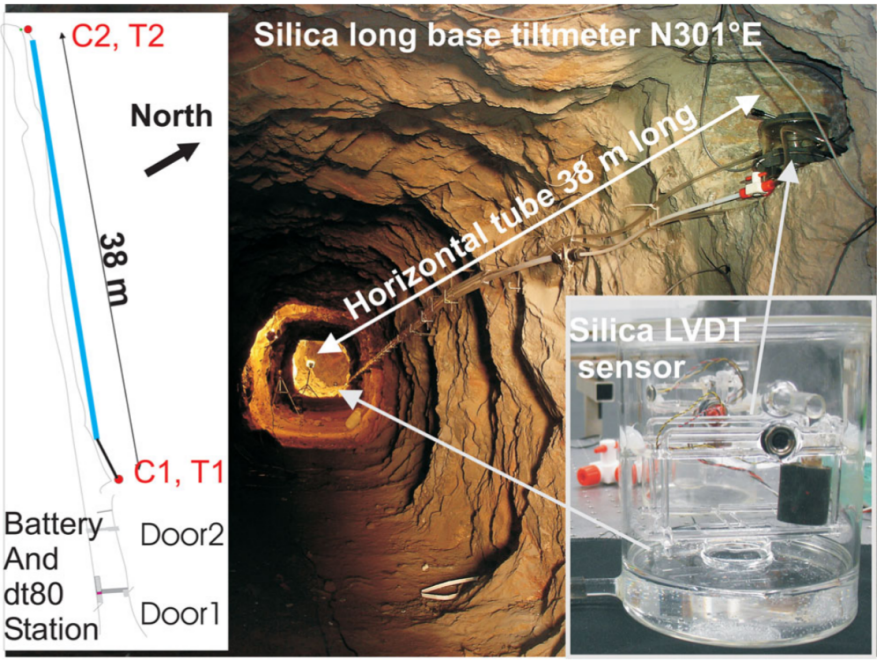

Figure 3.5: Figure from Boudin et al., 2022 showing a long-base hydraulic tiltmeter installed in a mine in North Chile. Two water leveling sensors are monitoring the fluid transfer along the 38-meter long tube.

instance with a piezoelectric material). But these technics are very specific and out the scope of our study.

In this PhD thesis, we use GNSS (including both cGNSS and sGNSS sites) and InSAR data, since these two techniques are the most adequate to measure postseismic or interseismic signals at a large scale. These two data sets are complementary: GNSS offers a higher temporal resolution and provides displacement on the three (East, North, Up) components, while InSAR offers a higher spatial resolution.

3.1.2 The GNSS technique

Basic principle

GNSS is the generic acronym used for satellite geopositioning and navigation systems. By antonomasia, we usually refer to GPS, which is the name of the GNSS system developed by the United States. GPS was a military project launched by the U.S. Department of Defense in 1973. The first satellite was launched in 1978 and the constellation of 24 satellites was fully operational in 1993. The system was opened to civilian use in 1988, but with a limited accuracy of 100 meters for non-military receivers. This limitation was removed in 2000. GPS is now commonly used by the general public with mobile receivers such as smartphones, or on-board navigation systems in cars or aircraft. In these devices, some additional inputs are used in order to maintain a meter accuracy on the move: inertial systems, additional triangulation with cellular networks, magnetometers (compass), distance traveled by the wheel (allowing to keep track in tunnels)... Over the years, other GNSS systems have been developed: the Soviet Union and Russia developed GLONASS that is fully operational since 2011 (26 satellites), and since 2020 the Chinese BeiDou (35 satellites) and European Galileo (27 satellites) systems are also fully operational. Some other systems are operating at a local scale, such as QZSS from Japan that can operate in Asia-Oceania, or NavIC from India that can operate on the Indian territory. While newest receivers are compatible with the four worldwide GNSS systems (GPS, GLONASS, Galileo, and BeiDou) they are often configured to operate mainly with the GPS constellation, which is also modernized along the years (31 satellites operational in 2025).

The GNSS positioning requires at least three satellites to be seen by the receiver at all time, then the receiver computes the distance to all of the visible satellites and by triangulation it is able to locate itself in space (Figure 3.6). The satellites are orbiting at a typical elevation of 20,000 km and are communicating with the receivers through electromagnetic microwaves (in the order of one GHz), transmitting their position and the current time. A fourth satellite is needed to set the time of the receiver. Broadcasting an accurate time information is crucial to obtain an accurate localization, thence

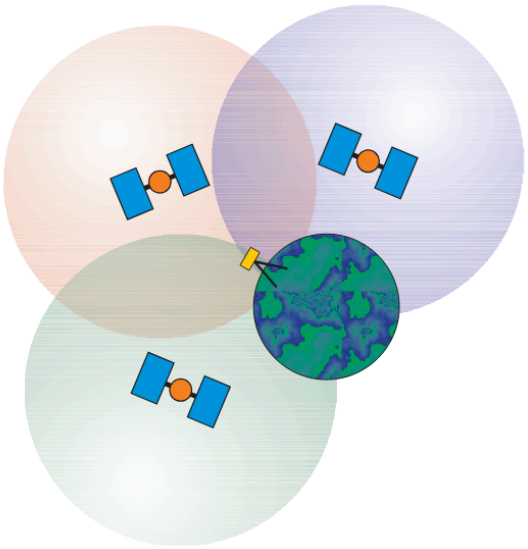

Figure 3.6: Illustration of the triangulation principle used to locate a GNSS receiver in space: the travel time, and so the distance, between each satellite and the receiver is computed. The intersection of the three circles gives the receiver location (from Teunissen and Montenbruck, 2017).

GNSS satellites are equipped with atomic clocks providing an accuracy in the order of a nanosecond per day. Control stations on the ground are also used to check satellites health and monitor their orbits.

On the physics of electromagnetic waves

Electromagnetic radiation, as transmitted by GNSS or SAR satellites, can be seen either as a wave characterized by its amplitude and wavelength, or as a flux of elementary particles called photons. A photon has no mass or electric charge, but it is characterized by a spin of 1, making it a boson, and has an energy equal to h.ν with h the Planck constant and ν the frequency. From now on, we will consider only the wave aspect of electromagnetic radiation. An electromagnetic wave is actually a transverse wave where both the electric field E and the magnetic induction B are perpendicular to the travel propagation, and perpendicular to each other (Figure 3.7). The relations between E and B were described in 1861 by James Clerk Maxwell, in its four famous homonym equations (Maxwell, 1861):

$$\nabla.E = \frac{\rho}{\varepsilon_0} \tag{3.1}$$

$$\nabla.B = 0 \tag{3.2}$$

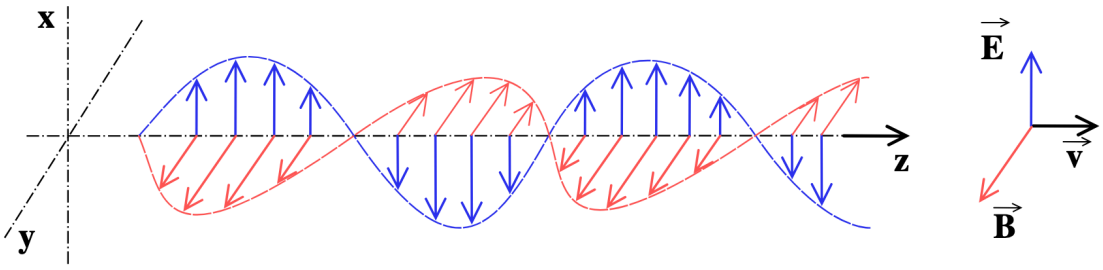

Figure 3.7: Linearly polarized electromagnetic wave propagating along the z-axis. The electric field E (blue) is oriented along the x-axis, while the magnetic field B (red) is oriented along the y-axis.

$$\nabla \times E = -\frac{\partial B}{\partial t} \tag{3.3}$$

$$\nabla \times B = \mu_0 J + \mu_0 \varepsilon_0 \frac{\partial E}{\partial t} \tag{3.4}$$

with ρ the electric charge density, ε_0 the vacuum dielectric permittivity, μ_0 the vacuum magnetic permeability, $\mathcal{J}$ the current density, and t the time.

The propagation speed v of an electromagnetic wave depends on the dielectric permittivity of the medium ε and the magnetic permeability μ:

$$v = \frac{1}{\sqrt{\mu\varepsilon}} \tag{3.5}$$

which in the vacuum is approximately equal to 3.10^8 m/s, and a relatively similar value in the atmosphere.

Sources of error

For monitoring the earthquake cycle, we are not interested in the accuracy on the move like for a car or an aircraft (real time positioning), instead we need a high static accuracy in order to monitor coseismic displacements of a few cm or interseismic displacements of a few mm/yr. Various factors of uncertainty have to be considered (Figure 3.8):

- The error on the receiver and satellite clocks. Receivers use quartz oscillators with a drift that can reach one second per day. This error can be corrected using the double-difference method by measuring the phase shift between two satellite-receiver pairs. GNSS satellites use atomic clocks with a drift in the order of a nanosecond per day, this drift can be corrected by downloading drift correction files.

- The error on the satellites' orbits: orbits are transmitted with an error of about 100 meters, which can induce an error of about 1 cm on the receiver position estimation. Precise orbits can be downloaded a few weeks after the acquisition, with a centimeter accuracy, mitigating this source of error.

- Delay due to crossing the ionosphere: the satellites orbiting at about 20,000 km, the signal has to cross the ionosphere between ~60 and ~1,000 km, which causes a delay by diffraction. This delay depends on the rate of ionization in the ionosphere (i.e., the density of free electrons), which tends to be higher in equatorial regions. Ionosphere is a dispersive medium, meaning that the delay is frequency-dependent, so using dual-frequency capabilities of the receivers we can correct for this delay.

- Delay due to the troposphere (from the ground to ~8-15 km): a *dry* delay depending on the thickness and density of the troposphere, and a *wet* delay depending on the humidity. Atmospheric models can be downloaded, with pressure and humidity evolution, to correct for these two types of delays.

- Multi-paths delays caused by reflections on objects surrounding the receiver (buildings, trees, radio antennas...). In order to prevent this, we try to install the GNSS antennas far from obstacles, especially metallic ones. Still, some indirect paths may remain (even the ground can reflect the signal) but they will average out during long sessions of measurement.

- Error on the phase centering in the receiver antenna: the signal from the satellite is recorded on a solenoid at the center of the receiver antenna, the actual recorded position may vary depending on the incidence of the ray. To account for this, we need to properly indicate the antenna model during the processing (including its height relative to the marker). The variation of incidence angle should also average out when performing long measurements. In addition, we adopt the convention of orienting the antenna to the North in order to account for the anisotropy inside the antenna.

- Relativistic effects: the frequency of the satellite clock oscillator is increased because of the high velocity (about 4 km/s) of the satellite relative to the receiver, according to special relativity, which is distorting the range estimation. In addition, general relativity effects due to the Earth's gravity field also curve the electromagnetic signal. These relativistic effects can easily be corrected by applying the equations of the special relativity (Einstein, 1905) and general relativity (Einstein, 1915), since we know the satellites positions and velocities.

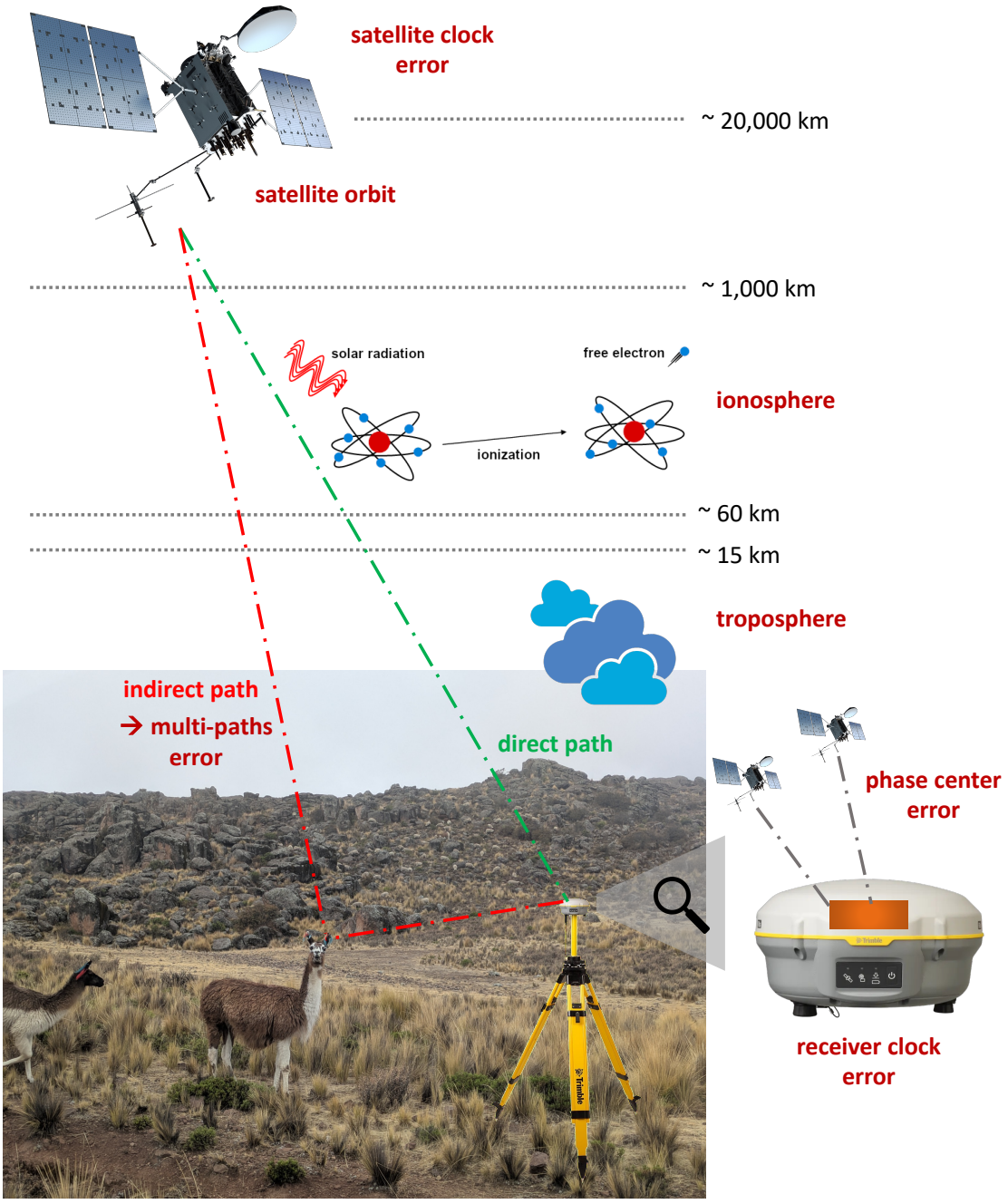

Figure 3.8: Main sources of error for static GNSS measurements: satellites orbits error, receiver and satellite clock errors, ionospheric delay, tropospheric delay, multi-paths error due to indirect reflected paths, and phase center error on the antenna's solenoid depending on the incidence angle.

GNSS networks in Central Andes

In Peru, several GNSS networks are operated, with continuous and survey measurements (Figure 3.9). The International GNSS Service (IGS) operates one cGNSS station in Arequipa city since 1993, which made it the first GNSS station in Peru, and one of the firsts in South America. Survey sites were measured starting from 1994 in the frame of the South America - Nazca Plate Project (SNAPP) project (Norabuena et al., 1998), some of these sites are still measured today by Instituto Geofísico del Perú (IGP) and ISTerre (about 50 sites). Continuous stations have been installed in South Peru by IGP, ISTerre, and Caltech starting from 2007. These 27 sites are maintained by IGP since 2015. The Insituto Geográfico Nacional (IGN) of Peru also installed its own 71 continuous stations starting from 2010, at various locations in Peru. More recently, 10 continuous and 26 additional survey sites have been installed in the frame of the DEEPtrigger project (Villegas-Lanza et al., 2025).

The Central Andes GPS Project (CAP) was deployed by American teams starting from 1993 with about 30 continuous and survey sites in Chile and Argentina (Bevis et al., 2001; Bevis et al., 2000; Kendrick et al., 1999; Kendrick et al., 2001). The GeoForschungsZentrum (GFZ) also started to monitor Chile and Argentina in 1993, deploying the very wide South American Geodynamic Activities (SAGA) network of 215 sites from 22°S to 42°S (Khazaradze and Klotz, 2003; Klotz et al., 1999; Klotz et al., 2001). Note that these two networks were focused on monitoring the Andean uplift, so many sites are located in the back-arc, which is not optimal to study the interseismic coupling. On the other hand, joint deployments from the Institut de Physique du Globe de Paris (IPGP) and Ecole Normale Supérieure (ENS) Paris were more aimed toward monitoring the seismic cycle related to the subduction. They deployed survey sites along the Chilean coast starting from 1996, and following during the 2000's (Ruegg et al., 2009; Vigny et al., 2009) and the 2010's (Klein et al., 2018; Métois et al., 2016). The Centro Sismológico Nacional of Chile (CSN) operates a network of more than 200 continuous GNSS stations since 2013 (Báez et al., 2018). 32 additional stations have been installed in the frame of the DEEPtrigger project. IGS also installed one station in Iquique city in 2002, and one in Antofagasta city in 2022.

In Argentina, the Red Argentina de Monitoreo Satelital Continuo (RAMSAC) started to install cGNSS stations in 1998 and it now operates more than 100 stations (Piñón et al., 2018).

Few survey and continuous GNSS measurements in Bolivia are available from Brooks et al., 2003 and Foster and Bevis, 2014. The later sites have been installed following the occurrence of the 2014 Mw8.1 Iquique earthquake.

Finally, cGNSS measurements are available in Brazil through the Brazilian Network for Continuous Monitoring of GPS (RBMC) network, operating since the late 1990's, in the frame of the Geodetic Reference System for the Americas (SIRGAS) initiative at about 200 sites.

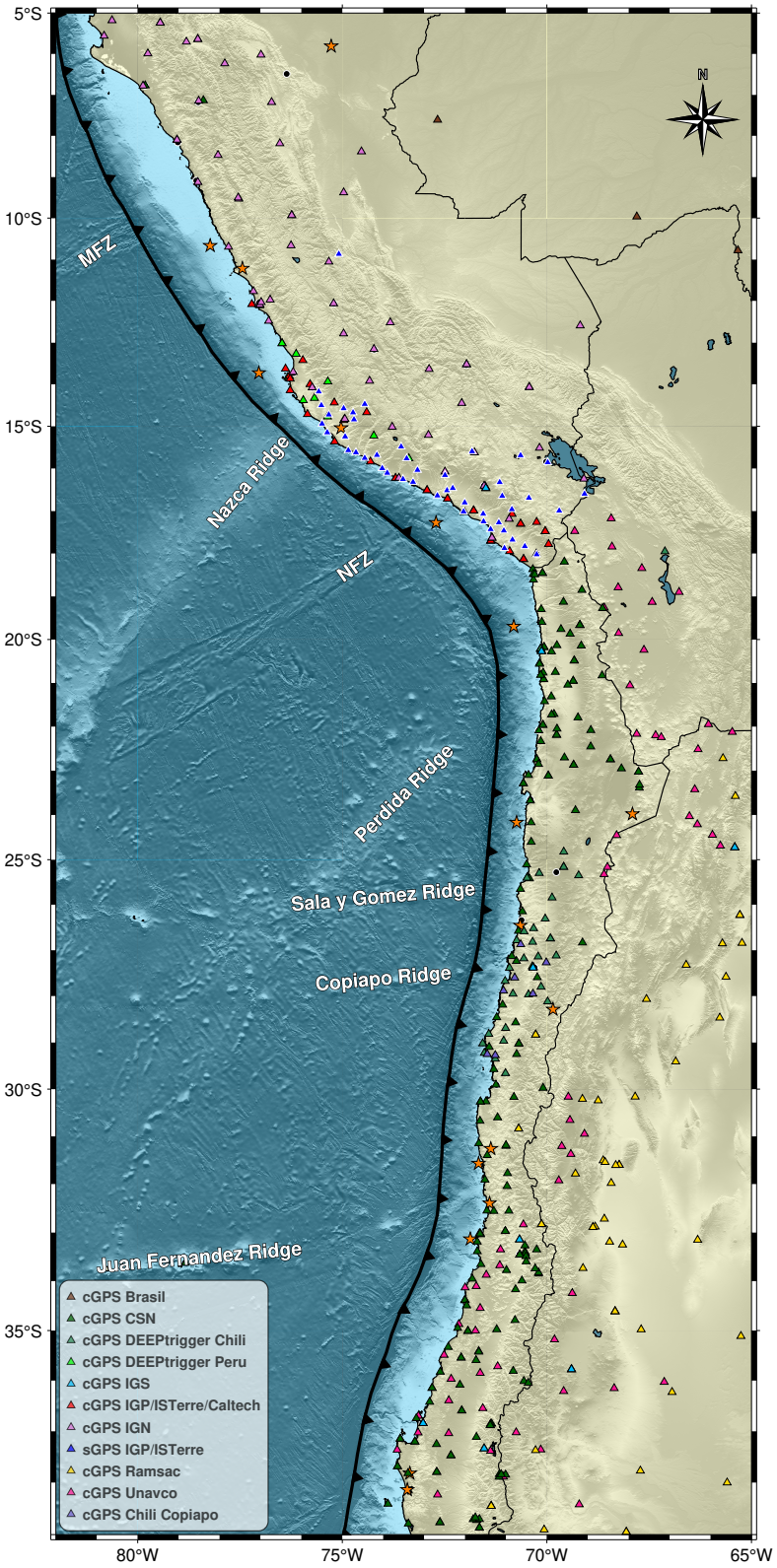

Figure 3.9: GNSS network used in this PhD thesis. The coordinates and measurement periods of every GNSS sites are reported in the annexes of this manuscript (Tables 9.1 to 9.11).

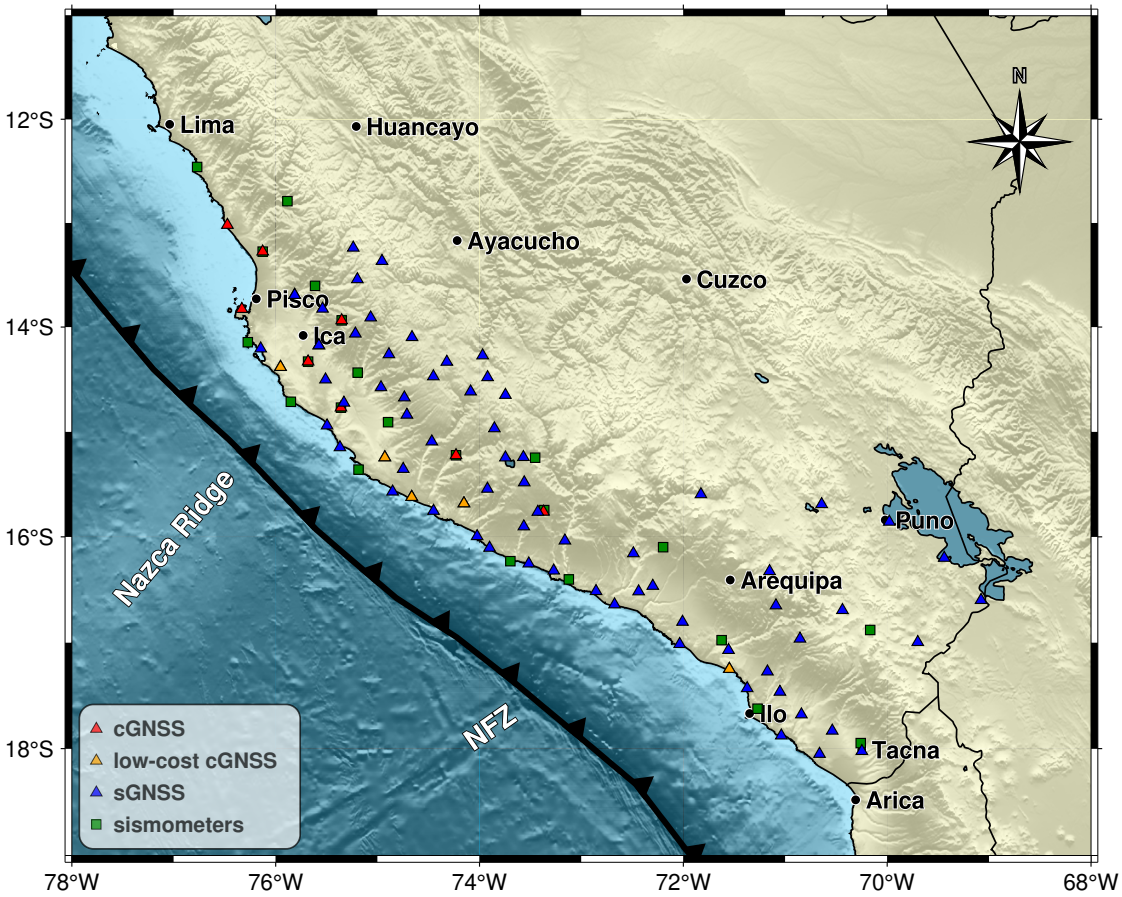

Figure 3.10: GNSS and seismic sites serviced during the field operations in Fall 2024. The low-cost cGNSS have been installed to replace some survey sites.

Installing a GNSS station

Field operations are regularly conducted in Peru and Chile by local institutes (IGP in Peru and CSN in Chile) and ISTerre. I was involved in one of these campaigns during two weeks in November-December 2024, that was performed in the frame of the DEEP-trigger projects and supported by IGP and Institut de recherche pour le développement (IRD). The objectives were to collect the data and perform basic maintenance operations at 8 cGNSS stations, to measure 57 sGNSS sites, to replace 5 sGNSS sites by permanent low-cost stations, and to dismantle 22 seismometers (Figure 3.10). We were split in four teams with people from ISTerre, IGP, and IRD, covering a large portion of South Peru from Lima to Tacna.

cGNSS stations are made of an antenna that is solidly fixed to the ground, and a receiver to decode the GNSS signal on various frequency bands (typical equipment in-

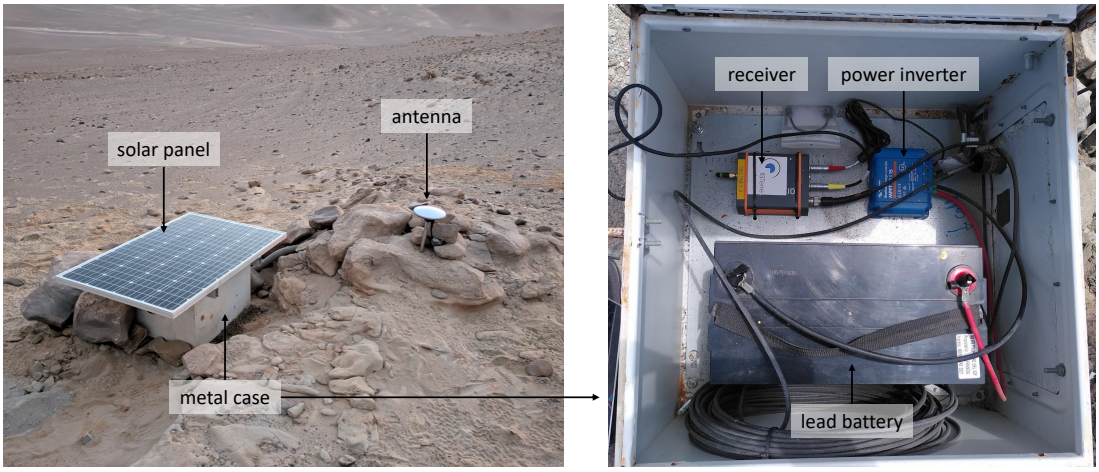

Figure 3.11: Typical setup for a cGNSS station. Here is shown a low-cost one with Septentrio mosaic-X5 GNSS receivers and ArduSimple antennas (setup similar to Vidal et al., 2024), but other cGNSS station use a similar setup, apart from more advanced antennas and receivers. The GNSS receiver is installed in a metallic case, sheltering it from the external elements (rain, sun, wind, dust...). The equipment is powered by a 12-volt lead-acid battery that is charged during the day by a solar panel. A power inverter converts the direct current from the solar panel and the battery to alternative current. The GNSS antenna is installed a few meters from the case in order to mitigate multi-paths errors. The cGNSS sites have the antenna screwed into the ground with a metallic rod.

clude Trimble NetR9 or NetRS, or Leica GR50 receivers). This equipment is supplied by electrical power from a 12-volt lead-acid battery, charged by a solar panel (Figure 3.11). The receiver is shielded in a metallic box with the solar panel on top. In order to avoid multi-paths effects, the antenna is installed several meters away from the box, with a cable buried into the ground. The antenna (facing North to improve phase centering) is screwed on a metallic support, a few tens of cm long, attached to a concrete slab in order to be stabilized, or directly to the bedrock (Figure 3.12). The equipment is recording the GNSS signal at any time and averages it to produce daily measurements, but higher rates of measurement are available. The data are stored on a SD flash memory card and need to be collected, as most of the stations are not connected to telemetry because of their remoteness. Basic maintenance operations are performed when we collect the data: cleaning the solar panel, checking the battery voltage and replacing the battery if needed, checking the connections as well as the strength of the GNSS signal...

sGNSS sites work in a similar fashion, but the equipment is only left for a few days on site so it is designed to be easily installed, dismantled, and carried (Figure



Figure 3.12: The ATIC cGNSS station installed close to the Atico city (between Chala and Camaná), installed by Caltech and now operated by IGP. Note that the antenna is equipped with a radome to mitigate wear and tear.

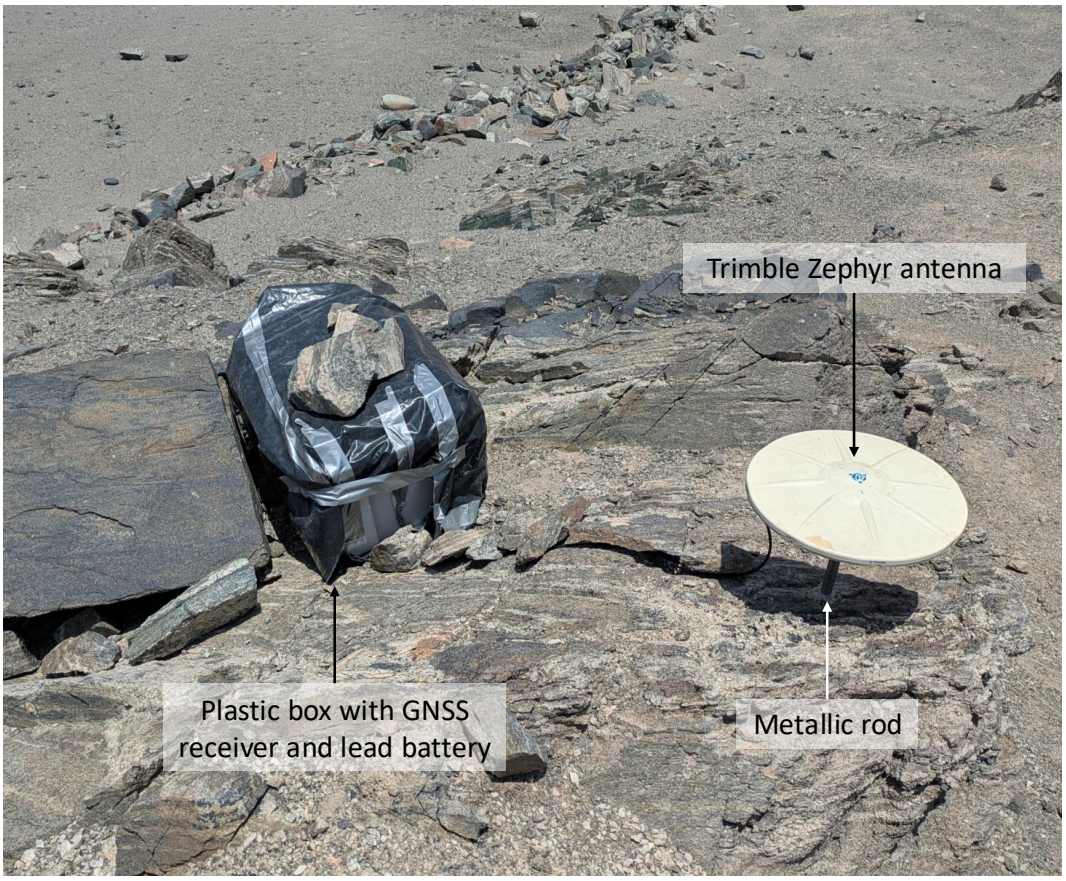

Figure 3.13: Typical setup for a sGNSS site. Compared to a cGNSS site, there is no solar panel and the case is made of plastic in order to be lighter to carry. This site has a screw pitch were we can screw the antenna with a metallic rod.

3.13). We still use a 12-volt lead-acid battery to supply the receiver and the antenna, however we do not need a solar panel as the battery capacity (~100 A·h) is enough to supply the equipment for several days. The receiver is shielded in a lightweight plastic box. Depending on the sites, the antenna is either screwed with a metallic rod into the ground where a screw pitch has been installed previously, or positioned above a marker drawn on the ground (Figure 3.14). For this latter setup, we can use a bipod or a tripod to center the antenna atop the marker after carefully leveling. The first method is more convenient as one just has to screw the antenna, removing the need for leveling and securing the bipod or tripod, and it reduces the sources of errors due to incorrect leveling or unwanted movements of the antenna during the recording. However, it requires some caution from the operator by using the adequate screw thread.

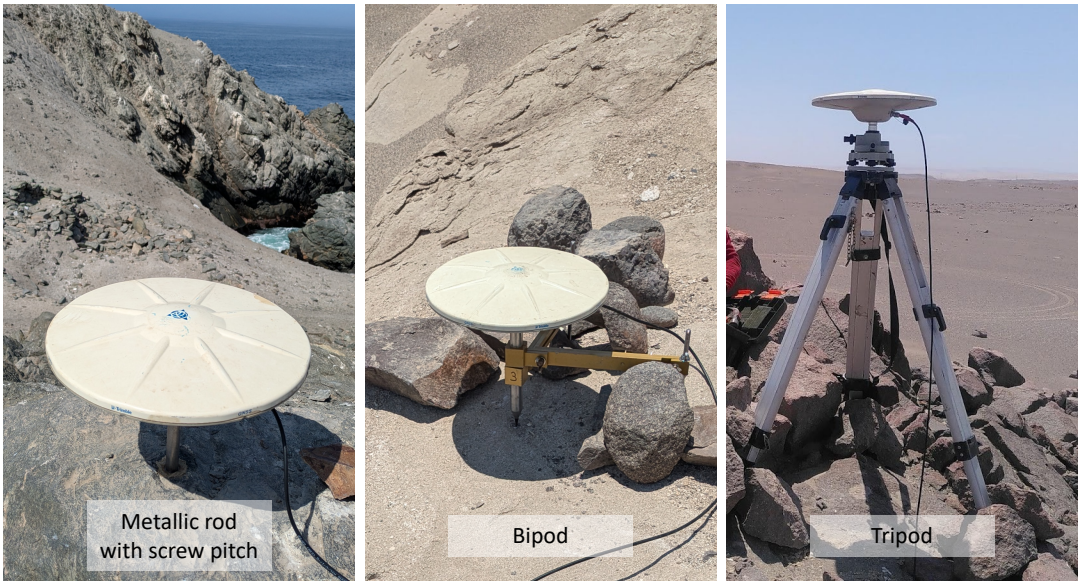

Figure 3.14: The three ways of installing the antenna for a sGNSS site: metallic rod with screw pitch, bipod, and tripod. If the site is already equipped with a screw pitch in the ground, one just have to screw the antenna with a metallic rod in the screw pitch. Otherwise, if there is just a marker, it is necessary to use either a bipod or a tripod to center and level the antenna above the marker. The bipod or tripod is then secured with some stones.

Either for installing a sGNSS or a cGNSS site, it is important to install the antenna far from obstacles such as buildings, fences, radio antennas... It reduces the multi-path indirect signals, and it maximizes the number of satellites that can be seen by the antenna. Another key point is to make sure that the antenna is firmly attached to the ground, and that it is not localized on a landslide or any area affected by a local deformation process. Usually, the antennas are attached to the bedrock or to a concrete slab. It is also important to make sure that the solar panel receives enough light, otherwise the battery may not charge enough, leading the station to shutdown at some times.

GNSS processing

In order to obtain accurate localization of the GNSS antenna at a millimeter scale, we need to process the raw data and correct for the various sources of error. The two main philosophies are double-difference (a.k.a. differential-GNSS, D-GNSS) and Precise Point Positionning (PPP) (Figure 3.15). The double-difference method process a given set of stations on the same batch, and references each station relative to each others. Some stations are used as references in order to compute absolute locations. This method has the advantage of correcting the receivers clock error by measuring

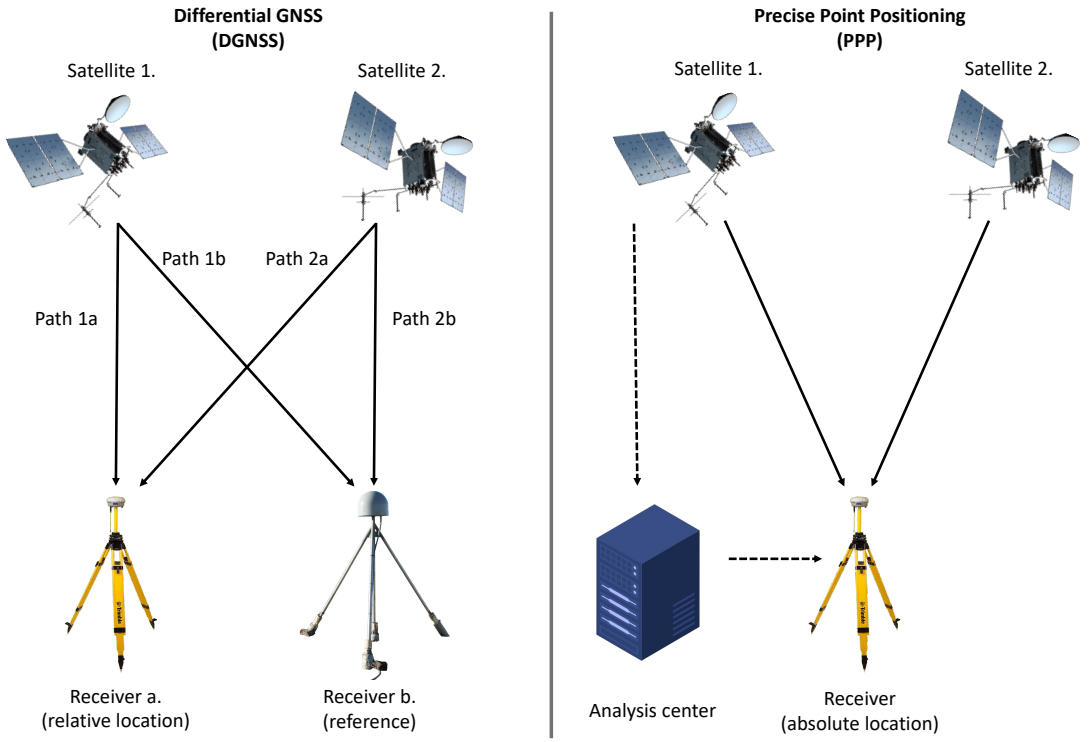

Figure 3.15: Differential GNSS (D-GNSS) vs. Precise Point Positioning (PPP). With the D-GNSS method, the stations are processed by batch. The various paths between multiple satellites and multiples receivers (here the paths 1a, 1b, 2a, and 2b) are used to cancel the satellite and receiver clocks errors. Each station of the network is referenced relative to reference stations. For PPP, we use correction tables provided by analysis centers to correct for the errors. Each station is processed independently and get an absolute location.

the phase shift between two satellite-receiver pairs. The GAMIT/GLOBK software has been commonly used for double-difference processing in multiple ground deformation studies (Klein et al., 2016; Métois et al., 2016). However, while this method provides a good accuracy, the processing is quite heavy and does not enable independent processing of the stations. In addition, it requires reference stations to be very precisely located and not affected by the geophysical process we study (Aoki and Kreemer, 2024). For these reasons, the GNSS data at ISTerre are instead processed using the PPP method, including the ones presented in this thesis. It allows absolute location of each independent station by using correction tables for satellite clocks and orbits provided by a network of continuously operating reference stations (CORS). With PPP the computation time is linearly proportional to the number of stations while it is exponential with D-GNSS, making PPP an efficient method for large-scale processing, as shown by several ground deformation studies (Blewitt et al., 2018; Naumowicz et al., 2024).

We use the GipsyX software from the Jet Propulsion Laboratory (JPL) for PPP processing at ISTerre (Bertiger et al., 2020). Wide-lane phase bias constraints provided by JPL are applied to resolve phase ambiguity. Orbit and clock estimations are taken from JPL final products, with NNR orbits. Ionospheric delays are canceled by using dual-frequency communications. The VMF1 (Boehm et al., 2006) tropospheric products are used to correct for tropospheric delay. Crustal deformation induced by ocean tide loading is corrected using the FES2014b tide model (Lyard et al., 2021). Phase center stability and multi-path protection are achieved using antenna calibration tables and by stacking GNSS measurements over the day to keep one position per day. Scaling, rotation and translation factors provided by JPL are then applied in the Helmert transformation to map the solution in the IGS2014 (Altamimi et al., 2016).

Time series modeling

Various processes are part of the GNSS time series, we model their respective contribution using a trajectory model based on the model proposed by Bevis and Brown, 2014 and implemented in the ITSA software (Marill et al., 2021). The station position along time *x(t)* is modeled as a sum of linear, Heaviside, logarithmic, and sinusoidal time functions:

$$x(t) = x_R + v(t - t_R) + \sum_{j=1}^{n_j} b_j H(t - t_j) + \sum_{i=1}^{n_i} a_i log_{10}\left(1 + \frac{t - t_i}{\tau_{Ra}}\right) + \sum_{k=1}^{2} [s_k sin(2k\pi(t - t_R)) + c_k cos(2k\pi(t - t_R))] + \sum_{a=1}^{n_a} b_a H(t - t_a) \quad (3.6)$$

- The first term x_R is the station's position at the initial time t=0.
- The second term $v(t - t_R)$ is the linear component corresponding to the interseismic velocity, with t_R the reference time of the last event.
- The third term is a Heaviside function modeling a coseismic displacement of amplitude b_j at a time t_j.
- The fourth term is a logarithmic decay modeling afterslip (Marone et al., 1991), with a characteristic time τ_{Ra} and a displacement a_i at a time t_i. For our applications, τ_{Ra} typically varies between 15 and 60 days.
- The fifth term is made of trigonometrical functions modeling annual and semi-annual seasonal oscillations caused by hydrological loading and temperature variations, weighted by coefficients s_k and c_k.

- Finally, the last term is accounting for antenna changes with a Heaviside function. We indicate when antenna changes happened on the field leading to a potential offset, especially on the vertical component, if the new antenna or its stand has a different height.

In order to limit the number of parameters that are considered at each GNSS site, coseismic and postseismic displacements associated with earthquakes are only modeled if the station lies within a given radius of influence from the earthquake. This radius $r(M_w)$ depends on the magnitude M_w of the earthquake, and is given by the empirical formula from Marill et al., 2021:

$$r(M_w) = 10^{(0.43M_w - 0.7)/1.15} \tag{3.7}$$

3.1.3 The InSAR technique

The interferometry by Synthetic Aperture Radar (SAR) is a geodetic technique using radar electromagnetic waves to estimate ground surface displacements. It is, with GNSS, one of the two geodetic techniques used in this PhD. In order to understand the possibilities and limitations of this technique, we start with some basics of radar theory, then we explain how SAR data are acquired, what are the factors of error that affect them, and how they are processed.

The radar theory

Radar, standing for radio detection and ranging, is an active system that sends electromagnetic radiations and measures the back-scattered signal in order to estimate a distance. Radar should not be confused with a sonar which uses acoustic wave, or a lidar which uses frequencies in the range of visible (or near-visible) light.

In the late 1880's Heinrich Hertz studied the propagation of electromagnetic waves in various media, and in 1899 Guglielmo Marconi showed that electromagnetic waves can be back-scattered. This led to the first use of electromagnetic waves for range estimation by the German inventor and physicist Christian Hülsmeyer in 1904. He developed a device, the *Telemobiloscope*, able to detect incoming ships by sending radio waves and ringing a bell when a back-scattered wave was detected. Hülsmeyer's invention is considered as the first radar, however it was not able to compute an actual distance to the object, but only detect the presence of an object. The introduction of radar pulsing was required to estimate the distance, by measuring the travel time of the signal. Developments in this direction during the 1920's allowed Albert Taylor, Leo Young, and Lawrence Hyland from the Carnegie Institution of Washington to develop a pulsed radar with appropriate encoding techniques that was able to measure

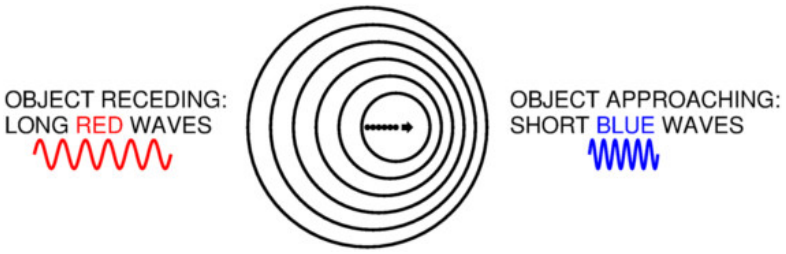

Figure 3.16: Illustration from UCLA of the Doppler effect: an electromagnetic wave transmitted from a receding object has its wavelength increased, while it is reduced to an approaching object. This effect can be observed on stars: the receding stars are *red-shifted*, while the approaching ones are *blue-shifted*.

the height of the ionosphere in 1924. At first, radar was primary used for military applications, but it also became essential in air traffic control, marine navigation, meteorology, or geophysical applications such as ground-penetrating radar and of course InSAR.

With modern radar devices, it is possible to measure the phase shift, and so the distance by making a hypothesis on the propagation velocity, but also the amplitude of the back-scattered signal. The amplitude attenuation gives information on the material of the surface reflecting the signal. In addition, using the Doppler effect we can estimate if an object is going away or toward the receiver: if the frequency of the back-scattered signal increases, the object is moving toward the receiver, while if the frequency is decreasing the object is moving away (Figure 3.16). The power Pr of the back-scattered signal is given by the radar range equation:

$$P_r = \frac{P_t G_t A_r \sigma F^4}{(4\pi)^2 R_t^2 R_r^2} \tag{3.8}$$

with Pt the transmitter power, Gt the gain of the transmitting antenna, Ar the surface of the receiving antenna, σ the scattering coefficient of the target, F the pattern propagation factor, Rt the distance between the transmitter and the target, and Rr the distance between the target and the receiver.

If the transmitter and the receiver are at the same position, we can simplify the radar equation:

$$P_r = \frac{P_t G_t A_r \sigma F^4}{(4\pi)^2 R^4} \tag{3.9}$$

meaning that the power of the back-scattered signal is declining at the fourth power of the distance R.

Acquisition geometry

Before digging into the subtleties of SAR, let's cover some essential notions and terminology. When a SAR satellite is scanning the Earth, it is following an orbit close to a North-South axis. The orbit is referred to as *ascending* when the satellite is going toward the North and *descending* when going toward the South (Figure 3.17). The antenna looks on one side of the satellite and sweeps an area of a given width that we call a *swath* (Figure 3.18). Two directions are defined to navigate on a SAR acquisition, the *azimuth* direction is parallel to the travel direction of the satellite, while the *range* direction is perpendicular to the travel direction and parallel to the direction at which the antenna is pointing (the line-of-sight, LOS). If we consider a satellite looking on the right (like Sentinel-1 that acquired the data used in this thesis) on an ascending orbit, the West side of the swath is the closest one from the satellite and is called *near range*, while the East side of the swath is the farthest from the satellite and is called the *far range*. We define the look angle as the difference between the direction where the antenna is looking and the *nadir*, a vertical axis between the satellite and the ground. The look angle varies between near and far range from 29 to 46° for Sentinel-1. This variation in the look angle implies that the sensitivity to vertical displacement is higher in the near range, while the sensitivity to horizontal displacement is higher in the far range.

The synthetic-aperture radar (SAR)

In order to increase the spatial resolution of a conventional radar system, a larger antenna is required. However, for remote sensing applications, the radar needs to stay relatively compact in order to be carried by a vehicle or a satellite. This limitation can be overcome by using synthetic-aperture radar (SAR), that can increase the aperture by using the displacement of the antenna over the area of interest while keeping the same antenna physical size. The idea is to send a succession of radio pulses and to record the back-scattered signal of each pulse at different positions (Figure 3.19). The various signals are then combined in order to mimic a larger *physical* aperture so to increase the spatial resolution in azimuth.

The resolution in range can be improved by using a *chirp* signal (Figure 3.20) for which a frequency modulation is applied around the carrier frequency in a given bandwidth. The range resolution is then inversely proportional to the bandwidth of the chirp signal.

The frequency modulation resulting from the chirp signal and the displacement in azimuth by Doppler effect has to be removed from the SAR acquisition. By applying fast Fourrier transforms, we obtain a single-look complex image (SLC) with amplitude and phase information.

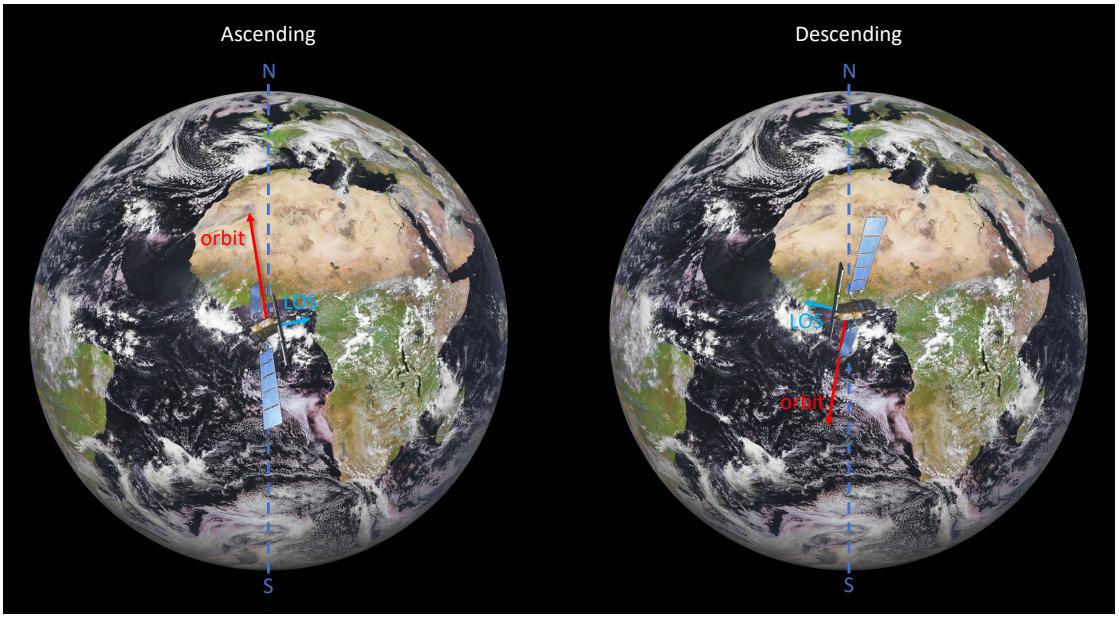

Figure 3.17: *Ascending* and *descending* orbits geometries for the Sentinel-1 SAR satellites. The travel direction is indicated by the red arrow, while the blue arrow corresponds to the line-of-sight (LOS) vector. Sentinel-1 is a *right-looking* satellite while some others are *left-looking*, and some even have the capability to look in both directions (like ALOS-2). Sentinel-1 orbits are tilted by about 8 degrees from the North-South axis.

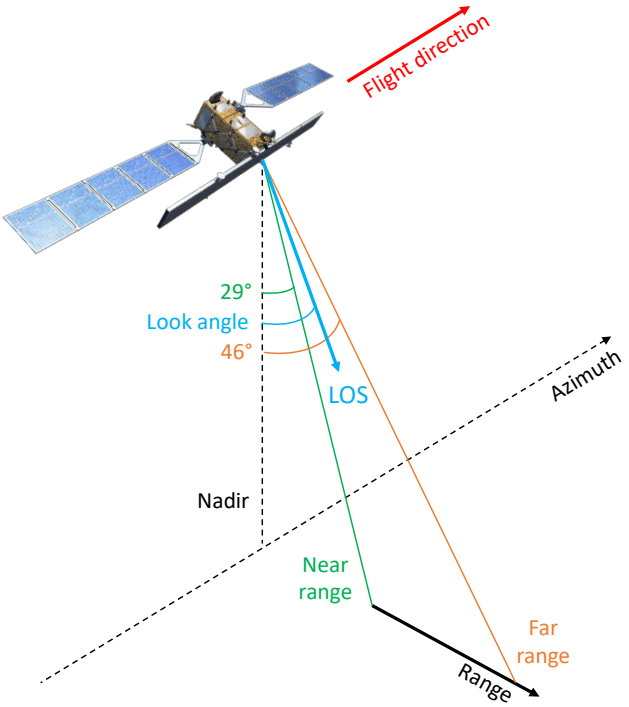

Figure 3.18: Acquisition geometry for the Sentinel-1 SAR satellites. The flight direction is indicated by the red arrow, while the line-of-sight (LOS) vector is indicated in blue. The look angle for Sentinel-1 in IW mode (most common acquisition mode, used in this PhD) is varying from 29° in near range to 46° in far range.

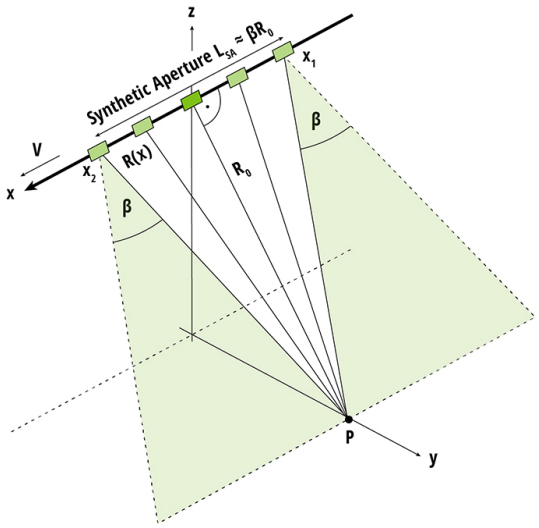

Figure 3.19: Figure from NASA showing the principle of synthetic aperture: it relies on the displacement of the satellite to measure successive back-scattered pulses, increasing the antenna aperture.

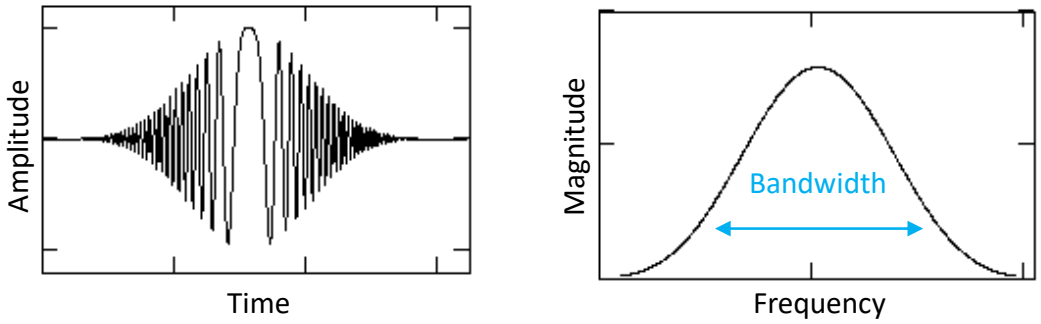

Figure 3.20: Chirp radar signal in time (left) and frequency (right) domains.

SAR can be used for remote sensing applications, either by using the amplitude attenuation or the phase delay between the transmitted and back-scattered signals (Figure 3.21). The amplitude can be used to detect changes in the nature of the surface, for instance to monitor oil-spill or changes in the vegetation cover. While the phase information can be used to measure the distance to the ground, allowing to map the terrain elevation and to monitor ground deformation. The SAR device can be carried on a car to monitor local processes, such as landslides (Frey et al., 2013). To monitor larger areas, and to overcome the fact that car-based measurements are limited by the terrain configuration, an aircraft such as a small drone or an airplane can be used. For frequent acquisitions on large areas, SAR satellites have been developed over the years. They orbit around the Earth following a close to North-South direction and can sweep the same area a few days apart.

An overview of SAR satellites

The use of SAR satellite for remote sensing started in 1978 with the launch of Seasat by NASA. It was aimed at monitoring the oceans, with the SAR device being used to measure the wave heights and the sea ice coverage. However, the mission ended after only three months due to a failure in the electrical system. InSAR really stepped up in the 1990's due to the launch of several SAR satellites by various space agencies (Figure 3.22): ERS-1 (1991) and ERS-2 (1995) by the European space agency (ESA), JERS-1 (1992) by the Japanese space agency (NASDA, now JAXA), and RADARSAT-1 (1995) by the Canadian space agency (CSA). All these satellites provided data during several years, with a world-wide coverage and orbits stable enough to perform interferometry. Notably, ERS acquisitions allowed mapping of coseismic and postseismic displacement associated with the 1992 Mw7.3 Landers earthquake in California (Fialko, 2004; Kohlhase et al., 2003; R. Michel et al., 1999; Price and Sandwell, 1998). ESA launched Envisat in 2002, which was used as a replacement for ERS satellites up to 2012. Envisat SAR data have been successfully used to measure the deformation associated with earthquakes, notably the 2003 Mw6.5 Bam earthquake in Iran (Fialko et al., 2005) and the 2009 Mw6.3 L'Aquila earthquake in Italy (Lanari et al., 2010). JAXA launched ALOS in 2006 as a replacement for JERS and ADEOS satellites up to 2011. Like Envisat, ALOS data were used to quantify earthquake-related deformation, including the 2008 Mw8.0 Sichuan earthquake in China (Hashimoto et al., 2010) and the 2011 Mw9.1 Tohoku earthquake in Japan (Park et al., 2013).

Nowadays, the most widely used SAR satellites for remote sensing are Sentinel-1 satellites from ESA, ALOS-2 and ALOS-4 from JAXA, TerraSAR-X and TanDEM-X from the German space agency (DLR), and COSMO-SkyMed from the Italian space agency (ASI). The NISAR satellite from NASA and the Indian space agency (ISRO) is also probably going to be a very popular platform in the incoming years. This variety

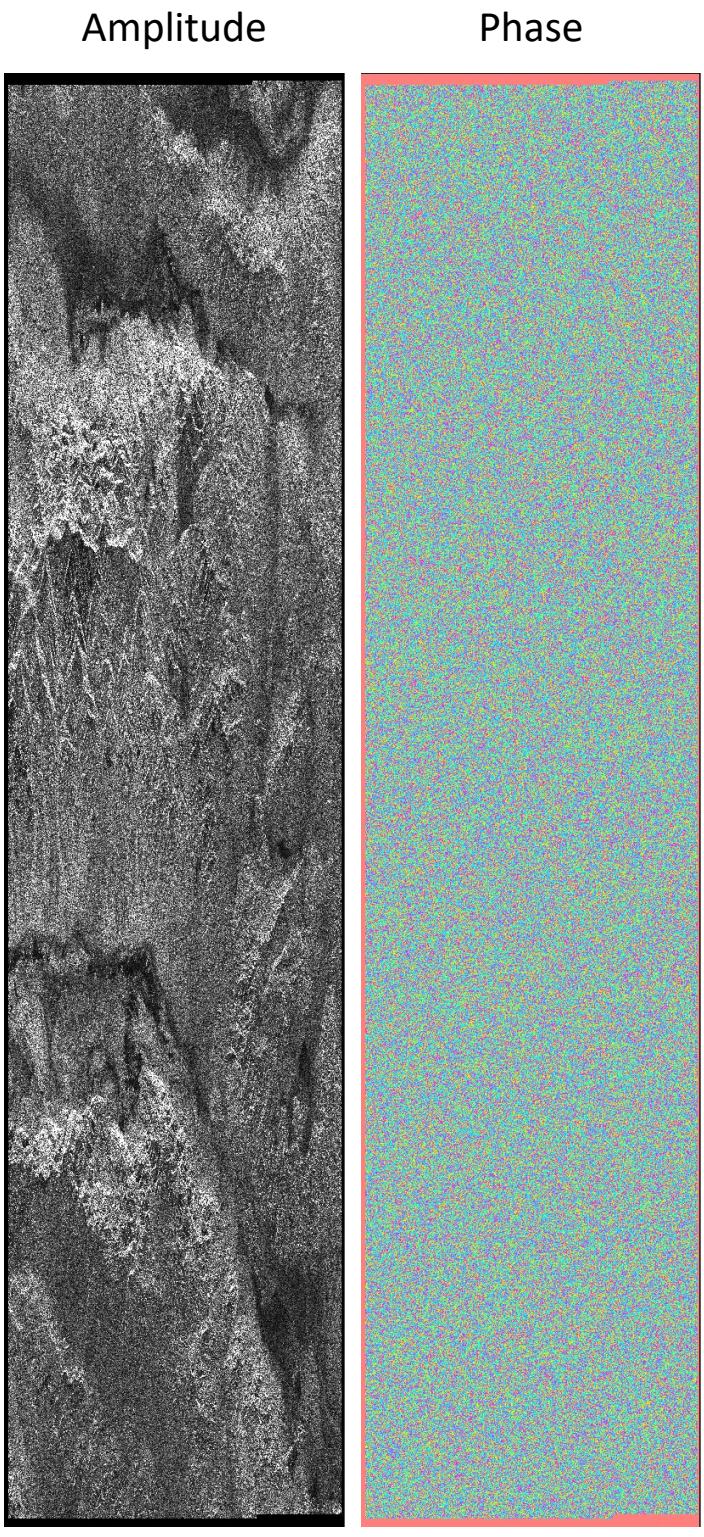

Figure 3.21: Amplitude (left) and phase (right) information of one subswath of a Sentinel-1 acquisition over the Ridgecrest area (California) on 2019-07-16, in radar geometry (processed with NSBAS). The amplitude image allows to see some patterns in the terrain geometry, while the phase information without interferometry is useless.

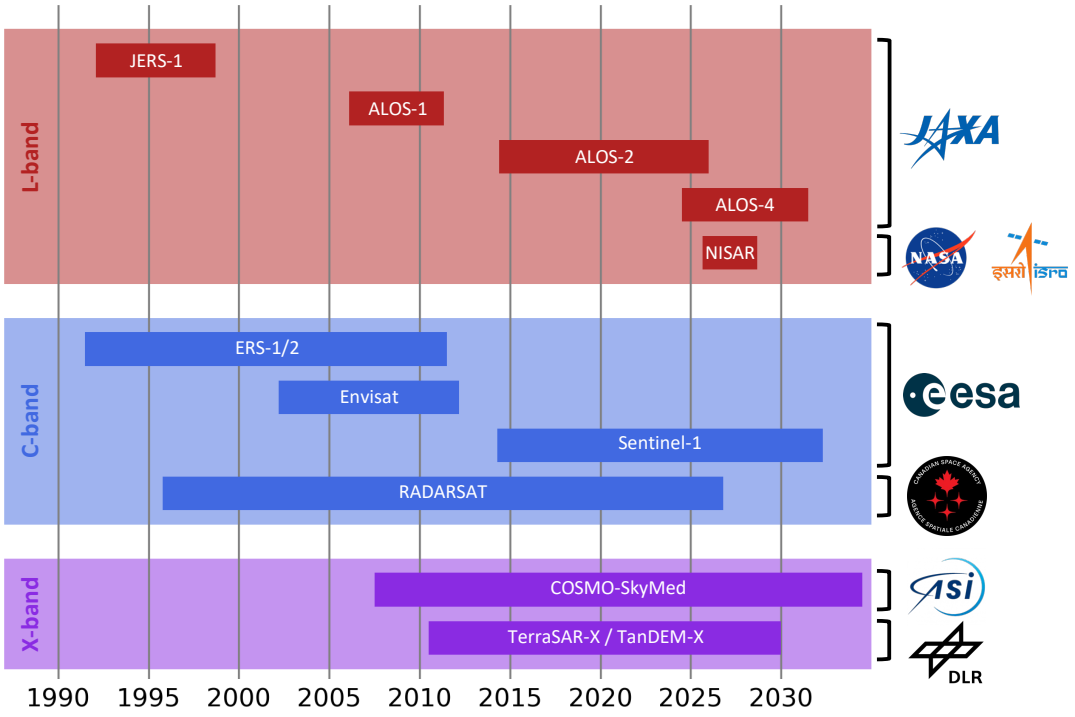

Figure 3.22: Non-exhaustive chronology of the main SAR satellites launched since the 1990's. Several constellations are still operating today, in 2025, so we reported the estimated operational periods from their respective operators. Note that NISAR is the only SAR satellite with dual-frequency capability (L-band and S-band) but it is going to operate primary with the L-band equipment.

of SAR satellites shows technical differences in the radar equipment, the acquisition techniques, or the data availability policies. One of the main difference between these platforms is the frequency of the transmitted radar signal, that we usually classify from lowest to highest frequency with the following nomenclature from the Institute of Electrical and Electronics Engineers (IEEE): L-band from 1 to 2 GHz (all ALOS satellites, NISAR), S-band from 2 to 4 GHz (NISAR), C-band from 4 to 8 GHz (ERS, Envisat, RADARSAT, Sentinel-1), and X-band from 8 to 12 GHz (TerraSAR-X & TanDEM-X, COSMO-SkyMed). Overall, a lower frequency improves the temporal coherence of the signal (less affected by decorrelation), which can be useful in areas with a surface prone to decorrelation (e.g., soft terrains, vegetated areas) or when the period between acquisitions is large. It is also able to measure stronger phase gradients than higher frequency signals, which can be an interesting feature for monitoring strong ground motion in the case of an earthquake or a landslide. In addition, the ability of L-band to penetrate the vegetation allows to observe the ground surface in highly vegetated areas. On the other hand, low frequencies such as L-band are more affected by the ionospheric effects, making it challenging to use in areas where the ionization rate is high (typically in equatorial regions). The spatial resolution in azimuth is also improved by using a higher frequency, as it is proportional to the ratio between the wavelength and the size of the antenna. Let's now briefly look at the main characteristics of the various SAR platforms available and explain why we chose to use Sentinel-1.

ALOS-2 is operated by JAXA and was built by Mitsubishi Heavy Industries. It was launched in 2014 and it is still operating in 2025. It is following a heliosynchronous orbit at 628 km. The radar instrument is transmitting on L-band, with various acquisition modes, allowing to maximize either the spatial resolution (down to 1 meter) or the spatial coverage (swath up to 490 km wide). Although the capabilities of this satellite are very good, with all the advantages provided by L-band, the sensitivity to ionospheric effects of L-band would have been an additional difficulty in Central Andes where the ionization rate is high. In addition, ALOS-2 data were not freely available to institutions outside of Japan, when the PhD started in 2022. ALOS-4 is an evolution of ALOS-2, launched in 2024, with increased maximal swath width (up to 700 km) and still using L-band. It is operating jointly with ALOS-2. ALOS-4 data were not available at the start of the PhD.

Sentinel-1 is a constellation of SAR satellites, operated in the frame of the Copernicus Programme from ESA. Three mostly identical satellites built by Thales Alenia Space have been launched: Sentinel-1A (April 2014), Sentinel-1B (April 2016), and Sentinel-1C (December 2024). Note that Sentinel-1B stopped to operate on December 2021 due to a critical failure in the electrical system. A fourth similar satellite, Sentinel-1D, is expected to be launched in late 2025. The idea of the Sentinel-1 project was to always have two twin satellites operating, reducing the revisit time from 12 to

6 days. Of course it was compromised due to the failure of Sentinel-1B in December 2021, but from 2016 to 2021 two satellites were operating together, and it is now again the case since 2025. The satellites are following heliosynchronous orbits at 693 km and are equipped with a C-band radar that can operate in various acquisition modes, maximimizing either the spatial resolution (down to 5 meters) or the spatial coverage (swath up to 400 km wide). C-band is a good compromise between L-band and X-band for many regions on Earth, except in densely vegetated areas where the radar beam cannot penetrate the vegetation, unlike with L-band. As Central Andes is a pretty dry area with mostly low vegetation, it was not an issue in our case. The short revisit time of 6 days with two satellites is a significant advantage, allowing to better monitor earthquakes or any process with a rapid time evolution. Finally, the Sentinel-1 data policy is very convenient as all the radar images are freely available through an online service, a few hours after the acquisition.

TerraSAR-X (TSX) and TanDEM-X (TDX) are twin satellites operated by a partnership between the DLR and EADS Astrium, launched in 2007 and 2010 respectively. They follow heliosynchronous orbits at 514 km, and are equipped with a X-band radar providing images down to a 1-meter resolution. The swath width can be up to 100 km with a 16-meter resolution. Unlike Sentinel-1, the two satellites are not used to lower the revisit time (11 days for TSX/TDX), instead they evolve at a few hundred meters from each other and are acquiring synchronously. This technique is used to measure the topography accurately, in order to build global DEMs such as the Copernicus DEM. The data policy is less flexible than for Sentinel-1, radar images have to be purchased to EADS Astrium. In addition, the X-band may not be ideal for tectonic applications since it is more prone to decorrelation and phase ambiguity in case of strong phase gradients.

COSMO-SkyMed is a constellation operated by ASI, with a first generation of four satellites (COSMO-1/2/3/4) launched from 2007 to 2010, and a second generation (CSG-1/2/3/4) with two satellites launched in 2019 and 2022 and two other ones expected to be launched in late 2025 and 2027. They are built by Thales Alenia Space, and they all use a X-band radar equipment. This constellation is mostly focused on Italy and the Mediterranean area, both for civilian and military applications. The data have to be purchased from the Telespazio company. It is not of great interest for monitoring Central Andes.

Finally, NISAR acquisitions were not available for this PhD as it was launched in July 2025, but this satellite is very promising for several reasons. It is a joint project from NASA and ISRO, aimed at monitoring Earth processes. NISAR is the first satellite to be equipped with dual frequency radars (L-band and S-band), allowing to combine the advantages of the two frequencies and to correct for ionospheric delays. The radar

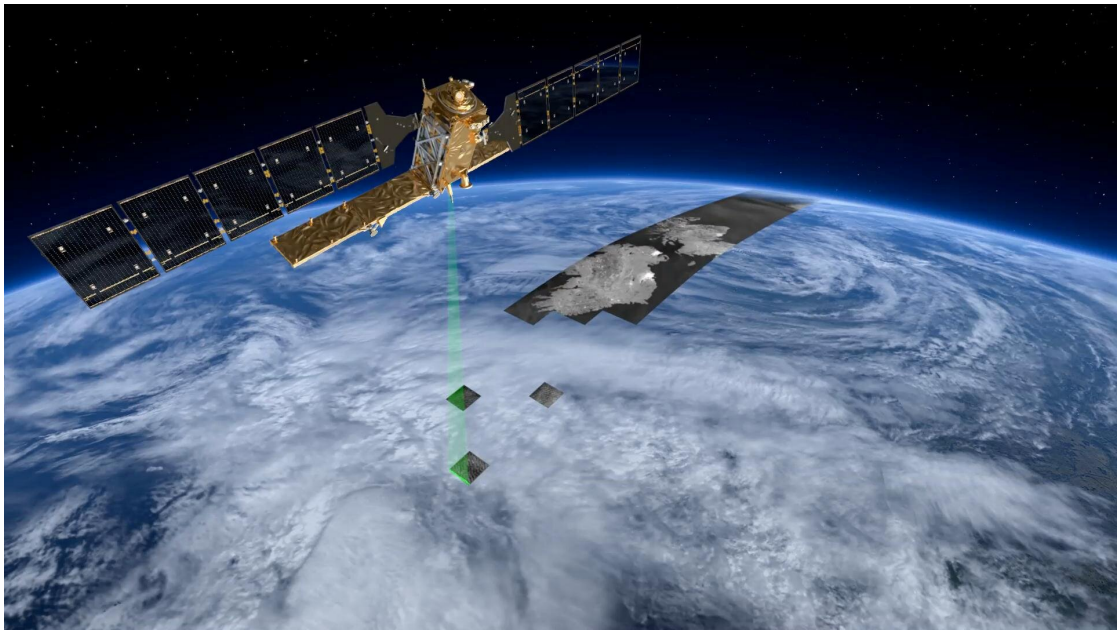

Figure 3.23: Artistic depiction from the ESA Medialab of a Sentinel-1 satellite acquiring over the Earth. The radar antenna is 12.3 m by 82 cm large and is acquiring on the right of the satellite in its travel direction. Note that the acquisition mode on the illustration just switched from *interferometric wide swath* (IW) mode to *wave* (WV) mode.

images, as well as already processed interferograms, are distributed openly through the Alaska Satellite Facility online service.

Sentinel-1 acquisition modes and characteristics

In order to understand how the InSAR products used in the frame of this PhD are produced, and to understand the inherent limitations, we will briefly discuss the acquisition techniques used by the Sentinel-1 satellites. Both Sentinel-1A and Sentinel-1B data are used in this study, but these two satellites are identical from an acquisition point of view. They follow a heliosynchronous orbit at 693 km with a 98.18° inclination, meaning that the orbits are close to a North-South axis. The revisit time for a given satellite is 12 days, with an orbital period of 98.6 minutes and 175 orbits per cycle. With two satellites, we have a 6-day revisit time. The radar antenna is looking on the right of the satellite along its travel direction, and acquisitions are performed both on ascending and descending orbits (Figure 3.23). The sensitivity to ground surface deformation will be different between ascending and descending tracks, since the LOS direction is different. For Central Andes, the LOS direction on ascending tracks is quasi-parallel to the Nazca - South America plates convergence vector, leading to a higher sensitivity to horizontal displacements compared to descending tracks. The look angle from

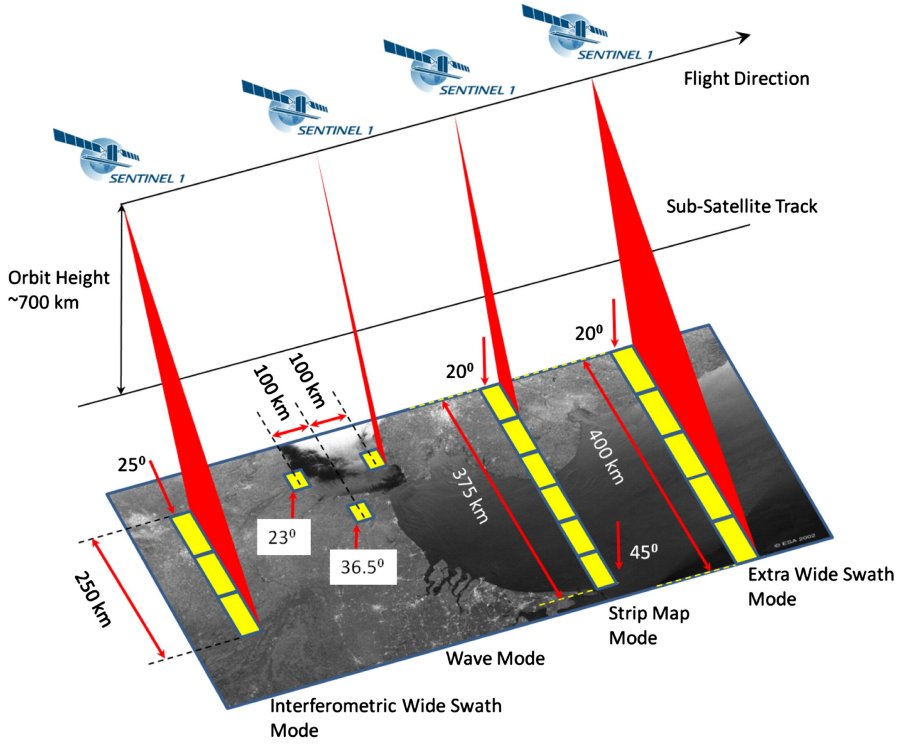

Figure 3.24: Figure from ESA showing the four acquisition modes of Sentinel-1: *stripmap* (SM), *interferometric wide swath* (IW), *extra-wide swath* (EW), and *wave* (WV). The main operational mode over continents is IW, that was used for all the SAR acquisitions used in this PhD thesis.

the nadir is varying from 29° in near range to 46° in far range, meaning that the sensitivity is also varying along the range direction, with higher sensitivity to horizontal displacements in the far range and higher sensitivity to vertical displacements in the near range.

Four acquisition modes are available for Sentinel-1, upon request from the operator (Figure 3.24):

- Stripmap mode (SM), that is the most accurate mode with a 5x5-meter resolution. Note that in this mode the pixels are square (same size in azimuth and range directions), which is not the case in the interferometric modes (IW and EW). The swath is 80-km wide. This mode is only used for monitoring special events and small areas, since it is more energy consuming and not suitable to map large areas.

- Interferometric wide swath (IW) mode, which is the main acquisition mode over lands, and the one used to acquire the data that were used for this PhD. This

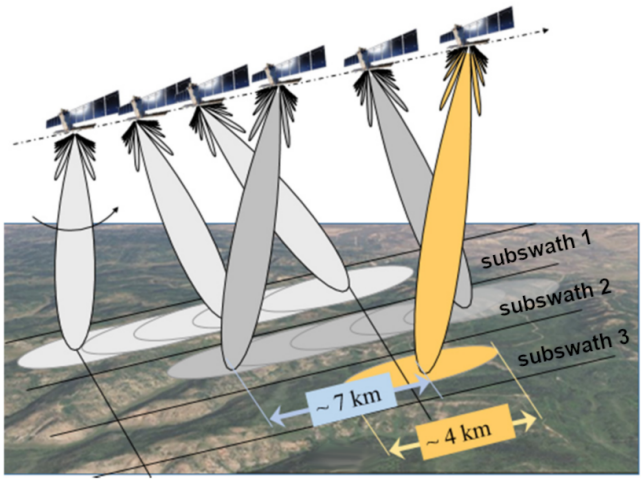

Figure 3.25: Figure modified from Monti-Guarnieri et al., 2017 showing the TOPSAR acquisition technology used by Sentinel-1 in IW and EW modes. The swath is divided into three subswaths along the range direction, and bursts are acquired cyclically, forward and backward, over the three subswaths. Bursts are about 4 km, with enough overlap to reconstitute the image smoothly.

mode, as well as the EW one, uses the TOPSAR (Terrain Observation with Progressive Scans SAR) technology (Figure 3.25). TOPSAR imaging uses electronic steering of the antenna both in range and azimuth directions to cyclically acquire various areas within the swath. Technical details can be found in De Zan and Monti Guarnieri, 2006. In this mode, the pixel is not square, with a 5-metre (range) by 20-metre (azimuth) size. The swath is 250-km wide (range direction) and is divided into three subswaths that need to be merged during the processing part (c.f., section *Processing InSAR data*).

- Extra-wide swath (EW) mode, that is working similarly to the IW mode but with larger swaths (400 km) and coarser resolution (25x40-metre). The swath is divided into five subswaths. This mode is used over drift ice, and to monitor ships positions or oil spills.

- Wave (WV) mode, which is a discontinuous acquisition mode used over oceans. It is less energy consuming than the other modes, and the resulting data are lighter. 20x20-km images are acquired at an interval of 100 km on two parallel lines along the travel direction, with a 5x5-metre resolution.

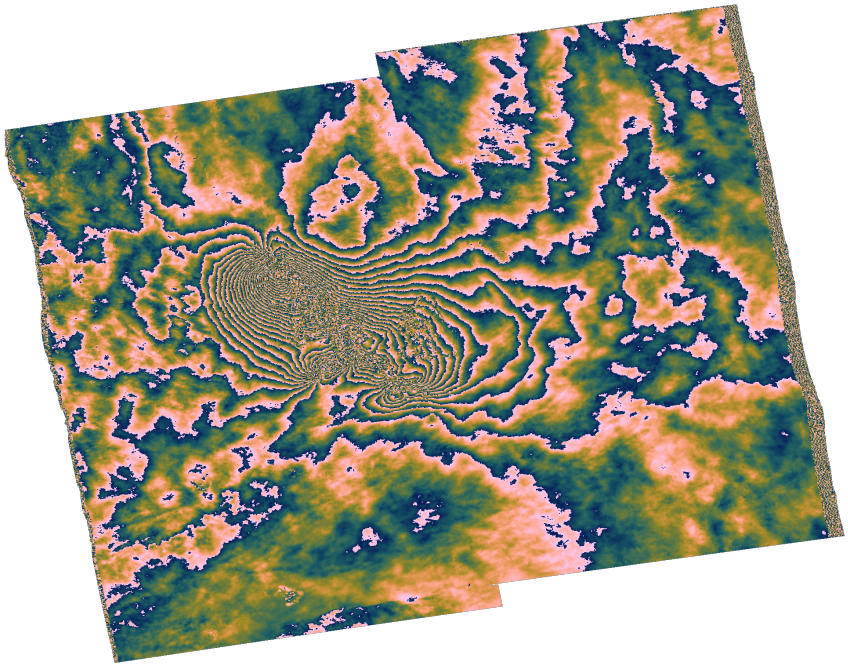

Figure 3.26: Thanks to interferometry, the phase information of Figure 3.26 at epoch 2019-07-16 can now be used with the phase information from another epoch 2019-07-04 to compute an interferogram, showing the differential phase between the two epochs. This interferogram is projected in terrain geometry, on two subswaths. We observe close-set fringes in the middle, caused by the coseismic ground displacement associated with the Mw7.1 Ridgecrest earthquake that happened on 2019-07-05.

The SAR interferometry

If the same region is observed by a SAR device at several epochs, it allows to compute the differential phase between two acquisitions (Figure 3.26). This is referred as SAR interferometry (InSAR). The differential phase can be used to quantify the displacement of the Earth surface along time. It is also possible to use a setup with two antennas going over the same area at the same time, and to use the differential phase between the two antennas to produce a digital elevation model (DEM). This kind of acquisition has been performed in 2000 by the Shuttle Radar Topography Mission (SRTM) which flew the Space Shuttle during 11 days around the Earth in order to produce a DEM with a resolution of 30 meters (size of the ground pixel). SAR interferometry is nowadays commonly used for monitoring volcanoes, landslides, land subsidence, or earthquakes.

Compared to other geodetic techniques, such as GNSS and optical correlation, InSAR has several advantages but also some drawbacks. With modern satellites InSAR can cover most of the Earth surface with a spatial resolution in the order of a few me-

ters. Unlike optical satellites, it is an active technology that is not sensitive to clouds. However, the resolution in time is limited by the revisit time of the satellite, which is at best of a few days: 6 days for Sentinel-1 on some areas when two satellites are operating, 12 days or more otherwise. In addition, the phase difference measured by InSAR is not always representative of the actual ground displacement, either because of the obstacles on the ground (vegetation, buildings...) or because of the perturbations in the troposphere or the ionosphere. There are also multiple other contributions that can affect InSAR measurements, requiring a careful interpretation of the data, that we are going to detail in the next section. Finally, InSAR only measures a displacement in the line-of-sight of the satellite, instead of measuring the three components (East, North, Up) like GNSS. We will see that it is possible in some cases to recover horizontal and vertical displacements with some hypothesis, but it is not as easy and reliable as for GNSS.

Sources of error in InSAR measurements

InSAR measurements are affected by various sources of error, which may be more or less preponderant depending on the acquiring satellite or the area of interest. Like GNSS, some errors are caused by factors altering the propagation of electromagnetic waves (e.g., ionospheric and tropospheric delays) or satellite orbits, but others are specific to InSAR.

Geometric distortions are inherent to radar acquisitions. A single radar antenna is able to measure the distance to an object but is not able to discriminate two objects at the same distance with different angular positions. Consequently, when a SAR image is acquired over an area with a sharp topography, some features may be incorrectly located, some areas distorted, or even hidden. The three effects involved are foreshortening, layover, and shadowing (Figures 3.27 and 3.28).

Foreshortening happens when the radar is scanning a hill with one slope facing the antenna. The slope facing the antenna will appear shortened on the image because the radar waves reflecting on the bottom and at the top are at a similar distance to the satellite, while the other slope will appear longer. Foreshortening is maximal in near range.

Layover occurs when a slope facing the antenna is steeper than the look angle of the satellite. In this case, a point on top of the slope will be closer to the satellite than a point at the bottom of the slope, affecting its horizontal localization on the image. Layover is maximal in the near range.

Shadowing refers to areas that are hidden by a tall feature, such as a mountain. The transmitted wave is reflected by the slope facing the antenna, while the slope behind is invisible to the radar. Shadowing is maximal in far range.

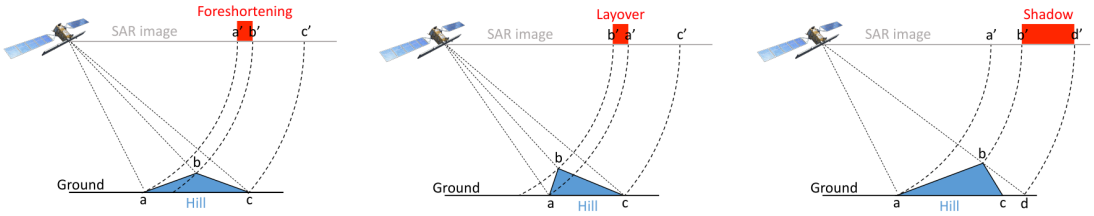

Figure 3.27: Geometric distortions that can occur with SAR acquisitions: foreshortening (left), layover (middle), and shadow (right).

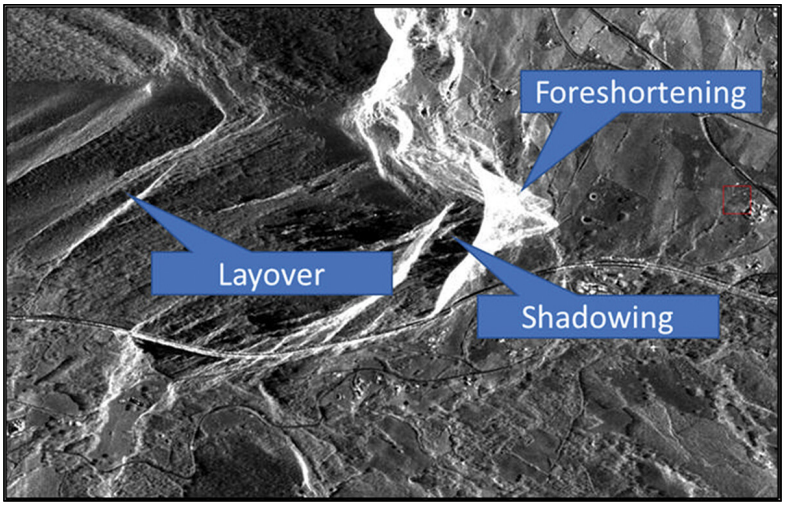

Figure 3.28: Figure from Bausilio et al., 2024 showing foreshortening, layover, and shadow effects on a SAR COSMO-SkyMed acquisition.

One of the main limiting factor with InSAR is decorrelation, which corresponds to strong discrepancies within pixels between two SAR acquisitions, introducing noise in the interferometric phase and preventing the track estimation of accurate surface displacements. This effect can be due to surfaces absorbing a significant part of the transmitted wave, or scattering energy in various directions. Vegetation or unstable surfaces such as sand or water show very strong decorrelation. In addition, the longer the time between two acquisitions, the higher is the decorrelation (known as *temporal* decorrelation). Loosely controlled orbits can also increase decorrelation because of higher variations in the acquisition geometry (known as *spatial* decorrelation). Note that this last point is less critical with modern satellites such as Sentinel-1 thanks to better constrained orbits. Finally, longer electromagnetic wavelength are less affected by decorrelation, especially on vegetated area because of the ability of larger wavelengths to penetrate through the vegetation. This latter point can influence the choice of the satellite instrumentation to study a vegetated area.

In order to retrieve the surface displacements from the differential phase in the interferograms, a step referred as *unwrapping* is required during the processing (see section *Processing InSAR data*). However, if the phase gradient is too strong, it can prevent the phase unwrapping. Indeed, according to the Nyquist frequency theorem, the sampling frequency to record a signal with a frequency f has to be at least two times f. Virtually, for InSAR applications we even consider that the spatial sampling frequency should be at least four times the signal frequency (Conroy et al., 2022). It means that the displacements in the LOS on one pixel should be less than one fourth of the radar wavelength λ in order to avoid phase ambiguity. For Sentinel-1, which has a wavelength λ = 5.5 cm and a 20-by-5 meters ground pixel, it means that the displacement gradient should not exceed 2.7 mm/m. For some events such as earthquakes this value can be exceeded, leading to incorrect unwrapping. Using a radar with a longer wavelength will mitigate this effect, for instance the ALOS-2 satellite signal has a wavelength of 24 cm, allowing to unwrap signals with phase gradients more than four times higher than for Sentinel-1. The interferograms are often sub-sampled in a step referred as *multilooking*, reducing the speckle, improving the signal-to-noise ratio, and reducing the size of the final products (Joughin and Winebrenner, 1994; Parizzi and Brcic, 2011). The multilook factor indicates the reduction of the lateral resolution, for instance a 8-look interferogram has a lateral resolution eight times lower than the original product.

Like GNSS, InSAR measurements can be affected by the electronic content of the ionosphere (Figures 3.29 and 3.30). But unlike GNSS, InSAR cannot rely on the dispersive properties of the ionosphere to cancel out this effect using dual frequency (except for the brand-new NISAR satellite from NASA and ISRO).

Actually, the interaction of the radar wave with the free electrons causes a phase advance and a group delay, leading to distortions on the images. In addition, due

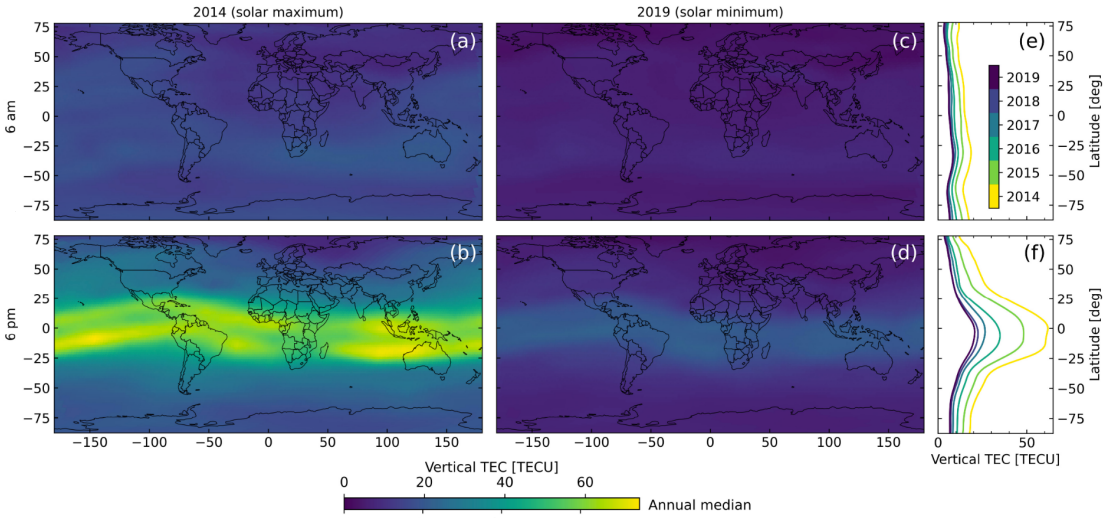

Figure 3.29: Figure modified from Yunjun et al., 2022 showing the annual median of vertical TEC (vTEC) in 2014 which corresponds to a solar maximum (a, b), and in 2019 which corresponds to a solar minimum (c, d). They are reported for 6 am (a, c) and 6 pm (b, d) solar times. It shows that vTEC is maximized at a solar maximum, and at 6 pm compared to 6 am. In addition, vTEC is significantly higher in the equatorial region (about three times higher in Ecuador than in France).

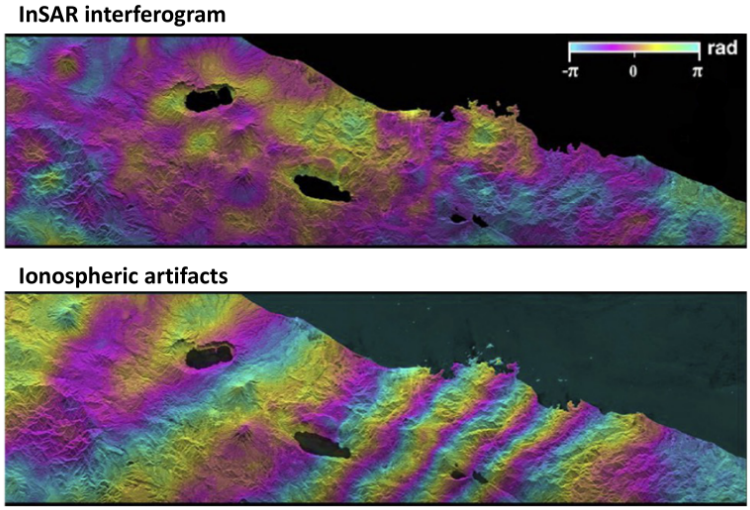

Figure 3.30: Figure modified from B. Zhang et al., 2022 showing an example of ionospheric artifacts on an InSAR interferogram.

to the magneto-optical Faraday effect, the interaction with the Earth magnetic field leads to a rotation of the polarization. Higher frequency signals are less affected by the ionosphere, meaning that a C-band satellite like Sentinel-1 (wavelength of 5.5 cm) may be favored over a L-band one like ALOS-2 (wavelength of 24 cm) in areas prone to ionospheric effects such as equatorial regions.

Several post-processing mitigation strategies exist, including using global ionosphere models (Marconato et al., 2024; Marconato et al., 2025), using GNSS-estimated ionospheric delays (Liao et al., 2020, or using data-based methods. Data-based methods do not rely on any ionosphere model, instead they assess the ionospheric delay based on some features in the SAR data. They rely either on the polarization rotation due to the Faraday effect, phase shift in the azimuth direction, or split-spectrum methods (B. Zhang et al., 2022).

In addition to ionospheric delay, InSAR is also affected by tropospheric delay (Figure 3.31). This delay results both from a slightly slower propagation velocity in the troposphere compared to vacuum and from refraction. The *dry* delay depends on the density of the troposphere (pressure and temperature), while the *wet* delay depends on the humidity. The stratified wet and dry delay can be modeled using global atmospheric models (pressure, temperature, humidity) (Ding et al., 2008; Jolivet et al., 2014; Z. Zhang et al., 2022), and is often correlated to the topography. The turbulent signal is more difficult to remove because it is a short wavelength signal, with a rapid evolution. Methods relying on dense GNSS networks are able to model the turbulent signal (Albino et al., 2025) but it can only be performed at a local scale.

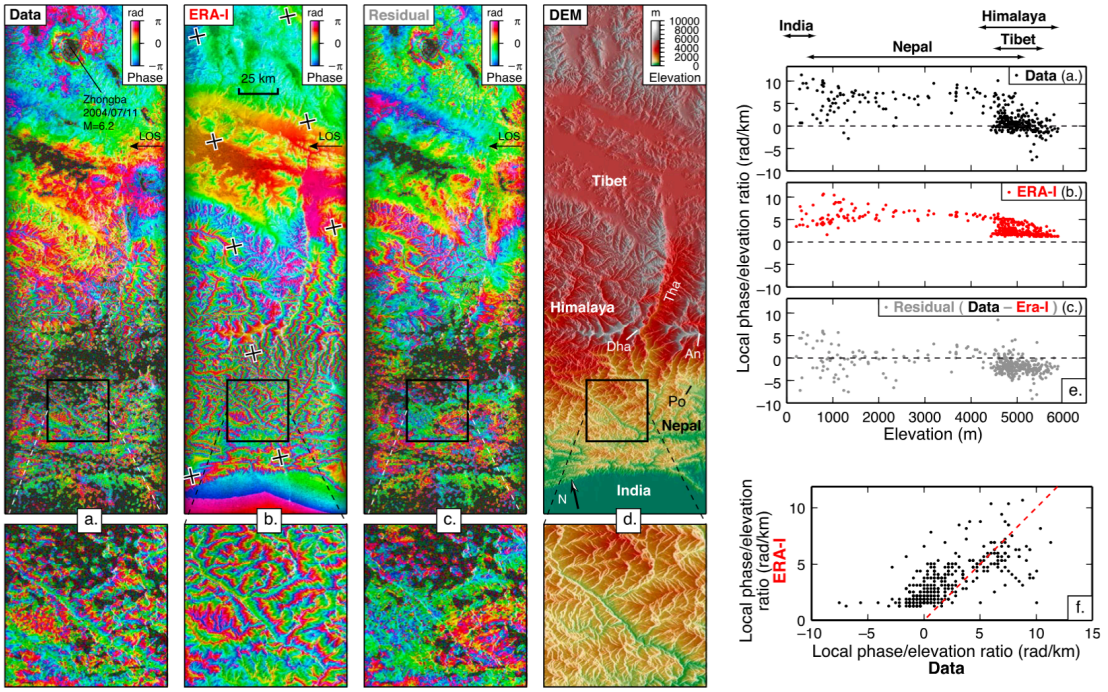

Figure 3.31: Figure from Jolivet et al., 2011 illustrating tropospheric delay on an interferogram. (a) Wrapped interferogram from ENVISAT acquisitions over Himalaya, in radar geometry. (b) Tropospheric correction computed from the ERA-I global atmospheric model. The black crosses indicate the ERA-I grid nodes. (c) Interferogram corrected from the tropospheric contribution. (d) SRTM digital elevation model. (e) Observations (top, black dots), tropospheric ERA-I predictions (middle, red dots), and residuals after tropospheric correction (bottom, gray dots) for local phase-elevation ratios. The dashed line shows zero mean phase-elevation ratio. We observe that the residuals are distributed close to the dashed line, meaning that they removed most of the elevation-correlated tropospheric signal. (f) Observed (x-axis) vs. predicted from the ERA-I model (y-axis) phase-elevation ratios. The red dashed line indicates the unit correlation. We observe a relatively significant correlation (coefficient of 0.67).

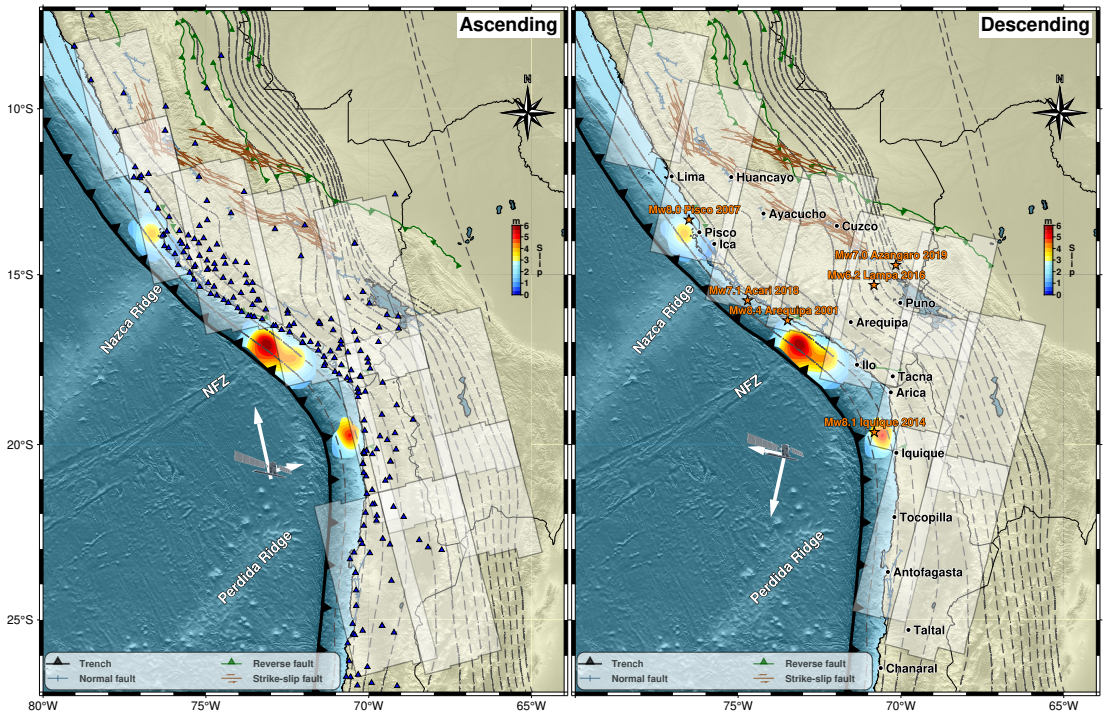

Figure 3.32: Footprints for the ascending (left) and descending (right) Sentinel-1 tracks processed in the frame of the FLATSIM Central Andes project.

The InSAR data used in this PhD

For this PhD thesis, we benefit from the Sentinel-1 InSAR data processed in the frame of the FLATSIM Central Andes project (principal investigator Mohamed Chlieh), resulting from a call for idea in 2020 for the FLATSIM service (FormaTerre, 2020). FLATSIM, which stands for FormaTerre LArge-scale multi-Temporal Sentinel-1 InterferoMetry, is an automated service provided by the FormaTerre Solid Earth data and service center that processed Sentinel-1 InSAR acquisitions for large-scale applications. The service is operated by the French national space agency (CNES), with the technical and scientific support of ISTerre/LGL-TPE/IPGP scientists and engineers. It benefits from its high-performance computing (HPC) platform, as well as its engineering and management team. Handling the processing on the CNES platform has the advantage of a direct access to the Sentinel-1 archive, which is a key factor for computing efficiency since InSAR processing is a very I/O-intensive task (i.e., reading and writing data is a strong limiting factor). The processing is following a small baseline approach and is based on the New Small temporal and spatial BASelines (NSBAS) InSAR processing chain (M.-P. Doin et al., 2011; Grandin, 2015), it is briefly explained in section *Processing InSAR data*, and more in-depth technical details can be found in Thollard et al., 2021, M.-P. Doin et al., 2011, and Lemrabet et al., 2023.

For the FLATSIM Central Andes project, 12 orbits have been processed spanning the 2015-2021 period, with 7 ascending and 5 ascending geometries, from 8°S to 26°S in latitude and from 79°W and 65°W in longitude. For processing purpose, some of the orbits have been split into two or three segments, leading to 21 segments in total that we refer as *tracks* (Figure 3.32). It covers a large area of about 900,000 km-square from Trujillo in Central Peru to the Copiapo Ridge in North Chile. Level-1 Standard Archive Format for Europe (SAFE) Sentinel-1 products from ESA are processed into interferograms, and then inverted into displacement time series. In total, 17,000 interferograms have been computed, which corresponds to more than 30 TB on disk. The temporal coherence, a proxy of the signal stability over time, is high on most of the processed area (>0.8) due to a dry climate with few vegetation (Figure 3.33). Areas with dense vegetation, such as the Amazonian Forest, show low coherence (<0.3), as well as salt lakes or water surfaces, leading to unsuccessful phase unwrapping. Resulting InSAR mean velocity maps show the areas where the unwrapping was successful (Figure 3.34), covering most of the Cordillera, the Altiplano, and the deserts (including the Atacama and Sechura deserts) within the processed latitude range. The final products are multi-looked to a 16-look resolution (320 meters), which is enough for tectonic application, improving signal coherence and reducing products size. The time series have about 140 epochs for most of the tracks, with one acquisition every 12 days when both satellites Sentinel-1A&B were operating together after the launch of Sentinel-1B in April 2016.

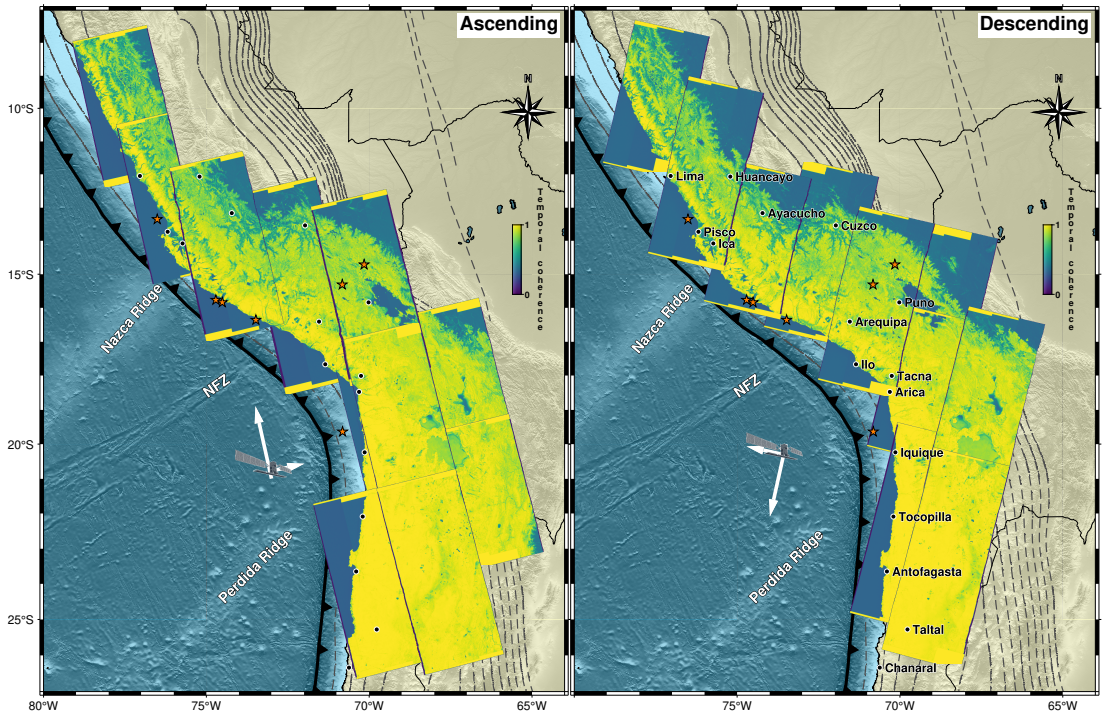

Figure 3.33: Temporal coherence, from 0 (no coherence) to 1 (perfect coherence). Most of the area westward of the Cordillera show a good coherence because of low vegetation.

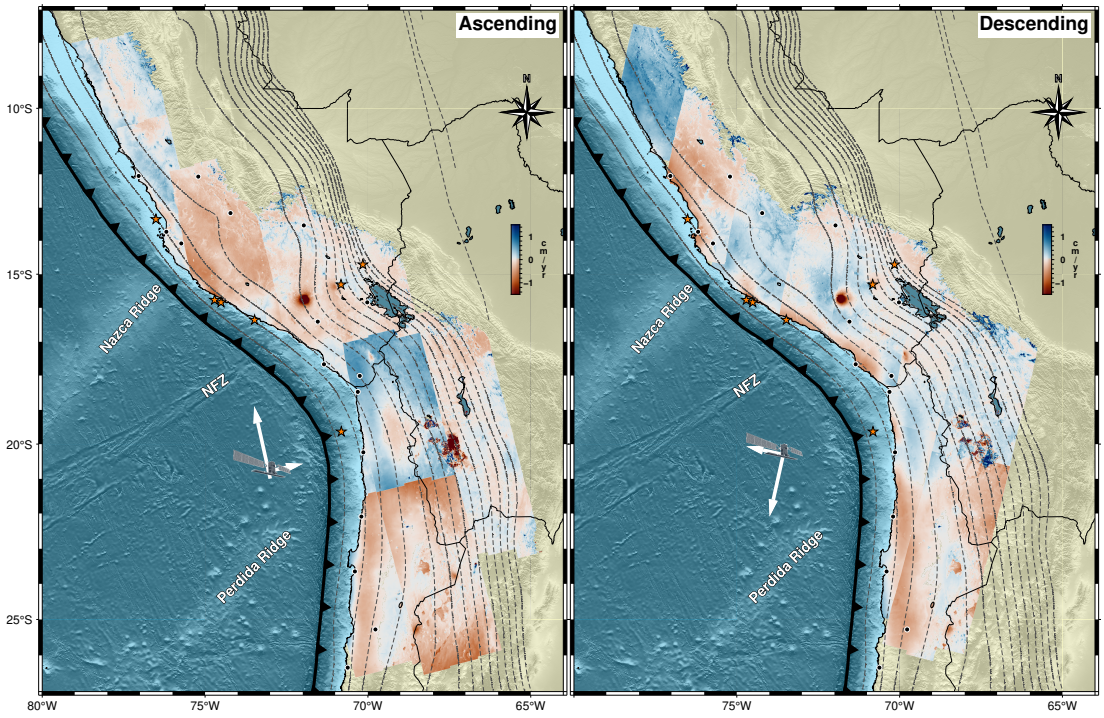

Figure 3.34: Mean velocity maps (2015-2021) in the line-of-sight (LOS) from FLATSIM, prior to any post-processing. Displacements are expressed positive when going away from the satellite.

Processing InSAR data

In this section, I briefly explain the processing scheme used by FLATSIM, without detailing all the technical subtleties, since I have not processed the data myself during this PhD. Readers can refer to Thollard et al., 2021 for full details on the FLATSIM service, to M.-P. Doin et al., 2011 for the NSBAS processing, and to Grandin, 2015 to see how the NSBAS processing chain has been adapted for the TOPSAR acquisition mode. NSBAS is based on the ROI_PAC package, for which technical details can be found in Rosen et al., 2004. The general processing scheme described here is to some extent representative of the general procedure used by other groups with other softwares, but some aspects may differ such as the atmospheric correction, the unwrapping, or the time series inversion.

First, raw SAFE products (in radar geometry) containing the amplitude and phase information are downloaded and converted to a *single-look complex* format (Figure 3.35). Precise orbits are also downloaded from ESA in order to compute accurately the perpendicular baseline between acquisitions. A reference image is chosen based on spatial and temporal baselines criteria: the reference image should be more or less in the middle of the studied time range and in the middle of the perpendicular baseline range, in order to minimize the discrepancies with other acquisitions. Then, the other acquisitions are referenced into the reference geometry with the help of a digital elevation model (DEM). For FLATSIM, the SRTM DEM was used with a 30-meter resolution.

Interferograms quantifying the differential phase delay between two given acquisitions can then be computed, following a network with various spatial and temporal baselines (Figure 3.37). Short temporal baseline interferograms are computed between every acquisition n and the n+1, n+2, and n+3 acquisitions. In addition, long temporal baseline interferograms are computed with a separation of 2-3 months and 1 year, and a perpendicular baseline of less than 100 meters. To account for the phase shift that occurs between the bursts when using the TOPSAR acquisition pattern, a spectral diversity correction is applied (Grandin, 2015). The interferograms are then down-sampled (multi-looked) to a given resolution, which was 16-look for FLATSIM Andes meaning that they are down-sampled by a factor 16 in azimuth and 64 in range, in order to increase the temporal coherence and to decrease the final product size. A merge of the three subswaths is performed in order to have a single smooth image along the swath width. The stratified topography-related tropospheric delay is corrected using the ERA5 global atmospheric model (Figure 3.38) containing information in the pressure, density, and humidity variables (M. .-P. Doin et al., 2009; Hersbach et al., 2020; Jolivet et al., 2011; Jolivet et al., 2014).

The interferograms are unwrapped, in order to raise the phase ambiguity and express the absolute phase difference (Figure 3.36). The algorithm is described in M.-P.

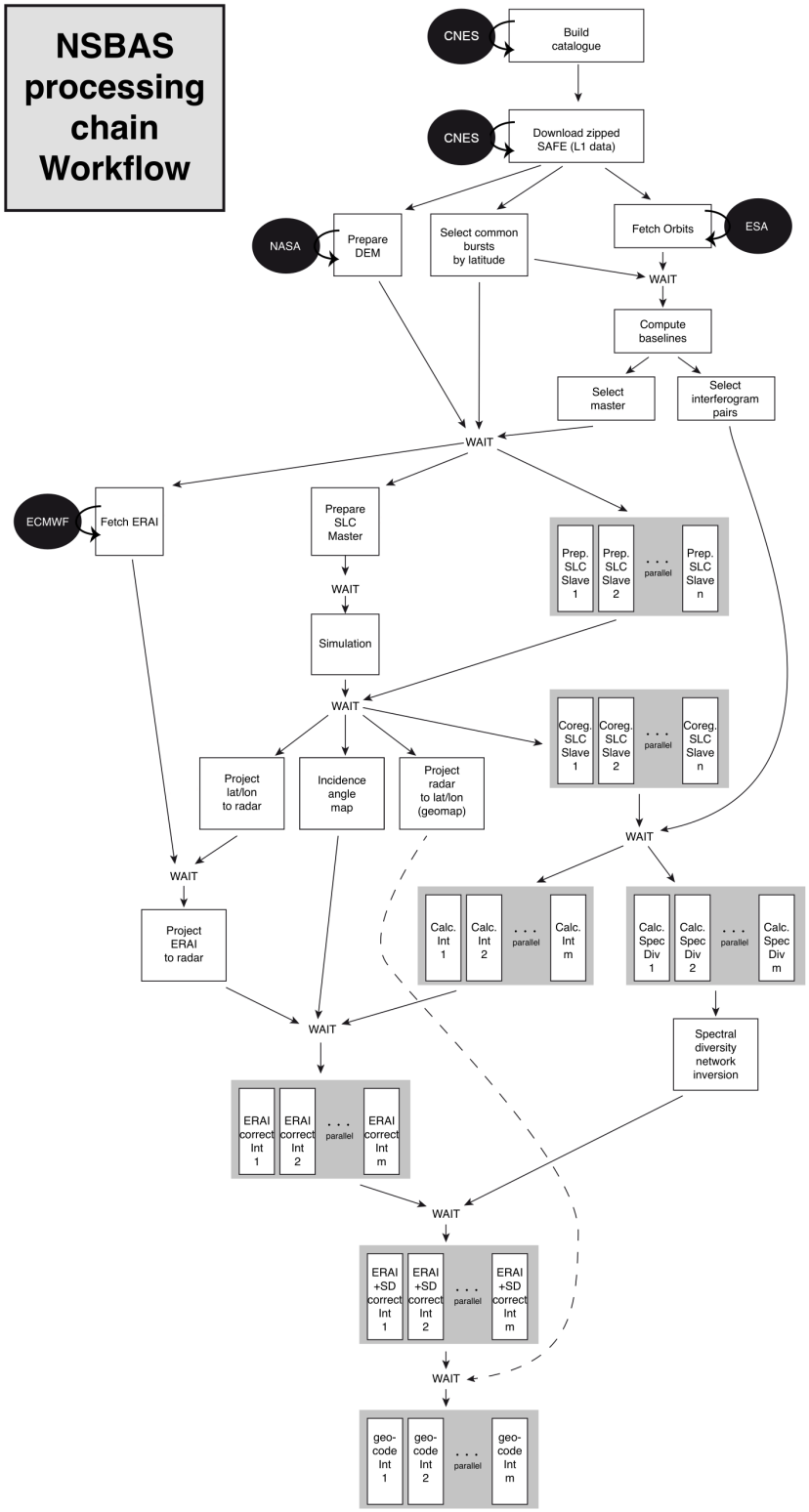

Figure 3.35: The typical NSBAS workflow, from the SAFE products to geocoded interferograms.

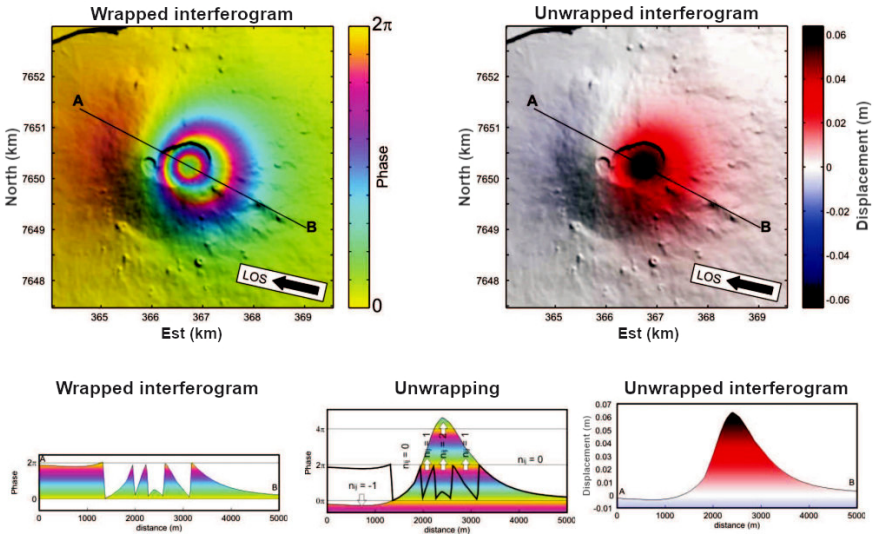

Figure 3.36: Figure modified from Augier, 2011 describing the process of unwrapping interferograms. The idea is to recover the actual displacement between the two acquisitions by summing the phase cycles. Unwrapping is performed progressively from a starting point with a high coherence.

Doin et al., 2023. Basically, it starts by unwrapping areas with a strong temporal coherence and then progressively unwraps neighboring areas. The software also geocodes the interferograms into the terrain geometry.

Using the unwrapped interferograms, displacements time series can be generated, expressing the displacement along time for each pixel of the acquisition (Figure 3.39). For that, interferograms are flattened by removing ramps (linear component of the signal) in azimuth and range directions before running the inversion. An iterative inversion scheme is used to compute the time series, reducing the weight of interferograms with high residual. Maps of average velocity are then computed from the timeseries, indicating the average velocity for each pixel on the acquisition period (2015-2021). The velocities then need to be referenced in a stable reference frame, such as ITRF, to be used for large-scale applications. This task is not handled by FLATSIM and can be achieved using various methods, often relying on GNSS velocities (Lemrabet et al., 2023; Metzger et al., 2021) or phase gradient stacking methods (H. Xu and Wang, 2025). Our approach, based on GNSS velocities, is described in Chapter 7.

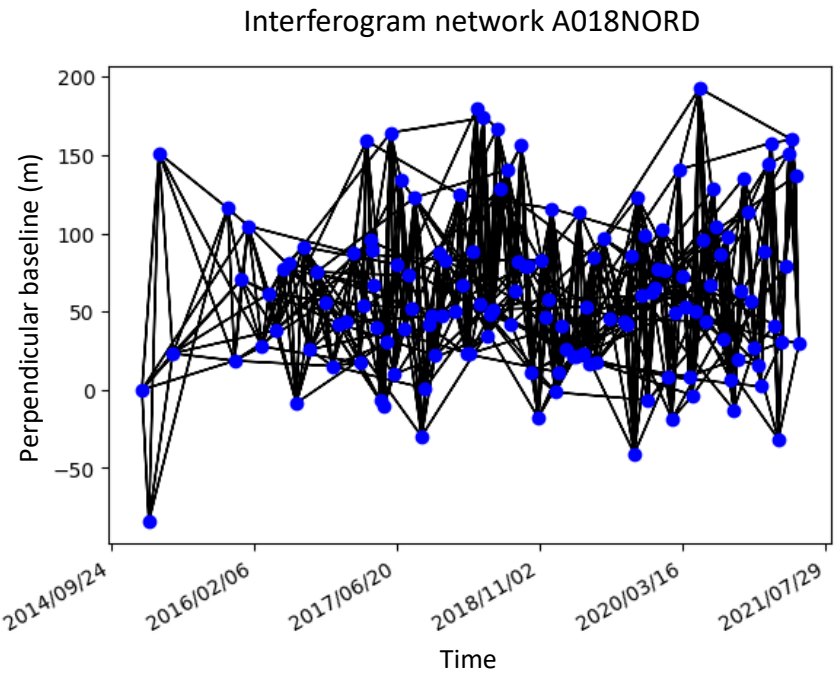

Figure 3.37: Interferogram network for the FLATSIM Central Andes A018NORD track. Each acquisitions (blue dots) are reported according to their respective epoch (x-axis) and perpendicular baseline (y-axis). Interferograms (black lines) are computed from acquisition pairs on short and long temporal baselines.

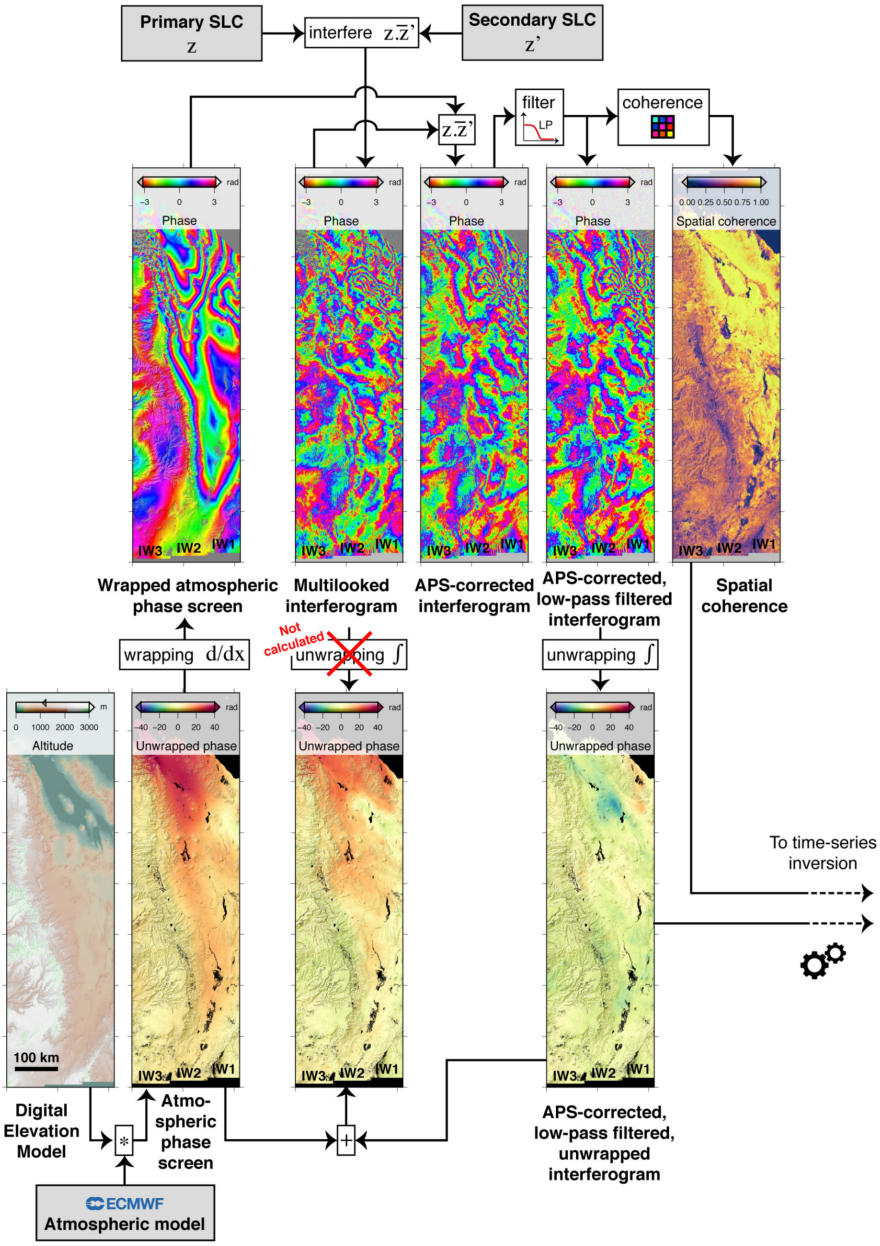

Figure 3.38: Figure from Thollard et al., 2021 showing the processing steps in NSBAS for computing filtered atmospheric-corrected unwrapped interferograms: computing interferograms from two SLC acquisitions, multilooking, computing atmospheric phase screen (APS) from the ECMWF ERA5 global model, unwrapping, filtering, and computing the spatial coherence.

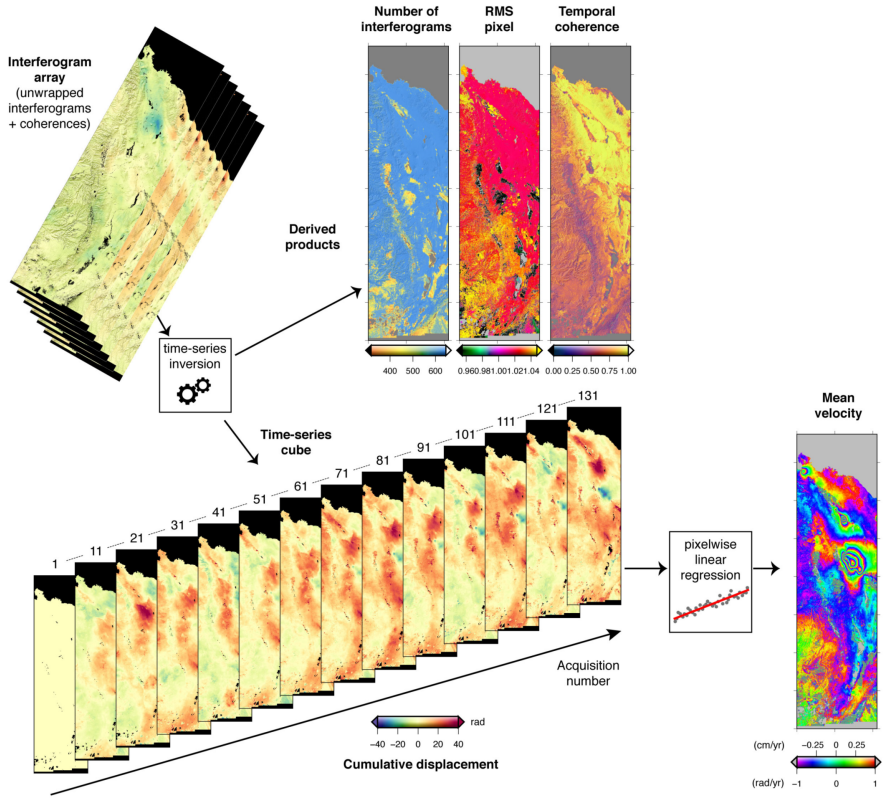

Figure 3.39: Figure from Thollard et al., 2021 illustrating the time series products. Interferograms with various temporal baselines are inverted into displacement time series, and some auxiliary products are provided: maps of the number of interferograms per pixel, root mean square, and temporal coherence. Then, mean velocity maps are computed through pixel-wise linear regression of the time series cube.

3.2 Technical aspects of the seismic cycle modeling

3.2.1 The inverse problem

The approach of computing the consequences of a process after defining its causal factors is known as *forward* or *direct* modeling. For instance, starting from the slip on the subduction interface related to a given process of the seismic cycle (coseismic slip, interseismic slip, or afterslip), one can model the displacements at the surface. The converse, is known as the *inverse problem* or simply *inversion*. In our study, we need to model the slip on the interface from the inversion of the observed surface displacements, known from the GNSS or InSAR measurements.

All the inversions we did in the following chapters have been performed using the linear least-square formulation of Tarantola and Valette (Radiguet et al., 2011; Tarantola, 2005; Tarantola and Valette, 1982). The geometry of the slip interface is shaped by the 3-D slab model from Slab2 (Hayes et al., 2018), and it is discretized into triangular elements that we refer as *sub-faults* (about 15 km large). On each of these sub-faults, a strike-slip and a dip-slip component of the slip vector is computed. The matrix d of surface displacements is then linked to the matrix m of slip on the fault:

$$d = G \cdot m \tag{3.10}$$

where G is the matrix of Green's functions that characterize the impulse response of the medium in a static case, neglecting the inertial effects. Green's functions are either calculated by considering an elastic half-space using the formulation of Meade, 2007 for triangular dislocations, or by considering a viscoelastic medium (see Chapter 5).

The inversion scheme is aimed at minimizing the cost function $S(m)$:

$$S(m) = \frac{1}{2}\left[(Gm - d)^t C_d^{-1}(Gm - d) + (m - m_0)^t C_m^{-1}(m - m_0)\right] \tag{3.11}$$

with m the slip on each sub-fault:

$$m = m_0 + C_m G^t (G C_m G^t + C_d)^{-1}(d - G m_0) \tag{3.12}$$

and m_0 the slip prior of the model (which can be selected from zero for a null slip prior, up to the plate convergence velocity for a fully-locked slip prior), C_d and C_m the data and model co-variance matrices, and G^t the transpose of the G matrix.

The data co-variance matrix C_d is diagonal, since we neglected the off-diagonal terms, and built from the uncertainties on the observed displacements. The model co-

variance matrix C_m smoothens the slip distribution between the neighboring sub-faults using an exponential formulation:

$$C_m(k,l) = \left(\sigma_m \frac{\lambda_0}{\lambda}\right)^2 e^{-\frac{d(k,l)}{\lambda}} \tag{3.13}$$

with λ the spatial correlation length, λ_0 the characteristic size of the sub-faults, *d(k,l)* the distance between two source elements k and l, and σ_m the uncertainty on the initial model that we use as a damping factor controlling the balance between minimizing the misfit and minimizing the distance to the initial model (slip prior).

The correlation length λ and the damping factor σ_m have to be tuned jointly by plotting *L-curves* that show the variation of the misfit as a function of a given metric (such as the maximal slip, the Manhattan distance L1, or the Euclidean norm L2 of the slip vectors) for various values of λ and σ_m.

The misfit between data d and model m is quantified by the reduced chi-square χ^2_{red}:

$$\chi^2_{red} = \frac{\chi^2}{\nu} \text{ with } \chi^2 = \sum_i \frac{(d_i - m_i)^2}{\sigma_i^2} \tag{3.14}$$

with σ^2 the variance and ν = n - p the degrees of freedom for n observations and p parameters.

Example of L-curves can be seen on Figure 3.40 or Figure S6 of Chapter 4. Note that in the inversion scheme used in Chapters 4 and 5 the maximal slip value is not constrained, which means that the smoothing has to be carefully tuned in order not to overcome the plate convergence velocity and having a non-physical coupling above 1. In Chapter 6, we modified our inversion scheme to have a bounded inversion where the maximal slip value is set, allowing more flexibility in the smoothing parametrization and more detailed slip distributions.

Due to the non-uniformity in the spatial distribution of the GNSS network, not all areas of the slab interface are resolved with the same confidence. Overall, we tend to have a lot of GNSS sites close to the coast, and less sites in the arc and back-arc. This is not really an issue and GNSS networks aimed at studying tectonic processes are generally designed this way, as the slip on the interface (either for coseismic, afterslip, or interseismic) is expected to be mainly distributed from the trench to a 60-km depth. A more limiting factor is the lack of GNSS sites close to the trench, since we do not have sea-floor measurements. The Peruvian and Chilean coasts are typically located between 100 and 200 km from the trench, which means that we may not map very accurately the slip on the shallowest part of the interface. To account for this limitation, we propose interseismic coupling models with a null or fully-locked (constrained by the plate convergence velocity) slip prior, leading to two end members. Also, we tend to have a sparser network in Central Peru, North of the Nazca ridge, compared to South

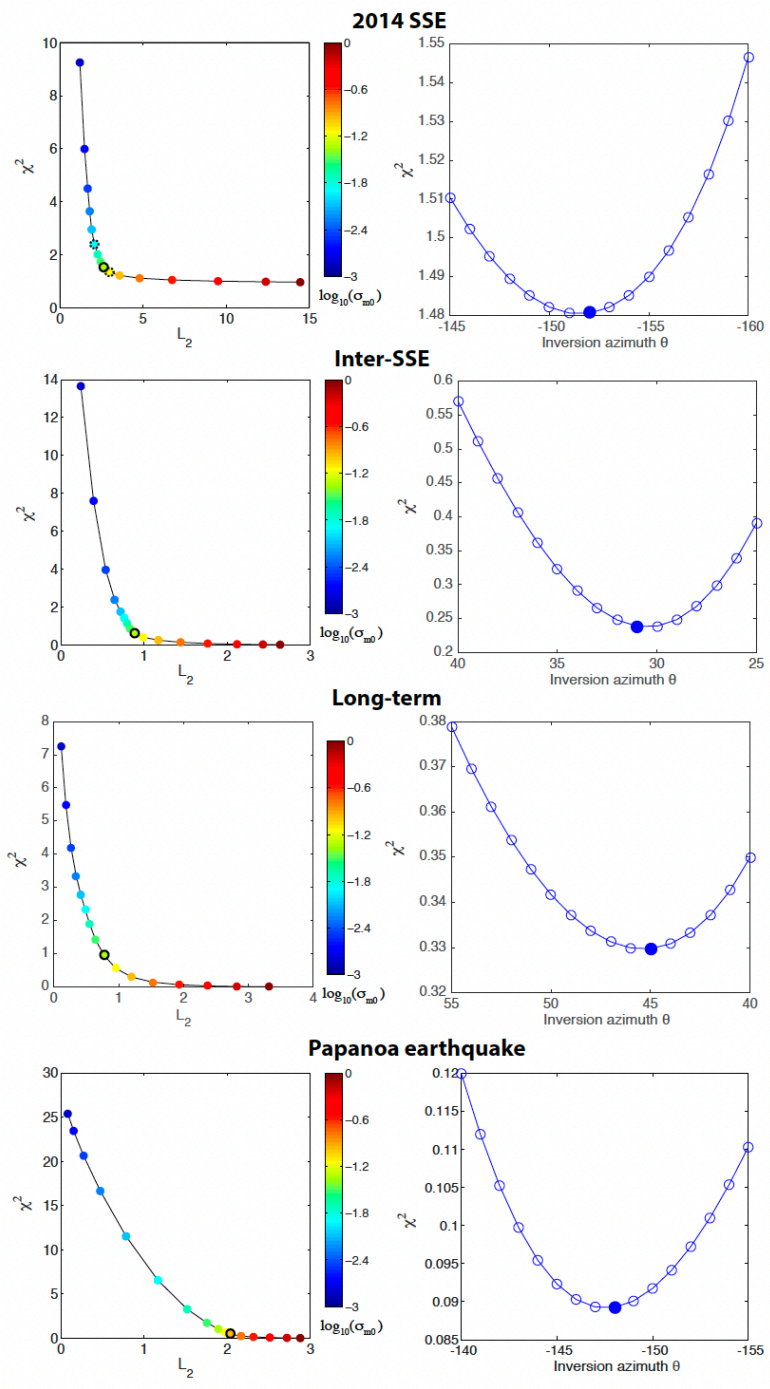

Figure 3.40: Figure from Radiguet et al., 2016 showing *L-curves* used to select the damping parameter (left). The data misfit (χ^2 and the associated average Euclidean norm of the slip vectors for each value of the damping parameter σ_m. The selected value, encircled in black, is chosen in the hollow part of the curve where the absolute value of the second derivative is the highest. On the right is shown the misfit in function of the selected convergence angle, they simply select the value for which the misfit is the lowest.

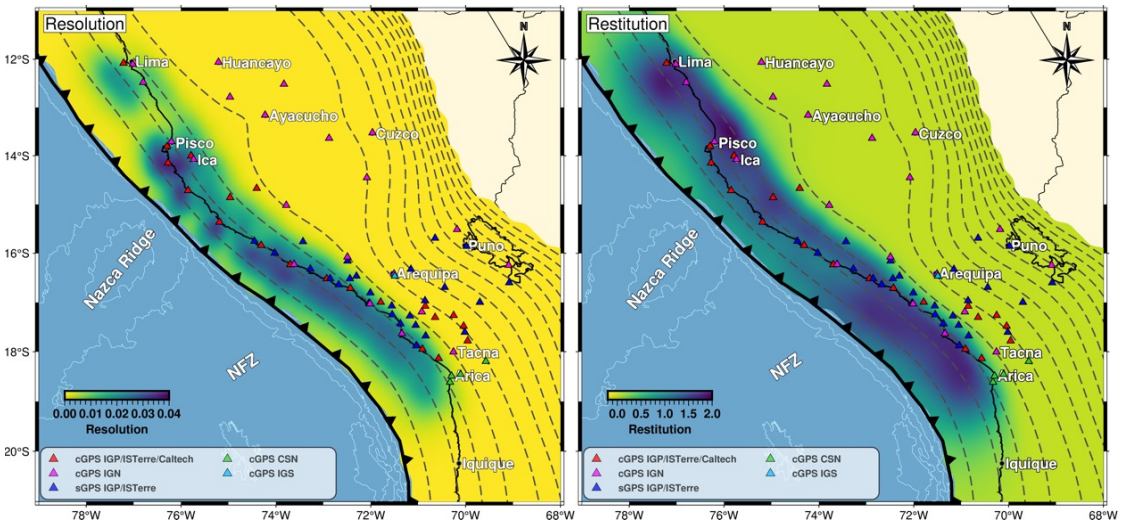

Figure 3.41: Diagonal values of the resolution matrix R (left) and restitution (right) on the slab, for the final interseismic model shown in Chapter 4. Whereas the diagonal elements of R inform us about how much the slip of a specific patch is accurately mapped on this patch by the program, the restitution informs us if this slip has been correctly projected onto other patches. We observe distinctly an edge effect near the 60-km iso-depth where the patches have a higher restitution because of the slip confinement, since the displacements on the stations more inland are mainly accommodated by these deep patches.

Peru or North Chile. To determine quantitatively the quality of the slip mapping on the interface, we define the resolution matrix R:

$$R = C_m G^t (G C_m G^t + C_d)^{-1} G \tag{3.15}$$

The higher the resolution is for a given sub-fault, the better is the slip mapping on this sub-fault. For a very well resolved model, the resolution matrix should tend toward the identity matrix. We also define the restitution as the sum of the rows of R, which indicates how well the slip of a given sub-fault has been accurately projected onto the other sub-faults (Figure 3.41).

Note that apart from these mathematical considerations, some hypothesis are made regarding the physics of the problem. First, we consider a uniform slip direction for all sub-faults. This hypothesis is sensible for modeling the coseismic or afterslip distributions of a subduction earthquake, which is extending on a relatively limited length along-strike (a few hundreds of km). It is also valid for modeling interseismic slip in South Peru or North Chile, since the estimated convergence direction is very uniform (Jaillard and Soler, 1996; Jarrin et al., 2023; Kendrick et al., 2003; Khazaradze and Klotz, 2003; Villegas-Lanza et al., 2016). This approach avoids having rotations of the

slip vectors from one sub-fault to another, which would allow a lower misfit due to the increase of model parameters at the cost of an unrealistic model. Still, using a uniform slip direction would become inadequate to map very large areas with a significant change in the convergence direction (e.g., modeling the whole Peru-Chile subduction from the Ecuador to South Chile, or the whole Japanese subduction).

The second hypothesis we did is to consider that the slip is constrained in the first 60 km of depth on the interface, following the laboratory experiments on rocks mechanical behavior (Kanaya and Hirth, 2018; Oleskevich et al., 1999; Tse and Rice, 1986) and the thermal models (Gagnon et al., 2005; Syracuse et al., 2010; Villegas-Lanza et al., 2016), indicating a ductile behavior beyond 60 km. Accordingly, we apply an exponential decay to taper the slip beyond 60 km.

Finally, for modeling interseismic coupling, we follow the back-slip hypothesis from Savage, 1983, for which the interseismic slip is defined as the difference between the plate convergence rate and the differential velocity between the subducting and overriding plates on the interface. It results in a null slip where the interface is freely slipping (creep), and a positive slip up to the plate convergence velocity where there is locking between the two plates.

3.2.2 Modeling the subduction by Finite Element Method

In order to model postseismic viscoelastic relaxation, and to compute Green's functions accounting for a more realistic structure and rheology, we developed 3-D Finite Element Method (FEM) models of the South Peru subduction. FEM is used in a wide range of applications (e.g., aeronautical and automotive industries, fluid dynamics, or design of critical infrastructures such as buildings or bridges) to numerically solve partial differential equations for discretized elements of a structure. The resolution of a FEM problem follows four main steps:

- Building a structure of the object of interest (such as a subduction zone, a car frame, or a building). The degree of complexity should be assessed depending on the required accuracy, what is known on the actual composition of the object, and the computational cost. Defining very detailed and tortuous shapes can be very time consuming both for designing the structure and running the simulation, and it can be more difficult to discretize, leading to errors. One also need to choose if the problem requires a 3-D structure, or if a 2-D structure is enough. A 2-D problem is easier to design, faster to run, and it can be tuned easily. For instance, if one wants to vary the slab geometry of a subduction zone, a 2-D problem is going to be significantly more convenient. On the other hand, if there are strong lateral variations such as a transition from flat slab to dipping slab (like in South Peru) a 2-D problem will not be appropriate. The spatial distribution

of the observations should also be considered, for instance if we study displacements at GNSS stations that are on the same profile a 2-D problem is fine, while modeling displacements along a 1000-km wide segment requires a 3-D model.

- Discretizing the structure into smaller elements, also known as *meshing*. Once the structure is defined, we need to discretize it in smaller elements (cells), that should be small enough to map accurately the deformation and large enough to have a reasonable computational cost. A variable cell size may also be considered if the required accuracy is not the same on various parts of the mesh. For our models, we chose to have smaller cells (5 km) close to the subduction interface and close to the GNSS sites and InSAR tracks footprints, and larger cells at the external boundaries (up to 100 km). As a rule of thumb, the cells should be at least two times smaller than the distance between stations. Various cell shapes can be used for the meshing, such as rectangular or triangular cells for a 2-D problem, and tetrahedral or hexahedral cell for a 3-D problem. We chose to use tetrahedral elements as it is often used for this type of problems and it tends to be more flexible. Actually, studies indicate that choosing tetrahedral or hexahedral elements result in similar efficiency and accuracy for most cases (Knupp, 2001; Schneider et al., 2022).

- Defining the material properties and the boundary conditions. Various material properties can be assigned to any of the defined bodies, including the viscoelastic properties with parameters such as Young's modulus, Poisson's ratio, or viscosity. Boundary conditions should also be defined in order to constrain the displacements at the external sides of the structure. For our models, we apply Dirichlet boundary conditions allowing tangential displacement while preventing radial displacement on the bottom, North, East, South, and West faces. The top surface is free.

- Solving the problem. After building the structure, meshing it, and defining all the properties of the model, differential equations can be solved at each cells and at various time-steps. The time-steps should be adapted in order to model correctly the displacement over time and avoiding aliasing, while minimizing the computational cost. One may for instance vary the time-step in function of the deformation gradient in time, with finer time-steps when the gradient is strong.

We used the commercial software CUBIT v2023.4 from the Coreform company to build and mesh the structure of the subduction zone in South Peru. The model is 2,000 by 2,000 km wide and 1,000 km deep, which may seems a bit over-sized but we wanted to avoid any edge effect that can arise when the mesh is too small. The tests from Cresseaux, 2024 showed that it is best to have a few hundreds kilometers between the

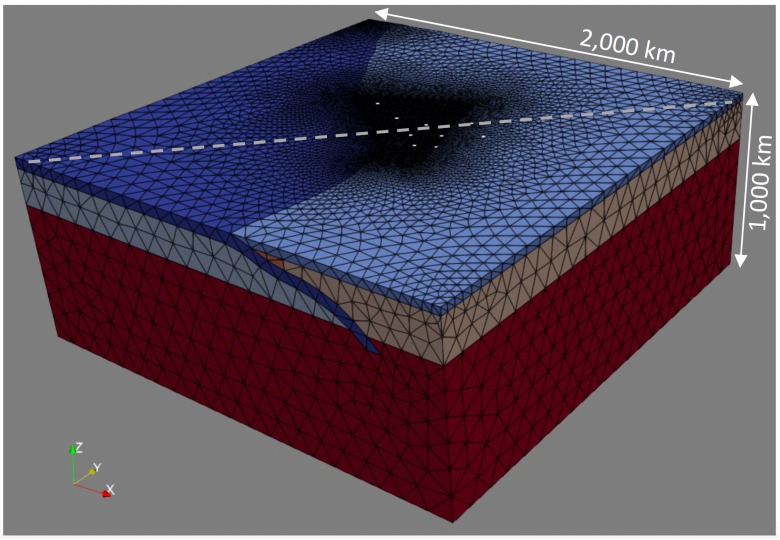

Figure 3.42: 3-D FEM model of the subduction zone in Southern Peru and Northern Chile. The slab is shaped by the Slab2 contours (Hayes et al., 2018), while bathymetry and topography come from SRTM15+ (Tozer et al., 2019). The mesh is 2,000 by 2,000-km wide and 1,000-km deep, using tetrahedral geometry. The cells are 5-km large close to the fault and the GNSS stations (white dots), and up to 100-km large at the external boundaries.

area of interest (such as the GNSS sites) and the external boundaries of the model. The slab interface is shaped by the Slab2 geometry (Hayes et al., 2018), while topography and bathymetry are following the SRTM15+ model (Tozer et al., 2019). Six blocks are defined: continental and oceanic lithospheres that are assigned elastic rheology, continental and oceanic asthenosphere that are assigned viscoelastic rheology (Maxwell or Burgers), lower mantle that is also viscoelastic, and the cold-nose that is assigned elastic rheology. Further details on the properties of the various bodies, and how we refined them, are available in Chapter 5.

Meshing was performed with tetrahedral cells that are about 5-km large close to the slab interface and close to the continental surface where the GNSS network and the InSAR tracks are located, and up to 100 km at the external boundaries. Then, the differential equations were solved using the open-source software PyLith v2.2.2 (B. T. Aagaard et al., 2013; B. Aagaard et al., 2019) published under the MIT license. This software is aimed at solving geophysical problems, including subduction related mechanisms. For studying the viscoelastic relaxation following the 2001 Mw8.4 Arequipa earthquake, we apply the coseismic slip distribution on the interface and we monitor the evolution of the medium by comparing the displacements at the surface with the geodetic observations. The simulations are run on about 30 years, with variable time-steps ranging from one day to a few weeks depending on the time since the earthquake (stronger displacement evolutions are observed in the early postseismic period).

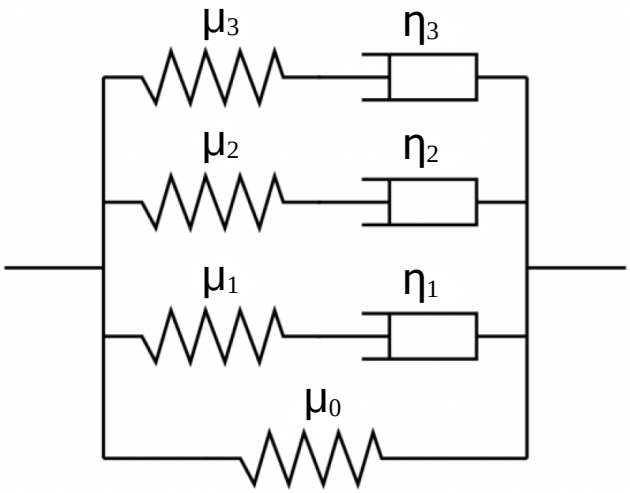

Figure 3.43: Generalized Maxwell with three Maxwell elements, characterized by their respective shear modulus μ and viscosity η, and a spring in parallel.

3.2.3 Defining Burgers rheology in PyLith

We would like to apply a bi-viscous Burgers rheology (see section 2.1.4) to the asthenospheric layers of our model, however this type of rheology is not implemented in PyLith. Instead, they propose a generalized Maxwell rheology (Wiechert, 1893) with three Maxwell elements in parallel (Figure 3.43).

A Burgers body can be expressed in the Kelvin (Figure 3.44, left) or the Maxwell (Figure 3.44, right) formalism. If we consider the generalized Maxwell body of Figure 3.43 with $\mu_0 = \mu_3 = 0$ and $\eta_3 = 0$, we obtain a Burgers body in the Maxwell formalism similar to Figure 3.44 (right).

We now have to express the shear modulus μ_{1K} and μ_{2K}, as well as the viscosities η_{1K} and η_{2K}, into the Maxwell formalism. In the Kelvin formalism, the system obeys the following constitutive equation with a stress σ and a strain ε:

$$\sigma + \left(\frac{\eta_{1K}}{E_{1K}} + \frac{\eta_{2K}}{E_{1K}} + \frac{\eta_{2K}}{E_{2K}}\right)\dot{\sigma} + \frac{\eta_{1K}\eta_{2K}}{E_{1K}E_{2K}}\ddot{\sigma} = \eta_{2K}\dot{\varepsilon} + \frac{\eta_{1K}\eta_{2K}}{E_{1K}}\ddot{\varepsilon} \tag{3.16}$$

while in the Maxwell formalism it obeys the following constitutive equation:

$$\sigma + \left(\frac{\eta_{1M}}{E_{1M}} + \frac{\eta_{2M}}{E_{2M}}\right)\dot{\sigma} + \frac{\eta_{1M}\eta_{2M}}{E_{1M}E_{2M}}\ddot{\sigma} = (\eta_{1M} + \eta_{2M})\dot{\varepsilon} + \frac{\eta_{1M}\eta_{2M}(E_{1M} + E_{2M})}{E_{1M}E_{2M}}\ddot{\varepsilon} \tag{3.17}$$

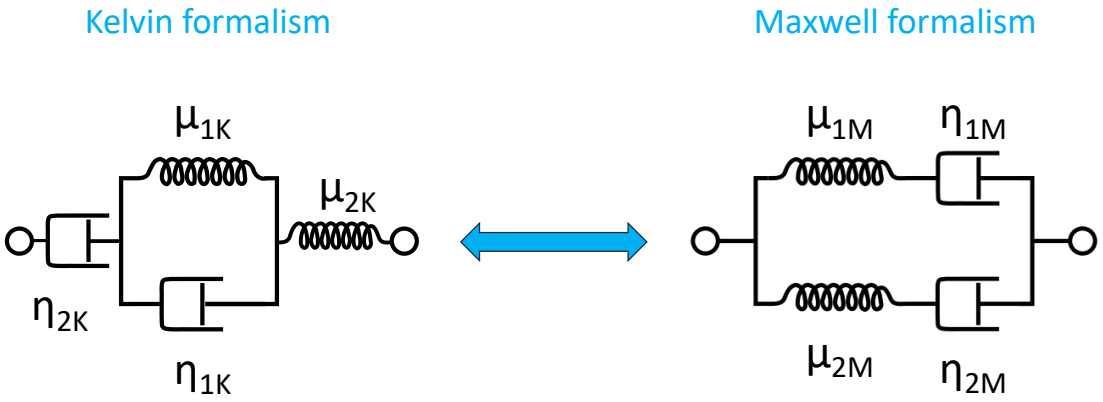

Figure 3.44: A Burgers body in the Kelvin (left) and Maxwell (right) formalisms, each spring and damper is characterized by their shear modulus μ or their viscosity η respectively. Note that the values of shear modulus and viscosity are not the same in the Kelvin and Maxwell formalisms (e.g., $\mu_{1M} \neq \mu_{1K}$).

Let's express equation 3.16 into the s-domain through a Laplace transform with a complex variable s:

$$E_{1K}E_{2K}\bar{\sigma}+(E_{2K}\eta_{2K}+E_{2K}\eta_{1K}+E_{1K}\eta_{2K})s\bar{\sigma}+E_{1K}E_{2K}s^2\bar{\sigma} = E_{1K}E_{2K}\eta_{2K}s\bar{\varepsilon}+E_{2K}\eta_{1K}\eta_{2K}s^2\bar{\varepsilon} \tag{3.18}$$

Stress σ and strain ε for each of the two Maxwell elements of the generalized Maxwell body of Figure 3.44 (right) are expressed:

$$\sigma_1 + \frac{\eta_{1M}}{E_{1M}}\dot{\sigma_1} = \eta_{1M}\dot{\varepsilon} \tag{3.19}$$

$$\sigma_2 + \frac{\eta_{2M}}{E_{2M}}\dot{\sigma_2} = \eta_{2M}\dot{\varepsilon} \tag{3.20}$$

Which gives the following Laplace transforms:

$$\bar{\sigma_1} + \frac{\eta_{1M}}{E_{1M}}s\bar{\sigma_1} = \eta_{1M}s\bar{\varepsilon} \tag{3.21}$$

$$\bar{\sigma_2} + \frac{\eta_{2M}}{E_{2M}}s\bar{\sigma_2} = \eta_{2M}s\bar{\varepsilon} \tag{3.22}$$

The total stress $\bar{\sigma}$ is then written:

$$\bar{\sigma} = \left(\frac{E_{1M}\eta_{1M}s}{E_{1M} + \eta_{1M}s} + \frac{E_{2M}\eta_{2M}s}{E_{2M} + \eta_{2M}s} \right) \bar{\varepsilon} \tag{3.23}$$

We finally obtain the relationships between viscosities η_{1M}, η_{2M} in the Maxwell formalism and viscosities η_{1K}, η_{2K} in the Kelvin formalism:

$$\eta_{1M} = \frac{\eta_{2K}\frac{\eta_{1M}}{E_{1M}} - \frac{\eta_{1K}\eta_{2K}}{E_{1K}}}{\frac{\eta_{1M}}{E_{1M}} - \frac{\eta_{2M}}{E_{2M}}} \tag{3.24}$$

$$\eta_{2M} = \frac{\frac{\eta_{1K}\eta_{2K}}{E_{1K}} - \eta_{2K}\frac{\eta_{2M}}{E_{2M}}}{\frac{\eta_{1M}}{E_{1M}} - \frac{\eta_{2M}}{E_{2M}}} \tag{3.25}$$

And the relationships between shear moduli E_{1M}, E_{2M} in the Maxwell formalism and E_{1K}, E_{2K} in the Kelvin formalism:

$$E_{1M} = \frac{\eta_{2K}\frac{\eta_{1M}}{E_{1M}} - \frac{\eta_{1K}\eta_{2K}}{E_{1K}}}{\frac{\eta_{1M}}{E_{1M}}\left(\frac{\eta_{1M}}{E_{1M}} - \frac{\eta_{2M}}{E_{2M}}\right)} \tag{3.26}$$

$$E_{2M} = \frac{\frac{\eta_{1K}\eta_{2K}}{E_{1K}} - \eta_{2K}\frac{\eta_{2M}}{E_{2M}}}{\frac{\eta_{2M}}{E_{2M}}\left(\frac{\eta_{1M}}{E_{1M}} - \frac{\eta_{2M}}{E_{2M}}\right)} \tag{3.27}$$

Chapter 4

Heterogeneous Locking and Earthquake Potential on the South Peru Megathrust from Dense GNSS Network

This first study has been published in January 2024 in *Journal of Geophysical Research: Solid Earth*. It was primarily aimed at providing an updated interseismic velocity field for South Peru, with a new model of interseismic coupling used to perform an earthquake potential assessment. Compared to the earlier study from Villegas-Lanza et al., 2016 that covered the whole Peruvian subduction, we benefit from extended GNSS measurements in South Peru, with 73 GNSS sites including 47 permanent stations and 26 survey sites. We have 57 GNSS sites between the Nazca Ridge and the Arica bend, compared to 7 in Villegas-Lanza et al., 2016, allowing to refine the interseismic model on this critical segment that hosted the 2001 Mw8.4 Arequipa and 1868 Mw~8.8 earthquakes. Longer GNSS time series, most of the sites having been measured on at least a decade, also allow to better identify and correct the coseismic and postseismic displacements affecting the measurements.

The GNSS time series were carefully analyzed using a trajectory model (Bevis and Brown, 2014; Marill et al., 2021) in order to isolate the interseismic velocity from other signals such as coseismic and postseismic displacements or seasonal variations. Therefore, we also provide coseismic slip distributions for the 2014 Mw8.1 Iquique earthquake and its Mw7.7 aftershock that we modeled from the coseismic offsets we measured at 37 continuous GNSS stations. An afterslip model for the Iquique earthquake is also provided from the postseismic signal that is observed in the GNSS time series. We also provide a coseismic slip model for the 2001 Mw8.4 Arequipa earthquake by inverting the coseismic offsets from Pritchard et al., 2007.

The interseismic velocities have been inverted in an elastic half space using a 3-D slab geometry based on Slab2 (Hayes et al., 2018) and a linear least-square inver-

sion method (Radiguet et al., 2011; Tarantola, 2005; Tarantola and Valette, 1982). The resulting interseismic coupling distribution shows strong heterogeneity, with lower coupling where the Nazca Ridge and Nazca Fracture Zone are subducting. A moment budget analysis performed using the methodology from Avouac, 2015 indicates that the South Peru segment could host a Mw8.4-9.0 earthquake with a recurrence time of 100 to 900 years.

4.1 Manuscript

Heterogeneous Locking and Earthquake Potential on the South Peru Megathrust from Dense GNSS Network

B. Lovery[1], M. Chlieh[1], E. Norabuena[2], J.C. Villegas-Lanza[2], M. Radiguet[1], N. Cotte[1], M. Langlais[1], A. Tsapong-Tsague[1], W. Quiroz[2], C. Sierra Farfán[3], M. Simons[4], J.M. Nocquet[5], H. Tavera[2], and A. Socquet[1]

[1]Univ. Grenoble Alpes, Univ. Savoie Mont Blanc, CNRS, IRD, Univ. Gustave Eiffel, ISTerre, 38000 Grenoble, France

[2]Instituto Geofísico del Perú, Lima, Peru

[3]Instituto Geográfico Nacional, Lima, Peru

[4]Caltech, USA

[5]Institut de Physique du Globe de Paris, IRD

Corresponding author: Bertrand Lovery (bertrand.lovery@univ-grenoble-alpes.fr)

ORCID: 0000-0002-3671-0608

Key Points:

- We present a dense interseismic velocity field at the scale of the South Peruvian Andes, from new decadal GNSS data at 73 locations
- Low locking (~0.4) is estimated along the Nazca Ridge and the Nazca Fracture Zone, delimiting wide patches of high locking (~0.9)
- Moment budget analysis shows that the South Peru segment could host a Mw=8.4-9.0 earthquake with a 100 to 1,000 years recurrence time

Abstract

The Central Andes subduction has been the theater of numerous large earthquakes since the beginning of the 21th Century, notably the 2001 M_w=8.4 Arequipa, 2007 M_w=8.0 Pisco and 2014 M_w=8.1 Iquique earthquakes. We present an analysis of 47 permanent and 26 survey GNSS measurements acquired in Central-South Peru between 2007 and 2022 to better understand the frictional properties of the megathrust interface. Using a trajectory model that mimics the different phases of the cycle, we extract a coherent interseismic GNSS field at the scale of the Central Andes from Lima to Arica (12-18.5°S). Interseismic models on a 3D slab geometry indicate that the locking level is relatively high and concentrated between 20 and 40-km depth. Locking distributions indicate a high spatial variability of the coupling along the trench, with the presence of many locked patches that spatially correlate with the seismotectonic segmentation. Our study confirms the presence of a creeping segment where the Nazca Ridge is subducting; we also observe a lighter apparent decrease of coupling related to the Nazca Fracture Zone (NFZ). However, since the Nazca Ridge appears to behave as a strong barrier, the NFZ is less efficient to arrest seismic rupture propagation. Considering various uncertainty factors, we discuss the implication of our coupling estimates with size and timing of large megathrust earthquakes considering both deterministic and probabilistic approaches. We estimate that the South Peru segment could have a Mw=8.4-9.0 earthquake potential depending principally on the considered seismic catalog and the seismic/aseismic slip ratio.

Plain Language Summary

Using dense global navigation satellite system (GNSS) data collected in the South-Central Peru, we extracted a large scale interseismic velocity (surface velocity between two earthquakes) field at the scale of the Central Andes of Peru, where the oceanic Nazca plate goes under the continental South America plate at a velocity of about 6 cm/yr. This area has been the theater of several great subduction earthquakes and tsunamis, then estimating the stress build-up on the subduction interface is key to better anticipate future large earthquakes. Through a modelling of the GNSS velocities on a 3D slab geometry, we were able to obtain useful informations on the location, size, magnitude and return period of future great earthquakes in South Peru. Thereby, we obtained a very heterogeneous spatial distribution of interseismic coupling (degree of locking between the two tectonic plates), with low-coupled areas where the Nazca Ridge and the Nazca Fracture Zone are subducting, but highly-coupled areas close to the coasts of Lima and Arequipa. Finally, we estimate that the South Peru segment between the Nazca Ridge and the Arica band could have the potential to host a Mw=8.4 to Mw=9.0 earthquake, with a one century and one millenial recurrence time respectively.

1 Introduction

The size and timing of large earthquakes is a major scientific and societal issue. In subduction zones, the slab interface called megathrust is a gigantic thrust fault that can slip suddenly of many meters generating large M_w>7.5, great M_w>8.5 or giant M_w>9.0 megathrust earthquakes. Among the most powerful earthquakes recorded, we can refer to the 1960 Mw=9.5 Valdivia (Chile) earthquake (Cifuentes, 1989; Kanamori & Cipar, 1974), the 2004 Mw=9.2 Sumatra (Indonesia) earthquake (Chlieh et al., 2007; Stein & Okal, 2005), or the 2011 Mw=9.1

Tohoku (Japan) earthquake (Ide et al., 2011; Koketsu et al., 2011; Simons et al., 2011). The seafloor uplift and subsidence induced by these earthquakes trigger tsunamis that can be a threat to the population that live near coastal areas (Takabatake et al., 2018). It is now widely recognized that the seismic sources of major earthquakes often overlap spatially well with locked patches issue from interseismic coupling models where the interseismic coupling is defined as the slip deficit over the long-term slip (Chlieh et al., 2008; Konca et al. 2008; Loveless & Meade, 2011; Metois et al., 2016; Moreno et al., 2010; Radiguet et al., 2016). It remains however challenging to deploy and maintain large and dense geodetic networks to obtain detailed mapping of the interseismic coupling, especially in subduction zone where a significant portion of the seismogenic zone lies below the seafloor and where seismic cycle deformation gradients affect distance of many hundreds of kilometers.

The heterogeneous pattern of the fault locking distributions indicate mechanical variations of the frictional properties of the fault interface. Highly locked fault patches with a coupling degree typically > 0.4 are supposed to host the seismic sources of future large earthquakes and are characterized by velocity weakening behavior (Chlieh et al., 2011). These apparent locked zones are often called asperities by abuse of language and may rather reflect a high density of smaller size 'real' asperities that lie in the stress shadow of each other making it difficult to dissociate them within an apparently locked patch (Bürgmann et al., 2005). Locked patches appear to be surrounded by creeping patches where the coupling degree is relatively lower. These creeping patches are dominated by velocity strengthening frictional behavior and supposed to act as partial or permanent barriers depending on their frictional and geometrical properties (Chlieh et al., 2008; Hetland & Simons, 2010; Kaneko et al., 2010; King & Nábělek, 1985; King, 1986; Saillard et al., 2017).

Here we present new GNSS measurements from the Central Andes of Peru issued from a long-term scientific collaboration between Peruvian, French and American institutions. The first GNSS stations were deployed in the aftermath of the 2007 M_w=8.0 Pisco earthquake with 5 continuous cGPS stations around the Paracas Peninsula (Perfettini et al., 2010). Between 2010 and 2012, 41 new continuous stations were installed along the coastline and in the Andes between Lima and Arica. In addition, 33 survey-mode sGPS points were deployed in 2012 and occupied every 2 years in average up to 2022, to densify the network along the coastline south from the Nazca ridge to Arica and in the Altiplano plateau up to the Titicaca Lake. This new data set is dense in the coastal areas and fills many gaps left by previous geodetic studies (Norabuena et al., 1998; Bevis et al., 2001; Chlieh et al., 2011; Nocquet et al., 2014; Villegas et al., 2016). One primary objective of this paper is to process and analyze simultaneously these observations to extract a coherent interseismic signal at the scale of the Andes of Central-South Peru.

In this study we provide a detailed mapping of creeping and locking patches and estimate the average moment deficit rate (MDR in Nm/yr) that is building up on a 3D megathrust interface. The uncertainties of the interseismic coupling models and associated MDR will be quantified including or not a Peruvian sliver (Villegas et al., 2016) and discussed together with historical and instrumental seismic catalogs to better understand the mechanical properties of the slab interface. Finally, we use these results to conduct a moment budget analysis in South Peru to balance the present-day loading rate and the seismicity rate over the long-term (Avouac, 2015; Mariniere et al., 2021). By exploring the related uncertainties, this analysis provides a quantitative estimate of the earthquake potential (M_{max}) and associated return period that could occur in this region.

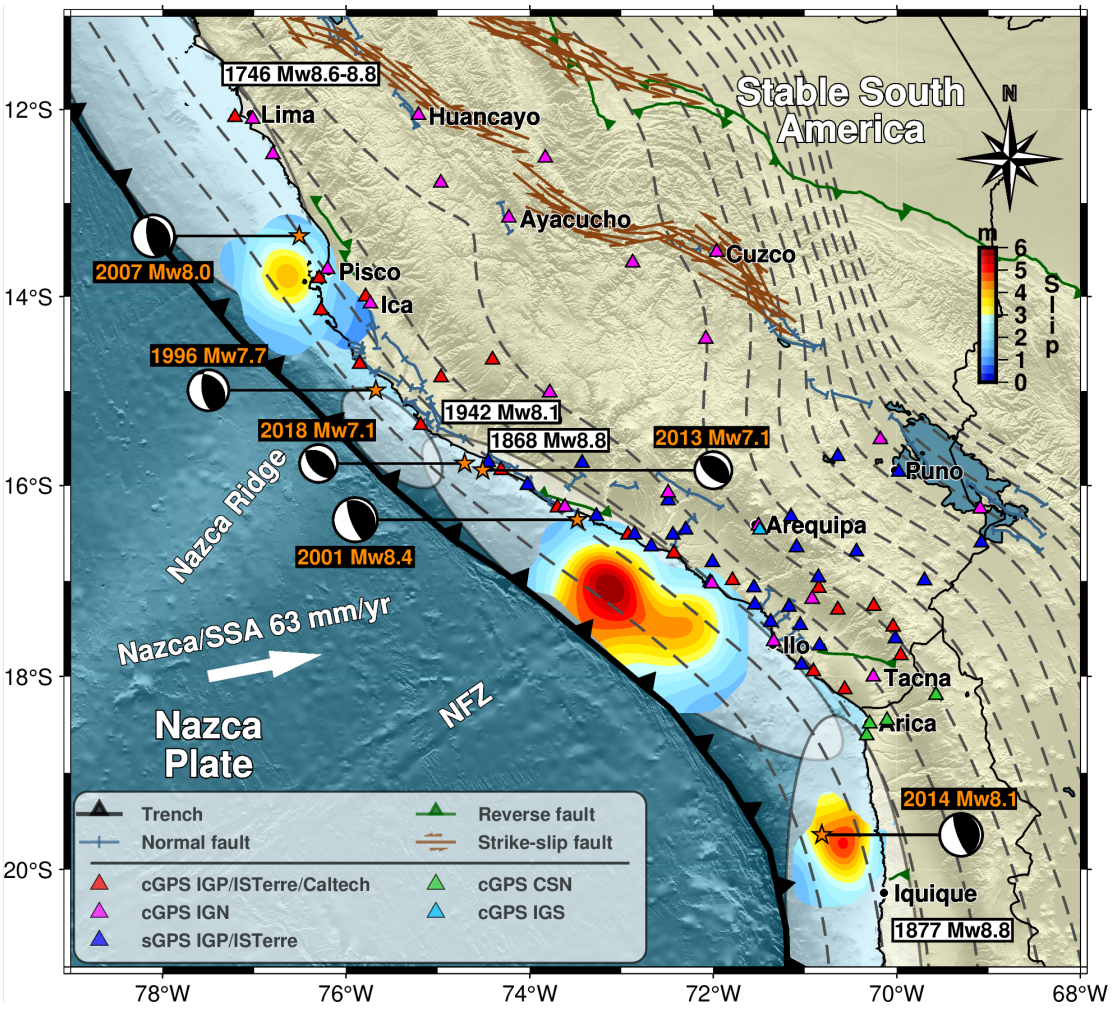

Figure 1: Seismotectonic background of the Central Andes subduction zone. Light gray ellipses indicate approximate rupture areas of major historical earthquakes since 1512 (Chlieh et al., 2011; Dorbath et al., 1990; Villegas et al., 2016). Focal mechanisms from major recent earthquakes are from the gCMT catalog. The approximate rupture areas of the M_w=8.1 2014 Iquique and M_w=8.4 2001 Arequipa earthquakes have been modelled in this study. M_w=8.0 2007 Pisco rupture is reported from Chlieh et al. (2011). Slab isodepth contours are reported every 20 km from Slab2 model (Hayes et al., 2018). The Nazca/Stable South America (SSA) convergence rate is depicted by the large white arrow (Kendrick et al., 2003). Major faults are from Veloza et al. (2011) and are depicted by blue (normal), green (reverse), and brown lines (strike-slip). Triangles show the location of GNSS stations used in this study, and are color coded according to their type (cGPS or sGPS) and their operator.

2 Seismotectonic context

Along the Western coast of the South America continent, the Nazca plate is subducting beneath the South American plate with a velocity of about 6 cm/yr (Altamimi et al., 2016; Kendrick et al., 2003). The Peruvian subduction zone is classically segmented into three main segments (Northern, Central, and Southern) of about 700 km each. The Northern segment extends from the Gulf of Guayaquil (3°S) to the Mendaña fracture zone (10°S). The Central segment is delimited

by the Mendaña fracture zone (10°S) and the Nazca Ridge (~15°S), while the Southern segment extends from that ridge up to the Arica bend (18.5°S) (Dorbath et al. 1990, Villegas et al. 2016). By contrast with the Northern segment that never experienced a great megathrust earthquake in the last 500 years (Nocquet et al., 2014; Villegas et al., 2016), the Central and Southern segments are characterized by recurrent great (Mw ≥ 8.5) earthquakes that occurred in 1746 in the Central and in 1604 and 1868 in the Southern segments. Large (Mw ≥ 7.5) megathrust earthquakes are even more frequent and occur in average every 20 years during the last five centuries (Bilek, 2010; Chlieh et al., 2011; Dorbath et al., 1990; Nishenko, 1991; Perfettini et al., 2010; Pritchard et al., 2007; Remy et al., 2016; Silgado, 1978; Sladen et al., 2010; Tavera et al., 2002; Tavera and Buforn, 1998; Villegas et al., 2016). The new GPS data presented here, recover the whole southern segment and the southern half of the Central segment (Figure 1).

In the North of Chile where the great 1877 M_w=8.8 earthquake occurred, the 2014 M_w=8.1 Iquique earthquake ruptured a segment between Iquique and Arica (Figure 1). This earthquake has significantly affected the GNSS network of Southern Peru. On the Southern Peru segment, the 1942 M_w=8.2 and the 2001 M_w=8.4 Arequipa earthquakes are the two largest events since the great 1868 M_w=8.8 event, and their cumulative ruptures have broken ~3/4 of the southern segment leaving an unbroken portion of about 150-200 km long between Ilo and Arica that can be considered as a seismic gap (Figure 1). Finally, in the Central segment offshore Lima, four large events with M_w~8.0 occurred in 1940, 1966, 1974 and 2007 (Pisco) with adjacent ruptures of about 150-200 km each that recover the whole Central segment (Beck et al., 1989; Beck et al., 1990; Dorbath et al., 1990; Langer & Spence, 1995; Perfettini et al., 2010; Sladen et al., 2010; Villegas et al, 2016).

Subandean shortening up to 10 mm/yr in South Peru has been reported by previous geodetic studies (Bevis et al., 2001; Métois et al., 2013; Norabuena et al., 1998; Villegas et al., 2016), while paleomagnetic studies reported up to 30 mm/yr of shortening (Arriagada et al., 2008). In the last decade, rigid sliver motion has been introduced to explain the deformation pattern in Central Andes (Nocquet et al., 2014; Villegas et al., 2016). Nocquet et al. (2014) defined a so-called Inca Sliver including southern Ecudador, Peru, and Bolivia extending from the trench to the Subandean belt. From an analysis of their GNSS velocities, they computed a Euler pole at 63.76°W, 22.47°N with a rate of 0.092°/Myr relative to the Stable South America frame (SSA). While Villegas et al. (2016) proposed a so-called Peruvian Sliver associated to a Euler pole at 67.23°W, 8.36°N with a rate of 0.104°/Myr, from the residuals of their inversions of interseismic velocities. This Peruvian Sliver (PS) encompass the whole GNSS network used in our study (12°S to 18°S), however it would be questionable to extend it further to the South, as the deformation pattern in Chile south of 19°S shows a different motion. Paleomagnetic studies reported in Arriagada et al. (2008) indicate an anti-clockwise rotation in the long-term displacement vectors north of 19°S, and a clockwise rotation south of 19°S. This pattern is also reported in geodetic studies (Chlieh et al., 2011; Métois et al., 2016). Yáñez-Cuadra et al. (2022) proposed a different approach, with diffuse continental deformation and mantle wedge viscoelastic relaxation, leading to minimal rigid motion needed to explain the surface displacements in the Atacama region (23°S to 30°S). In this study, we remain on a rigid block motion approach, with purely elastic rheology, as the analysis of intracontinental deformation is beyond the scope of this paper, although we acknowledge that viscoelasticity is a physical process that plays a key role in the deformation of subduction zones. Our results are compared in part 5.3 to the data-model misfits expected from a fully relaxed viscoelastic model (Li et al., 2015).

174

175

176 **3. Data analysis and Trajectory Models**

177 **3.1 Permanent and campaign GNSS Networks**

178 We analyze here the crustal motion recorded by 73 GNSS sites (Figure 2) deployed
179 between 1993 and 2022 in the Andes of Central and Southern Peru between latitudes 12°S to 18°S
180 and longitudes 60°W to 78°W. We also used continuous GNSS time series in South Peru and North
181 Chile in order to assess the contribution of co and post-seismic deformation associated with recent
182 earthquakes, notably the 2014 M_w=8.1 Iquique earthquake in North Chile (~20°S) and the 2001
183 M_w=8.4 Arequipa earthquake (Figure S20) in South Peru (~17°S) which have significantly
184 affected the southern Peruvian stations. In Peru, this GNSS network is composed of:

185 - 21 continuous GNSS (cGPS) stations deployed in the frame of a collaboration between the
186 Instituto Geofísico del Perú (IGP), the Institut des Sciences de la Terre (ISTerre), and the
187 California Institute of Technology (Caltech). They are maintained since 2015 by the IGP.
188 Maximum data coverage is between 2007 and 2022, but several stations do not provide data for
189 such a long time-range because of operating issues. Most of the stations are located between
190 latitudes 16°S and 18°S.

191 - 21 continuous GNSS stations deployed by the Instituto Geográfico Nacional (IGN) of Peru
192 covering the 2010-2018 time period. These stations are spread on a large area between latitudes
193 12°S and 18°S.

194 - 1 continuous IGS (Johnston et al., 2017) GNSS station installed in 1993, the AREQ station
195 located close to Arequipa city.

196 - 26 survey GNSS points (sGPS) deployed by IGP and ISTerre and measured on average every 2
197 years, when possible, between 2012 and 2022. Campaigns have been performed in June 2012, June
198 2013, October 2013, April 2014, October 2015, November 2016, June 2018, November 2018, and
199 March 2022.

200 - 4 continuous GNSS time series from the Centro Sismológico Nacional (CSN) of Chile.

201 Finally, to correct properly the GNSS campaign measurements from the displacements
202 generated by the 2014 M_w=8.1 Iquique earthquake, we used 21 CSN cGPS stations located close
203 to the rupture area (Figure S2).

204 All the GNSS time series with their trajectory model are available in the supplementary
205 material.

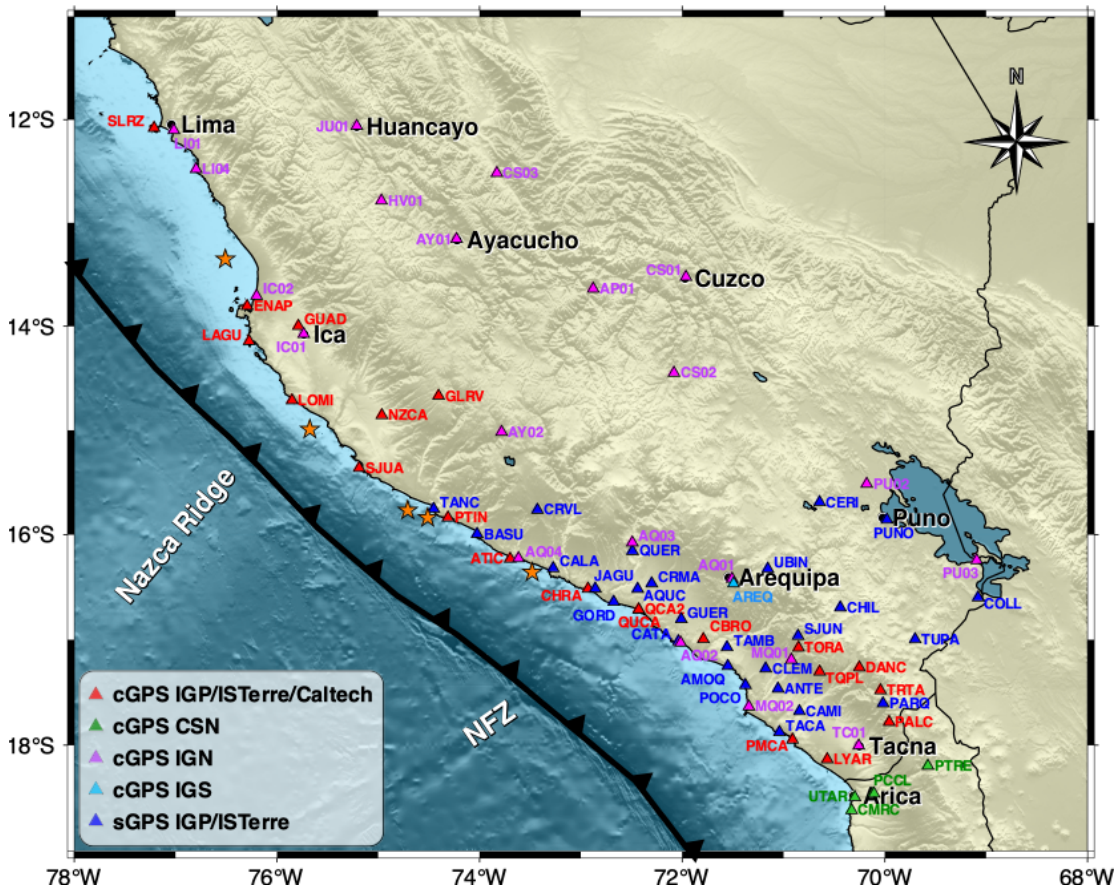

Figure 2: GNSS network used to extract the interseismic velocity field. Stations are color coded according to their type (cGPS or sGPS) and their operator.

3.2 Data Processing

Data were processed following a Precise Point Positioning (PPP) approach at ISTerre using the GipsyX software v1.5 from the Jet Propulsion Laboratory (JPL) (Bertiger et al., 2020). To resolve the phase ambiguity, GipsyX imposes wide-lane phase bias constraints provided by JPL. Orbit and clock estimations are taken from JPL final products. NNR orbits are used. Ionospheric delays are canceled by using dual-frequency communications. No second order ionospheric correction is applied. The VMF1 (Boehm et al., 2006) is used to estimate the tropospheric zenith delay parameters. Tropospheric delays are inverted from the data: a delay is inverted every 5 minutes and two horizontal gradients are accounted for per session of 24 hours. We use the FES 2014b model to correct from ocean tide loading (Lyard et al., 2021). Phase center stability and multi-path protection are achieved using antenna calibration tables and by stacking GNSS measurements over the day to keep one position per day. In the case of GNSS campaigns, the positioning of the antenna precisely above the campaign point is usually an issue, that is minimized using a forced-centering system at most points. Scaling, rotation and translation factors provided by JPL are then applied in the Helmert transformation to map the solution in the IGS2014 (Altamimi et al., 2016). The processed GNSS time series indicate the daily positions of the station covering a time window of several years, as shown in Figure 3 and time-series in supplements. The displacements extracted from our GNSS data are given in the ITRF2014 reference frame

(Altamimi et al., 2016). To express them relatively to the Stable South America (SSA) reference frame, we used the ITRF2014/SSA Euler pole located at 18.68°S and 128.69°W with an angular velocity of 0.122°Myr^{-1} (Altamimi et al., 2016). We double-checked the stability of our reference frame by processing various GNSS sites located in Brazil, and expressed in the SSA frame (Figure S14).

3.3 Trajectory modeling of the continuous GNSS time series

To model the GNSS time series, we applied a trajectory model that mimics the position of a GNSS station as a function of time using the ITSA software (Marill et al., 2021). The trajectory model used here is the sum of sub-models that sketch individually processes such as the secular motion of the station, instantaneous jumps either due to earthquakes or antenna changes, post-seismic relaxation and seasonal oscillations (Bevis & Brown, 2014; Marill et al., 2021). A schematic view of the process is given in Figure S1. Because no obvious signature of slow slip events has been detected in our processed GNSS time series, no term is assigned to that process here. Mathematically, the evolution of the station position x(t) is expressed as the summation of linear, Heaviside, logarithmic and sinusoidal time functions that are described as follows:

$$\boldsymbol{x(t)} = \boldsymbol{x_R} + \boldsymbol{v(t-t_R)} + \sum_{j=1}^{n_j} \boldsymbol{b_j}\, \boldsymbol{H(t-t_j)} + \sum_{i=1}^{n_j} \boldsymbol{a_i}\, \boldsymbol{\log_{10}}\left(\boldsymbol{1} + \frac{\boldsymbol{t-t_i}}{\boldsymbol{\tau_{Ra}}}\right)$$

$$+ \sum_{k=1}^{2}\left[\boldsymbol{s_k}\, \boldsymbol{\sin}\left(\boldsymbol{2k\pi(t-t_R)}\right) + \boldsymbol{c_k}\, \boldsymbol{\cos}\left(\boldsymbol{2k\pi(t-t_R)}\right)\right] + \sum_{a=1}^{n_A} \boldsymbol{b_a}\, \boldsymbol{H(t-t_a)} \quad (1)$$

- The first term x_R being the station position at t=0.

- The second term $v(t - t_R)$ is a linear term corresponding to the secular velocity, including a steady-state interseismic velocity with t_R being the reference time.

- The third term corresponds to coseismic displacements modeled by a Heaviside function where the coefficient b_j characterizes the coseismic jump at time t_j. Major seismic events (M_w > 6.4) reported in the ISC are considered, if they are in a radius of influence (in km) defined as $r(M_w)=10^{(0.43Mw-0.7)/1.15}$, M_w being the moment magnitude of the considered event.

- The fourth term corresponds to the postseismic deformation detectable after major seismic events, that is classically modeled by a decaying logarithmic function with a characteristic time $\boldsymbol{\tau_{Ra}}$ and a displacement a_i at time t_i. A value of $\boldsymbol{\tau_{Ra}}$ = 30 days was found adequate for our data.

- The fifth term corresponds to annual and semi-annual seasonal oscillations, due to hydrological loading and temperature variations weighted by the coefficients s_k and c_k.

- Finally, the last term is related to antenna changes leading to artificial jumps b_a at time t_a in the time series if the characteristics of the new antenna are different. These jumps are especially visible on the vertical component of the time series and are corrected from field work records.

To better appreciate the variability of the signals recorded by permanent stations, Figure 3 reports the norm of the horizontal components of four GNSS time series with their respective trajectory model, and the large earthquakes that occurred in that region during the time of observation (2007-

2022). All the stations shown are located along the coastline between the Paracas Peninsula and Arica. These time series are all expressed in the Stable South America (SSA) reference frame. Station LAGU, located near the Paracas Peninsula and installed right after the 2007 M_w=8.0 Pisco earthquake shows the postseismic relaxation and reloading process that have followed. Station LYAR installed in South Peru has recorded the 2014 M_w=8.1 Iquique earthquake and its postseismic relaxation. Finally, station SJUA located between LAGU and LYAR was sensitive to the 2013 and 2018 M_w=7.1 Acari earthquakes.

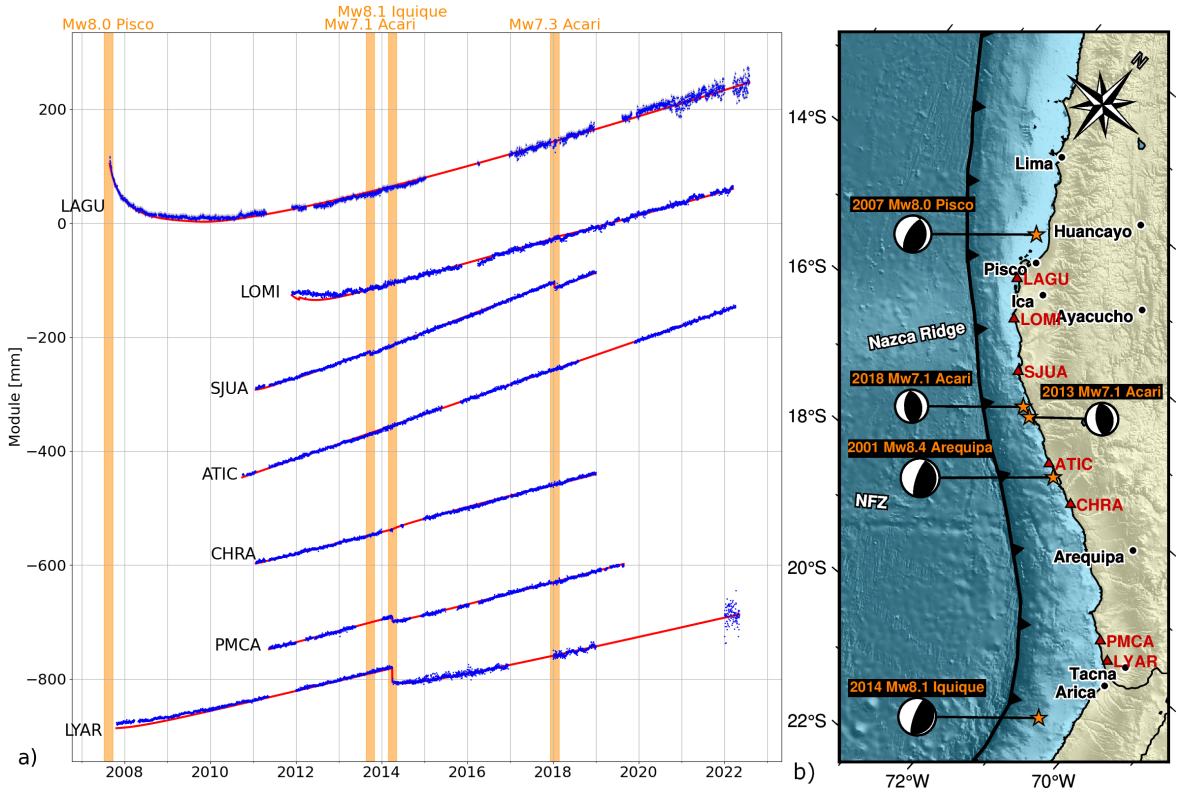

Figure 3: Time series on the norm of the horizontal components of continuous GNSS stations along the coast (a), relative to SSA, and corrected from antenna jumps and seasonal variations: LAGU, LOMI, SJUA, ATIC, CHRA, PMCA, and LYAR. Data points are displayed in blue, while the trajectory model is in red. The time series are arranged from North (top) to South (bottom). Coseismic and postseismic displacements from the M_w=8.1 2014 Iquique earthquake at LYAR, PMCA and SJUA stations are clearly noticeable. At the LAGU station, we observe the postseismic relaxation of the M_w=8.0 2007 Pisco earthquake. On the right panel (b), are displayed the station locations and the earthquakes accommodated in the time series.

It is worth noting that this trajectory model software is only relevant when the time series has enough data points (>100) and an appropriate temporal distribution (at least one year of data). Although it is not a binding criterion for the data extracted from our cGPS stations, it prevents the use of the trajectory model for our sGPS time series. Consequently, we use another methodology to correct our sGPS time series.

3.4 Corrections of survey-mode GNSS velocities

In the purpose of correcting properly the coseismic jumps and afterslip offsets generated by the 2014 Iquique seismic sequence at each of the survey-mode sGPS station, we estimate the

displacements associated with the 2014 M_w=8.1 Iquique mainshock on April 1st, its main M_w=7.7 aftershock on April 3rd, and the 30 first days of postseismic afterslip at 14 continuous cGPS stations in South Peru and 21 cGPS stations in north Chile (Figure S2). The coseismic displacements tables associated with each of these earthquakes as well as the afterslip motion after 30 days are listed in Table S2 of the supplements. Then, using the inversion procedure described below (section 4.1), we performed static slip inversions of these displacements constrained by the seismic moment and rake vector from the gCMT. The derived slip sources are then used to predict through forward modelling the coseismic jumps to be corrected at each of the survey-mode GNSS sites in South Peru. Figure S2 shows the coseismic and afterslip recorded displacements by the permanent GNSS stations in South Peru used for the slip inversions, and the predicted displacements that have been used to correct survey GNSS points (Table S3). We retained a regularization length $\boldsymbol{\lambda}$ =10 km and a damping parameter $\boldsymbol{\sigma_m(k)} = 10^{-1.2}$, as it provides a good balance between a low misfit and a reasonable consideration of inter-stations distances (see section 4.1 for definition of the parameters). A 250 degrees azimuth from North (clockwise) was selected, as it is consistent with the slip vector from gCMT and the plate convergence direction. The modelled slip distribution is in quite good agreement with Jara et al. (2018).

In addition to the modelling of the Iquique earthquake coseismic and postseismic displecements, we modelled the seasonal displacements at each sGPS point based on the approach of Hoffmann et al. (2018). We extract the seasonal signal modelled at each cGPS stations by the ITSA trajectory model, as depicted on Figure S15. Then, we spatialy interpolate this seasonal signal at the sGPS locations, and we substract it from the sGPS time series. Since the GNSS campaigns are often performed at the same season one year from another, the seasonal correction is not very strong. Nevertheless, we observed a reduction of 2% in the standard deviation when correcting the sGPS time series for the seasonal, as well as a velocity change of up to 5% at some sGPS points.

3.5 Extracting the interseismic velocity field from cGPS and sGPS analysis

Using our trajectory model for cGPS stations by keeping only the linear term, and performing a linear regression in our corrected sGPS position time series, we finally extracted the interseismic velocities on the horizontal components (East, North) for each of the 73 stations. We chose not to consider the vertical component for the inversions. Indeed, the errors on the vertical component is much larger, especially on sGPS sites. In addition, the vertical deformation is very sensitive to non-tectonic processes, such as hydrological processes, volcanic activity, or local terrain subsidence (Itoh et al., 2019). The observed vertical interseismic velocities at cGPS sites are reported on Figure S21. We observe that they are very heterogeneous, even at a relatively local scale, which would be an issue for the modelling. All these velocities are listed in a Stable South America (SSA) reference frame in Table S1 of the supplement and shown in Figure 4. Uncertainties on the velocities have been estimated through a statistical analysis of the time series using Median Interannual Difference Adjusted for Skewness (MIDAS) described in Blewitt et al. (2016). In a nutshell, MIDAS is a trend estimator method working with pairs of data, assuming a majority of the data have a Gaussian probability distribution function, adopting an unbiased Theil-Sen method. In SSA reference frame, all the interseismic GNSS velocities are oriented toward the Cordillera, coherently with the relative Nazca/South America convergence direction. Velocity gradients decrease with increasing distance from the trench axis consistently with gradients

expected from interseismic locking models. Trench-lateral variations in the amplitudes of the velocities suggest lateral variations in the locking distribution (See cross section Figure 4).

It is worth noting that the AREQ station, located in Arequipa and recording since 1993, is still affected by the effects of the 2001 Arequipa earthquake. These effects are discussed in section 5.2 and may affect other stations in the close area.

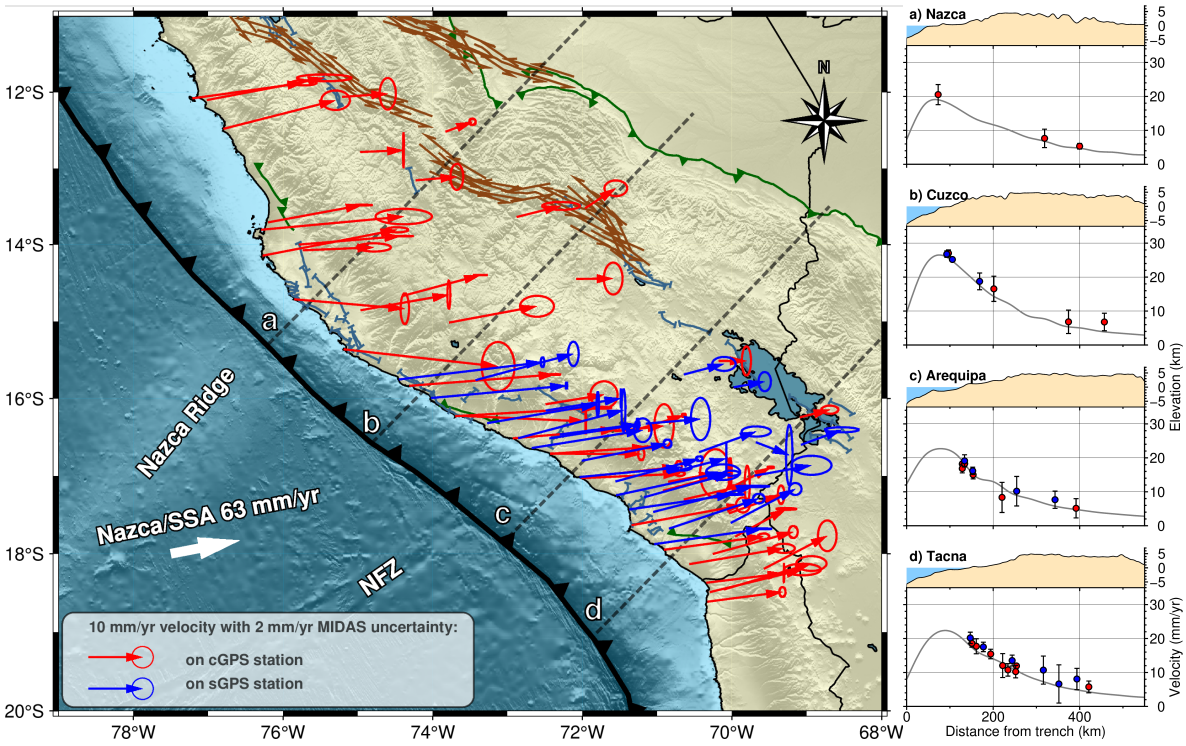

Figure 4: Interseismic velocity field relative to the Stable South America frame. Velocities on continuous GNSS stations (cGPS) are displayed in red, while velocities on survey GNSS points (sGPS) are displayed in blue. Velocity uncertainties from MIDAS (Blewitt et al., 2016) are depicted by ellipses. Major faults are from Veloza et al. (2011). Four cross-sections (a, b, c, d) are plotted perpendicular to the trench, with 100-km wide tracks. The norm of the velocity at each station is displayed in red (cGPS) and blue (sGPS), the model shown in Figure 5 (SSA, with $\lambda = 30$ km) being depicted by the gray line. The topography is plotted above.

4. GNSS-derived interseismic slip inversion

4.1 Slip inversion procedure

In order to obtain an interseismic coupling model on the megathrust interface, we first build a 3D slab geometry based on the South American slab contours of the Slab2 model between latitudes 10°S and 25°S (Hayes et al., 2018). Our modeled slab interface shown in Figure S3 is discretized into 6,700 15-km wide elementary triangular dislocations, with source points placed at the center.

The inversion procedure follows the formulation of Tarantola & Valette (Radiguet et al., 2011; Tarantola, 2005; Tarantola & Valette, 1982), implemented within the static inversion of the Principal Component Analysis Inversion Model (PCAIM) software (Kositsky & Avouac, 2010). To model the interseismic coupling, we used a backslip approach (Savage, 1983) on the 3D slab geometry embedded in a purely elastic medium with a shear modulus μ of 40 GPa. We define interseismic coupling as the fraction between the slip rate on a patch and the plate convergence velocity, the interseismic coupling is therefore ranging from zero for a fully creeping patch to one for a fully locked patch. The shear modulus (a.k.a. rigidity) is difficult to estimate accurately, as it depends on the location, and more generally it increases with depth (Bilek and Lay, 1999). The retained value of 40 GPa is a compromise of the various values found in the literature (Bilek and Lay, 1999; Villegas et al., 2016), considering the average depth of our coupling distribution. The slip amplitude and rake are fixed consistently with the horizontal projection of the relative plate convergence vector V_{pl}. The slip on the megathrust interface can be decomposed into a strike-slip and a dip-slip component for each sub-fault patch. The matrix *d* of surface displacements can then be obtained by the following formula:

$$d = G.m \qquad (2)$$

where *m* is the matrix of slip rate on the fault at depth, and *G* the associated Green's function. Green's functions are computed based on the analytical equations from Meade (2007). A linear least-squares inversion is used to minimize the cost function *S(m)* defined as:

$$\boldsymbol{S(m) = \frac{1}{2}\left[(Gm - d)^t C_d^{-1}(Gm - d) + (m - m_0)^t C_m^{-1}(m - m_0)\right]} \qquad (3)$$

and the modeled slip rates *m* on each source element:

$$m = m_0 + C_m G^t (G C_m G^t + C_d)^{-1}(d - G m_0) \qquad (4)$$

m_0 being the prior model, C_d and C_m the co-variance matrices for data and model, G^t the transpose matrix of *G*. The data co-variance matrix C_d is defined as the diagonal matrix of the associated uncertainties on the measurements. We neglect the co-variances, so all terms outside the diagonal become zero. The model co-variance matrix C_m is used to regularize the slip distribution between neighboring elementary patches which is achieved by an exponential smoothing function expressed as:

$$\boldsymbol{C_m(k,l) = \left(\sigma_m \frac{\lambda_0}{\lambda}\right)^2 e^{-\frac{d(k,l)}{\lambda}}} \qquad (5)$$

d(k,l) being the distance between source elements *k* and *l*, λ_0 a scaling factor (characteristic size of fault patch), λ the spatial correlation length, and σ_m the damping parameter controlling the relative weight of the distance to initial model versus data misfit. In practice, we adjust the regularization length λ and σ_m in order to maintain an interseismic coupling between zero and one (cf. part 4.2). Finally, we impose the coupling to taper at 60 km depth of the slab interface, as the thermodynamics conditions deeper should prevent fault locking (Gagnon et al., 2005).

To quantify the misfit between the observation and the model, we define the reduced chi-square criteria as:

$$\chi^2_{red} = \frac{\chi^2}{\nu} \text{ with } \chi^2 = \sum_i \frac{(d_i - m_i)^2}{\sigma_i^2} \quad (6)$$

d being the data, *m* being the model, σ^2 the variance, and $\nu=n-p$ the degrees of freedom for *n* observational data and *p* fitted parameters.

In order to determine which areas are modeled with confidence, we can define the resolution matrix *R*:

$$R = C_m G^t (G C_m G^t + C_d)^{-1} G \quad (7)$$

where C_m and C_d are the co-variance matrices for model and data parameters and *G* the matrix of Green's functions. The closer the resolution matrix *R* is to the identity matrix *Id*, the better the model is resolved (Radiguet al., 2011). Then, we define the restitution as the sum of the rows of the resolution matrix *R*. Both the restitution and the diagonal elements of the resolution matrix are plotted on Figure S4. Whereas the diagonal elements of *R* inform us about how much the slip of a specific patch is accurately mapped, the restitution informs us if this slip has been correctly projected onto other patches.

Considering the 3D slab geometry and the location of the GNSS sites presented above, we found that the diagonal values of the resolution matrix *R* are relatively low due to the high number of small patches (6,700) for a relatively low amount of GNSS sites (73), in order not to impose too much constraint on the slip location. The diagonal values are higher where the density of station is high, indicating a better resolution there. The same goes for the restitution, except that the distribution is smoother. Overall, we can state that the spatial resolution of slip in the seismogenic zone above 60-km depth of the slab interface is relatively high between latitudes 12°S and 18°S.

4.2 Results of Interseismic coupling models

Following the inversion procedure described above and considering a creeping slip prior model (i.e. $m_0=0$), we tested different values of regularization length and damping parameter in order to find the optimum GNSS fitting parameters. Figures S5 and S6 displayed L-curves that compare the χ^2 for variable parameters. We searched for the parameter values which offer an adequate compromise between the misfit and model complexity (Radiguet et al., 2011; Florsch et al., 2014). In other words, we seek to minimize the misfit, while keeping a regularization length in the same order as the average distance between the GNSS sites and a maximal slip bounded by the plate the plate convergence rate.

Rather than showing the so-called best model, we propose a family of acceptable solutions for regularization lengths λ of 15, 30, or 200 km that all provide an acceptable GNSS misfit with χ^2 ranging from 0.28 to 0.47. Figure 5 reports the coupling distributions for various smoothing factors λ =15, 30, and 200 km. The rough solutions may better reflect the coupling in the Southern segment where the slip resolution and restitution are much better. Low coupling is shown close to the trench, however this area is not very well resolved by the model (cf Figure S4). Consequently, we also run inversions with a locked slip prior (Figure S16), showing high coupling close to the trench. In all these models, it appears that the coupling distributions tend to extend up to 60-km depth where it is supposed to creep due to the high temperatures there (>400°C according to Villegas et al., 2016). This may suggest that an element is missing in our model, like a sliver

motion proposed by Nocquet et al. (2014) and Villegas et al. (2016), that we are going to discuss in part 5.1.

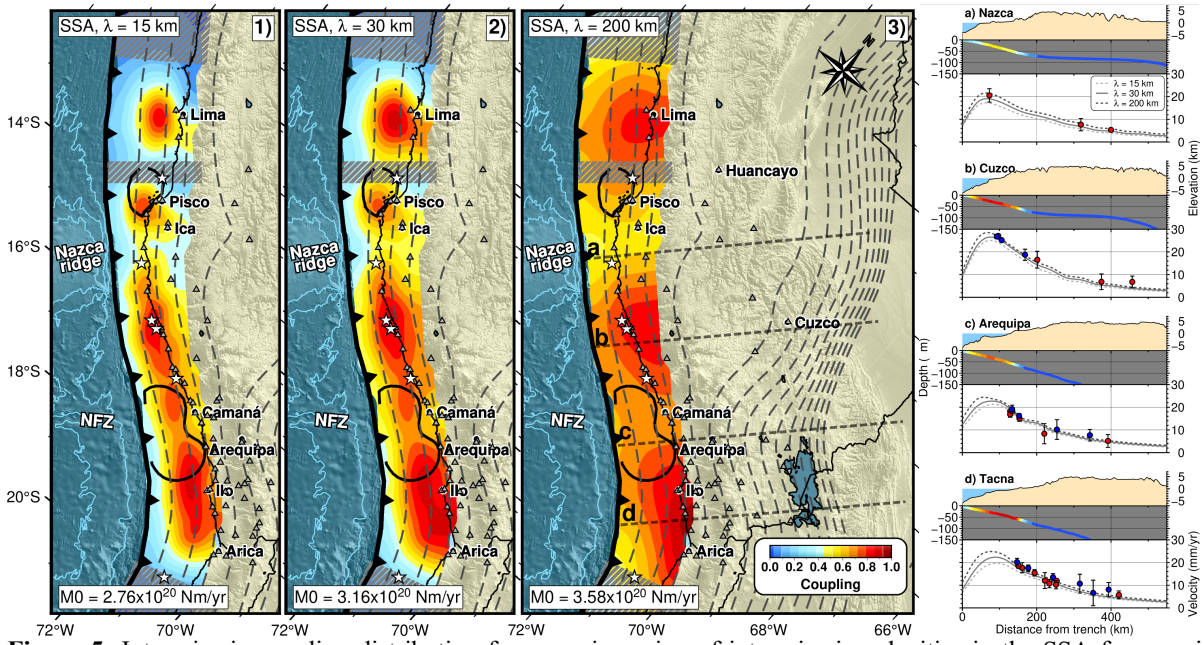

Figure 5: Interseismic coupling distribution from our inversion of interseismic velocities in the SSA frame, with various smoothing (λ = 15, 30, and 200 km). Slab contours (dashed lines) are reported every 20-km depth, from the Slab2 model (Hayes et al. 2018). The interseismic coupling is highly heterogeneous reflecting strong variations of the frictional properties on the slab interface. Thus, there are four highly coupled areas: a very-highly coupled area close to Lima, a less coupled area near Ica, a large band of high-coupling between the Nazca Ridge and the Nazca Fracture Zone (NFZ), and a highly coupled area between the NFZ and the Arica bend. GNSS sites are depicted by grey triangles. Discontinuities can be observed where the Nazca Ridge and the NFZ are subducting below the South America plate. The approximate rupture area of the Mw=8.4 2001 Arequipa has been estimated in this study, while the Mw=8.0 2007 Pisco earthquake rupture is reported from Chlieh et al. (2011). Patches with gray hachure pattern depict areas that are not well resolved by the model. Four cross-sections (a, b, c, d) are plotted perpendicular to the trench, with 100-km wide tracks. The norm of the velocity at each station is displayed in red (cGPS) and blue (sGPS), the three models (λ = 15, 30, and 200 km) are plotted with gray lines. The topography and slab profile are plotted above. Interseismic coupling from the model in panel 2 (λ = 30 km) is indicated by the color scale on the slab interface.

We define the moment deficit rate (dMo_{inter}/dt) of a coupling model as:

$$\frac{dMo_{inter}}{dt} = \int \mu\left(V_{pl} - V_{back}\right) dS \qquad (8)$$

the integration being computed over the surface S of the slab interface, and where (V_{pl} -V_{back}) is the back-slip offset rate across the fault. In practice, we compute for each discretized patch k its local moment deficit that we sum up over a specific surface. For instance, if we integrate over the whole megathrust up to 60-km depth from Lima to Arica, we find moment deficit rates ranging from 2.76 to 3.58×10^{20} Nm/yr respectively for models with λ =15 and 200 km.

4.3 Extension of the Peruvian Sliver to South Peru?

Figures 6 and S18 show the GNSS residuals (data minus model) associated with the coupling distribution shown in Figure 5-2, inland GNSS residuals located in the Cordillera between 300 and 500 km from the trench indicate a southeastward motion of about 4 mm/yr (Figure 6a). This coherent motion is observable along ~700 km at all GNSS sites located in the Cordillera west of Lima up to Lake Titicaca. This tendency disappears when using the Peruvian Sliver (PS) reference frame proposed by Villegas et al. 2016 (Figure 6b), suggesting that there is room for a rigid sliver moving about 4 mm/yr southwestward, within which all our stations are included (Figure S13). Considering that Peruvian Sliver as a reference frame, the relative Nazca / Peruvian Sliver convergence rate would be reduced to ~55 mm/yr.

When the velocities rotated in the Peruvian reference frame are inverted to obtain the coupling, the orientation of the residual velocities is randomly distributed along the coastline.

If we consider the interseismic GNSS velocities in that Peruvian sliver reference and perform similar inversions to those described above, the data misfit is improved compared to previous models without sliver ($\chi^2 = 0.24$ with the sliver, while $\chi^2 = 0.30$ with the interseismic velocities in SSA reference). In addition, the new coupling distributions highlight much better the variations of the downdip limit of the locked subduction zone (compare Figures 5 and 8, or refer to Figure S19). The fact that these inversions with the sliver naturally contain the slip in the first 50-60 km of depth is a strong physical argument in favor of this sliver motion, compared to the model in the SSA frame which required a deeper coupling to fit the data. Increasing the smoothing factor tends to extend the coupling near the trench. The resulting global moment deficit rates are about 25% lower than for the previous models without sliver.

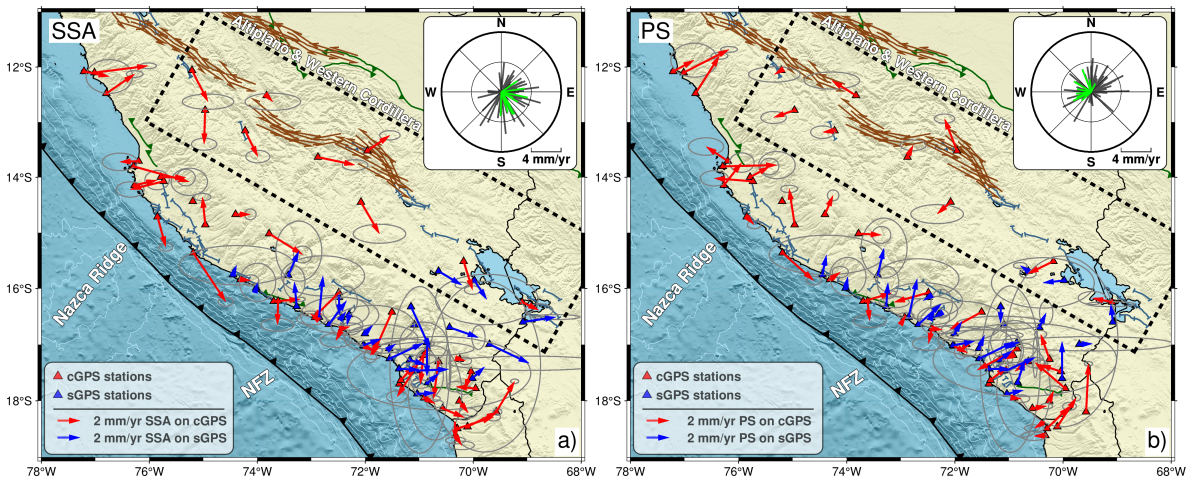

Figure 6: Residuals from our inversions using GNSS data in the Stable South America frame (a) and in the Peruvian Sliver frame (b), for a regularization length $\lambda = 30$ km. Most of the residuals are below 4 mm/yr, although some have higher values. Survey GNSS points are in blue, while continuous GNSS stations are in red. Uncertainties computed by MIDAS (Blewitt et al., 2016) are depicted by gray ellipses. Residuals at inland stations, within the black dashed rectangle, are highlighted in green on the roses. In a Stable South America frame, we see a southwestward direction that dominates in the residuals, especially well seen in the GNSS sites far away from the trench. In the Peruvian Sliver reference frame, residuals are distributed randomly and might be due to internal deformation within the Andes or long-term viscous effect associated with recent large earthquakes that we do not account for here (Perfettini et al., 2005).

5 Discussion

5.1 Comparison with previously published interseismic coupling models

Norabuena et al. (1998) and Bevis et al. (2001) have published preliminary insights on interseismic coupling in the area. Norabuena et al. (1998) obtained a good fit to the data by considering a locking of about 50% up to 20-km depth and 12 mm/yr of shortening, while Bevis et al. (2001) retained a locking close to 100% from 10 to 50-km depth and a 5-6 mm/yr shortening. However, both studies rely on only one continuous station (AREQ) and about 20 survey points between Lima and Arica with only two years of data (1994 and 1996 SNAPP measurements). In addition, no detailed slab geometry was available at the time, and they do not account for the seismic events or seasonal variations that could have affected their measurements. A decade later, new studies from Chlieh et al. (2011) and Villegas et al. (2016) were able to present more detailed interseismic coupling distributions thanks to new developments.

Compared to Villegas et al. (2016) and Chlieh et al. (2011), our results confirm some features while refining their restitution. The best fitting models from the three studies show a highly coupled area close to the coast of Lima, one close to Pisco, one south of the Nazca Ridge, and one between the NFZ and the Arica bend. These four highly coupled areas are separated by three low coupled areas: one between Lima and Pisco, and two where the Nazca Ridge and the NFZ are subducting.

In our study, the decoupling between Lima and Pisco is centered at about 13.5°S, while in Villegas et al. (2016) and Chlieh et al. (2011) this decoupling is observed at about 12.5°S. However, this area is not well resolved, therefore the apparent decoupling may in fact be related to a lack of data and should be considered with caution. Regarding the creeping area where the Nazca Ridge is subducting, it is a persistent feature in all the models, with a width of at least 70 km and even 150-200 km in Chlieh et al. (2011). It is difficult to assess accurately the width of this creeping area, as the GNSS sites are at least 50 km apart in this area.

It is on the Southern segment that our study provides the most clarification, with a significant increase in station density. There were 7 stations between the Nazca Ridge and the Arica bend in Chlieh et al. (2011), 8 in Villegas et al. (2016), and 57 in our study. This improved resolution highlights a high coupling between the Nazca Ridge and the Arica bend, lowered where the NFZ is subducting but not as much as in Villegas et al. (2016) or Chlieh et al. (2011). Having a lot of stations both on the coast and inland, up to Lake Titicaca, is a substantial improvement to constrain the depth of coupling compared to older studies. In addition, when accounting for a Peruvian Sliver as defined by Villegas et al. (2016), the maximum coupling depth is 10 km shallower. Apart from the number of stations, the type of station and observed time range also differ between the three studies. In South Peru, Chlieh et al. (2011) essentially based their analysis on survey points measured between 1993 and 2003, while Villegas et al. (2016) used mostly continuous stations measured between 2007 and 2013. In our study, we analyzed a mix of continuous (47) and survey (26) points, measured in the 2007-2022 and 2012-2022 periods respectively. The extensive use of continuous measurements and longer time range reduce uncertainties compared to older studies. It is worth noting that the interseismic velocities from Chlieh et al. (2011) are representative of an earlier time period, mostly before the 2001 Arequipa earthquake. Our interseismic velocities at cGPS sites are extracted using a more comprehensive trajectory model, by accounting for various

526 coseismic, postseismic, or seasonal displacements. While for sGPS sites we account for seasonal
527 variations, as well as coseismic and postseismic displacements induced by the 2014 Iquique
528 earthquake. Finally, our inversions are performed using a 3-D slab model (Hayes et al., 2018).

529

530 **5.2 Long-living effects of post-seismic viscous relaxation**

531 Some of the far-field residuals located on the Altiplano and Western Cordillera are pointing toward
532 the trench (in the PS frame) and could be associated either with long-term postseismic viscous
533 effects of the 2001 Arequipa and 2007 Pisco earthquakes (Hergert & Heidbach, 2006; Klein et al.,
534 2016; Remy et al., 2016), or with internal deformation within the Andes (Kley & Monaldi, 1998).
535 The Arequipa (AREQ) continuous station, installed in 1993 and operating until now, was the only
536 one active during the 2001 earthquake in Southern Peru. We remark that the reversal time of
537 motion of the AREQ station is about 7 years after the 2001 earthquake (Figure 7) suggesting that
538 during that period the record of that station was dominated by postseismic (afterslip and viscous)
539 relaxation. After 2008, the interseismic loading process became the most dominant process and
540 the velocity increased gradually to nearly reach its pre-2001 velocity at the beginning of 2020. We
541 quantify the velocity change at the AREQ station between the period prior to the 2001 event (1997-
542 2001) and our period of observation on the GNSS network in South Peru (2012-2023 for most
543 stations), by computing the average interseismic velocity (module of the North and East
544 components) on the two periods at the station. We found that during our period of observations
545 (2012-2023), the interseismic velocity measured at the Arequipa (AREQ) station is reduced by
546 about 15% in the SSA frame, and 30% in the PS frame, compared to the velocity measured prior
547 to 2001, suggesting that our estimates of moment deficit rate (MDR) may be a lower bound in the
548 region surrounding the 2001 rupture. However, the AREQ station is located close to the earthquake
549 centroid (less than 200 km), and therefore probably more affected than most of the stations in the
550 South Peru segment. These estimates of 15% (SSA) and 30% (PS) should therefore be seen as a
551 maximum post-seismic effect on the the MDR.

552

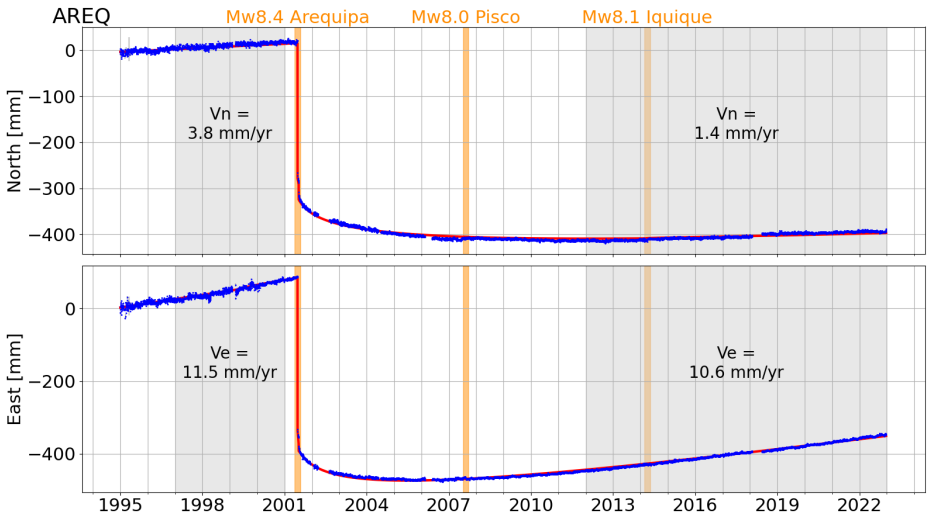

553

554 **Figure 7:** Time series for the AREQ station, located in the city of Arequipa on the horizontal
555 components (North, East), corrected from antenna jumps and seasonal variations. Data points are
556 displayed in blue, while the trajectory model is displayed in red. North and East velocities are
557 reported for two time ranges: 1997-2001 and 2012-2022, in order to compare the interseismic
558 velocity before the 2001 event to the velocity in recent years.

559

560 **5.3 Possible effect of viscoelastic rheology on the interseismic deformation field**

561 In order to estimate the effect of viscoelastic rheology on the interseismic deformation field, Li et
562 al. (2015) computed elastic and viscoelastic interseismic models on the North Chile subduction
563 zone. They applied a uniform locking from the trench to a given maximum locking depth, varying
564 from 30 to 80 km, and they quantified the misfit on the horizontal GNSS observations. From this
565 approach, they observed an improved minimum of misfit when applying the viscoelastic model,
566 especially when considering the backarc sites only. In addition, the locking depth corresponding
567 to the minimum of misfit is lowered with the viscoelastic model: from ~55 to ~45 km with all the
568 data, and from ~55 to ~50 km with backarc data only.

569 In a similar way, we tested models with uniform fully locked megathrust interface from the trench
570 to various depths varying from 20 to 80 km. Then, we quantified the evolution of the reduced $\boldsymbol{\chi^2}$
571 as function of the maximum locking depth. Results are reported on Figure S17, when considering
572 all the GNSS sites (left) or only the backarc GNSS sites (right) indicated on Figure 6. We consider
573 either SSA (in blue) or the PS (in orange) reference frames. We observe on both cases that the
574 minimum value of $\boldsymbol{\chi^2}$is significantly reduced when considering the PS frame relative to the SSA
575 frame: from 0.82 to 0.45 with all the GNSS sites, and from 0.32 to 0.18 when considering the
576 backarc GNSS sites only. Furthermore, the maximum locking depth corresponding to this
577 minimum is also reduced when considering the PS frame: from 45 to 40 km with all the GNSS
578 data, and from 52 to 35 km with the backarc points only. This behavior is very similar to the one
579 observed by Li et al. (2015) when comparing viscoelastic and purely elastic models. Consequently,
580 considering a rigid PS block motion shows relatively similar geodetic fit.

581 Performing a full viscoelastic model of the loading on the subduction is beyond the scope of this
582 paper. We therefore chose to model internal deformation by a sliver and estimate the variability in
583 the models to assess the seismic potential and its uncertainties (cf. next section). A viscoelastic
584 model that accounts for viscoelastic deformation, including the relaxation following the 2001
585 Arequipa and the 2007 Pisco earthquake, should ideally be performed to move towards a better
586 mechanical interpretation of the deformation field in the central Andes that account for the whole
587 seismic cycle (e.g. Li & Chen, 2023).

588

589 **5.4 Along-strike Variations of the Moment deficit rate, and seismotectonic parameters**
590 **controlling the seismic segmentation**

591 We compute between Lima and Arica the along trench-strike variations of the MDR (Figure 8) by
592 summing up the MDR of all nodes down to 60-km depth within 15-km wide strips normal to the

trench. Although the final coupling distributions indicate noticeable differences, the MDR integrated at the scale of the studied area remains in a limited range of 2.0 to 2.9 × 10^{20} Nm/yr (~Mw=7.4-7.6), respectively for λ varying between 15 to 200 km (Tables 1 and S4). The MDR increases with λ, however this increase is relatively low in the South Peru segment where it evolves from 1.4 to 1.8 × 10^{20} Nm/yr, compared to the Central Peru segment where the MDR dispersion between models is much higher (0.6 to 1.1 × 10^{20} Nm/yr). On Figure S16 are displayed the models with a locked slip prior, the corresponding MDR values are reported in Table 1. Overall, a locked slip prior increases the MDR of ~80% when integrating from Lima to Arica, however this raise is limited to ~20% when integrating from Nazca to Arica, the later area being better constrained by the data. The moment budget analysis described in part 5.5 will be carried out on the Nazca-Arica segment.

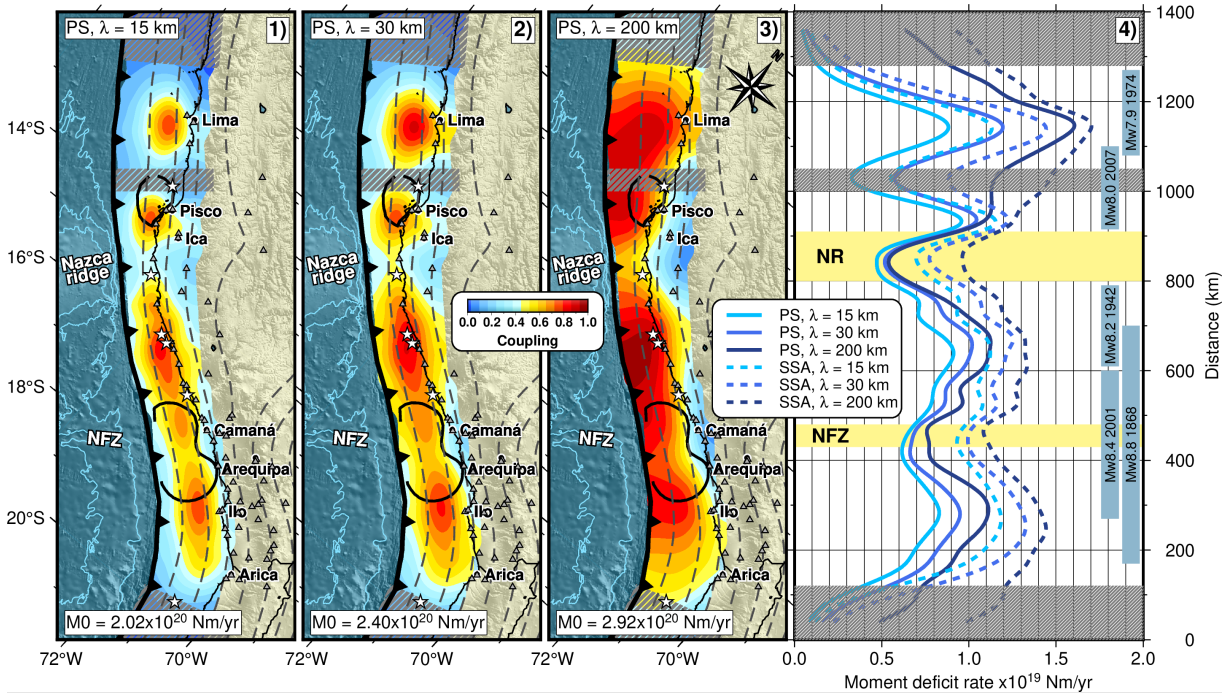

Figure 8: Interseismic coupling distribution from our inversion of interseismic velocities in the PS frame, with three different smoothing (λ of 15, 30 and 200 km). Slab contours (dashed lines) are reported every 20-km depth, from the Slab2 model (Hayes et al. 2018). GNSS sites are depicted by grey triangles. The interseismic coupling is highly heterogeneous reflecting strong variations of the frictional properties of the slab interface. Thus, there are four highly-coupled areas: a very-highly coupled area close to Lima, a less highly-coupled area near Ica, a large band of high-coupling between the Nazca Ridge and the Nazca Fracture Zone (NFZ), and a highly-coupled area between the NFZ and the Arica bend. Discontinuities can be observed where the Nazca Ridge and the NFZ are subducting below the South America plate. The approximate rupture area of the Mw=8.4 2001 Arequipa has been estimated in this study, while the Mw=8.0 2007 Pisco earthquake rupture is reported from Chlieh et al. (2011). On the right panel are displayed the moment deficit rate by along-trench distance for models in the PS and SSA frame, and with various smoothing (λ of 15, 30 and 200 km), computed over 10-km wide segments. Patches with gray hachure pattern depict areas that are not well resolved by the model. Rupture extents from major seismic events are reported as blue segments.

618

Reference frame	Slip prior	λ (km)	$\log_{10}(\sigma_m)$	Moment (Nm/yr) Lima-Arica	Moment (Nm/yr) Nazca-Arica	Displayed on:
SSA	creeping	15	-1.53	2.76×10^{20}	2.04×10^{20}	Fig. 5-1
SSA	creeping	30	-1.32	3.16×10^{20}	2.24×10^{20}	Fig. 5-2
SSA	creeping	100	-1.00	3.47×10^{20}	2.39×10^{20}	/
SSA	creeping	200	-0.70	3.58×10^{20}	2.44×10^{20}	Fig. 5-3
PS	creeping	15	-1.58	2.02×10^{20}	1.48×10^{20}	Fig. 8-1
PS	creeping	30	-1.35	2.40×10^{20}	1.67×10^{20}	Fig. 8-2
PS	creeping	100	-0.65	2.86×10^{20}	1.85×10^{20}	/
PS	creeping	200	-0.35	2.92×10^{20}	1.87×10^{20}	Fig. 8-3
SSA	locked	15	-1.53	4.15×10^{20}	2.96×10^{20}	/
SSA	locked	30	-1.32	3.93×10^{20}	2.74×10^{20}	/
SSA	locked	100	-1.00	3.75×10^{20}	2.54×10^{20}	/
SSA	locked	200	-0.70	3.67×10^{20}	2.49×10^{20}	/
PS	locked	15	-1.58	3.37×10^{20}	2.04×10^{20}	Fig. S16-1
PS	locked	30	-1.35	3.22×10^{20}	1.99×10^{20}	Fig. S16-2
PS	locked	100	-0.65	3.15×10^{20}	1.92×10^{20}	/
PS	locked	200	-0.35	3.12×10^{20}	1.89×10^{20}	Fig. S16-3

619 **Table 1:** Misfit and moment deficit over the whole resolved area (Lima to Arica) or restrained to
620 the South Peru segment (Nazca to Arica) for various models. Each line corresponds to a specific
621 smoothing (λ and σ_m), combined with a given reference frame (SSA or PS) and slip prior (creeping
622 or locked).

623

Control of Lateral variation of coupling: Entering in subduction of Seafloor geomorphological features

The dense GNSS network used in this study highlights creeping areas at the locations of the Nazca Ridge and the NFZ characterized by a rate-strengthening friction. These creeping areas are well resolved by the density of GNSS sites and appear to be persistent features of our coupling models. Because of its relatively high along-strike width of ~ 60 km and its historical behavior to stop systematically large and great earthquakes, the Nazca Ridge segment is considered a strong barrier. By contrast, the NFZ segment, which is ~ 20-km long is often crossed by the rupture of large events and rarely appears to have acted as a barrier in the last five centuries of seismic history. In addition, the decrease of coupling where the NFZ is subducting may be overestimated due to the visco-elastic relaxation following the 2001 Arequipa earthquake. Indeed, the location of this creeping intersegment falls in the middle of the 2001 rupture area, it is therefore difficult to discriminate between what may be related to the visco-elastic relaxation and what may be actually creeping. Robinson et al. (2006) have shown that this fracture zone stalled the 2001 M_w=8.4 Arequipa seismic rupture but was not efficient enough to arrest its southward propagation. The probability that an earthquake ruptures through a creeping barrier depends on the resistance and the efficiency of this barrier to arrest the seismic rupture propagation (Kaneko et al., 2010). The resistance of a barrier ($R_{vs} = \Delta T_{vs} \times L_{vs}$) is the product to its length L_{vs} (measured along the trench strike) and to the stress increase ΔT_{vs} required for the velocity strengthening patch to sustain the seismic slip to propagate through it. The efficiency *B* of a barrier is defined as:

$$B = (\Delta T_{vs} / \beta \Delta T_{vw}). (L_{vs} / L_{vw}), \qquad (9)$$

where ΔT_{vw} is the stress drop transferred from the ruptured velocity weakening segment of length L_{vw} to the velocity strengthening patch and β a geometrical factor taken equal to 1/6 in the 3D models of Kaneko et al. (2010). A barrier is supposed to be strong when the probability of an earthquake rupturing through the barrier is low, which is the case when $B > 1$. Applied to the Nazca Ridge segment and considering L_{vs}= 60 km, L_{vw} = 180 km and β = 1/6 (from 3D models of Kaneko et al., 2010), we find $\Delta T_{vs} > \Delta T_{vw} / 2$, meaning that the required stress increase on the velocity strengthening patch should be higher than half of the seismic stress drop to stop the seismic rupture propagation.

When the efficiency tends to zero, this means that the probability that an earthquake ruptures through a creeping segment is high. If we consider that the NFZ is an inefficient barrier this would mean that ΔT_{vs} tends to zero. Because ΔT_{vs} is proportional to (a - b), this would suggest that NFZ segment might tend to a velocity neutral frictional behavior, efficient enough to slow down the seismic rupture propagation (Robinson et al., 2006) but inefficient to arrest it as attested by historical records (Figure 9).

On Figure S7 are displayed the thrust events with $M_w \geq 5.5$ (from gCMT), on top of a map indicating the dominating friction law, velocity weakening or velocity strengthening. Plots of the seismicity for various catalogues are given in Figures S8, S9, and S10, with cross-sections. We consider areas with coupling below 0.4 to be in the velocity strengthening regime, while areas with coupling above 0.4 are considered in the velocity weakening regime. We observe a convincing overlap between the seismic dataset and the velocity weakening domain, both in along-strike and along-dip variations, which support our interseismic coupling distribution. While on Figure S12 we displayed all seismic events, including small magnitude events, the IGP catalog being complete at $Mw \geq 4.5$. In this case, we observe a high cumulative seismicity at the location of creeping areas, especially where the Nazca ridge and the NFZ are subducting. This result was expected, as

creeping areas are known to host a high amount of low magnitude seismic events (Rubin et al., 1999; Scholz, 1990).

Seismic Segmentation, Characteristic earthquakes and Return Period

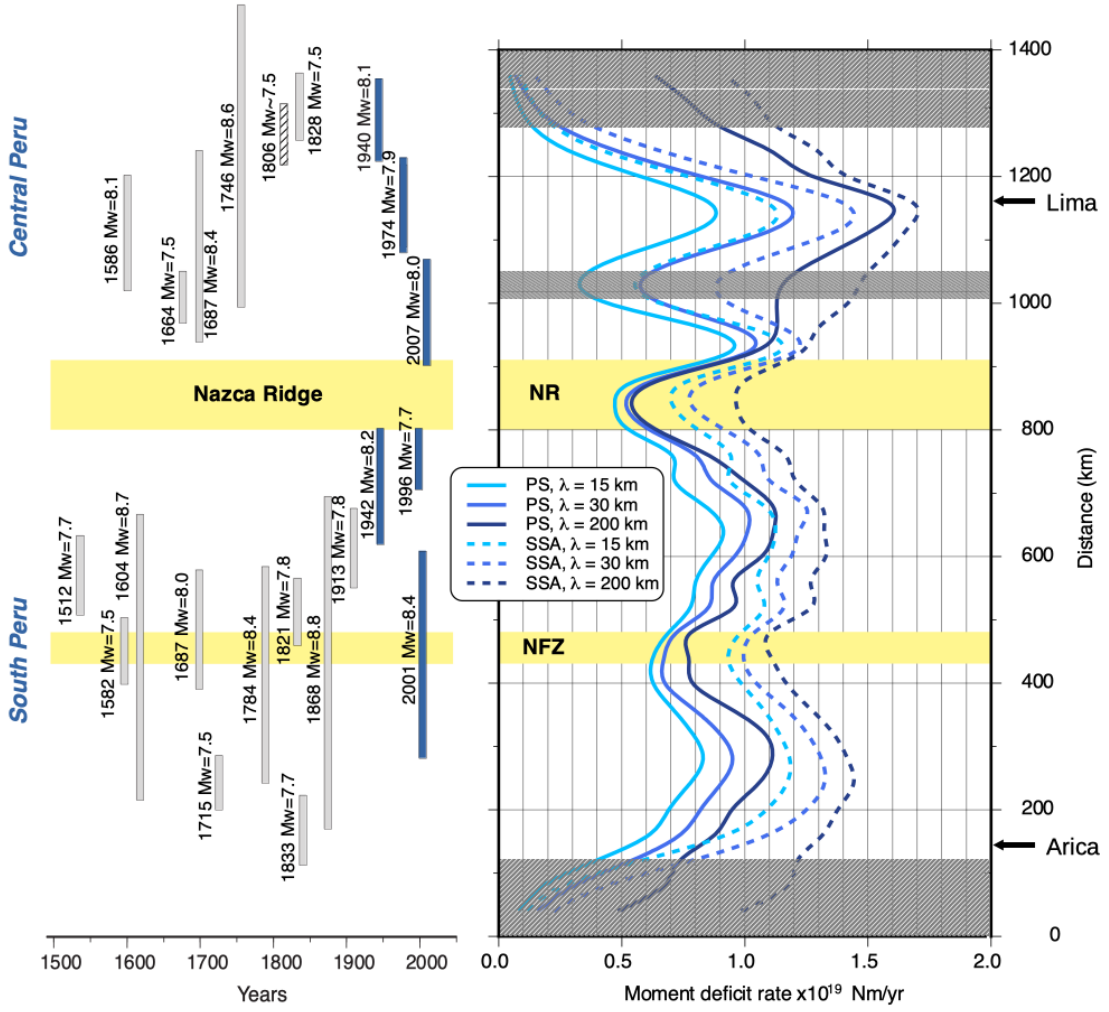

Figure 9: *Left:* Approximate rupture lengths of large subduction earthquakes (Mw>7.5) since the 16th century, taken from Villegas et al. (2016). Recent earthquakes are displayed in blue, while historical earthquakes are displayed in gray. Extension of the Nazca Ridge and the Nazca Fracture Zone are reported in yellow. *Right:* Moment deficit rate by latitude for models in the PS and SSA frame, and with various smoothing (λ of 15, 30 and 200 km), computed over 5-km wide segments. Patches with gray hachure pattern depict areas that are not well resolved by the model. Rupture extents from major seismic events are reported as blue segments.

In the Central Peru segment, our coupling maps recover about half of that segment and specifically the rupture areas of the 1974 M_w=7.9 Lima and 2007 M_w=8.0 Pisco earthquakes. Both 1974 and 2007 seismic ruptures appear to correlate quite well with two highly locked patches. At the rates

of moment deficit of our coupling models, we found that the 1974 rupture area can easily host a similar event if the locked patch off-shore Lima breaks individually.

In the Southern Peru segment, historical and instrumental seismic catalogs indicate that this segment can be subdivided into three sub-segments corresponding to the rupture areas of the 1942 M_w=8.2 Nazca (200 km), 2001 M_w=8.4 Arequipa (300 km) and 1833 M_w=7.8 Ilo-Arica (150 km) earthquakes. The largest events of 1604 M_w=8.7 and 1868 M_w=8.8 appear to have ruptured simultaneously the Arequipa and Ilo-Arica sub-segments.

In the 1942 rupture area, the 1996 M_w=7.7 event as well as the 2013 & 2018 M_w=7.1 Acari events which all ruptured within the 1942 rupture suggesting that the locked patch there is relatively fragmented. Considering the actual moment deficit rate integrated over the 1942 Nazca rupture, this segment would be mature today to host a $M_w \sim 8.0 \pm 0.1$ seismic event.

In the wake of the 2001 Arequipa and 2014 Iquique earthquakes, the 150-km long Ilo-Arica portion is clearly identified as a seismic gap. In the historical catalog that segment appears to have broken individually in 1833 and together with the 2001 Arequipa rupture area during the great 1868 M_w=8.8 mega-event. Considering the moment deficit rates of our models, we found that the Ilo-Arica segment is mature for a seismic event with a moment magnitude Mw > 8.0.

Now if we consider the 450-km long rupture area of the great 1604 and 1868 $M_w \sim 8.7$-8.8 megathrust earthquakes, one way to estimate the return period $T(Mw_{char})$ of such characteristic earthquakes can be defined as:

$$T(Mw_{char}) = M0_{char} / (dMo_{inter}/dt) \qquad (10)$$

, where dMo_{inter}/dt is the moment deficit rate integrated over the characteristic rupture area. At the actual moment deficit rate integrated over the 450-km long rupture, we find a return period of Tr ~ 103-171 years, a period much shorter than the 264 years that separates these two great events. This difference can be partially explained by the fact that the seismic moments released by other large events in that same rupture area, like the 1784 M_w=8.4 and 1687 M_w=8.0 events are not taken into account with that approach, neither aseismic slip as postseismic that follow such events.

This deterministic approach is informative, but it tends to underestimate the return period of characteristic earthquakes and does not provide insight on the maximum-magnitude earthquake. Also, this approach does not take into account the frequency-magnitude of the background seismicity that varies from one region to another, nor aseismic slip events which indicate the limitations of that deterministic approach.

5.5 Moment budget analysis and earthquake potential

To conclude our analysis, we perform a moment budget at the scale of the South Peru segment since this segment is well resolved by our data, and because it cannot be excluded that it could rupture at once. For that we integrated the moment deficit rate of our interseismic models within a polygon that goes from the trench down to 60-km depth, and from the Nazca Ridge to the Arica bend (see polygon contours on Figure S11, the three southern polygons are considered).

To balance the seismicity rate with the moment deficit rate that is accumulating annually on the Southern Peru megathrust interface, we considered four instrumental catalogs that are homogeneous in magnitude (Figure 10): ISC-GEM (Di Giacomo et al., 2018; Storchak et al., 2013; Storchak et al., 2015), ISC (Willeman & Storchak, 2001), gCMT (Dziewonski et al., 1981; Ekström et al., 2012), and Instituto Geofísico del Perú (IGP), covering respectively the 1906-2022, 1978-2022, 1976-2022, and 1906-2022 periods. The two main differences are that the global catalogues (ISC-GEM, ISC and gCMT) have a similar magnitude of completeness of M_w=5.2 and a b-value of 0.68, 0.73, and 0.72 respectively, while the local catalog from IGP has a magnitude of completeness of M_w=4.5 and a b-value of 1.03. Compared to others subduction zone, the Peruvian subduction zone is characterized by a low b-value (Bilek & Lay, 2018).

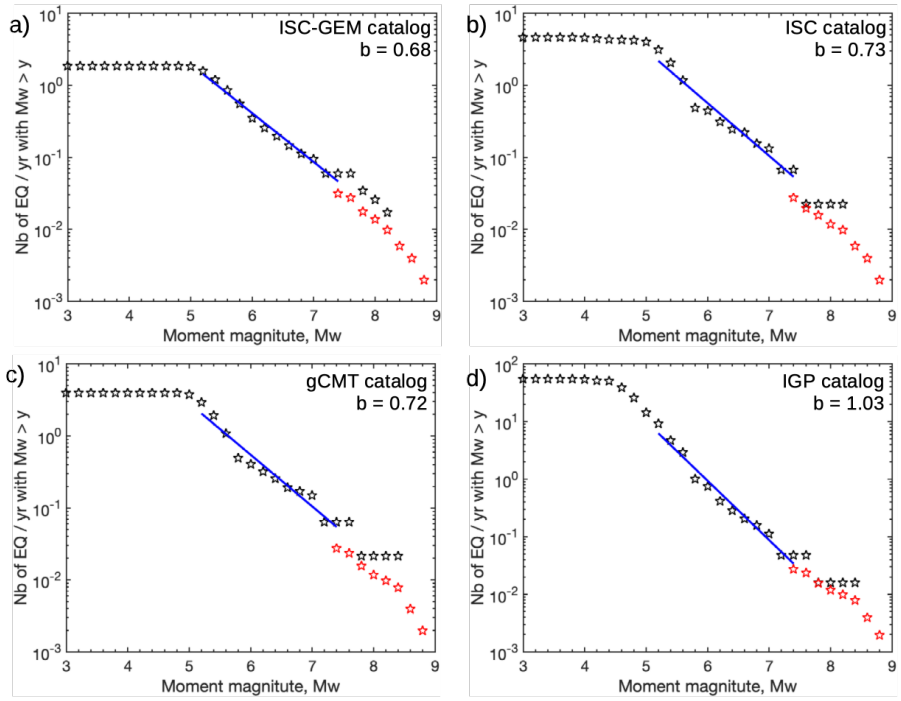

Figure 10: Frequency-magnitude distribution for various seismic catalogs on the South Peru segment: ISC-GEM (a), ISC (b), gCMT (c), IGP (d). The b-value of the corresponding Gutenberg-Richter law is reported for each catalog in the magnitude range 5.2-7.4 (blue line). Red stars correspond to strong events above magnitude 7.5, including historical events from Villegas et al. (2016).

Assuming the frequency–magnitude distribution for these catalogs, the mean recurrence time of the associated earthquake potential T(Mmax) is defined as (Avouac, 2015; Molnar, 1979):

$$\boldsymbol{T(M_{max})} = \frac{1}{\left(1-\frac{2b}{3}\right)\alpha}\frac{\boldsymbol{M_{max}}}{\dot{\boldsymbol{M}}_{\boldsymbol{0}}} \qquad (11)$$

where α is the fraction of transient slip that is seismic during the cycle and is written as:

$$\alpha = \frac{M_0^{seismic}}{M_0^{seismic} + M_0^{aseismic}} \qquad (12)$$

with $Mo^{seismic}$ the seismic moment, $Mo^{aseismic}$ the aseismic moment including postseismic afterslip and slow slip episodes that occur during the cycle (Matsu'ura, 2015). When $\alpha = 1$ and $b = 0$, one will find the formulation of the recurrence time for a characteristic earthquake. Then, the frequency of the earthquake potential depends on the moment deficit rate and the b-value of seismic catalogs (see Figure 11) for which we have some estimations and the parameter α that we still need to bound.

The moment deficit rates of the family of acceptable coupling models range from 1.15 to 2.81x10^{20} Nm/yr. However, we discussed in part 5.2 that the visco-elastic relaxation following the 2001 Arequipa earthquake may still affect the observed velocity at some of the stations, notably close to the epicenter. The rupture area of this event was in the middle of the region considered for moment budget analysis, between the Nazca Ridge and the Arica bend. It is unlikely that all the stations in the area have been affected in the same proportion than the AREQ station, located in Arequipa city, still we adopt here a conservative approach and consider for uncertainties that the total moment deficit on the South Peru segment may be underestimated by up to 15% in the SSA frame and up to 30% in the PS frame. Measuring a velocity trend on less than a decade is not supposed to be strictly representative of the long-term secular motion, subsequently the trend velocity measured before the Arequipa earthquake could also be accelerated and may not be representative either of the secular interseismic trend.

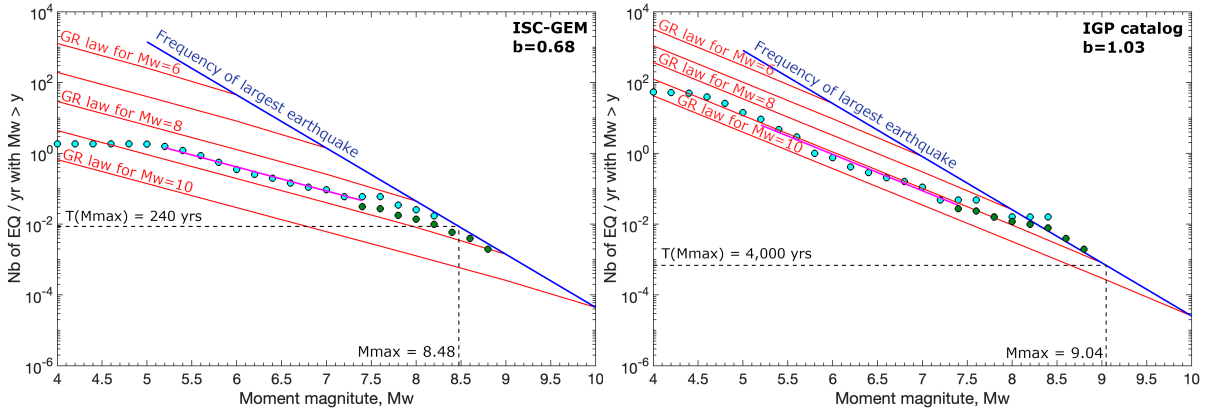

Figure 11: Estimation of maximum expected magnitude with $\alpha = 0.7$ and $\mu = 40$ GPa, in the PS frame and with a smoothing $\lambda = 30$ km, for the ISC-GEM catalog (left) and the IGP catalog (right). The earthquake potential is Mw=8.48 with a 240 years recurrence time for the ISC-GEM catalog, while the earthquake potential is Mw=9.04 with a 4000 years recurrence time for the IGP catalog. Instrumental earthquakes from the catalogs are depicted by cyan dots, historical earthquakes from Villegas et al. (2016) by green dots. The red lines are Gutenberg-Richter laws for maximum magnitude of 6,7,8,9 and 10 from top to bottom respectively. The GR law of our catalog is shown by the pink line. The blue line is the frequency of the maximum magnitude event.

Using the maximum moment deficit rates found of 2.4 (SSA) / 1.9 (PS) x10^{20} Nm/yr (models with λ=200km), we varied α between 0.1 and 1 for both catalogs to explore its impact on the estimate of the earthquake potential (Figure 12). A lower bound for α can be assessed from the largest magnitude event recorded in the instrumental catalogs, in our case the 2001 M_w=8.4 earthquake,

for which magnitude is reached when α=0.21/0.27 with the IGP catalog and α=0.37/0.47 with the ISC-GEM catalog. An upper bound for α can be estimated considering that the afterslip moment released during the postseismic period corresponds to at least 25% of the seismic moment (i.e., $\alpha \leq 0.8$). This value is an average from various afterslip studies in subduction zones (Jara et al., 2018; Perfettini et al, 2010; Pritchard et al., 2007; Remy et al., 2016), and from our own analysis. In the specific case where α=0.8 we find an earthquake potential of Mw=9.6/9.4 (Tr ~5300/3400 years) with the IGP catalog and Mw=8.8/8.7 (Tr ~190/170 years) with the ISC-GEM catalog.

If now we suppose that during a full cycle, $Mo_{seismic} = Mo_{aseismic}$, then $\alpha = 0.5$ and we find an earthquake potential of Mw=9.2/9.0 (Tr ~2100/1350 years) with the IGP catalog and Mw=8.6/8.4 (Tr ~150/100 years) with the ISC-GEM catalog. In this case, the ISC-GEM catalog has an earthquake potential lower or equal to the maximum-magnitude of historical seismic records which is possible considering the uncertainties on the seismic moment for the 1604 and 1868 events, with a recurrence time of about Tr ~125 ± 25 years consistent with the four M_w>8.4 of the 500-years historical catalog. Considering the IGP catalog, this would suggest a maximum-magnitude earthquake of $M_w \geq 9.0$ with a return period of Tr≥1350 yr much longer than the period covered by the historical catalog.

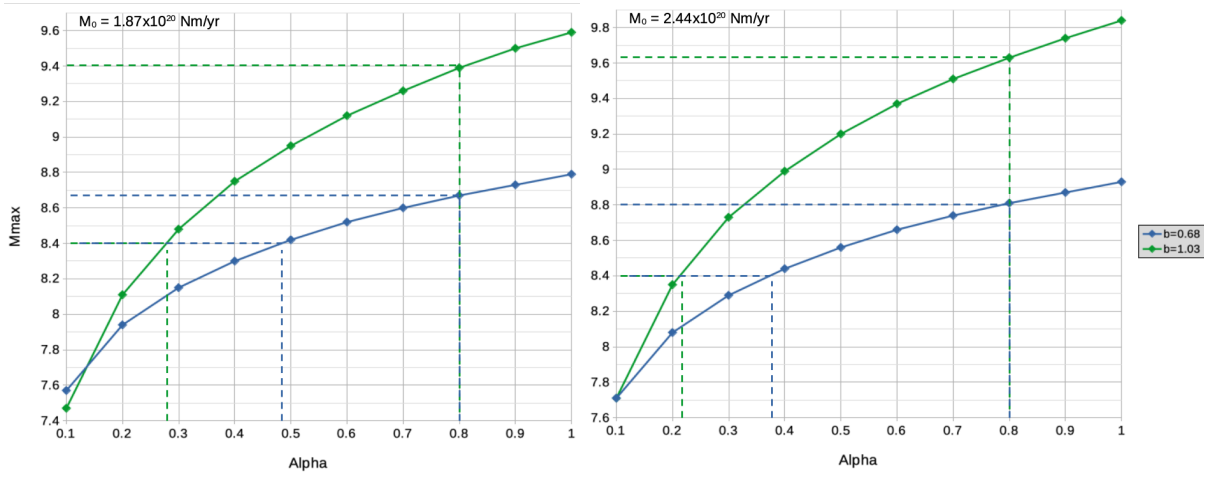

Figure 12: Variation of the estimated earthquake potential in the Peruvian sliver (left) and in the Stable South America (right) frames, for various values of alpha, from 0.1 to 1. The benchmarked model has a regularization length λ = 200 km, a rigidity μ = 45 GPa, and a b-value of 0.68 (blue) or 1.03 (green) corresponding to the ISC-GEM and IGP catalogs respectively. The minimum boundary for alpha is determined from the maximum-magnitude event of instrumental catalogs (which is the 2001 Mw=8.4 Arequipa earthquake). The maximum boundary is considering a minimum 20% aseismic slip.

Finally, Figure 13 reports the maximum-magnitude and its variability for the various parameters and uncertainties discussed:

- The influence of the sliver motion, by correcting or not from the Peruvian Sliver. Applying the sliver correction tends to lower the moment deficit (see Table 1).

- The slip prior of the model, considering a creeping (no coupling) or a locked (full coupling) slip prior. This parameter has a strong influence on poorly resolved area, for instance close to the trench.

- The smoothing of the interseismic slip model, with regularization length λ = 15, 30, and 200 km. All these values allow a good fit to the data and a realistic slip distribution, but increasing the smoothing tends to increase the moment deficit (see Table 1).

- The rigidity μ = 35, 40, and 45 GPa. We consider this range plausible considering the average depth of our slip distribution (Bilek and Lay, 1999). The moment deficit is proportional to the rigidity.

- The impact of a potential underestimation of the moment deficit, due to the postseismic viscous relaxation following the 2001 Arequipa earthquake. We consider as an upper boundary an underestimation of 15% on the moment deficit in the SSA frame, and 30% in the PS frame.

- The rate of seismic events alpha = 0.3, 0.55, and 0.8. The lower boundary and upper boundaries were selected based on the analysis described above (see Figure 12).

- The seismic catalog considered, ISC-GEM (b=0.68), gCMT (b=0.72), ISC (b=0.73), and IGP (b=1.03).

We computed 864 combinations of these parameters, following the logical tree on Figure 14, and we displayed the median (circles), as well as the 15th and 85th percentiles (vertical bars), for each value of these parameters. Models in the PS and SSA frames are weighted by a factor 2/3 and 1/3 respectively, as we consider these models more likely (best fit to the data). In the same way, models accounting or not for an eventual moment underestimation following the Arequipa earthquake are weighted by a factor 1/3 and 2/3 respectively, as the correction corresponds to an extreme upper boundary.

The b-value of instrumental catalogs as well as the amount of aseismic slip in the transient slips are the two parameters that show the largest variability in the determination of the Mmax, with a variability of ~0.6 in M_w. The presence or not of the sliver, as well as the rigidity, or the viscoelastic relaxation associated with the Arequipa earthquake can influence that determination of ~0.15 in M_w. The slip prior induced a variability of ~0.12 in Mw, and the smoothing factor of the interseismic models a variability of ~0.08 in Mw.

Overall, we found a median value of Mw=8.55, a 15th percentile at Mw=8.15, and a 85th percentile at Mw=9.0. Considering the largest earthquake recorded on the South Peru segment was the 2001 Mw=8.4 Arequipa earthquake, we can state that the earthquake potential on this segment is at least Mw=8.4. The recurrence time for a Mw=8.4 would be ~100 years, while it would be ~1,000 years for a Mw=9.0. A better characterization of the b-value and the amount of aseismic slip over the cycle are the two main parameters to improve the assessment of the earthquake potential. It is also essential to note that our moment budget analysis being restricted to the South Peru segment, our computed magnitudes are bounded by the size of this segment. In fact, an earthquake rupturing

both the South Peru segment and another segment, crossing the Nazca Ridge or the Arica bend, could exceed our estimates.

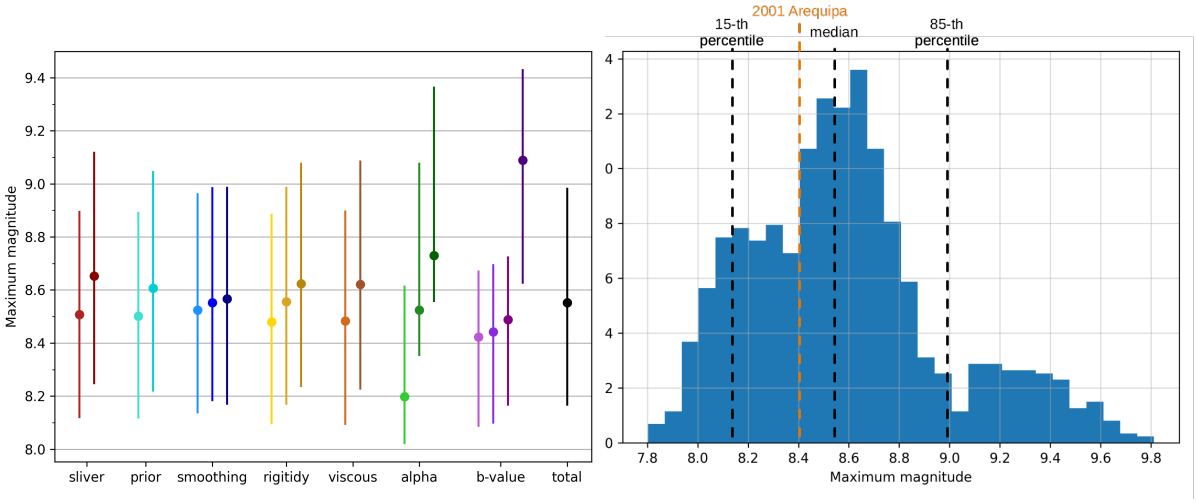

Figure 13: *Left:* Earthquake potential in function of various parameters, from left to right: sliver motion (with and without Peruvian sliver), slip prior (creeping or locked), smoothing (λ = 15, 30, and 200 km), average medium rigidity (35, 40, and 45 GPa), neglecting or not viscous behavior following the 2001 Arequipa earthquake, rate of seismic events α (0.3, 0.55, and 0.8), b-value of seismic catalog (ISC-GEM: 0.68, gCMT: 0.72, ISC: 0.73, and IGP: 1.03), and the total range. Models in the PS and SSA frames are weighted by a factor 2/3 and 1/3 respectively, and models accounting or not for viscous behavior following the Arequipa earthquake are weighted by a factor 1/3 and 2/3 respectively. The dots represent the median M_w value, while the vertical bars represent the variability between the 15th and 85th percentiles on the 864 models considered. *Right:* Distribution of the earthquake potential for the 864 computed models, accounting for all the discussed factors of uncertainty. Median, 15th and 85th percentiles are depicted by dashed lines.

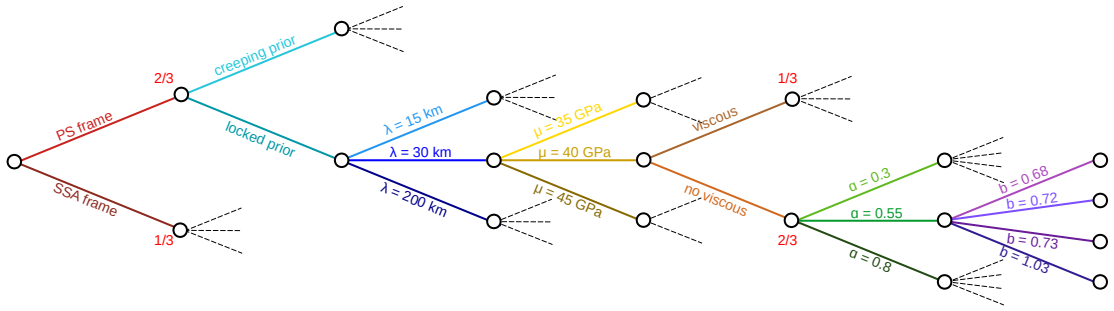

Figure 14: Logic tree used for exploration of uncertainties on Figure 13. We explore from left to right: sliver motion (with and without Peruvian sliver), specified slip prior (creeping or locked), smoothing (λ = 15, 30, and 200 km), average medium rigidity (35, 40, and 45 GPa), neglecting or not viscous behavior following the 2001 Arequipa earthquake, rate of seismic events α (0.3, 0.55, and 0.8), and b-value of seismic catalog (ISC-GEM: 0.68, gCMT: 0.72, ISC: 0.73, and IGP: 1.03). Models in the PS and SSA frames are weighted by a factor 2/3 and 1/3 respectively, and models accounting or not for viscous behavior following the Arequipa earthquake are weighted by a factor 1/3 and 2/3 respectively.

6 Conclusions

To summarize, we have extracted a dense interseismic velocity field at the scale of the South Peruvian Andes from time series analysis of 73 GNSS sites (47 cGPS and 26 sGPS), including a significant amount of unpublished data. From that, we obtained a map of interseismic coupling, with an unprecedented resolution, through an inversion process based on the Tarantola-Valette formulation. It highlights a highly heterogeneous coupling distribution, with strongly coupled patches offshore Lima (12°S), Atico (16°S) and Ilo (17.5°S) cities. Low coupling areas were observed where the Nazca ridge, and more tenuously where the Nazca fracture zone, are subducting below the continent. From this distribution, we estimate that the South Peru segment which extends from the Nazca ridge to the Arica bend could host a M_w=8.4 (recurrence time of 100 years) to Mw=9.0 (recurrence time of 900 years). In addition, we observe that the region near the coast of Lima could have a high seismic potential due to its very high coupling, according to our model. The estimation of the earthquake potential depends on several factors, like the chosen seismic catalog, the rate of seismic events over all transient parameters, correcting or not for a sliver motion, or accounting for long-term visco-elastic relaxation following the 2001 Arequipa earthquake. Among these factors, the two main sources of uncertainty are the seismic catalog and the rate of seismic events.

Further developments may include the use of InSAR data, allowing for a large-scale mapping with a very high resolution in space compared to GNSS. It would help to better constrain the depth of the transition between brittle and ductile rheology, as well as the amount and extension of intracontinental deformation. In addition, it would help to estimate the extent of visco-elastic relaxation following megathrust events, like the 2001 Arequipa earthquake. The increased resolution would also be a key point to overcome the lack of constraint on the models we encounter in some areas, for example South of Lima. We may also include a denser monitoring of creeping areas to assess if the aseismic creep is released continuously or through bursts of slow slip, in order to better constrain the frictional behavior of those barriers, and the actual value of the rate of seismic events α. Finally, the use of more complex rheology, with visco-elastic or visco-elasto-plastic behaviors would be a significant progress in order to account for large-scale intracontinental deformation (Li et al., 2015). It would also be a step in the direction of a general interseismic coupling model at the scale of central Andes, extending south of the Arica bend where a rotation of the long-term slip direction was suggested by Arriagada et al. (2008) and Métois et al. (2016).

Acknowledgments

This work was supported by funding from ERC, CNES, CNRS-INSU and LabEx Osug@2020 (Investissements d'avenir – ANR10LABX56). A. Socquet received funding from the European Research Council (ERC) CoG 865963 DEEP-trigger. B. Lovery salary was covered by grants from CNES and ERC DEEPtrigger. We thank all organizations and persons that are supporting and operating continuous GNSS stations and campaign measurements used in this study. The continuous GNSS stations in Chile used in this work are maintained and distributed by the Centro Simologico Nacional, Universidad de Chile. The IGP/ISTerre/Caltech GNSS stations in Peru were

installed by ISTerre and Caltech in collaboration with IGP, and are now maintained by the Instituto Geofisico del Peru. The IGN network in Peru is maintained by the Instituto Geográfico Nacional. We thank the French national pool of portable geodetic instruments GPSMOB-RESIF (INSU-CNRS) for providing the geodetic instruments for the GNSS campaigns. Finally, we thank former engineers who worked on the operational implementation of the GipsyX GNSS processing at ISTerre, including Gaëlle Deschamps-Huygen and Rémi Molaro-Maqua.

Open Research

All GNSS time series used in this manuscript are available at (Socquet et al., 2023e): https://doi.org/10.17178/GNSS.products.SouthAmerica_GIPSYX.daily. RINEX data from CSN network are available at http://gps.csn.uchile.cl. RINEX data from RBMC are available at https://www.ibge.gov.br/en/geosciences/geodetic-positioning/geodetic-networks/19213-brazilian-network-for-continuous-monitoring-of-the-gnss-systems.html?=&t=downloads. RINEX data from SNAPP campaigns are available from UNAVCO (Simons et al., 2010): 1994 campaign at https://www.unavco.org/data/gps-gnss/data-access-methods/dai1/data_request.php?gid=1325&ds=1&parent_link=Campaign&pview=original, 1996 campaign at https://www.unavco.org/data/gps-gnss/data-access-methods/dai1/data_request.php?gid=1493&ds=2&parent_link=Campaign&pview=original, and 2001 campaign at https://www.unavco.org/data/gps-gnss/data-access-methods/dai1/data_request.php?gid=2128&ds=1&parent_link=Campaign&pview=original. RINEX data from campaigns in South Peru between 2012 and 2022 are available through the following links: 2012 campaign (Socquet et al., 2023a) at https://doi.org/10.15148/12160e27-0951-41b7-be97-efc4fec7ff96, 2013 campaign (Socquet et al., 2023d) at https://doi.org/10.15148/14ab8f86-3453-4a44-b921-ec3b0a133ef6, 2015 campaign (Socquet & Norabuena, 2023c) at https://doi.org/10.15148/376f13e4-e333-4da1-aa10-76f4eae08ffc, 2016 campaign (Nocquet & Socquet, 2023) at https://doi.org/10.15148/f410d57f-2e67-4174-9e7e-17ae3fd55d99, 2018 campaign (Socquet et al., 2023b) at https://doi.org/10.15148/94cc6056-84d5-4c92-a043-6db8b769babf, and 2022 campaign (Socquet et al., 2023f) at https://gpscope.dt.insu.cnrs.fr/campagnes/data/2022-041/rinex/. RINEX data from IGP/ISTerre/Caltech continuous stations in South Peru are available at https://doi.osug.fr/data/public/GNSS_products/Peru/RINEX/peru_igp/. RINEX data from IGN network are available at https://doi.osug.fr/data/public/GNSS_products/Peru/RINEX/peru_ign/. The trajectory model analysis has been performed using the ITSA software, hosted on GriCAD GitLab repository (https://gricad-gitlab.univ-grenoble-alpes.fr/isterre-cycle/itsa), and described in Marill et al. (2021). Geographical illustrations were made using the Generic Mapping Tools (GMT) version 6 package (Wessel et al., 2019) licensed under LGPL version 3 or later, available at https://www.generic-mapping-tools.org/. Other illustrations were made with Matplotlib v3.7.1 (Hunter, 2007), available under the Matplotlib license at https://matplotlib.org.

References

Altamimi, Z., Rebischung, P., Métivier, L., & Collilieux, X. (2016). ITRF2014: A new release of the International Terrestrial Reference Frame modeling nonlinear station motions. *Journal of Geophysical Research: Solid Earth*, *121*(8), 6109–6131. https://doi.org/10.1002/2016JB013098

Arriagada, C., Roperch, P., Mpodozis, C., & Cobbold, P. R. (2008). Paleogene building of the Bolivian Orocline: Tectonic restoration of the central Andes in 2-D map view. *Tectonics*, *27*(6). https://doi.org/10.1029/2008TC002269

Avouac, J.-P. (2015), From geodetic imaging of seismic and aseismic fault slip to dyamic modeling of the seismic cycle. *Annu. Rev. Earth Planet. Sci.* , *43*, 233-271.

Beck, S. L., & Ruff, L. J. (1989). Great earthquakes and subduction along the Peru trench. *Phys. Earth Planet. Inter*., 57(3–4), 199–224, doi:10.1016/0031-9201(1089)90112-X.

Beck, S. L., & Nishenko, S. P. (1990). Variations in the mode of great earthquake rupture along the central Peru subduction zone. *Geophys. Res. Lett.*, 17, 1969–1972, doi:10.1029/GL017i011p01969.

Bertiger, W., Bar-Sever, Y., Dorsey, A., Haines, B., Harvey, N., Hemberger, D., et al. (2020). GipsyX/RTGx, a new tool set for space geodetic operations and research. *Advances in Space Research*, *66*(3), 469–489. https://doi.org/10.1016/j.asr.2020.04.015

Bevis, M., Kendrick, E., Smalley Jr., R., Brooks, B., Allmendinger, R., & Isacks, B. (2001). On the strength of interplate coupling and the rate of back arc convergence in the central Andes: An analysis of the interseismic velocity field. *Geochemistry, Geophysics, Geosystems*, *2*(11). https://doi.org/10.1029/2001GC000198

Bevis, M., & Brown, A. (2014). Trajectory models and reference frames for crustal motion geodesy. *Journal of Geodesy*, *88*(3), 283–311. https://doi.org/10.1007/s00190-013-0685-5

Bilek, S. L., & Lay, T. (1999). Rigidity variations with depth along interplate megathrust faults in subduction zones. *Nature*, *400*(6743), 443–446. https://doi.org/10.1038/22739

Bilek, S. L. (2010), Invited review paper: Seismicity along the South American subduction zone: Review of large earthquakes, tsunamis, and subduction zone complexity. *Tectonophysics, 495*, 2-14. https://doi.org/10.1016/j.tecto.2009.02.037.

Bilek, S. L., & Lay, T. (2018). Subduction zone megathrust earthquakes. *Geosphere*, *14*(4), 1468–1500. https://doi.org/10.1130/GES01608.1

Blewitt, G., Kreemer, C., Hammond, W. C., & Gazeaux, J. (2016). MIDAS robust trend estimator for accurate GPS station velocities without step detection. *Journal of Geophysical Research: Solid Earth*, *121*(3), 2054–2068. https://doi.org/10.1002/2015JB012552

Boehm, J., Werl, B., & Schuh, H. (2006). Troposphere mapping functions for GPS and very long baseline interferometry from European Centre for Medium-Range Weather Forecasts operational analysis data. *Journal of Geophysical Research: Solid Earth*, *111*(B2). https://doi.org/10.1029/2005JB003629

Bürgmann, R., Kogan, M. G., Steblov, G. M., Hilley, G., Levin, V. E., & Apel, E. (2005). Interseismic coupling and asperity distribution along the Kamchatka subduction zone. *Journal of Geophysical Research: Solid Earth*, *110*(B7). https://doi.org/10.1029/2005JB003648

1004 Chlieh, M., Avouac, J.-P., Hjorleifsdottir, V., Song, T.-R. A., Ji, C., Sieh, K., et al. (2007).
1005 Coseismic Slip and Afterslip of the Great Mw 9.15 Sumatra–Andaman Earthquake of 2004.
1006 *Bulletin of the Seismological Society of America*, *97*(1A), S152–S173.
1007 https://doi.org/10.1785/0120050631
1008
1009 Chlieh, M., Avouac, J. P., Sieh, K., Natawidjaja, D. H., & Galetzka, J. (2008). Heterogeneous
1010 coupling of the Sumatran megathrust constrained by geodetic and paleogeodetic measurements.
1011 *Journal of Geophysical Research: Solid Earth*, *113*(B5). https://doi.org/10.1029/2007JB004981
1012
1013 Chlieh, M., Perfettini, H., Tavera, H., Avouac, J.-P., Remy, D., Nocquet, J.-M., et al. (2011).
1014 Interseismic coupling and seismic potential along the Central Andes subduction zone. *Journal of*
1015 *Geophysical Research: Solid Earth*, *116*(B12). https://doi.org/10.1029/2010JB008166
1016
1017 Cifuentes, I. L. (1989). The 1960 Chilean earthquakes. *Journal of Geophysical Research: Solid*
1018 *Earth*, *94*(B1), 665–680. https://doi.org/10.1029/JB094iB01p00665
1019
1020 Di Giacomo, D., Engdahl, E. R., & Storchak, D. A. (2018). The ISC-GEM Earthquake Catalogue
1021 (1904–2014): status after the Extension Project. *Earth System Science Data*, *10*(4), 1877–1899.
1022 https://doi.org/10.5194/essd-10-1877-2018
1023
1024 Dorbath, L., Cisternas, A., & Dorbath, C. (1990), Assesment of the size of large and great historical
1025 earthquakes in Peru. *Bulletin of the Seismological Society of America, 80*, 551-576.
1026 https://doi.org/10.1785/BSSA0800030551
1027
1028 Dziewonski, A. M., Chou, T. A., & Woodhouse, J. H., (1981), Determination of earthquake source
1029 parameters from waveform data for studies of global and regional seismicity, *J. Geophys. Res.*, *86*,
1030 2825-2852. https://doi.org/10.1029/JB086iB04p02825
1031
1032 Ekström, G., Nettles, M., & Dziewoński, A. M. (2012). The global CMT project 2004–2010:
1033 Centroid-moment tensors for 13,017 earthquakes. *Physics of the Earth and Planetary Interiors*,
1034 *200–201*, 1–9. https://doi.org/10.1016/j.pepi.2012.04.002
1035
1036 Florsch, N., Revil, A., & Camerlynck, C. (2014). Inversion of generalized relaxation time
1037 distributions with optimized damping parameter. *Journal of Applied Geophysics*, *109*, 119–132.
1038 https://doi.org/10.1016/j.jappgeo.2014.07.013
1039
1040 Gagnon, K., Chadwell, C. D., & Norabuena, E. (2005). Measuring the onset of locking in the Peru–
1041 Chile trench with GPS and acoustic measurements. *Nature*, *434*(7030), 205–208.
1042 https://doi.org/10.1038/nature03412
1043
1044 Hayes, G. P., Moore, G. L., Portner, D. E., Hearne, M., Flamme, H., Furtney, M., & Smoczyk, G.
1045 M. (2018). Slab2, a comprehensive subduction zone geometry model. *Science*, *362*(6410), 58–61.
1046 https://doi.org/10.1126/science.aat4723
1047

Hetland, E. A., & Simons, M. (2010). Post-seismic and interseismic fault creep II: Transient creep and interseismic stress shadows on megathrusts. *Geophysical Journal International*, *181*(1), 99-112

Hergert, T., & Heidbach, O. (2006). New insights into the mechanism of postseismic stress relaxation exemplified by the 23 June 2001 Mw = 8.4 earthquake in southern Peru. *Geophysical Research Letters*, *33*(2). https://doi.org/10.1029/2005GL024858

Hoffmann, F., Metzger, S., Moreno, M., Deng, Z., Sippl, C., Ortega-Culaciati, F., & Oncken, O. (2018). Characterizing Afterslip and Ground Displacement Rate Increase Following the 2014 Iquique-Pisagua Mw 8.1 Earthquake, Northern Chile. *Journal of Geophysical Research: Solid Earth*, *123*(5), 4171–4192. https://doi.org/10.1002/2017JB014970

Hunter, J. D. (2007). Matplotlib: A 2d graphics environment. *Computing in Science & Engineering*, *9*(3), 90–95. https://doi.org/10.1109/MCSE.2007.55

Ide, S., Baltay, A., & Beroza, G. C. (2011). Shallow Dynamic Overshoot and Energetic Deep Rupture in the 2011 Mw 9.0 Tohoku-Oki Earthquake. *Science*. Retrieved from https://www.science.org/doi/10.1126/science.1207020

Itoh, Y., Wang, K., Nishimura, T., & He, J. (2019). Compliant Volcanic Arc and Backarc Crust in Southern Kurile Suggested by Interseismic Geodetic Deformation. *Geophysical Research Letters*, *46*(21), 11790–11798. https://doi.org/10.1029/2019GL084656

Jara, J., Sánchez-Reyes, H., Socquet, A., Cotton, F., Virieux, J., Maksymowicz, A., et al. (2018). Kinematic study of Iquique 2014 Mw 8.1 earthquake: Understanding the segmentation of the seismogenic zone. *Earth and Planetary Science Letters*, *503*, 131–143. https://doi.org/10.1016/j.epsl.2018.09.025

Johnston, G., Riddell, A., & Hausler, G. (2017), The International GNSS Service. Teunissen, Peter J.G., & Montenbruck, O. (Eds.), *Springer Handbook of Global Navigation Satellite Systems* (1st ed., pp. 967-982). Cham, Switzerland: Springer International Publishing. https://doi.org/10.1007/978-3-319-42928-1

Kanamori, H., & Cipar, J. J. (1974). Focal process of the great Chilean earthquake May 22, 1960. *Physics of the Earth and Planetary Interiors*, *9*(2), 128–136. https://doi.org/10.1016/0031-9201(74)90029-6

Kaneko, Y., Avouac, J.-P., & Lapusta, N. (2010). Towards inferring earthquake patterns from geodetic observations of interseismic coupling. *Nature Geoscience*, *3*(5), 363–369. https://doi.org/10.1038/ngeo843

Kendrick, E., Bevis, M., Smalley, R., Brooks, B., Vargas, R. B., Lauría, E., & Fortes, L. P. S. (2003). The Nazca–South America Euler vector and its rate of change. *Journal of South American Earth Sciences*, *16*(2), 125–131. https://doi.org/10.1016/S0895-9811(03)00028-2

King, G., and Nábělek, J. (1985). Role of fault bends in the initiation and termination of earthquake rupture. *Science* 228.4702, 984-987.

King, G. (1986). Speculations on the geometry of the initiation and termination processes of earthquake rupture and its relation to morphology and geological structure. *Pure and applied geophysics* 124, 567-585.

Klein, E., Fleitout, L., Vigny, C., & Garaud, J. D. (2016). Afterslip and viscoelastic relaxation model inferred from the large-scale post-seismic deformation following the 2010 Mw 8.8 Maule earthquake (Chile). *Geophysical Journal International*, *205*(3), 1455–1472. https://doi.org/10.1093/gji/ggw086

Kley, J., & Monaldi, C. R. (1998). Tectonic shortening and crustal thickness in the Central Andes: How good is the correlation? *Geology*, *26*(8), 723–726. https://doi.org/10.1130/0091-7613(1998)026<0723:TSACTI>2.3.CO;2

Koketsu, K., Yokota, Y., Nishimura, N., Yagi, Y., Miyazaki, S., Satake, K., et al. (2011). A unified source model for the 2011 Tohoku earthquake. *Earth and Planetary Science Letters*, *310*(3), 480–487. https://doi.org/10.1016/j.epsl.2011.09.009

Konca, A. O., Avouac, J.-P., Sladen, A., Meltzner, A. J., Sieh, K., Fang, P., et al. (2008). Partial rupture of a locked patch of the Sumatra megathrust during the 2007 earthquake sequence. *Nature*, *456*(7222), 631–635. https://doi.org/10.1038/nature07572

Kositsky, A. P., & Avouac, J.-P. (2010). Inverting geodetic time series with a principal component analysis-based inversion method. *Journal of Geophysical Research: Solid Earth*, *115*(B3). https://doi.org/10.1029/2009JB006535

Langer, C. J., & Spence, W. (1995). The 1974 Peru earthquake series. *Seismol. Soc. Am.*, 85(3), 665–687.

Li, S., Moreno, M., Bedford, J., Rosenau, M., & Oncken, O. (2015). Revisiting viscoelastic effects on interseismic deformation and locking degree: A case study of the Peru-North Chile subduction zone. *Journal of Geophysical Research: Solid Earth*, *120*(6), 4522–4538. https://doi.org/10.1002/2015JB011903

Li, S., & Chen, L. (2023). How Long Can the Postseismic and Interseismic Phases of Great Subduction Earthquake Sustain? Toward an Integrated Earthquake-Cycle Perspective. *Geophysical Research Letters*, *50*(11), e2023GL103976. https://doi.org/10.1029/2023GL103976

Loveless, J. P., & Meade, B. J. (2011). Spatial correlation of interseismic coupling and coseismic rupture extent of the 2011 MW = 9.0 Tohoku-oki earthquake. *Geophysical Research Letters*, *38*(17). https://doi.org/10.1029/2011GL048561

Lyard, F. H., Allain, D. J., Cancet, M., Carrère, L., & Picot, N. (2021). FES2014 global ocean tide atlas: design and performance. *Ocean Science*, *17*(3), 615–649. https://doi.org/10.5194/os-17-615-2021

Marill, L., Marsan, D., Socquet, A., Radiguet, M., Cotte, N., & Rousset, B. (2021). Fourteen-Year Acceleration Along the Japan Trench. *Journal of Geophysical Research: Solid Earth*, *126*(11), e2020JB021226. https://doi.org/10.1029/2020JB021226

Mariniere, J., Beauval, C., Nocquet, J.-M., Chlieh, M., & Yepes, H. (2021), Earthquake recurrence model for the Colombia–Ecuador subduction zone constrained from seismic and geodetic data, implication for PSHA. *Bulletin of the Seismological Society of America*, *111*(3), 1508-1528.

Matsu'ura, T. (2015). Late Quaternary uplift rate inferred from marine terraces, Muroto Peninsula, southwest Japan: Forearc deformation in an oblique subduction zone. *Geomorphology*, *234*, 133–150. https://doi.org/10.1016/j.geomorph.2015.01.012

Meade, B. J. (2007). Algorithms for the calculation of exact displacements, strains, and stresses for triangular dislocation elements in a uniform elastic half space. *Computers & Geosciences*, *33*(8), 1064–1075. https://doi.org/10.1016/j.cageo.2006.12.003

Métois, M., Socquet, A., Vigny, C., Carrizo, D., Peyrat, S., Delorme, A., et al. (2013). Revisiting the North Chile seismic gap segmentation using GPS-derived interseismic coupling. *Geophysical Journal International*, *194*(3), 1283–1294. https://doi.org/10.1093/gji/ggt183

Métois, M., Vigny, C., & Socquet, A. (2016). Interseismic Coupling, Megathrust Earthquakes and Seismic Swarms Along the Chilean Subduction Zone (38°–18°S). *Pure and Applied Geophysics*, *173*(5), 1431–1449. https://doi.org/10.1007/s00024-016-1280-5

Molnar, P. (1979), Earthquake recurrence intervals and plate tectonics. *Bulletin of the Seismological Society of America, 69(1)*, 115-133. https://doi.org/10.1785/BSSA0690010115

Moreno, M., Rosenau, M., & Oncken, O. (2010). 2010 Maule earthquake slip correlates with pre-seismic locking of Andean subduction zone. *Nature*, *467*(7312), 198–202. https://doi.org/10.1038/nature09349

Nishenko, S. P. (1991). Circum-Pacific seismic potential, *U.S. Geological Survey, National Earthquake Information Center*

Nocquet, J.-M., Socquet, A. (2023). *EPOS-France - GPSMob data - Mission n° 16-153 - Perou (2016) - 2016-08-24 / 2016-12-06 - 36 points* [Dataset]. OSU OREME. http://doi.org/10.15148/F410D57F-2E67-4174-9E7E-17AE3FD55D99

Nocquet, J.-M., Villegas-Lanza, J. C., Chlieh, M., Mothes, P. A., Rolandone, F., Jarrin, P., et al. (2014). Motion of continental slivers and creeping subduction in the northern Andes. *Nature Geoscience*, *7*(4), 287–291. https://doi.org/10.1038/ngeo2099

1184 Norabuena, E., Leffler-Griffin, L., Mao, A., Dixon, T., Stein, S., Sacks, I. S., et al. (1998). Space
1185 Geodetic Observations of Nazca-South America Convergence Across the Central Andes. *Science*,
1186 *279*(5349), 358–362. https://doi.org/10.1126/science.279.5349.358
1187
1188 Perfettini, H., Avouac, J.-P., & Ruegg, J.-C. (2005). Geodetic displacements and aftershocks
1189 following the 2001 Mw = 8.4 Peru earthquake: Implications for the mechanics of the earthquake
1190 cycle along subduction zones. *Journal of Geophysical Research: Solid Earth*, *110*(B9).
1191 https://doi.org/10.1029/2004JB003522
1192
1193 Perfettini, H., Avouac, J.-P., Tavera, H., Kositsky, A., Nocquet, J.-M., Bondoux, F., et al. (2010).
1194 Seismic and aseismic slip on the Central Peru megathrust. *Nature*, *465*(7294), 78–81.
1195 https://doi.org/10.1038/nature09062
1196
1197 Pritchard, M. E., Norabuena, E. O., Ji, C., Boroschek, R., Comte, D., Simons, M., et al. (2007).
1198 Geodetic, teleseismic, and strong motion constraints on slip from recent southern Peru subduction
1199 zone earthquakes. *Journal of Geophysical Research: Solid Earth*, *112*(B3).
1200 https://doi.org/10.1029/2006JB004294
1201
1202 Radiguet, M., Cotton, F., Vergnolle, M., Campillo, M., Valette, B., Kostoglodov, V., & Cotte, N.
1203 (2011). Spatial and temporal evolution of a long term slow slip event: the 2006 Guerrero Slow Slip
1204 Event. *Geophysical Journal International*, *184*(2), 816–828. https://doi.org/10.1111/j.1365-
1205 246X.2010.04866.x
1206
1207 Radiguet, M., Perfettini, H., Cotte, N., Gualandi, A., Valette, B., Kostoglodov, V., et al. (2016).
1208 Triggering of the 2014 Mw7.3 Papanoa earthquake by a slow slip event in Guerrero, Mexico.
1209 *Nature Geoscience*, *9*(11), 829–833. https://doi.org/10.1038/ngeo2817
1210
1211 Remy, D., Perfettini, H., Cotte, N., Avouac, J. P., Chlieh, M., Bondoux, F., et al. (2016).
1212 Postseismic relocking of the subduction megathrust following the 2007 Pisco, Peru, earthquake.
1213 *Journal of Geophysical Research: Solid Earth*, *121*(5), 3978–3995.
1214 https://doi.org/10.1002/2015JB012417
1215
1216 Robinson, D. P., Das, S., & Watts, A. B. (2006), Earthquake rupture stalled by a subducting
1217 fracture zone. *Science, 312*(5777), 1203-1205. https://doi.org/10.1126/science.1125771
1218
1219 Rubin, A. M., Gillard, D., & Got, J.-L. (1999). Streaks of microearthquakes along creeping faults.
1220 *Nature*, *400*(6745), 635–641. https://doi.org/10.1038/23196
1221
1222 Saillard, M., Audin, L., Rousset, B., Avouac, J.-P., Chlieh, M., Hall, S. R., et al. (2017). From the
1223 seismic cycle to long-term deformation: linking seismic coupling and Quaternary coastal
1224 geomorphology along the Andean megathrust. *Tectonics*, *36*(2), 241–256.
1225 https://doi.org/10.1002/2016TC004156
1226
1227 Savage, J. C. (1983). A dislocation model of strain accumulation and release at a subduction zone.
1228 *Journal of Geophysical Research: Solid Earth*, *88*(B6), 4984–4996.
1229 https://doi.org/10.1029/JB088iB06p04984

Scholz, C. H. (1990), The Mechanics of Earthquakes and Faulting, *Cambridge Univ. Press*, 413.

Silgado, E. (1978). Recurrence of tsunamis in the western coast of South America. *Marine Geodesy*, *1*(4), 347–354. https://doi.org/10.1080/01490417809387980

Simons, M., Galetzka, J., Genrich, J. F., Ortega, F., Comte, D., et al. (2010). Central Andean Tectonic Observatory Geodetic Array [Dataset]. UNAVCO, Inc. http://doi.org/10.7283/T50P0X37

Simons, M., Minson, S. E., Sladen, A., Ortega, F., Jiang, J., Owen, S. E., et al. (2011). The 2011 Magnitude 9.0 Tohoku-Oki Earthquake: Mosaicking the Megathrust from Seconds to Centuries. *Science*, *332*(6036), 1421–1425. https://doi.org/10.1126/science.1206731

Sladen, A., Tavera, H., Simons, M., Avouac, J. P., Konca, A. O., Perfettini, H., et al. (2010). Source model of the 2007 Mw 8.0 Pisco, Peru earthquake: Implications for seismogenic behavior of subduction megathrusts. *Journal of Geophysical Research: Solid Earth*, *115*(B2). https://doi.org/10.1029/2009JB006429

Socquet, A., Cotte, N., Bondoux, F., Norabuena, E. (2023a). *EPOS-France - GPSMob data - Mission n° 12-136b - Sud Pérou (2012) - 2012-06-23 / 2012-07-04 - 24 points* [Dataset]. OSU OREME. http://doi.org/10.15148/12160E27-0951-41B7-BE97-EFC4FEC7FF96

Socquet, A., Nocquet, J.-M., Norabuena, E., Villegas, J. C., Chlieh, M. (2023b). *EPOS-France - GPSMob data - Mission n° 18-135 - Perou (2018) - 2018-11-02 / 2018-11-21 - 26 points* [Dataset]. OSU OREME. http://doi.org/10.15148/94CC6056-84D5-4C92-A043-6DB8B769BABF

Socquet, A., Norabuena, E. (2023c). *EPOS-France - GPSMob data - Mission n° 15-265 - Pérou (2015) - 2015-10-22 / 2015-11-01 - 27 points* [Dataset]. OSU OREME. http://doi.org/10.15148/376F13E4-E333-4DA1-AA10-76F4EAE08FFC

Socquet, A., Norabuena, E., Cotte, N. (2023d). *EPOS-France - GPSMob data - Mission n° 13-136 - Sud Pérou (2013) - 2013-06-09 / 2013-06-15 - 2 points* [Dataset]. OSU OREME. http://doi.org/10.15148/14AB8F86-3453-4A44-B921-EC3B0A133EF6

Socquet, A., Tsapong-Tsague, A., Lovery, B., Janex, G., & Radiguet, M. (2023e). Metadata and GNSS daily position solutions for permanent GNSS stations in South America [Dataset]. These datasets include station metadata and GNSS daily solutions for over 700 GNSS stations in South America. CNRS, OSUG, ISTERRE. https://doi.org/10.17178/GNSS.PRODUCTS.SOUTHAMERICA_GIPSYX.DAILY

Socquet, A., Villegas, J. C., Langlais, M., Doubre, C., Donniol, B., Costantino, G., Chouli, A., Jung, A. (2023f). *EPOS-France - GPSMob data - Mission n° 22-041 - Perou (2022) - 2022-03-12 / 2022-08-07 - 69 points.* OSU OREME. [Dataset]. DOI: https://doi.org/10.15148/289f31dd-9109-49ba-8116-5217191226e5

Stein, S., & Okal, E. A. (2005). Speed and size of the Sumatra earthquake. *Nature*, *434*(7033), 581–582. https://doi.org/10.1038/434581a

Storchak, D.A., Di Giacomo, D., Bondár, I., Engdahl, E.R., Harris, J., Lee, W.H.K., Villaseñor, A., & Bormann, P. (2013), Public Release of the ISC-GEM Global Instrumental Earthquake Catalogue (1900-2009). *Seism. Res. Lett.*, *84*(5), 810-815. https://doi.org/10.1785/0220130034

Storchak, D. A., Di Giacomo, D., Engdahl, E. R., Harris, J., Bondár, I., Lee, W. H. K., et al. (2015). The ISC-GEM Global Instrumental Earthquake Catalogue (1900–2009): Introduction. *Physics of the Earth and Planetary Interiors*, *239*, 48–63. https://doi.org/10.1016/j.pepi.2014.06.009

Takabatake, T., Shibayama, T., Esteban, M., & Ishii, H. (2018). Advanced casualty estimation based on tsunami evacuation intended behavior: case study at Yuigahama Beach, Kamakura, Japan. *Natural Hazards*, *92*(3), 1763–1788. https://doi.org/10.1007/s11069-018-3277-0

Tarantola, A. (2005), Inverse problem theory and methods for model parameter estimation. *Society for Industrial and Applied Mathematics*.

Tarantola, A., & Valette, B. (1982). Generalized nonlinear inverse problems solved using the least squares criterion. *Reviews of Geophysics*, *20*(2), 219–232. https://doi.org/10.1029/RG020i002p00219

Tavera, H., Buforn, E., Bernal, I., Antayhua, Y., Vilacapoma, L. (2002), The Arequipa (Peru) earthquake of June 23, 2001. *Journal of Seismology, 6*, 279–283.

Tavera, H., & Buforn, E. (1998). Sismicidad y sismotectónica de Perú. *Física de la Tierra*, *10*, 187-219.

Veloza, G., Styron, R., Taylor, M., & Mora, A. (2011), Open source archive of active faults for northwest South America. *Gsa Today*, *22*(10), 4-10. https://doi.org/10.1130/GSAT-G156A.1

Villegas-Lanza, J. C., Chlieh, M., Cavalié, O., Tavera, H., Baby, P., Chire-Chira, J., & Nocquet, J.-M. (2016). Active tectonics of Peru: Heterogeneous interseismic coupling along the Nazca megathrust, rigid motion of the Peruvian Sliver, and Subandean shortening accommodation. *Journal of Geophysical Research: Solid Earth*, *121*(10), 7371–7394. https://doi.org/10.1002/2016JB013080

Wessel, P., Luis, J. F., Uieda, L., Scharroo, R., Wobbe, F., Smith, W. H. F., & Tian, D. (2019), The Generic Mapping Tools version 6. *Geochemistry, Geophysics, Geosystems*, 20, 5556–5564. https://doi.org/10.1029/2019GC008515

Willemann, R. J., Storchak, D. A. (2001), Data Collection at the International Seismological Centre, Seis. Res. Lett., *72*, 440-453. https://doi.org/10.1785/gssrl.72.4.440

Yáñez-Cuadra, V., Ortega-Culaciati, F., Moreno, M., Tassara, A., Krumm-Nualart, N., Ruiz, J., et al. (2022). Interplate Coupling and Seismic Potential in the Atacama Seismic Gap (Chile): Dismissing a Rigid Andean Sliver. *Geophysical Research Letters*, *49*(11), e2022GL098257. https://doi.org/10.1029/2022GL098257

4.2 Supplements

Journal of Geophysical Research: Solid Earth

Supporting Information for

Heterogeneous Locking and Earthquake Potential on the South Peru Megathrust from Dense GNSS Network

B. Lovery[1], M. Chlieh[1], E. Norabuena[2], J.C. Villegas-Lanza[2], M. Radiguet[1], N. Cotte[1], M. Langlais[1], A. Tsapong-Tsague[1], W. Quiroz[2], C. Sierra Farfán[3], M. Simons[4], J.M. Nocquet[5], H. Tavera[2], and A. Socquet[1]

[1]Univ. Grenoble Alpes, Univ. Savoie Mont Blanc, CNRS, IRD, Univ. Gustave Eiffel, ISTerre, 38000 Grenoble, France

[2] Instituto Geofísico del Perú, Lima, Peru

[3]Instituto Geográfico Nacional, Lima, Peru

[4]Caltech, USA

[5]Institut de Physique du Globe de Paris, IRD

Contents of this file

Figures S1 to S21
Tables S2 to S4

Additional Supporting Information (Files uploaded separately)

Caption for Table S1: Interseismic velocities (mm/yr) in the Stable South America frame at each GNSS station. Longitude and latitude of the stations are specified, as well as interseismic velocities along North, East, and Up components, with their associated uncertainties from MIDAS (Blewitt et al., 2016).

Caption for Dataset S1: GNSS timeseries are displayed on NEU components, with data points in blue and uncertainties from GipsyX in grey. For survey GNSS stations, the data points prior to Iquique correction (mainshock + aftershock + postseismic) are displayed in cyan. Model from our trajectory model (ITSA) is depicted by the red line for continuous GNSS stations.

Introduction

In this material, we provide additional information on the analysis, notably on the trajectory model, the slip inversion process, and the moment budget analysis. For instance, we include coseismic and postseismic models of the 2014 Mw=8.1 Iquique earthquake with slip distribution and tables. Resolution tests and L-curves related to the slip inversion process are also included. GNSS timeseries and interseismic velocities are available as separate files, Dataset S1 and Table S1 respectively.

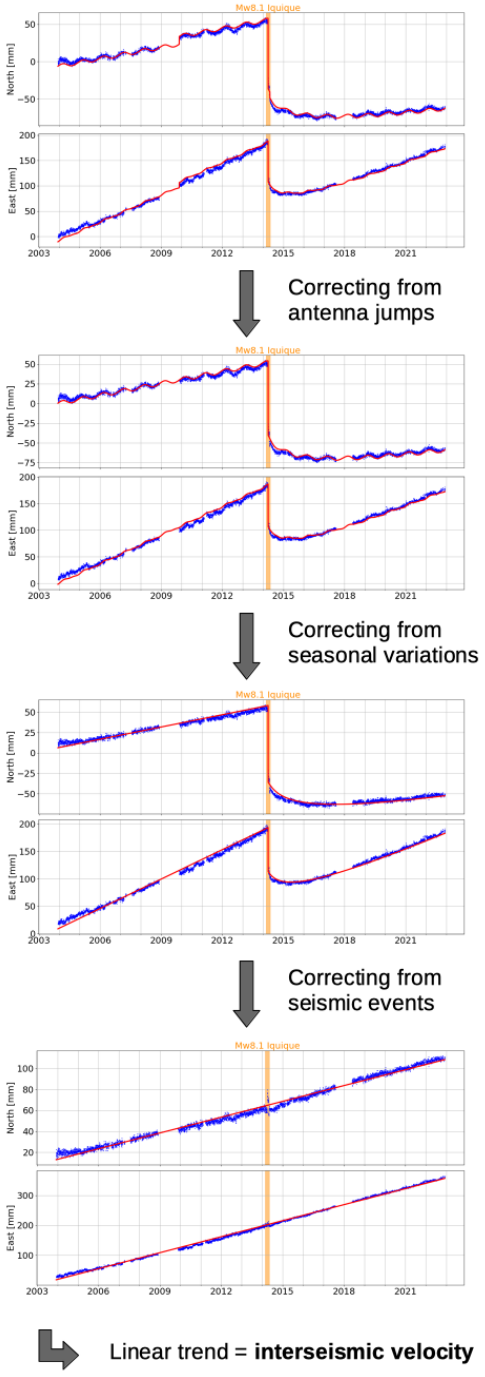

Figure S1: Explanation of the trajectory model. From top to bottom, the time series is corrected from antenna jumps, seasonal variations, seismic events (coseisic and postseismic displacements). At the end, we obtained a linear trend, depicting the secular motion in a given reference frame. We consider this motion as the interseismic velocity.

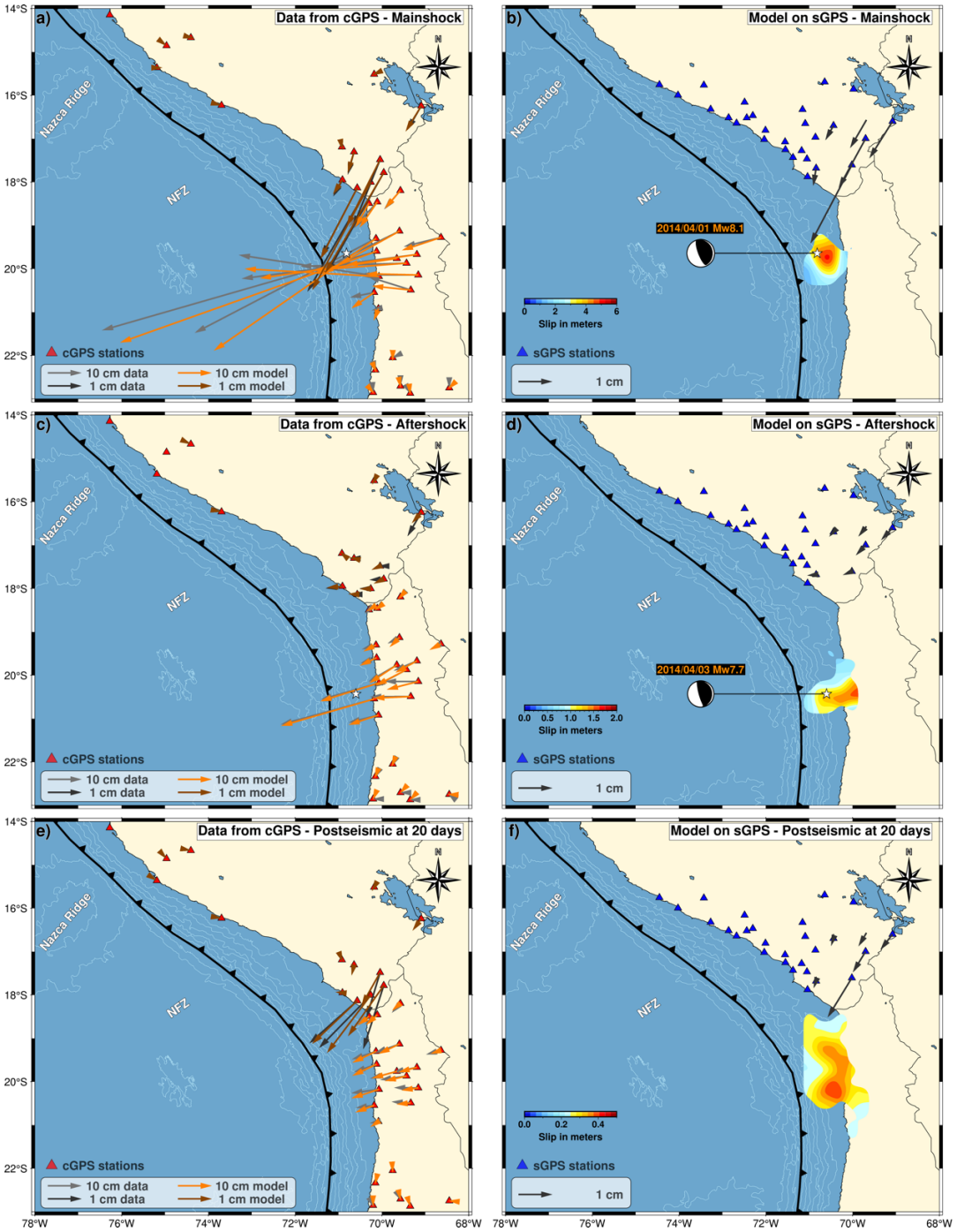

Figure S2: *Top:* Predicted coseismic displacements (right) associated with the M_w=8.1 2014 Iquique earthquake mainshock at the survey GNSS sites. These displacements were estimated from our inversion of co-seismic displacements measured with our trajectory model at 37 continuous GNSS sites in South Peru and Chile (left). Our associated co-seismic slip model on the subduction interface is depicted by the color scale. Slip contours are reported every 1 m. Focal mechanism is from the Global CMT catalog. *Middle:* Same, but for the M_w=7.7 2014 Iquique earthquake aftershock. *Bottom:* Same, but for the postseismic displacements at 20 days after the M_w=8.1 Iquique earthquake.

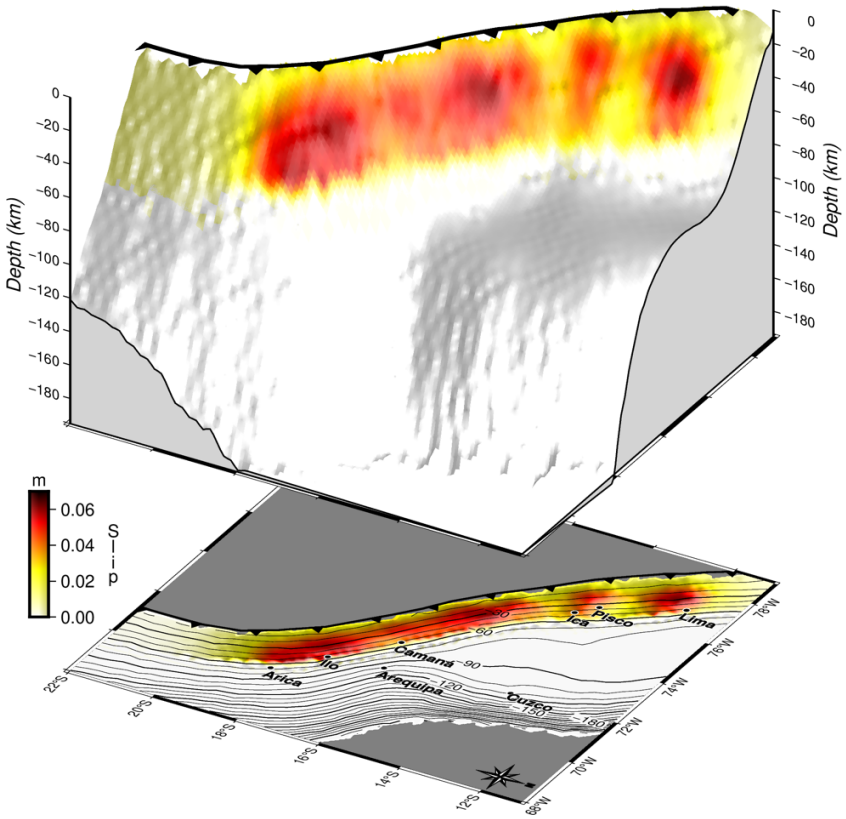

Figure S3: Interseismic slip distribution on the 3D slab model, based on Slab2 contours (Hayes et al., 2018). The model displayed here has been obtained with data in the SSA frame, and a spatial correlation length λ=30km. Slab contours are reported every 10 km.

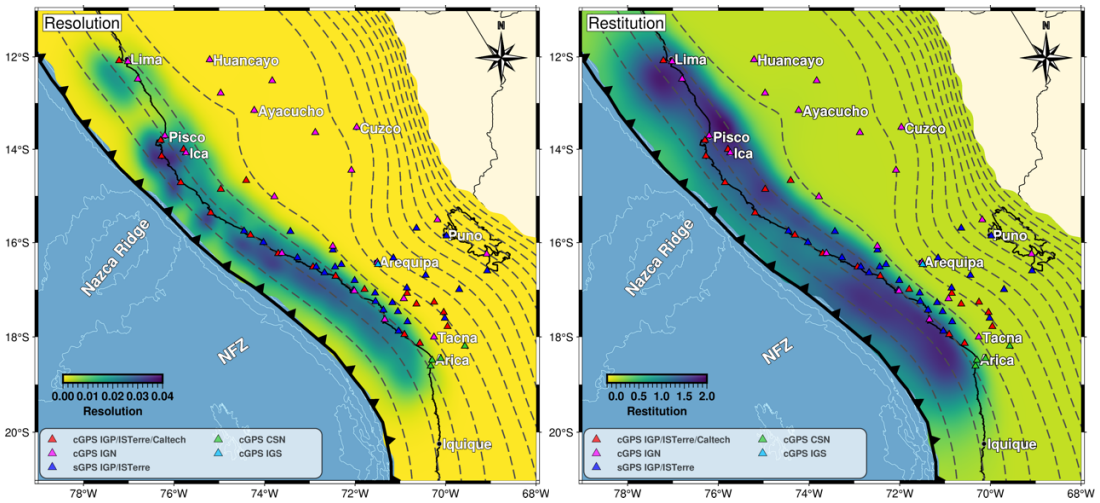

Figure S4: Diagonal values of the resolution matrix R (left) and restitution (right) on the slab, for a correlation length λ of 30 km. Whereas the diagonal elements of R inform us about how much the slip of a specific patch is accurately mapped on this patch by the program, the restitution informs us if this slip has been correctly projected onto other patches. Overall, we can notice that our diagonal values of R are low because we have defined a high number of small patches on our slab (6,700) for a relatively low amount of GNSS stations (73), in order not to impose a strong constraint on the slip locations. The diagonal values are higher where the density of station is high, indicating a better resolution, and are close to zero above 60 km depth because we confine the slip in the first 60 km depth of our model. The same goes for the restitution, except that the distribution is smoother. We can observe distinctly an edge effect near the 60 km iso-depth where the patches have a higher restitution because of the slip confinement, since the displacements on the stations more inland are only accommodated by these deep patches.

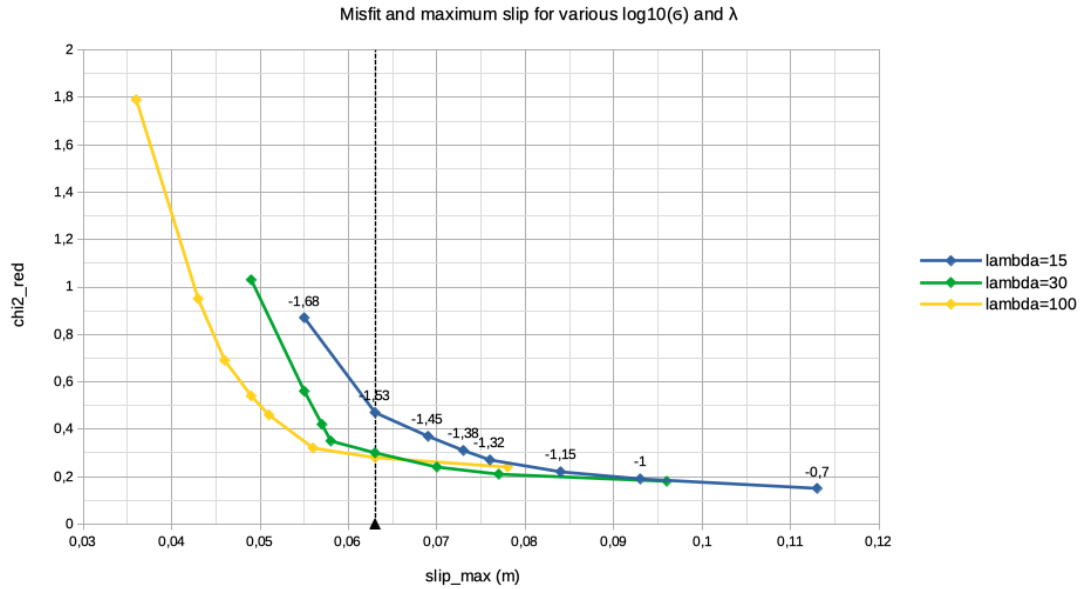

Figure S5: Variations of damping factor σ_m for various correlation lengths λ, we expressed the associated misfit (chi2_red) and maximum slip on the fault (slip_max), for data in the SSA frame. The vertical black line indicates the Nazca/SSA plate convergence velocity of 63 mm/yr. We retained the parameters for which the black line crosses the L-curve at its apex, corresponding to λ = 30 km and $\log_{10}(\sigma_m)$ = -1.32.

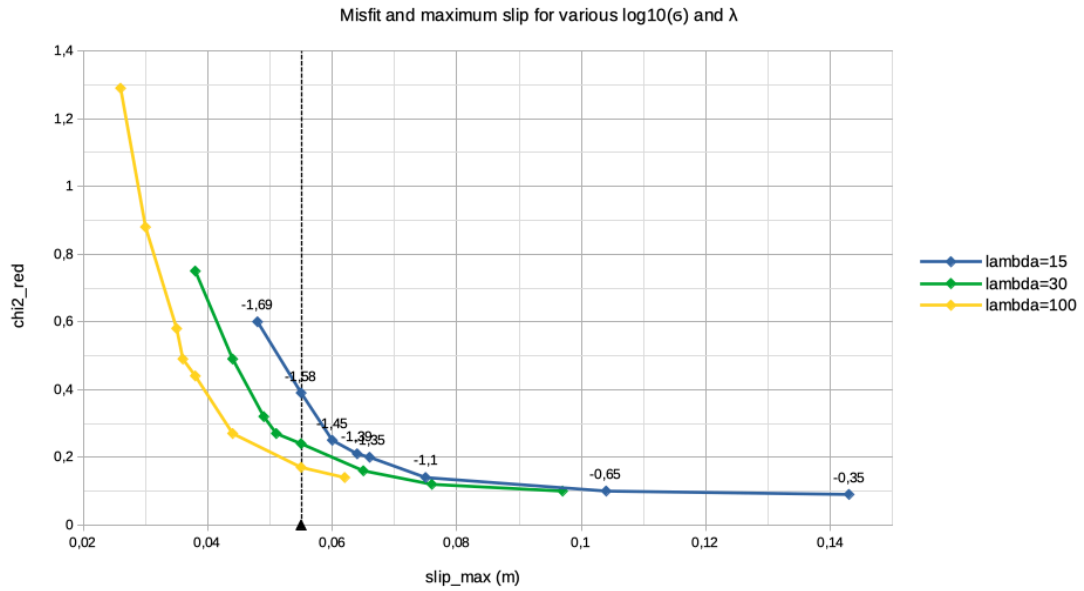

Figure S6: Variations of damping factor σ_m for various correlation lengths λ, we expressed the associated misfit (chi2_red) and maximum slip on the fault (slip_max), for data in the PS frame. The vertical black line indicates the Nazca/Sliver plate convergence velocity of 55 mm/yr. We retained the parameters for which the black line crosses the L-curve at its apex, corresponding to λ = 30 km and $\log_{10}(\sigma_m)$ = -1.35.

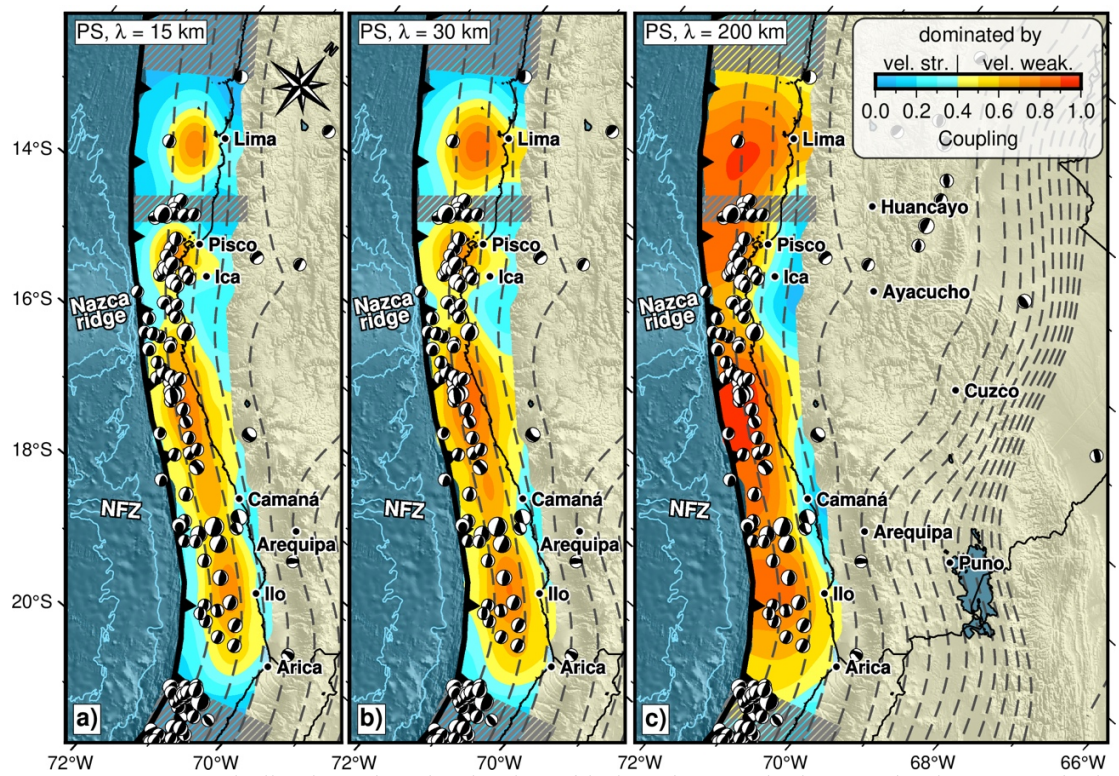

Figure S7: Map indicating the dominating friction law, velocity weakening or velocity strengthening, based on the interseismic coupling distribution for a model in the Peruvian Sliver frame and various λ values (15, 30, and 200 km). We consider areas with coupling below 0.4 to be in the velocity strengthening regime, while areas with coupling above 0.4 are considered in the velocity weakening regime. Velocity weakening areas should be more conducive to host seismic events. Seismicity from the gCMT catalog is plotted on top, cherry-picking thrusts events with Mw>5.5 and up to 70 km depth. We can observe a convincing overlap between the seismicity and the velocity weakening domain.

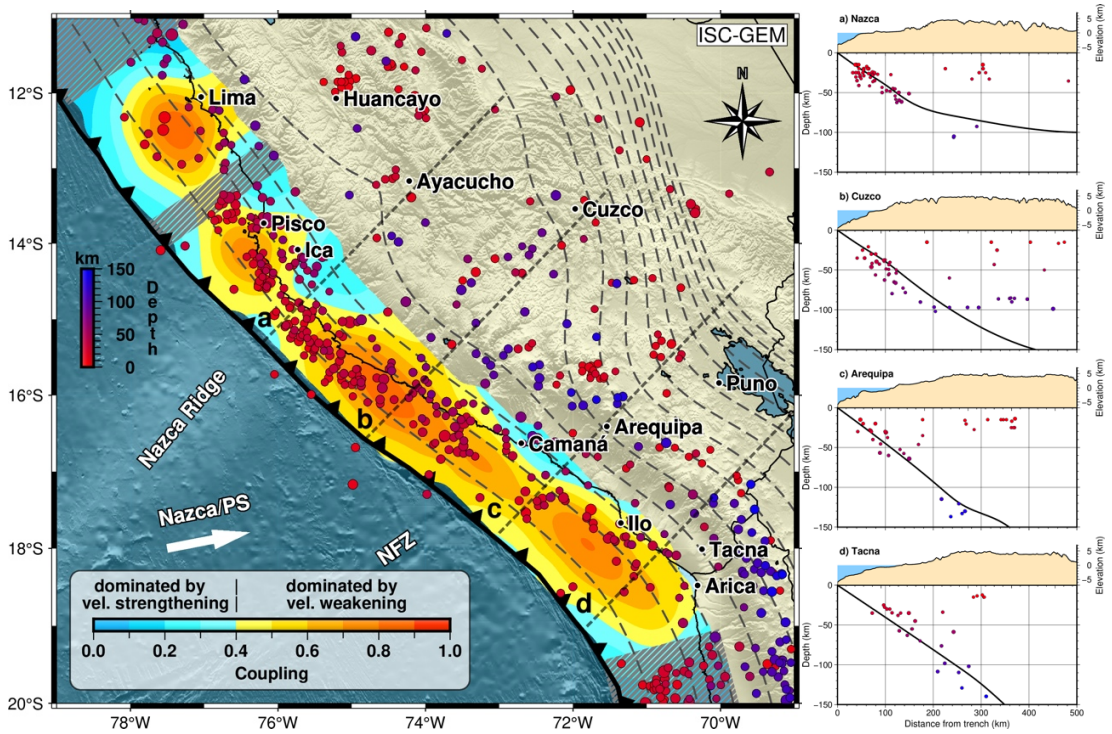

Figure S8: Cartography of the seismicity from the ISC-GEM catalog, for events with Mw>5 and and up to 150-km depth. Events are color-coded according to their depth and displayed with a radius proportional to their magnitude. The friction-law distribution is plotted as background (cf Figure S7). On the right panel are displayed four cross-sections, displaying the seismicity on top of the slab contours from Slab2 (Hayes et al. 2018) and the topography.

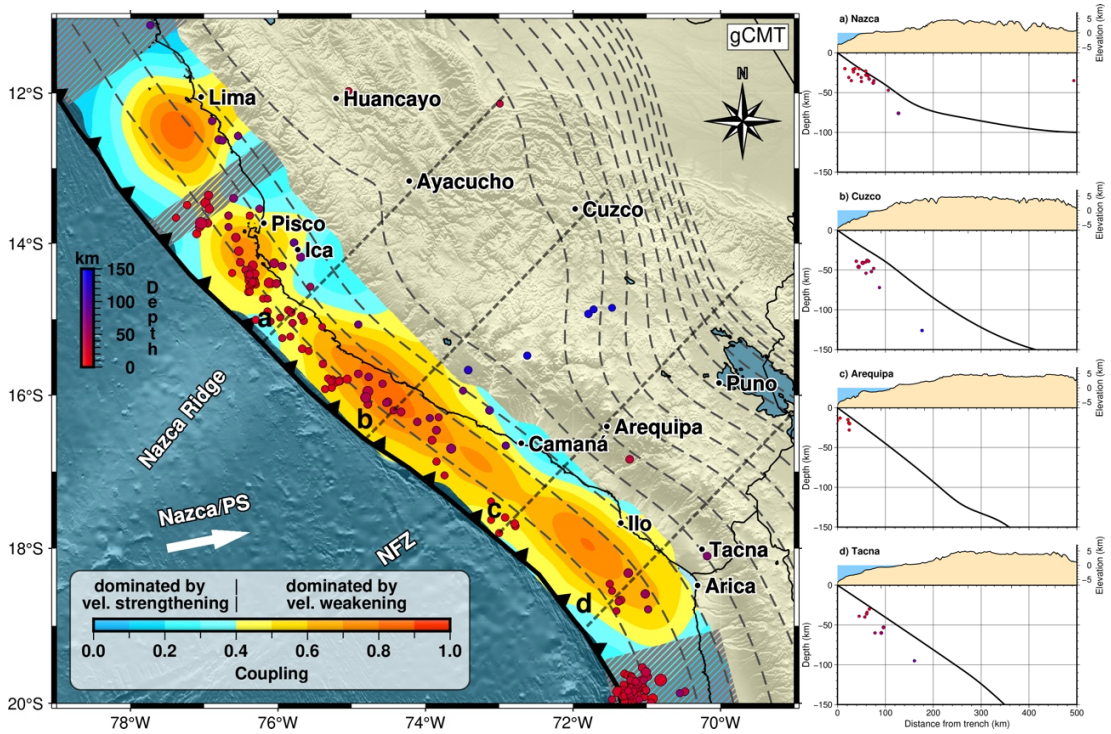

Figure S9: Cartography of the seismicity from the gCMT catalog, for events with Mw>5 and and up to 150-km depth. Events are color-coded according to their depth and displayed with a radius proportional to their magnitude. The friction-law distribution is plotted as background (cf Figure S7). On the right panel are displayed four cross-sections, displaying the seismicity on top of the slab contours from Slab2 (Hayes et al. 2018) and the topography.

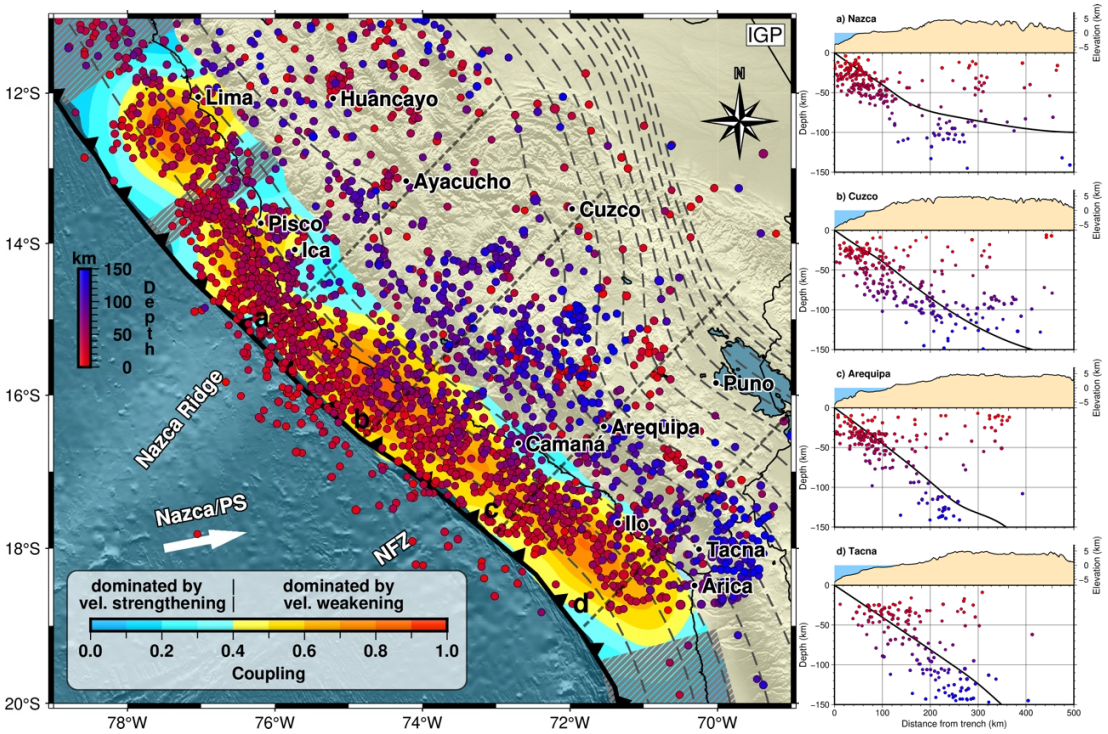

Figure S10: Cartography of the seismicity from the IGP catalog, for events with M>5 and and up to 150-km depth. Events are color-coded according to their depth and displayed with a radius proportional to their magnitude. The friction-law distribution is plotted as background (cf Figure S7). On the right panel are displayed four cross-sections, displaying the seismicity on top of the slab contours from Slab2 (Hayes et al. 2018) and the topography.

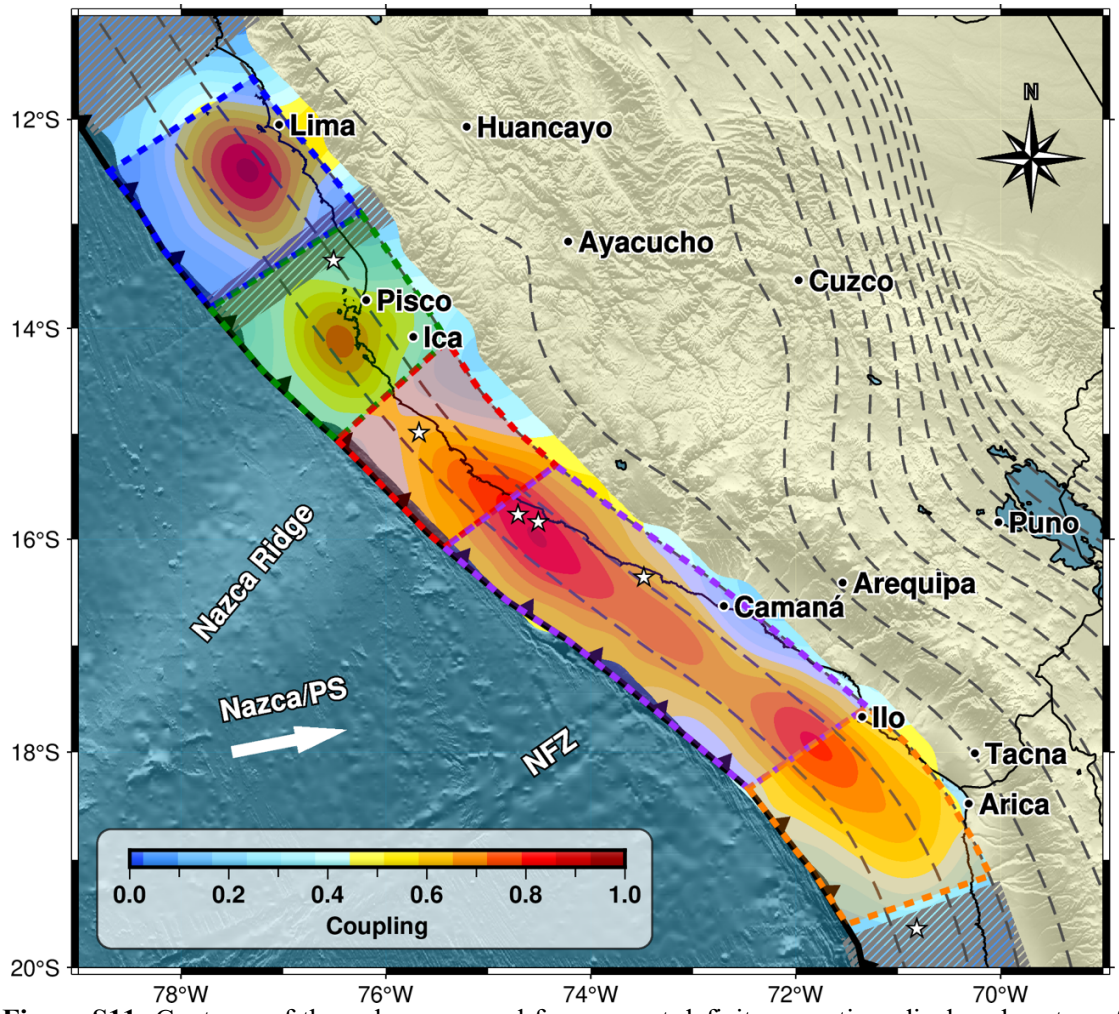

Figure S11: Contours of the polygones used for moment deficit computing, displayed on top of the interseismic coupling distribution (model in PS frame, with λ = 30 km). From top to bottom: the blue polygone is located on the segment where 1974 Mw=7.9 earthquake ruptured, the green one corresponds to the 2007 Mw=8.0 Pisco earthquake rupture, the red one corresponds to the 1942 Mw=8.2 rupture, the purple one corresponds to the 2001 Mw=8.4 Arequipa earthquake rupture, and the orange one corresponds to the 1833 Mw=7.7 Arica earthquake rupture.

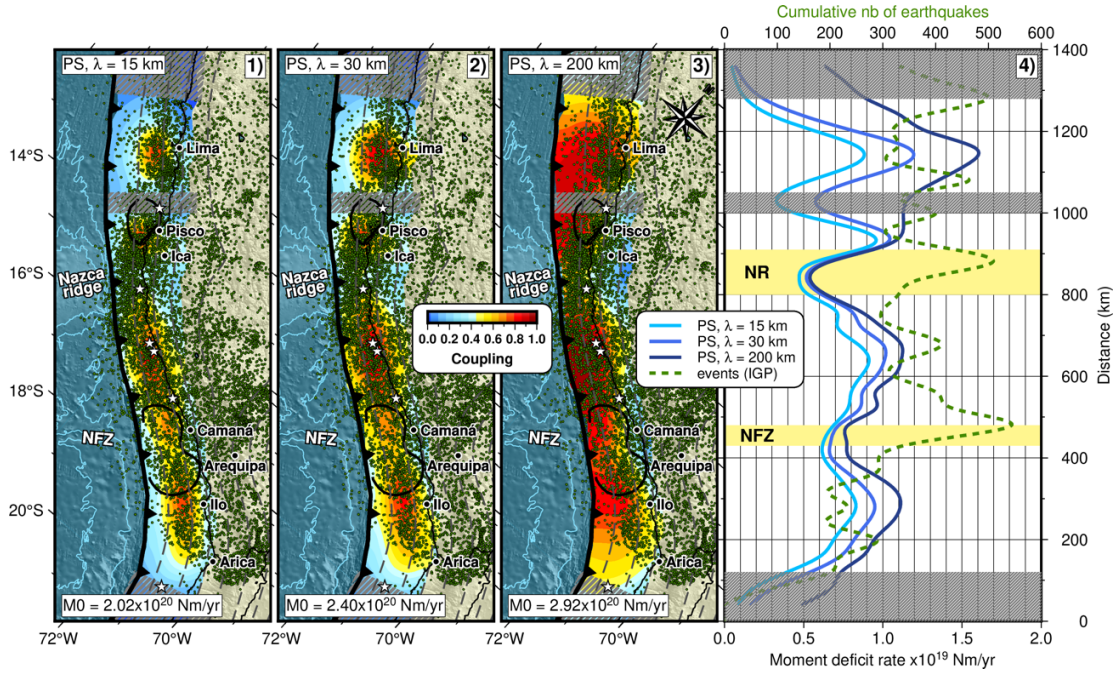

Figure S12: Interseismic coupling distribution from our inversion of interseismic velocities in the PS frame, with three different smoothing (λ of 15, 30 and 200 km). Slab contours (dashed lines) are reported every 20 km depth, from the Slab2 model (Hayes et al., 2018). The approximate rupture area of the Mw=8.4 2001 Arequipa has been estimated in this study, while the Mw=8.0 2007 Pisco earthquake rupture is reported from Chlieh et al. (2011). Seismic events from the IGP catalog (all magnitudes) are depicted by green dots. On the right panel are displayed the moment deficit rate by latitude for models with various smoothing (λ of 15, 30 and 200 km), computed over 15-km wide segments. Patches with gray hachure pattern depict areas that are not well resolved by the model. Cumulative seismicity from the IGP catalog is depicted by the green dashed line.

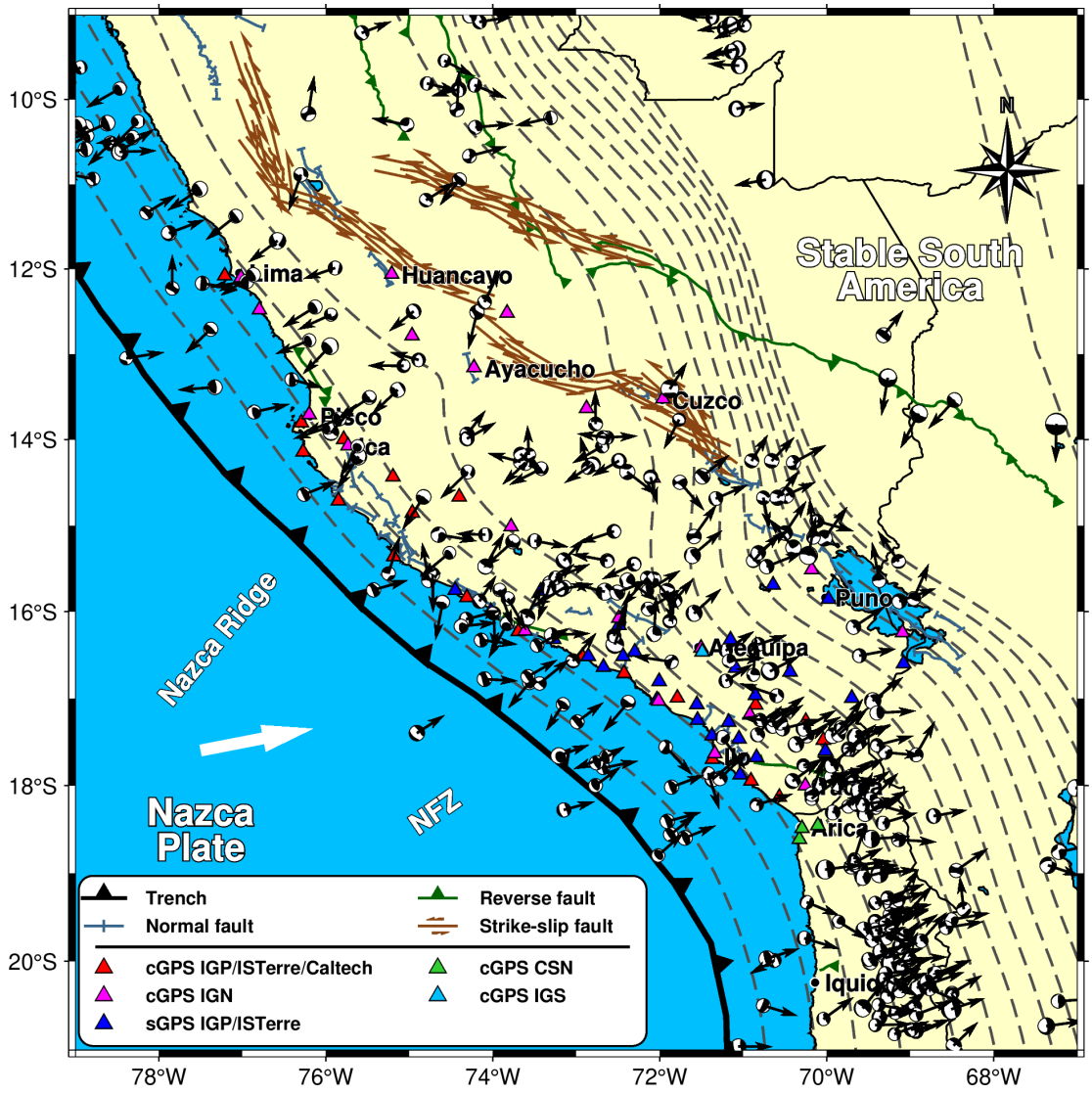

Figure S13: Map showing seismicity from the gCMT with their associated slip vector, cherry-picking events deeper than 40 km in order to keep essentially inter-slab events. Major faults from Veloza et al. (2011) are depicted by blue (normal), green (reverse), and brown lines (strike-slip). Triangles show the location of GNSS stations used in this study, and are color coded according to their type (cGPS or sGPS) and their operator. We observe that our GNSS network seems to belong to the same tectonic block.

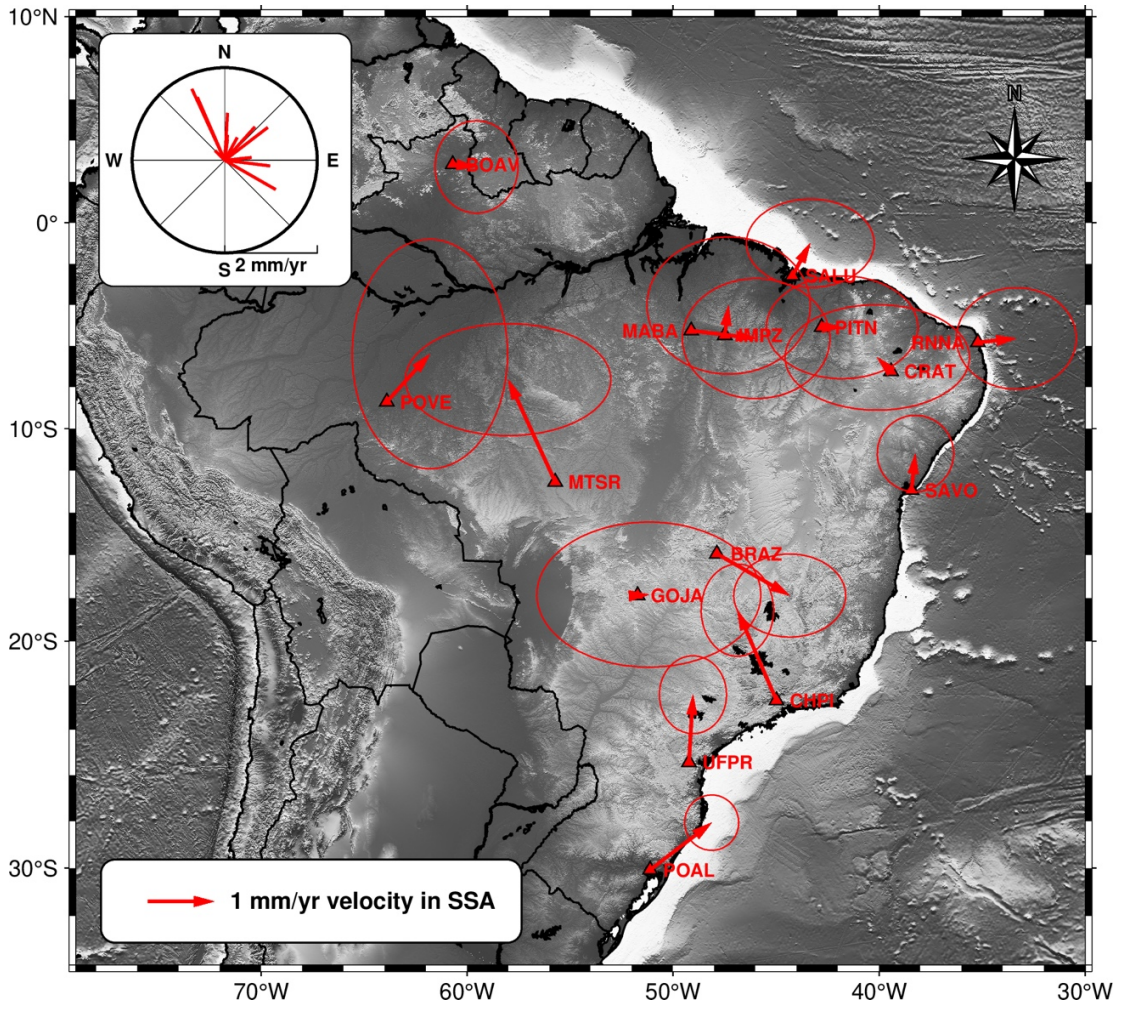

Figure S14: Various GNSS sites in Brazil, with their velocity expressed in the Stable South America frame. Ellipses indicate their uncertainties computed by MIDAS (Blewitt et al., 2016). Residual velocities are between 0.3 and 1.7 mm/yr and distributed in various directions, indicating that our reference frame is stable.

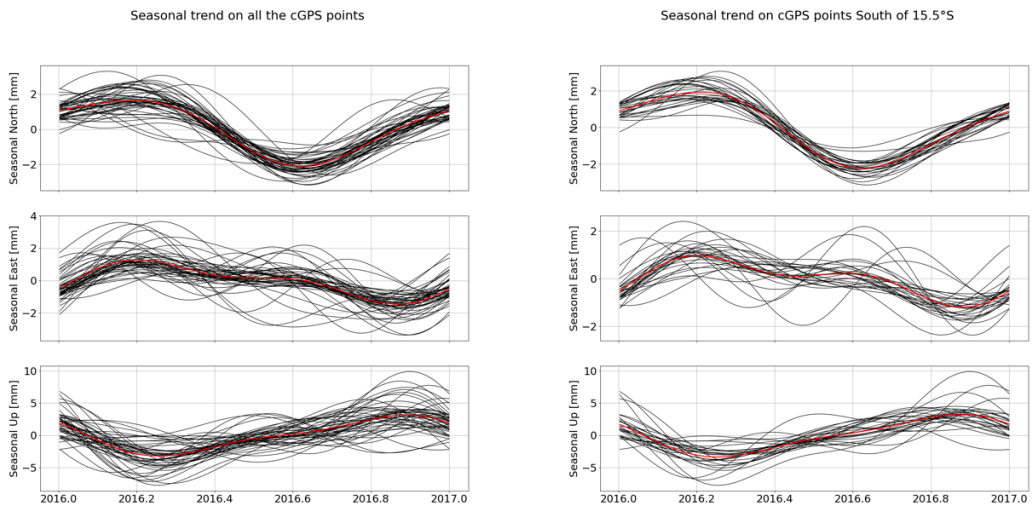

Figure S15: Seasonal trend on the N,E,U components extracted by the ITSA trajectory model on every cGPS stations (left) or restrained to the stations South of 15.5°S (right). The latter being more representative of the area where the sGPS points are located. In red is displayed the average trend.

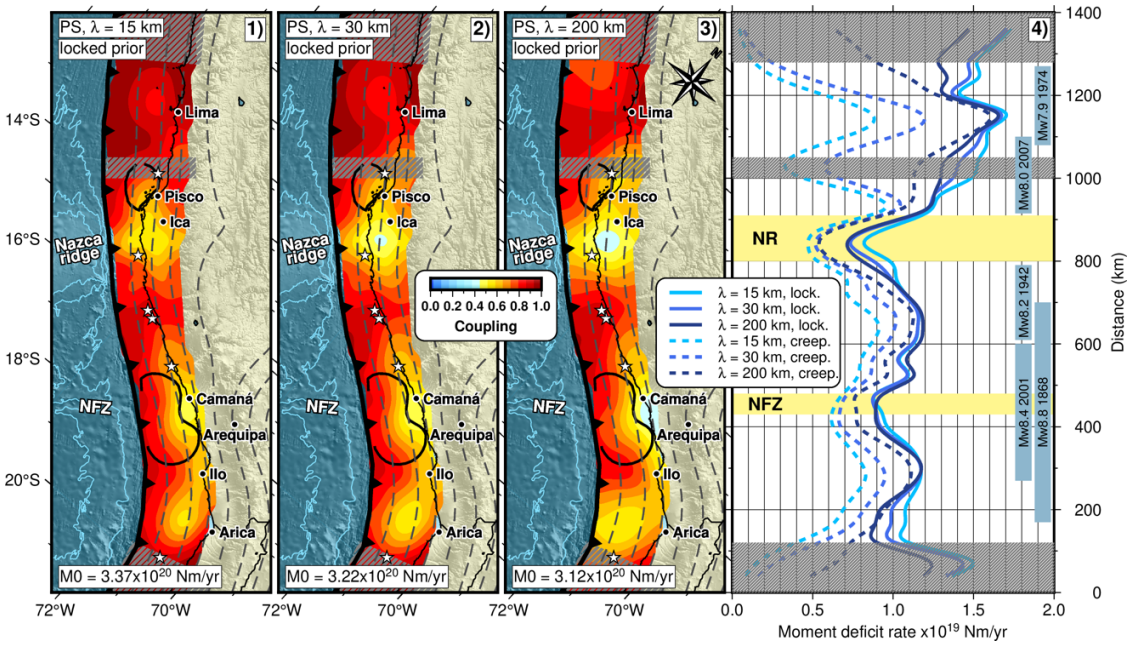

Figure S16: Interseismic coupling distribution from our inversion of interseismic velocities in the PS frame, with three different smoothing (λ of 15, 30 and 200 km) and a locked slip prior. Slab contours (dashed lines) are reported every 20-km depth, from the Slab2 model (Hayes et al. 2018). The interseismic coupling is highly heterogeneous reflecting strong variations of the frictional properties of the slab interface. Thus, there are four highly-coupled areas: a very-highly coupled area close to Lima, a less highly-coupled area near Ica, a large band of high-coupling between the Nazca Ridge and the Nazca Fracture Zone (NFZ), and a highly-coupled area between the NFZ and the Arica bend. Discontinuities can be observed where the Nazca Ridge and the NFZ are subducting below the South America plate. The approximate rupture area of the Mw=8.4 2001 Arequipa has been estimated in this study, while the Mw=8.0 2007 Pisco earthquake rupture is reported from Chlieh et al. (2011). On the right panel are displayed the moment deficit rate by latitude for models with a creeping or locked slip prior, and with various smoothing (λ of 15, 30 and 200 km), computed over 10-km wide segments. Patches with gray hachure pattern depict areas that are not well resolved by the model. Rupture extents from major seismic events are reported as blue segments.

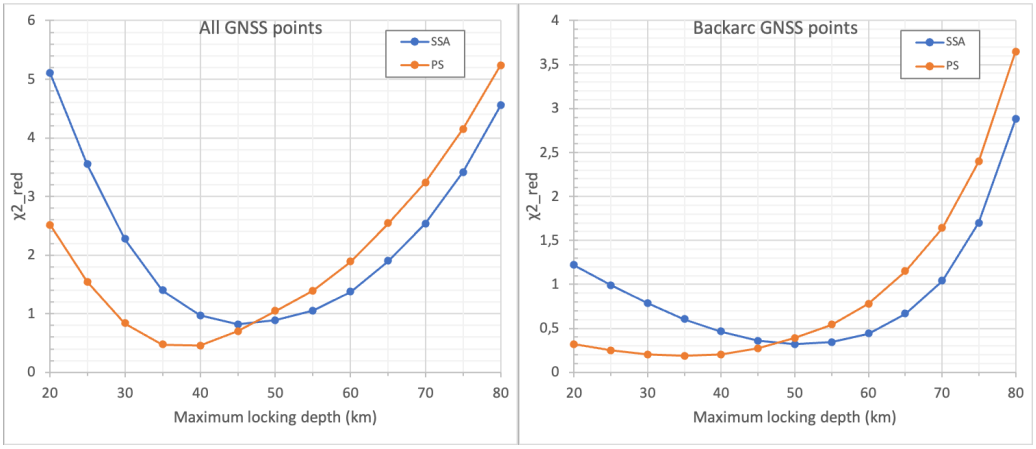

Figure S17: Evolution of the reduced χ^2 in function of the maximum locking depth, for GNSS data in both SSA (blue curve) and PS (orange curve) frames, including all the GNSS points (left) or only the backarc points (right) indicated on Figure 7. We consider a direct model with uniform locking from the trench to the specified maximum locking depth. We observe on both cases that the minimum value of χ^2 is reduced when considering the PS frame relative to the SSA frame: from 0.82 to 0.45 with all the GNSS points, and from 0.32 to 0.18 with the backarc points only. Furthermore, the maximum locking depth corresponding to this minimum is also reduced when considering the PS frame: from 46 to 38 km with all the GNSS points, and from 52 to 35 km with the backarc points only. This behavior is very similar to the one observed by Li et al. (2015) in Northern Chile when benchmarking a viscoelastic model against a purely elastic model, with varied uniform locking depth extending from the trench: when considering a viscoelastic model, both the fit to the data and the maximum locking depth are decreased. Subsequently, applying the PS solid block motion is similar in some way as adding a viscous behavior to the model, at least when considering the effects on the fit to the data and the maximum locking depth.

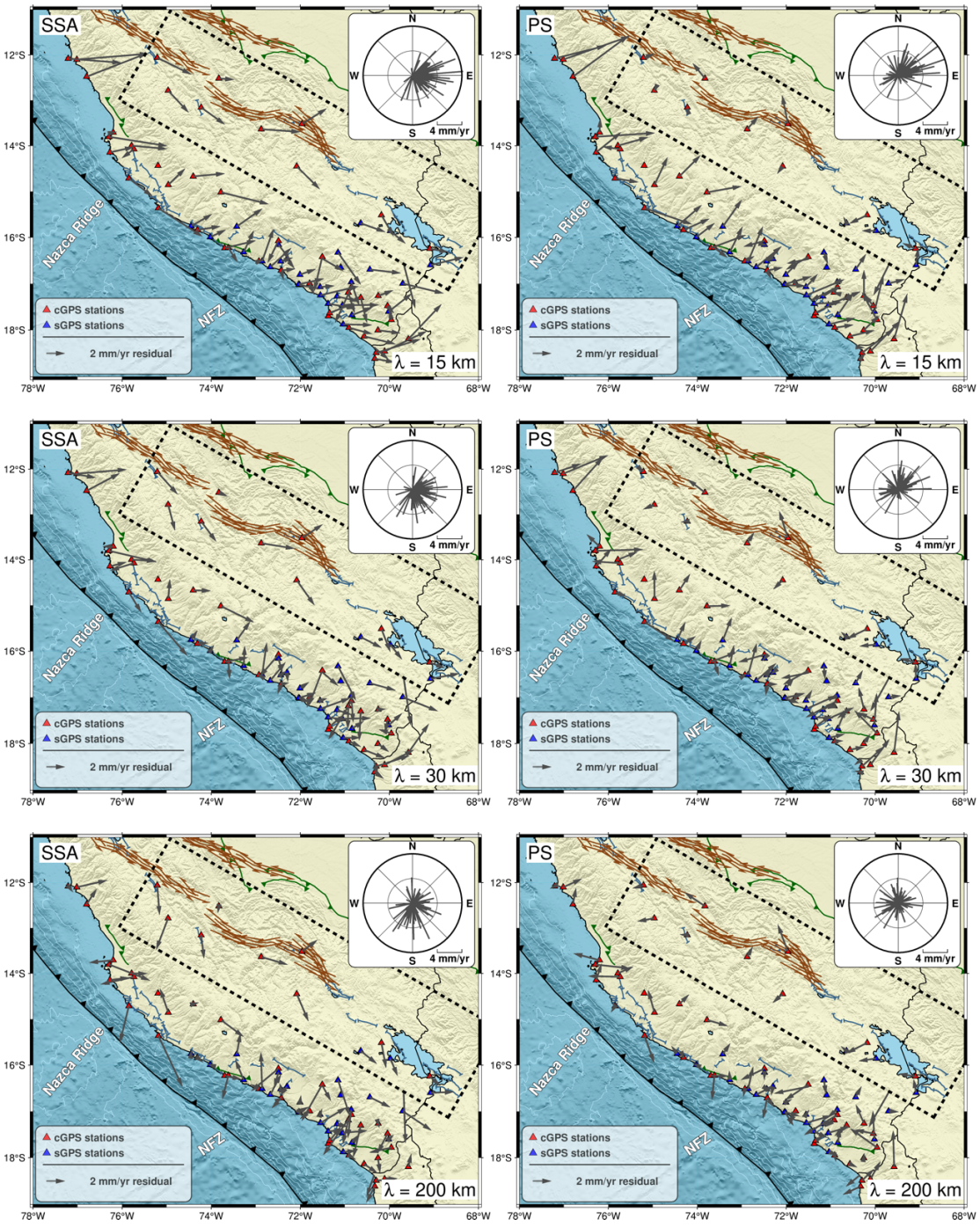

Figure S18: Residuals from our inversions using GNSS data in the Stable South America frame (left) and in the Peruvian Sliver frame (right), for various regularization lengths λ = 15 km (top), 30 km (middle), and 200 km (bottom). Most of the residuals are below 4 mm/yr, although some have higher values. Survey GNSS points are in blue, while continuous GNSS stations are in red.

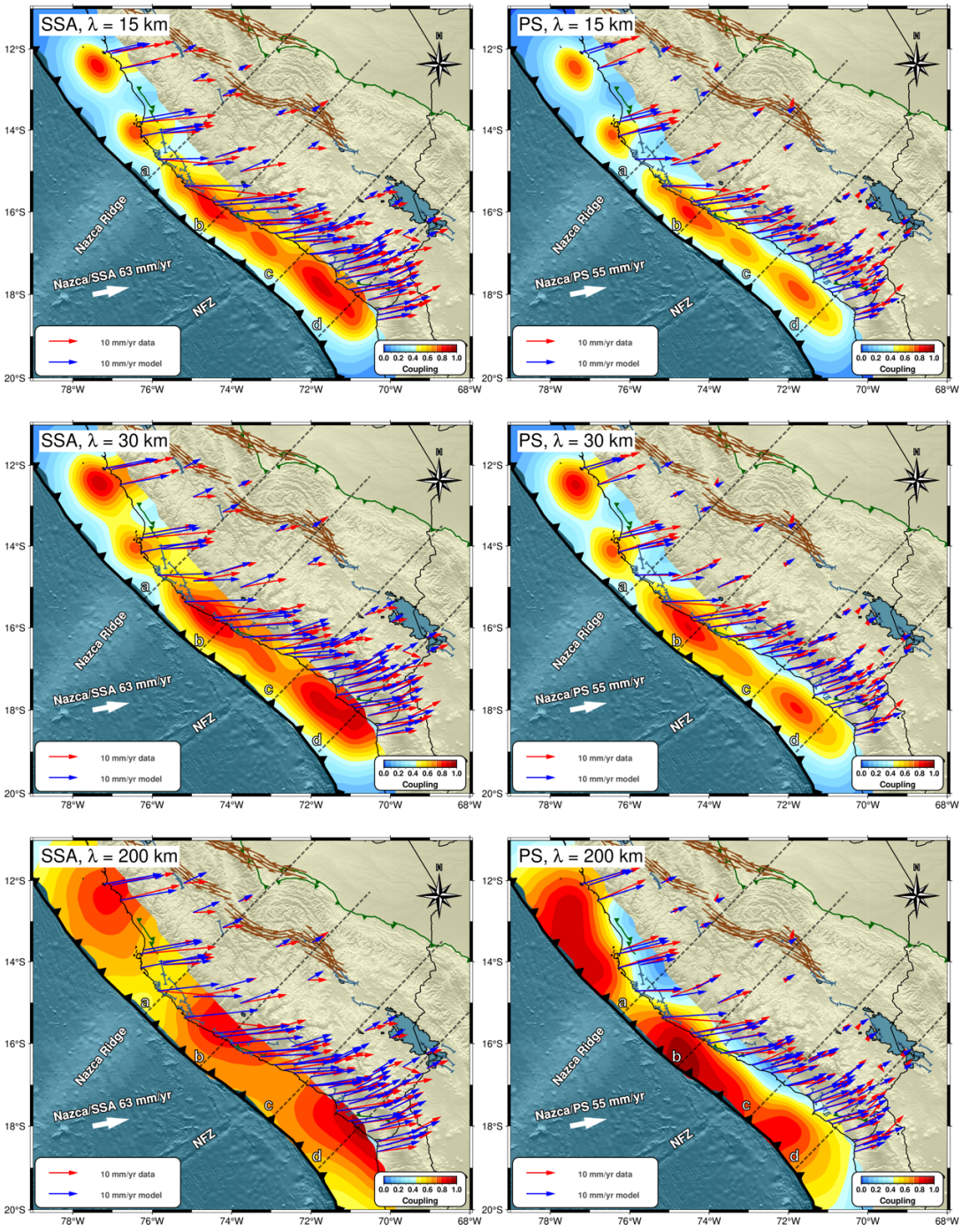

Figure S19: Interseismic coupling distributions for models in the SSA (left) and PS (right) reference frames, with various regularization lengths: 15 km (top), 30 km (middle), and 200 km (bottom). The measured interseismic velocities at each GNSS sites are depicted by red vectors, while the modeled velocities are depicted by blue vectors. Cross-section profiles a, b, c, d are reported on Figures 5, 6, and 9. Major faults are from Veloza et al. (2011).

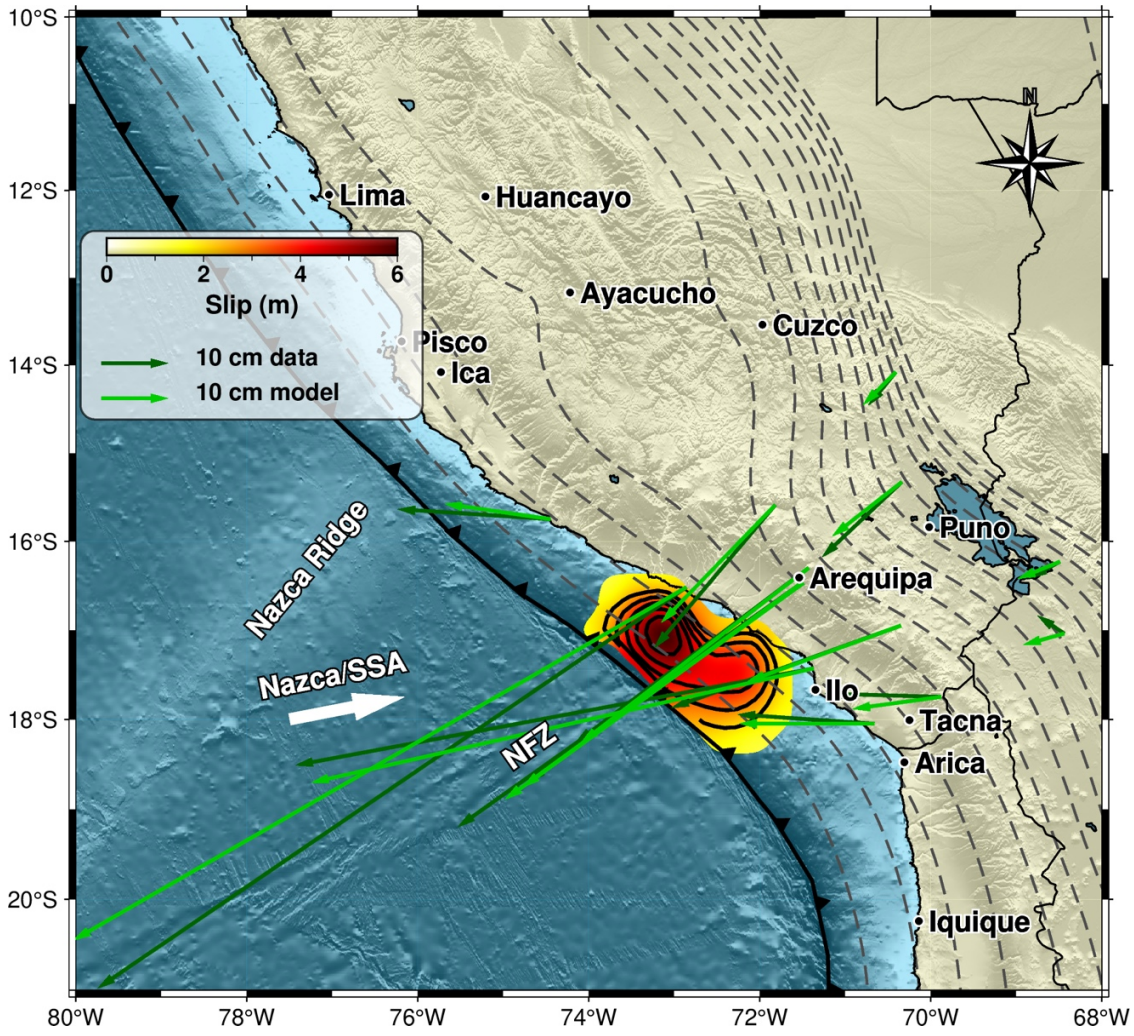

Figure S20: Coseismic slip distribution of the 2001 Mw=8.4 Arequipa earthquake, modelled in this study from the GNSS measurement of Pritchard et al. (2007). The inversion has been carried out in an elastic half-space, using the Tarantola & Valette method described in Radiguet et al. (2011). We retained a regularization length $\boldsymbol{\lambda}$ =10 km and a damping parameter $\boldsymbol{\sigma_m(k)} = 10^{-1.2}$. The slip contours are reported every meter. The GNSS-measured displacements from Pritchard et al. (2007) are depicted by dark green vectors, and the modeled displacements by bright green vectors.

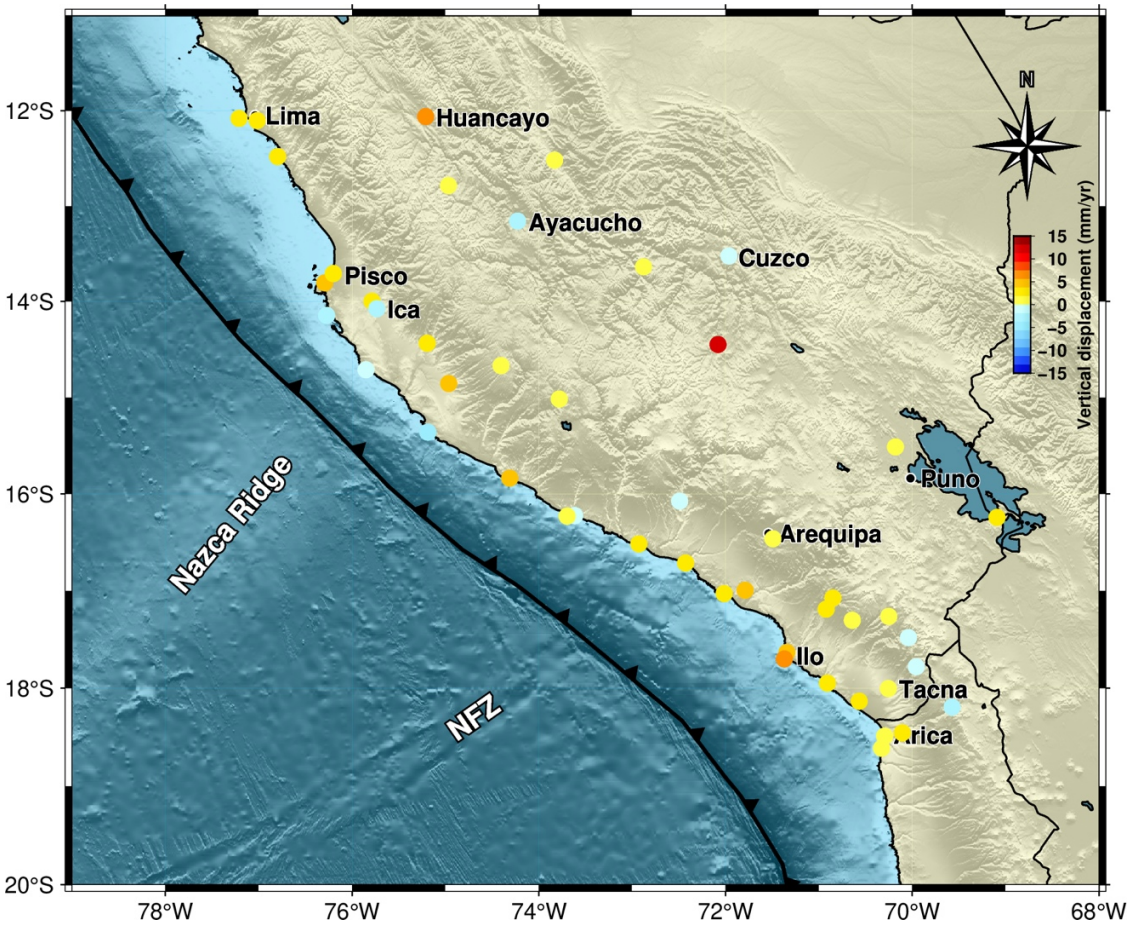

Figure S21: Observed vertical interseismic velocities at permanents GNSS sites (mm/yr). Most sites appear to uplift during the interseismic period. The distribution is quite heterogeneous and we chose not to take the vertical displacement rates into account in the modelling so far.

Station	Lon.	Lat.	Mainshock		Aftershock		Postseismic	
			East	North	East	North	East	North
AEDA	-70.178	-20.546	-0.072	-0.015	-0.277	-0.076	-0.055	-0.007
ATJN	-70.137	-19.301	-0.539	-0.281	-0.041	-0.013	-0.071	-0.024
CBAA	-68.448	-22.746	0	-0.001	-0.004	0.003	0	0
CGTC	-70.069	-20.177	-0.416	0.064	-0.173	-0.049	-0.082	-0.011
CHM2	-69.194	-19.669	-0.231	-0.031	-0.068	-0.029	-0.072	-0.015
COLC	-68.639	-19.276	-0.110	-0.027	-0.029	-0.013	-0.044	-0.012
CRSC	-70.08	-20.918	-0.020	-0.005	-0.088	-0.022	-0.025	-0.005
MNMI	-69.596	-19.131	-0.254	-0.125	-0.034	-0.017	-0.073	-0.026
PB03	-69.752	-22.049	-0.002	-0.001	-0.003	-0.006	0	0
PB04	-70.150	-22.335	0.001	-0.004	-0.002	-0.003	0	0
PB05	-70.203	-22.853	0	-0.001	0	0	0.003	-0.005
PB06	-69.572	-22.706	0	0	-0.001	0	0.002	-0.004
PB08	-69.161	-20.143	-0.178	0	-0.099	0	-0.071	0.001
PB11	-69.656	-19.761	-0.461	-0.060	-0.083	-0.049	-0.079	-0.021
PCCL	-70.107	-18.458	-0.071	-0.078	-0.007	-0.007	-0.036	-0.027
PCHA	-69.432	-19.869	-0.316	-0.009	-0.095	-0.051	-0.078	-0.011
PICC	-69.335	-20.490	-0.126	0.040	-0.120	-0.001	-0.057	0.003
PSGA	-70.123	-19.597	-0.816	-0.235	-0.047	-0.016	-0.067	-0.023
PTRE	-69.574	-18.194	-0.048	-0.056	-0.005	-0.006	-0.025	-0.028
SRGD	-69.348	-22.871	0.001	-0.002	-0.002	0	0	0
UTAR	-70.297	-18.491	-0.060	-0.070	-0.012	-0.012	-0.034	-0.024
ATIC	-73.697	-16.231	0	0	0	0	0	0
GLRV	-74.404	-14.670	0	0	0	0	0	0
LAGU	-76.273	-14.145	0	0	0	0	0	0
LYAR	-70.569	-18.134	-0.011	-0.020	-0.002	0	-0.014	-0.013
NZCA	-74.964	-14.856	0	0	0	0	0	0
PALC	-69.957	-17.781	-0.017	-0.030	-0.004	0	-0.006	-0.019
PMCA	-70.909	-17.949	-0.003	-0.005	-0.005	-0.001	0	0
SJUA	-75.188	-15.363	0	0	0	0	0	0
TQPL	-70.643	-17.304	-0.002	-0.007	-0.001	0	0	0
TRTA	-70.041	-17.482	-0.008	-0.020	0	0	-0.004	-0.013
LI01	-77.017	-12.103	0	0	0	0	0	0
LI04	-76.797	-12.482	0	0	0	0	0	0
MQ01	-70.922	-17.191	0	0	0	0	0	0
PU02	-70.179	-15.514	0	0	0	0	0	0
PU03	-69.093	-16.245	-0.004	-0.007	-0.004	-0.007	0	0
TC01	-70.257	-18.004	-0.019	-0.033	-0.003	0	-0.015	-0.016

Table S2: Measured coseismic displacements (in meters) at continuous GNSS sites associated with the 2014 Mw=8.1 Iquique earthquake mainshock, the Mw=7.7 aftershock, and the postseismic displacement at 20 days.

Station	Lon.	Lat.	Mainshock		Aftershock		Postseismic	
			East	North	East	North	East	North
AMOQ	-71.548	-17.252	0.0039	0.0039	-0.0026	0.0002	0.0010	0.0016
ANTE	-71.052	-17.466	0.0013	0.0006	-0.0018	-0.0015	0.0005	0.0007
AQUC	-72.439	-16.518	0.0047	0.0017	0.0000	0.0007	0.0008	0.0004
BASU	-74.024	-15.996	0.0029	-0.0002	0.0006	-0.0002	0.0006	-0.0001
CALA	-73.272	-16.321	0.0032	0.0010	0.0006	0.0003	0.0006	0.0002
CAMI	-70.841	-17.679	-0.0009	-0.0052	-0.0026	-0.0002	-0.0007	-0.0021
CATA	-72.036	-17.017	0.0056	0.0029	-0.0009	0.0011	0.0012	0.0009
CERI	-70.644	-15.691	-0.0008	0.0001	-0.0003	-0.0001	-0.0003	-0.0007
CHIL	-70.439	-16.696	-0.0024	-0.0043	-0.0012	-0.0014	-0.0007	-0.0022
CLEM	-71.175	-17.275	0.0017	0.0022	-0.0016	-0.0003	0.0006	0.0009
COLL	-69.080	-16.600	-0.0069	-0.0109	-0.0034	-0.0036	-0.0036	-0.0046
COND	-69.681	-16.568	-0.0048	-0.0083	-0.0023	-0.0030	-0.0023	-0.0040
CRMA	-72.300	-16.467	0.0043	0.0015	-0.0004	0.0009	0.0006	0.0004
CRVL	-73.428	-15.763	0.0022	-0.0003	0.0003	0.0001	0.0003	0.0000
GORD	-72.675	-16.641	0.0051	0.0019	0.0006	0.0005	0.0010	0.0004
GUER	-72.009	-16.806	0.0048	0.0023	-0.0012	0.0013	0.0009	0.0007
JAGU	-72.857	-16.515	0.0046	0.0016	0.0007	0.0004	0.0009	0.0003
PARQ	-70.017	-17.606	-0.0123	-0.0233	-0.0026	-0.0010	-0.0072	-0.0117
POCO	-71.374	-17.432	0.0031	0.0044	-0.0023	-0.0018	0.0009	0.0023
PUNO	-69.980	-15.858	-0.0014	-0.0016	-0.0010	-0.0018	-0.0009	-0.0017
QUER	-72.490	-16.158	0.0037	0.0009	-0.0002	0.0007	0.0004	0.0003
SJUN	-70.856	-16.966	-0.0005	-0.0013	-0.0005	0.0006	0.0001	-0.0008
TACA	-71.038	-17.877	-0.0003	-0.0005	-0.0051	-0.0019	-0.0007	0.0035
TAMB	-71.557	-17.072	0.0035	0.0031	-0.0027	0.0015	0.0008	0.0011
TANC	-74.452	-15.754	0.0025	0.0010	0.0006	0.0003	0.0005	0.0002
TUPA	-69.700	-16.997	-0.0080	-0.0146	-0.0029	-0.0030	-0.0038	-0.0062
UBIN	-71.154	-16.327	-0.0001	0.0001	-0.0006	0.0016	0.0001	0.0000

Table S3: Estimated coseismic displacements (in meters) at survey GNSS sites, associated with the 2014 Mw=8.1 Iquique earthquake mainshock, the Mw=7.7 aftershock, and the postseismic displacement at 20 days.

Reference frame	λ (km)	$\log_{10}(\sigma_m)$	Moment (Nm/yr) Lima	Moment (Nm/yr) Pisco	Moment (Nm/yr) 1942	Moment (Nm/yr) Arequipa	Moment (Nm/yr) Ilo-Arica
SSA	15	-1.53	4.08×10^{19}	3.76×10^{19}	3.54×10^{19}	1.09×10^{20}	5.29×10^{19}
SSA	30	-1.32	5.42×10^{19}	4.43×10^{19}	3.95×10^{19}	1.17×10^{20}	6.07×10^{19}
SSA	100	-1.00	6.50×10^{19}	5.18×10^{19}	4.18×10^{19}	1.22×10^{20}	6.71×10^{19}
SSA	200	-0.70	6.83×10^{19}	5.28×10^{19}	4.28×10^{19}	1.24×10^{20}	6.97×10^{19}
PS	15	-1.58	3.05×10^{19}	2.90×10^{19}	2.57×10^{19}	8.10×10^{19}	3.61×10^{19}
PS	30	-1.35	4.31×10^{19}	3.53×10^{19}	2.95×10^{19}	8.92×10^{19}	4.26×10^{19}
PS	100	-0.65	6.11×10^{19}	4.46×10^{19}	3.21×10^{19}	9.89×10^{19}	4.90×10^{19}
PS	200	-0.35	6.31×10^{19}	4.67×10^{19}	3.26×10^{19}	1.00×10^{20}	4.95×10^{20}

Table S4: Moment deficit over the five segments defined on Figure S12, for various models. Each line corresponds to a specific smoothing (λ and σ_m), combined with a given reference frame (SSA or PS).

Chapter 5

Viscoelastic Relaxation Following the 2001 Mw8.4 Arequipa Earthquake and Its Impact on the Interseismic Coupling of the South Peru Megathrust

This second study has been published in June 2025 in *Geophysical Research Letters*. It has two main purposes: modeling the postseismic viscoelastic relaxation associated with the 2001 Mw8.4 Arequipa earthquake in order to correct the interseismic coupling distribution, and to provide some insight on the rheology of the South Peru subduction zone. It starts from the observation made in Lovery et al., 2024 that the time series of the AREQ GNSS station installed in 1993 in Arequipa city is still affected by some postseismic displacements following the 2001 Mw8.4 Arequipa earthquake. We expected this trend to affect GNSS sites within a larger area onshore of the 2001 rupture, however most of the other GNSS sites were installed more recently (between 2007 and 2015 for most of the sites) which does not allow to estimate the postseismic displacements with a trajectory model like we did for the 2014 Mw8.1 Iquique earthquake.

In order to model the viscoelastic relaxation of the asthenosphere following the earthquake, which is the main process explaining long-term postseismic displacements (more than a decade), we developed a 3-D Finite Element Method (FEM) model of the subduction zone. The meshing was performed using the commercial software CUBIT from Coreform, and the simulations were run with the open-source software PyLith (B. T. Aagaard et al., 2013). The model incorporates a viscoelastic asthenosphere below an elastic lithosphere, with an elastic cold nose. It was constrained by the 30-year time series of the AREQ continuous GNSS station and 8 survey GNSS sites measured since 1994. We retained a Burgers rheology in the asthenosphere to fit the data with a Maxwell viscosity $\eta_M = 9 \times 10^{18}$ Pa·s and a Kelvin viscosity $\eta_K = 5 \times 10^{18}$ Pa·s.

The interseismic velocities from Lovery et al., 2024 have been corrected from the modeled postseismic contribution, and viscoelastic Green's functions have been computed using the estimated rheology. It allowed to release a viscoelastic interseismic coupling model for South Peru, accounting for the postseismic displacements following the 2001 Mw8.4 Arequipa earthquake, raising by 9% the estimated moment deficit rate (which is still within the uncertainties from Lovery et al., 2024).

5.1 Manuscript

Viscoelastic Relaxation Following the 2001 Mw8.4 Arequipa Earthquake and its Impact on the Interseismic Coupling of the South Peru Megathrust

B. Lovery[1], M. Radiguet[1], M. Chlieh[1], E. Norabuena[2], J.C. Villegas-Lanza[2], J. Cresseaux[1], T. Ragon[1], A. Tsapong-Tsague[1], H. Tavera[2], and A. Socquet[1]

[1]Univ. Grenoble Alpes, Univ. Savoie Mont Blanc, CNRS, IRD, Univ. Gustave Eiffel, ISTerre, 38000 Grenoble, France

[2]Instituto Geofísico del Perú, Lima, Peru

Corresponding author: Bertrand Lovery (bertrand.lovery@univ-grenoble-alpes.fr)

ORCID: 0000-0002-3671-0608

Key Points:

- The postseismic phase following the 2001 Mw8.4 Arequipa megathrust earthquake is still ongoing after two decades
- The surface displacements associated with viscoelastic relaxation can be modelled using a bi-viscous Burgers rheology
- Accounting for postseismic processes increases the moment deficit rate by 9% on the South Peru segment

Abstract

Postseismic displacements associated with the 2001 Mw8.4 Arequipa earthquake have been observed on a continuous GNSS timeseries in Arequipa for over two decades (~30 cm on horizontal components). Using Finite Element Method (FEM), we explore the rheological properties of the South Peru subduction zone to model this temporal evolution, and we quantify the effects of the postseismic processes on the interseismic coupling assessment with viscoelastic Green's functions. Using one continuous and eight survey GNSS timeseries as constraints, we found that a Burgers rheology in the asthenosphere (Maxwell viscosity $\eta_M = 9 \cdot 10^{18}$ Pa.s, Kelvin viscosity $\eta_K = 5 \cdot 10^{18}$ Pa.s) with an elastic cold-nose fits best the pattern. The postseismic processes affect the interseismic coupling distribution and moment deficit rate, raising their values by 9% over the South Peru segment and up to 24% in the vicinity of the 2001 Arequipa earthquake rupture. These values remain within the uncertainties from Lovery et al. (2024a).

Plain Language Summary

When a large earthquake happens on an ocean-continent subduction like the Peru-Chile margin, sudden slip on the plate interface generates an oceanward motion of the land on the overriding plate. It is followed by a slower transient deformation which can last several years to decades, referred as the postseismic phase of the seismic cycle. Then, the overriding plate motion resumes to its stable landward velocity, characteristic of the interseismic loading until the next large earthquake occurs. Monitoring displacements on the Earth surface using Global Navigation Satellite System, is a way to estimate the slip deficit accumulating during the interseismic period and hence the earthquake potential of a subduction segment. However, the observed velocities could represent a mix between interseismic loading and a long-lasting postseismic signal, affecting the estimation of slip deficit accumulated and earthquake potential. In this study we show that the postseismic signal following the 2001 Mw8.4 Arequipa earthquake is still ongoing two decades later. We also show that it can be modelled using a viscoelastic Finite Element Method model of the subduction. Using this model, we corrected the observed interseismic velocities over South Peru, leading to a 9% increase in the estimated energy accumulating on the subduction interface.

1 Introduction

Large earthquakes are followed by postseismic deformation signals of variable timescales. Postseismic displacements can be explained by poroelastic rebound (Peltzer et al., 1996) or afterslip (Marone et al., 1991) that can last months to years respectively. However, long-term postseismic signal may be better explained by viscoelastic relaxation of the asthenosphere, up to decades after the earthquake (Barbot et al., 2010; Hu et al., 2004; Klein et al., 2016; Li et al., 2018; Nur et al., 1974; Qiu et al., 2018; Sun et al., 2014; Wang et al., 2007; Wang et al., 2012). For instance, the 1960 Mw9.5 Valdivia earthquake was followed by viscoelastic relaxation that is expected to last for about 70 years (Hu et al., 2004; Wang et al., 2007). Wang et al. (2012) showed that viscoelastic relaxation is prevalent for earthquakes of Mw8+. Monitoring of the postseismic phase over several decades can therefore provide key information on the viscosity of the mantle at different characteristic timescales, allowing to discriminate between Maxwell fluid and more complex rheology involving transient viscosities (Boulze et al., 2022). Several studies showed that viscoelastic relaxation generates deformation at the continental scale (Boulze et al., 2022; Klein et al., 2016; Pollitz et al., 2006; Wang et al., 2012), making it a fundamental process to discriminate the slip on the slab interface from intracontinental deformation. Viscoelasticity has been a subject of growing interest over the last two decades allowing to link postseismic and interseismic displacements at various stages of the earthquake cycle. For instance, by revisiting the deformation on the Nankai subduction, Li & Chen (2024) showed the importance of accounting for viscoelastic relaxation to explain the surface displacements and model properly the interseismic loading. This has been shown to impact the estimated moment deficit and related seismic potential on the subduction zone (Pollitz, 2025), but as it depends on the rheology, it is important to assess this contribution with local observations for each region considered.

In Peru, the Mw8.4 Arequipa earthquake occurred in 2001. It was followed by a postseismic deformation that has been studied by Perfettini et al. (2005), Hergert & Heidbach (2006), and Sun et al. (2018), but on a limited time range of 2, 3.5, and 12 years after the earthquake respectively. With 23 years of postseismic recording since the earthquake we can now better assess the rheology over the South Peru megathrust.

South Peru has been the theater of several other large megathrust earthquakes in the last decades, including the 2007 Mw8.0 Pisco and the 1996 Mw7.7 earthquakes, and is also known to have

hosted larger events such as the 1868 Mw8.8 earthquake that ruptured the whole segment from the Nazca Ridge (NR) to the Arica bend (Dorbath et al., 1990). The megathrust is characterized by a heterogeneous coupling distribution, with a lower coupling where the NR and the Nazca Fracture Zone (NFZ) are subducting (Lovery et al., 2024a). The NR is known to behave as a strong barrier against seismic rupture propagation (Chlieh et al., 2011; Lovery et al., 2024a; Villegas-Lanza et al., 2016), while the NFZ has stalled the Arequipa earthquake rupture without stopping its propagation (Robinson et al., 2006). However, Lovery et al. (2024a) observed that postseismic deformation following the 2001 Arequipa earthquake is still ongoing and may impact the assessment of the secular surface deformation and of the interseismic coupling (ISC). The GNSS position timeseries of the station AREQ located in Arequipa city shows a horizontal velocity on the 2012-2023 period that is lowered by ~15% in the Stable South America (SSA) frame compared to its value prior to the Arequipa earthquake on the 1995-2001 period (Figure 1, bottom). It was the only continuously operating GNSS station (cGNSS) in South Peru at that time, but this velocity change may have affected the whole area around the 2001 rupture. In this study we focus on quantifying more accurately the postseismic processes (afterslip + viscoelastic relaxation) following the Arequipa earthquake, and how it affected the estimates of the ISC distribution and associated moment deficit rate in South Peru.

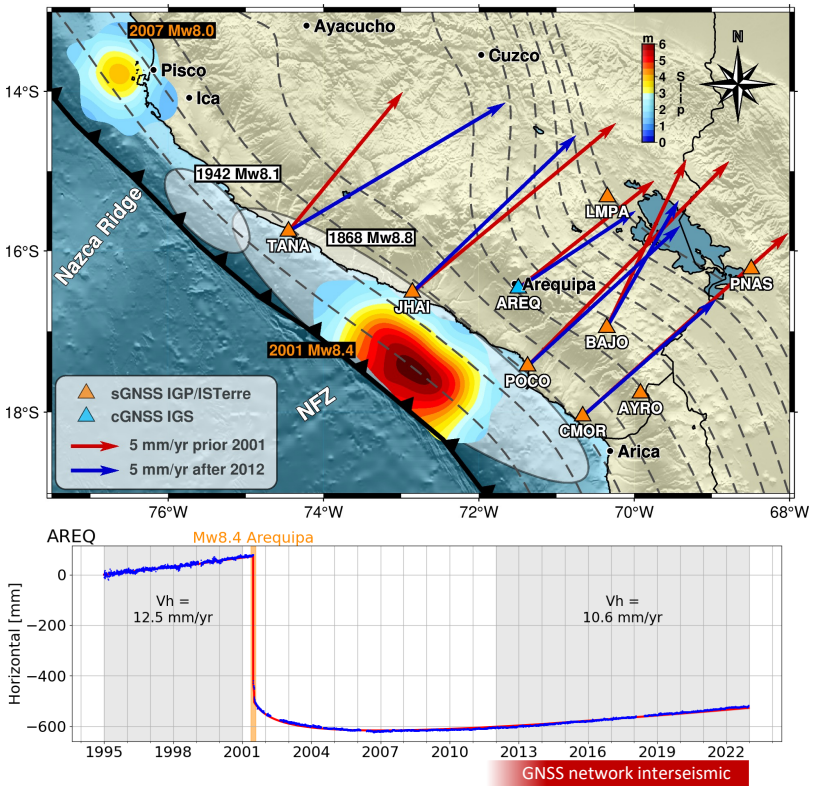

Figure 1: *Top:* Interseismic velocities at AREQ and sGNSS SNAPP sites (when available) in South Peru (Norabuena et al., 1998), prior to the Arequipa earthquake (red) and after 2012 (blue). The slip distribution of the 2001 Mw8.4 Arequipa (this study) and 2007 Mw8.0 Pisco (Chlieh et al., 2011) earthquakes are reported by the colormap (cf. section 3). Gray ellipses indicate approximate historical ruptures (Villegas-Lanza et al., 2016). Slab contours (dashed lines) are reported every 20-km depth, from the Slab2 model (Hayes et al. 2018). *Bottom:* Horizontal component of the AREQ timeseries, corrected from antenna jumps and seasonal variations. Observations are displayed in blue, and the trajectory model in red (cf. section 3). Velocities are reported for two time-ranges: 1995-2001 and 2012-2023, in order to compare the interseismic velocity over the last decade (observation period used for interseismic velocity assessment in Lovery et al., 2024a) to the one prior to the earthquake.

2 Finite Element Method model

To model the surface displacements related to the Arequipa earthquake and its postseismic phase, we use a 3-D Finite Element Method (FEM) model of the subduction zone in South Peru (Figures 2 and S1, Table S1, Text S1). Following the viscoelastic structure of Luo & Wang (2021), thermal models (Araya Vargas et al., 2021; Springer, 1999; Wada & Wang, 2009), and gravimetry (Tassara et al., 2006; Tassara & Echaurren, 2012), we use 40-km thick oceanic and 30-km thick

continental elastic layers, while the underlying layers are considered viscoelastic (Figures 2 and S1). The stagnant forearc mantle is materialized by a cold-nose that extends down to 85-km depth (Luo & Wang, 2021; Sun & Wang, 2015), consistent with the thermal insights from Wada & Wang (2009), the seismic tomography from Gao et al. (2021), and the results from temperature-controlled postseismic models (Sobolev & Muldashev, 2017). For simplicity, elastic properties in the various layers are taken from the PREM model (Dziewonski & Anderson, 1981). We set the oceanic asthenosphere to be ten times more viscous than the continental one, which is typical for subduction (Hu et al., 2004; Luo and Wang, 2021; Wang et al., 2012).

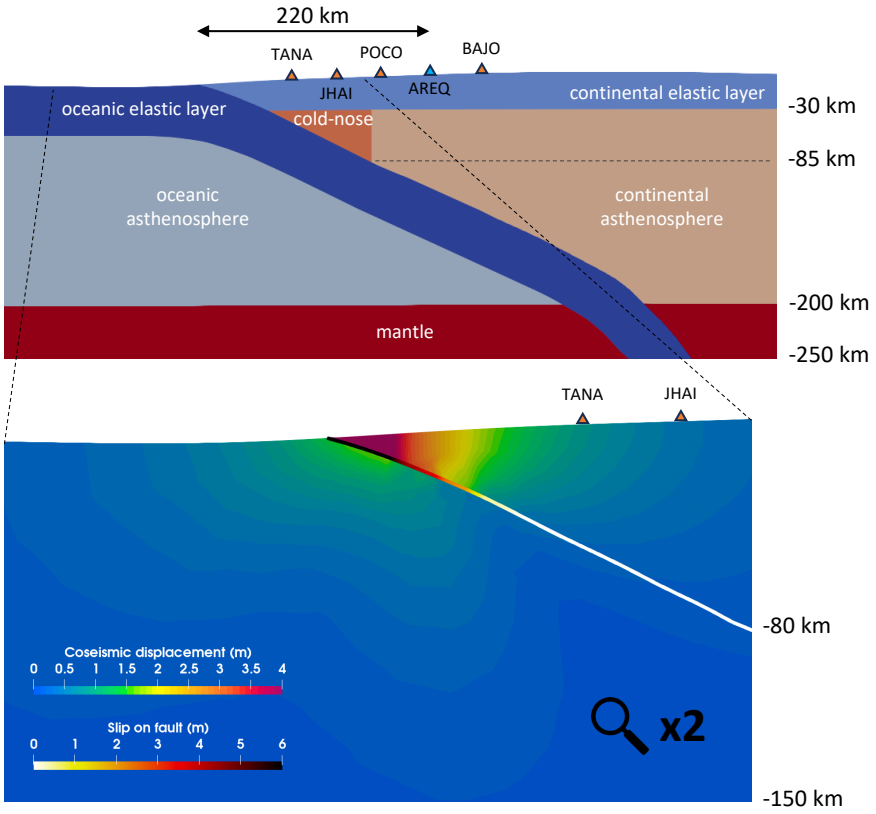

Figure 2: *Top:* Slicing of the 3-D subduction model, passing by AREQ station. Triangles indicate the projected locations of cGNSS (blue) and sGNSS (orange). See Figure S1 for full-size structure. *Bottom:* Absolute values of coseismic displacement and slip amplitude on the interface associated with the Arequipa earthquake, zoomed-in, according to the model.

3 Accommodating observed postseismic surface displacements

3.1 GNSS data used to constrain the models

We analyze the cGNSS station AREQ (Johnston et al., 2017), located at 225 km from the trench (Figure 1, bottom). It allows to get precise measurements on horizontal and vertical components since 1994. In addition, eight sGNSS sites have been measured during 14 campaigns performed between April 1994 and March 2022 by the Instituto Geofísico del Perú (IGP) and the Institut des Sciences de la Terre (ISTerre). Among them, five have been measured several times before and after the Arequipa earthquake (Figure 1, top, and Figures S2 to S5): BAJO, CMOR, JHAI, POCO, and TANA. These sGNSS data, not included in previous studies (Hergert & Heidbach, 2006; Perfettini et al., 2005; Sun et al., 2018), provide quite robust horizontal displacements. Data processing is described in Text S2.

We separate the postseismic displacements from the interseismic loading by detrending the timeseries from the velocity prior to the Arequipa earthquake. Computing the pre-Arequipa horizontal velocity on the AREQ timeseries is reliable, as we have 7 years of daily recording. However, we only have two campaigns in 1994 and 1996 for POCO and TANA, and three in 1994, 1996, and 1999 for AYRO, BAJO, CMOR, JHAI, LMPA, and PNAS (Table S2). We do not consider the vertical component at sGNSS sites because of its high dispersion. Even at the cGNSS AREQ the assessment of the pre-Arequipa vertical velocity is difficult.

3.2 Assessing model parameters

To model the Arequipa postseismic phase, we inverted the coseismic offsets from Pritchard et al. (2007) following the Tarantola-Valette formulation (Kositsky & Avouac, 2010; Radiguet et al., 2011; Tarantola & Valette, 1982) with similar parameters as in Lovery et al. (2024a), except we set a three times higher weight to AREQ. The resulting coseismic slip distribution (Figures S6 and S7) is applied to our FEM model. To constrain the viscoelastic postseismic model parameters, we compare the displacements predicted by the model to the horizontal and vertical components of the AREQ timeseries, as well as to the horizontal components of the sGNSS timeseries (Figure 3). As uncertainties are higher on sGNSS, we focus first on fitting the AREQ timeseries. At AREQ we observe a ~40 cm East and ~35 cm North coseismic offset followed by a decelerating postseismic displacement of ~30 cm East and ~15 cm North up to 2024. The vertical component displayed a ~3 cm coseismic subsidence, followed by a ~2 cm transient uplift until 2006, and then

a long-term subsidence of ~5 cm up to 2024. The vertical trend on the 2010-2024 period is almost linear, with no apparent return to the pre-earthquake values.

Since the ISC in Lovery et al. (2024a) was computed mostly with stations installed in 2012, we focus on fitting the 2012-2023 period to assess the impact of long-term relaxation (>10 years after the earthquake) on the estimation of the ISC. sGNSS have been measured a few weeks after the earthquake, so the offsets observed on sGNSS timeseries include early afterslip. To account for the early afterslip, we apply an afterslip term *as(t)* with a logarithmic formulation (Marone et al., 1991) to fill the gap in the timeseries (Figure S8 and S9):

$$\text{as(t)} = \text{A}\cdot log\left(1 + \frac{t}{\tau}\right)$$

with amplitude A, time t in days, and characteristic time τ. A is computed for each station by least-square minimization of the data-model residual, while τ = 5 days has been assessed using the AREQ timeseries only in order to fit the short-term trend.

Figure 3 displays the fit to the GNSS timeseries for various rheological structures, with viscosities optimized based on root mean square error (RMSE) (cf. Figures S10 to S12). The best model is characterized by a Burgers rheology (cf. Text S3) in the asthenosphere (40-200 km depth) with a Maxwell viscosity $\eta_M = 9\cdot10^{18}$ Pa.s and a Kelvin viscosity $\eta_K = 5\cdot10^{18}$ Pa.s, and an elastic cold-nose down to 85 km depth. A detailed explanation on the assessment of the model parameters is available in Text S4 and S5. Our optimal value for the long-term Maxwell viscosity in the asthenosphere (cf. Figures S10 to S12), $9\cdot10^{18}$ Pa.s (RMS = 0.013 vs. 0.019 for $8\cdot10^{18}$ Pa.s vs. 0.018 for $1\cdot10^{19}$ Pa.s) is similar to Wang et al. (2012) who reported viscosities in the order of 1.10^{19} Pa.s at subduction zones, as well as Li et al. (2018) on the volcanic arc in Chile. Socquet et al. (2024) found a viscosity of $2\cdot10^{19}$ Pa.s for the area surrounding the 2014 Mw8.1 Iquique earthquake. It is also within the 0.5-3$\cdot10^{19}$ Pa.s range reported by Trubienko et al. (2013) for large subduction earthquakes in South-East Asia and for Tohoku. Sun et al. (2018) found a slightly lower viscosity of $5\cdot10^{18}$ Pa.s for the Arequipa earthquake, but on a shorter timescale (12 vs. 23 years) and neglecting afterslip.

Our model does not fit the vertical component after 2005, when the uplift trend reversed to subsidence. One possible model fits both horizontal and vertical components with $\eta_M = 4\cdot10^{19}$ Pa.s and $\eta_K = 4\cdot10^{18}$ Pa.s, and a viscoelastic cold-nose, with a Maxwell rheology $\eta_{MCN} = 1\cdot10^{19}$ Pa.s

(turquoise curve on Figure 3, Figure S13). However, such possibility is questionable because the cold-nose is supposed to be either purely elastic as in Luo & Wang (2021), or highly viscous relative to the asthenosphere, of the order of 10^{22} Pa.s as found by Dhar et al. (2022) and Muto et al. (2016), or 10^{20}-10^{21} Pa.s in Muto et al. (2019). Given the uncertainties regarding the vertical component (especially in the pre-2001 period that is used for detrending), and that it is only available at one location, we chose to stick with a model fitting primarily the horizontal component, rather than trying to fit absolutely both components with a somewhat unrealistic model. The vertical component is more sensible to non-tectonic processes such as volcanic activity or hydrological loading (Itoh et al., 2019). AREQ is located within the volcanic arc, close to major active volcanoes such as Misti (15 km northeast), Chachani (20 km north), Ubinas (65 km east) and Sabancaya (70 km northwest). Volcanic activity at Sabancaya since 2013 and potentially earlier has been reported by Boixart et al. (2020), MacQueen et al. (2020), and Machacca et al. (2023), with a significant inflation trend over the last decade (~2 cm/yr). This inflation trend at the volcano could lead to a subsidence in the surrounding area (Chaussard et al., 2016; Shreve et al., 2021), including in Arequipa, also observed by Lovery et al. (2024b) on InSAR timeseries. Reath et al. (2019) also report a raising thermal anomaly starting from 2004 at Sabancaya, approximately at the same time as the observed transition from uplift to subsidence.

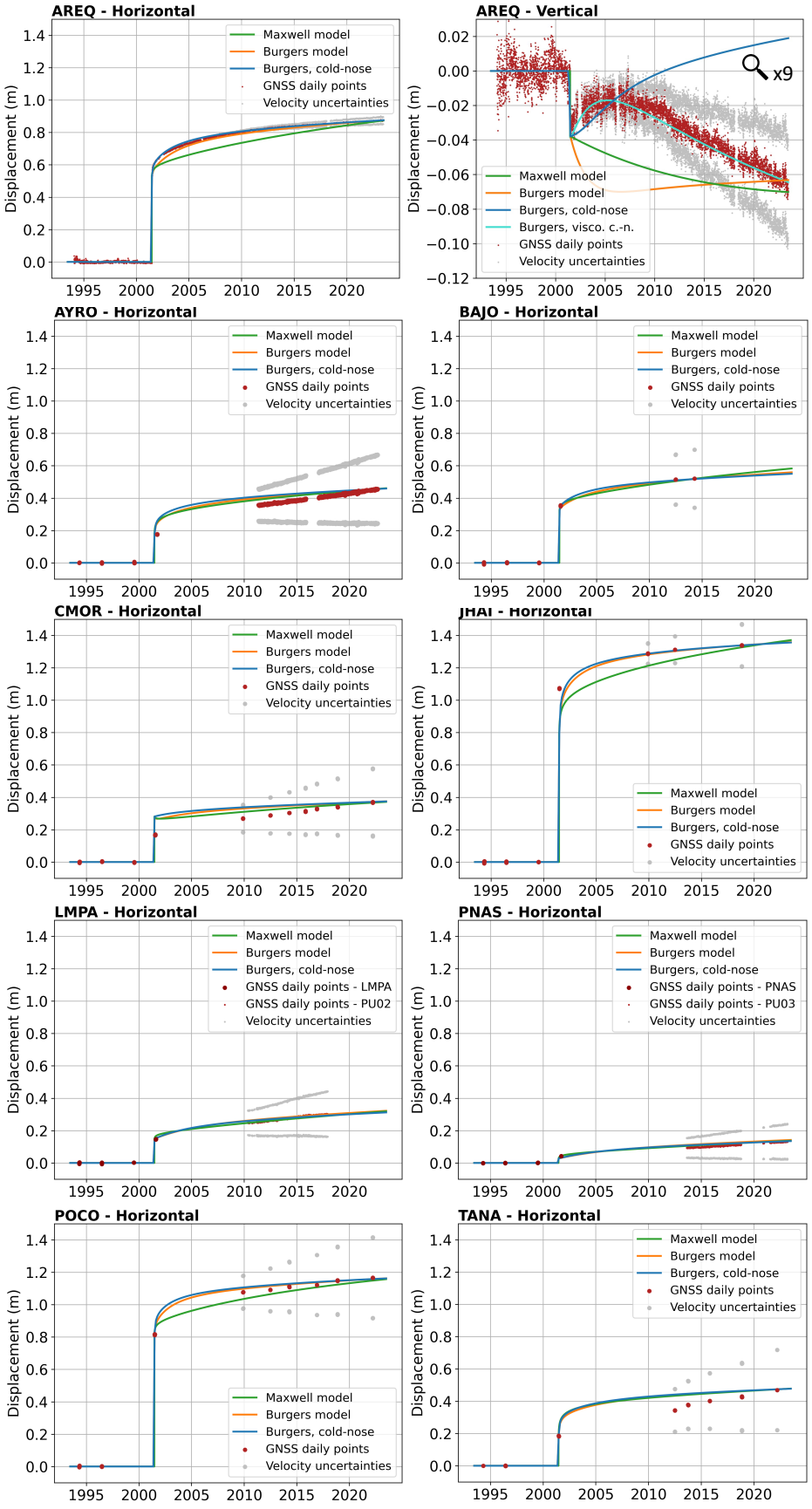
AREQ - Horizontal
AREQ - Vertical
AYRO - Horizontal
BAJO - Horizontal
CMOR - Horizontal
JHAI - Horizontal
LMPA - Horizontal
PNAS - Horizontal
POCO - Horizontal
TANA - Horizontal
Displacement (m)
Maxwell model
Burgers model
Burgers, cold-nose
Burgers, visco. c.-n.
GNSS daily points
GNSS daily points - LMPA
GNSS daily points - PU02
GNSS daily points - PNAS
GNSS daily points - PU03
Velocity uncertainties
x9

Figure 3: Displacement timeseries at AREQ (horizontal and vertical) and at the various sGNSS sites (AYRO, BAJO, CMOR, JHAI, LMPA, PNAS, POCO, and TANA) on the horizontal component. The timeseries cover the 1994-2024 period and have been corrected from coseismic steps related to other earthquakes, seasonal variations, and detrended from the pre-Arequipa velocities. Daily GNSS solutions are reported by red dots. Uncertainties at 3σ on the slope after 2001, computed using MIDAS, are indicated by gray dots. The vertical component is zoomed-in by a factor nine compared to the horizontal. Four models are displayed: Maxwell rheology without cold-nose (green), Burgers rheology without cold-nose (yellow), Burgers rheology with an elastic cold-nose (blue, best model), and Burgers rheology with a Maxwell viscoelastic cold-nose (turquoise on AREQ vertical component, cf. Figure S13). For every model, the afterslip term is included (cf. Figure S8).

4 Impact on the ISC and moment deficit rate

4.1 Modelling ISC using viscoelastic Green's functions

To model the ISC, we use the inversion scheme described in Lovery et al. (2024a). However, in order to keep this analysis consistent between postseismic and interseismic models, we introduced viscoelastic Green's functions (GF) instead of pure elastic ones. The procedure is described in Text S6 (see also Figure S14). Introducing viscoelasticity for modelling ISC is often expected to improve the fit in the far-field and to reduce the locking depth (Itoh et al., 2019; Li et al., 2015 & 2018). Indeed, we get larger displacements in the back-arc (Figure S15 to S16), but the change in locking depth is less striking than what is observed by Li et al. (2015, 2018) in Chile, or Li & Chen (2024) over Nankai and Cascadia. While we observe about 15-km shallower coupling over the large locked asperity between the NR and the 2001 rupture, the locking depth on the other segments remains similar. It could be related to the presence of the elastic cold-nose, or to the flat to dipping slab transition in South Peru (in the flat slab zone there is much less continental asthenosphere, which changes the viscoelastic effect in that area). Also, ISC is increased between the NR and the NFZ, while it is lowered from the NFZ to the Arica bend. The latter segment is now showing two distinct asperities instead of one. The moment deficit rate over the South Peru segment (delimited by the purple polygon on Figure 4) remains quite similar: $2.21 \cdot 10^{20}$ Nm/yr vs. $2.24 \cdot 10^{20}$ Nm/yr for viscoelastic and elastic GF respectively.

4.2 Accounting for postseismic displacements

Using the rheology inferred in section 3, we model the surface displacements over time on the GNSS network used for ISC assessment. For each site, we model the expected postseismic rate

over the observation period (Figure S17, Table S3), which is about 2012-2023 for most sites. We subtract this contribution to the interseismic velocities estimated in Lovery et al. (2024a). Then we invert the corrected velocities using viscoelastic GF, like in section 4.1.

The obtained ISC distribution (Figure 4b) shows a higher coupling in the area overlapping the Arequipa rupture (Figure S18) compared to the model not accounting for postseismic (Figure 4a). Also, the decrease in coupling where the NFZ subducts is less pronounced, and may partially result from the Arequipa postseismic phase. The large locked asperity between the NR and the 2001 rupture overlaps the ruptures of the 1942 Mw8.1 and 1913 Mw7.8 earthquakes (Villegas-Lanza et al., 2016). Note that the shallow part of the segment between the NFZ and the Arica bend (from the trench to the 20-km slab contour) may actually be more coupled than what we observe as the resolution is a bit lower due to higher distance between the trench and the GNSS stations (Figure S19).

In order to validate our findings against independent data, we compare our ISC distribution with seismicity. On Figure S20 are displayed the thrust events with $M_w \geq 5.5$ from gCMT (Dziewonski et al., 1981; Ekström et al, 2012), on top of our ISC distribution. We observe a convincing overlap between the events distribution and the areas of high coupling (> 0.4), especially for the model corrected from postseismic where the mainshock and aftershocks of the Arequipa earthquake now lie in an area of very high coupling (> 0.8). While on Figure S21 are displayed all seismic events from the IGP catalog (magnitude of completeness M_c=4.5). We observe a high cumulative seismicity at the location of creeping areas, especially where the NR and the NFZ are subducting, as creeping areas are known to host most of low-magnitude seismic events (Bassett et al., 2025; Jiang & Lapusta, 2017; Métois et al., 2016; Rubin et al., 1999; Scholz, 1990; Sippl et al., 2021).

The moment deficit rate over the South Peru segment is increased by 9% when accounting for postseismic processes, going from $2.21 \cdot 10^{20}$ Nm/yr to $2.42 \cdot 10^{20}$ Nm/yr. This increase is significant, but remains within the uncertainties from Lovery et al. (2024a) who considered an increase up to 15% in their exploration of uncertainties for maximum earthquake magnitude assessment. Note that locally the impact can be significantly higher, we observe a 24% increase at the center of the Arequipa rupture (Figures 4c, S18 and S21 to S24).

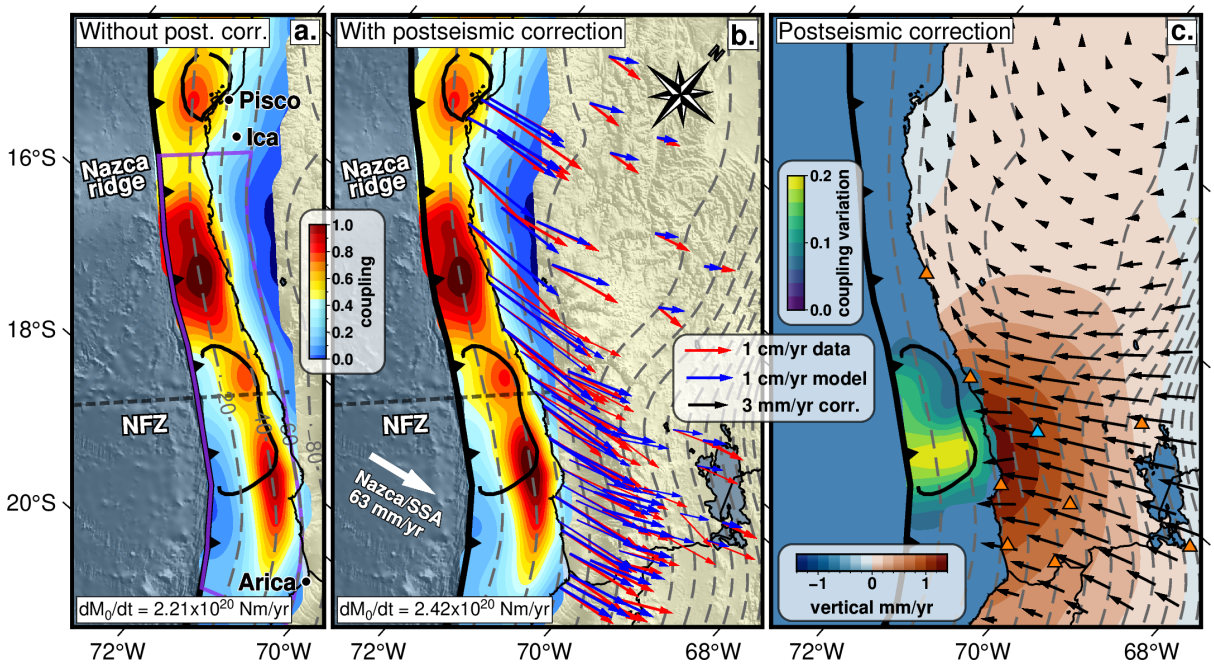

Figure 4: ISC distribution without (a) and with (b) postseismic correction. Slab contours (dashed lines) are reported every 20-km depth, from the Slab2 model (Hayes et al. 2018). The approximate 2001 Arequipa and 2007 Pisco ruptures are reported by black contours. Observed and modelled interseismic velocities are depicted by red and blue vectors respectively. The low-coupled area where the NFZ (indicated by the dashed black line) is subducting is less pronounced for the model accounting for postseismic displacements. In the latter, higher coupling leads to a 9% increase in moment deficit rate (dM_0/dt) over the South Peru segment delimited by the purple polygon. (c) The greenish colormap shows the difference between (a) and (b) ISC distributions. We report postseismic velocity on the 2012-2023 period on the horizontal (black vectors) and vertical (blue-red colormap) components. The locations of the GNSS sites are indicated by the orange(sGNSS) and blue (cGNSS) triangles.

5 Conclusions

The present-day velocities have not resumed to their pre-2001 values, confirming that the Mw8.4 Arequipa earthquake postseismic phase is still ongoing. Revisiting the legacy sGNSS data confirmed the observation made previously on the AREQ continuous timeseries, all of the eight sGNSS showing a significant change in velocity between the pre-earthquake period and the last decade. Using viscoelastic GF, we provide an ISC model considering a Burgers rheology with an elastic cold-nose. Correcting for the postseismic processes following the Arequipa earthquake increases the estimation of the ISC, and the moment deficit rate by 9%. Low coupling where the NR is subducting remains a persistent feature on the ISC distribution, suggesting that it acts as a strong seismic barrier. However, the decrease in coupling where the NFZ is subducting is less pronounced.

This study also provides proxies for the mantle rheology in South Peru, which can be modelled with Burgers viscosity in the asthenosphere (η_M = $9{\cdot}10^{18}$ Pa.s, η_K = $5{\cdot}10^{18}$ Pa.s in the continental domain) and an elastic cold-nose. At this point, it is difficult to settle on the vertical velocity change and its implications regarding the rheological structure considering the weak constraints and the potential contaminations on the vertical component. Vertical deformation over the seismic cycle at subduction zones is still relatively poorly understood and should be analyzed more thoroughly on better instrumented cases, as advocated by Luo & Wang (2021) and Li & Chen (2024). As shown by other authors (Li & Chen, 2024; Moreno et al., 2011; Pollitz, 2025; Trubienko et al., 2013; Wang et al., 2007; Wang et al., 2012), it is important to perform viscoelastic models taking into account the postseismic processes to properly model the loading on the megathrust, associated seismic potential, and along-strike segmentation. Viscoelastic ISC models, as proposed in this study, are fundamental to discriminate the slip on the slab interface from internal deformation. Finally, the shallow locking observed south of the NR should be considered in risk assessment as shallow oceanic ruptures are often associated with a higher risk of tsunami (Bilek & Lay, 2002; Carvajal et al., 2022; Villegas-Lanza, 2016).

Acknowledgments

This work was supported by funding from European Research Council (ERC), CNES, Instituto Geofísico del Perú (IGP), CNRS-INSU, and LabExOsug@2020 (Investissements d'avenir—ANR10LABX56). A. Socquet received funding from the ERC CoG 865963 DEEPtrigger. B. Lovery salary was covered by grants from CNES (convention n°5100020593) and ERC DEEPtrigger. J. Cresseaux salary was covered by ERC DEEPtrigger. The IGP/ISTerre/Caltech GNSS stations in Peru were installed by ISTerre and Caltech in collaboration with IGP, and are now maintained by IGP. The IGN network in Peru is maintained by the Instituto Geografico Nacional. We thank the Computational Infrastructure for Geodynamics (http://geodynamics.org) which is funded by the National Science Foundation under awards EAR-0949446, EAR-1550901,

and EAR-2149126. Most computing was made on the GriCAD infrastructure (https://gricad.univ-grenoble-alpes.fr). We thank the Editor Germán Prieto, the Associate Editor Ake Fagereng, Carlos Peña, and an anonymous reviewer for their detailed and constructive comments, as well as M.-P. Doin for useful discussion.

Open Research

All GNSS timeseries used in this manuscript are available at Socquet et al. (2023d). RINEX data from SNAPP campaigns are available from UNAVCO (Simons et al., 2010): 1994 campaign at https://www.unavco.org/data/gps-gnss/data-access-methods/dai1/data_request.php?gid=1325&ds=1&parent_link=Campaign&pview=original, 1996 campaign at https://www.unavco.org/data/gps-gnss/data-access-methods/dai1/data_request.php?gid=1493&ds=2&parent_link=Campaign&pview=-original, and 2001 campaign at https://www.unavco.org/data/gps-gnss/data-access-methods/dai1/data_request.php?gid=2128&ds=1&parent_link=Campaign&pview=original. RINEX data from campaigns in South Peru between 2012 and 2022 are available at Socquet et al. (2023a) for the 2012 campaign, Socquet et al. (2023c) for the 2013 campaign, Socquet & Norabuena (2023) for the 2015 campaign, Nocquet & Socquet (2023) for the 2016 campaign, Socquet et al. (2023b) for the 2018 campaign, and Socquet et al. (2023e) for the 2022 campaign.

The trajectory model analysis has been performed using the ITSA software (Marill et al., 2021) available on the Software Heritage permanent repository (https://archive.softwareheritage.org/swh:1:dir:78f41876979eea6263221ed4e14873557152860c) and on the GriCAD GitLab repository (https://gricad-gitlab.univ-grenoble-alpes.fr/isterre-cycle/itsa). We use PyLith 2.2.2 (Aagaard et al., 2013) published under the MIT license and available at https://geodynamics.org/resources/pylith. Geographical illustrations were made using the Generic Mapping Tools version 6 package (Wessel et al., 2019) licensed under LGPL version 3 or later,

343 available at https://www.generic-mapping-tools.org/. Other illustrations were made with Matplotlib
344 v3.7.1 (Hunter, 2007), available under the Matplotlib license at https://matplotlib.org.
345

346 **References**

347 Aagaard, B.T.; Knepley, M.G.; Williams, C.A. (2013), A domain decomposition approach to
348 implementing fault slip in finite-element models of quasi-static and dynamic crustal deformation,
349 *Journal of Geophysical Research: Solid Earth, 118 (6)*, 3059-3079.
350 https://doi.org/10.1002/jgrb.50217
351
352 Araya Vargas, J., Sanhueza, J., & Yáñez, G. (2021). The Role of Temperature in the Along-Margin
353 Distribution of Volcanism and Seismicity in Subduction Zones: Insights From 3-D
354 Thermomechanical Modeling of the Central Andean Margin. *Tectonics*, *40*(11), e2021TC006879.
355 https://doi.org/10.1029/2021TC006879
356
357 Barbot, S., & Fialko, Y. (2010). A unified continuum representation of post-seismic relaxation
358 mechanisms: semi-analytic models of afterslip, poroelastic rebound and viscoelastic flow. In
359 Geophysical Journal International (Vol. 182, Issue 3, pp. 1124–1140). Oxford University Press
360 (OUP). https://doi.org/10.1111/j.1365-246x.2010.04678.x
361
362 Bassett, D., Shillington, D. J., Wallace, L. M., & Elliott, J. L. (2025). Variation in slip behaviour
363 along megathrusts controlled by multiple physical properties. *Nature Geoscience*, *18*(1), 20–31.
364 https://doi.org/10.1038/s41561-024-01617-9
365
366 Bilek, S. L., & Lay, T. (2002). Tsunami earthquakes possibly widespread manifestations of
367 frictional conditional stability. *Geophysical Research Letters*, *29*(14), 18-1-18–4.
368 https://doi.org/10.1029/2002GL015215
369
370 Boixart, G., Cruz, L. F., Miranda Cruz, R., Euillades, P. A., Euillades, L. D., & Battaglia, M.
371 (2020). Source Model for Sabancaya Volcano Constrained by DInSAR and GNSS Surface
372 Deformation Observation. *Remote Sensing*, *12*(11), 1852. https://doi.org/10.3390/rs12111852
373
374 Boulze, H., Fleitout, L., Klein, E., & Vigny, C. (2022). Post-seismic motion after 3 Chilean
375 megathrust earthquakes: a clue for a linear asthenospheric viscosity. *Geophysical Journal*
376 *International*, *231*(3), 1471–1478. https://doi.org/10.1093/gji/ggac255
377
378 Carvajal, M., Sun, T., Wang, K., Luo, H., & Zhu, Y. (2022). Evaluating the tsunamigenic potential
379 of buried versus trench-breaching megathrust slip. *Journal of Geophysical Research: Solid Earth*,
380 127, e2021JB023722. https://doi.org/10.1029/2021JB023722
381
382 Chaussard, E. (2016). Subsidence in the Parícutin lava field: Causes and implications for
383 interpretation of deformation fields at volcanoes. *Journal of Volcanology and Geothermal*
384 *Research*, *320*, 1–11. https://doi.org/10.1016/j.jvolgeores.2016.04.009
385

Chlieh, M., Perfettini, H., Tavera, H., Avouac, J.-P., Remy, D., Nocquet, J.-M., et al. (2011). Interseismic coupling and seismic potential along the Central Andes subduction zone. *Journal of Geophysical Research: Solid Earth*, *116*(B12). https://doi.org/10.1029/2010JB008166

Dhar, S., Muto, J., Ito, Y., Miura, S., Moore, J. D. P., Ohta, Y., & Iinuma, T. (2022). Along-arc heterogeneous rheology inferred from post-seismic deformation of the 2011 Tohoku-oki earthquake. In Geophysical Journal International (Vol. 230, Issue 1, pp. 202–215). Oxford University Press (OUP). https://doi.org/10.1093/gji/ggac063

Dorbath, L., Cisternas, A., & Dorbath, C. (1990), Assesment of the size of large and great historical earthquakes in Peru. *Bulletin of the Seismological Society of America, 80*, 551-576. https://doi.org/10.1785/BSSA0800030551

Dziewonski, A. M., & Anderson, D. L. (1981). Preliminary reference Earth model. *Physics of the Earth and Planetary Interiors*, *25*(4), 297–356. https://doi.org/10.1016/0031-9201(81)90046-7

Dziewonski, A. M., Chou, T. A., & Woodhouse, J. H., (1981), Determination of earthquake source parameters from waveform data for studies of global and regional seismicity, *J. Geophys. Res.*, *86*, 2825-2852. https://doi.org/10.1029/JB086iB04p02825

Ekström, G., Nettles, M., & Dziewoński, A. M. (2012). The global CMT project 2004–2010: Centroid-moment tensors for 13,017 earthquakes. *Physics of the Earth and Planetary Interiors*, *200–201*, 1–9. https://doi.org/10.1016/j.pepi.2012.04.002

Gao, Y., Tilmann, F., van Herwaarden, D.-P., Thrastarson, S., Fichtner, A., Heit, B., et al. (2021). Full Waveform Inversion Beneath the Central Andes: Insight Into the Dehydration of the Nazca Slab and Delamination of the Back-Arc Lithosphere. *Journal of Geophysical Research: Solid Earth*, *126*(7), e2021JB021984. https://doi.org/10.1029/2021JB021984

Hayes, G. P., Moore, G. L., Portner, D. E., Hearne, M., Flamme, H., Furtney, M., & Smoczyk, G. M. (2018). Slab2, a comprehensive subduction zone geometry model. *Science*, *362*(6410), 58–61. https://doi.org/10.1126/science.aat4723

Hergert, T., & Heidbach, O. (2006). New insights into the mechanism of postseismic stress relaxation exemplified by the 23 June 2001 Mw = 8.4 earthquake in southern Peru. *Geophysical Research Letters*, *33*(2). https://doi.org/10.1029/2005GL024858

Hu, Y., Wang, K., He, J., Klotz, J., & Khazaradze, G. (2004). Three-dimensional viscoelastic finite element model for postseismic deformation of the great 1960 Chile earthquake. In Journal of Geophysical Research: Solid Earth (Vol. 109, Issue B12). American Geophysical Union (AGU). https://doi.org/10.1029/2004jb003163

Hunter, J. D. (2007). Matplotlib: A 2d graphics environment. *Computing in Science & Engineering*, *9*(3), 90–95. https://doi.org/10.1109/MCSE.2007.55

Itoh, Y., Wang, K., Nishimura, T., & He, J. (2019). Compliant Volcanic Arc and Backarc Crust in Southern Kurile Suggested by Interseismic Geodetic Deformation. *Geophysical Research Letters*, *46*(21), 11790–11798. https://doi.org/10.1029/2019GL084656

Jiang, J., & Lapusta, N. (2017). Connecting depth limits of interseismic locking, microseismicity, and large earthquakes in models of long-term fault slip. *Journal of Geophysical Research: Solid Earth*, *122*(8), 6491–6523. https://doi.org/10.1002/2017JB014030

Johnston, G., Riddell, A., Hausler, G. (2017). The International GNSS Service. Teunissen, Peter J.G., & Montenbruck, O. (Eds.), *Springer Handbook of Global Navigation Satellite Systems* (1st ed., pp. 967-982). Cham, Switzerland: Springer International Publishing. https://doi.org/10.1007/978-3-319-42928-1

Klein, E., Fleitout, L., Vigny, C., & Garaud, J. D. (2016). Afterslip and viscoelastic relaxation model inferred from the large-scale post-seismic deformation following the 2010Mw8.8 Maule earthquake (Chile). In Geophysical Journal International (Vol. 205, Issue 3, pp. 1455–1472). Oxford University Press (OUP). https://doi.org/10.1093/gji/ggw086

Kositsky, A. P., & Avouac, J.-P. (2010). Inverting geodetic time series with a principal component analysis-based inversion method. *Journal of Geophysical Research: Solid Earth*, *115*(B3). https://doi.org/10.1029/2009JB006535

Li, S., Moreno, M., Bedford, J., Rosenau, M., & Oncken, O. (2015). Revisiting viscoelastic effects on interseismic deformation and locking degree: A case study of the Peru-North Chile subduction zone. *Journal of Geophysical Research: Solid Earth*, *120*(6), 4522–4538. https://doi.org/10.1002/2015JB011903

Li, S., Bedford, J., Moreno, M., Barnhart, W. D., Rosenau, M., & Oncken, O. (2018). Spatiotemporal variation of mantle viscosity and the presence of cratonic mantle inferred from 8 years of postseismic deformation following the 2010 Maule, Chile, earthquake. *Geochemistry, Geophysics, Geosystems*, 19, 3272–3285. https://doi.org/10.1029/2018GC007645

Li, S., & Chen, L. (2024). Revisiting interseismic deformation in Nankai: focusing on slip-deficit accumulation in the ETS zone and comparison with Cascadia. *Earth, Planets and Space*, *76*(1), 108. https://doi.org/10.1186/s40623-024-02054-z

Lovery, B., Chlieh, M., Norabuena, E., Villegas-Lanza, J. C., Radiguet, M., Cotte, N., et al. (2024a). Heterogeneous locking and earthquake potential on the South Peru megathrust from dense GNSS network. *Journal of Geophysical Research: Solid Earth*, 129, e2023JB027114. https://doi.org/10.1029/2023JB027114

Lovery, B., Doin, M. P., Chlieh, M., Socquet, A., Radiguet, M., Villegas-Lanza, J. C., et al. (2024b). Using Sentinel-1 Timeseries for Large-scale Tectonic Applications in Central Andes. *AGU24*.

Luo, H., Wang, K. Postseismic geodetic signature of cold forearc mantle in subduction zones. *Nat. Geosci.* 14, 104–109 (2021). https://doi.org/10.1038/s41561-020-00679-9

Machacca, R., Lesage, P., Tavera, H., Pesicek, J. D., Caudron, C., Torres, J. L., et al. (2023). The 2013–2020 seismic activity at Sabancaya Volcano (Peru): Long lasting unrest and eruption. *Journal of Volcanology and Geothermal Research*, *435*, 107767. https://doi.org/10.1016/j.jvolgeores.2023.107767

MacQueen, P., Delgado, F., Reath, K., Pritchard, M., Bagnardi, M., Milillo, P. Lundgren, P., Macedo, O., Aguilar, V., Ortega, M., Anccasi, R., Lazarte, I., Miranda, R. (2020) Volcano-Tectonic Interactions at Sabancaya Volcano, Peru: Eruptions, Magmatic Inflation, Moderate Earthquakes, and Fault Creep. JGR- Solid Earth. https://doi.org/10.1029/2019JB019281

Marill, L., Marsan, D., Socquet, A., Radiguet, M., Cotte, N., & Rousset, B. (2021). Fourteen-Year Acceleration Along the Japan Trench. *Journal of Geophysical Research: Solid Earth*, *126*(11), e2020JB021226. https://doi.org/10.1029/2020JB021226

Marone, C. J., Scholtz, C. H., & Bilham, R. (1991). On the mechanics of earthquake afterslip. *Journal of Geophysical Research: Solid Earth*, *96*(B5), 8441–8452. https://doi.org/10.1029/91JB00275

Métois, M., Vigny, C., & Socquet, A. (2016). Interseismic Coupling, Megathrust Earthquakes and Seismic Swarms Along the Chilean Subduction Zone (38°–18°S). *Pure and Applied Geophysics*, *173*(5), 1431–1449. https://doi.org/10.1007/s00024-016-1280-5

Moreno, M., Melnick, D., Rosenau, M., Bolte, J., Klotz, J., Echtler, H., et al. (2011). Heterogeneous plate locking in the South–Central Chile subduction zone: Building up the next great earthquake. *Earth and Planetary Science Letters*, *305*(3), 413–424. https://doi.org/10.1016/j.epsl.2011.03.025

Muto, J., Shibazaki, B., Iinuma, T., Ito, Y., Ohta, Y., Miura, S., & Nakai, Y. (2016). Heterogeneous rheology controlled postseismic deformation of the 2011 Tohoku-Oki earthquake. In Geophysical Research Letters (Vol. 43, Issue 10, pp. 4971–4978). American Geophysical Union (AGU). https://doi.org/10.1002/2016gl068113

Muto, J., Moore, J. D. P., Barbot, S., Iinuma, T., Ohta, Y., & Iwamori, H. (2019). Coupled afterslip and transient mantle flow after the 2011 Tohoku earthquake. *Science Advances*, *5*(9), eaaw1164. https://doi.org/10.1126/sciadv.aaw1164

Nocquet, J.-M., & Socquet, A. (2023). *EPOS-France - GPSMob data - Mission n° 16-153 - Perou (2016) - 2016-08-24 / 2016-12-06 - 37 points* [Dataset]. OSU OREME. http://doi.org/10.15148/F410D57F-2E67-4174-9E7E-17AE3FD55D99

Norabuena, E., Leffler-Griffin, L., Mao, A., Dixon, T., Stein, S., Sacks, I. S., et al. (1998). Space Geodetic Observations of Nazca-South America Convergence Across the Central Andes. *Science*, *279*(5349), 358–362. https://doi.org/10.1126/science.279.5349.358

Nur, A., & Mavko, G. (1974). Postseismic Viscoelastic Rebound. In Science (Vol. 183, Issue 4121, pp. 204–206). American Association for the Advancement of Science (AAAS). https://doi.org/10.1126/science.183.4121.204

Peltzer, G., Rosen, P., Rogez, F., & Hudnut, K. (1996). Postseismic Rebound in Fault Step-Overs Caused by Pore Fluid Flow. In Science (Vol. 273, Issue 5279, pp. 1202–1204). American Association for the Advancement of Science (AAAS). https://doi.org/10.1126/science.273.5279.1202

Perfettini, H., Avouac, J.-P., & Ruegg, J.-C. (2005). Geodetic displacements and aftershocks following the 2001 Mw = 8.4 Peru earthquake: Implications for the mechanics of the earthquake cycle along subduction zones. *Journal of Geophysical Research: Solid Earth*, *110*(B9). https://doi.org/10.1029/2004JB003522

Pollitz, F. F., Bürgmann, R., & Banerjee, P. (2006). Post-seismic relaxation following the great 2004 Sumatra-Andaman earthquake on a compressible self-gravitating Earth. *Geophysical Journal International*, *167*(1), 397–420. https://doi.org/10.1111/j.1365-246X.2006.03018.x

Pollitz, F. F. (2025). 3D Viscoelastic Models of Slip-Deficit Rate Along the Cascadia Subduction Zone. *Journal of Geophysical Research: Solid Earth*, *130*(1), e2024JB029847. https://doi.org/10.1029/2024JB029847

Press, W., A. Teukolsky, W. Vetterling, and B. Flannery (2002), Numerical Recipes in C: the Art of Scientific Computing, Cambridge Univ Press, Cambridge, U. K.

Pritchard, M. E., Norabuena, E. O., Ji, C., Boroschek, R., Comte, D., Simons, M., et al. (2007). Geodetic, teleseismic, and strong motion constraints on slip from recent southern Peru subduction zone earthquakes. *Journal of Geophysical Research: Solid Earth*, *112*(B3). https://doi.org/10.1029/2006JB004294

Qiu, Q., Moore, J. D. P., Barbot, S., Feng, L., & Hill, E. M. (2018). Transient rheology of the Sumatran mantle wedge revealed by a decade of great earthquakes. *Nature Communications*, *9*(1), 1–13. https://doi.org/10.1038/s41467-018-03298-6

Radiguet, M., Cotton, F., Vergnolle, M., Campillo, M., Valette, B., Kostoglodov, V., & Cotte, N. (2011). Spatial and temporal evolution of a long term slow slip event: the 2006 Guerrero Slow Slip Event. *Geophysical Journal International*, *184*(2), 816–828. https://doi.org/10.1111/j.1365-246X.2010.04866.x

Reath, K., Pritchard, M., Poland, M., Delgado, F., Carn, S., Coppola, D., et al. (2019). Thermal, deformation, and degassing remote sensing time series (CE 2000–2017) at the 47 most active volcanoes in Latin America: Implications for Volcanic Systems. Journal of Geophysical Research: Solid Earth, 124, 195–218. https://doi.org/10.1029/2018JB016199

Robinson, D. P., Das, S., & Watts, A. B. (2006), Earthquake rupture stalled by a subducting fracture zone. *Science, 312*(5777), 1203-1205. https://doi.org/10.1126/science.1125771

Rubin, A. M., Gillard, D., & Got, J.-L. (1999). Streaks of microearthquakes along creeping faults. *Nature*, *400*(6745), 635–641. https://doi.org/10.1038/23196

Scholz, C. H. (1990), The Mechanics of Earthquakes and Faulting, *Cambridge Univ. Press*, 413.

Shreve, T., Grandin, R., Smittarello, D., Cayol, V., Pinel, V., Boichu, M., & Morishita, Y. (2021). What Triggers Caldera Ring-Fault Subsidence at Ambrym Volcano? Insights From the 2015 Dike Intrusion and Eruption. *Journal of Geophysical Research: Solid Earth*, *126*(6), e2020JB020277. https://doi.org/10.1029/2020JB020277

Simons, M., Galetzka, J., Genrich, J. F., Ortega, F., Comte, D., Glass, B., et al. (2010). Central Andean Tectonic Observatory Geodetic Array [Dataset]. UNAVCO, Inc. https://doi.org/10.7283/T50P0X37

Sippl, C., Moreno, M., & Benavente, R. (2021). Microseismicity Appears to Outline Highly Coupled Regions on the Central Chile Megathrust. *Journal of Geophysical Research: Solid Earth*, *126*(11), e2021JB022252. https://doi.org/10.1029/2021JB022252

Sobolev, S. V., & Muldashev, I. A. (2017). Modeling Seismic Cycles of Great Megathrust Earthquakes Across the Scales With Focus at Postseismic Phase. *Geochemistry, Geophysics, Geosystems*, *18*(12), 4387–4408. https://doi.org/10.1002/2017GC007230

Socquet, A., & Norabuena, E. (2023). *EPOS-France - GPSMob data - Mission n° 15-265 - Pérou (2015) - 2015-10-22 / 2015-11-01 - 28 points* [Dataset]. OSU OREME. http://doi.org/10.15148/376F13E4-E333-4DA1-AA10-76F4EAE08FFC

Socquet, A., Cotte, N., Bondoux, F., & Norabuena, E. (2023a). *EPOS-France - GPSMob data - Mission n° 12-136b - Sud Pérou (2012) - 2012-06-23 / 2012-07-04 - 33 points* [Dataset]. OSU OREME. http://doi.org/10.15148/12160E27-0951-41B7-BE97-EFC4FEC7FF96

Socquet, A., Nocquet, J.-M., Norabuena, E., Villegas, J. C., & Chlieh, M. (2023b). *EPOS-France - GPSMob data - Mission n° 18-135 - Perou (2018) - 2018-11-02 / 2018-11-21 - 26 points* [Dataset]. OSU OREME. http://doi.org/10.15148/94CC6056-84D5-4C92-A043-6DB8B769BABF

Socquet, A., Norabuena, E., & Cotte, N. (2023c). *EPOS-France - GPSMob data - Mission n° 13-136 - Sud Pérou (2013) - 2013-06-08 / 2013-10-08 - 15 points* [Dataset]. OSU OREME. http://doi.org/10.15148/14AB8F86-3453-4A44-B921-EC3B0A133EF6

Socquet, A., Tsapong-Tsague, A., Lovery, B., Janex, G., Metois, M., & Radiguet, M. (2023d). Metadata and GNSS daily position solutions for permanent GNSS stations in South America [Dataset]. These datasets include station metadata and GNSS daily solutions for over 700 GNSS

612 stations in South America. CNRS, OSUG, ISTERRE.
613 https://doi.org/10.17178/GNSS.PRODUCTS.SOUTHAMERICA_GIPSYX.DAILY
614
615 Socquet, A., Villegas, J. C., Langlais, M., Doubre, C., Donniol, B., Costantino, G., Chouli, A., &
616 Jung, A. (2023e). *EPOS-France - GPSMob data - Mission n° 22-041 - Perou (2022) - 2022-03-*
617 *12 / 2022-08-07 - 70 points.* OSU OREME. [Dataset]. DOI: https://doi.org/10.15148/289f31dd-
618 9109-49ba-8116-5217191226e5
619
620 Socquet, A., Cresseaux, J., Lovery, B., Radiguet, M. (2024). Loading rate changes following
621 megathrust earthquakes explored with viscoelastic models. *AGU24*.
622
623 Springer, M. (1999). Interpretation of heat-flow density in the Central Andes. *Tectonophysics*,
624 *306*(3), 377–395. https://doi.org/10.1016/S0040-1951(99)00067-0
625
626 Sun, T., Wang, K., Iinuma, T., Hino, R., He, J., Fujimoto, H., et al. (2014). Prevalence of
627 viscoelastic relaxation after the 2011 Tohoku-oki earthquake. Nature, 514(7520), 84–87.
628 https://doi.org/10.1038/nature13778
629
630 Sun, T. and Wang, K. (2015), Viscoelastic relaxation following subduction earthquakes and its
631 effects on afterslip determination. *J. Geophys. Res. Solid Earth*, 120: 1329–1344.
632 https://doi.org/10.1002/2014JB011707
633
634 Sun, T., Wang, K., & He, J. (2018). Crustal Deformation Following Great Subduction Earthquakes
635 Controlled by Earthquake Size and Mantle Rheology. *Journal of Geophysical Research: Solid*
636 *Earth*, *123*(6), 5323–5345. https://doi.org/10.1029/2017JB015242
637
638 Tarantola, A., & Valette, B. (1982). Generalized nonlinear inverse problems solved using the least
639 squares criterion. *Reviews of Geophysics*, *20*(2), 219–232.
640 https://doi.org/10.1029/RG020i002p00219
641
642 Tassara, A., Götze, H.-J., Schmidt, S., & Hackney, R. (2006). Three-dimensional density model
643 of the Nazca plate and the Andean continental margin. *Journal of Geophysical Research: Solid*
644 *Earth*, *111*(B9). https://doi.org/10.1029/2005JB003976
645
646 Tassara, A., & Echaurren, A. (2012). Anatomy of the Andean subduction zone: three-dimensional
647 density model upgraded and compared against global-scale models: Anatomy of the Andean
648 subduction zone. *Geophysical Journal International*, *189*(1), 161–168.
649 https://doi.org/10.1111/j.1365-246X.2012.05397.x
650
651 Trubienko, O., Fleitout, L., Garaud, J.-D., & Vigny, C. (2013). Interpretation of interseismic
652 deformations and the seismic cycle associated with large subduction earthquakes. In
653 Tectonophysics (Vol. 589, pp. 126–141). Elsevier BV. https://doi.org/10.1016/j.tecto.2012.12.027
654
655 Villegas-Lanza, J. C., Chlieh, M., Cavalié, O., Tavera, H., Baby, P., Chire-Chira, J., & Nocquet,
656 J.-M. (2016). Active tectonics of Peru: Heterogeneous interseismic coupling along the Nazca
657 megathrust, rigid motion of the Peruvian Sliver, and Subandean shortening accommodation.

Journal of Geophysical Research: Solid Earth, *121*(10), 7371–7394. https://doi.org/10.1002/2016JB013080

Wada, I., & Wang, K. (2009). Common depth of slab-mantle decoupling: Reconciling diversity and uniformity of subduction zones. In Geochemistry, Geophysics, Geosystems (Vol. 10, Issue 10). American Geophysical Union (AGU). https://doi.org/10.1029/2009gc002570

Wang, K., Hu, Y., Bevis, M., Kendrick, E., Smalley Jr., R., Vargas, R. B., & Lauría, E. (2007). Crustal motion in the zone of the 1960 Chile earthquake: Detangling earthquake-cycle deformation and forearc-sliver translation. *Geochemistry, Geophysics, Geosystems*, *8*(10). https://doi.org/10.1029/2007GC001721

Wang, K., Hu, Y. & He, J. (2012). Deformation cycles of subduction earthquakes in a viscoelastic Earth. *Nature* 484, 327–332. https://doi.org/10.1038/nature11032

Wessel, P., Luis, J. F., Uieda, L., Scharroo, R., Wobbe, F., Smith, W. H. F., & Tian, D. (2019), The Generic Mapping Tools version 6. *Geochemistry, Geophysics, Geosystems*, 20, 5556–5564. https://doi.org/10.1029/2019GC008515

References From the Supporting Information

Aagaard, B.T.; Knepley, M.G.; Williams, C.A. (2013), A domain decomposition approach to implementing fault slip in finite-element models of quasi-static and dynamic crustal deformation, *Journal of Geophysical Research: Solid Earth, 118 (6)*, 3059-3079. https://doi.org/10.1002/jgrb.50217

Abers, G. A., van Keken, P. E., & Hacker, B. R. (2017). The cold and relatively dry nature of mantle forearcs in subduction zones. Nature Geoscience, 10(5), 333–337. https://doi.org/10.1038/ngeo2922

Altamimi, Z., Rebischung, P., Métivier, L., & Collilieux, X. (2016). ITRF2014: A new release of the International Terrestrial Reference Frame modeling nonlinear station motions. *Journal of Geophysical Research: Solid Earth*, *121*(8), 6109–6131. https://doi.org/10.1002/2016JB013098

Angiboust, S., Menant, A., Gerya, T., & Oncken, O. (2022). The rise and demise of deep accretionary wedges: A long-term field and numerical modeling perspective. *Geosphere*, *18*(1), 69–103. https://doi.org/10.1130/GES02392.1

Bertiger, W., Bar-Sever, Y., Dorsey, A., Haines, B., Harvey, N., Hemberger, D., et al. (2020). GipsyX/RTGx, a new tool set for space geodetic operations and research. *Advances in Space Research*, *66*(3), 469–489. https://doi.org/10.1016/j.asr.2020.04.015

Bevis, M., & Brown, A. (2014). Trajectory models and reference frames for crustal motion geodesy. *Journal of Geodesy*, *88*(3), 283–311. https://doi.org/10.1007/s00190-013-0685-5

Blewitt, G., Kreemer, C., Hammond, W. C., & Gazeaux, J. (2016). MIDAS robust trend estimator for accurate GPS station velocities without step detection. *Journal of Geophysical Research: Solid Earth*, *121*(3), 2054–2068. https://doi.org/10.1002/2015JB012552

Boulze, H., Fleitout, L., Klein, E., & Vigny, C. (2022). Post-seismic motion after 3 Chilean megathrust earthquakes: a clue for a linear asthenospheric viscosity. *Geophysical Journal International*, *231*(3), 1471–1478. https://doi.org/10.1093/gji/ggac255

Chlieh, M., Perfettini, H., Tavera, H., Avouac, J.-P., Remy, D., Nocquet, J.-M., et al. (2011). Interseismic coupling and seismic potential along the Central Andes subduction zone. *Journal of Geophysical Research: Solid Earth*, *116*(B12). https://doi.org/10.1029/2010JB008166

Dziewonski, A. M., Chou, T. A., & Woodhouse, J. H., (1981), Determination of earthquake source parameters from waveform data for studies of global and regional seismicity, *J. Geophys. Res.*, *86*, 2825-2852. https://doi.org/10.1029/JB086iB04p02825

Ekström, G., Nettles, M., & Dziewoński, A. M. (2012). The global CMT project 2004–2010: Centroid-moment tensors for 13,017 earthquakes. *Physics of the Earth and Planetary Interiors*, *200–201*, 1–9. https://doi.org/10.1016/j.pepi.2012.04.002

Fang, R., Lv, H., Shu, Y., Zheng, J., Zhang, K., & Liu, J. (2021). Improved performance of GNSS precise point positioning for high-rate seismogeodesy with recent BDS-3 and Galileo. In Advances in Space Research (Vol. 68, Issue 8, pp. 3255–3267). Elsevier BV. https://doi.org/10.1016/j.asr.2021.06.012

Gao, Y., Tilmann, F., van Herwaarden, D.-P., Thrastarson, S., Fichtner, A., Heit, B., et al. (2021). Full Waveform Inversion Beneath the Central Andes: Insight Into the Dehydration of the Nazca Slab and Delamination of the Back-Arc Lithosphere. *Journal of Geophysical Research: Solid Earth*, *126*(7), e2021JB021984. https://doi.org/10.1029/2021JB021984

Hayes, G. P., Moore, G. L., Portner, D. E., Hearne, M., Flamme, H., Furtney, M., & Smoczyk, G. M. (2018). Slab2, a comprehensive subduction zone geometry model. *Science*, *362*(6410), 58–61. https://doi.org/10.1126/science.aat4723

Hoffmann, F., Metzger, S., Moreno, M., Deng, Z., Sippl, C., Ortega-Culaciati, F., & Oncken, O. (2018). Characterizing Afterslip and Ground Displacement Rate Increase Following the 2014 Iquique-Pisagua Mw 8.1 Earthquake, Northern Chile. *Journal of Geophysical Research: Solid Earth*, *123*(5), 4171–4192. https://doi.org/10.1002/2017JB014970

Itoh, Y., Wang, K., Nishimura, T., & He, J. (2019). Compliant Volcanic Arc and Backarc Crust in Southern Kurile Suggested by Interseismic Geodetic Deformation. *Geophysical Research Letters*, *46*(21), 11790–11798. https://doi.org/10.1029/2019GL084656

Kositsky, A. P., & Avouac, J.-P. (2010). Inverting geodetic time series with a principal component analysis-based inversion method. *Journal of Geophysical Research: Solid Earth*, *115*(B3). https://doi.org/10.1029/2009JB006535

Li, S., Moreno, M., Bedford, J., Rosenau, M., & Oncken, O. (2015). Revisiting viscoelastic effects on interseismic deformation and locking degree: A case study of the Peru-North Chile subduction zone. *Journal of Geophysical Research: Solid Earth*, *120*(6), 4522–4538. https://doi.org/10.1002/2015JB011903

Li, S., Bedford, J., Moreno, M., Barnhart, W. D., Rosenau, M., & Oncken, O. (2018). Spatiotemporal variation of mantle viscosity and the presence of cratonic mantle inferred from 8 years of postseismic deformation following the 2010 Maule, Chile, earthquake. *Geochemistry, Geophysics, Geosystems*, 19, 3272–3285. https://doi.org/10.1029/2018GC007645

Li, S., & Chen, L. (2024). Revisiting interseismic deformation in Nankai: focusing on slip-deficit accumulation in the ETS zone and comparison with Cascadia. *Earth, Planets and Space*, *76*(1), 108. https://doi.org/10.1186/s40623-024-02054-z

Lin, Y. N., Kositsky, A. P., and Avouac, J.-P. (2010). PCAIM joint inversion of InSAR and ground-based geodetic time series: Application to monitoring magmatic inflation beneath the Long Valley Caldera, Geophys. Res. Lett., 37, L23301, https://doi.org/10.1029/2010GL045769

Lovery, B., Chlieh, M., Norabuena, E., Villegas-Lanza, J. C., Radiguet, M., Cotte, N., et al. (2024a). Heterogeneous locking and earthquake potential on the South Peru megathrust from dense GNSS network. *Journal of Geophysical Research: Solid Earth*, 129, e2023JB027114. https://doi.org/10.1029/2023JB027114

Luo, H., Wang, K. Postseismic geodetic signature of cold forearc mantle in subduction zones. *Nat. Geosci.* 14, 104–109 (2021). https://doi.org/10.1038/s41561-020-00679-9

Marill, L., Marsan, D., Socquet, A., Radiguet, M., Cotte, N., & Rousset, B. (2021). Fourteen-Year Acceleration Along the Japan Trench. *Journal of Geophysical Research: Solid Earth*, *126*(11), e2020JB021226. https://doi.org/10.1029/2020JB021226

Peña, C., Metzger, S., Heidbach, O., Bedford, J., Bookhagen, B., Moreno, M., et al. (2022). Role of poroelasticity during the early postseismic deformation of the 2010 Maule megathrust earthquake. Geophysical Research Letters, 49, e2022GL098144. https://doi.org/10.1029/2022GL098144

Press, W., A. Teukolsky, W. Vetterling, and B. Flannery (2002), Numerical Recipes in C: the Art of Scientific Computing, Cambridge Univ Press, Cambridge, U. K.

Radiguet, M., Cotton, F., Vergnolle, M., Campillo, M., Valette, B., Kostoglodov, V., & Cotte, N. (2011). Spatial and temporal evolution of a long term slow slip event: the 2006 Guerrero Slow Slip Event. *Geophysical Journal International*, *184*(2), 816–828. https://doi.org/10.1111/j.1365-246X.2010.04866.x

Socquet, A., Cresseaux, J., Lovery, B., Radiguet, M. (2024). Loading rate changes following megathrust earthquakes explored with viscoelastic models. *AGU24*.

Sun, T. and Wang, K. (2015), Viscoelastic relaxation following subduction earthquakes and its effects on afterslip determination. *J. Geophys. Res. Solid Earth*, 120: 1329–1344. https://doi.org/10.1002/2014JB011707

Sun, T., Wang, K., & He, J. (2018). Crustal Deformation Following Great Subduction Earthquakes Controlled by Earthquake Size and Mantle Rheology. *Journal of Geophysical Research: Solid Earth*, *123*(6), 5323–5345. https://doi.org/10.1029/2017JB015242

Tarantola, A., & Valette, B. (1982). Generalized nonlinear inverse problems solved using the least squares criterion. *Reviews of Geophysics*, *20*(2), 219–232. https://doi.org/10.1029/RG020i002p00219

Tozer, B, Sandwell, D. T., Smith, W. H. F., Olson, C., Beale, J. R., & Wessel, P. (2019). Global bathymetry and topography at 15 arc sec: SRTM15+. *Earth and Space Science*, 6, 1847–1864. https://doi.org/10.1029/2019EA000658

Trubienko, O., Fleitout, L., Garaud, J.-D., & Vigny, C. (2013). Interpretation of interseismic deformations and the seismic cycle associated with large subduction earthquakes. In Tectonophysics (Vol. 589, pp. 126–141). Elsevier BV. https://doi.org/10.1016/j.tecto.2012.12.027

Wada, I., & Wang, K. (2009). Common depth of slab-mantle decoupling: Reconciling diversity and uniformity of subduction zones. In Geochemistry, Geophysics, Geosystems (Vol. 10, Issue 10). American Geophysical Union (AGU). https://doi.org/10.1029/2009gc002570

Wang, K., Hu, Y. & He, J. (2012). Deformation cycles of subduction earthquakes in a viscoelastic Earth. *Nature* 484, 327–332. https://doi.org/10.1038/nature11032

Wang, Y., Wang, K., He, J., & Zhang, L. (2023). On unusual conditions for the exhumation of subducted oceanic crustal rocks: How to make rocks hotter than models. *Earth and Planetary Science Letters*, *615*, 118213. https://doi.org/10.1016/j.epsl.2023.118213

5.2 Supplements

Geophysical Research Letters

Supporting Information for

Viscoelastic Relaxation Following the 2001 Mw8.4 Arequipa Earthquake and its Impact on the Interseismic Coupling of the South Peru Megathrust

B. Lovery[1], M. Radiguet[1], M. Chlieh[1], E. Norabuena[2], J.C. Villegas-Lanza[2], J. Cresseaux[1], T. Ragon[1], A. Tsapong-Tsague[1], H. Tavera[2], and A. Socquet[1]

[1]Univ. Grenoble Alpes, Univ. Savoie Mont Blanc, CNRS, IRD, Univ. Gustave Eiffel, ISTerre, 38000 Grenoble, France

[2]Instituto Geofísico del Perú, Lima, Peru

Contents of this file

Texts S1 to S6
Figures S1 to S24
Tables S1 to S3

The meshing has been performed using the software CUBIT 2023.4 from Coreform, while we use the open-source PyLith v2.2.2 software (Aagaard et al., 2013) to solve the problem. We use tetrahedral cells, going from a 5-km resolution close to the fault and the GNSS stations, to a 100-km resolution at the external boundaries of the model. The mesh is 2,000 by 2,000-km wide and 1,000-km deep, Dirichlet boundary conditions are applied at the external boundaries. Slab contours are derived from the Slab2 model (Hayes et al., 2018), while topography and bathymetry come from SRTM15+ (Tozer et al., 2019).

Text S1: Technical details about the FEM model and meshing.

GNSS data were processed at ISTerre by Precise Point Positioning (PPP) using the GipsyX software v1.5 from the Jet Propulsion Laboratory (Bertiger et al., 2020) and expressed in the ITRF2014 reference frame (Altamimi et al., 2016) using the strategy described in Lovery et al. (2024a) (Figure S5). For the continuous station, we applied a trajectory model (Bevis & Brown, 2014) using the ITSA software (Marill et al., 2021) to correct for coseismic displacements (other than the Arequipa earthquake) and seasonal variations. For survey sites, we removed the contribution from coseismic and postseismic slip related to the 2014 Iquique seismic sequence (Mw8.1 mainshock and Mw7.7 aftershock) modelled in Lovery et al. (2024a). We also corrected for the seasonal displacements at each sGNSS site using the approach from Hoffman et al. (2018) and Lovery et al. (2024a). The AYRO site (measured between 1994 and 2014) was located at only 9 km from the cGNSS site PALC, installed in 2012, so we tied the two timeseries in order to have a timeseries covering the 1994-2022 period (cf. Figures S2 and S3). Measurement at LMPA and PNAS sites ended in 2001, so we tied their timeseries with the cGNSS timeseries PU02 (2010-2017, 28 km from LMPA) and PU03 (2013-2023, 64 km from PNAS) respectively. Unlike AYRO, there was no temporal overlap between LMPA and PU02, and between PNAS and PU03, so they are merged with a step in order to maintain continuity (cf. Figures S2 and S5).

Text S2: GNSS data processing.

The viscoelastic behavior can be modelled by a Maxwell fluid composed of an elastic spring and a viscous damper in series, for which the stress σ and the strain ε are linked by the equation

$$\frac{\dot{\boldsymbol{\sigma}}}{\mathbf{E_M}} + \frac{\boldsymbol{\sigma}}{\boldsymbol{\eta_M}} = \dot{\boldsymbol{\varepsilon}}$$

with E_M and η_M the Maxwell Young's modulus and viscosity.

While a Kelvin solid composed of an elastic spring and a viscous damper in parallel would behaves as

$$\boldsymbol{\sigma} = \mathbf{E_K}\boldsymbol{\varepsilon} + \boldsymbol{\eta_K}\dot{\boldsymbol{\varepsilon}}$$

with E_K and η_K the Kelvin Young's modulus and viscosity.

When we link these two bodies together, we obey a bi-viscous Burgers rheology, applied to subduction zones by various authors (Boulze et al., 2022; Li et al., 2018; Li & Chen, 2024; Sun & Wang, 2015; Wang et al., 2012), with two characteristic times given by the Maxwell and Kelvin viscosities and Young's moduli:

$$\boldsymbol{\sigma} + \left(\frac{\boldsymbol{\eta_K}}{\mathbf{E_K}} + \frac{\boldsymbol{\eta_M}}{\mathbf{E_K}} + \frac{\boldsymbol{\eta_M}}{\mathbf{E_M}}\right)\dot{\boldsymbol{\sigma}} + \frac{\boldsymbol{\eta_K}\boldsymbol{\eta_M}}{\mathbf{E_K}\mathbf{E_M}}\ddot{\boldsymbol{\sigma}} = \boldsymbol{\eta_M}\dot{\boldsymbol{\varepsilon}} + \frac{\boldsymbol{\eta_K}\boldsymbol{\eta_M}}{\mathbf{E_K}}\ddot{\boldsymbol{\varepsilon}}$$

Text S3: Explanation about Maxwell and Burgers rheology.

Figure 3 displays the fit to the GNSS timeseries for various rheological structures, with viscosities optimized based on root mean square error (RMSE) (cf. Figures S10 and S11). First, we consider a Maxwell rheology (cf. Text S3) with a viscosity $\eta_M = 1 \cdot 10^{19}$ Pa.s (Figure 3, green curve). While this model provides a good fit to the horizontal data on the long-term, it is at the cost of a poor fit on the short to mid-term (2001-2012). Consequently, we introduced a bi-viscous Burgers rheology. Using this Burgers rheology in the asthenosphere (40-200 km depth) with a Maxwell viscosity $\eta_M = 9 \cdot 10^{18}$ Pa.s and a Kelvin viscosity $\eta_K = 5 \cdot 10^{18}$ Pa.s (Figure 3, orange curve) gives a better fit to the horizontal component over the entire timeseries (RMS = 0.023 vs. 0.040 for the previous model). As we are especially interested in modeling the last decade, we prioritize the long-term fit (2012-2024) at the expense of the short-term. In the mantle (200-1,000 km depth) we maintain a simple Maxwell rheology $\eta_M = 5 \cdot 10^{20}$ Pa.s. Considering the striking evidence for a stagnant cold-nose on most subduction zones, including along the Peru-Chile subduction (Angiboust et al., 2022; Gao et al., 2021; Li & Chen, 2024; Luo & Wang, 2021; Sun & Wang, 2015; Wada & Wang, 2009; Wang et al., 2023), we add an elastic cold-nose to our model down to 85 km depth. It lowers the RMS (0.013 vs 0.023) and it generates postseismic uplift (Figure 3, blue curve). This cold-nose may be partially serpentinized (Abers et al., 2017). We performed a F-test (Peña et al., 2022), showing that the variance reductions associated with the introduction of Burgers rheology and cold-nose are significant (Text S5).

Using the Burgers model described above with an elastic cold-nose, we obtain a very good fit at AREQ on the horizontal component (RMS = 0.007), as well as a relatively good fit at AYRO, BAJO, JHAI, LMPA, and POCO (RMS = 0.013). The fit at CMOR, PNAS, and TANA is less satisfying (RMS = 0.02), but it may be related to a bad constraint on the pre-seismic velocity used for detrending. To assess the uncertainties associated to the detrending, we computed the 3σ uncertainties on the pre-earthquake GNSS velocity using the MIDAS software (Blewitt et al., 2016), the effect of these uncertainties on the post-earthquake velocity is reported on Figure 3 by gray dots, it shows that the slope is relatively poorly constrained at sGNSS. In addition, the displacements at these sites are significantly smaller, which could lead to a proportionally higher misfit. Early GNSS measurements from the nineties are also expected to be less stable (Fang et al., 2021). Our optimal value for the long-term Maxwell viscosity in the asthenosphere (cf. Figures S10 and S11), $9 \cdot 10^{18}$ Pa.s (RMS = 0.013 vs. 0.019 for $8 \cdot 10^{18}$ Pa.s vs. 0.018 for $1 \cdot 10^{19}$ Pa.s) is similar to Wang et al. (2012) who reported viscosities in the order of 1.10^{19} Pa.s at subduction

zones, as well as Li et al. (2018) on the volcanic arc in Chile. Socquet et al. (2024) found a viscosity of $2 \cdot 10^{19}$ Pa.s for the area surrounding the 2014 Mw8.1 Iquique earthquake. It is also within the 0.5-$3 \cdot 10^{19}$ Pa.s range reported by Trubienko et al. (2013) for large subduction earthquakes in Indonesia and Tohoku. Sun et al. (2018) found a slightly lower viscosity of $5 \cdot 10^{18}$ Pa.s for the Arequipa earthquake, but on a shorter timescale (12 vs. 23 years) and neglecting afterslip. On Figure S12 is reported the misfit depending on cold-nose edge depth and continental elastic layer thickness.

Text S4: Detailed explanation on the various models tested to accommodate the postseismic displacements.

Following the methodology described in Peña et al. (2022), we performed a F-test to check if the variance reduction induced by the adjunction of an additional parameter in the model is statically significant (Lin et al., 2010; Press et al., 2002). We compared the Burgers model (model B) against the Maxwell model (model A), and the Burgers model with cold-nose (model C) against the Burgers model without cold-nose (model B). First, we compute the F-values using the following formulation:

$$\mathrm{F} = \frac{(S_1^2 - S_2^2) \times df_2}{(df_1 - df_2) \times S_2^2}$$

with S_1^2 and S_2^2 the residual sum of the squares of the model with fewer and higher parameters respectively. df_1 and df_2 are the associated degrees of freedom, expressed as N – P with N the number of data samples and P the number of model parameters. Then, the p-values, expressing the probability that the variance reduction is due to chance, are computed using the routine scipy.stats.f, and the test is considered successful (i.e. the variance reduction is statically significant) when $p < 0.05$.

- Burgers model vs. Maxwell model:

  $df_1(A) = N - P = 9 - 1 = 8$
  $df_2(B) = N - P = 9 - 2 = 7$

  $$F = \frac{(0.5^2 - 0.2^2) \times 7}{(8-7) \times 0.2^2} = 36.75$$

  → $p = 4.9 \cdot 10^{-5} < 0.05$ → the test is successful

- Burgers model with cold-nose vs. Burgers model without cold-nose:

  $df_1(B) = N - P = 9 - 2 = 7$
  $df_2(C) = N - P = 9 - 3 = 6$

  $$F = \frac{(0.2^2 - 0.14^2) \times 6}{(7-6) \times 0.14^2} = 6.24$$

  → $p = 0.02 < 0.05$ → the test is successful

Text S5: F-test on variance reduction.

Both the postseismic and the interseismic simulations were performed using viscoelastic rheology. For the interseismic inversion, we use viscoelastic Green's functions instead of pure elastic ones as was done in Lovery et al. (2024a). We used a similar approach to what is described in Li et al. (2015). To compute the viscoelastic Green's functions, we run individual PyLith simulations for each patch of the fault (6,008 patches) with a unit coseismic slip, both in dip-slip and in strike-slip (12,016 simulations in total). The structure and rheology are the same as for our prefered postseismic model. The simulations are run for 200 years in order to get fully-relaxed Green's functions (cf. Figure S14).

The displacement computed 200 years after the simulated coseismic slip at the location of the 73 GNSS sites used to build the Green's function matrix *G.* The *G* matrix is linking the matrix *d* of surface displacements with the matrix *m* of slip rate on the fault:

$$d = G \cdot m$$

The viscoelastic *G* matrix is then used to invert for the interseismic coupling with the PCAIM software (Kositsky & Avouac, 2010) and a Tarantola-Valette inversion scheme (Radiguet et al., 2011; Tarantola & Valette, 1982). A comparison of the interseismic coupling model with viscoelastic Green's functions against pure elastic Green's functions, also generated with PyLith using the same mesh and elastic parameters, is shown on Figure S15. Larger displacements in the far-field are observed with viscoelastic Green's functions, as already reported by other studies over various areas (Itoh et al., 2019; Li et al., 2015 & 2018).

Text S6: Technical details about the computation of viscoelastic Green's functions.

Body	Rheology	Depth (km)	Shear modulus μ (GPa)	Maxwell shear modulus	Kelvin shear modulus	Maxwell viscosity (Pa.s)	Kelvin viscosity (Pa.s)
Oceanic elastic layer	elastic	0 – 40	59	-	-	-	-
Continental elastic layer	elastic	0 – 30	59	-	-	-	-
Cold-nose	- / - / elastic / Maxwell	30 – 85	70	- / - / - / $\frac{2}{3}\mu$	- / - / - / $\frac{1}{3}\mu$	- / - / - / 1.10^{19}	-
Oceanic asthenosphere	Maxwell / Burgers / Burgers / Burgers	40 – 200	70	- / $\frac{2}{3}\mu$ / $\frac{2}{3}\mu$ / $\frac{2}{3}\mu$	- / $\frac{1}{3}\mu$ / $\frac{1}{3}\mu$ / $\frac{1}{3}\mu$	1.10^{20} / 9.10^{19} / 9.10^{19} / 9.10^{19}	- / 5.10^{19} / 5.10^{19} / 5.10^{19}
Continental asthenosphere	Maxwell / Burgers / Burgers / Burgers	30 – 200	70	- / $\frac{2}{3}\mu$ / $\frac{2}{3}\mu$ / $\frac{2}{3}\mu$	- / $\frac{1}{3}\mu$ / $\frac{1}{3}\mu$ / $\frac{1}{3}\mu$	1.10^{19} / 9.10^{18} / 9.10^{18} / 9.10^{18}	- / 5.10^{18} / 5.10^{18} / 5.10^{18}
Mantle	Maxwell	200 – 1,000	105 - 294	μ	-	5.10^{20}	-

Table S1: Viscoelastic properties of the various blocks for the four models displayed on Figure 3: Maxwell model / Burgers model / Burgers model with elastic cold-nose / Burgers model with viscoelastic cold-nose.

Site	1994	1996	1999	2001	2009	2012	2013	2014	2015	2016	2018	2022	Tied cGNSS data
AYRO	•	•	•	•				•					2011-2022
BAJO	•	•	•	•		•		•					
CMOR	•	•	•	•	•	•		•	•	•	•	•	
JHAI	•	•	•	•	•	•					•		
LMPA	•	•	•	•									2010-2017
PNAS	•	•	•	•									2013-2023
POCO	•	•		•	•	•		•		•	•	•	
TANA	•	•		•		•	•		•		•	•	

Table S2: Survey GNSS sites used in the study, with their respective measurement years. When survey GNSS timeseries are tied with continuous GNSS timeseries (cf. Text S2), the timespan of the latter is indicated in the last column.

Site	Longitude	Latitude	East (mm)	North (mm)	Up (mm)
AMOQ	-71.55	-17.25	-2.48	-2.30	1.47
ANTE	-71.05	-17.47	-2.23	-1.92	1.54
AQ02	-72.02	-17.03	-3.00	-2.57	1.49
AQ03	-72.49	-16.08	-2.67	-1.64	1.85
AQUC	-72.44	-16.52	-2.47	-1.78	1.20
ATIC	-73.70	-16.23	-0.98	-0.39	0.05
BAJO	-70.35	-16.95	-3.33	-1.61	1.05
BASU	-74.02	-16.00	-0.68	-0.22	0.01
CALA	-73.27	-16.32	-1.32	-0.69	0.17
CATA	-72.04	-17.02	-2.42	-2.12	1.12
CBRO	-71.79	-17.00	-3.78	-3.28	2.49
CERI	-70.64	-15.69	-3.30	-2.06	-0.21
CHRA	-72.93	-16.52	-1.79	-1.13	0.42
CLEM	-71.17	-17.28	-2.55	-2.20	1.95
CMOR	-70.66	-18.05	-1.59	-1.35	0.76
COLL	-69.08	-16.60	-2.93	-1.07	-0.20
COND	-69.68	-16.57	-3.78	-1.57	-0.33
CRMA	-72.30	-16.47	-2.74	-1.98	1.63
CRVL	-73.43	-15.76	-1.27	-0.51	0.24
GORD	-72.68	-16.64	-1.97	-1.39	0.55
GUER	-72.01	-16.81	-2.79	-2.30	1.74
JHAI	-72.86	-16.52	-1.95	-1.25	0.52
MADG	-71.83	-15.60	-2.69	-1.71	1.52
POCO	-71.37	-17.43	-2.26	-2.16	1.28
PU02	-70.18	-15.51	-4.23	-2.60	-0.63
PU03	-69.09	-16.24	-2.39	-1.02	-0.25
PUNO	-69.98	-15.86	-3.38	-1.84	-0.49
QCA2	-72.43	-16.72	-1.95	-1.51	0.75
QUER	-72.49	-16.16	-2.57	-1.63	1.72
SJUN	-70.86	-16.97	-2.68	-1.75	2.10
TAMB	-71.56	-17.07	-2.75	-2.44	2.01
TANA	-74.45	-15.75	-0.48	-0.08	-0.02
TUPA	-69.70	-17.00	-2.78	-1.07	0.16

Table S3: Velocity corrections associated with the postseismic processes during the observation period of the GNSS network used for interseismic coupling assessment (~2012-2023), at each GNSS sites used for interseismic coupling assessment (cf. Figure S17).

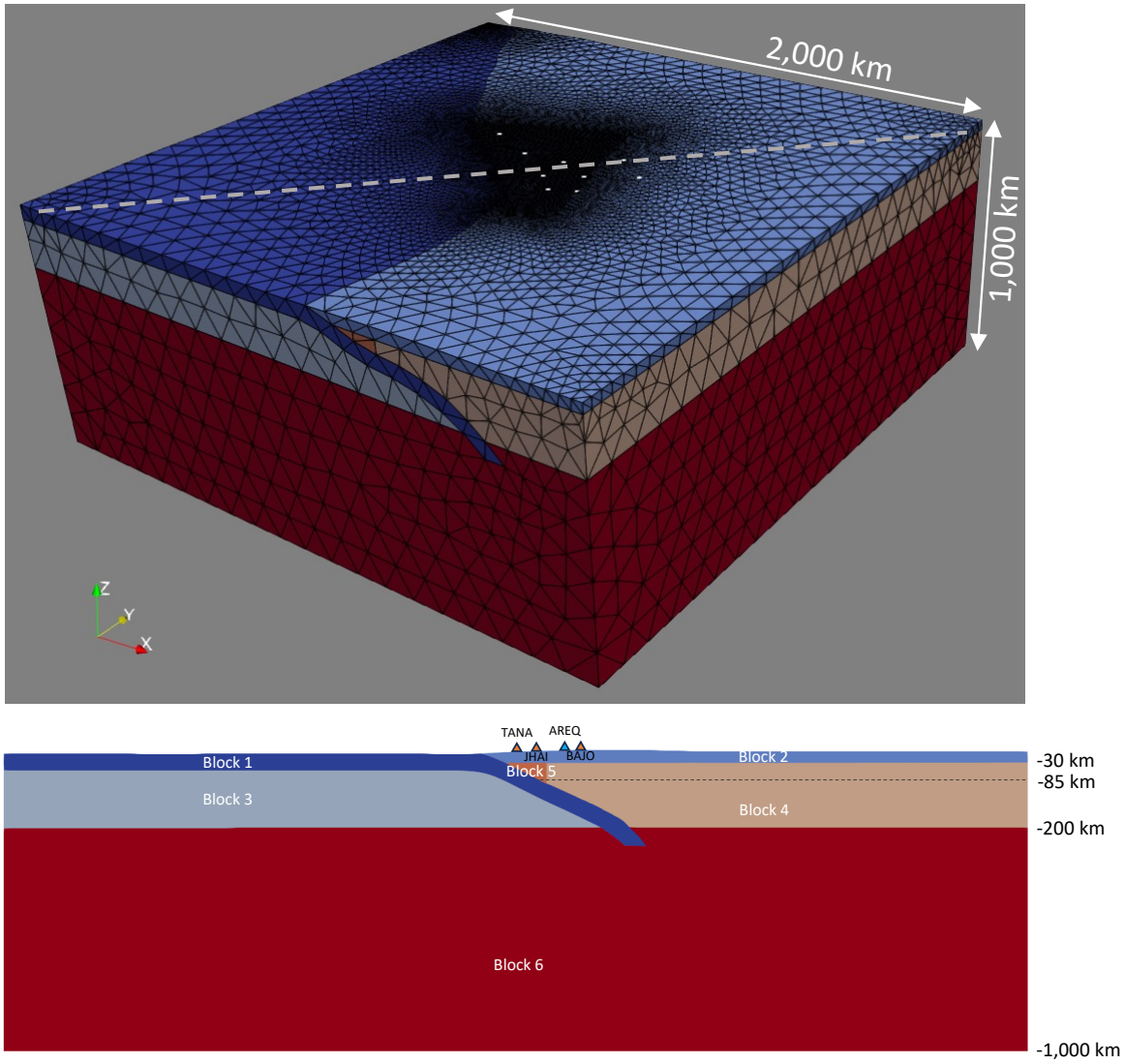

Figure S1: *Top:* 3-D FEM model of the subduction zone in Southern Peru and Northern Chile. The slab is shaped by the Slab2 contours (Hayes et al., 2018), while bathymetry and topography come from SRTM15+ (Tozer et al., 2019). The mesh is 2,000 by 2,000-km wide and 1,000-km deep, using tetrahedral geometry. The cells are 5-km large close to the fault and the GNSS stations, and up to 100-km large at the external boundaries. The dashed gray line indicates the location of the slicing. *Bottom:* Slicing of the 3-D FEM model of the subduction zone, passing by Arequipa city on the full-size mesh. The locations of the GNSS sites are indicated by the orange (sGNSS) and blue (cGNSS) triangles. The model is composed of six blocks: oceanic elastic layer (block 1), continental elastic layer (block 2), ocean asthenosphere (block 3), continental asthenosphere (block 4), cold-nose (block 5), and mantle (block 6). Zoomed-in representation is showed on Figure 2.

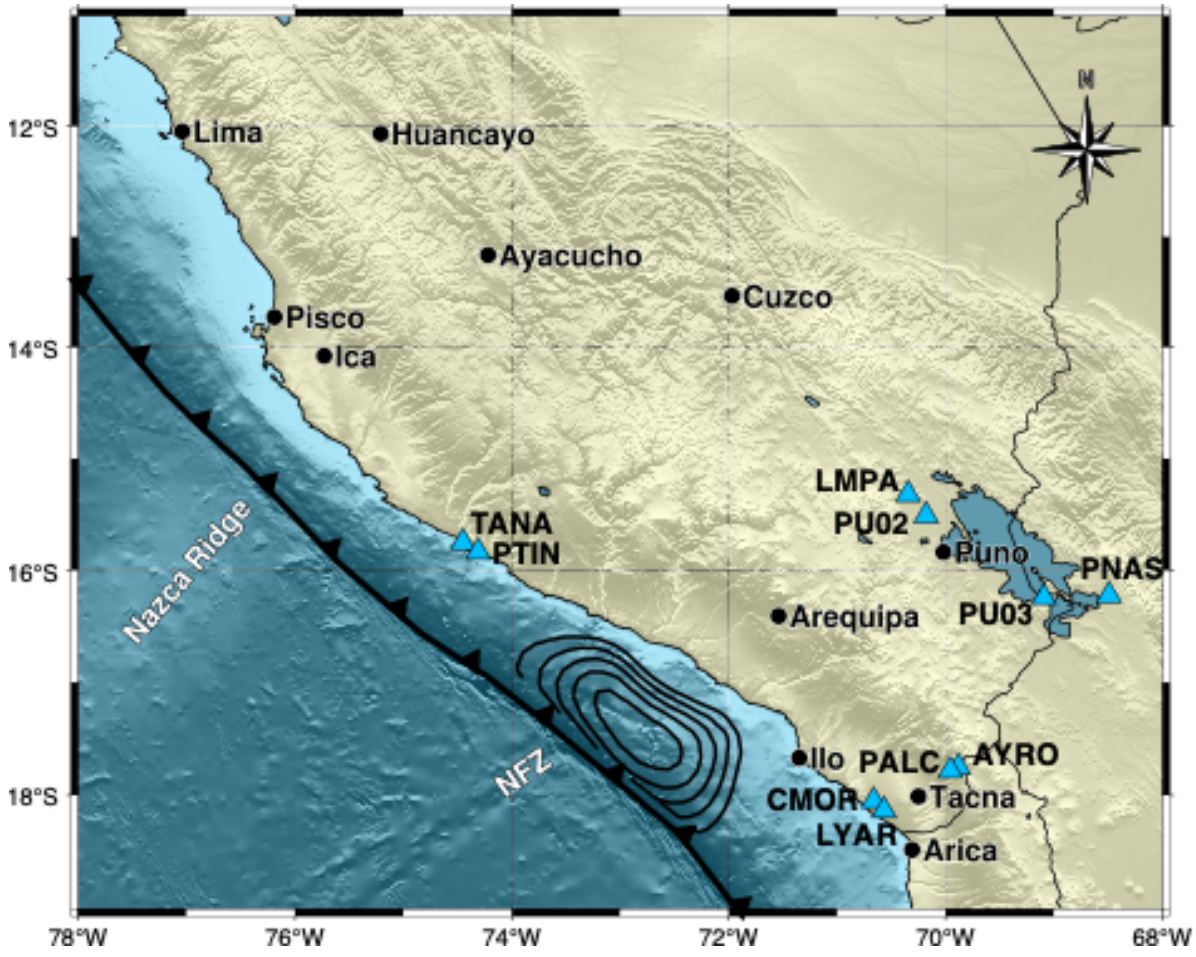

Figure S2: Location of sGNSS sites (AYRO, CMOR, LMPA, PNAS, and TANA) and nearby cGNSS sites (PALC, LYAR, PU02, PU03, and PTIN) shown by blue triangles. The approximate rupture area of the 2001 Mw8.4 Arequipa earthquake is reported by the black 1-m slip contours. Black dots indicate the main cities.

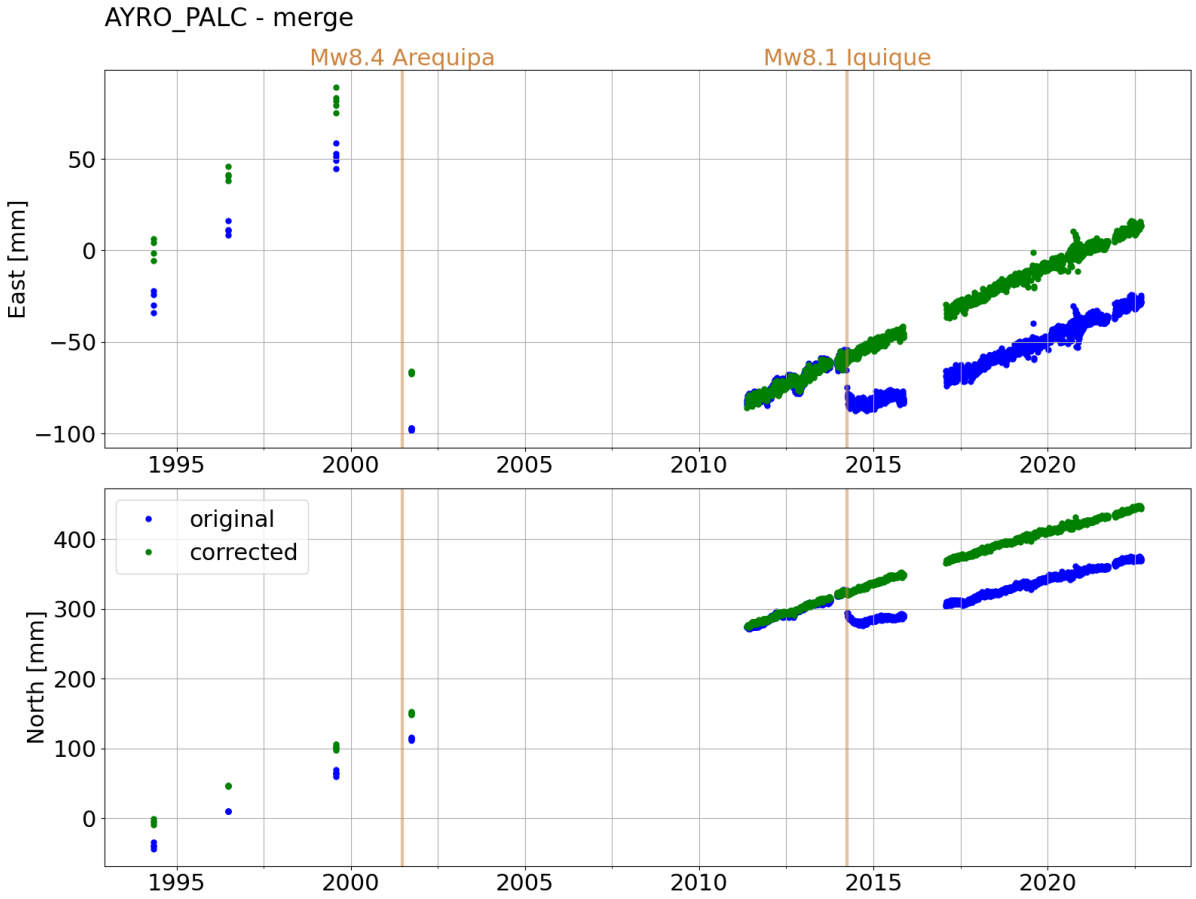

Figure S3: *Top:* Displacement timeseries at sGNSS site AYRO, merged with cGNSS site PALC. Original daily GNSS solutions are displayed as blue dots, and solutions corrected from coseismic and postseismic displacements related to the 2014 Mw8.1 Iquique earthquake and seasonal variations as green dots. Epochs corresponding to the 2001 Mw8.4 Arequipa and 2014 Mw8.1 Iquique earthquakes are depicted by yellow vertical lines.

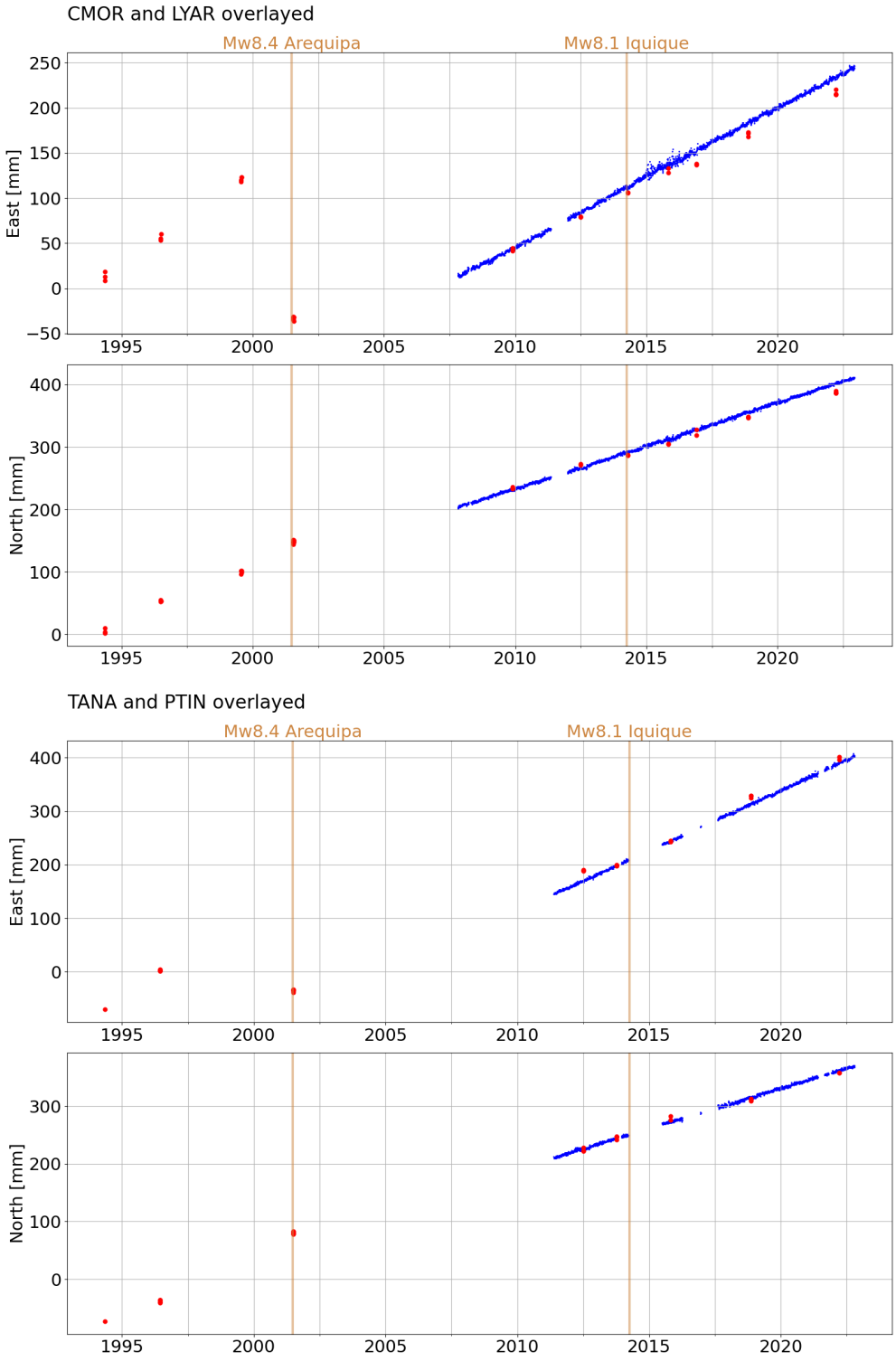

Figure S4: *Top:* Displacement timeseries at sGNSS site CMOR after correcting from coseismic and postseismic displacements related to the 2014 Mw8.1 Iquique earthquake, and accounting for seasonal variations, compared to nearby cGNSS site LYAR. Daily sGNSS and cGNSS solutions are displayed as red and blue dots respectively. Epochs corresponding to the 2001 Mw8.4 Arequipa and 2014 Mw8.1 Iquique earthquakes are depicted by yellow vertical lines. *Bottom:* The same with sGNSS site TANA and nearby cGNSS site PTIN.

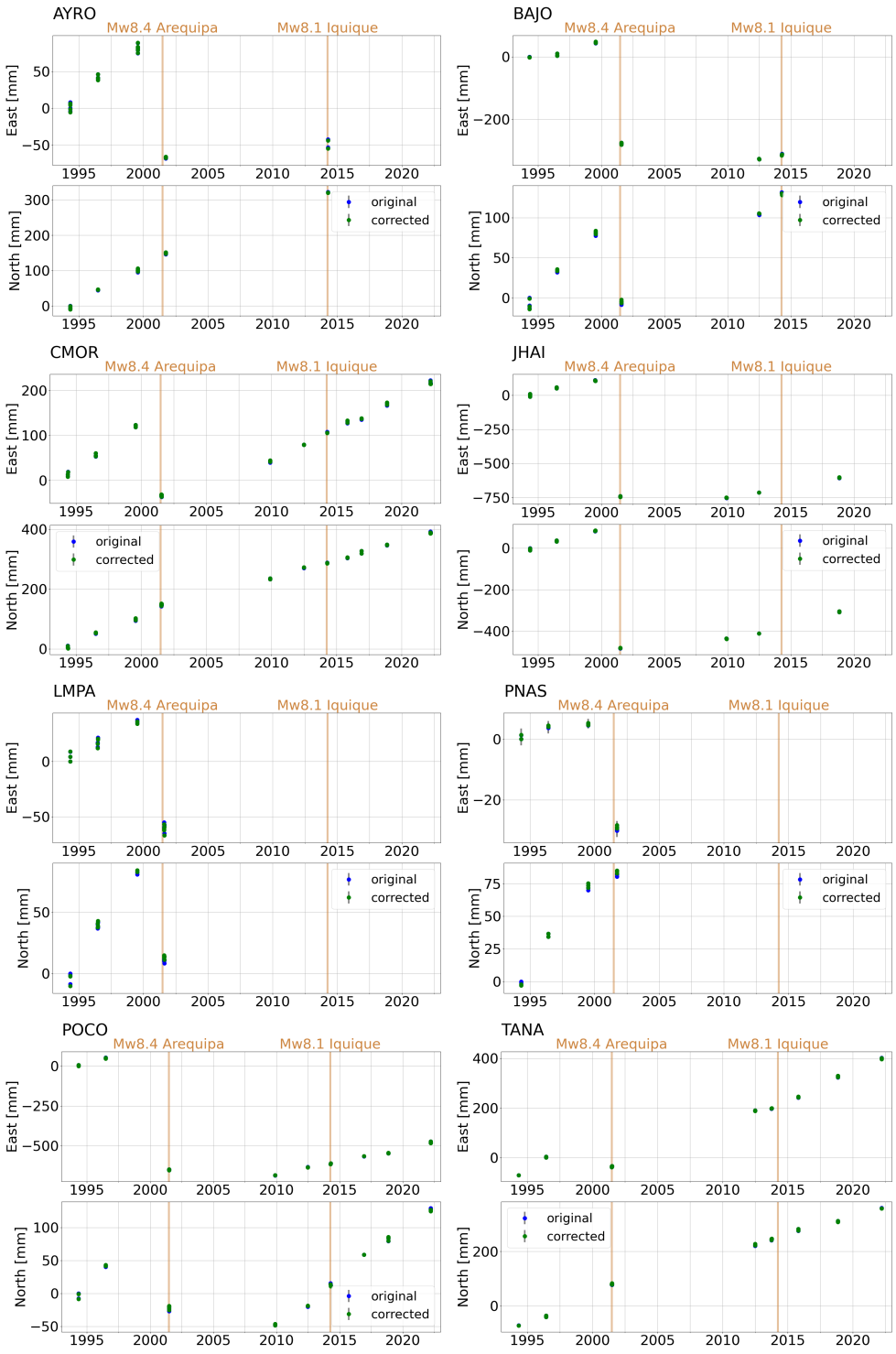

Figure S5: Displacement timeseries at sGNSS sites AYRO, BAJO, CMOR, JHAI, LMPA, PNAS, POCO, and TANA, without any correction (blue) or after correcting from coseismic and postseismic displacements related to the 2014 Mw8.1 Iquique earthquake, as well as accounting for seasonal variations (green). Daily GNSS solutions are displayed as blue dots, with their uncertainty indicated by the gray error bars. Epochs corresponding to the 2001 Mw8.4 Arequipa and 2014 Mw8.1 Iquique earthquakes are depicted by yellow vertical lines.

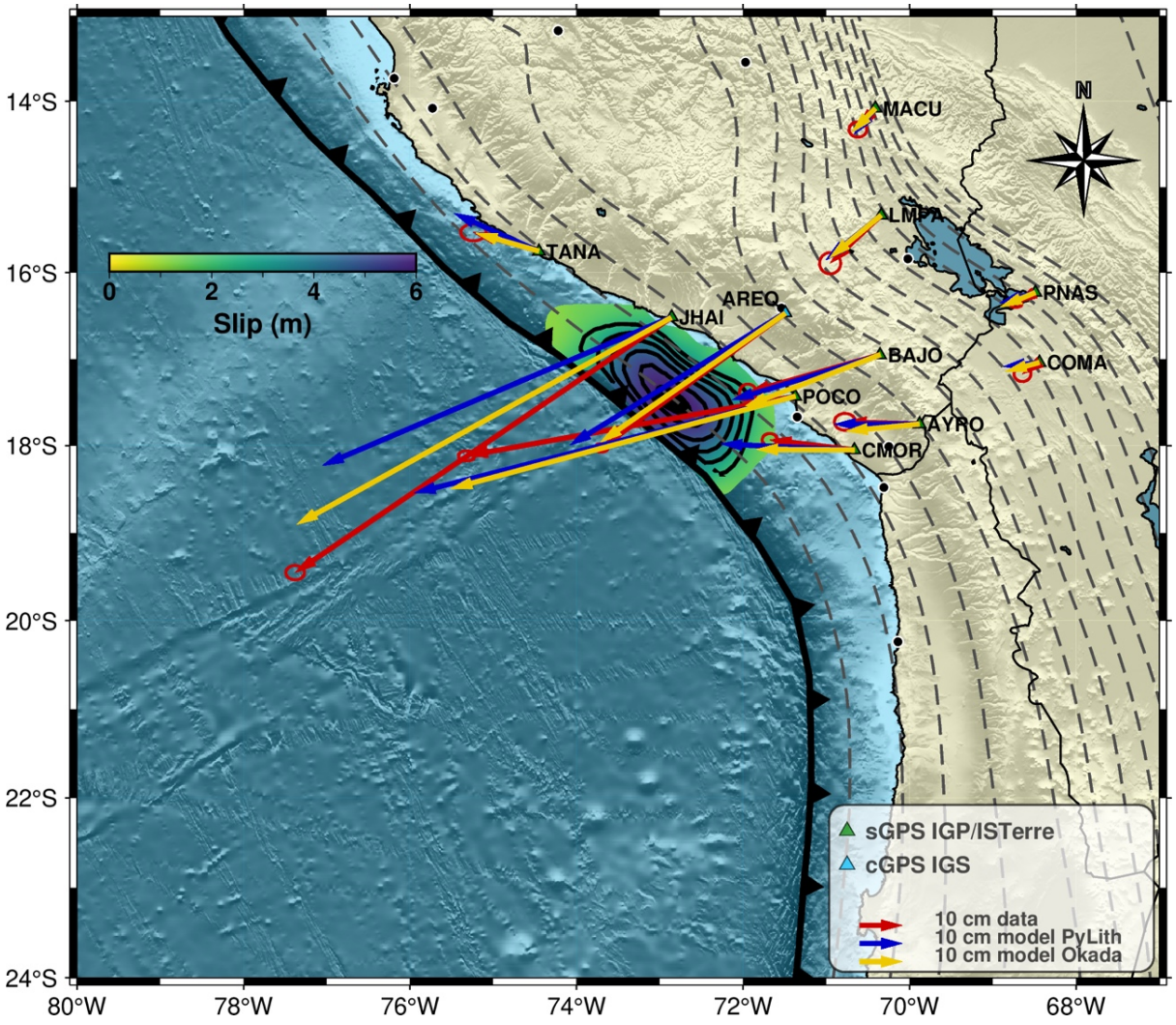

Figure S6: Coseismic displacements associated with the 2001 Mw8.4 Arequipa. Observed coseismic offsets at GNSS sites are displayed in red, the modelled coseismic offsets using the Okada model from Lovery et al. (2024a) in yellow, and the modelled coseismic offsets using PyLith in blue.

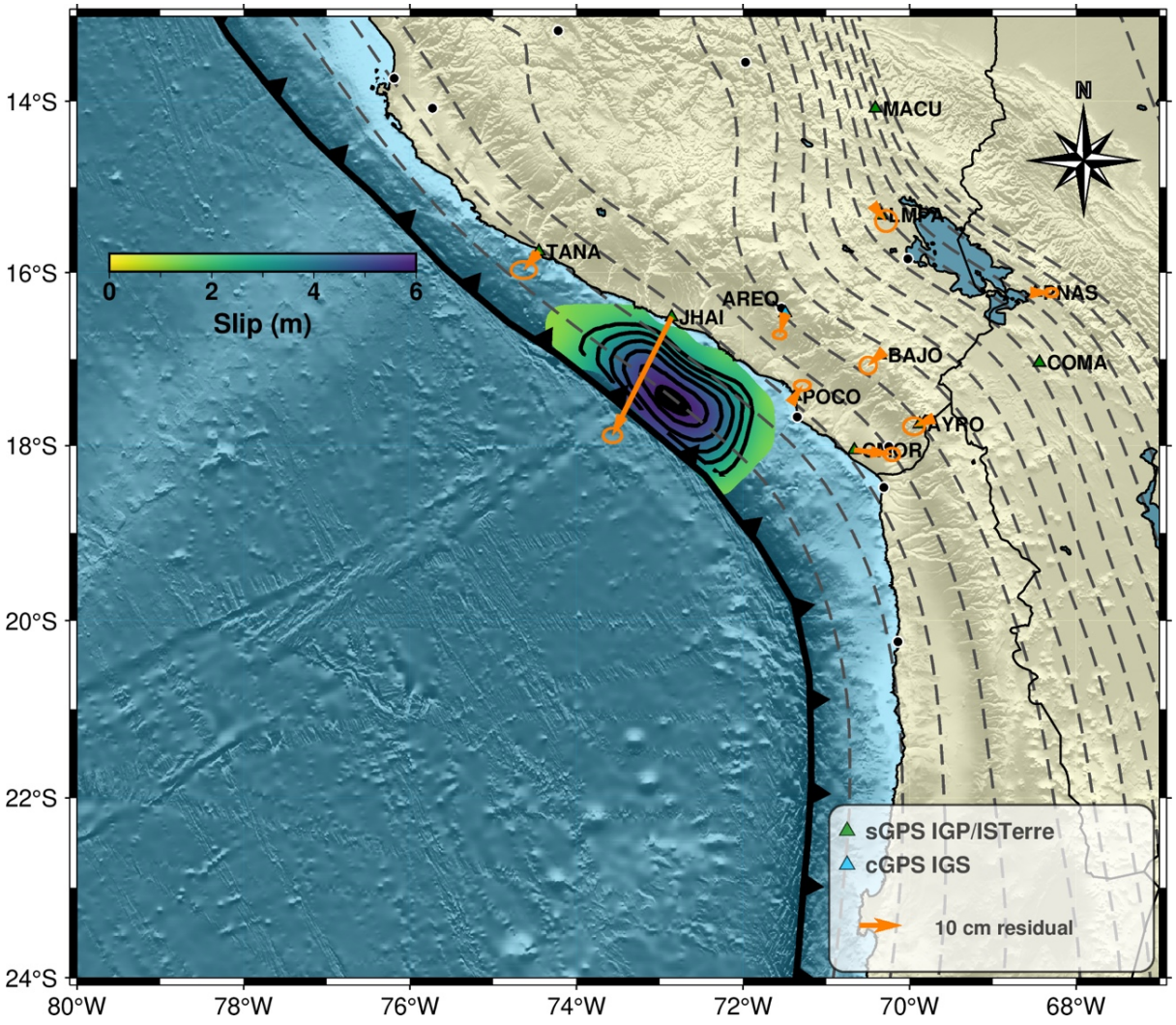

Figure S7: Residuals between the observed coseismic offsets at GNSS sites and the modelled coseismic offsets using PyLith (Figure S6).

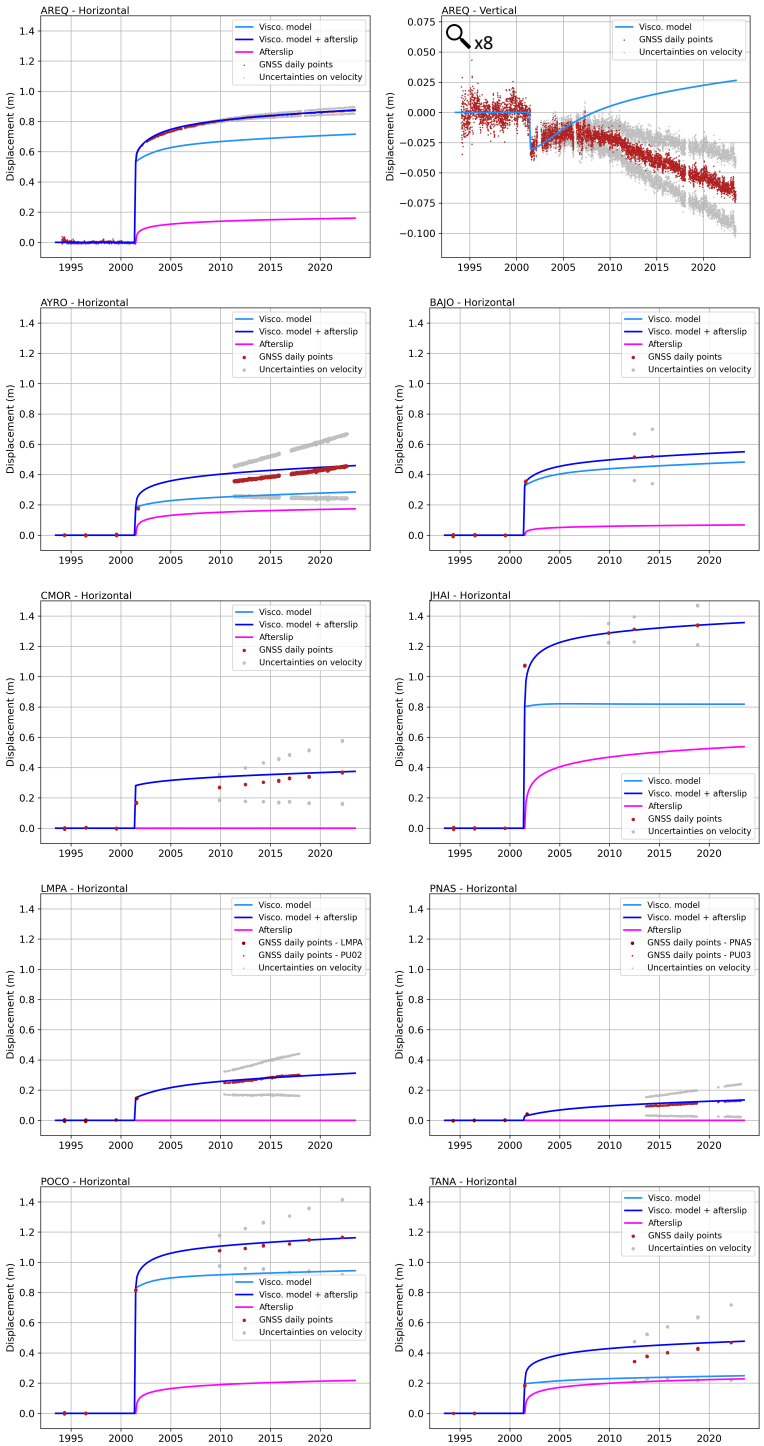

Figure S8: Displacement timeseries at the AREQ cGNSS station and at the various sGNSS sites (AYRO, BAJO, CMOR, JHAI, LMPA, PNAS, POCO, and TANA) on the horizontal components, as well as the vertical component for AREQ. The timeseries cover the 1994-2024 period and has been corrected from coseismic steps related to other earthquakes, seasonal variations, and detrended from the pre-Arequipa velocities. Daily GNSS solutions are reported by the red dots. Uncertainties at 3σ on the slope after 2001, computed using MIDAS, are indicated by gray dots. Note that the vertical component is zoomed-in by a factor eight compared to the horizontal. Pure viscoelastic displacements are depicted by the light blue line, afterslip by the magenta line, and their sum by the dark blue line.

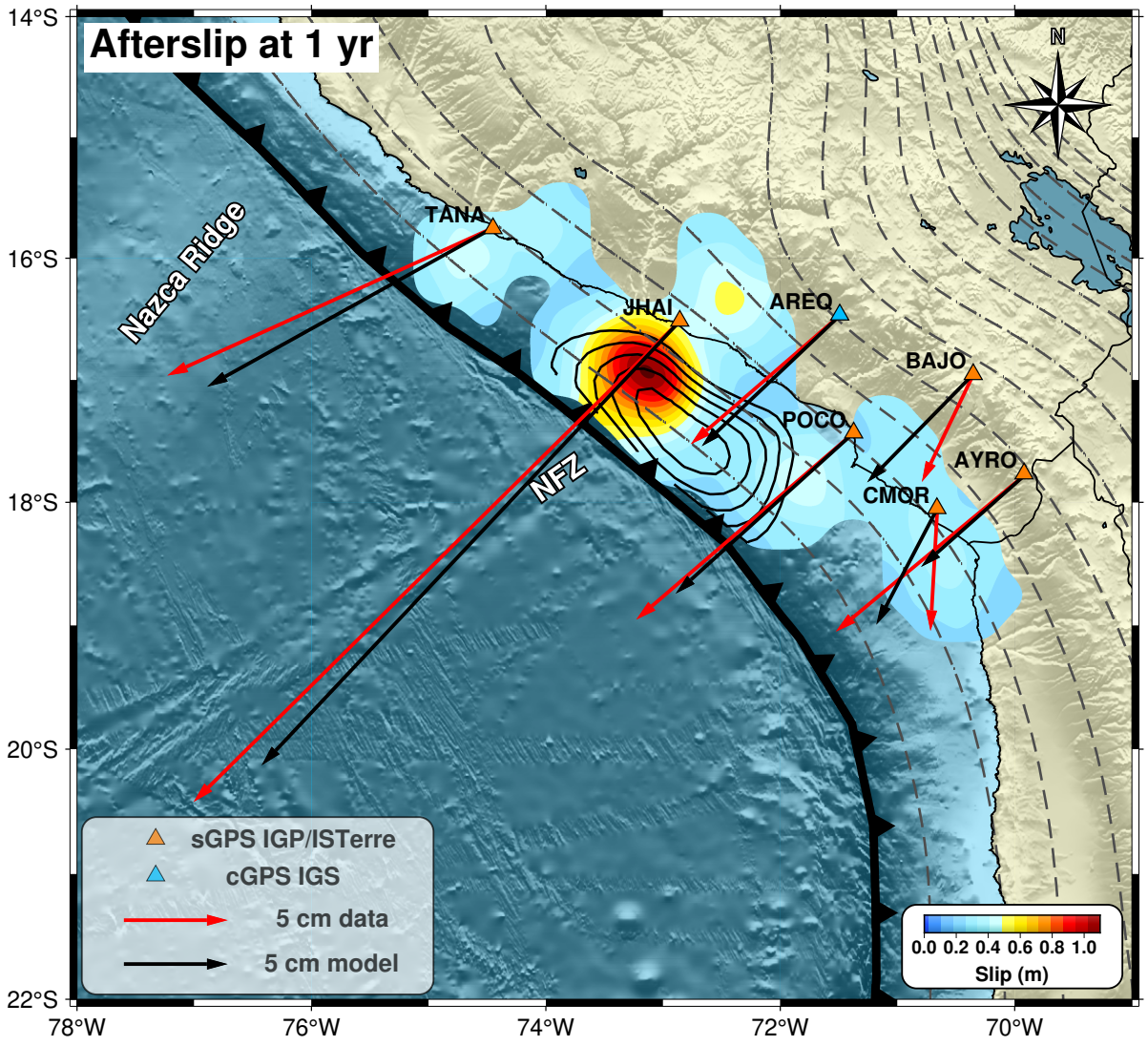

Figure S9: 1-year cumulated afterslip displacements estimated at GNSS sites (Figure S8) for the 2001 Mw8.4 Arequipa earthquake is reported by red vectors, while modelled displacements using viscoelastic Green's functions are reported by the black vectors. The resulting afterslip distribution is reported by the colormap. Slab contours (dashed lines) are reported every 20-km depth, from the Slab2 model (Hayes et al. 2018). The 2001 Mw8.4 Arequipa earthquake coseismic slip distribution is reported by the black 1-m slip contours.

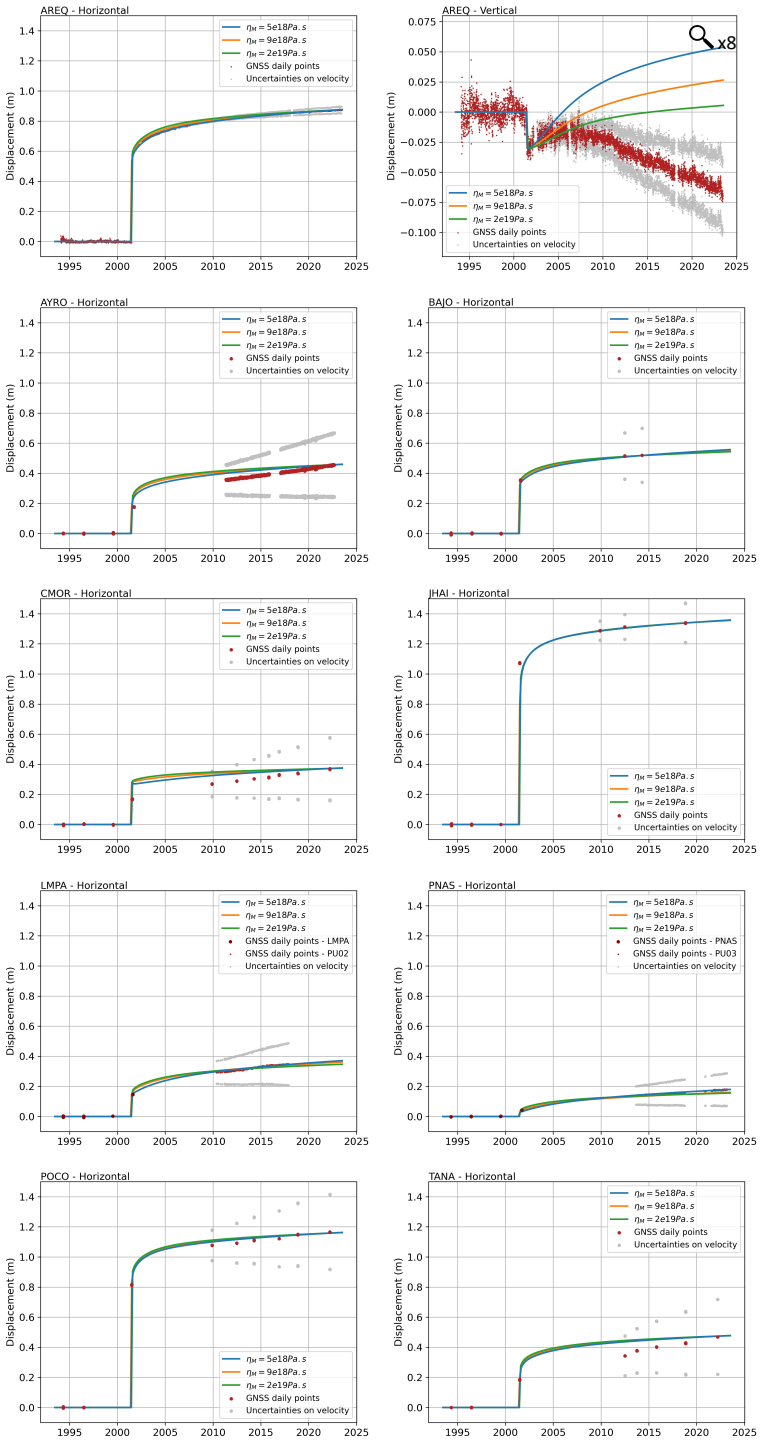

Figure S10: Displacement timeseries at the AREQ cGNSS station and at the various sGNSS sites (AYRO, BAJO, CMOR, JHAI, LMPA, PNAS, POCO, and TANA) on the horizontal components, as well as the vertical component for AREQ. The timeseries cover the 1994-2024 period and has been corrected from coseismic steps related to other earthquakes, seasonal variations, and detrended from the pre-Arequipa velocities. Daily GNSS solutions are reported by the red dots. Uncertainties at 3σ on the slope after 2001, computed using MIDAS, are indicated by gray dots. Note that the vertical component is zoomed-in by a factor eight compared to the horizontal. Three models with various Maxwell η_M viscosities are displayed: $5{\cdot}10^{18}$ Pa.s (blue), $9{\cdot}10^{18}$ Pa.s (yellow), and $2{\cdot}10^{19}$ Pa.s (green).

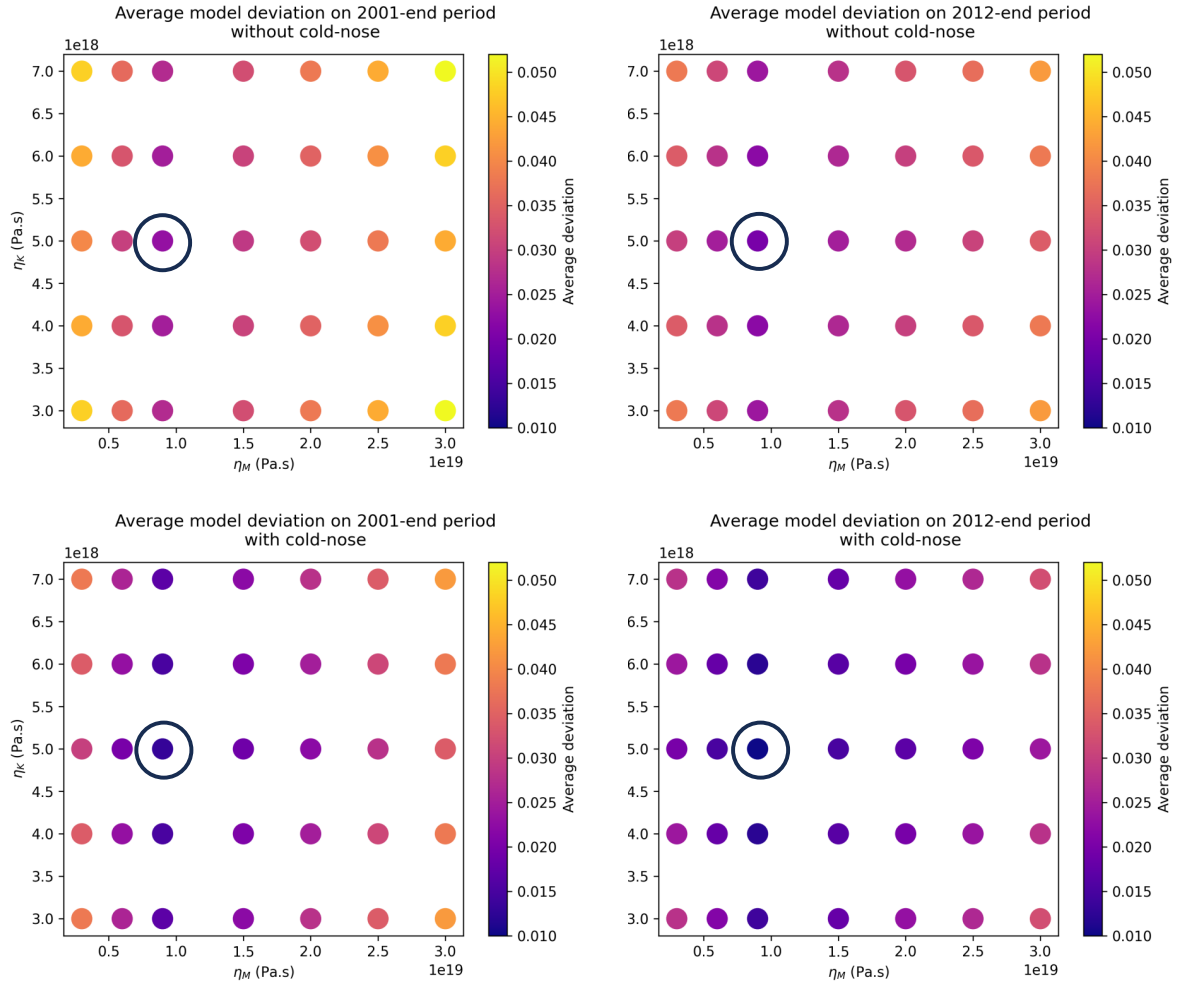

Figure S11: Average data-model deviation on the horizontal component at the GNSS stations, depending on asthenosphere Maxwell viscosity η_M (x-axis) and asthenosphere Kelvin viscosity η_K (y-axis), starting from 2001 (left) or 2012 (right), with (bottom) or without (top) elastic cold-nose. For each case, the best model is indicated by the black circle.

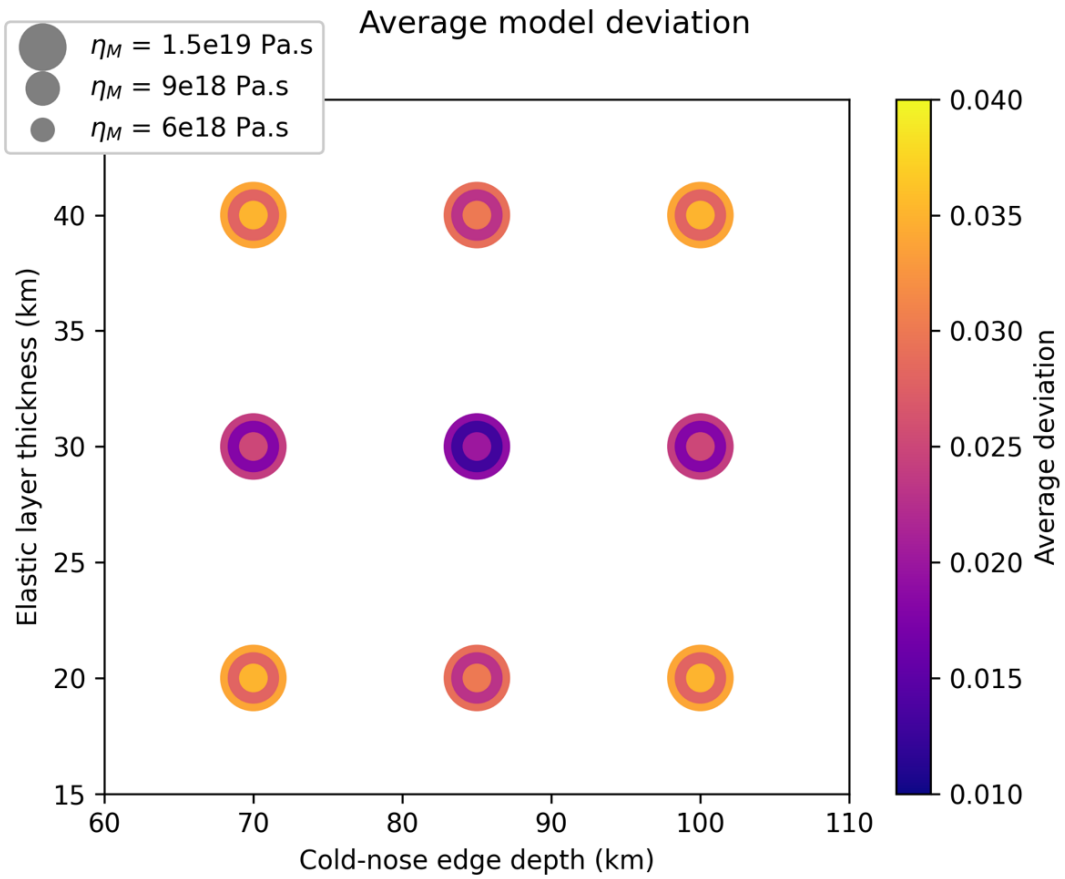

Figure S12: Average data-model deviation on the horizontal component at the GNSS stations, depending on cold-nose edge depth (x-axis), continental elastic layer thickness (y-axis), and asthenosphere Maxwell viscosity η_M (small to large circles).

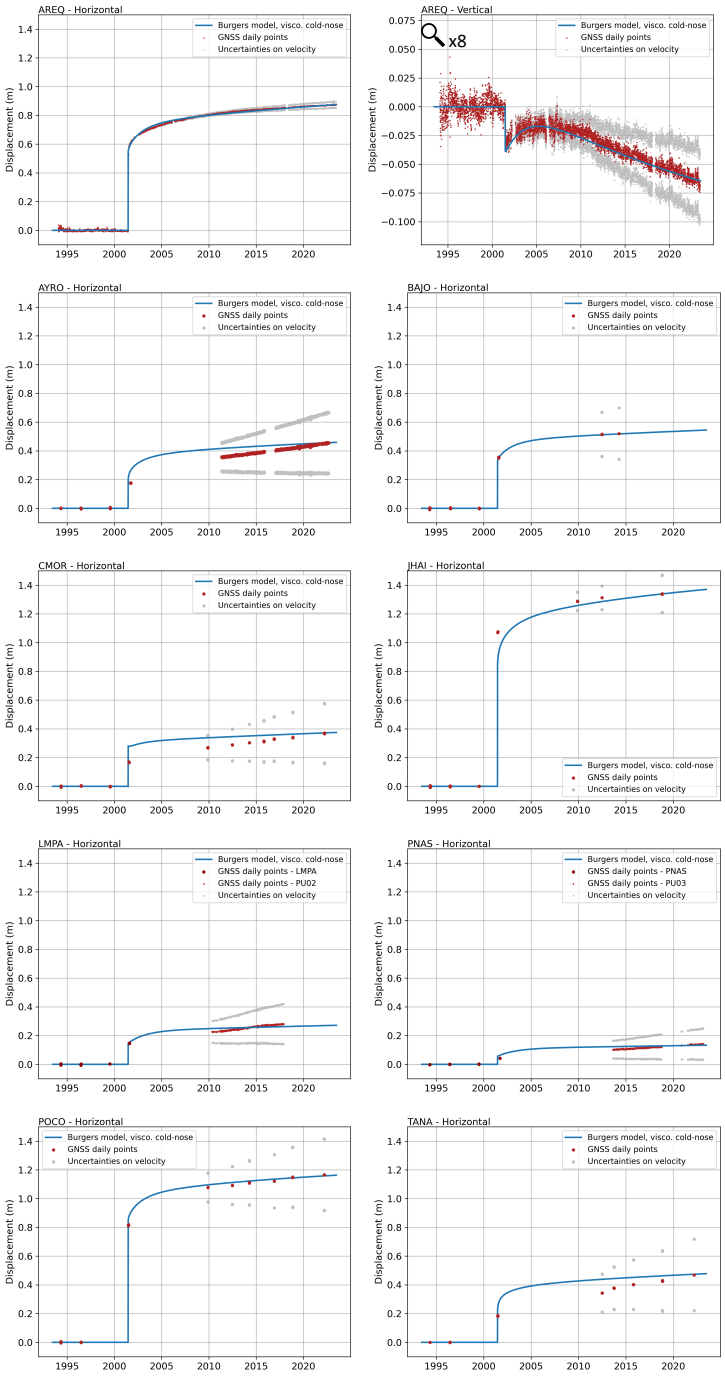

Figure S13: Displacement timeseries at the AREQ cGNSS station and at the various sGNSS sites (AYRO, BAJO, CMOR, JHAI, LMPA, PNAS, POCO, and TANA) on the horizontal component, as well as the vertical component for AREQ. The timeseries cover the 1994-2024 period and has been corrected from coseismic steps related to other earthquakes, seasonal variations, and detrended from the pre-Arequipa velocities. Daily GNSS solutions are reported by the red dots. Uncertainties at 3σ on the slope after 2001, computed using MIDAS, are indicated by gray dots. Note that the vertical component is zoomed-in by a factor eight compared to the horizontal. The displayed model features a lower viscosity in the cold-nose block, with a Maxwell rheology of $1 \cdot 10^{19}$ Pa.s, and a higher viscosity in the remaining asthenosphere ($\eta_M = 4 \cdot 10^{19}$ Pa.s and $\eta_K = 4 \cdot 10^{18}$ Pa.s). This model fits well the horizontal and vertical components, but we consider its constitution unrealistic.

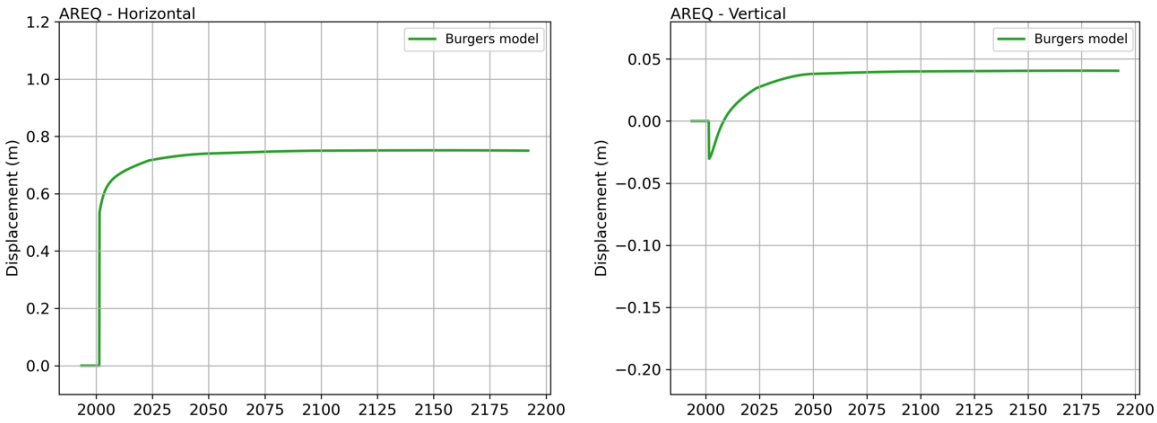

Figure S14: Horizontal (left) and vertical (right) displacements at AREQ over 200 years, from our best postseismic model (Burgers model with elastic cold-nose) used to build viscoelastic Green's functions. We observe that the system is fully-relaxed over the last 100 years of the timeseries.

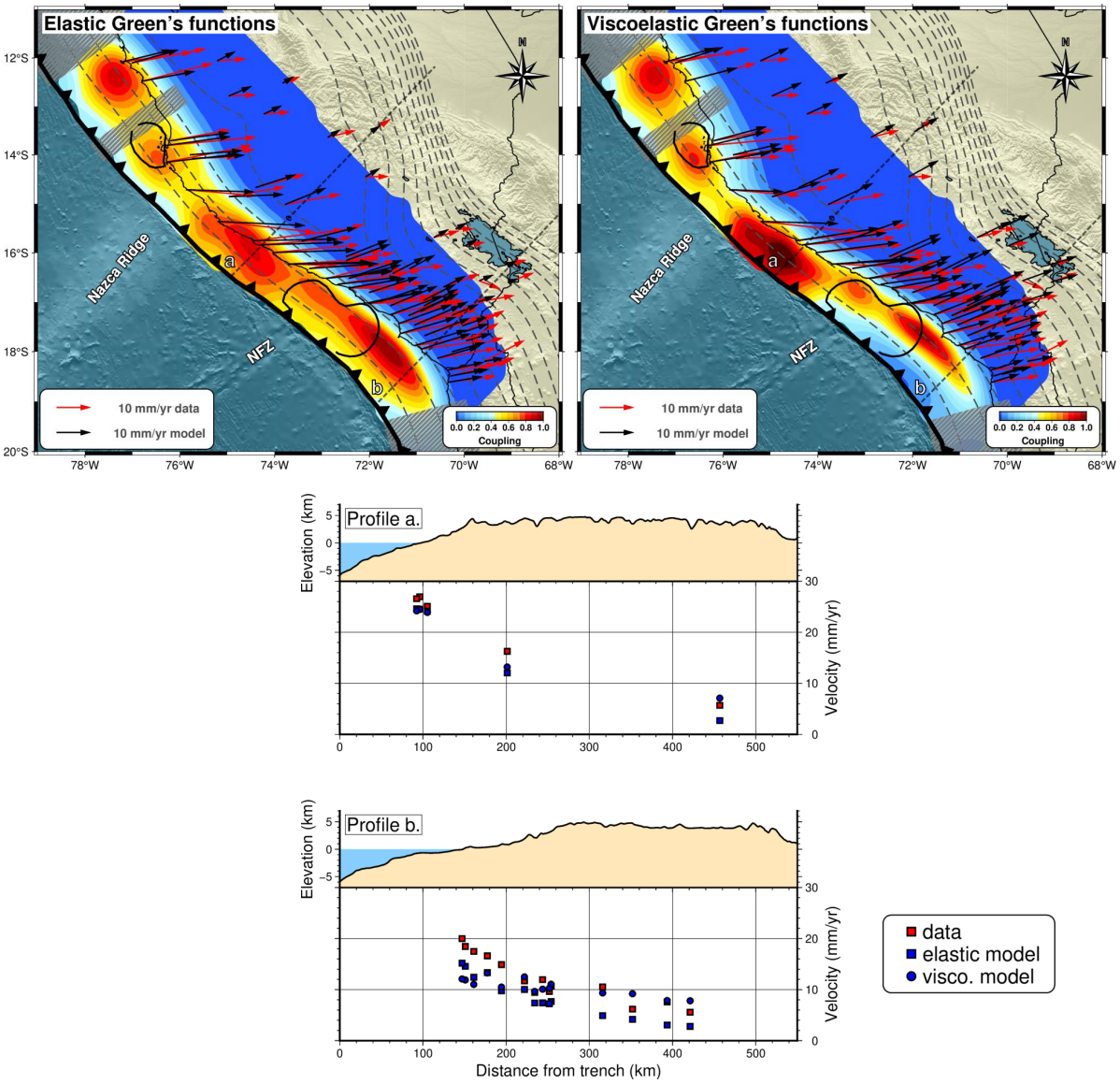

Figure S15: Interseismic coupling distribution derived from the interseismic GNSS velocities from Lovery et al. (2024a), using elastic (top-left) and viscoelastic (top-right, similar to the model shown on Figure 4a) Green's functions. Observed and modelled interseismic velocities are depicted by red and blue vectors respectively. Slab contours (dashed lines) are reported every 20-km depth, from the Slab2 model (Hayes et al. 2018). The approximate rupture area of the 2001 Mw8.4 Arequipa and 2007 Mw8.0 Pisco earthquakes are reported by the black contours. Two profiles (a and b) are reported on cross-sections (bottom panel) with horizontal displacements at GNSS sites from the data (red squares), and from the elastic (blue squares) and viscoelastic interseismic models (blue dots).

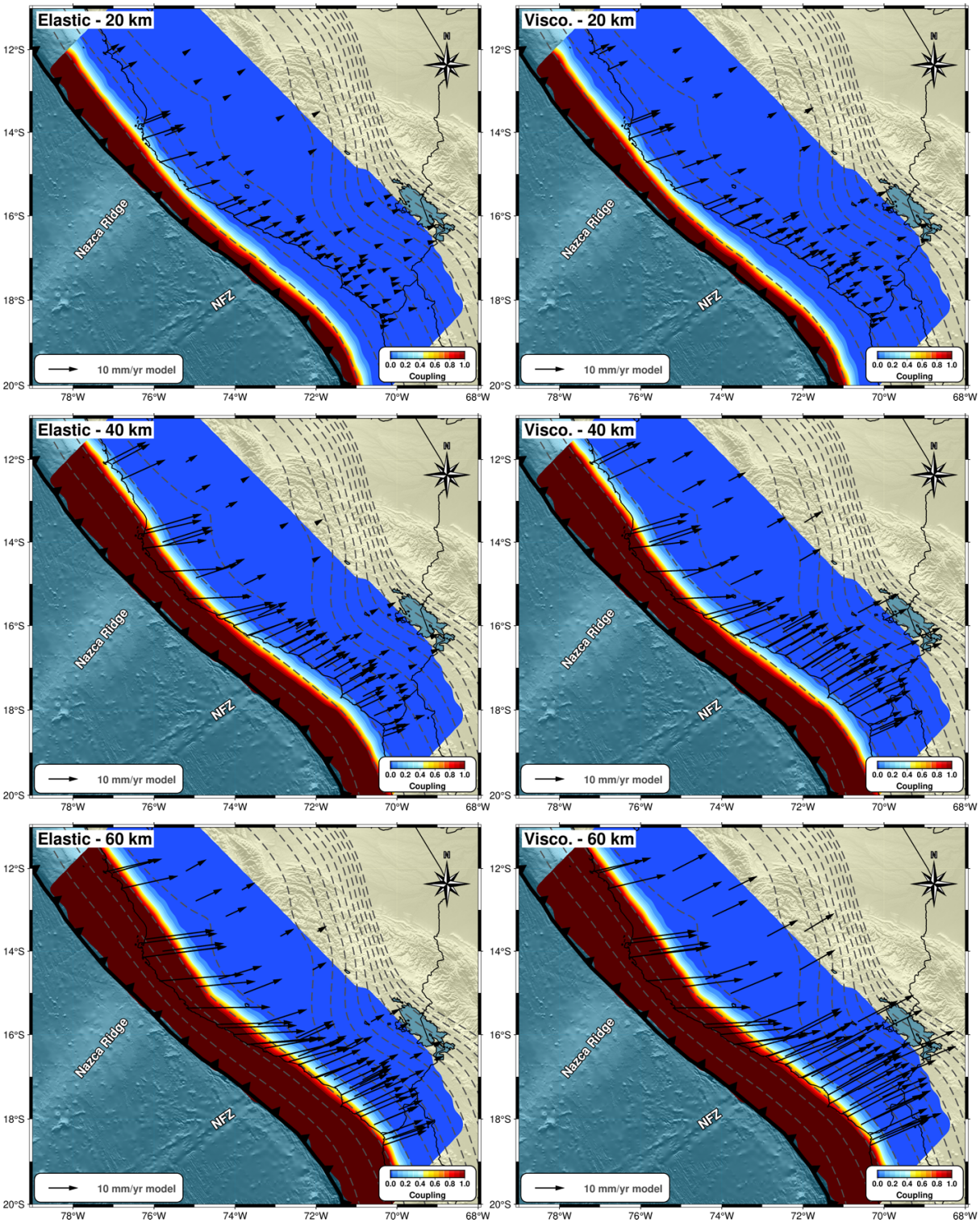

Figure S16: Forward models of displacement using a fully-locked interface down to a given depth (20, 40, or 60 km), with elastic (left) or viscoelastic (right) Green's functions. The modelled surface displacements are depicted by the black vectors. Slab contours (dashed lines) are reported every 20-km depth, from the Slab2 model (Hayes et al. 2018). Larger displacements are observed in the far-field and on the southern segment when using viscoelastic Green's functions.

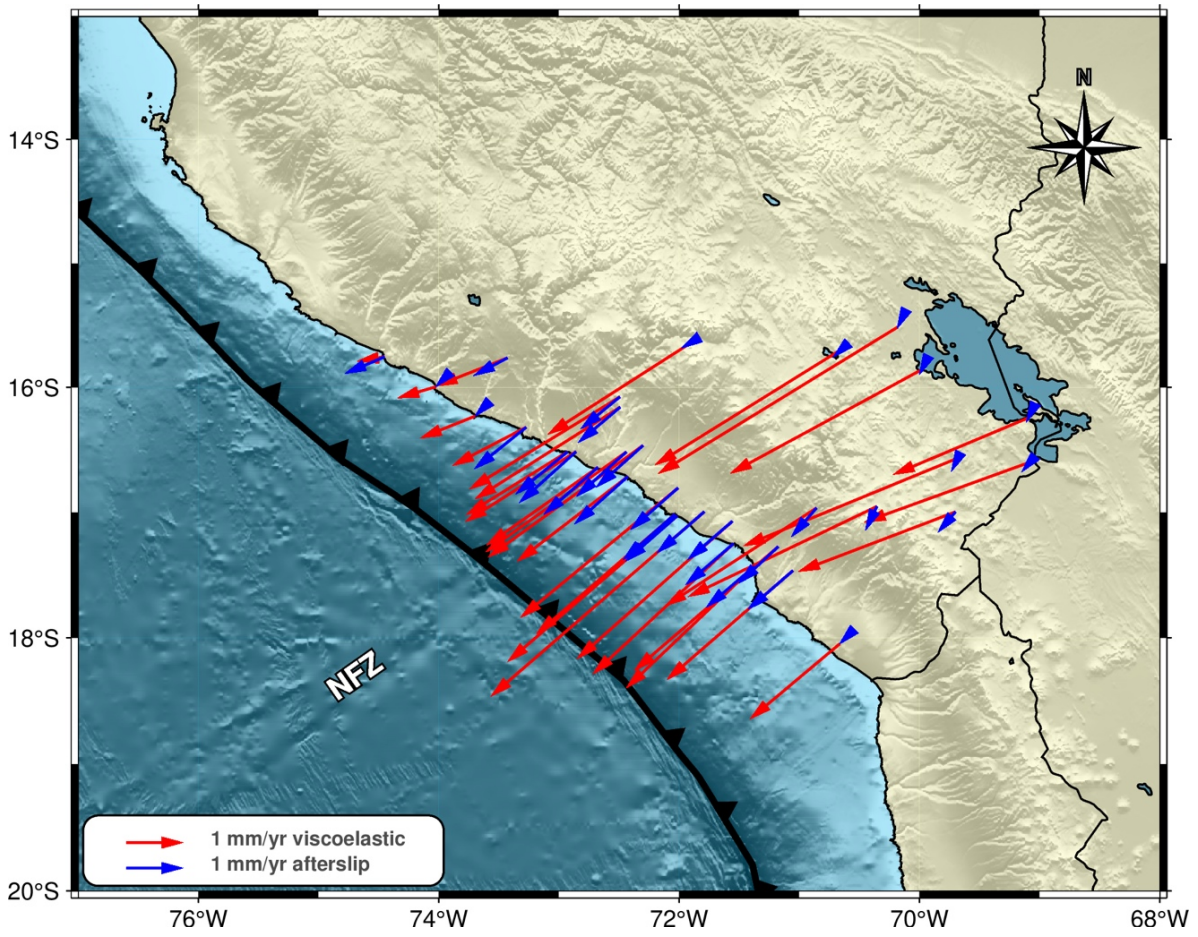

Figure S17: Velocity associated with the viscoelastic relaxation (red) and afterslip (blue) during the observation period of the GNSS network used for interseismic coupling modelling (~2012-2023), at each GNSS sites used for interseismic coupling assessment (cf. values on Table S3).

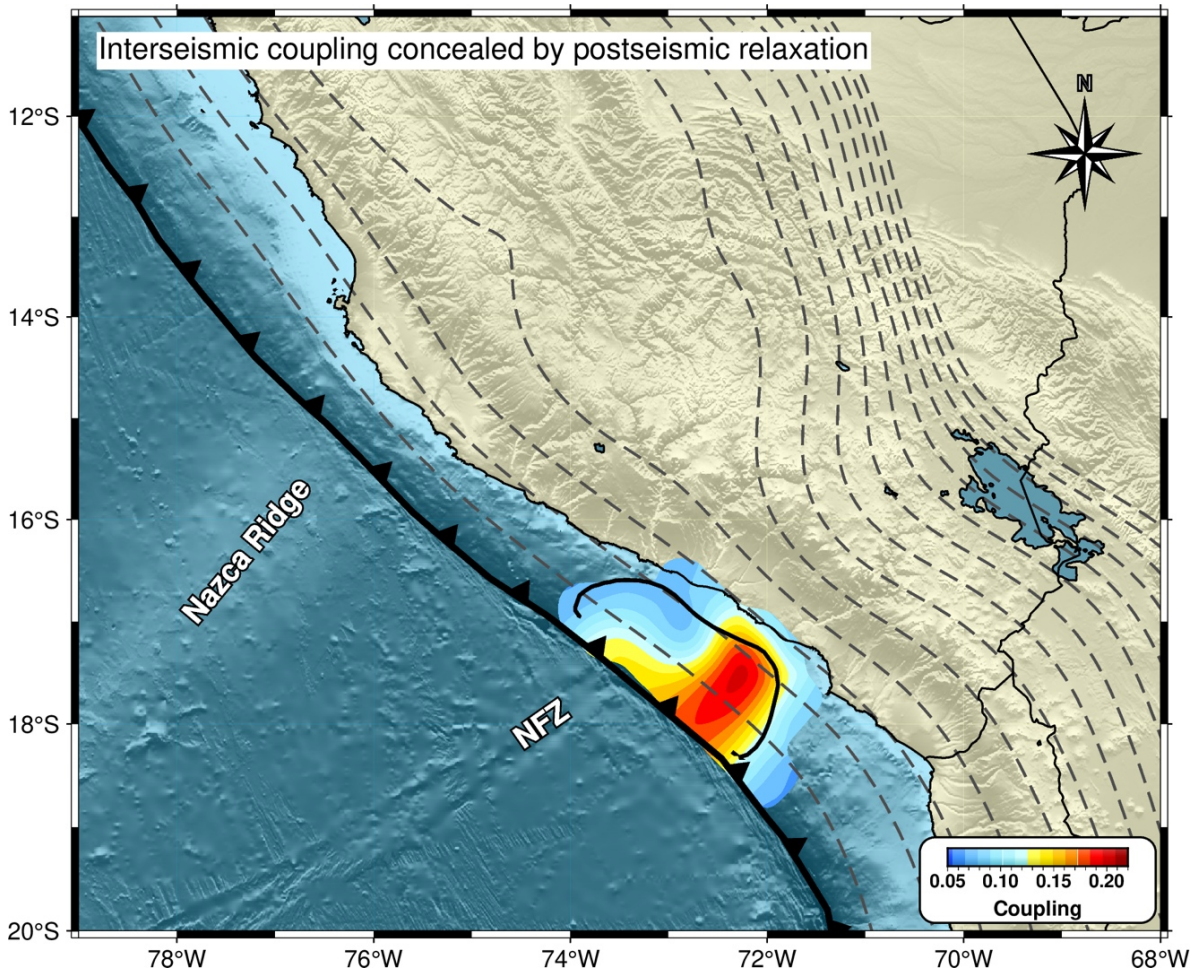

Figure S18: Difference between interseismic coupling distribution corrected or not from postseismic processes (Figure 4). Slab contours (dashed lines) are reported every 20-km depth, from the Slab2 model (Hayes et al. 2018). The approximate rupture area of the 2001 Mw8.4 Arequipa earthquake is reported by the black contour. Note that the coupling difference can reach up to 24% locally.

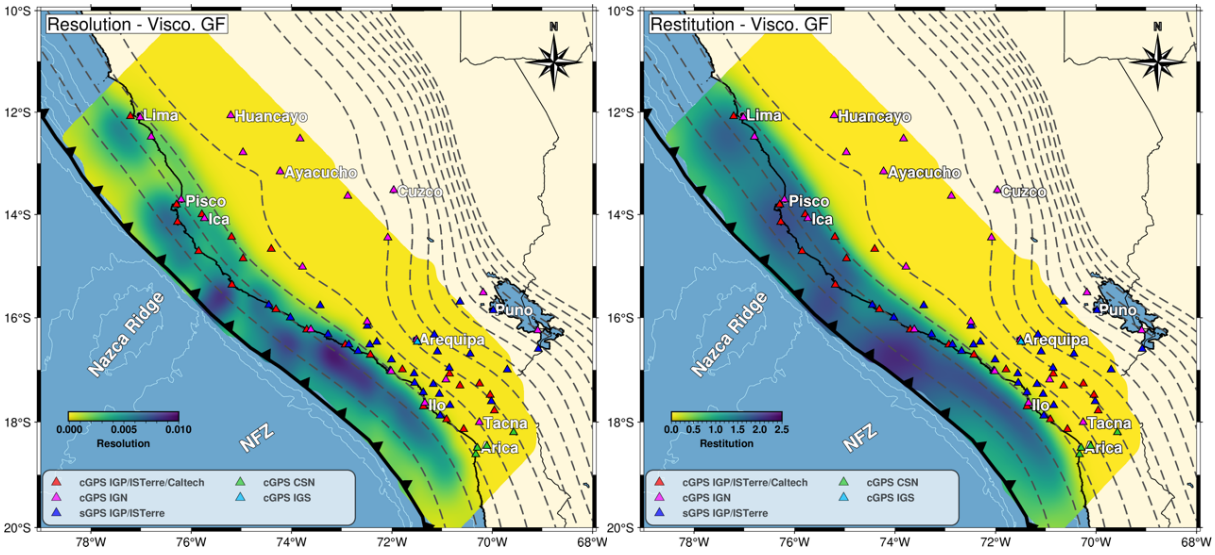

Figure S19: Diagonal values of the resolution matrix R (left) and restitution (right) on the slab, for a correlation length λ of 30 km. Whereas the diagonal elements of R inform us about how much the slip of a specific patch is accurately mapped on this patch by the program, the restitution informs us if this slip has been correctly projected onto other patches (Lovery et al., 2024a; Radiguet et al., 2011). Overall, we can notice that our diagonal values of R are low because we have defined a high number of small patches on our slab (6,008) for a relatively low amount of GNSS stations (73), in order not to impose a strong constraint on the slip locations. The diagonal values are higher where the density of station is high, indicating a better resolution, and are close to zero above 60 km depth because we confine the slip in the first 60 km depth of our model. The same goes for the restitution, except that the distribution is smoother. We can observe distinctly an edge effect near the 60 km iso-depth where the patches have a higher restitution because of the slip confinement, since the displacements on the stations more inland are only accommodated by these deep patches.

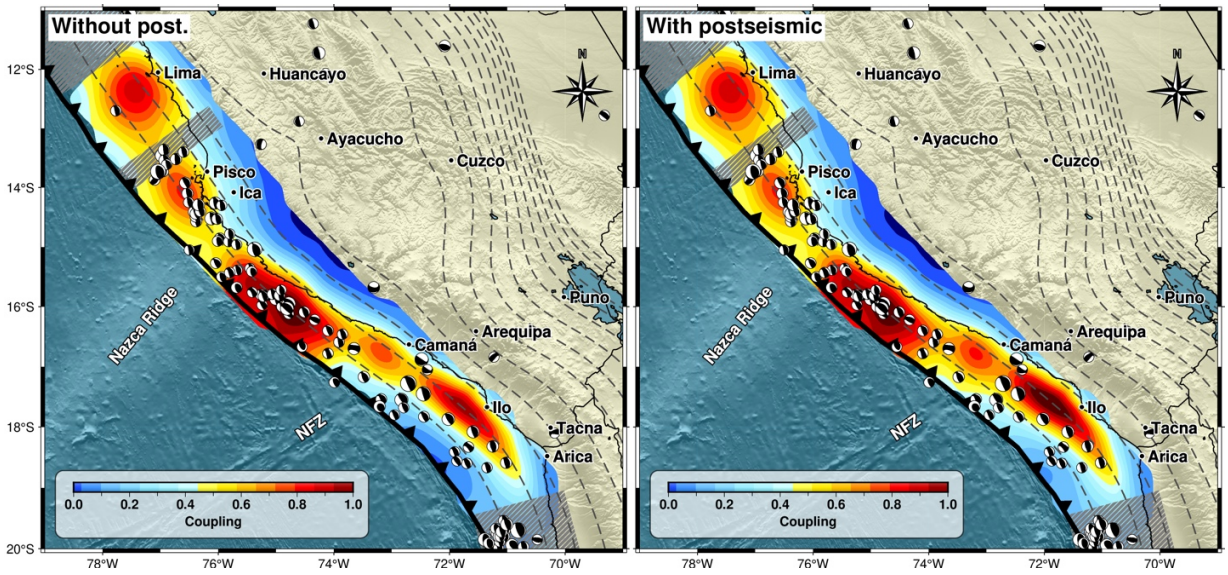

Figure S20: Interseismic coupling distribution before (left) and after (right) postseismic correction. Areas with high coupling are prone to host large seismic events. Seismicity from the gCMT catalog (Dziewonski et al., 1981; Ekström et al, 2012) is plotted on top, cherry-picking thrusts events with Mw>5.5 and up to 70 km depth. We can observe a convincing overlap between the seismicity and highly-coupled areas (coupling > 0.4).

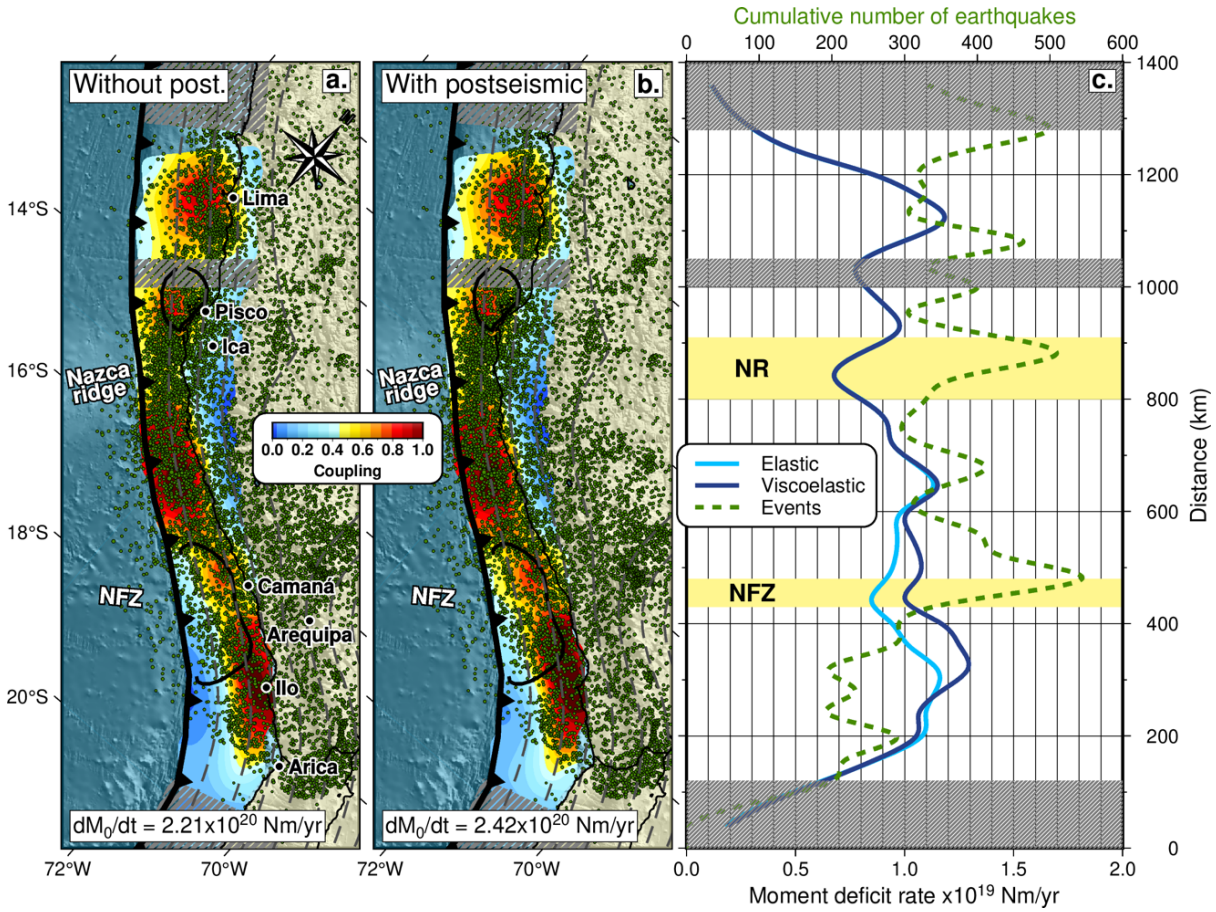

Figure S21: Interseismic coupling distribution from our inversion of interseismic velocities before (a) and after (b) postseismic correction. Slab contours (dashed lines) are reported every 20 km depth, from the Slab2 model (Hayes et al., 2018). The approximate rupture area of the Mw8.4 2001 Arequipa earthquake has been estimated in this study, while the Mw8.0 2007 Pisco earthquake rupture is reported from Chlieh et al. (2011). Seismic events from the Instituto Geofisico del Peru (IGP) catalog (all magnitudes, magnitude of completeness M_c=4.5) are depicted by green dots. On the panel (c) are displayed the moment deficit rate by latitude for elastic and viscoelastic models, computed over 15-km wide segments. Patches with gray hachure pattern depict areas that are not well resolved by the model. Cumulative seismicity from the IGP catalog is depicted by the green dashed line.

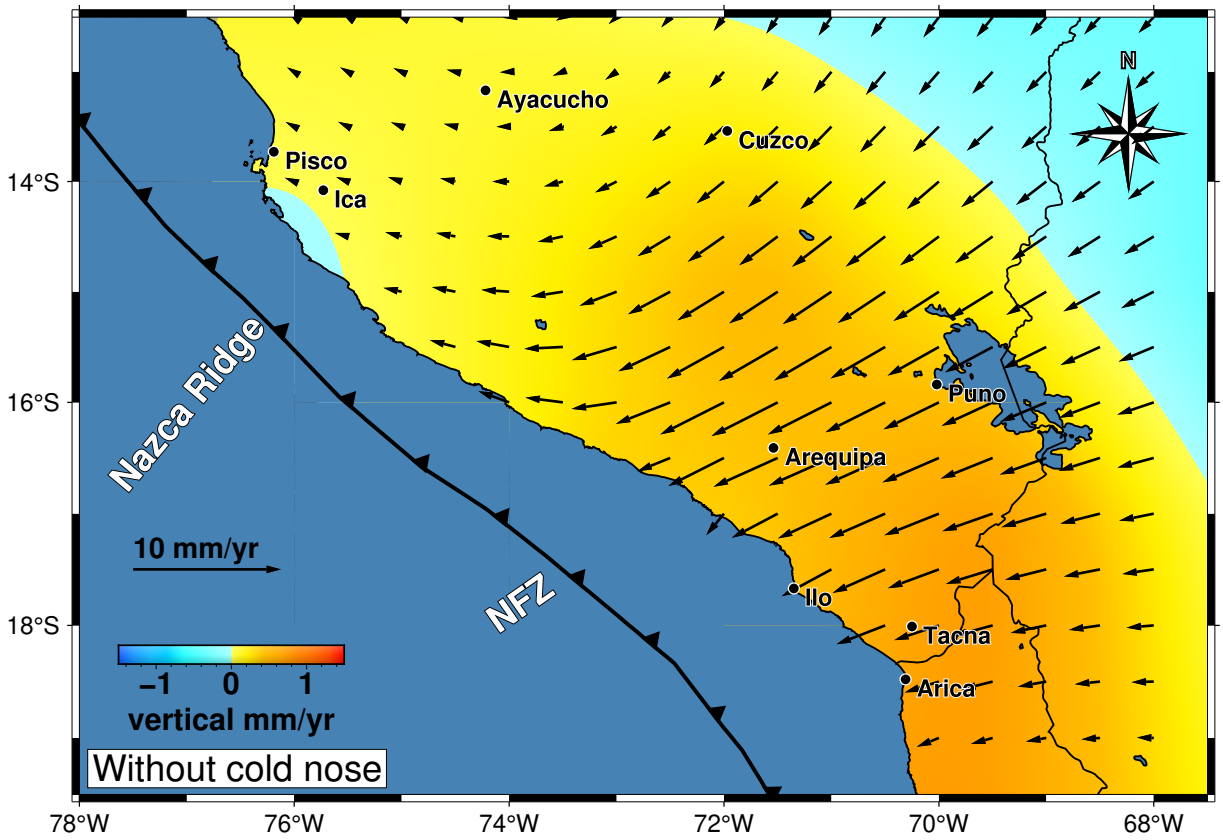

Figure S22: Postseismic velocity on the 2015-2024 period from the model without cold-nose shown on Figure 3 (orange line), on the horizontal (black vectors) and vertical (colorscale) components. Projection on this time period could be used to correct Sentinel-1 InSAR data, which started operation on 2015.

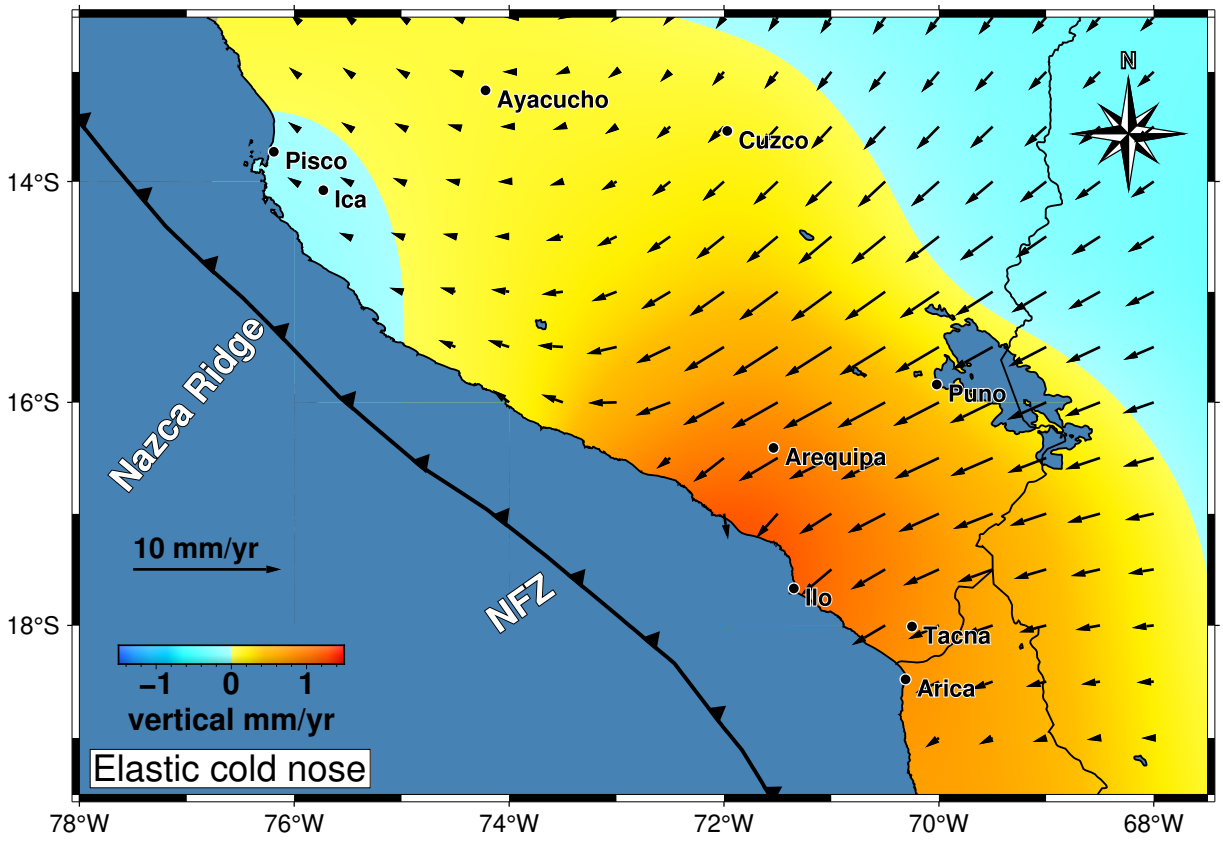

Figure S23: Postseismic velocity on the 2015-2024 period from the model with elastic cold-nose shown on Figure 3 (blue line), on the horizontal (black vectors) and vertical (colorscale) components. Projection on this time period could be used to correct Sentinel-1 InSAR data, which started operation on 2015.

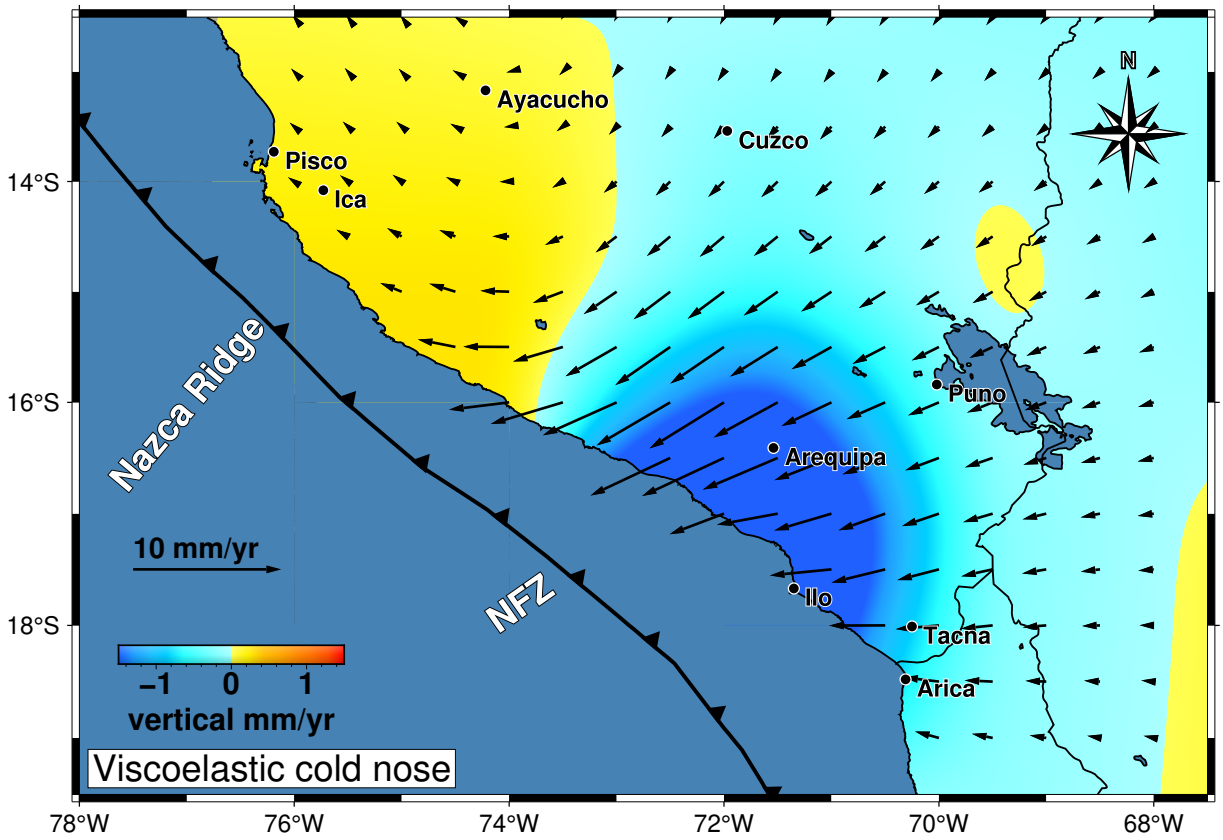

Figure S24: Postseismic velocity on the 2015-2023 period from the model with viscoelastic cold-nose shown on Figure S13, on the horizontal (black vectors) and vertical (colorscale) components. Projection on this time period could be used to correct Sentinel-1 InSAR data, which started operation on 2015.

Chapter 6

Modeling non-tectonic signals in InSAR phase ramps

In order to use InSAR mean velocity maps for large-scale tectonic applications, they have to be referenced in a stable reference frame such as ITRF. Two strategies can be applied: either we choose to reference the InSAR maps on the GNSS by applying ramps (i.e., linear phase gradients) in range and azimuth directions, or we estimate the ramps associated to non-tectonic effects affecting the InSAR data and we remove them. The second approach may appears to be more elegant as it allows to have a dataset totally independent from the GNSS data. In addition to avoiding the potential biases affecting the GNSS data, it could allow the use of InSAR for large-scale applications in areas without GNSS instrumentation. For these reasons, we first tried to model the ramps related to non-tectonic processes: ocean tide loading (OTL), solid Earth tides (SET), and ionospheric delay. Although we obtained some interesting results by doing so, we ended up relying solely on GNSS to reference our InSAR velocity maps used in Chapter 7 because the ramp corrections were not sufficient to offer a satisfying agreement between InSAR and GNSS datasets in Central Andes.

The following article from Marconato et al. has been accepted for publication in *Geophysical Research Letters*, in November 2025. Although the main contributor to this work is Léo Marconato, who wrote most of the manuscript and carried out the final modeling of ionospheric phase delay, I contributed to the study by modeling the phase ramps associated to the SET and OTL in Central Andes.

6.1 Manuscript

Long-Wavelength Ionospheric Compensation of InSAR Time-Series Based on Global Ionosphere Maps

L. Marconato[1], M.-P. Doin[1], B. Lovery[1], L. Rolland[2], P. Durand[3]

[1]Univ. Grenoble Alpes, Univ. Savoie Mont Blanc, CNRS, IRD, Univ. Gustave Eiffel, ISTerre, 38000 Grenoble, France
[2]Université Côte d'Azur, CNRS, IRD, Observatoire de la Côte d'Azur, Géoazur, 06560 Valbonne, France
[3]Centre National d'Études Spatiales, Toulouse, France

Key Points:

- Ionosphere significantly contributes to the long-wavelength component of Sentinel-1 InSAR time-series, even far from equatorial regions
- Global ionosphere maps (GIMs) efficiently remove the low-frequency ionospheric contributions in long-wavelength displacement time-series
- GIM-based corrections, together with tidal corrections, improve the agreement between InSAR and GNSS for measuring tectonic plate motion

Corresponding author: Léo Marconato, leo.marconato@univ-grenoble-alpes.fr

Abstract

Uncorrected long-wavelength contributions remain a major limitation for interpreting InSAR time-series over large areas (>100 km). Among them, the ionosphere can impact InSAR measurements across various timescales, potentially biasing secular velocity estimates. We use Global Ionosphere Maps (GIMs) to predict ionospheric effects for >15,000 Sentinel-1 acquisitions in France, Tibet, and Central Andes. We evaluate GIM-based corrections using phase ramps (planar functions fitted to interferograms) as proxies for long-wavelength signals, enabling analysis of their temporal evolution. After correcting for solid Earth tides and oceanic tidal loading, GIM-derived predictions show a strong temporal consistency with observed ramps, effectively capturing seasonal and multi-year fluctuations with amplitudes of ∼0.2 mm/km. The highest-resolution GIM also corrects part of the strong daily fluctuations of along-track ramps observed on ascending tracks over equatorial regions. These corrections reduce ramp rate uncertainty and improve agreement with GNSS, paving the way toward direct InSAR measurement of tectonic plate motion.

Plain Language Summary

Satellite radar interferometry (InSAR) allows to measure the deformation of the Earth's surface over time, and can detect tiny displacements related to processes such as interseismic loading around tectonic faults. However, over large areas (>100 km), these measurements become less reliable due to the superposition of other signals to the ones actually related to ground motion. One such source of error comes from the propagation of radar waves in the ionosphere. In this study, we show that these ionospheric effects can be tracked and removed efficiently using publicly available Global Ionosphere Maps (GIMs). We analyze massively processed InSAR data over France, Tibet, and Central Andes, demonstrating that GIMs reproduce very well the temporal variations of the spatially smooth component of the measurements, at the scale of months to years. Correcting the InSAR results with this approach improves the accuracy of long-term ground motion measurements, and make them more reliable for studying tectonic motion over large areas.

1 Introduction

The study of ground deformation using Synthetic Aperture Radar Interferometry (InSAR) is now a well established method, which has undergone significant improvements over the past decade. The Sentinel-1 mission, with its systematic, freely available acquisitions, triggered the development of automated processing services to leverage its vast archive (Bekaert et al., 2019; Morishita et al., 2020; Thollard et al., 2021), enabling the computation of velocity maps at a few mm/yr accuracy over regions of 100 000 km^2. Such products open new possibilities for studying tectonic deformation at a continental scale with an unprecedented resolution, previously achievable only with scattered GNSS measurements (Weiss et al., 2020; Lemrabet et al., 2023; Watson et al., 2024; Fang et al., 2024).

InSAR provides relative measurements in time and space due to the inherent phase ambiguity in the ground-satellite distance. The uncertainty on the InSAR phase difference between two points increases with the distance between the points (Parizzi et al., 2021), due to various effects that contribute to the interferometric phase at long spatial wavelengths. As improvements of the orbit determination in recent generations of satellites, including Sentinel-1, have significantly reduced orbital errors (Fattahi & Amelung, 2014; Peter et al., 2017), other sources must dominate the residual long-wavelength signals. Parizzi et al. (2021) emphasized the dominating impact of tropospheric delays at long wavelengths (>100 km). The influence of solid Earth tides (SET) on the long-wavelength content of InSAR time-series was investigated by Xu and Sandwell (2020) and Lemrabet et al. (2023). Recently, Stephenson et al. (2022) and Liu et al. (2025) isolated the long-wavelength contribution due to tectonic plate motion after correcting for SET, tropospheric and ionospheric perturbations.

Most often, the long-wavelength signals are simply discarded from InSAR data by subtracting the best-fitting two-dimensional linear function, or 'phase ramps', for example. GNSS data is then used to complement the missing information and allow the interpretation of InSAR results in terms of crustal deformation in a given reference-frame (e.g., Fialko, 2006; Tong et al., 2013; Weiss et al., 2020; Marconato, Audin, et al., 2024). However, this approach is limited by the density and the heterogeneity of the GNSS network. Using GNSS to substitute for InSAR's long-wavelength information requires to prove that all missing spatial scales in filtered InSAR data are captured by the GNSS data (Xu & Sandwell, 2020). Alternatively, one could use GNSS to estimate a single offset in order to place InSAR velocity maps within the orbital reference field. This approach first requires to remove efficiently all long-wavelength signals unrelated to plate tectonic motion, such as atmospheric delays or tidal loading. In an attempt to retrieve the largest wavelengths from InSAR, Lemrabet et al. (2023) showed that the time-series of phase ramps, once corrected for tropospheric delays and solid Earth tides, were accurate enough to estimate trends of ramp time-series (ramp rates) and reference multiple InSAR velocity maps with minimal reliance on GNSS (Figure 1a). However, this study did not account for ionospheric effects.

Due to the ionosphere dispersive property, the low-frequency SAR sensors, such as L-band sensors, are more severely affected than C-band sensors, as Sentinel-1. Nevertheless, significant ionospheric phase contributions have been reported in Sentinel-1 InSAR time-series over various regions (Gomba et al., 2017; Liang et al., 2019; Liao et al., 2018), and its impact on the long-wavelength measurements is clearly identified, resulting in gradients of up to 0.03 mm/km/yr in line-of-sight (LOS) velocities (Stephenson et al., 2022; Liu et al., 2025). Ionosphere's effect on the interferometric phase is controlled by both the spatial variations of Total Electron Content (TEC) and the variations of incidence angle across-track.

Global ionosphere maps (GIMs) quantify the ionospheric TEC thanks to empirical models and assimilation of GNSS measurements (Hernández-Pajares et al., 2009; Feltens et al., 2011; Martire et al., 2024). They can be used to compute ionospheric cor-

rections for InSAR in a straightforward and computationally efficient way (Belcher, 2008), especially compared to methods based on the SAR data itself, such as *range split-spectrum* (Gomba et al., 2016; Fattahi et al., 2017). This latter method is computationally demanding and requires extensive filtering and interpolation in low-coherence areas, limiting the correction accuracy and applicability to systematic processing (e.g., Marconato, Doin, et al., 2024). GIMs have received little attention in the InSAR community, likely due to their limited spatial resolution (1-5° of longitude/latitude), significantly coarser than that of InSAR products (generally a few hundred meters). Yunjun et al. (2022) showed that GIMs can efficiently reduce SAR geolocation errors, but they didn't investigate their impact on phase measurements. The GIM provided by the Center for Orbit Determination in Europe (CODE) is used to compute the ionospheric correction layer of the Sentinel-1 Extended Time Annotation Products products (Gisinger et al., 2022), however the performance of this correction has not yet been thoroughly evaluated.

Here, we focus on the potential of GIMs to correct the long-wavelength contribution of ionosphere to InSAR time-series, with a strategy defined in Figure 1a. As in Lemrabet et al. (2023), we use phase ramps in range (or *across-track*) and azimuth (or *along-track*) as a simple, two parameters, quantification of the largest wavelength signals contained in InSAR, including both plate motion and non-tectonic signals. Phase ramp coefficients can be easily represented through time to statistically assess their daily, seasonal and pluriannual fluctuations. We use several TEC models to predict phase ramps due to ionosphere and compare them to the ramp time-series from a massive dataset over France, Tibet and Central Andes. Eventually, we investigate the impact of the GIM-based correction on the referencing of long-wavelength InSAR velocities using the approach based on ramp rates from Lemrabet et al. (2023).

2 Data and Methods

2.1 FLATSIM Datasets and Processing

InSAR time-series were computed using the FormaTerre LArge-Scale Multi-Temporal Sentinel-1 InterferoMetry (FLATSIM) service (FormaTerre, 2020; Thollard et al., 2021), based on the NSBAS processing chain (Doin et al., 2011; Grandin, 2015). It allows massive interferometric processing of SAR data acquired by the Sentinel-1 mission over large regions (>250,000 km^2). Long tracks are processed by several ∼500-700 km long units, hereafter referred as *tracks*. The methodological details regarding the processing and products are described in Thollard et al. (2021).

Three case-study regions — France, eastern Tibet and Central Andes — feature 21 to 30 Sentinel-1 tracks each, divided almost evenly between ascending and descending geometries (Figure 1b). The processed data covers the time period from 2014 to 2021 (2020 for Tibet), totalizing more than 15,000 time steps in 77 time-series (Tables S1 to S3). Note that the France dataset includes acquisitions down to every 6 days, while Tibet and Andes have a minimum revisit time of 12 days. France and Tibet, located at mid-latitudes, are characterized by medium variations of TEC (Figure 1b). The Andes dataset, located in the equatorial ionospheric region, undergoes stronger TEC variations (Figure 1b). Ascending tracks are acquired in the late afternoon, close to sunset, when the TEC has just passed its maximum (∼18 h, local solar time). They are thus more impacted by ionospheric effects than descending tracks, acquired just before sunrise, close to the daily minimum of TEC (∼6 h) (Liang et al., 2019).

2.2 Ramp time-series as a proxy for long-wavelength signals

Linear phase ramps in range and in azimuth are fitted on each interferogram. The corresponding ramp coefficients (in mm/km) are then inverted to retrieve a cumulative time-series of phase ramp coefficients (Figure 1a; Biggs et al., 2007; Thollard et al., 2021).

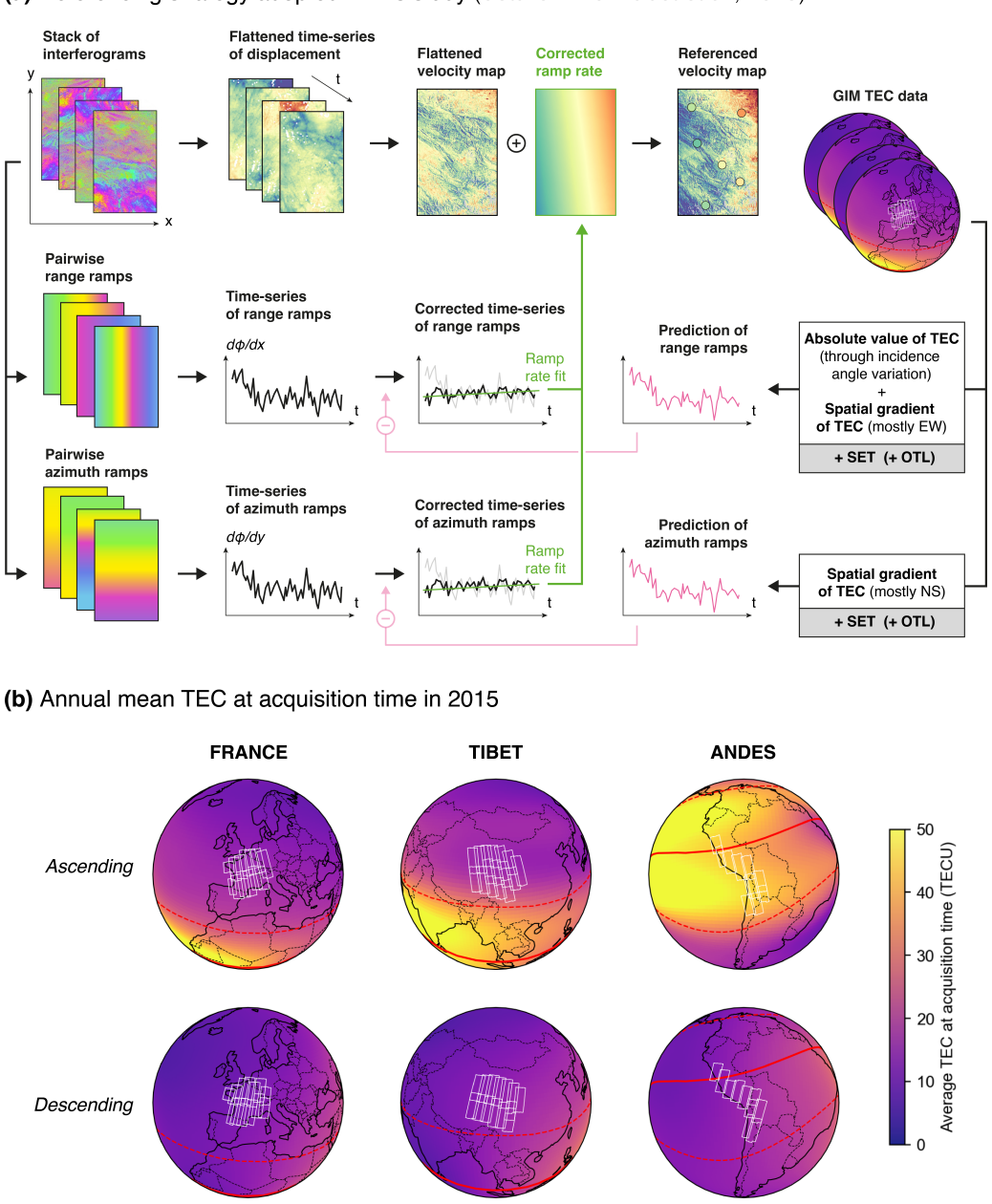

Figure 1. (a) Sketch of the referencing strategy used in this study, whose methodological details are explained in Lemrabet et al. (2023). (b) Average TEC maps related to the three datasets used in this study. The TEC from the JPLD model (Martire et al., 2024) is averaged over all acquisitions during the year 2015, at the acquisition time of ascending and descending tracks. Footprints of the processed tracks are shown by white polygons. The geomagnetic equator and +/-20° parallels are shown by solid and dashed red lines, respectively.

These ramp time-series represent a robust estimation of the largest spatial scales included in the InSAR signal in range or azimuth, over footprints of about 250 km in range by ~600 km in azimuth. The ramp coefficient time-series thus offer a good proxy to ana-

lyze fluctuations and trends of the largest wavelength signals on a simple 1-dimensional temporal axis. Note that due to the variation of look angle from near range to far range, the range ramps are not only sensitive to spatial gradients but also to any source of unmodeled absolute delay between satellite and ground, such as orbit error, atmospheric delays or Earth's surface loading (Xu & Sandwell, 2020). Ramp coefficients are computed on interferograms for which positive values represent motion away from the satellite. As a result, a decrease of the absolute vertical delay (e.g., homogeneous uplift) will for instance create a positive ramp in range.

2.3 Corrections of Tidal Effects

The Earth's surface deforms under the effect of solid Earth tides (SET), caused by gravitational interactions between the Earth, Moon, and Sun. These spatially smooth displacements, mainly vertical, reach several tens of centimeters and produce significant ramps in InSAR data (Xu & Sandwell, 2020; Lemrabet et al., 2023). Lunar tides are strongly aliased in Sentinel-1 data, while solar tides, being sampled at a fixed time of the day, cannot be observed. We model SET displacements using IERS conventions (McCarthy et al., 2004), as in Lemrabet et al. (2023). Tidal forcing also drives ocean tide loading (OTL), which deforms the lithosphere near coastlines creating vertical and horizontal displacements of up to several centimeters and affecting InSAR measurements in these regions (Yu et al., 2020; Wang et al., 2024). We derive OTL corrections at a ground resolution of $1/30^\circ$ using IERS conventions (McCarthy et al., 2004), the FES2022 tide model (Carrere et al., 2022) and the SPOTL software (Agnew, 2013). Eleven tidal constituents (K1, K2, M2, Mf, Mm, N2, O1, P1, Q1, S2, Ssa) from both solar and lunar origin are taken into account, with M2 having the largest effect. SET and OTL displacements are then projected into the satellite line-of-sight (LOS).

2.4 GIM-based Ionospheric Corrections

The International GNSS Service (IGS) publicly provides a compilation of several GIMs, computed by various institutes using a few hundreds of worldwide-distributed GNSS stations (Hernández-Pajares et al., 2009). These models, expressed on a spatial grid of 2.5° in latitude by 5° in longitude with a 2-hour temporal sampling, differ mostly by the model used for the assimilation of GNSS data (Table S4). In complement, we also use the higher resolution TEC maps provided by the Jet Propulsion Laboratory (JPLD model; Martire et al., 2024), featuring 1° spatial and 15 minutes temporal resolutions. For France, we also use a local TEC model provided by the French National Geographic Institute and constrained by the french permanent GNSS network (RGP, $\sim$500 stations). This hourly local model is not expressed on a grid but as a Taylor expansion in space.

We compute ionospheric phase screens by interpolating TEC maps in space and time, accounting for Earth rotation, and converting them into LOS InSAR phase. This workflow, described in detail in Text S1, mostly follows the methodology proposed by Gisinger et al. (2022) and Yunjun et al. (2022). Given the different orbital heights between SAR and GNSS satellites, a scaling factor must be applied to the GIM-derived TEC values beforehand. We use a constant value of 0.84 for this parameter, estimated using the empirical ionosphere model NeQuick2, that provides a 3D monthly description of the ionospheric electronic density (Nava et al., 2008, Figure S1). Note that due to Sentinel-1 TOPS acquisition mode, ionosphere can create phase jumps between bursts (Liang et al., 2019), which are not considered here since they do not impact the long-wavelength measurements.

3 Results

Linear ramp coefficients in range and in azimuth are then fitted on the tidal and ionospheric LOS maps, for each acquisition, using the actual spatial distribution of valid InSAR time-series. To better isolate the effect of each correction (SET, OTL, and GIM-based ionosphere), we evaluate them individually after applying all other corrections. Note that since the FLATSIM workflow includes a tropospheric correction based on the ECMWF ERA5 global weather model (Doin et al., 2009; Jolivet et al., 2014), the observed ramp time-series are already corrected from tropospheric delays and therefore we do not focus on this contribution. An example of observed and predicted ramp time-series is shown for range and azimuth ramps in Figures 2 and S2, respectively.

3.1 The long-wavelength contribution from tidal effects

The predicted ramp time-series due to SET show typical aliasing patterns (Figures 2a, S2), i.e., mostly high frequencies with a seasonal amplitude modulation. These ramps have similar amplitudes for the three studied regions and are systematically stronger for range ramps (amplitudes up to 0.1-0.2 mm/km) than for azimuth ramps ($<$0.03 mm/km). This is expected since SET create spatially smooth displacement patterns, impacting the InSAR ramps mostly by the effect of the look angle variation. Overall, the agreement between SET ramp predictions and the observed ramps corrected from all other contributions is very good for almost all tracks. This is reflected in the systematic reduction of the variance of ramp time-series after correcting SET (shown for all tracks on Figure S3). On average, this correction reduces the standard deviation of the residue by 20 to 50% for range ramps and by about 5% for azimuth ramps.

Like SET, OTL impacts the high-frequencies of the ramp time-series (Figures 2b, S2). The OTL-induced LOS displacement presents gradients near the coast, but also large-scale patterns. Its effect on ramps is the largest in the western and northern coasts of France, where oceanic tides are among the most important on Earth (Yu et al., 2020). For tracks located in Brittany, this contribution is dominating, creating ramp variations with amplitudes of up to 0.2 mm/km in range and 0.1 mm/km in azimuth (example on Figures 2b, S2). As a result, the OTL correction reduces the variance of ramps by up to 40% in these regions (Figure S3), but this impact decreases rapidly for tracks away from the coast. The OTL correction has a small impact in the Andes, and they were not computed for Tibet, since it is located far from the sea.

3.2 The long-wavelength contribution from the ionosphere

Figure S4 displays an example of the impact of GIM correction on a LOS displacement time-series. To quantify this impact, we provide here an in-depth statistical assessment of the ability of GIM predictions to correct the long-wavelength signals observed in InSAR time-series. The main results are summarized for ascending tracks in Figure 3, which illustrates the temporal agreement between observed and predicted ramps and the associated variance reduction for each region. Complementary figures in the Supplementary Materials provide detailed results for descending tracks (Figure S5), as well as the temporal variograms for all datasets (Figures S6 and S7).

Overall, the GIM-predicted ramps have stronger amplitudes in range than in azimuth (Figures 3, S5), because the effect of incidence angle variation adds to the spatial variability of TEC along range. Furthermore, as expected, larger variations can be observed in ascending tracks than in descending ones, due to the difference of solar activity at their respective acquisition times. The main observations on the GIM-predicted ramp time-series (Figures 2c, 3, S2, S5) are as follows:

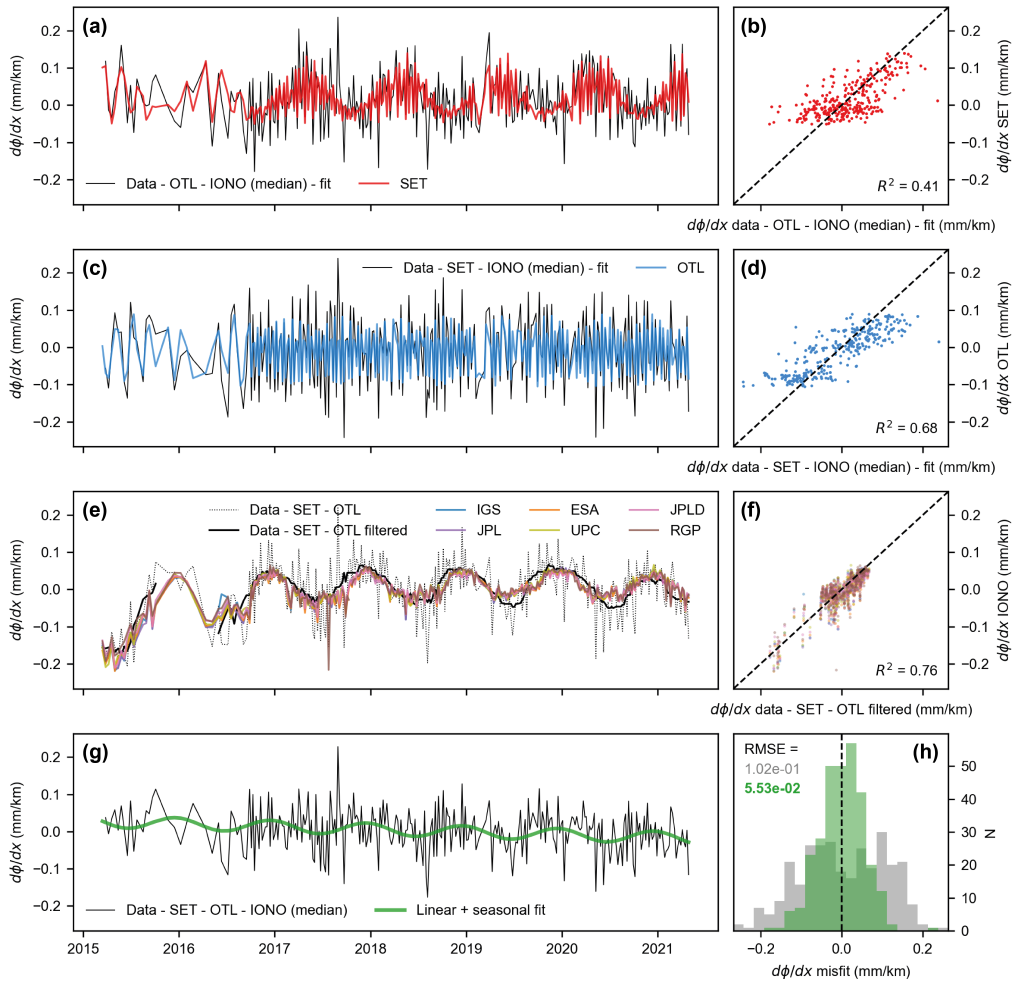

Figure 2. Example of SET, OTL and GIM corrections on a time-series of range ramps for the ascending track A030NORD in France. Left panels show the ramp time-series, with in black, data with all corrections applied except one, which is displayed in color. These colored and black time-series are compared in the right panels with the predicted correction on the y-axis, along with the squared correlation coefficient. For the two top rows, the linear plus seasonal fit shown in the lowest panel is also removed from the data. (a, b) SET correction. (c, d) OTL correction. (e, f) GIM-based ionospheric corrections. On panel e, the dotted (solid, respectively) black line shows the raw (low-pass filtered, respectively) ramps. On panel f, the low-pass filtered ramps are used for comparison. (g) Parametric fit (in green), composed of a linear and a seasonal term, computed on the data residuals after the three previous corrections (in black). (h) Distribution of the residuals with respect to the parametric fit on the raw data (in grey) and on the fully corrected data (in green), with corresponding RMSE values in mm/km.

- Range ramps present a clear seasonal oscillation, with opposite phase in France and Tibet (located in the Northern hemisphere) compared to the Andes (located in the Southern hemisphere). A faint seasonality is also visible on azimuth ramps, especially over France.
- The amplitude of this seasonal signal decreases over time from 2016 to 2020.
- In the Andes, a semi-annual oscillation of smaller amplitude is particularly visible in range ramps for ascending tracks (Figure 3e).
- Daily oscillations are relatively larger on ascending tracks than on descending tracks, along azimuth than along range, and in Andes than in France or Tibet. These high-frequency fluctuations dominate the time-series of azimuth ramps.
- The time-series show strong pluri-annual trends, often with a parabolic shape (Figure 3a-f).

The comparison between observed and predicted ramps shows that low-frequency fluctuations in GIM-based ionospheric ramps closely match those in the observed ramps. Low-pass temporal filtering (sliding median with 0.2 yr window) highlights this strong correlation, suggesting that most large-scale residual seasonality in InSAR ramp time-series has an ionospheric origin.

Interestingly, these low-frequency components of modeled ramp time-series are very consistent between the different GIMs, for both range and azimuth ramps (Figures 2, 3, S2, S5). The only significant discrepancies between GIMs occur for the Central Andes dataset, which is prone to the most intense ionospheric activity. In this case, the JPLD model better reproduces the oscillations of azimuth ramps in ascending tracks (Figure 3f,h), leading to a variance reduction twice as large as that obtained with other GIMs (Figure 3i).

Temporal variograms of the ramp time-series before and after corrections (Figures 3g,h, S6, S7) show that the GIM correction impacts the whole frequency range. The decrease of variance at short lags demonstrates the ability of GIMs to correct short-term ionospheric effects, while the further decrease at annual and longer lags indicates the effectiveness of the correction at low frequencies. In Central Andes, for azimuth ramps (Figure 3h), the improvement brought by the JPLD model compared to the IGS ones is particularly clear, starting from the highest frequencies.

The better performance of the JPLD model in correcting the large azimuth ramps observed in the Central Andes likely stems from its ability to capture the ionosphere's rapid spatio-temporal dynamics (Milanowska et al., 2021). This suggests that the resolution of the ionospheric model plays an important role in the performance of GIM-based corrections in contexts of strong ionospheric activity, such as in equatorial regions. By contrast, range ramp predictions are less sensitive to GIM resolution, since they are dominated by the effect of incidence angle variations rather than by local TEC gradients. In this case, the IGS low-resolution models are sufficient to constrain the ionospheric ramps and yield sometimes even slightly better results than the JPLD model. Note that in France, the local RGP model delivers ramp predictions similar to those of global models (Figure 3a,b). Finally, ramp time-series computed directly with the NeQuick2 model for a few examples show a very good agreement with those derived from GIMs (Figure S8), suggesting that empirical models could also be used to correct InSAR long-wavelength ionospheric contributions.

After applying all corrections (SET, OTL where applicable, and GIM), most ramp time-series still exhibit a small seasonal signal (Figures 2g, S6, S7) and varying levels of high-frequency noise. A characteristic feature of ionospheric noise is that it affects ascending tracks more strongly than descending ones, due to their different acquisition times. The residual seasonality has similar amplitude for both ascending and descending tracks, suggesting that most of the low-frequency components of ionospheric noise are effectively

corrected by the GIMs. Thus, remaining seasonal signals likely originate from uncorrected sources, such as hydrological or atmospheric loading. In contrast, high-frequency residuals are significantly larger for ascending tracks than for descending ones (Figures S6, S7), indicating that low-resolution GIMs — and, to a lesser extent, the JPLD model — cannot fully correct the daily, long-wavelength ionospheric fluctuations. This is probably owing to the limited spatial and/or temporal resolution of TEC models, or the lack of GNSS data to constrain it accurately in some regions.

4 Impact on the Referencing of InSAR Velocity Maps

One purpose of correcting non-tectonic contributions to InSAR ramps is eventually to produce referenced velocity maps directly in the orbital reference frame with a minimal input from GNSS. To that end, the trend of the ramp time-series (hereafter, ramp rate) should represent the effect of tectonic plate motions in the ITRF (Stephenson et al., 2022; Liu et al., 2025). The referencing strategy proposed by Lemrabet et al. (2023) is to extract ramp rates from ramp time-series corrected non-tectonic contributions, and to reintroduce them in the form of a velocity ramp added to the flattened velocity map for each track (Figure 1a). With such an approach, the performance of the referencing both relies on the quality of the ramp rate fit, and thus the noise level in the ramp time-series, and on the assumption that all non-tectonic contributions that can bias the trend have been removed.

Tidal corrections remove mostly high-frequencies and improve the ramp rate estimate by noise level reduction. In contrast, ionospheric corrections significantly impact the trend of ramp time-series. Indeed, the 11-year solar cycle is sampled asymmetrically by the FLATSIM time-series, with a mostly decreasing solar activity on the period between 2014 and 2019 (Figure S9). The evolution of solar activity explains the modulation of the seasonal oscillations in the ramp time-series and the change in decadal ramp rates (e.g., Figures 3, 4). As GIM-based ramp corrections appear to constrain these low-frequency variations effectively, they should significantly improve the estimated ramp rates and, thereby, the quality of the final referencing.

To verify this, we compare ramp rates estimated from InSAR data with ramp rates simulated independently with GNSS data. Lemrabet et al. (2023) applied a similar approach to show an overall agreement in Tibet after the SET correction, but without ionospheric correction and while masking the early portion of the time-series affected by strong ionospheric contributions. Here, we use their GNSS-derived ramp-rate predictions, based on the data from Wang and Shen (2020), to perform a similar analysis, but including the GIM-based ionospheric correction and without masking any part of the time-series. An example of the impact of this correction on velocity maps is shown in Figure S10. Figures 4a and b show that our proposed correction strategy (SET+GIM) improves the match between GNSS- and InSAR-derived ramp rates for Tibet. After applying these corrections, the RMSE between both measurements is reduced by 33% in range and 10% in azimuth. Moreover, uncertainties in the InSAR-derived ramp rates are greatly reduced (Figure 4), owing to the variance reduction stemming from both corrections (Figure S3).

While the applied corrections generally improve the consistency between InSAR and GNSS ramp rates, some discrepancies remain (RMS = 0.77–0.87 mm/km/yr). In some cases, corrections appear to increase the mismatch. A perfect match is however not expected, mainly because the sparse GNSS sites (Figure S11) sample unevenly the InSAR LOS velocity maps that can be strongly affected by tectonic deformation, but also because vertical velocity is neglected in the GNSS LOS projection and the observation period of InSAR and GNSS data differs. Despite this, based on Figures 4a and b, one may question whether the trends observed in InSAR ramp time-series still contain residual physical contributions, unrelated to plate motion in the ITRF. We observe in particular that, on average, there is a small shift between range ramp rates predicted by GNSS

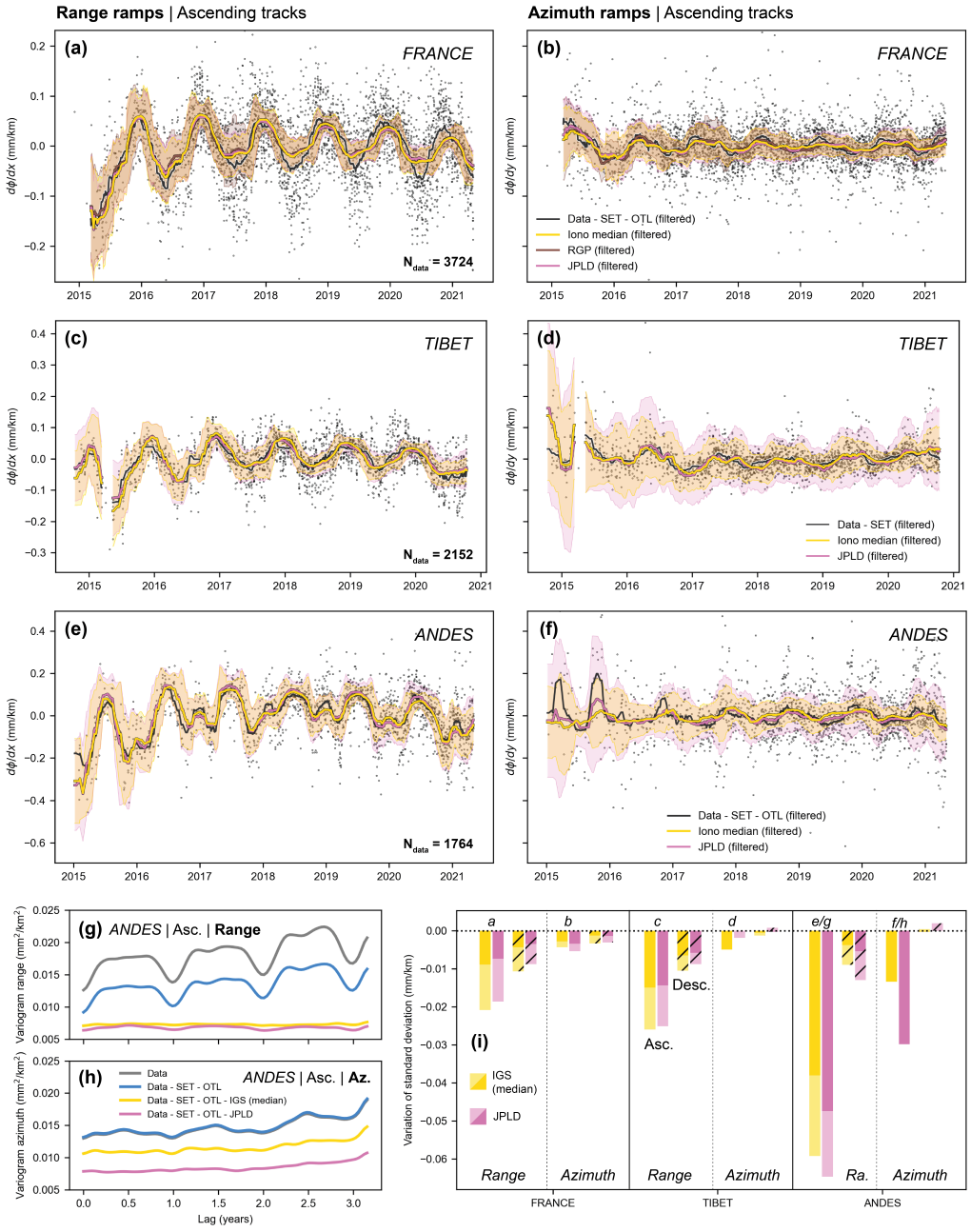

Figure 3. Comparison of range (a, c, e) and azimuth (b, d, f) ramps predicted by GIMs with the observed ramps, gathered for all ascending tracks in France (a, b), Tibet (c, d) and the Andes (e, f). Ramps corrected for tides and detrended for each track independently are shown as black dots, with the black line representing a sliding median of these datasets. The yellow, pink, and brown lines show the time-series of ramps predicted by the median of IGS (low-resolution) models, the JPLD (high-resolution) model, and the RGP model (for France only), respectively, using the same temporal smoothing. Shaded envelopes indicate twice the standard deviation within the sliding window (0.2 yr). (g, h) Examples of 1-D variogram for the range (g) and azimuth (h) ramps of ascending tracks in the Andes, as a function of temporal lag, for raw ramps (gray), ramps corrected from SET and OTL (blue), and after GIM correction, either with the median of IGS models (yellow) or the JPLD model (pink). (i) Standard deviation change associated to GIM correction, for all datasets. The impact of IGS (median) and JPLD corrections are shown in yellow and pink, respectively. Hatched bars denote the descending tracks. The saturated or light bars show the change in standard deviation for raw or smoothed (sliding median) ramp time-series, respectively.

and those obtained using InSAR after ionospheric correction, larger for descending tracks. This probably reflects a systematic bias, which, based on a fit to residual ramp rates in both LOS, would correspond to an unaccounted uniform increase in vertical delay between satellite and ground of 8.3 mm/yr combined with an eastward uniform drift of 1.2 mm/yr (Figure 4a). Such bias could originate from unmodeled orbital drift, Earth's center of mass motion, or uncertainties in decadal trends of tropospheric or ionospheric models.

5 Conclusions and perspectives

We have demonstrated that GIMs can effectively be used to model and correct long-wavelength ionospheric contributions in InSAR time-series, and thereby to improve the referencing of InSAR velocity maps. By taking advantage of extensive Sentinel-1 InSAR datasets in France, Tibet, and Central Andes, we showed that the GIM-based corrections systematically capture the dominant seasonal and pluri-annual variations observed in InSAR phase ramps. Furthermore, the high-resolution JPLD GIM model significantly reduces the strong daily fluctuations in InSAR ramps observed in equatorial regions. We also applied corrections for SET and OTL, which contribute to reduce the high-frequency noise in ramps time-series. Once applied, these three corrections reduce discrepancies between InSAR- and GNSS-derived ramp rates, showing that they substantially improve the large-scale referencing of InSAR measurements.

The proposed GIM-based corrections can be easily applied in a systematic way and have a low computational cost compared to other ionospheric compensation methods. They are limited by the resolution and reliability of GIMs, depending on the distribution of GNSS stations, which is uneven across regions. Also, the scaling factor used to account for the part of the ionosphere located above the satellite orbit should be further investigated, since it may vary through time (Yunjun et al., 2022). Additionally, other long-wavelength contributions beyond those corrected in this work probably affect InSAR measurements, including hydrological and atmospheric loading, polar tides and potential drifts in residuals orbit errors. A better understanding and modeling of these effects will be essential to move towards the use of InSAR as an accurate standalone geodetic tool capable of measuring plate tectonic motions over large regions, as advocated in, e.g., Lemrabet et al. (2023) or Liu et al. (2025).

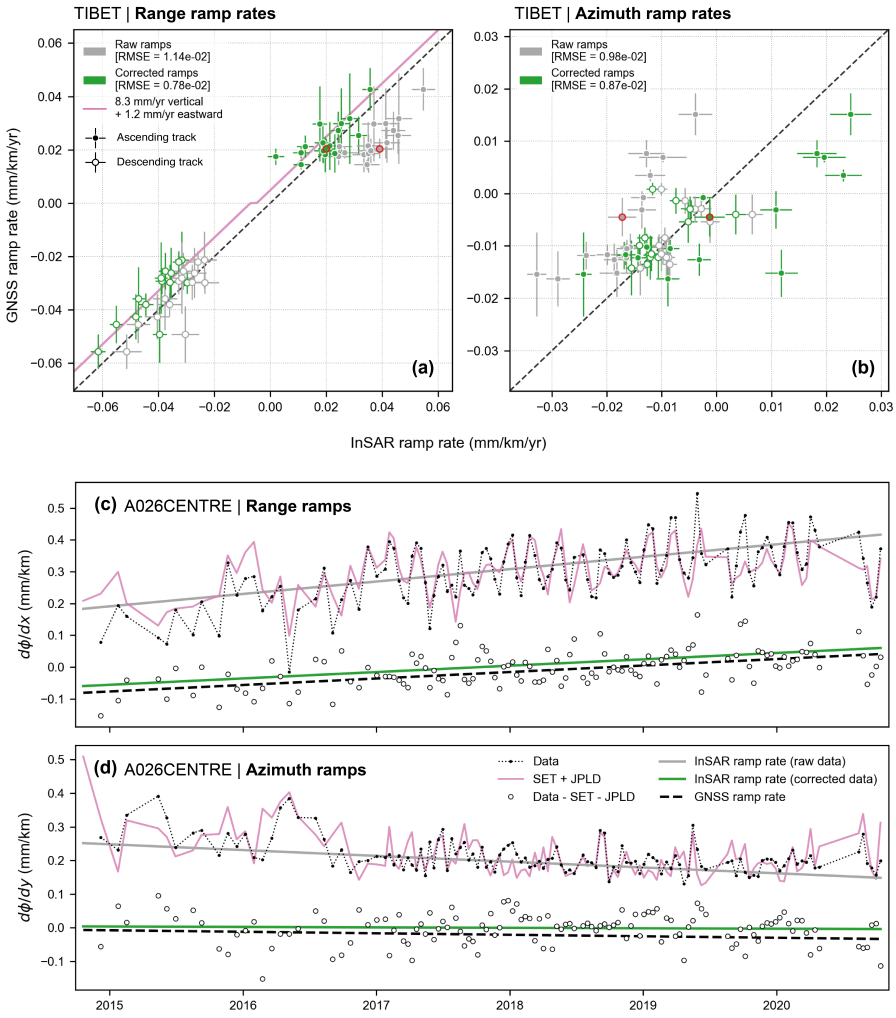

Figure 4. (a, b) Comparison between ramp rates measured with InSAR and the ones predicted by GNSS in Tibet. Panels a and b show the range and azimuth ramp rates, respectively. Ascending and descending tracks are shown by full and empty circles, respectively. InSAR rates computed on raw ramps are shown in grey, while ramp rates computed on time-series corrected from SET and GIM (JPLD model) are shown in green. In panel a, the pink line shows the impact of a combined increase of 8.3 mm/yr in vertical delay and of 1.2 mm/yr in eastward delay, which best explains the residuals between GNSS and InSAR rates. (c, d) Ramp time-series before (dashed line) and after (empty circles) removing the prediction of SET and ionosphere (pink line), for the track A026CENTRE (highlighted by red circles in panels a and b). Rates fitted in the raw and corrected InSAR ramps are shown in grey and green, respectively, and the GNSS ramp rate is shown by the black dashed line.

Open Research Section

The Sentinel-1 data used in this work is open and can be accessed, for instance, from ASF DAAC (2020/2023). All GIMs used in this study are available on JPL (2024), RGP (2025) and IGS (2025). 10.7cm Radio Flux data is available on NOAA (2025). The

NeQuick2 code is available on ITU (2023). Solid Earth tides have been computed with the Solid program (Milbert, 2024). Oceanic tides have been computed with the SPOTL program (Agnew, 2013). The GIM-based correction codes are available on Marconato (2025). GNSS data from Wang & Shen (2020) is available on Shen (2019). All ramp time-series data analyzed in this work, including observed ramps and corrections, are available on Marconato et al. (2025), together with plots similar to Figure 2 for all the studied tracks.

Acknowledgments

We thank the FLATSIM project team (M.-P. Doin, C. Lasserre, C. Proy, M. Diament, P. Durand, F. Thollard, C. Laurent, E. Pathier, R. Grandin, E. Pointal, E. Deschamps-Ostanciaux, D. Clesse) for building and operating the FLATSIM service (FormaTerre, 2020). Post-processing computations presented in this paper were performed using the GRICAD infrastructure (`https://gricad.univ-grenoble-alpes.fr/`), which is supported by Grenoble research communities. The project REF-InSAR was financially supported by CNES as an application of the Sentinel-1 mission. L. Marconato benefited from a 6 months allowance by CNES to accomplish this work. We thank the reviewers and the editor for their constructive comments, which helped improve this manuscript.

Conflict of Interest Statement

The authors have no conflicts of interest to disclose.

References

Agnew, D. C. (2013). *SPOTL: Some Programs for Ocean-Tide Loading.* Retrieved from `https://igppweb.ucsd.edu/~agnew/Spotl/spotlmain.html`

ASF DAAC. (2020/2023). *Alaska Satellite Facility DAAC.* Retrieved from `https://asf.alaska.edu/asf/asf-services-data-discovery/`

Bekaert, D. P., Karim, M., Linick, J. P., Hua, H., Sangha, S., Lucas, M., ... Lai-Norling, J. (2019, December). Development of open-access Standardized InSAR Displacement Products by the Advanced Rapid Imaging and Analysis (ARIA) Project for Natural Hazards. In (Vol. 2019, pp. G23A–04). Retrieved 2025-06-24, from `https://ui.adsabs.harvard.edu/abs/2019AGUFM.G23A..04B` (ADS Bibcode: 2019AGUFM.G23A..04B)

Belcher, D. (2008, December). Theoretical limits on SAR imposed by the ionosphere. *IET Radar, Sonar & Navigation*, *2*(6), 435–448. Retrieved 2022-03-17, from `https://digital-library.theiet.org/content/journals/10.1049/iet-rsn_20070188` doi: 10.1049/iet-rsn:20070188

Biggs, J., Wright, T., Lu, Z., & Parsons, B. (2007, September). Multi-interferogram method for measuring interseismic deformation: Denali Fault, Alaska. *Geophysical Journal International*, *170*(3), 1165–1179. Retrieved 2023-03-02, from `https://academic.oup.com/gji/article/170/3/1165/634759` doi: 10.1111/j.1365-246X.2007.03415.x

Carrere, L., Lyard, F., Cancet, M., Allain, D., Dabat, M.-L., Fouchet, E., ... Picot, N. (2022). A new barotropic tide model for global ocean: FES2022. *CNES*. doi: 10.24400/527896/A03-2022.3287

Doin, M.-P., Guillaso, S., Jolivet, R., Lasserre, C., Lodge, F., Ducret, G., & Grandin, R. (2011). Presentation of the small baseline NSBAS processing chain on a case example: The Etna deformation monitoring from 2003 to 2010 using Envisat data. In (pp. 3434–3437). ESA SP-697, Frascati, Italy.

Doin, M.-P., Lasserre, C., Peltzer, G., Cavalié, O., & Doubre, C. (2009, September). Corrections of stratified tropospheric delays in SAR interferometry: Validation with global atmospheric models. *Journal of Applied Geophysics*, *69*(1), 35–50.

Retrieved 2022-01-11, from https://linkinghub.elsevier.com/retrieve/pii/S0926985109000603 doi: 10.1016/j.jappgeo.2009.03.010

Fang, J., Houseman, G. A., Wright, T. J., Evans, L. A., Craig, T. J., Elliott, J. R., & Hooper, A. (2024, June). The Dynamics of the India-Eurasia Collision: Faulted Viscous Continuum Models Constrained by High-Resolution Sentinel-1 InSAR and GNSS Velocities. *Journal of Geophysical Research: Solid Earth*, *129*(6), e2023JB028571. Retrieved 2024-08-07, from https://agupubs.onlinelibrary.wiley.com/doi/10.1029/2023JB028571 doi: 10.1029/2023JB028571

Fattahi, H., & Amelung, F. (2014, October). InSAR uncertainty due to orbital errors. *Geophysical Journal International*, *199*(1), 549–560. Retrieved 2024-12-21, from http://academic.oup.com/gji/article/199/1/549/733573/InSAR-uncertainty-due-to-orbital-errors doi: 10.1093/gji/ggu276

Fattahi, H., Simons, M., & Agram, P. (2017, October). InSAR Time-Series Estimation of the Ionospheric Phase Delay: An Extension of the Split Range-Spectrum Technique. *IEEE Transactions on Geoscience and Remote Sensing*, *55*(10), 5984–5996. Retrieved 2021-10-08, from http://ieeexplore.ieee.org/document/7987747/ doi: 10.1109/TGRS.2017.2718566

Feltens, J., Angling, M., Jackson-Booth, N., Jakowski, N., Hoque, M., Hernández-Pajares, M., ... Zandbergen, R. (2011, December). Comparative testing of four ionospheric models driven with GPS measurements. *Radio Science*, *46*(6), 2010RS004584. Retrieved 2024-06-07, from https://agupubs.onlinelibrary.wiley.com/doi/10.1029/2010RS004584 doi: 10.1029/2010RS004584

Fialko, Y. (2006, June). Interseismic strain accumulation and the earthquake potential on the southern San Andreas fault system. *Nature*, *441*(7096), 968–971. Retrieved 2025-06-24, from https://www.nature.com/articles/nature04797 doi: 10.1038/nature04797

FormaTerre. (2020). *FLATSIM Data Products: Data Products generated by FLATSIM (FormaTerre LArge-scale multi-Temporal Sentinel-1 InterferoMetry)*. CNES. Retrieved 2025-06-24, from https://flatsim.cnes.fr doi: 10.24400/253171/FLATSIM2020

Gisinger, C., Libert, L., Marinkovic, P., Krieger, L., Larsen, Y., Valentino, A., ... Miranda, N. (2022). The Extended Timing Annotation Dataset for Sentinel-1—Product Description and First Evaluation Results. *IEEE Transactions on Geoscience and Remote Sensing*, *60*, 1–22. Retrieved 2024-06-04, from https://ieeexplore.ieee.org/document/9841598/ doi: 10.1109/TGRS.2022.3194216

Gomba, G., Parizzi, A., De Zan, F., Eineder, M., & Bamler, R. (2016, March). Toward Operational Compensation of Ionospheric Effects in SAR Interferograms: The Split-Spectrum Method. *IEEE Transactions on Geoscience and Remote Sensing*, *54*(3), 1446–1461. Retrieved 2021-10-08, from http://ieeexplore.ieee.org/document/7308047/ doi: 10.1109/TGRS.2015.2481079

Gomba, G., Rodriguez Gonzalez, F., & De Zan, F. (2017, January). Ionospheric Phase Screen Compensation for the Sentinel-1 TOPS and ALOS-2 ScanSAR Modes. *IEEE Transactions on Geoscience and Remote Sensing*, *55*(1), 223–235. Retrieved 2023-11-07, from http://ieeexplore.ieee.org/document/7570182/ doi: 10.1109/TGRS.2016.2604461

Grandin, R. (2015, May). Interferometric Processing of SLC Sentinel-1 TOPS Data. In *Proceedings of Fringe 2015: Advances in the Science and Applications of SAR Interferometry and Sentinel-1 InSAR Workshop*. European Space Agency. Retrieved 2022-04-27, from http://proceedings.esa.int/fringe2015/page_paper116.php doi: 10.5270/Fringe2015.pp116

Hernández-Pajares, M., Juan, J. M., Sanz, J., Orus, R., Garcia-Rigo, A., Feltens,

J., ... Krankowski, A. (2009, March). The IGS VTEC maps: a reliable source of ionospheric information since 1998. *Journal of Geodesy*, *83*(3-4), 263–275. Retrieved 2024-06-07, from http://link.springer.com/10.1007/s00190-008-0266-1 doi: 10.1007/s00190-008-0266-1

IGS. (2025). *IGS combined global ionospheric maps (GIM).* International GNSS Service. Retrieved from https://cdaweb.gsfc.nasa.gov/pub/data/gps/tec2hr_igs/

ITU. (2023). *Ionospheric propagation data and prediction methods required for the design of satellite networks and systems.* International Telecommunication Union. Retrieved from https://www.itu.int/rec/R-REC-P.531-15-202308-I/en

Jolivet, R., Agram, P. S., Lin, N. Y., Simons, M., Doin, M., Peltzer, G., & Li, Z. (2014, March). Improving InSAR geodesy using Global Atmospheric Models. *Journal of Geophysical Research: Solid Earth*, *119*(3), 2324–2341. Retrieved 2022-01-11, from https://onlinelibrary.wiley.com/doi/abs/10.1002/2013JB010588 doi: 10.1002/2013JB010588

JPL. (2024). *Global Ionospheric Maps for Research - JPLD Data Product.* California Institute of Technology. Retrieved from https://sideshow.jpl.nasa.gov/pub/iono_daily/gim_for_research/jpld/

Lemrabet, L., Doin, M., Lasserre, C., & Durand, P. (2023, July). Referencing of Continental-Scale InSAR-Derived Velocity Fields: Case Study of the Eastern Tibetan Plateau. *Journal of Geophysical Research: Solid Earth*, *128*(7), e2022JB026251. Retrieved 2023-08-09, from https://agupubs.onlinelibrary.wiley.com/doi/10.1029/2022JB026251 doi: 10.1029/2022JB026251

Liang, C., Agram, P., Simons, M., & Fielding, E. J. (2019, September). Ionospheric Correction of InSAR Time Series Analysis of C-band Sentinel-1 TOPS Data. *IEEE Transactions on Geoscience and Remote Sensing*, *57*(9), 6755–6773. Retrieved 2021-10-08, from https://ieeexplore.ieee.org/document/8706258/ doi: 10.1109/TGRS.2019.2908494

Liao, H., Meyer, F. J., Scheuchl, B., Mouginot, J., Joughin, I., & Rignot, E. (2018, May). Ionospheric correction of InSAR data for accurate ice velocity measurement at polar regions. *Remote Sensing of Environment*, *209*, 166–180. Retrieved 2021-10-20, from https://linkinghub.elsevier.com/retrieve/pii/S0034425718300580 doi: 10.1016/j.rse.2018.02.048

Liu, Y., Yunjun, Z., & Simons, M. (2025, June). Inferring Tectonic Plate Rotations From InSAR Time Series. *Geophysical Research Letters*, *52*(12), e2025GL115137. Retrieved 2025-06-25, from https://agupubs.onlinelibrary.wiley.com/doi/10.1029/2025GL115137 doi: 10.1029/2025GL115137

Marconato, L. (2025). *FlatsimCorr: Correction of Long-wavelength non-tectonic contribution in Flatsim time-series.* Retrieved from https://github.com/leomarconato/FlatsimCorr

Marconato, L., Audin, L., Doin, M.-P., Nocquet, J.-M., Jarrin, P., Rolandone, F., ... Cisneros, D. (2024, September). Internal deformation of the North Andean Sliver in Ecuador-southern Colombia observed by InSAR. *Geophysical Journal International*, ggae338. Retrieved 2025-01-10, from https://academic.oup.com/gji/advance-article/doi/10.1093/gji/ggae338/7759724 doi: 10.1093/gji/ggae338

Marconato, L., Doin, M.-P., Audin, L., & Pathier, E. (2024, June). Ionospheric compensation in L-band InSAR time-series: Performance evaluation for slow deformation contexts in equatorial regions. *Science of Remote Sensing*, *9*, 100113. Retrieved 2024-01-19, from https://linkinghub.elsevier.com/retrieve/pii/S266601722300038X doi: 10.1016/j.srs.2023.100113

Marconato, L., Doin, M.-P., Lovery, B., Rolland, L., & Durand, P. (2025, August).

Data from "Long-Wavelength Ionospheric Compensation of InSAR Time-Series Based on Global Ionosphere Maps". Zenodo. Retrieved from https://doi.org/10.5281/zenodo.16844331 doi: 10.5281/zenodo.16844331

Martire, L., Runge, T. F., Meng, X., Krishnamoorthy, S., Vergados, P., Mannucci, A. J., ... Green, D. W. (2024, May). The JPL-GIM algorithm and products: multi-GNSS high-rate global mapping of total electron content. *Journal of Geodesy*, *98*(5), 44. Retrieved 2024-12-06, from https://link.springer.com/10.1007/s00190-024-01860-3 doi: 10.1007/s00190-024-01860-3

McCarthy, D. D., Petit, G., & International Earth Rotation and Reference Systems Service (Eds.). (2004). *IERS Conventions (2003)* (No. 32). Frankfurt am Main: Verl. des Bundesamtes für Kartographie und Geodäsie.

Milanowska, B., Wielgosz, P., Krypiak-Gregorczyk, A., & Jarmołowski, W. (2021). Accuracy of global ionosphere maps in relation to their time interval. *Remote Sensing*, *13*(18). Retrieved from https://www.mdpi.com/2072-4292/13/18/3552 doi: 10.3390/rs13183552

Milbert, D. (2024). *Solid Earth Tide computation program.* Retrieved from https://geodesyworld.github.io/SOFTS/solid.htm

Morishita, Y., Lazecky, M., Wright, T., Weiss, J., Elliott, J., & Hooper, A. (2020, January). LiCSBAS: An Open-Source InSAR Time Series Analysis Package Integrated with the LiCSAR Automated Sentinel-1 InSAR Processor. *Remote Sensing*, *12*(3), 424. Retrieved 2025-06-24, from https://www.mdpi.com/2072-4292/12/3/424 doi: 10.3390/rs12030424

Nava, B., Coïsson, P., & Radicella, S. (2008, December). A new version of the NeQuick ionosphere electron density model. *Journal of Atmospheric and Solar-Terrestrial Physics*, *70*(15), 1856–1862. Retrieved 2025-01-15, from https://linkinghub.elsevier.com/retrieve/pii/S1364682608000357 doi: 10.1016/j.jastp.2008.01.015

NOAA. (2025). *Daily Solar Activity Data.* Space Weather Prediction Center - National Oceanic and Atmospheric Administration. Retrieved from https://www.ngdc.noaa.gov/stp/space-weather/swpc-products/annual_reports/daily_solar_indices_summaries/daily_solar_data/

Parizzi, A., Brcic, R., & De Zan, F. (2021, October). InSAR Performance for Large-Scale Deformation Measurement. *IEEE Transactions on Geoscience and Remote Sensing*, *59*(10), 8510–8520. Retrieved 2022-06-07, from https://ieeexplore.ieee.org/document/9280350/ doi: 10.1109/TGRS.2020.3039006

Peter, H., Jäggi, A., Fernández, J., Escobar, D., Ayuga, F., Arnold, D., ... Fémé-nias, P. (2017). Sentinel-1a – first precise orbit determination results. *Advances in Space Research*, *60*(5), 879-892. Retrieved from https://www.sciencedirect.com/science/article/pii/S0273117717303794 doi: https://doi.org/10.1016/j.asr.2017.05.034

RGP. (2025). *Modèles Ionosphériques RGP.* Institut National de l'Information Géographique et Forestière. Retrieved from ftp://rgpdata.ign.fr/pub/products/ionosphere/calcul/

Shen, Z. (2019). *Present-Day Crustal Deformation of Continental China Derived from GPS and its Tectonic Implications.* Harvard Dataverse. Retrieved from https://doi.org/10.7910/DVN/C1WE3N doi: 10.7910/DVN/C1WE3N

Stephenson, O. L., Liu, Y., Yunjun, Z., Simons, M., Rosen, P., & Xu, X. (2022, November). The Impact of Plate Motions on Long-Wavelength InSAR-Derived Velocity Fields. *Geophysical Research Letters*, *49*(21), e2022GL099835. Retrieved 2024-12-21, from https://agupubs.onlinelibrary.wiley.com/doi/10.1029/2022GL099835 doi: 10.1029/2022GL099835

Thollard, F., Clesse, D., Doin, M.-P., Donadieu, J., Durand, P., Grandin, R., ... Specht, B. (2021, September). FLATSIM: The ForM@Ter LArge-Scale Multi-Temporal Sentinel-1 InterferoMetry Service. *Remote Sensing*, *13*(18), 3734.

592 Retrieved 2022-11-15, from https://www.mdpi.com/2072-4292/13/18/3734
593 doi: 10.3390/rs13183734
594 Tong, X., Sandwell, D. T., & Smith-Konter, B. (2013, January). High-resolution
595 interseismic velocity data along the San Andreas Fault from GPS and In-
596 SAR. *Journal of Geophysical Research: Solid Earth*, *118*(1), 369–389. Re-
597 trieved 2022-02-01, from https://onlinelibrary.wiley.com/doi/10.1029/
598 2012JB009442 doi: 10.1029/2012JB009442
599 Wang, M., & Shen, Z. (2020, February). Present-Day Crustal Deformation of Con-
600 tinental China Derived From GPS and Its Tectonic Implications. *Journal of*
601 *Geophysical Research: Solid Earth*, *125*(2), e2019JB018774. Retrieved 2025-
602 03-07, from https://agupubs.onlinelibrary.wiley.com/doi/10.1029/
603 2019JB018774 doi: 10.1029/2019JB018774
604 Wang, M., Wang, Q., Zhang, H., He, W., Xiao, F., & Li, J. (2024). Analysis of
605 Ocean Tide Loading Displacement Correction for Long-Strip InSAR Mea-
606 surements in Coastal Areas of France. *IEEE Journal of Selected Topics in*
607 *Applied Earth Observations and Remote Sensing*, *17*, 6818–6824. Retrieved
608 2024-10-10, from https://ieeexplore.ieee.org/document/10462181/ doi:
609 10.1109/JSTARS.2024.3374520
610 Watson, A. R., Elliott, J. R., Lazecký, M., Maghsoudi, Y., McGrath, J. D., & Wal-
611 ters, R. J. (2024, May). An InSAR-GNSS Velocity Field for Iran. *Geophys-*
612 *ical Research Letters*, *51*(10), e2024GL108440. Retrieved 2025-06-24, from
613 https://agupubs.onlinelibrary.wiley.com/doi/10.1029/2024GL108440
614 doi: 10.1029/2024GL108440
615 Weiss, J. R., Walters, R. J., Morishita, Y., Wright, T. J., Lazecky, M., Wang, H.,
616 ... Parsons, B. (2020, September). High-Resolution Surface Velocities
617 and Strain for Anatolia From Sentinel-1 InSAR and GNSS Data. *Geophys-*
618 *ical Research Letters*, *47*(17), e2020GL087376. Retrieved 2025-06-24, from
619 https://agupubs.onlinelibrary.wiley.com/doi/10.1029/2020GL087376
620 doi: 10.1029/2020GL087376
621 Xu, X., & Sandwell, D. T. (2020, January). Toward Absolute Phase Change Re-
622 covery With InSAR: Correcting for Earth Tides and Phase Unwrapping Am-
623 biguities. *IEEE Transactions on Geoscience and Remote Sensing*, *58*(1), 726–
624 733. Retrieved 2025-02-17, from https://ieeexplore.ieee.org/document/
625 8850313/ doi: 10.1109/TGRS.2019.2940207
626 Yu, C., Penna, N. T., & Li, Z. (2020, August). Ocean Tide Loading Effects
627 on InSAR Observations Over Wide Regions. *Geophysical Research Let-*
628 *ters*, *47*(15), e2020GL088184. Retrieved 2024-10-10, from https://
629 agupubs.onlinelibrary.wiley.com/doi/10.1029/2020GL088184 doi:
630 10.1029/2020GL088184
631 Yunjun, Z., Fattahi, H., Pi, X., Rosen, P., Simons, M., Agram, P., & Aoki, Y.
632 (2022). Range Geolocation Accuracy of C-/L-Band SAR and its Im-
633 plications for Operational Stack Coregistration. *IEEE Transactions on*
634 *Geoscience and Remote Sensing*, *60*, 1–19. Retrieved 2023-11-07, from
635 https://ieeexplore.ieee.org/document/9759304/ doi: 10.1109/
636 TGRS.2022.3168509

6.2 Supplements

Supporting Information for "Long-Wavelength Ionospheric Compensation of InSAR Time Series Based on Global Ionosphere Maps"

L. Marconato[1], M.-P. Doin[1], B. Lovery[1], L. Rolland[2], P. Durand[3]

[1]Univ. Grenoble Alpes, Univ. Savoie Mont Blanc, CNRS, IRD, Univ. Gustave Eiffel, ISTerre, 38000 Grenoble, France

[2]Université Côte d'Azur, CNRS, IRD, Observatoire de la Côte d'Azur, Géoazur, 06560 Valbonne, France

[3]Centre National d'Études Spatiales, Toulouse, France

Contents of this file

- Text S1
- Figures S1 to S11
- Tables S1 to S4

Text S1. Methodological details regarding the computation of ionospheric phase screens based on Global Ionospheric Maps (GIMs).

Sources of TEC

The characteristic of the different TEC data sources used in this study are summarized in Table S4. Besides their different resolutions, the GIMs differ also by the mapping function used to assimilate the GNSS observation et convert it to vertical TEC. The JPLD mode, for instance, is the one based on the most complex mapping function (3-layers model). Note that although several layers are used in some GIMs to model GNSS data, only the vertically integrated TEC is provided in the final product. We thus use a single layer mapping function to convert TEC to the InSAR phase contribution (see details below in *Mapping Function*). The impact of the vertical distribution of TEC is largely negligible in this work given the resolution of the TEC models used, but should be considered as a possible improvement if higher-resolution models are developed in the future.

Interpolation strategy

The spatial resolution of the GIMs used in the study is much coarser than that of the FLATSIM InSAR products. Therefore, a spatial interpolation of the Total Electron Content datasets must be performed to compute ionospheric phase screens. However, interpolating at the resolution of interferograms ($\sim$100 m) would be computationally expensive and useless given the smoothness of the TEC maps. We thus interpolate the TEC maps on a grid in radar coordinates with a $\sim$10 km sampling on ground, using a

bicubic interpolation method. This grid is enough to capture the spatial variation of TEC constrained by the GIMs, whose resolution is in the best case of the order of 100 km.

For each point in the radar image geometry, with given latitude ρ and longitude Φ, we compute the ionospheric piercing point (IPP), i.e., the intersection between the radar rays and the idealized ionospheric thin shell. IPP coordinates $(\rho_{\mathrm{IPP}}, \Phi_{\mathrm{IPP}})$ can be computed from the ground coordinates (ρ, Φ) using the incidence angle θ and the look angle β (measured from the north with anti-clockwise as positive, considering LOS from target to SAR platform), following Yunjun et al. (2022):

$$\begin{cases} \rho_{\mathrm{IPP}} = \arcsin[\sin(\rho)\cos(\theta - \theta_{\mathrm{IPP}}) + \cos(\rho)\sin(\theta - \theta_{\mathrm{IPP}})\cos(\beta)] \\ \Delta\Phi = \mathrm{atan2}[-\sin(\theta - \theta_{\mathrm{IPP}})\cos(\rho)\sin(\beta),\ \cos(\theta - \theta_{\mathrm{IPP}}) - \sin(\rho)\sin(\theta_{\mathrm{IPP}})] \\ \Phi_{\mathrm{IPP}} = \mathrm{mod}(\Phi + \Delta\Phi + \pi, 2\pi) - \pi \end{cases} \tag{1}$$

where θ_{IPP} is the incidence angle on the ionospheric thin-shell and can be computed from the ground incidence angle θ as follows:

$$\theta_{\mathrm{IPP}} = \arcsin\left(\frac{Re.\sin\theta}{Re + h_{\mathrm{IPP}}}\right) \tag{2}$$

where Re is the Earth's radius and h_{IPP} is the height of the ionospheric idealized layer (here set to 400 km).

We also need to perform a temporal interpolation of the TEC between the GIM time steps before and after the SAR acquisition time. As the SAR acquisition duration of one FLATSIM chunk (250 by 500 km) is of the order of one minute, the SAR acquisition duration can be considered as instantaneous with respect to the temporal resolution of the ionospheric models. Since the ionosphere exhibits more stable patterns in a Sun-fixed reference frame, it is essential to account for Earth's rotation when performing temporal interpolation of ionospheric TEC. The ionosphere is largely driven by solar radiation, which induces daily variations that are more coherent when viewed relative to the

Sun rather than to a terrestrial reference frame. Neglecting this $\sim$15° per hour rotation can lead to apparent rapid variations in TEC that do not correspond to actual physical changes. By interpolating in a Sun-synchronous framework, one minimizes these artifacts and better captures the underlying spatiotemporal coherence of TEC variations. Thus, similarly to the way the GIM-based ionospheric corrections are build in the ETAD products (Gisinger et al., 2022), we linearly interpolate the values of the previous $\mathrm{TEC}^{t_{before}}$ and next $\mathrm{TEC}^{t_{after}}$ time steps at the acquisition time t_{acq} by shifting the longitude Φ_{IPP} proportionally to the Earth's rotation rate ω (15°/h):

$$\mathrm{TEC}^{t_{acq}}_{\Phi_{\mathrm{IPP}}} = \frac{t_{after} - t_{acq}}{t_{after} - t_{before}} \times \mathrm{TEC}^{t_{before}}_{\Phi_{\mathrm{IPP}}+\omega(t_{acq}-t_{before})} + \frac{t_{acq} - t_{before}}{t_{after} - t_{before}} \times \mathrm{TEC}^{t_{after}}_{\Phi_{\mathrm{IPP}}-\omega(t_{after}-t_{acq})} \tag{3}$$

This effect is quite small for the 15-minute JPLD model, but it can represent important shifts for the other models whose temporal sampling is 2 hours. In this case, the 30° rotation between two time steps cannot be neglected, particularly during periods of rapid ionospheric changes (sunrise or sunset).

The RGP model is not expressed on a spatio-temporal grid, but as a two-dimensional Taylor series expansion with respect to the latitude and sun-fixed longitude. Thus, the Earth's rotation is already taken into account in the model, and the TEC can be directly computed at the point corresponding to the latitude and longitude of the IPP at the time of acquisition. The Taylor expansion coefficients are provided each hour, and the continuity is not ensured between two consecutive models. Therefore, we use the two models encompassing the acquisition time, separated by one hour, to compute two estimations of the TEC at the exact SAR acquisition time. Then, an average of both TEC models,

weighted proportionally to the position of the acquisition time with respect to each model times, is computed and used in the following.

Mapping function

Once TEC maps have been interpolated spatially and temporally on the radar image geometry taking into account the IPP position for each radar image pixel, it must be converted to an ionospheric phase screen (IPS), or the actual phase advance due in the two-way propagation of the SAR signal. This can be easily computed using Appelton–Hartree equation (Belcher, 2008):

$$\phi_{iono} = -\frac{4\pi K}{c f_0}\text{sTEC} \tag{4}$$

where sTEC represents the integral of the TEC in the line-of-sight (LOS) of the satellite, or slant TEC, $K = 40.3$ m^3/s^2, c is the speed of light in vacuum and f_0 the frequency of the wave. We use the following simple mapping function based on the thin-shell ionosphere approximation (Yunjun et al., 2022) to project the vertically integrated TEC values provided by the GIMs (vTEC) into slant TEC:

$$\text{sTEC} = \frac{\text{vTEC}}{\cos(\theta_{\text{IPP}})} \tag{5}$$

Note that the refraction effect, advocated as non negligible by Yunjun et al. (2022), is not taken into account here. Indeed, we found a dimensional inconsistency in the Equation 9 of their article, leading to a large overestimation of the refraction angles. Indeed, the vertically integrated TEC should be replaced by the electron density in the equation (9)

of their paper. Electron density, taken as TEC divided by the actual thickness of the ionospheric layer (a few hundred of kilometers) is a much smaller number than TEC. Consequently, the refraction angles which we then computed using the correct formula turned out to be very small, and we conclude that the refraction effect is completely negligible at the frequency bands used for SAR imaging.

Scaling factor

All the TEC models used here are based on GNSS data, whose signals are crossing the entire ionosphere (the orbital height for the GPS constellation is ∼20,000 km). By contrast, the SAR satellites fly at lower altitudes (693 km for Sentinel-1) and thus part of the ionosphere is located above their orbits. This should be taken into account to correct only for the TEC located below the satellites orbits and actually affecting the InSAR phase. No consensual approaches have been proposed to estimate the scaling factor quantifying the sub-orbital part of the ionosphere $\alpha = \mathrm{TEC}_{sub-orbital}/\mathrm{TEC}_{total}$ to accurately scale the TEC values from the GIMs. For ETAD corrections, a constant scaling factor of $\alpha = 0.9$ is used, based on a single analysis of TerraSAR-X data (Gisinger et al., 2022). Yunjun et al. (2022) estimate the topside TEC using the GNSS data of the receiver located onboard the Sentinel-1 platforms for one ascending track in Chile. By comparing these measurements with the JPLD GIM, they provide a time-series of the α coefficient for this track, showing strong variations, mostly ranging between 0.3 and 0.85, with a median value of 0.69. They observe a seasonal behavior of the α values, such as a pluri-annual decrease of the ratio between 2015 (close to the solar maximum) and 2020 (close to the solar minimum). Although limited to a single region and a single time of

day, both characterized by strong ionospheric activity, this analysis suggests lower values of α when the ionospheric activity is lower (in winter and close to the solar minimum). Unfortunately, uncertainties on the topside TEC measurements are not provided and thus their accuracy cannot be quantified. Anyhow, applying this method would have implied heavy GNSS processing which is beyond the scope of this study.

We investigated predictions of the α ratio made by an empirical ionospheric model, namely the NeQuick2 model (Nava et al., 2008). This model takes as parameters the position (longitude, latitude, altitude), the month, the time of the day and the daily solar activity (given by the 10.7cm solar radio flux) and outputs the electron density profile. It can also be used to compute integrated TEC along slant profile between two points. We computed for the three geographical regions (France, Tibet, and Andes) studied in the following, the ratio between the TEC integrated vertically up to 693 km (the height of the Sentinel-1 orbits) and up to 20,000 km (typical height of the GNSS orbits), equivalent to α.

The values of α predicted by NeQuick2 show relatively small variations, between 0.81 and 0.85, and are similar across regions. A slight increase of the ratio can be observed from the solar maximum to the solar minimum, as opposed to the trend found by the data of Yunjun et al. (2022). Globally, the variations of the ratio predicted by NeQuick2 are small and would not impact the correction significantly. We thus use the median value of these predictions, i.e $\alpha = 0.84$, to scale the GIM-based corrections shown in the following.

We also computed for a few tracks the ramps directly predicted by the NeQuick2 model (Figure S7). Using such a 3D empirical ionospheric model to derive TEC does not require

any interpolation nor the use of a mapping function. Indeed, NeQuick2 allows a direct computation of the slant integrated TEC between the satellite and the ground for each point of the coarse grid defined above. Then, the TEC maps are converted to IPS using Equation 4, and then ramps were fitted in this IPS.

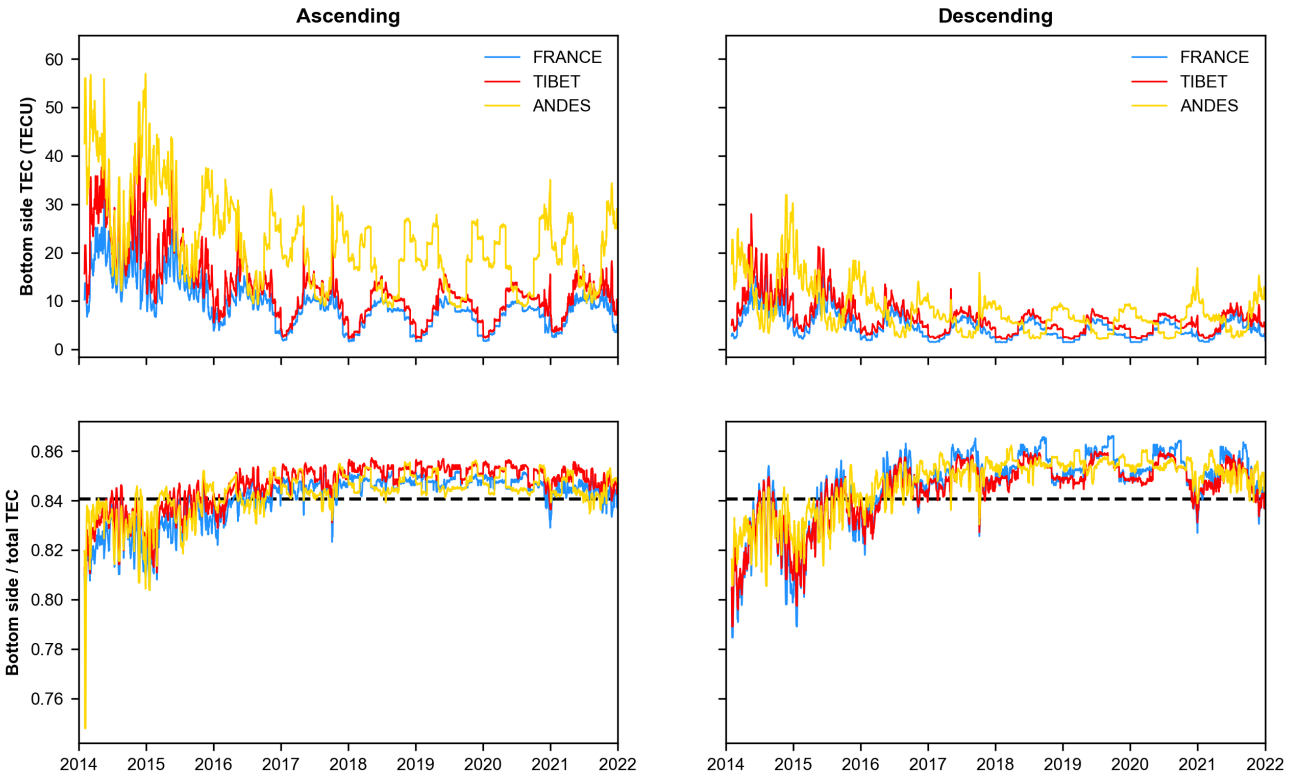

Figure S1. TEC estimations using the NeQuick2 model (Nava et al., 2008) in the three regions of study, at the time of ascending (a) and descending (b) Sentinel-1 acquisitions. The top panels show the vertical TEC below the Sentinel-1 orbits and the bottom panels show the α coefficient. See Text S1 for details.

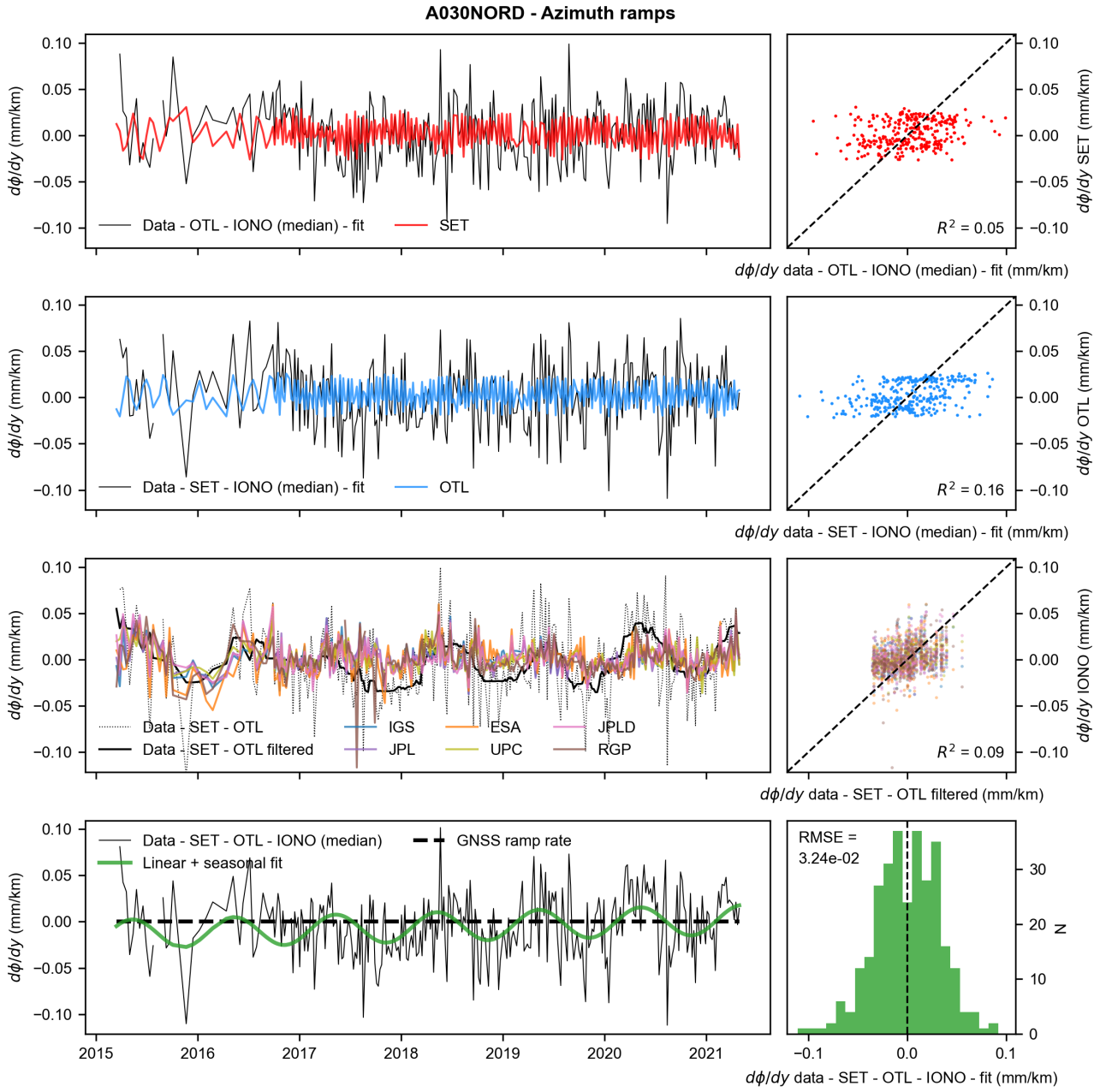

Figure S2. Same as Figure 2 for azimuth ramps.

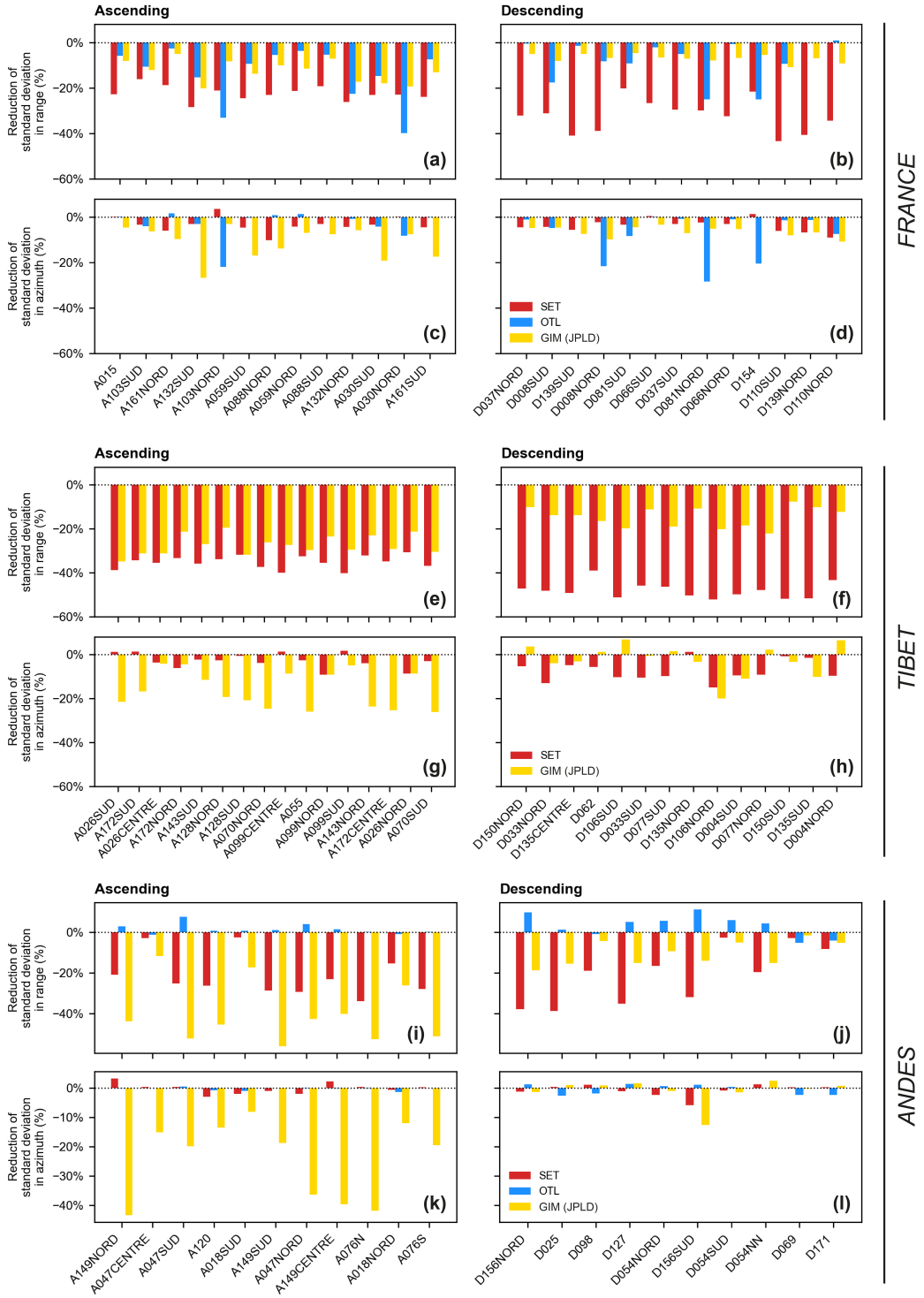

Figure S3. Reduction of the standard deviation of ramp time-series associated to each of the following correction: solid Earth's tide (red), ocean tide loading (blue) and GIM-based ionospheric (yellow) corrections. The impact of each correction is evaluated once time series are corrected from the two others. For each track in the France (a-d), Tibet (e-h), and Andes (i-l) datasets, range ramps are shown in the top row and azimuth ramps in the bottom row.

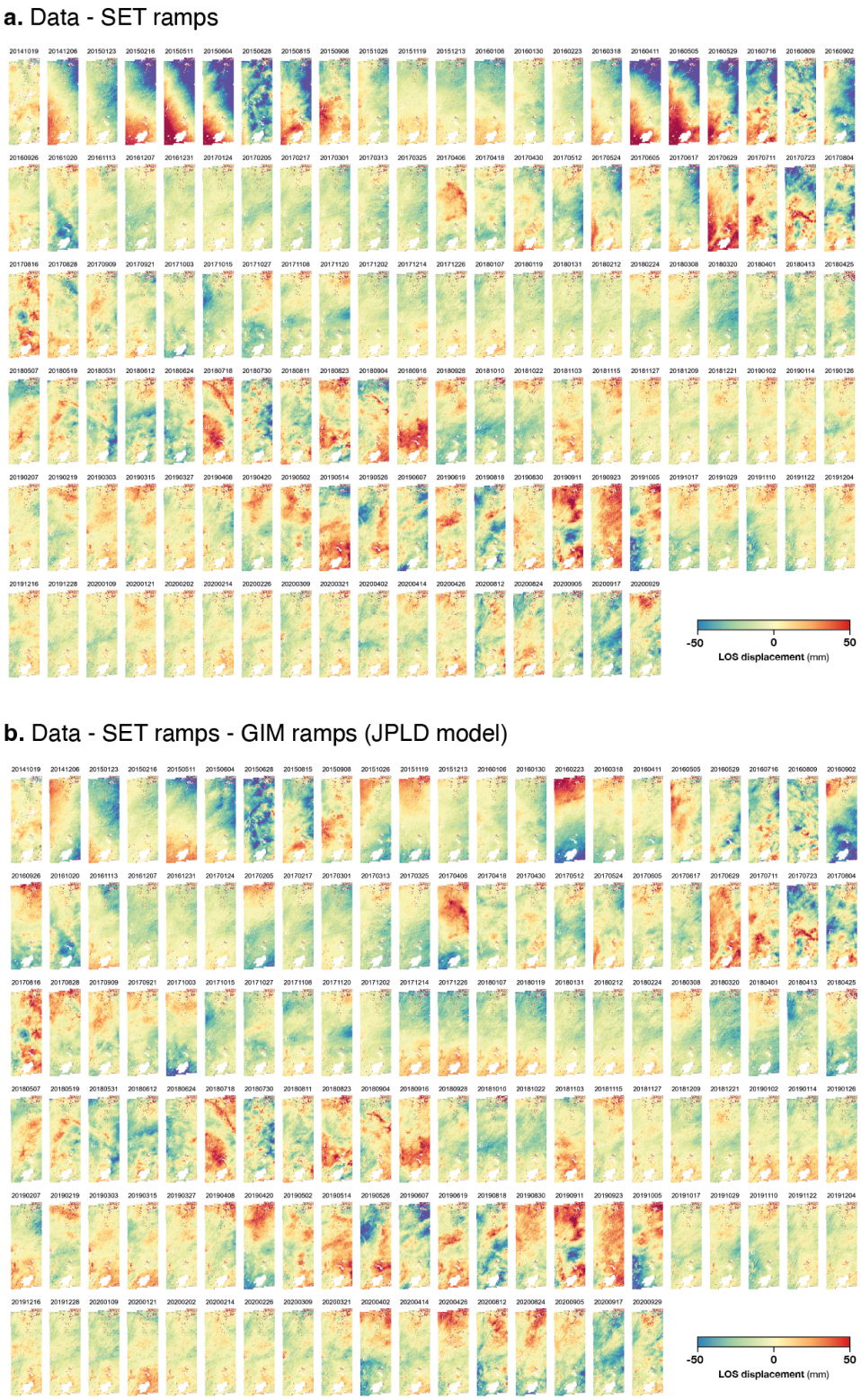

Figure S4. Time-series of cumulative LOS displacement in radar geometry for the track A026CENTRE in Tibet. (a) Time-series corrected only for the SET ramps. (b) Time-series corrected for the SET ramps and the GIM ramps (JPLD model).

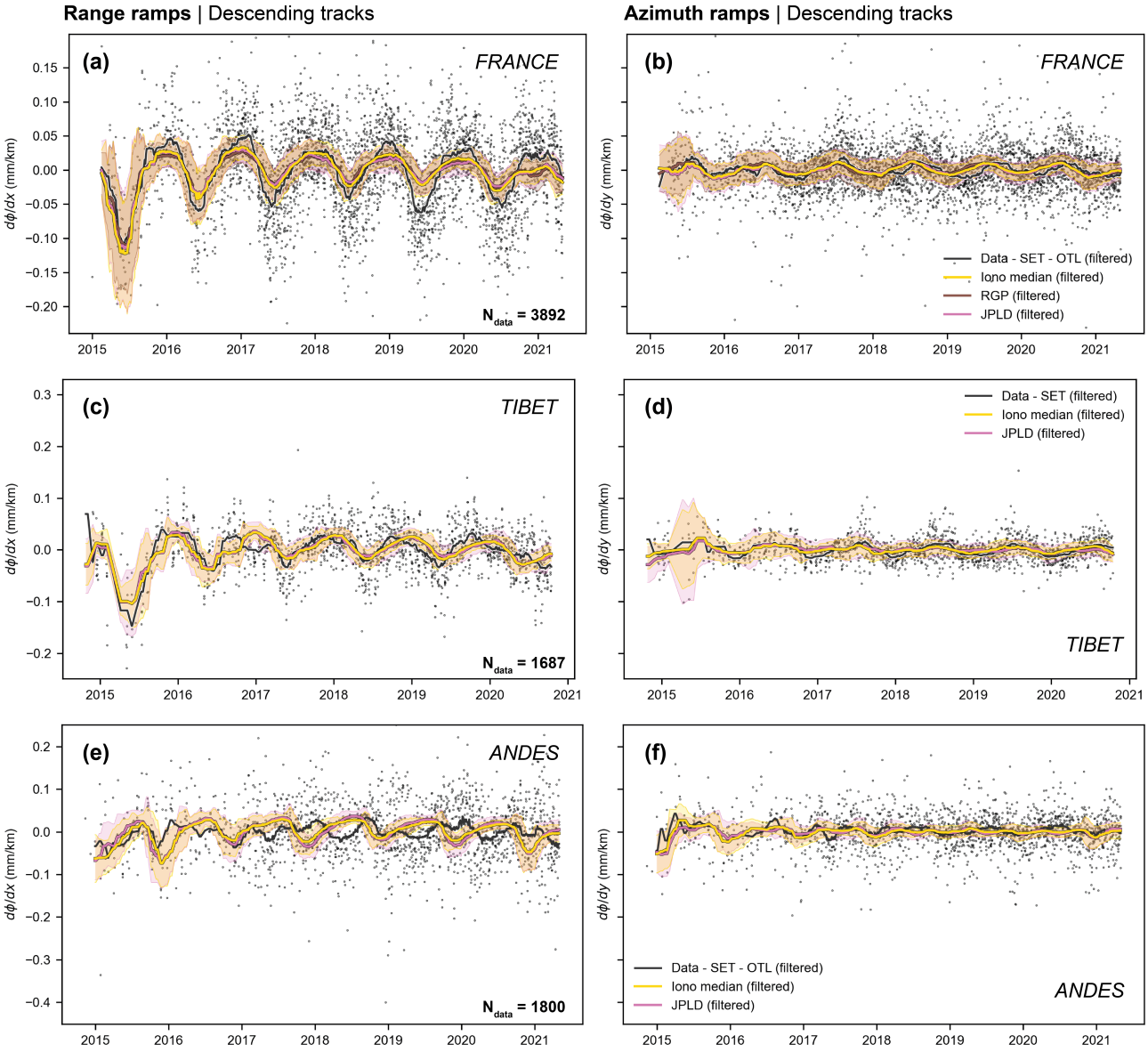

Figure S5. Same as Figure 3 (a-f) for descending tracks.

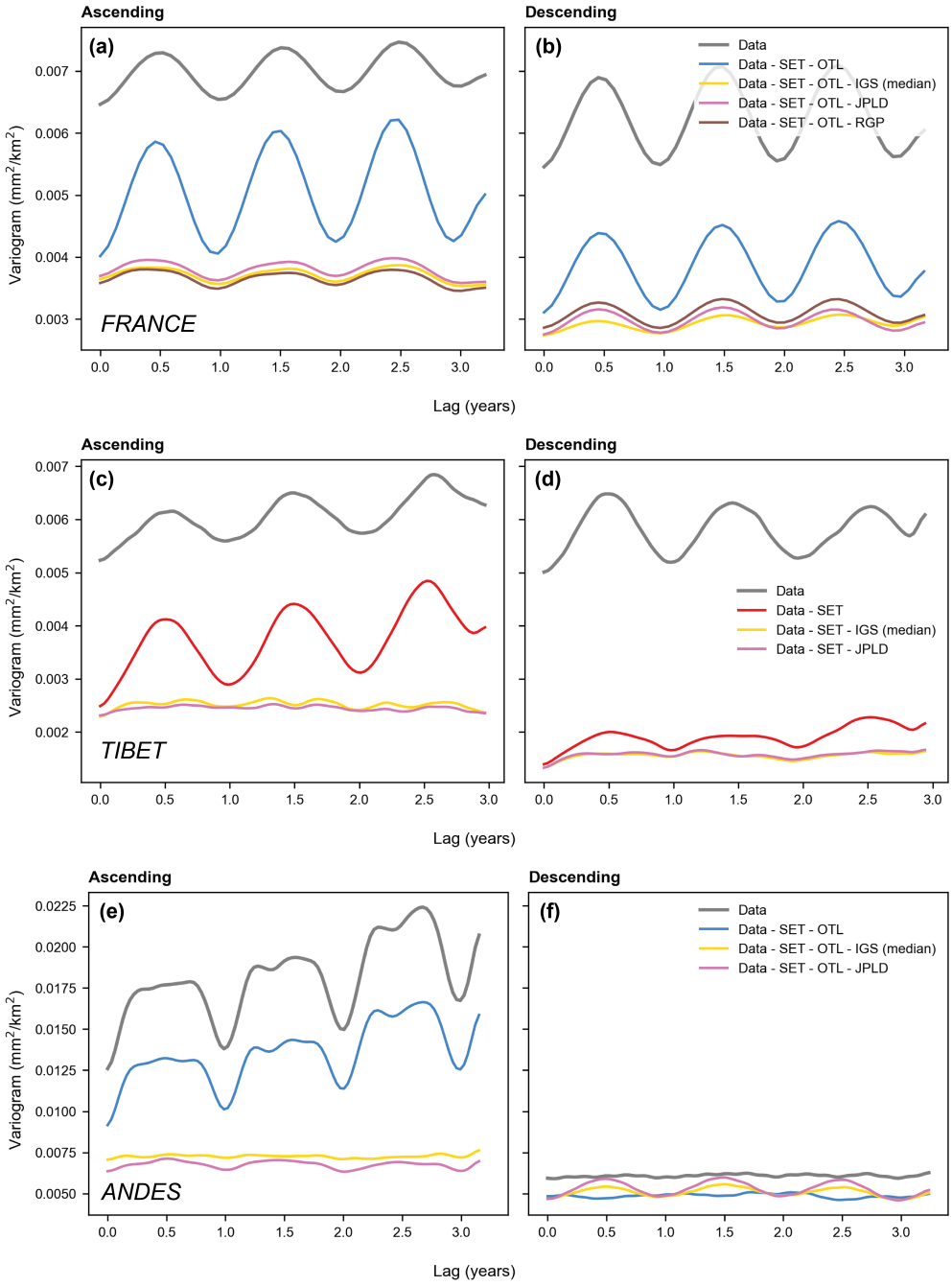

Figure S6. 1D variograms for the time-series of range ramps of ascending (a, c, e) and descending (b, d, f) tracks in France (a, b), Tibet (c, d) and Andes (e, f). Variance is shown as a function of temporal lag for raw ramps (gray), ramps corrected from SET and OTL (blue, only SET in Tibet), and adding the GIM correction, either with the median of IGS models (yellow) or the JPLD model (pink).

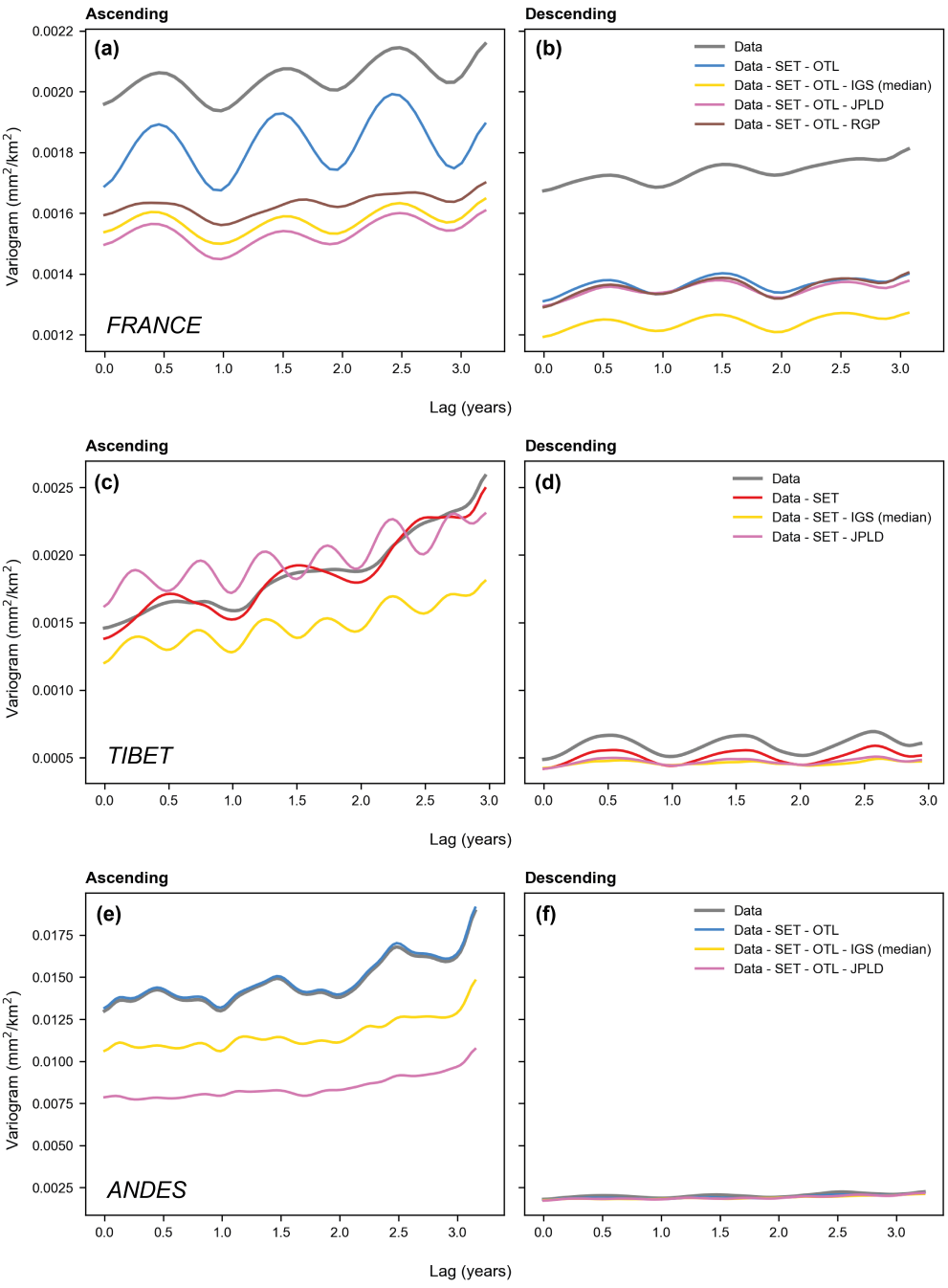

Figure S7. Same as Figure S5 for azimuth ramps.

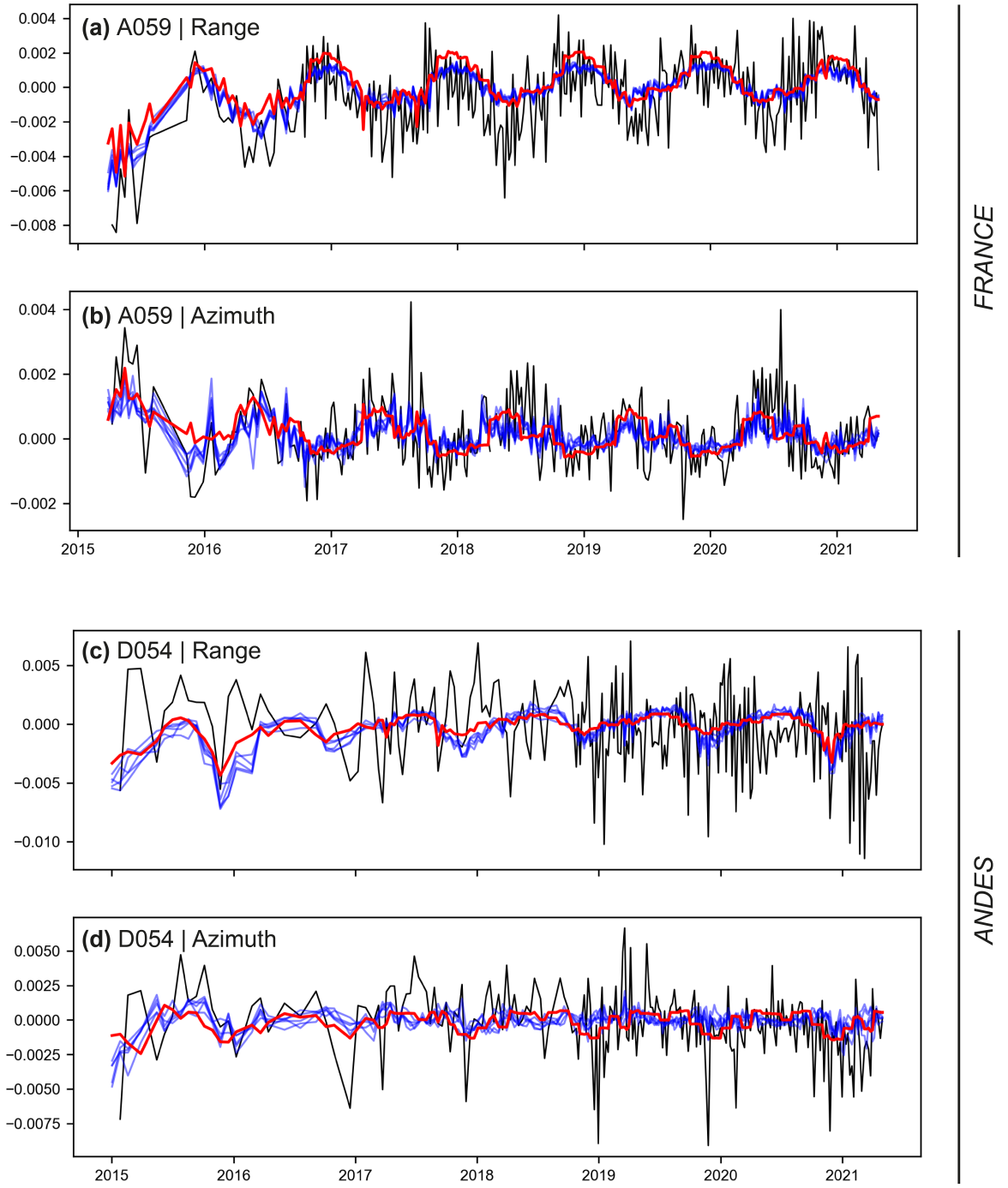

Figure S8. Comparison of ramps predicted by the NeQuick2 empirical model (red line) with the ones predicted by the different GIMs used in this study (blue line). The black line shows the observed ramps corrected from SET and OTL. (a, b) Ramp time-series of track A059 in France for range and azimuth, respectively. (c, d) Same for track D054 in Central Andes.

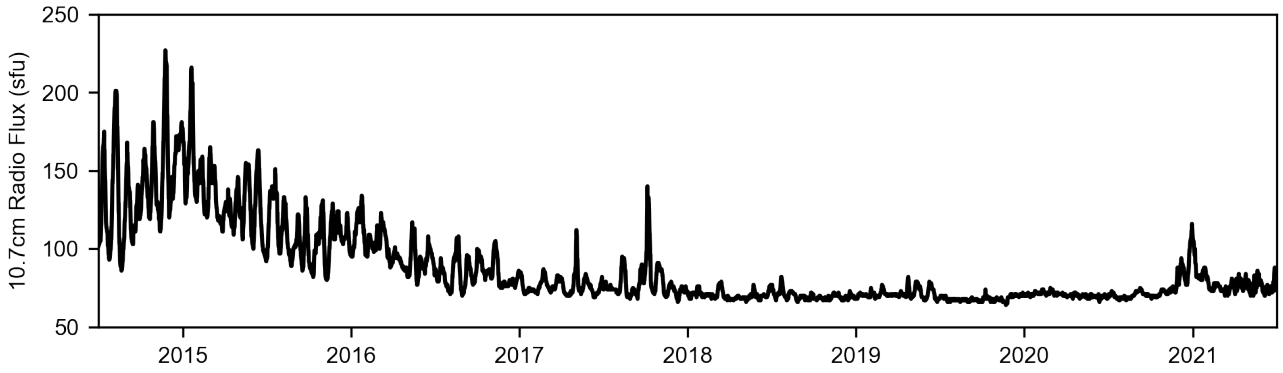

Figure S9. Solar activity during the time period of the Sentinel-1 data used in this work, from 10.7cm Radio Flux data provided by Space Weather Prediction Center (National Oceanic and Atmospheric Administration).

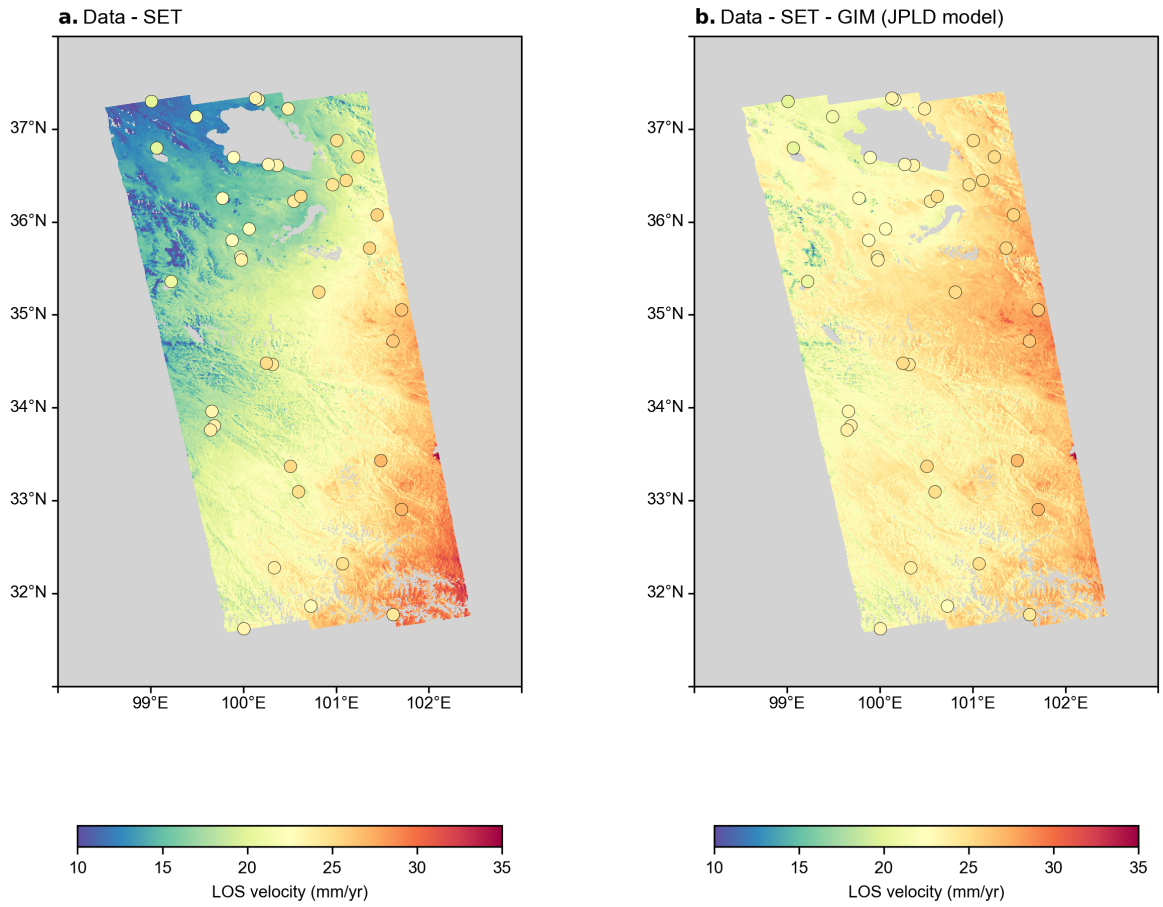

Figure S10. LOS velocity maps in ground geometry for the track A026CENTRE in Tibet. (a) Velocity map obtained after correction of SET ramps only. (b) Velocity map obtained after correction of SET ramps and GIM ramps (JPLD model). A constant velocity offset was adjusted to the GNSS velocities from Wang & Shen (2020) projected in the LOS (shown by colored dots).

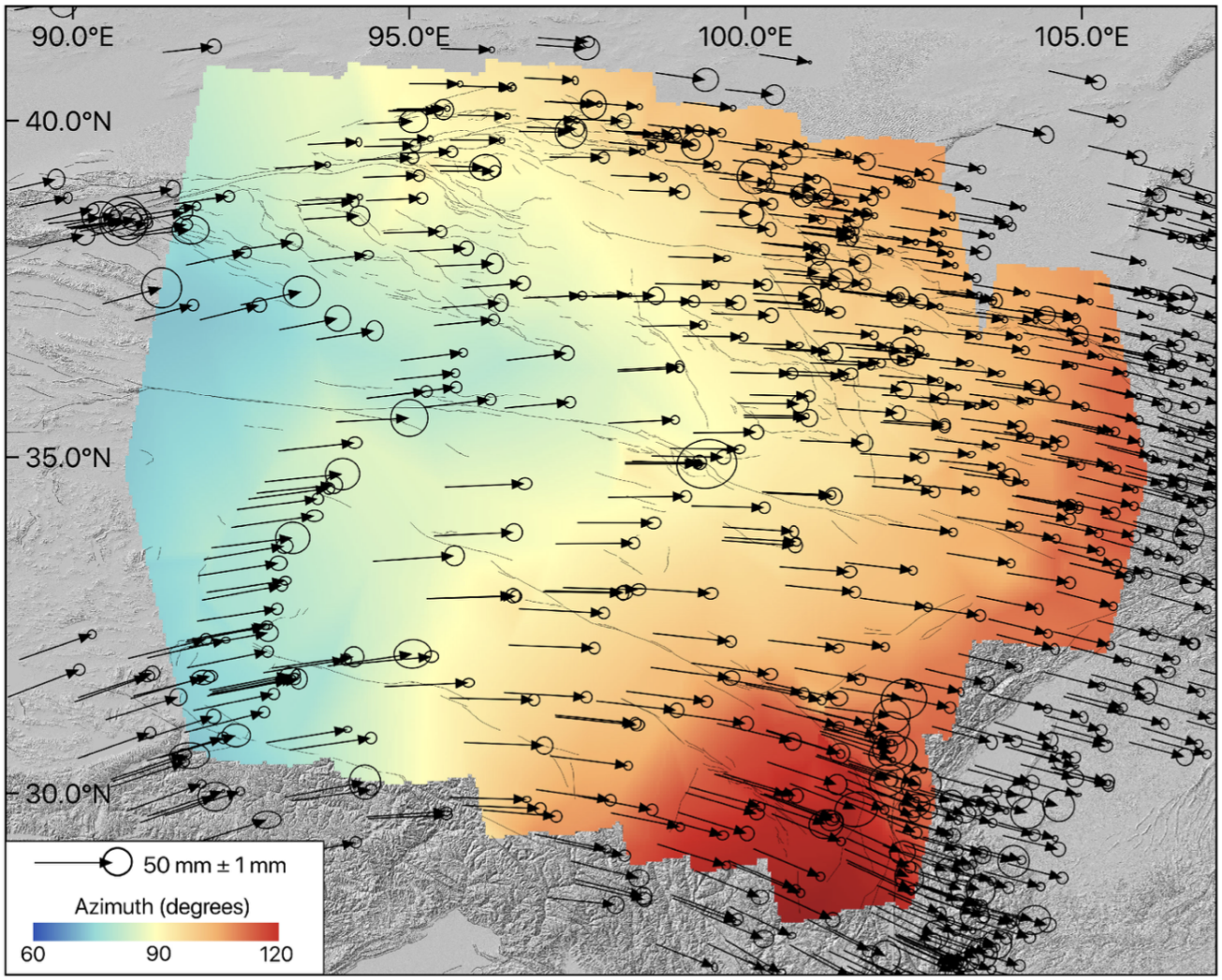

Figure S11. GNSS velocities expressed in ITRF2008 reference frame used for the computation of simulated ramp rates in Tibet. Data is from Wang & Shen (2020). Azimuth, measured clockwise from North, of the interpolated GNSS field is shown in background over the Tibet FLATSIM processing area. Figure from Lemrabet et al. (2023).

Table S1. Information about Sentinel-1 tracks of the France dataset.

Track	Number of acquisitions	First acquisition	Last acquisition
A015	273	20151106	20210426
A103SUD	262	20150329	20210426
A161NORD	301	20150426	20210430
A132SUD	254	20150307	20210428
A103NORD	258	20150504	20210426
A059SUD	305	20150326	20210429
A088NORD	302	20150503	20210425
A059NORD	300	20150501	20210429
A088SUD	306	20150503	20210425
A132NORD	239	20150307	20210428
A030SUD	311	20150312	20210427
A030NORD	301	20150312	20210427
A161SUD	312	20141121	20210430
D037NORD	310	20141219	20210428
D008SUD	309	20150203	20210426
D139SUD	277	20141015	20210429
D008NORD	303	20150416	20210426
D081SUD	310	20150103	20210425
D066SUD	285	20150806	20210430
D037SUD	309	20150313	20210428
D081NORD	311	20141116	20210425
D066NORD	261	20151110	20210430
D154	312	20150508	20210430
D110SUD	311	20141130	20210427
D139NORD	284	20141015	20210429
D110NORD	310	20150330	20210427
	7616		

Table S2. Information about Sentinel-1 tracks of the Tibet dataset.

Track	Number of acquisitions	First acquisition	Last acquisition
A026SUD	137	20141019	20201011
A172SUD	132	20141017	20201009
A026CENTRE	128	20141019	20201011
A172NORD	129	20141110	20201009
A143SUD	141	20141015	20201007
A128NORD	136	20141014	20201006
A128SUD	138	20141014	20201006
A070NORD	135	20141022	20201002
A099CENTRE	135	20141012	20201004
A055	132	20141021	20201013
A099NORD	136	20141012	20201004
A099SUD	136	20141012	20201004
A143NORD	142	20141015	20201007
A172CENTRE	130	20141110	20201009
A026NORD	129	20141019	20201011
A070SUD	136	20141022	20201002
D150NORD	130	20141027	20201007
D033NORD	132	20141031	20201011
D135CENTRE	91	20141026	20201006
D062	134	20141102	20201013
D106SUD	132	20141024	20201004
D033SUD	129	20141031	20201011
D077SUD	128	20141103	20201002
D135NORD	117	20141026	20201006
D106NORD	132	20141211	20201004
D004SUD	109	20141029	20201009
D077NORD	123	20141103	20201002
D150SUD	128	20141027	20201007
D135SUD	84	20141213	20201006
D004NORD	118	20141029	20201009
	3839		

Table S3. Information about Sentinel-1 tracks of the Andes dataset.

Track	Number of acquisitions	First acquisition	Last acquisition
A149NORD	140	20150107	20210423
A047CENTRE	87	20150205	20210422
A047SUD	144	20150313	20210428
A120	123	20150105	20210421
A018SUD	87	20141217	20210426
A149SUD	250	20150107	20210429
A047NORD	139	20150430	20210428
A149CENTRE	225	20150320	20210429
A076N	212	20150114	20210430
A018NORD	141	20150110	20210426
A076S	216	20150114	20210430
D156NORD	236	20150213	20210430
D025	141	20150216	20210427
D098	149	20150209	20210420
D127	153	20150118	20210422
D054NORD	229	20150101	20210429
D156SUD	239	20150402	20210430
D054SUD	226	20150101	20210429
D054NN	147	20150101	20210429
D069	135	20150102	20210430
D171	145	20141017	20210425
	3564		

Table S4. Characteristics of the different TEC data sources used in this study (Hernández-Pajares et al., 2009; Martire et al., 2024).

Name	Spatial resolution	Temporal resolution	Coverage	Type of model
IGS	2.5 × 5°	2h	Global	Weighted mean of several models
JPL	2.5 × 5°	2h	Global	Extended slab
UPC	2.5 × 5°	2h	Global	2-shell
ESA	2.5 × 5°	2h	Global	1-shell
JPLD	1 × 1°	15’	Global	3-shell
RGP	Undefined (local Taylor expansion)	1h	France	1-shell

References

Belcher, D. (2008, December). Theoretical limits on SAR imposed by the ionosphere. *IET Radar, Sonar & Navigation*, *2*(6), 435–448. Retrieved 2022-03-17, from https://digital-library.theiet.org/content/journals/10.1049/iet-rsn_20070188 doi: 10.1049/iet-rsn:20070188

Gisinger, C., Libert, L., Marinkovic, P., Krieger, L., Larsen, Y., Valentino, A., ... Miranda, N. (2022). The Extended Timing Annotation Dataset for Sentinel-1—Product Description and First Evaluation Results. *IEEE Transactions on Geoscience and Remote Sensing*, *60*, 1–22. Retrieved 2024-06-04, from https://ieeexplore.ieee.org/document/9841598/ doi: 10.1109/TGRS.2022.3194216

Hernández-Pajares, M., Juan, J. M., Sanz, J., Orus, R., Garcia-Rigo, A., Feltens, J., ... Krankowski, A. (2009, March). The IGS VTEC maps: a reliable source of ionospheric information since 1998. *Journal of Geodesy*, *83*(3-4), 263–275. Retrieved 2024-06-07, from http://link.springer.com/10.1007/s00190-008-0266-1 doi: 10.1007/s00190-008-0266-1

Lemrabet, L., Doin, M., Lasserre, C., & Durand, P. (2023, July). Referencing of Continental-Scale InSAR-Derived Velocity Fields: Case Study of the Eastern Tibetan Plateau. *Journal of Geophysical Research: Solid Earth*, *128*(7), e2022JB026251. Retrieved 2023-08-09, from https://agupubs.onlinelibrary.wiley.com/doi/10.1029/2022JB026251 doi: 10.1029/2022JB026251

Martire, L., Runge, T. F., Meng, X., Krishnamoorthy, S., Vergados, P., Mannucci, A. J., ... Green, D. W. (2024, May). The JPL-GIM algorithm and products: multi-GNSS high-rate global mapping of total electron content. *Journal of Geodesy*, *98*(5), 44. Retrieved 2024-12-06,

from https://link.springer.com/10.1007/s00190-024-01860-3 doi: 10.1007/s00190-024-01860-3

Nava, B., Coïsson, P., & Radicella, S. (2008, December). A new version of the NeQuick ionosphere electron density model. *Journal of Atmospheric and Solar-Terrestrial Physics*, *70*(15), 1856–1862. Retrieved 2025-01-15, from https://linkinghub.elsevier.com/retrieve/pii/S1364682608000357 doi: 10.1016/j.jastp.2008.01.015

Wang, M., & Shen, Z. (2020, February). Present-Day Crustal Deformation of Continental China Derived From GPS and Its Tectonic Implications. *Journal of Geophysical Research: Solid Earth*, *125*(2), e2019JB018774. Retrieved 2025-03-07, from https://agupubs.onlinelibrary.wiley.com/doi/10.1029/2019JB018774 doi: 10.1029/2019JB018774

Yunjun, Z., Fattahi, H., Pi, X., Rosen, P., Simons, M., Agram, P., & Aoki, Y. (2022). Range Geolocation Accuracy of C-/L-Band SAR and its Implications for Operational Stack Coregistration. *IEEE Transactions on Geoscience and Remote Sensing*, *60*, 1–19. Retrieved 2023-11-07, from https://ieeexplore.ieee.org/document/9759304/ doi: 10.1109/TGRS.2022.3168509

Chapter 7

Large Scale InSAR and GNSS Timeseries Analysis over the Central Andes

This chapter is a draft of an article that shall be submitted in the future. The objective is to publish the InSAR mean velocity maps processed in the framework of the FLATSIM Central Andes project, referenced and corrected from major coseismic and postseismic events affecting the acquisitions, and to perform joint inversions of interseismic velocities using InSAR and GNSS datasets at the scale of South Peru. We also investigate how this dense mapping of surface deformation can help to assess the partitioning of the deformation in the upper plate, notably the role of crustal faults such as the Cuzco fault system and the Cordillera Blanca.

1 Introduction

Central Andes (8°S to 26°S) is an area subject to various geophysical processes, including a history of strong seismicity beyond magnitude 8 (M. E. Beck, 1998; Dorbath et al., 1990), intense volcanic activity (Aguilera et al., 2022), and landslides (Zerathe et al., 2016). This activity is strongly related to the subduction of the Nazca plate below the South America continent at a velocity of about 6 cm/yr (Jarrin et al., 2023; Kendrick et al., 2003) along the Peru-Chile trench, leading to the formation of the Andean Central Volcanic Belt (15°S to 30°S) which hosts 44 active and potentially active stratovolcanoes (Aguilera et al., 2022) such as the Sabancaya and Casiri volcanoes in South Peru (Figure 7.1), that both showed signs of activity in the recent years (Boixart et al., 2020; Machacca et al., 2023; MacQueen et al., 2020; Vargas-Alva and Villegas-Lanza, 2021).

With elevations up to 6,768 meters in the Cordillera Blanca, Central Andes are the testimony of a significant permanent deformation of the upper plate. Saillard et al., 2017 and Jolivet et al., 2020 considered that a fraction of the uplift during the interseismic period transfers to permanent uplift (tenths of mm/yr) of the fore-arc over the

seismic cycle in Central Andes, observed on raised terraces in Chile and Peru (Regard et al., 2010; Saillard et al., 2017; Saillard et al., 2009; Saillard et al., 2011), through plastic deformation. On the other hand, Melnick, 2016 suggests that the permanent uplift is built by intermediate-depth subduction earthquakes, instead of the interseismic loading. Saillard et al., 2017 also observed an along-strike correlation between areas with a high uplift rate, peninsulas, and low-coupled areas. They interpret this observation as an indication that creeping segments are affected by higher shear stress leading to an uplift of the coastal domain. Crustal faults can also play a role in the partitioning of the deformation in the upper plate. Indeed, from the various interseismic coupling models that have been developed to better assess the seismic potential in Central to South Peru (Chlieh et al., 2011; Gagnon et al., 2005; Lovery et al., 2024; Lovery et al., 2025; Norabuena et al., 1998; Villegas-Lanza et al., 2016) and North Chile (Béjar-Pizarro et al., 2013; Chlieh et al., 2011; Hoffmann et al., 2018; Jolivet et al., 2020; S. Li et al., 2015; Métois et al., 2016; Yáñez-Cuadra et al., 2022), several of these studies introduced a third plate, known as *sliver*, to which a rigid block motion is affected. In Peru, Villegas-Lanza et al., 2016 defined a so-called Peruvian Sliver divided into a Western part with a ~5 mm/yr South-East velocity and an Eastern part with a ~3 mm/yr North-East velocity, that are supposed to be separated by the Cuzco fault system and the Cordillera Blanca. In North Chile, Métois et al., 2016 defined a so-called Andean Sliver with a North-East velocity of about 8 mm/yr. The Andean sliver is delimited by the Subandean fold and thrust belt on its oriental front, on which Shi et al., 2020 reported a ~3 mm/yr creep caused by viscous mantle flow. These slivers have been introduced to improve the fit of interseismic models to observed surface velocities, however their actual delimitation remains unclear, and their affected velocities are not driven by strong geological evidences. In addition, Yáñez-Cuadra et al., 2022 and S. Li et al., 2015 argue that the Andean sliver is not required when accounting for diffuse internal deformation or viscoelasticity, respectively. Therefore, it appears necessary to investigate for evidences of such slivers in surface velocity fields, notably by assessing the relative displacement across the crustal faults that are expected to bound them. However, despite the continuous efforts to increase the density of GNSS networks in Central Andes, GNSS sites are often tens of kilometers apart and often very sparse in the back-arc (Lovery et al., 2024; Métois et al., 2016; Villegas-Lanza et al., 2016).

In this paper, we take advantage of a massive processing of InSAR time series (2015-2021) done over the Central Andes in the framework of the FLATSIM project (FormaTerre, 2020) to map the surface deformation in the Central Andes (Figure 7.1), in addition to the tens of continuous and survey GNSS sites that have been deployed during the last 15 years (Socquet et al., 2023). Processing such amount of data (12 ascending and descending orbits, 900,000 km^2, 17,000 interferograms) was a technical challenge for the operating team in order to process long time series while avoiding the potential sources of error in InSAR processing (e.g., decorrelation, tropospheric delays, incorrect

phase unwrapping). In addition, using InSAR time series for large-scale tectonic applications requires to reference each orbit into a stable reference frame, what we did using GNSS velocities. The data are affected by a variety of geophysical signals, including megathrust and crustal earthquakes coseismic displacements, postseismic displacements following large earthquakes, volcanic deformation, and landslides. These signals are reviewed and either corrected or masked. We focus on South Peru, where recent locking models based on GNSS measurements have been published (Lovery et al., 2024; Lovery et al., 2025; Villegas-Lanza et al., 2016), to show how InSAR measurements can help to characterize both the interseismic coupling on the megathrust and the deformation transferred to the upper plate. Using spatially continuous mapping of the deformation by InSAR, we invert for interseismic coupling with viscoelastic Green's functions and we analyze the deformation across major crustal faults that localize deformation in the fore-arc or that delimit the continental sliver in the back-arc.

2 Seismotectonic context

During the last thirty years, Central Andes hosted six large megathrust earthquakes of magnitude Mw > 7.5, from North to South: the 2007 Mw8.0 Pisco, 1996 Mw7.7 Nazca, 2001 Mw8.4 Arequipa, 2014 Mw8.1 Iquique, 2007 Mw7.7 Tocopilla, and 1995 Mw8.1 Antofagasta earthquakes. Looking back in time, we can identify some segmentation of the seismicity. The Peruvian side is often split into three segments by authors (Chlieh et al., 2011; Nocquet et al., 2014; Villegas-Lanza et al., 2016): the North, Central, and South Peru segments. North of the Mendaña fracture zone (MFZ, 10°S), the North Peru segment is characterized by a smaller seismicity with only two events of magnitude Mw $\geq$ 7.5 during the last century in 1960 (Mw7.6) and 1996 (Mw7.5), and by a propensity to host shallow tsunami earthquake ruptures (Villegas-Lanza et al., 2016). The Central Peru segment, between the MFZ and the Nazca Ridge (15°S) ruptured on all its length through four large earthquakes since 1940, from North to South in 1996 (Mw8.0), 1940 (Mw8.1), 1974 (Mw7.9), and 2007 (Mw8.0). The whole segment is expected to have ruptured during the 1746 Mw~8.6 earthquake (S. L. Beck and Nishenko, 1990). The South Peru segment, from the Nazca Ridge to the Arica bend (18.5°S) ruptured on most of its length during the 1868 Mw~8.8 earthquake (Carvajal et al., 2025) and partially from North to South in 1996 (Mw7.7), 1942 (Mw8.2), and 2001 (Mw8.4). In Chile, the Northern segment from the Arica bend to the Perdida ridge (22°S) ruptured in 1877 through a Mw~8.3 earthquake. This segment ruptured partially on its Northernmost part during the 2014 Mw8.1 Iquique earthquake (Duputel et al., 2015; Hoffmann et al., 2018), leaving a seismic gap from 20 to 22°S (Delouis et al., 2009; Métois et al., 2013). South of the 1877 rupture, between the Perdida ridge and the Sala y Gomez ridge (25.5°S), the interface was ruptured from North to South during the 2007 Mw7.7 Tocopilla and 1995 Mw9.0 Antofagasta earthquakes. Note that long-lasting (more than

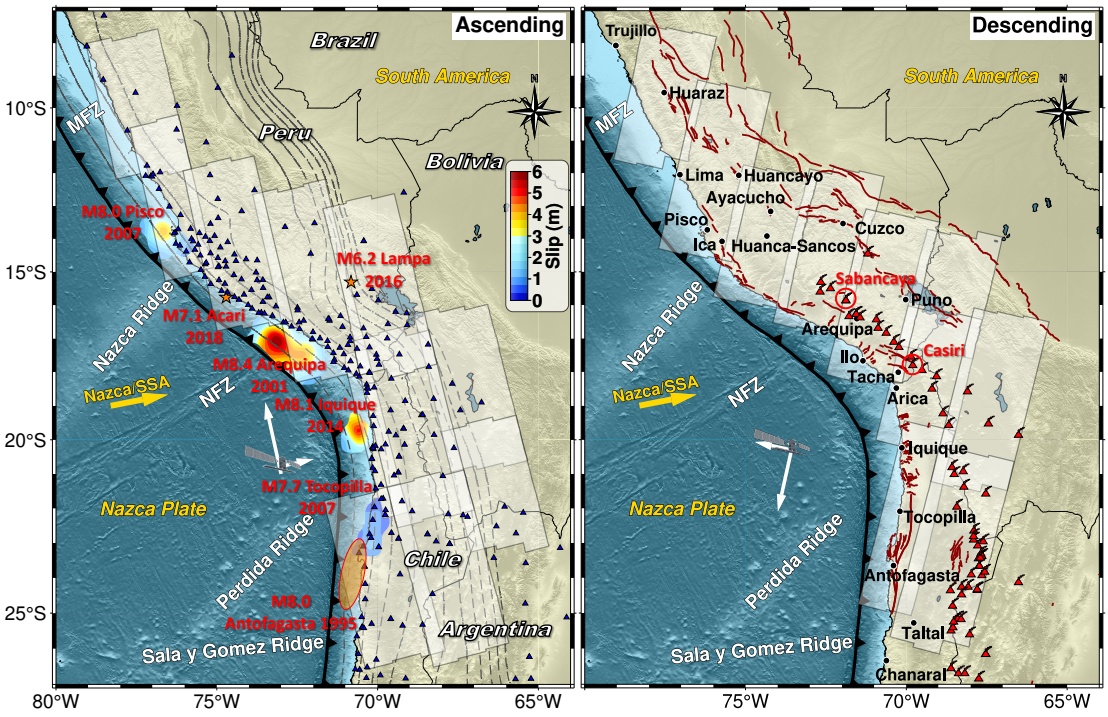

Figure 7.1: Footprints for the ascending (left) and descending (right) Sentinel-1 tracks processed in the framework of the FLATSIM Andes project. On the left panel are reported the GNSS sites as blue triangles (Socquet et al., 2023), the slab contours every 20 km as gray dashed lines (Hayes et al., 2018), and the main earthquakes affecting the area. The slip distributions for the 2001 Arequipa and 2014 Iquique earthquakes are reported from Lovery et al., 2024, from Béjar-Pizarro et al., 2010 for the 2007 Tocopilla earthquakes, and from Chlieh et al., 2011 for the 1995 Antofagasta earthquake. The epicenters of the 2016 Lampa and 2018 Acari earthquakes are reported from the ISC seismic catalog (Bondár and Storchak, 2011). On the right panel are reported the Holocene volcanoes in red, the major cities as black dots, and the main active faults as solid dark burgundy lines from the GEM Active Faults Database (Styron and Pagani, 2020) and the Chilean Database of Active Faults (Maldonado et al., 2021).

a decade) postseismic displacements have been reported following large earthquakes such as the 2001 Mw8.4 Arequipa (Hergert and Heidbach, 2006; Lovery et al., 2025; Perfettini et al., 2005; Sun et al., 2018) or the 2014 Mw8.1 Iquique (Hoffmann et al., 2018; Itoh et al., 2023; Lovery et al., 2024) events.

From this overview of the seismicity, we notice that oceanic structures play an important role in the rupture segmentation, notably the Nazca, Perdida, and Sala y Gomez ridges. The Nazca Ridge is even considered as a strong seismic barrier (Dorbath et al., 1990; Kaneko et al., 2010; Philibosian and Meltzner, 2020; Villegas-Lanza et al., 2016), due to its ability to stop the rupture propagation of the 2007 Mw8.0 Pisco, 1996 Mw7.7, and 1942 Mw8.2 earthquakes. It has also been reported as a low-coupling anomaly in several interseismic coupling models (Chlieh et al., 2011; Lovery et al., 2024; Lovery et al., 2025; Villegas-Lanza et al., 2016). Also, the Nazca Fracture Zone (NFZ) is reported to have slowed down the rupture of the 2001 Mw8.4 Arequipa earthquake (Robinson et al., 2006).

3 Data and methods

3.1 GNSS data

More than 200 GNSS time series (Socquet et al., 2023) are used in this study (Figure 7.1), either to reference InSAR velocity maps or to quantify tectonic signals (coseismic, postseismic, or interseismic deformation). In Peru, we use 152 sites, including 83 cGNSS stations (43 IGN, 22 IGP/ISTerre/Caltech, 8 DEEPtrigger, and 1 IGS stations) and 69 sGNSS sites measured during surveys from IGP, ISTerre, and DEEPtrigger. Compared to Lovery et al., 2024 and Lovery et al., 2025, we added about 30 GNSS sites where the Nazca Ridge (NR) is subducting thanks to the installation of new cGNSS stations and several GNSS surveys (in 2018, 2019, 2022, and 2024), improving significantly the resolution on this area (Villegas-Lanza et al., 2025). In Chile, 83 cGNSS stations are used (66 CSN, and 17 DEEPtrigger stations). We also use 12 cGNSS stations in Bolivia and 10 cGNSS stations in Argentina (RAMSAC). Early measurements started in the mid-1990's in Peru with the SNAPP campaign (1994) and the installation of the AREQ cGNSS station from IGS in 1993, and in Chile with the CAP and SAGA networks (Brooks et al., 2003; Khazaradze and Klotz, 2003), but most of the sites were installed later, in the mid-2000's to the mid-2010's for many sites in Peru, Chile, Bolivia, and Argentina.

GNSS data were processed by Precise Point Positioning (PPP) at ISTerre (Socquet et al., 2023) using the GipsyX software v2.3 from the Jet Propulsion Laboratory (Bertiger et al., 2020), expressed in the ITRF2014 reference frame (Altamimi et al., 2016), and converted into the Stable South America (SSA) frame using the Euler pole from Altamimi et al., 2016. The interseismic displacements at continuous GNSS (cGNSS) stations are

extracted by applying a trajectory model (Bevis and Brown, 2014) using the ITSA software (Marill et al., 2021) to correct for coseismic, postseismic, and seasonal displacements. Survey sites are corrected from the coseismic and postseismic displacements associated with the 2014 Iquique seismic sequence using the slip models from Lovery et al., 2024, and from seasonal displacements using the methodology from Hoffmann et al., 2018 and Lovery et al., 2024. Interseismic velocities are also corrected from the postseismic displacements associated with the 2001 Mw8.4 Arequipa earthquake using the postseismic model from Lovery et al., 2025.

3.2 InSAR data - the FLATSIM Central Andes project

The InSAR data used in this study come from the FLATSIM Central Andes project (FormaTerre, 2020). FLATSIM (FormaTerre LArge-scale multi-Temporal Sentinel-1 InterferoMetry) is an InSAR processing service from FormaTerre Solid Earth data and services center and is operated by the French national space agency (CNES). It is based on the New Small temporal and spatial BASelines (NSBAS) InSAR processing chain (M.-P. Doin et al., 2011; Grandin, 2015), processing level-1 Sentinel-1 products from ESA into interferograms (wrapped and unwrapped, geocoded or not) and displacement time series. The InSAR data are acquired in interferometric wideswath (IW) mode, with the three subswaths merged into a single 250-km wide track. The detailed processing approach is described in Thollard et al., 2021 and Lemrabet et al., 2023.

For the Central Andes, between latitudes 8°S and 26°S, and longitudes 79°W and 65°W, 12 orbits have been processed spanning the 2015-2021 period, including 7 ascending and 5 descending (Figure 7.1). Some of the orbits have been split in two or three segments for ease of processing, leading to 21 segments in total that we refer as *tracks*. It covers a large area of about 900,000 km^2 from Trujillo in Central Peru to Chañaral in North Chile (Figure 7.1). The temporal coherence that fluctuates between 0 and 1 (Figure 7.2) is a proxy of the signal stability over time. It is high (>0.8) on most of the processed area due to a dry climate with little vegetation. Areas with dense vegetation, such as the Amazonian Forest, show low coherence (<0.3), as well as salt lakes or water surfaces, leading to unsuccessful phase unwrapping. Resulting InSAR mean velocity maps (Figure 7.3) show the areas where the unwrapping was successful (i.e., where the temporal coherence was strong enough, typically above 0.7), covering most of the Cordillera, the Altiplano, and part of the Atacama and Sechura deserts within the processed latitude range.

Disposing of both ascending and descending orbits allows us to measure displacements with two different line-of-sights. As the Sentinel-1 satellites are right-looking, it points toward East-northeast in the ascending orbits, a direction very similar to the Nazca – Stable South America (SSA) plate convergence, leading to a high sensitivity to horizontal displacements, and toward West-northwest in the descending orbits that are

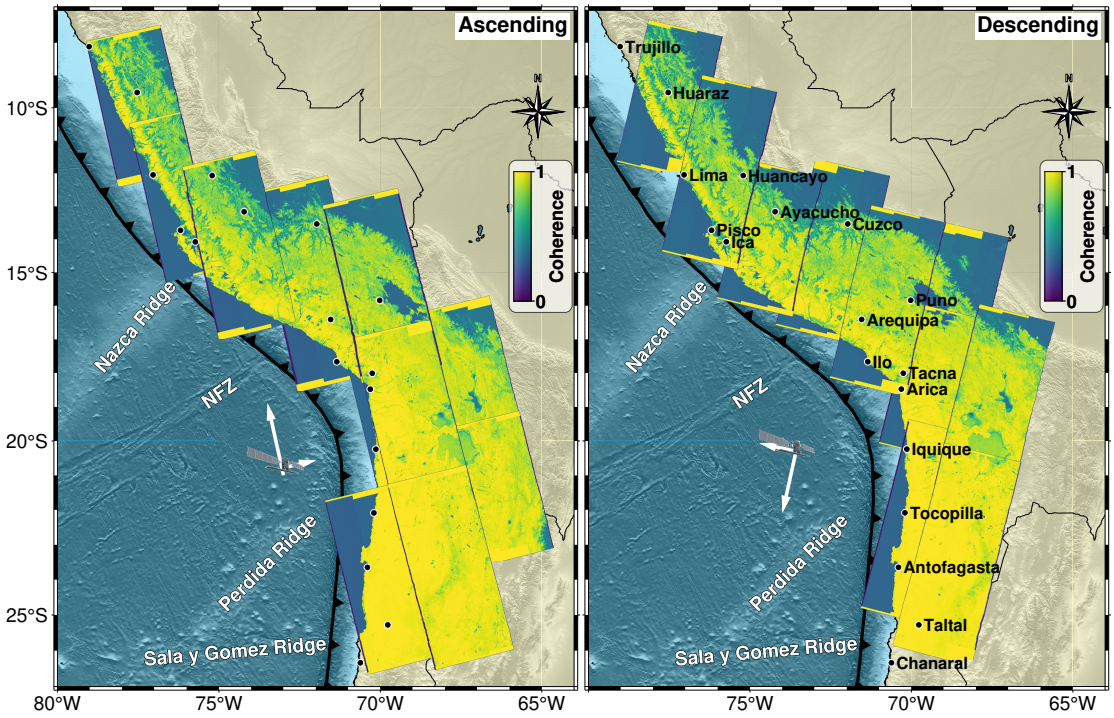

Figure 7.2: Temporal coherence, from 0 (lost coherence) to 1 (perfect coherence) for ascending (left) and descending (right) tracks. Most of the area westward of the Cordillera shows a good coherence because of low vegetation, while we lose the coherence in the Subandean regions.

relatively more sensitive to vertical displacements. The final products are multi-looked to a 16-look resolution (320 m), improving signal coherence and reducing products size. The time series have about 140 epochs for most of the tracks, with one acquisition every 12 days when both satellites Sentinel-1A&B were operating simultaneously after the launch of Sentinel-1B in April 2016.

3.3 Referencing InSAR acquisitions

The FLATSIM service provides mean velocity maps in the line-of-sight (LOS) of the satellite (Figure 3) computed from the displacement time series. Displacements in radian/yr are converted to cm/yr by a factor λ / 4π with λ the wavelength of the radar pulse (5.55 cm), and expressed as positive when the satellite to ground distance increases. The mean velocity maps have been flattened (i.e., linear ramps in range and azimuth are removed). As a result, these maps are expressed in a floating reference frame. Consequently, we need to reference them in a stable reference frame such as ITRF2014 (Altamimi et al., 2016) for large-scale applications. We chose to reference the velocity maps using the wide GNSS network in Central Andes, overlapping with the tracks' footprints (Figure 7.1).

First, we selected the GNSS sites with adequate time coverage in the 2015-2021 time window (i.e., with at least 80% of complete daily measurements) and with a reliable signal on both horizontal and vertical components (i.e., stable enough to extract an average velocity on horizontal and vertical components). It withdraws sGNSS sites, for which the vertical component is not stable enough, and some sites known to be affected by local events such as landslides. This leaves us with 94 sites distributed over the area covered by the InSAR data, in spite of a few data gaps, notably in the Eastern part of the Central Andes. We computed the average velocity on the 2015-2021 period for the three components (East, North, Up) in ITRF2014 and projected them into the LOS using the LOS vector at the exact location of each GNSS station and for each track. We computed an interpolated grid at a 0.5° resolution to improve the spatial distribution. In order to overcome the lack of GNSS stations in the back-arc, seven additional sites are added in the back-arc that are assigned the motion of SSA in ITRF2014.

These velocities projected in LOS are used to add the missing linear gradients (ramps) in range and azimuth direction to the InSAR velocity maps. We need to adjust the ramps of the mean velocity maps to fit the best the ones from GNSS, while maximizing the continuity between the tracks. For this purpose, we first stitch the common tracks of a given orbit along the azimuth direction (for the orbits that are split into several segments) by minimizing the difference on the overlaps. Then, we apply ramps in range and azimuth on each orbit, plus an offset, to minimize both the difference between GNSS and InSAR LOS velocities at all stations weighted according

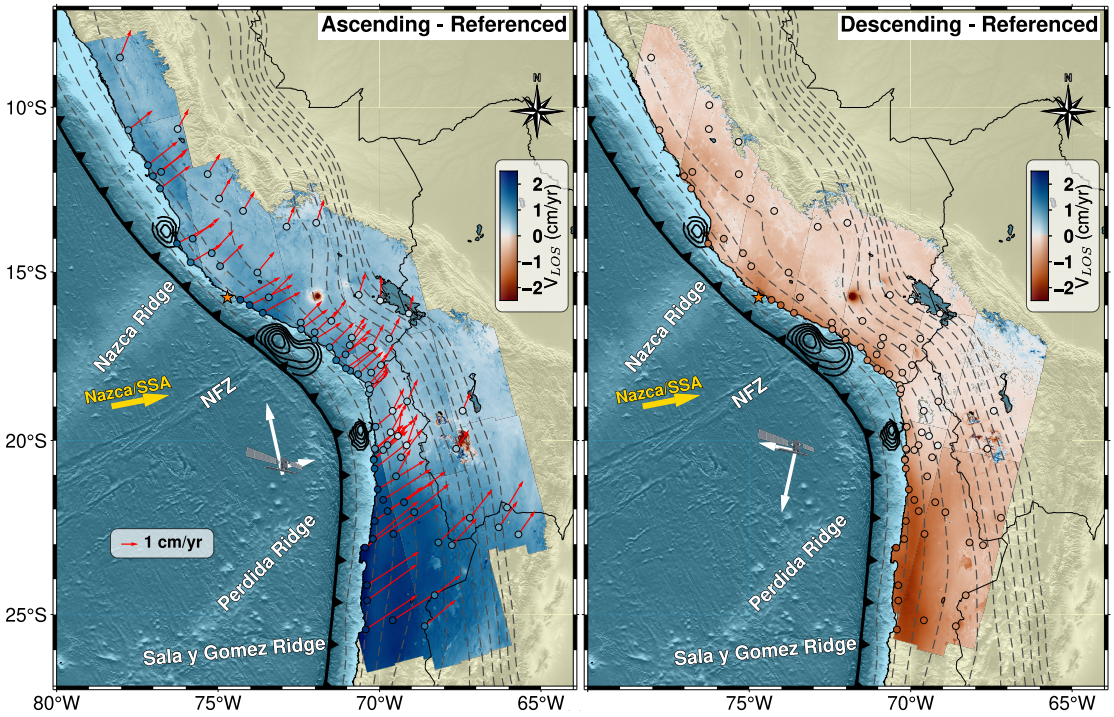

Figure 7.3: InSAR mean velocity maps on the 2015-2021 period in the line-of-sight (LOS) after referencing from GNSS for ascending (left) and descending (right) tracks. Positive velocities (blueish colors) indicate an elongation of the satellite to ground distance, while negative velocities (reddish colors) indicate a shortening. Average GNSS velocities on the same period are displayed by red vectors, while the projections into LOS are reported within black circles. One-meter slip contours for the 2007 Pisco, 2001 Arequipa, and 2014 Iquique earthquakes are reported as solid black lines from North to South. The epicenter of the 2018 Acari earthquake is indicated by the orange star.

to their MIDAS uncertainties (Blewitt et al., 2016) and the difference within the overlaps between the orbits accounting for the look angle variation between near and far range (for Sentinel-1, the angle from the nadir is ranging from 29° in near range to 46° in far range). On Figure 7.3 are displayed the resulting referenced InSAR mean velocity maps, in good agreement with the GNSS LOS values. With the InSAR data referenced in ITRF2014, the large-wavelength component of the signal is controlled by the GNSS, while the short-wavelength is still controlled by the InSAR.

3.4 Horizontal-vertical decomposition

By decomposing referenced InSAR mean velocity maps, we estimate mean velocity maps for the East and Up components. We use an approach similar to D. Wang et al.,

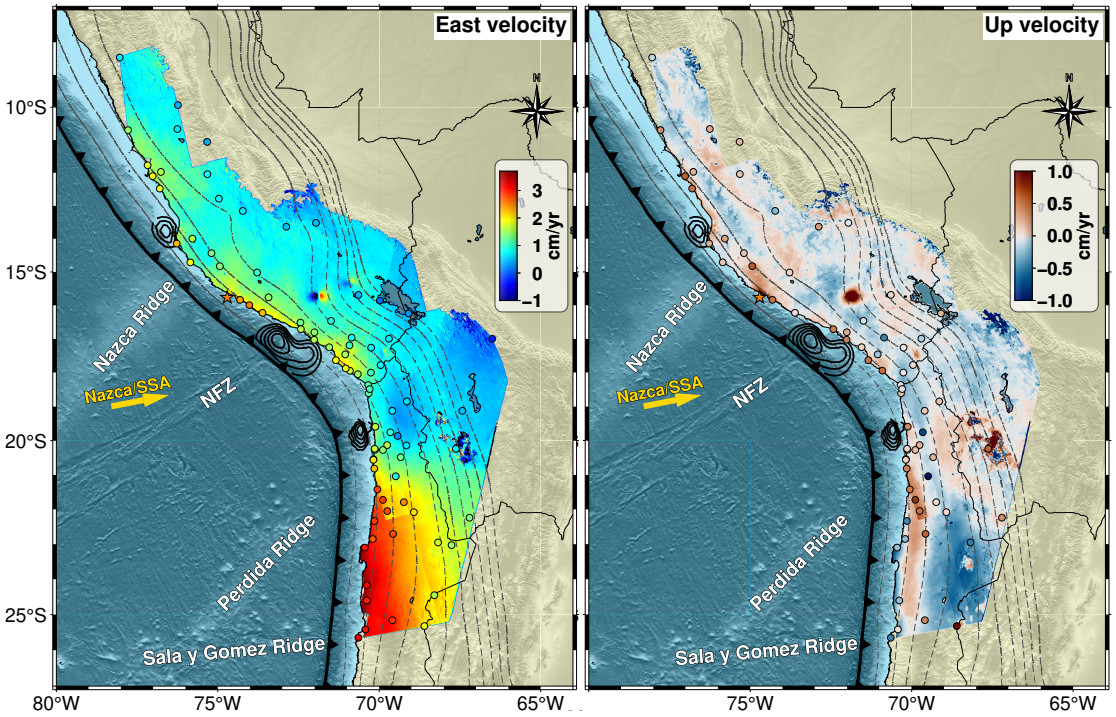

Figure 7.4: East (left) and up (right) InSAR mean velocity maps on the 2015-2021 period after decomposition. Average East (left) and Up (right) GNSS velocities on the same period are reported within black circles. One-meter slip contours for the 2007 Pisco, 2001 Arequipa, and 2014 Iquique earthquakes are reported as solid black lines from North to South. The epicenter of the 2018 Acari earthquake is indicated by the orange star.

2024, where we solve the equation

$$V_{LOS} - e_N.V_N = e_E.V_E + e_U.V_U \tag{7.1}$$

with V the velocities and (e_N, e_E, e_U) the components of the LOS vector for each pixel. The North velocity is computed by bi-linear interpolation of the GNSS North velocities. We solve the system of equations in the areas where ascending and descending tracks overlap. As the Nazca-SSA convergence is mostly West-East oriented, the East component captures most of the tectonic signal. The resulting East and Up velocity maps are displayed on Figure 7.4, showing an overall satisfying agreement between GNSS and InSAR velocities (the difference at most sites is below 15%). Note that fewer GNSS sites are showed on the Up velocity map than on the East velocity map because the vertical component was not always stable enough at some sites.

4 Description of the main signals observable in the InSAR maps

In this section we review the variety of geophysical signals that can be observed in the richness of these InSAR data. First, we describe the large-wavelength patterns visible in the mean velocity maps and we do a comparison with previous studies performing large-scale InSAR mapping of Central Andes (Béjar-Pizarro et al., 2013; Chlieh et al., 2004; Chlieh et al., 2011; Jolivet and Simons, 2018; Jolivet et al., 2020; Kosari et al., 2024). Then we focus on quantifying the displacements across crustal faults at the Cuzco fault system and at the Cordillera Blanca, that were proposed by Villegas-Lanza et al., 2016 as boundaries for the Peruvian Sliver. Finally, we review the others signals affecting the velocity maps, including co and postseismic displacements, volcanic deformation, and a landslide at the Huanca-Sancos city.

4.1 Large-scale features associated to subduction and its segmentation

Several features are easily noticeable on the InSAR mean velocity maps, both in LOS (Figures 7.3 and 7.9) and on the horizontal-vertical decomposition (Figures 7.4, 7.5, and 7.6). At first order, a long-wavelength pattern showing maximum eastward velocity close to the coast and diminishing inland is observed in Peru and Chile: it appears in reddish colors on the LOS velocity maps and it is associated with an eastward displacement up to about 2 cm/yr in Peru and 3-4 cm/yr in Chile, and a band of uplift along the coast up to about 1 cm/yr (c.f., profiles on Figures 7.5 for Peru and 7.6 for Chile). We observe some discontinuities in this pattern, notably where the Nazca Ridge and the NFZ are subducting, and at the location of the Arica bend. The along-trench segmentation of this pattern of displacement is consistent with the interseismic coupling models in Peru (Chlieh et al., 2011; Lovery et al., 2024; Lovery et al., 2025; Villegas-Lanza et al., 2016) and Chile (Béjar-Pizarro et al., 2013; Jolivet et al., 2020; Kosari et al., 2024; S. Li et al., 2015; Métois et al., 2016).

Significant displacement, both in LOS and on the East component, is observed along the coast of Peru North (Figure 7.5, profiles a to c) and South (Figure 7.5, profiles d to g) of the Nazca Ridge with up to about 2 cm/yr on the East component. The observed East displacement is lowered to less than 1 cm/yr where the Nazca Ridge and the NFZ are subducting, which are persistent features in the interseismic coupling models (Chlieh et al., 2011; Lovery et al., 2024; Lovery et al., 2025; Villegas-Lanza et al., 2016). More to the South and close to the border with Chile, the East displacement in the vicinity of the Arica bend is dropping close to zero (profile h on Figure 7.5). In Chile,

the coastal signal is very strong (Figure 7.6), up to about 3-4 cm/yr on the East component, for a number of compounding reasons: a decrease of the trench - coast distance, an increase of the Nazca - South America relative velocity (Jarrin et al., 2023; Kendrick et al., 2003), a change of trench azimuth, and likely an increase of interseismic coupling on the megathrust which is consistent with the high locking observed on interseismic coupling models (Chlieh et al., 2011; Jolivet et al., 2020; S. Li et al., 2015; Métois et al., 2016). Note that East displacement is dropping below 1.5 cm/yr in the vicinity of the 2014 Mw8.1 Iquique earthquake rupture at about 20°S (Figure 7.6, profiles b and c), which is likely related to its postseismic deformation (Hoffmann et al., 2018; Itoh et al., 2023; Lovery et al., 2024). Also, the 2001 Mw8.4 Arequipa earthquake is known to have generated a long-lasting postseismic signal due to the viscoelastic relaxation of the asthenosphere (Hergert and Heidbach, 2006; Lovery et al., 2025; Perfettini et al., 2005; Sun et al., 2018), that is still affecting the GNSS time series in Arequipa with a decrease of about 15% on the velocity over the last decade compared to the preseismic velocity (Lovery et al., 2025). Therefore, the deformation in the Arequipa region (in front of the NFZ) is quite complex, with the superposition of multiple signals: the interseismic locking, the viscoelastic relaxation associated with the Arequipa earthquake, the large-scale deformation induced by the inflation of the Sabancaya volcano (see section *Volcanic deformation*) with possibly some subsidence surrounding the volcano as reported on other volcanic areas (Chaussard, 2016; Shreve et al., 2021), and the postseismic deformation following the Iquique earthquake.

The vertical component shows a more heterogeneous pattern, with mostly uplift between the 40 and 60-km depth slab contours corresponding to the transition from locking to creep on the megathrust (Jolivet et al., 2020; S. Li et al., 2015; Lovery et al., 2024; Métois et al., 2016; Villegas-Lanza et al., 2016), except where the NR is subducting. This zone of uplift is about 70-km wide. The maximum of uplift (3-4 mm/yr) is located at about 120-130 km from the trench, both in Peru and in Chile, which approximately corresponds to the down-dip limit of the highly-locked (coupling > 0.7) asperities of the interseismic coupling models from Métois et al., 2016, Chlieh et al., 2011, and Yáñez-Cuadra et al., 2022. Moderate subsidence (~2 mm/yr) is observed South of Arica (18.5°S to 19.5°S), onshore of the 2014 Iquique rupture (profile a on Figure 7.6). This subsidence could be related to the postseismic displacements associated with the Iquique earthquake, still Melnick, 2016 reports quaternary uplift rates about two to three times lower than on the Tocopilla segment (22 to 23°S). The trench-to-coast distance is also significantly larger, with up to 160 km at Arica compared to about 90 km at Iquique city.

4.2 Inland vertical deformation

We observe some subsidence between the 60 and 80-km contours (2-4 mm/yr). On some segments, we observe a secondary uplift zone (about 2 mm/yr) beyond the 80-km depth contour at about 250 km from the trench. This secondary uplift zone is observed on the Peruvian flat-slab segment from 9°S to 15°S (profiles a to e on Figure 7.5, also between Ilo and the Titicaca lake (profile g), and along the Chilean Western Cordillera from 19°S to 22°S (profiles b to d on Figure 7.6). The Central Andean plateau (Altiplano) in Bolivia, for which quaternary uplift has been reported (Brooks et al., 2003; Ehlers and Poulsen, 2009; Garzione et al., 2008; Isacks, 1988), is mostly affected by subsidence (about 2 mm/yr) on our maps, notably between 16 and 19°S, but it appears to be partially uplifting between 19 and 22°S. Note that the observations in the Central Andean plateau are made difficult by the patterns of locally strong uplift or subsidence (up to more than 1 cm/yr) we observe at various salt lakes, including Salar de Uyuni, Salar de Atacama, and Salar de Colpasa (see Figure 7.6). However, this last observation should be taken with a grain of salt, since it could be biased by phase artifacts related to the soil moisture (Devlin and Lohman, 2025; M.-P. Doin et al., 2023; Karami et al., 2025).

The presence of a secondary uplift zone in the volcanic arc has been reported in viscoelastic models with a cold nose (stagnant and cold mantle wedge) during the late interseismic stage by Luo et al., 2025. The secondary uplift zone appears to be co-located with areas of high topography and positive gravity anomaly (Molina et al., 2021; Sandwell et al., 2014), notably in Chile where the uplift pattern follow the curvature of the Western Cordillera that is gradually bending Eastward South of 20°S. In the Antofagasta region (21°S to 26°S), where the volcanic arc is located at about 280 km from the coast at 23°S compared to about 140 km at the latitude of the Iquique city (20.2°S), we observe a strong subsidence (3 to 100 mm/yr). These observations accredit the theory from Saillard et al., 2017, Jolivet et al., 2020, and Kosari et al., 2024, that the permanent uplift is mostly generated by partial plastic deformation during the interseismic period. Some authors (Ragon and Simons, 2023; van Dinther et al., 2019) proposed that great earthquakes generate a secondary uplift zone a few hundred kilometers from the trench, resulting from coseismic elastic rebound in conjunction with a return flow caused by slab penetration, or from afterslip. While this earthquake-driven secondary uplift can contribute to the long-term permanent uplift, it is unlikely that it caused the secondary uplift zone observed on our InSAR velocity maps, since it is not aligned with the 2014 Iquique earthquake rupture.

4.3 Comparison with previously published InSAR maps

Kosari et al., 2024 released East and vertical velocity maps in North Chile (20.5°S to 26°S), derived from Sentinel-1 acquisitions spanning on a similar period of six years, allowing a direct comparison with our results on the first 100 to 150 kilometers from the coast (their velocity maps are not covering the more inland areas). Their observations are very similar, with a Eastward velocity up to 3.5 cm/yr at the coast and diminishing down to about 2 cm/yr below the 60-km slab contour. They also observe a decrease of the East velocity down to 2 cm/yr in the vicinity of Iquique. The vertical velocity map is also consistent with our results: subsidence is observed at the coast, notably on the Mejillones peninsula (up to 6 mm/yr of subsidence), while an uplift band is observed between the 40 and 60-km slab contours with a maximum of 6 mm/yr in the vicinity of the Tocopilla city. These observations differ from the interseismic uplift model from Jolivet et al., 2020, based on GNSS data and Envisat InSAR time series spanning on the 2003 to 2010 period (Jolivet and Simons, 2018), for which they indicate uplift of about 2 mm/yr at the Mejillones peninsula and significantly smaller uplift in the vicinity of Tocopilla (less than 1 mm/yr vs. 6 mm/yr in our study and Kosari et al., 2024). Overall, it seems that the uplift pattern from Jolivet et al., 2020 is shifted ocean-ward of about 50 km compared to our study and Kosari et al., 2024. This may be partially related to the different observation period (2003-2010 vs. 2015-2021), which was not impacted by the 2014 Mw8.1 Iquique earthquake in Jolivet et al., 2020 but which was affected by the 2007 Mw7.7 Tocopilla earthquake, slightly North of the Mejillones peninsula. Although the authors accounted for the coseismic displacement associated with the Tocopilla earthquake, the mean velocity may be affected by some postseismic displacement related either to the Tocopilla or 1995 Mw8.0 Antofagasta earthquakes. Even on the mean LOS velocity maps provided by Jolivet et al., 2020 and Jolivet and Simons, 2018 it appears that the maximum uplift is located at the coast, while it is about 50 km inland on our LOS velocity maps. Note that the look angle of the Envisat satellite (15 to 45°) is different from Sentinel-1 (29 to 46°), which may result in a different sensitivity in LOS between the acquisitions used by Jolivet et al., 2020 and our study. Béjar-Pizarro et al., 2013 report a maximum LOS velocity of about 18 mm/yr at about 30 km from the coast using Envisat SAR acquisitions on a similar period (2003 to 2009) but on a different track. Chlieh et al., 2011 also provided a mean velocity map in LOS, obtained from a long temporal baseline ERS interferogram between October 1995 and May 1999, from 18.5°S to 23°S (Northern edge of the Mejillones peninsula). It shows consistent velocities compared to our study, except that the signal is decreasing to less than 5 mm/yr in the vicinity of the Mejillones peninsula, which may reflect the postseismic displacements following the 1995 Antofagasta earthquake.

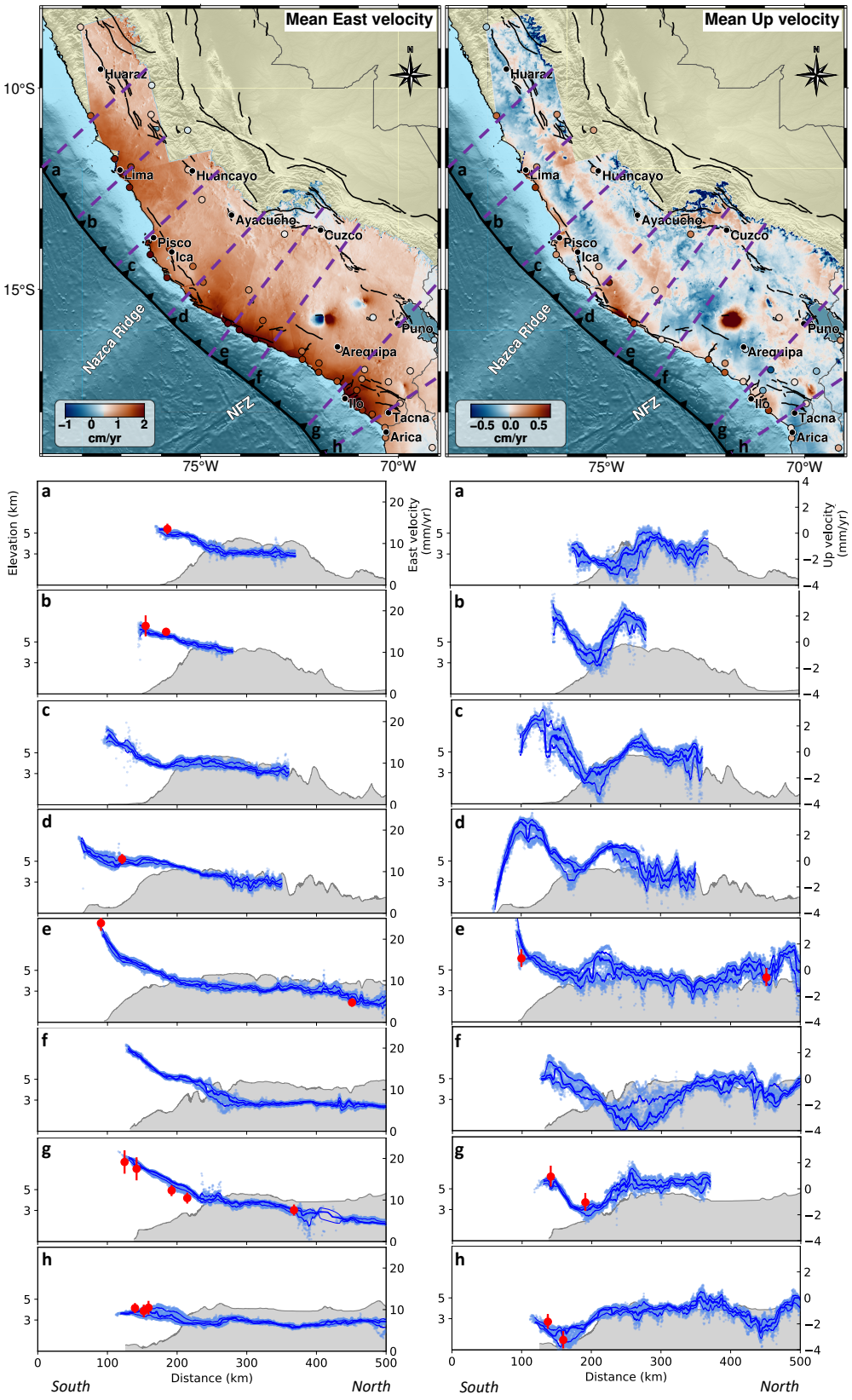

Figure 7.5: Cross-sections (a, b, c, d, e, f, g, h) along the Peru subduction, on the InSAR mean East (left) and Up (right) velocities. InSAR data within 100-km wide boxes are displayed as light blue dots on the cross-sections, with the median and quarters indicated by thick and thin solid blue lines respectively. The average GNSS velocities and associated uncertainties projected in LOS are in red. The topography is indicated by the light gray line.

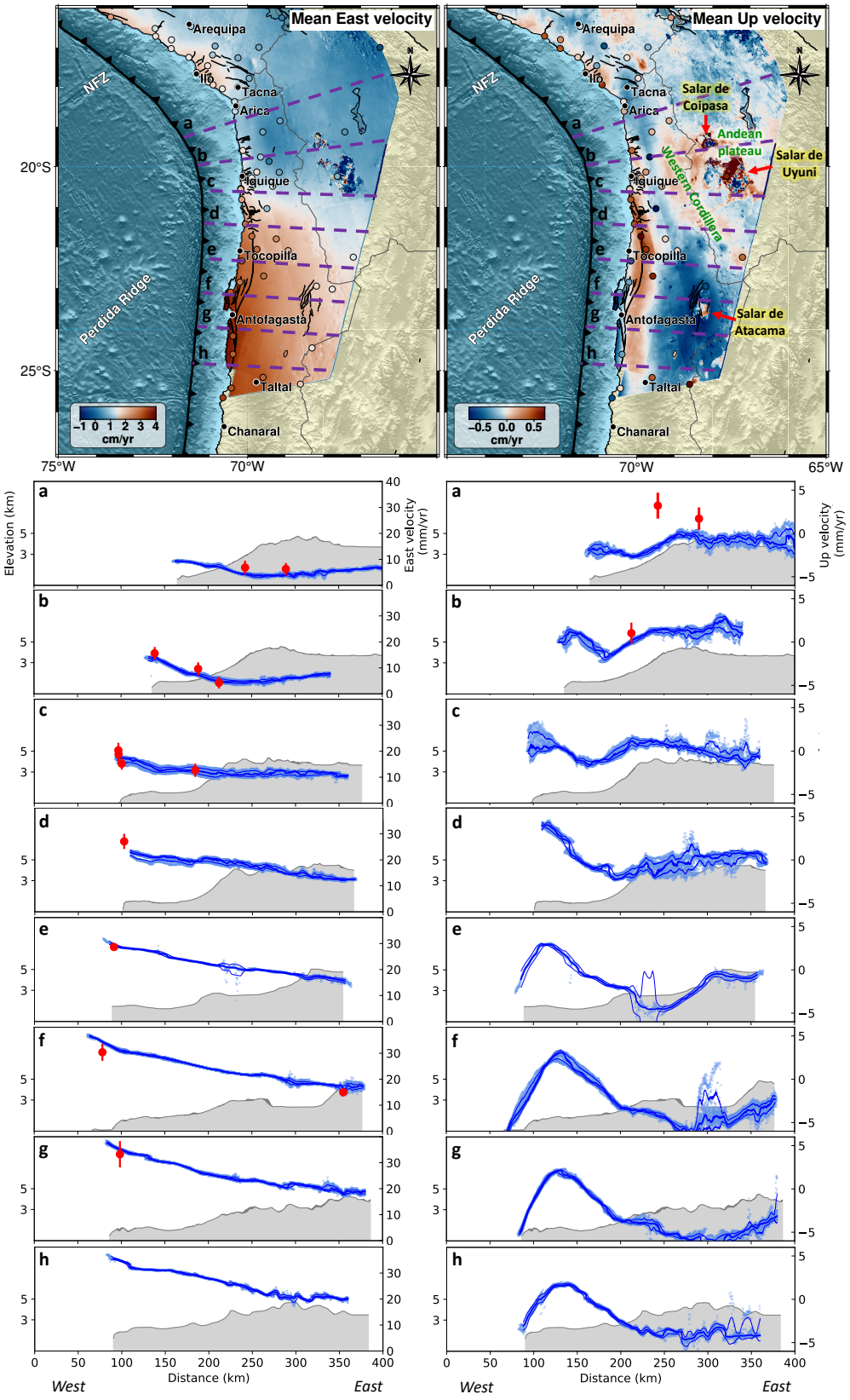

Figure 7.6: Cross-sections (a, b, c, d, e, f, g, h) along the Chile subduction, on the InSAR mean East (left) and Up (right) velocities. InSAR data within 100-km wide boxes are displayed as light blue dots on the cross-sections, with the median and quarters indicated by thick and thin solid blue lines respectively. The average GNSS velocities and associated uncertainties projected in LOS are in red. The topography is indicated by the light gray line.

4.4 Mapping the displacement across active faults

On Figure 7.7 we show some profiles across the main branch of the Cuzco fault system. This system is composed of the Cuzco fault that crosses the city of Cuzco, the Zurite-Huaraconda fault on the West, and the Tambomachay and Pachatusan faults on the East. It is expected to have hosted several significant earthquakes such as in 1650 and 1950 with magnitudes of about 7.2 and 6.0, respectively (epicenter in the vicinity of the Cuzco city, see Figure 7.7) (García et al., 2025; Silgado, 1978; Tavera and Buforn, 2001). The Cuzco fault system is mostly oriented in a West-northwest to South-southeast direction. It is not totally clear to the authors (Benavente et al., 2018; García et al., 2025) if the Cuzco fault has some splays or not, and where exactly the fault is located in the valley. We observe a pretty sharp velocity change when crossing the fault in the InSAR velocity maps, with a left-lateral offset of up to 2.8 mm/yr on the East component (see profiles a to d on Figure 7.7). On profiles b and c, we also observe a secondary offset of about 2 mm/yr at about 25 km North. Looking at the elevation profiles, we note that the signals observed across the faults cannot be related to residual stratified atmospheric effects. We modeled the East velocity V_E on the main fault (the Zurite-Huaraconda fault on profiles a and b, and the Cuzco fault on profiles c and d) with an arctangent model (Segall, 2010):

$$V_E(x) = \frac{A}{\pi} tan^{-1}\left(\frac{x}{D}\right) \tag{7.2}$$

with x the position along the profile, A the amplitude of the offset, and D the locking depth on the fault.

We measured an offset between 2.2 and 2.8 mm/yr, and a locking depth ranging from 0.6 km on the Eastern side (profile d) to 1.5 km on the Western side (profile a).

An uplift of about 2 mm/yr is observed when crossing the Zurite-Huaracondo fault from North to South (profile a). An area of subsidence (about 1.5 mm/yr) is observed between the Zurite-Huaracondo fault and the splay fault located about 5 km to the South (profile b). This zone of subsidence extends to the East in the valley along the Cuzco fault (profiles c and d), with an amplitude of about 1.5 mm/yr on a width of about 15 km, which may indicate the presence of a releasing bend in the Cuzco valley.

The location of the transitions appears to be consistent with the fault location from Benavente et al., 2018. The observations indicate a left-lateral strike-slip component along the Zurite-Huaracondo and Cuzco fault systems. The total East displacement along the profiles a to e is about 3 to 4 mm/yr, which is partially accommodating the ~5 mm/yr motion (mostly oriented parallel to the Cuzco fault profile) of the Western Peruvian Sliver proposed by Villegas-Lanza et al., 2016. These faults are also expected to have a normal component (Benavente et al., 2018; García et al., 2025) but it would require observations on the North component to measure it due to the East-West orientation of the fault system.

Another fault that pops up on the InSAR velocity maps is the Cordillera Blanca fault. On the East component, we measure an offset up to 1.5 mm/yr when crossing the fault trace from West to East (Figure 7.8, profiles b to d), and up to 3 mm/yr of uplift on the vertical component (profiles a to e). A subsidence of about 2 mm/yr from West to East is observed in the Santa valley (a.k.a. Callejón de Huaylas) West of the Cordillera Blanca, which implies a total uplift of less than 1 mm/yr along the full profiles. The velocity gradients appear to be located on the Western flank of the Cordillera Blanca, and East of the Santa valley, well centered on the fault location. This suggests that the signal observed across the fault is of tectonic origin, and not due to residual stratified tropospheric effects. However, further analysis will be necessary to disentangle these two components, especially on the vertical velocity map.

The observed signal on the East component may be smaller than the actual horizontal displacement on the fault due to the North-northwest to South-southeast orientation of the fault, which would limit the observation of a strike-slip component. An observation on the North component would have been helpful to estimate more accurately the potential of the fault. Still, the observations are compatible with a partitioning between a left-lateral strike-slip mechanism and a normal mechanism reported by Benavente et al., 2018. The localization of the deformation also corroborates the fault trace from Benavente et al., 2018. According to Villegas-Lanza et al., 2016 the Cordillera Blanca fault is supposed to accommodate a Southeast displacement of about 4 mm/yr between the Western and Eastern Peruvian Slivers but it is difficult to constrain the amplitude of the displacement due to the lack of observation on the North component.

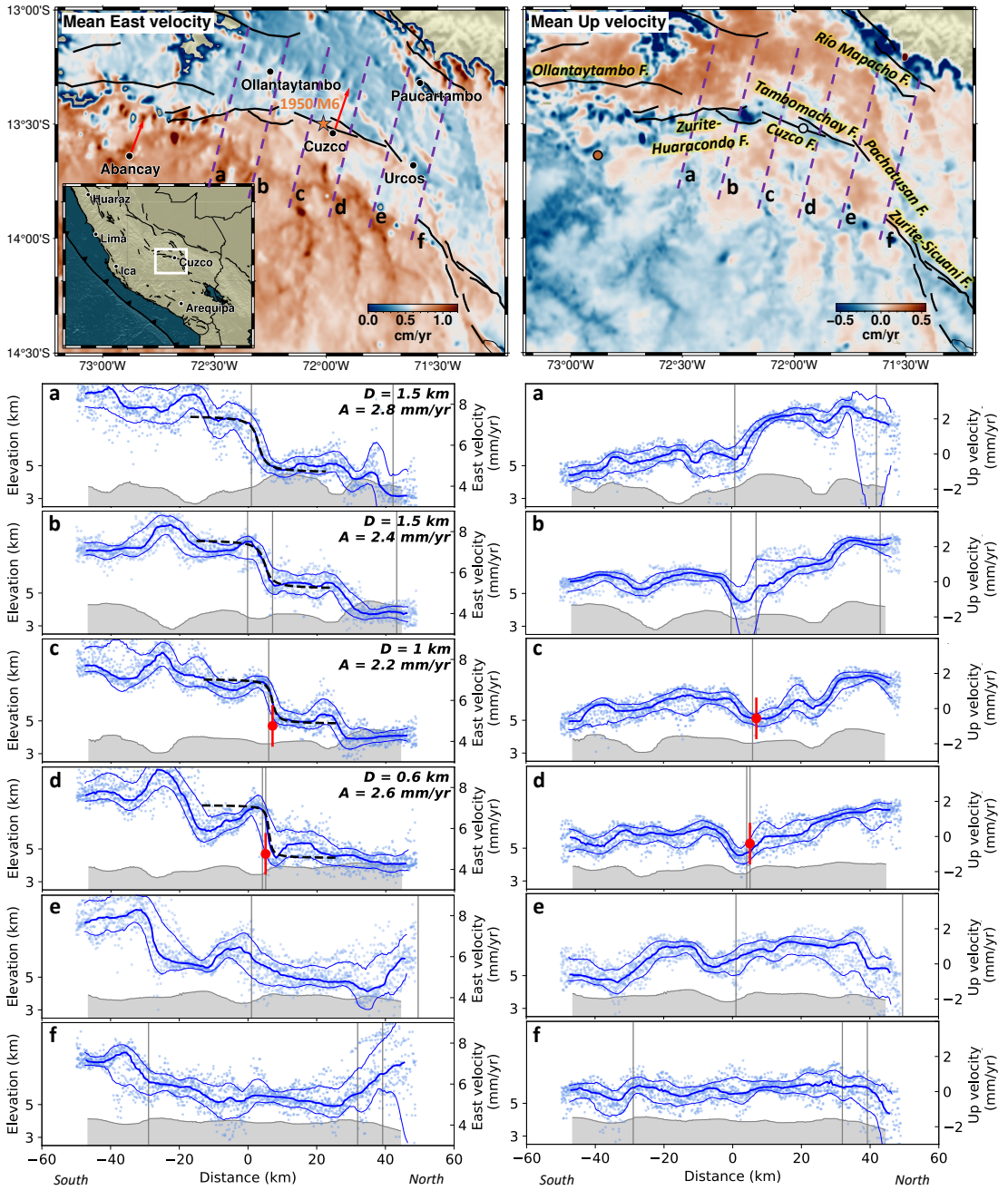

Figure 7.7: Cross-sections (a, b, c, d, e, f) across the main Cuzco fault, on the InSAR mean East (left) and Up (right) velocities. InSAR data within 50-km wide boxes are displayed as light blue dots on the cross-sections, with the median and quarters indicated by thick and thin solid blue lines respectively. The topography is indicated by the light gray line, the fault locations (Styron and Pagani, 2020) by vertical dark gray lines, and the average GNSS velocities by the red dots. On some profiles (a, b, c, d) an arctangent model of East displacement on the Cuzco fault is displayed as a dashed black line. The corresponding locking depth D and the velocity shift A across the fault are reported next to the profile.

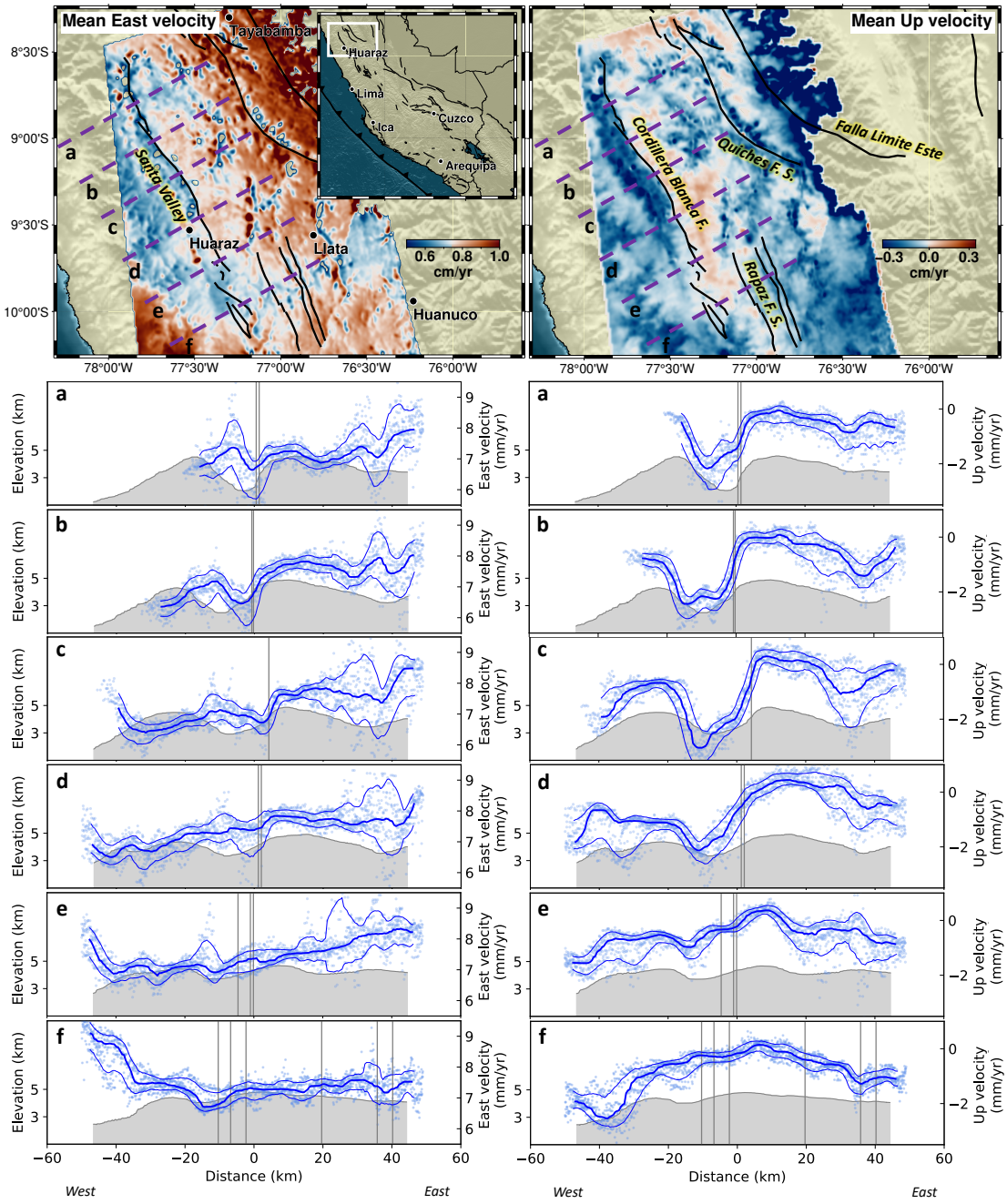

Figure 7.8: Cross-sections (a, b, c, d, e, f) across the Cordillera Blanca, on the InSAR East (left) and Up (right) velocity maps. InSAR data within 50-km wide boxes are displayed as light blue dots on the cross-sections, with the median and quarters indicated by thick and thin solid blue lines respectively. The topography is indicated by the light gray line, the fault locations (Styron and Pagani, 2020) by vertical dark gray lines.

4.5 Co and postseismic displacements

The coseismic displacements associated with two earthquakes in Peru are easily noticeable: the 2018 Mw7.1 Acari and the 2016 Mw6.2 Lampa earthquakes. The 2018 Acari earthquake was a thrust event on the slab interface that nucleated at a similar location as the Mw7.1 2013 and Mw7.2 2024 events (Eberle et al., 2024; Jiang and Li, 2023). The signal of the Acari earthquake is mostly located close to the coast, so it is mixed with the interseismic signal on the InSAR mean velocity maps, however, in the time series, we observe a sharp step (of up to about 4 cm) in January 2018 at the time of the earthquake (January 14) (Figure 7.9). Since the InSAR acquisitions are taken 12 days apart, it does not capture a pure coseismic displacement and it includes some postseismic displacement. The Lampa earthquake was located farther inland, at about 200 km from the coast, and it ruptured a shallow crustal normal fault (Aguirre et al., 2021; Tavera et al., 2016; G. Xu et al., 2019). We observe very clearly the separation between the area going away from the satellite (in blue on Figure 7.9) which is associated with a westward motion and some uplift, and the area going toward the satellite (in red on Figure 7) associated with an eastward motion. The timeseries indicates a displacement of up to 4 cm in the LOS, however, the spatial wavelength of the signal is too small (about 50 km) to impact the observed interseismic velocity if properly masked (see section 4.1 *Inversion method*).

The InSAR data also captured postseismic deformation signal associated with the 2014 Mw8.1 Iquique earthquake in North Chile. The InSAR time series started only one year after the Iquique earthquake, so the observed average velocity is significantly affected: we observe a significant decrease in the Eastward velocity compared to the Southern segment (about 1 cm/yr vs. 3 cm/yr), as well as subsidence at the coast onshore of the Iquique rupture (2-3 mm/yr). The low East velocity would not be compatible with the high interseismic locking expected in this area (Hoffmann et al., 2018; S. Li et al., 2015; Métois et al., 2016) without considering the Iquique earthquake postseismic displacement. Hoffmann et al., 2018, Itoh et al., 2023, Shrivastava et al., 2019, and Lovery et al., 2024 proposed afterslip models for the Iquique earthquake. Hoffmann et al., 2018 also accounted for the viscoelastic relaxation of the asthenosphere following the earthquake. These models predict a trench-ward displacement of about 10 cm of displacement on the acquisition period (2015 to 2021), which corresponds to about 1.5 cm/yr on the mean velocity.

4.6 Volcanic deformation

Other notable features include surface deformation related to volcanic activity, notably at the Sabancaya and Casiri volcanoes. The deformation trend at the Sabancaya volcano affects a 70-km wide circular area encompassing also the ancient Hualca Hualca

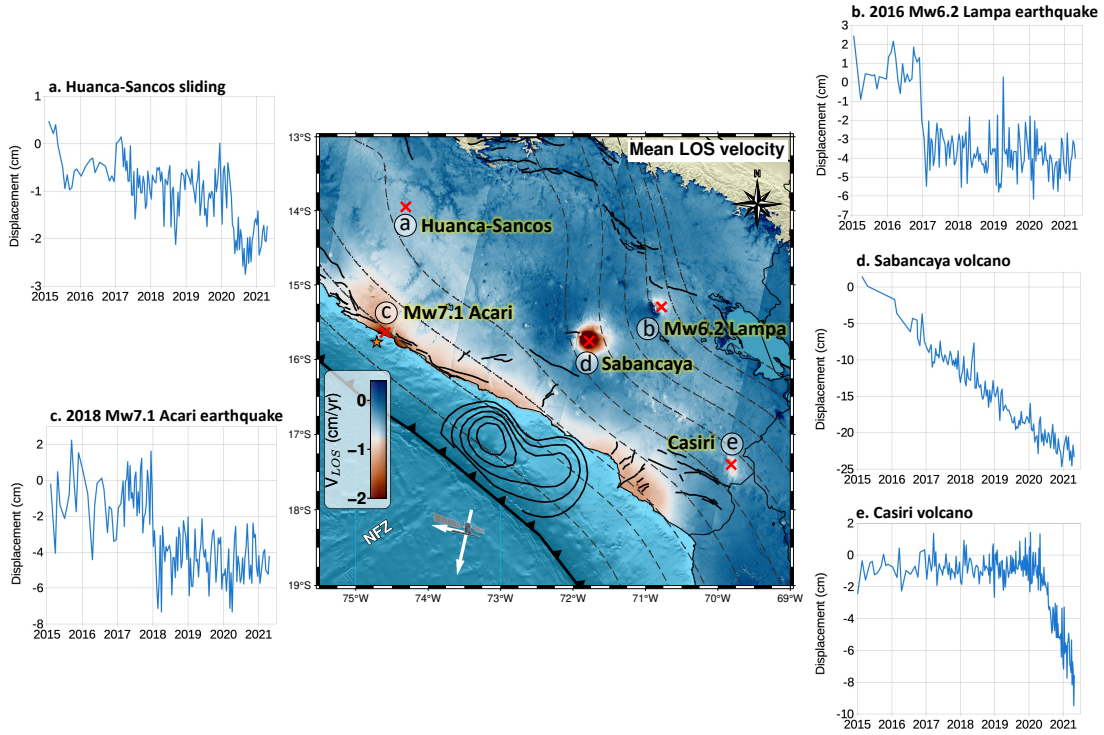

Figure 7.9: Referenced InSAR mean velocity map in LOS on the 2015-2021 period, for descending tracks in South Peru. The reddish pattern close to the coast indicates significant displacement toward the satellite, mostly related to the interseismic locking near the coast. We also observe the coseismic (and maybe some postseismic) displacements associated to the Mw6.2 Lampa crustal earthquake (December 1 2016) and to the Mw7.1 Acari subduction earthquake (January 14 2018) (c), as displayed by a clear offset in the time series at the dates of the earthquakes. The sustained inflation of the Sabancaya volcano (d) is also very noticeable, as well as the abrupt inflation of the Casiri volcano starting in 2020 (e). We observe a sliding at the Huanca-Sancos city (a) affected by several transient displacements. The slip distribution for the 2001 Mw8.4 Arequipa earthquake is reported from Lovery et al., 2024 by 1-meter black contours. The epicenter of the 2018 Acari earthquake is reported from the ISC seismic catalog (Bondár and Storchak, 2011). Main active faults from the GEM Active Faults Database (Styron and Pagani, 2020) are reported as solid black lines. Slab contours (gray dashed lines) are reported every 20-km depth, from the Slab2 model (Hayes et al., 2018). InSAR time series (averaged on 4 pixels) at the corresponding locations indicated by the red crosses are reported as insets for the various events.

volcano. The uplift rate is relatively linear in the 2015-2021 time window covered by the data, with a velocity of up to about 5 cm/yr in LOS (descending tracks, Figure 7.9). Deformation related to the Sabancaya since 2013 has been reported by Boixart et al., 2020 and Machacca et al., 2023. The volcano was reported to be relatively quiet since 1998, then seismic activity resumed in 2013 until the start of eruptive activity on November 6 2016 (Machacca et al., 2023). The East and vertical velocities confirm that this deformation is related to an inflation of the area, with a relatively uniform uplift of about 2 cm/yr within the circular area (Figure 7.4). A westward motion of about 3 cm/yr is observed on the Western part of the circular area, as well as an eastward motion of similar amplitude on the Eastern side. We cannot state on the North displacement as we do not recover this component on our InSAR data, but we can expect the inflation to be relatively isotropic. The modeling from Machacca et al., 2023 and the magnetotellurics observation from Torres et al., 2025 conclude that the magmatic reservoir supplying the Sabancaya is located beneath the Hualca Hualca (8 km North of Sabancaya) at about 12 km depth. The area in the vicinity of the Sabancaya volcano, including Arequipa city, is undergoing subsidence (as discussed in Lovery et al., 2025).

The inflation trend at the Casiri volcano is also significant, with a velocity of up to about 6 cm/yr in LOS (Figure 7.9). Unlike at Sabancaya, we captured the beginning of the inflation in mid-2020, the signal being mostly flat beforehand. The deformation at Casiri has also been reported by Vargas-Alva and Villegas-Lanza, 2021, as well as Biggs et al., 2022 and Popescu et al., 2025 using supervised and unsupervised machine learning, respectively. The deformation started jointly with the occurrence of several earthquakes of magnitude Mw>4 on July 25 and 26 (Antayhua et al., 2021) and appears relatively linear until the end of the timeseries in September 2021.

4.7 The Huanca-Sancos landslide

Although the 16-look resolution is a bit coarse to study small landslides, some large landslides can still be identified, including the instability at the Huanca-Sancos city in the Ayacucho department (Figure 7.10). Huanca-Sancos is a small city of about 4,000 inhabitants located on the Western flank of a valley. A continuous GNSS station (AY03) is operated by IGN in the center of the city. The GNSS time series, recorded from January 2017 to January 2019, indicates three significant eastward displacements during the period: a ~15 mm displacement in March 2017 spanning about two weeks, a ~35 mm displacement in May 2018 spanning about one month, and a ~20 mm displacement in August 2018 spanning about three weeks (Figure 7.10). These displacements are not related to known earthquakes, and are anyway too spread in time to be coseismic displacements. Figure 7.10 shows InSAR displacement time series in LOS for the ascending A120 (red) and descending D098 (green) tracks at two locations: point 1 (left) is located at the position of the AY03 GNSS station in the Huanca-Sancos city

center, while point 2 is located on the Eastern flank of the valley across the river. The displacement observed in March 2017 on the GNSS time series is also observed on the InSAR data, and interestingly it is observed on both sides of the valley at points 1 and 2. The InSAR time series is a bit too noisy to state on the displacements observed in May and August 2018 on the GNSS data, however we observe a crisp step in April 2020 at point 1 of about 30 mm. The major added value of InSAR time series analysis compared to GNSS to monitor this landslide is to observe the spatial extent of the sliding area. We observe that most of the city center is located on the landslide, on a circular area of about 600 m of diameter.

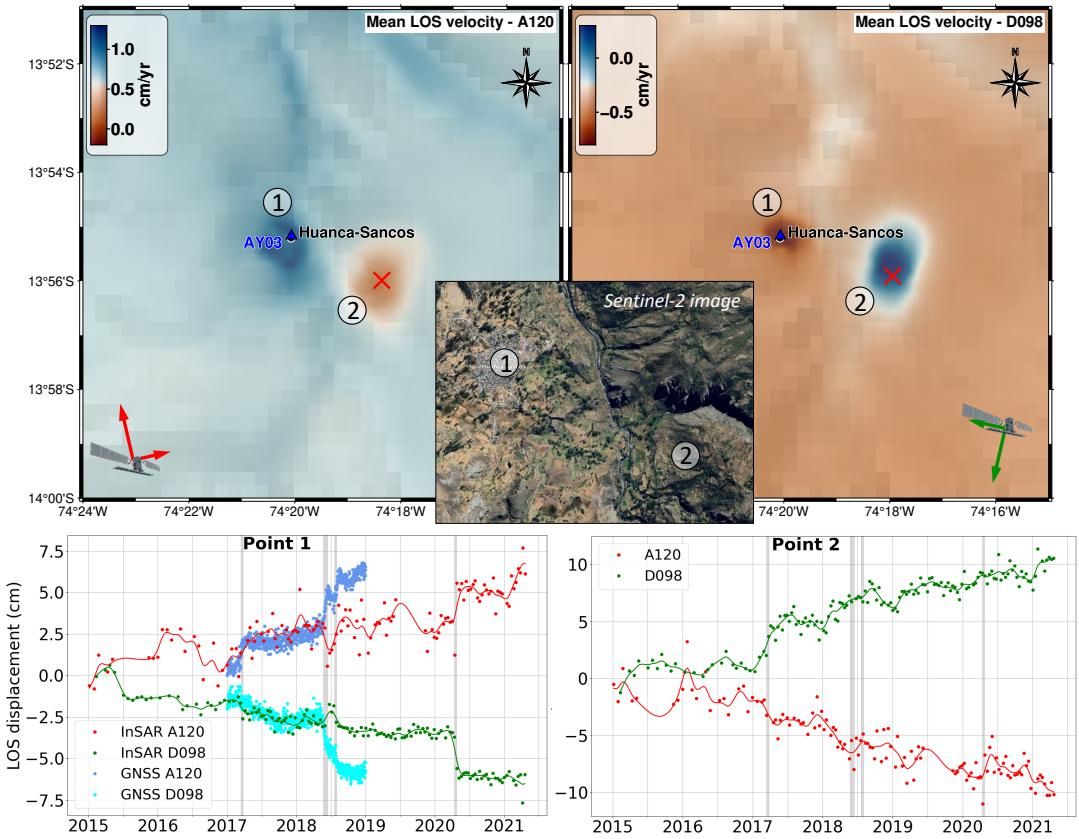

Figure 7.10: *Top:* Mean velocity maps in LOS for the ascending A120 (left) and descending D098 (right) tracks, zoomed on Huanca-Sancos. The AY03 GNSS station is located in the city. *Bottom:* InSAR displacement time series in LOS for the ascending A120 (red) and descending D098 (green) tracks at two locations: point 1 (left) is located at the position of the AY03 GNSS station in the Huanca-Sancos city center, while point 2 is located on the Eastern flank of the valley across the river. The GNSS time series at AY03, projected in LOS for the A120 and D098 geometries, are reported in blue and cyan respectively.

5 Modeling interseismic coupling

5.1 Inversion method

In order to model the interseismic coupling in Central and South Peru (11°S to 19°S), we use a linear-least square inversion procedure following the Tarantola & Valette formulation (Radiguet et al., 2011; Tarantola, 2005; Tarantola and Valette, 1982), implemented in the PCAIM software (Kositsky and Avouac, 2010), and using a 3-D slab geometry based on Slab2.0 (Hayes et al., 2018). We refer to Lovery et al., 2024 for full technical details on the inversion procedure. Viscoelastic Green's functions are computed using the methodology from Lovery et al., 2025 in a fully-relaxed state, in order to model the interseismic coupling with a viscoelastic rheology. Note that compared to Lovery et al., 2024 and Lovery et al., 2025 we modified the inversion code to have a bounded inversion algorithm where we specify the maximum value of back-slip, which is constrained by the plate convergence rate of 63 mm/yr in South Peru (Jarrin et al., 2023; Kendrick et al., 2003; Villegas-Lanza et al., 2016). It allows to have interseismic coupling models with less smoothing without exceeding the convergence rate. Finally, we impose the interseismic coupling to taper below a 60-km depth in order to avoid unrealistic slip at depths where the rocks are expected to become too ductile to lock the interface (Gagnon et al., 2005; Villegas-Lanza et al., 2016). Misfit between observed (d_i) and modeled (m_i) velocities is quantified by a reduced chi-square criteria:

$$\chi^2_{red} = \frac{\chi^2}{\nu} \text{ with } \chi^2 = \sum_i \frac{(d_i - m_i)^2}{\sigma_i^2} \tag{7.3}$$

where σ^2 is the variance and ν = n - p the degrees of freedom for n observations and p parameters.

For inverting InSAR velocities, we correct the LOS mean velocity maps from the 2001 Mw8.4 Arequipa earthquake postseismic deformation using the correction proposed by Lovery et al., 2025, who modeled the viscoelastic relaxation of the asthenosphere by finite element method, and from the 2014 Mw8.1 Iquique earthquake postseismic deformation using the afterslip model from Lovery et al., 2024. We also correct from the 2018 Mw7.1 Acari earthquake coseismic displacement using the slip model from Juan Carlos Villegas-Lanza (personal communication). We mask some areas with signals of short spatial wavelength that are not related to the deformation generated by the subduction megathrust: the Sabancaya and Casiri volcanoes, and the 2016 Mw6.2 Lampa earthquake (Figure 7.11). Then, we subsample the corrected LOS velocity maps (in the SSA reference frame) with a sampling step decreasing from 10 to 40 km with the distance to the slab, using a similar approach as Socquet et al., 2019 and Grandin

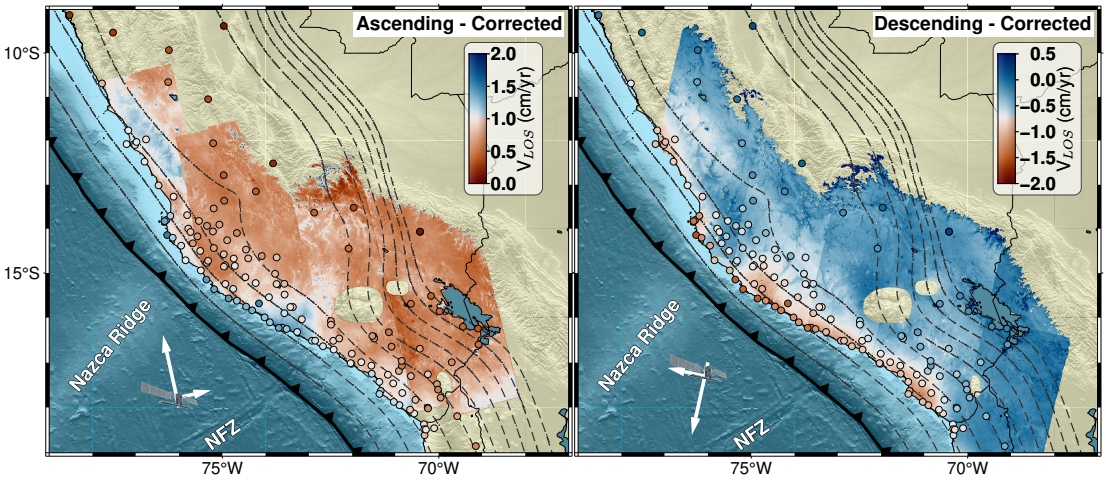

Figure 7.11: InSAR mean velocity maps on the 2015-2021 period in LOS, referenced and corrected from the 2001 Mw8.4 Arequipa and 2014 Mw8.1 Iquique earthquakes postseismic displacements, and from the 2018 Mw7.1 Acari earthquake coseismic step. GNSS velocities on the same period are reported within black circles.

et al., 2009. We consider four ascending and six descending tracks in a joint inversion, for which the LOS vector is given for each pixel.

5.2 Results of interseismic velocities inversion

We apply a fixed convergence direction that we refer as *tectonic angle*, which is defined as the counterclockwise angle from the East vector (e.g., a tectonic angle of 0 degree corresponds to a pure East convergence, while a 90-degree value corresponds to a pure North convergence). On Figure 7.12 is reported the reduced chi-square as a function of the tectonic angle for values between 12 and 22 degrees. We retain a 17-degree angle for all the inversions performed in this study, since it is the value for which the misfit is the lowest. In addition, this value is in agreement with the estimated convergence vectors (Jarrin et al., 2023; Kendrick et al., 2003; Villegas-Lanza et al., 2016) and the focal mechanisms of major earthquakes in the area, including the 2001 Mw8.4 Arequipa earthquake (Giovanni et al., 2002; Hergert and Heidbach, 2006; Tavera and Buforn, 2001; Tavera et al., 2006).

Then, we searched for the optimal damping factor σ_m and correlation length λ (Lovery et al., 2024; Radiguet et al., 2016), that need to be adjusted together, by computing some *L-curves* (Figure 7.13). We vary the damping parameter from $\sigma_m = 10^{-2}$ to $10^{-0.2}$ for three values of correlation length (λ = 10, 20, and 30 km), and we express the misfit (reduced chi-square) and the Manhattan distance (L1 norm) on the x and y axis

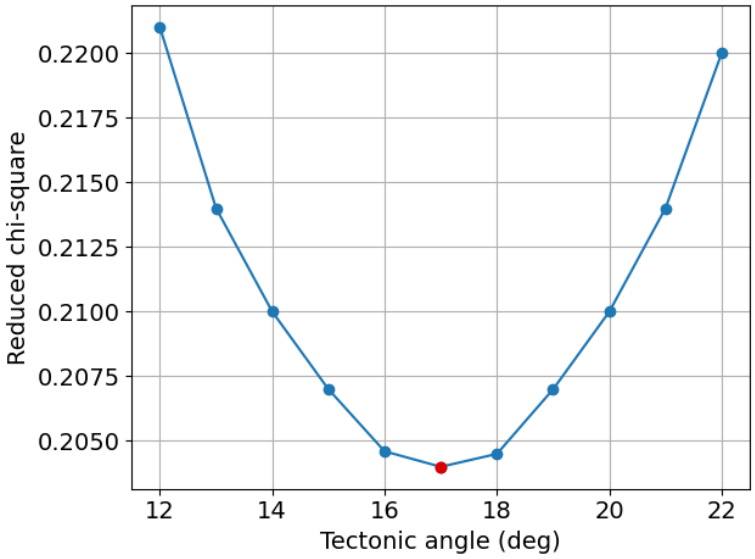

Figure 7.12: Variation of reduced chi-square in function of the tectonic angle, defined anti-clockwise from the East vector. We retain an angle of 17 degrees, for which the reduced chi-square is the lowest (highlighted in red).

respectively. We retained the parameters λ = 20 km and $\sigma_m = 10^{-1.1}$ that correspond to the hollow part of the curve, for which the misfit is significantly lowered without requiring too much slip or too much model complexity (Florsch et al., 2014; Radiguet et al., 2016).

After setting the inversion parameters (tectonic angle, damping factor, and correlation length), we explore the relative weight of GNSS vs. InSAR (Figure 7.14). The reduced chi-square for GNSS and InSAR datasets, and the total reduced chi-square which is the sum of the two, are expressed in function of a weighting factor W_{factor} defined as:

$$W_{factor} = \frac{W_{GNSS}}{W_{GNSS} + W_{InSAR}} \tag{7.4}$$

with W_{GNSS} and W_{InSAR} the weights of the GNSS and InSAR respectively. For instance, W_{factor} = 0 and W_{factor} = 1 correspond to InSAR-only and GNSS-only models. In order to lower the total misfit we retain a factor W_{factor} = 0.6, equivalent to a weighting of 60% for the GNSS dataset.

Results of an inversion with GNSS interseismic velocities only are showed on Figure 7.15. The fit is satisfying for most sites (χ^2_{red} = 0.22), from the coast to the back-arc. The few sites in Northern Chile show a relatively poorer fit, which may indicate that

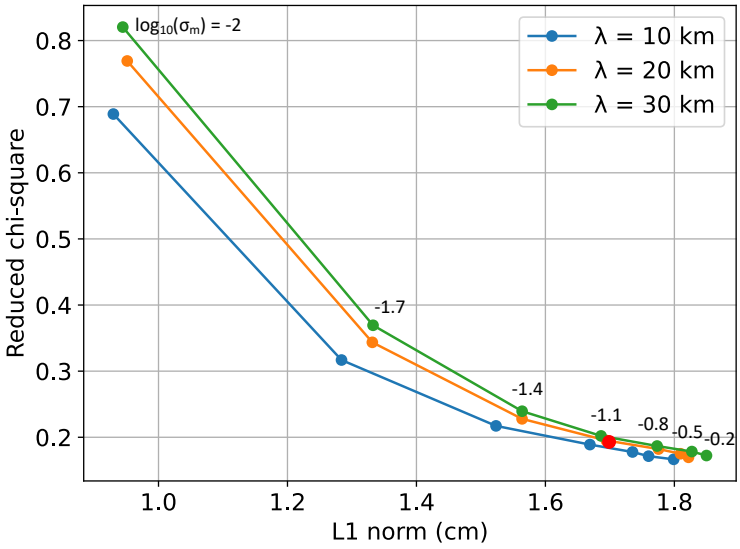

Figure 7.13: Adjustment of the damping factor σ_m for various correlation lengths λ. The Manhattan distance (L1 norm) and the associated reduced chi-square are reported on the x and y axis respectively. We retained the parameters λ = 20 km and $log_{10}(\sigma_m)$ = -1.1, highlighted in red.

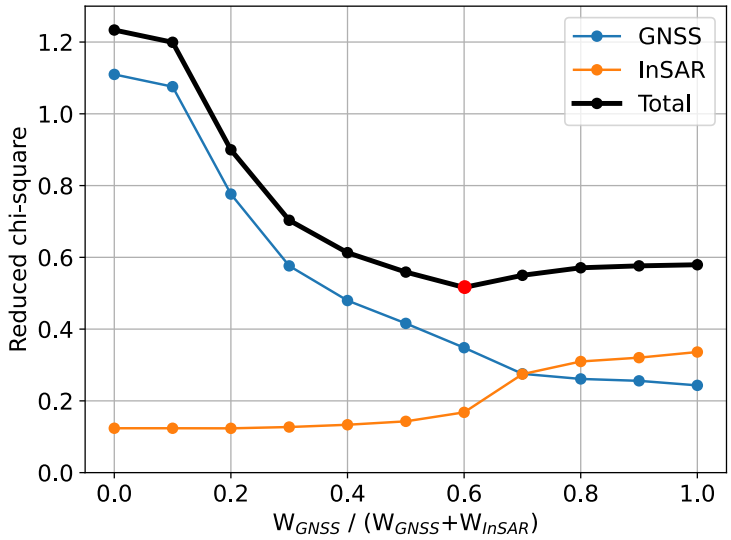

Figure 7.14: Variation of reduced chi-square in function of the relative weight of GNSS vs. InSAR. We retained a weighting of 60% for GNSS, for which the total misfit is the lowest (highlighted in red).

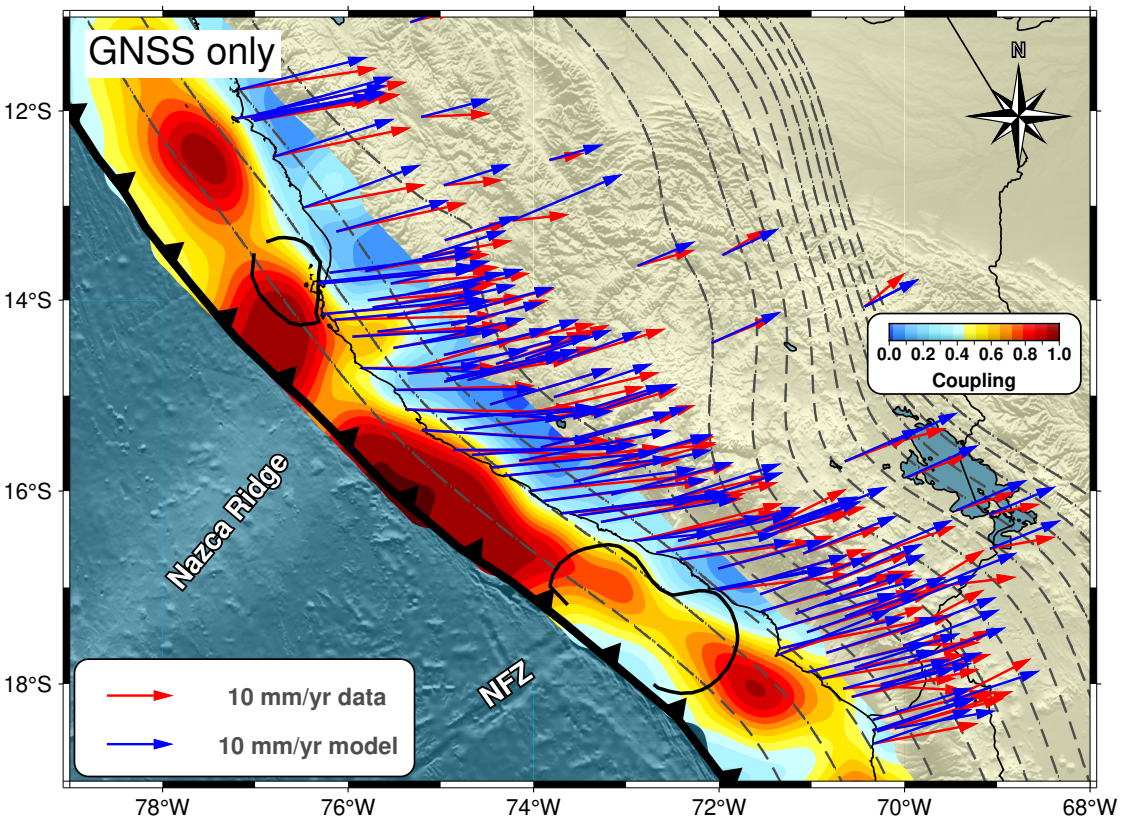

Figure 7.15: Interseismic coupling distribution from our inversion of GNSS-only interseismic velocities. Slab contours (dashed lines) are reported every 20-km depth, from the Slab2 model (Hayes et al., 2018). The approximate rupture area of the 2001 Mw8.4 Arequipa is reported from Lovery et al., 2024, while the 2007 Mw8.0 Pisco earthquake rupture is reported from Chlieh et al., 2011. Observed and modeled interseismic velocities are reported by red and blue vectors respectively.

the model structure and rheology is not optimal for North Chile, or that an additional block motion may be required as suggested by Métois et al., 2016 or Chlieh et al., 2004.

On Figure 7.16 the results of the joint inversion of the InSAR and GNSS datasets are reported with the optimal parametrization described previously. Compared to the inversion with GNSS only, the fit at GNSS sites is slightly poorer, but most of them still show a residual (data minus model) below 2 mm/yr. The residuals on InSAR velocities are also relatively good, both on ascending and descending tracks, with values below 4 mm/yr for most of the sites. However, it appears that the area in the vicinity of the 2018 Mw7.1 Acari earthquake is affected by higher residuals (up to 1 cm/yr at some very localized InSAR sites), which may indicate that the coseismic correction is not totally adequate.

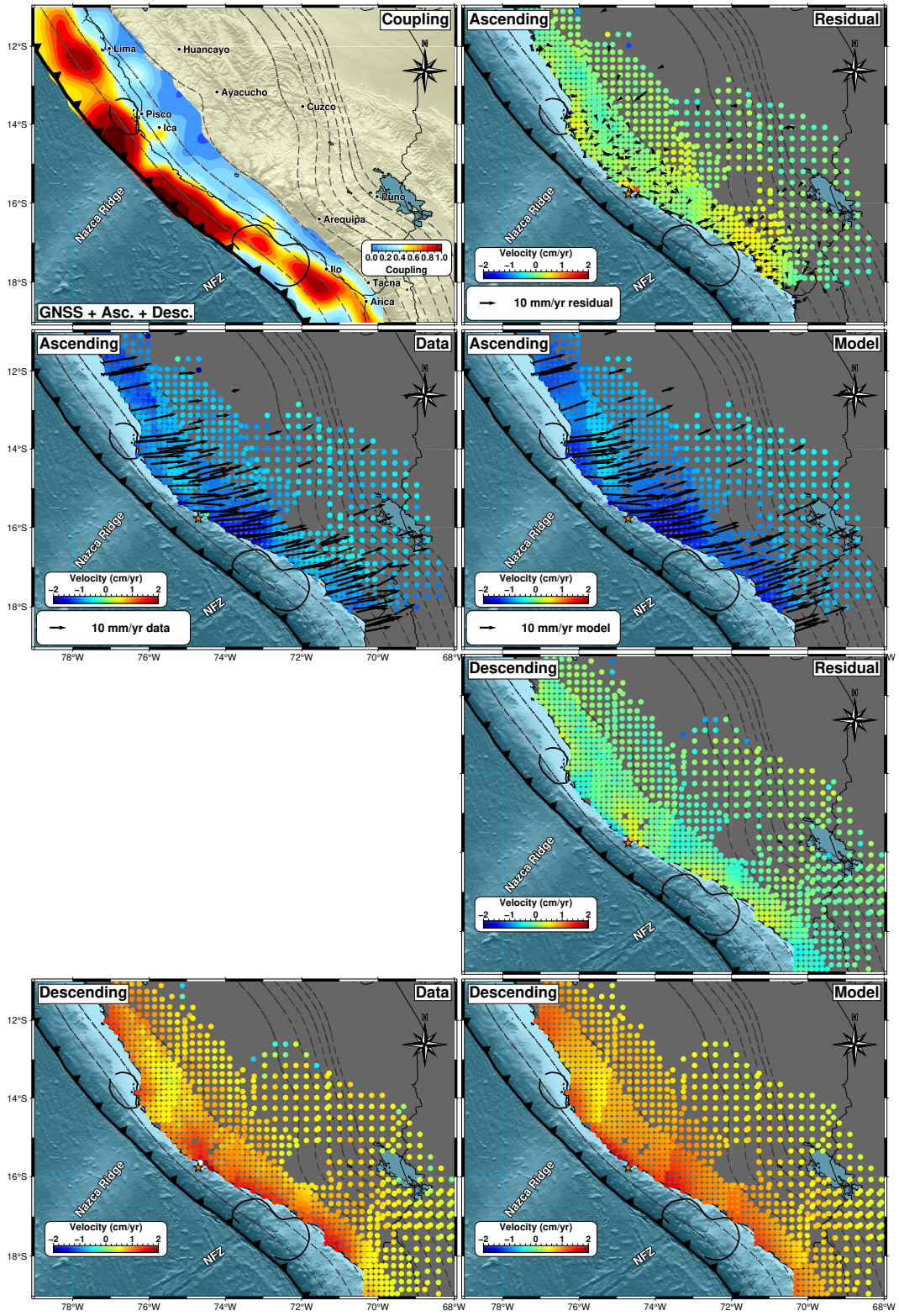

Figure 7.16: Interseismic coupling distribution from joint inversion of GNSS and InSAR interseismic velocities. Slab contours (dashed lines) are reported every 20-km depth, from the Slab2 model (Hayes et al., 2018). The approximate ruptures of the 2001 Mw8.4 Arequipa and 2007 Mw8.0 Pisco earthquakes are reported from Lovery et al., 2024 and Chlieh et al., 2011 respectively. LOS velocities at InSAR discretized sites are reported by the *jet* colormap for data, model, and residual. Horizontal velocities at GNSS sites are reported by black vectors for data, model, and residual. The epicenter of the 2018 Acari earthquake is reported from the ISC seismic catalog (Bondár and Storchak, 2011) as an orange star.

5.3 Discussion of the interseismic coupling models

From GNSS velocities only

Compared to the interseismic coupling model proposed by Lovery et al., 2025, we have about doubled the amount of GNSS sites (150 vs. 73 sites). The improvement in spatial coverage is especially noticeable on the segment where the Nazca Ridge is subducting. Earlier studies (Lovery et al., 2024; Lovery et al., 2025; Villegas-Lanza et al., 2016) have gaps of about 80 km between the coastal stations in this area (about 14 to 16°S), which was a significant limiting factor for assessing accurately the interseismic coupling on this segment. We observe an increase of interseismic coupling where the Nazca Ridge is subducting (Figure 7.15), especially in the shallow part (less than 20 km deep), from about 0.5 to 0.7. It indicates that the substantial decrease in coupling in front of the Nazca Ridge that was reported in the previous geodetic studies (Chlieh et al., 2011; Jara et al., 2024; Lovery et al., 2024; Lovery et al., 2025; Villegas-Lanza et al., 2016) was overestimated due to the lack of resolution. Still, the decrease in coupling where the ridge is subducting is very noticeable on the model, especially in the deeper part (more than 20 km deep), fully locked asperities being observed South and North of the ridge. This is an important result, the Nazca Ridge being considered a strong seismic barrier (Dorbath et al., 1990; Lovery et al., 2024; Philibosian and Meltzner, 2020; Villegas-Lanza et al., 2016). From all the large subduction earthquakes (Mw $\geq$ 7.5) that the Peruvian subduction hosted since 1512, no event nucleated on the ridge and no seismic rupture propagated on the ridge (Chlieh et al., 2011; Dorbath et al., 1990; Villegas-Lanza et al., 2016). For instance, the rupture propagation of the 2007 Mw8.0 Pisco earthquake (Sladen et al., 2010; Tavera and Bernal, 2008) was stopped North of the ridge, and South of the ridge for the 1996 Mw7.7 and 1942 Mw8.2 earthquakes (Dorbath et al., 1990; Villegas-Lanza et al., 2016). Aside from these observations on the Nazca Ridge segment, the interseismic coupling distribution from GNSS velocities is highly heterogeneous and quite similar to Lovery et al., 2025. High coupling (> 0.8) is observed offshore of Lima (12 to 13°S), offshore of Pisco (14 to 15°S), from the Nazca Ridge to the NFZ, and from the NFZ to the Arica bend. Lower coupling (< 0.8) is still observed where the NFZ is subducting.

From GNSS and InSAR velocities

The joint inversion of InSAR and GNSS interseismic velocities (Figure 7.16) results in a comparable interseismic coupling distribution at the first order, compared to the inversion based only on GNSS (Figure 7.15). It indicates a good agreement between GNSS and InSAR datasets, which is something we expected since the InSAR velocity maps have been referenced using GNSS so the long-wavelength InSAR signal is mostly controlled by GNSS. Still, the short-wavelength InSAR signal brings independent ob-

servations at smaller scale. Also, the InSAR is very sensitive to the vertical component, while about half of the GNSS sites are survey sites for which the vertical component is not used. These features of the InSAR dataset lead to two main changes with respect to the GNSS-only inversion: increased seismic coupling on the Northwestern segment (11 to 13°S), and where the NFZ is subducting (17 to 18°S).

The increased coupling on the Northwestern segment amounts about 50% compared to GNSS-only. It is probably related to the sparse distribution of stations in the area, where InSAR brings a significant improvement in spatial coverage. It is an important result for seismic potential assessment in the area, where a large earthquake offshore of Lima could be a serious threat. The degree of locking we observe with InSAR is consistent with the seismic history of this segment that ruptured in front of Lima in 1974 (Mw7.9) and North of Lima in 1940 (Mw8.1), the largest event that has stroke the segment was of magnitude Mw~8.6 and occurred in 1746 (Dorbath et al., 1990).

The increase of coupling where the NFZ is subducting (about 30% compared to GNSS-only) indicates that some GNSS velocities may have been underestimated. Earlier interseismic coupling models (Chlieh et al., 2011; Lovery et al., 2024; Lovery et al., 2025; Villegas-Lanza et al., 2016) reported low-coupling in this segment, overlapping the 2001 Mw8.4 Arequipa earthquake rupture, but it was not clear whether this apparent lower coupling was caused by a sparser GNSS network (notably in Chlieh et al., 2011 and Villegas-Lanza et al., 2016), by the postseismic displacements following the 2001 earthquake, or by an actual decrease in coupling. We now benefit from dense GNSS and InSAR observations in this area, we apply a postseismic correction (Lovery et al., 2025) on the interseismic velocities, and we still observe a lower coupling compared to the locked segments South and North of the NFZ. The increased coupling brought by InSAR is in better adequacy with what is expected from an area hosting a Mw8.4 earthquake, but it seems that the subduction of the NFZ effectively lowers the coupling. The NFZ is considered as a weak barrier, reported to have slowed down the rupture propagation of the 2001 Arequipa earthquake (Robinson et al., 2006).

The residuals on the InSAR tracks (Figure 7.17) show a stripe of respectively positive and negative velocity on the ascending and descending tracks (about 3 mm/yr) close to the trench in front of the Nazca Ridge from about 14°S to 15.5°S. Note that in this area the coast is closer from the trench, at about 100 km vs. 150 to 200 km on the other segments. More inland, we observe a stripe of respectively negative and positive residual (the opposite compared to the coastal stripe) on the ascending and descending tracks (about 2 mm/yr). Also, we observe an increase of about 2 mm/yr in the residuals when crossing the Cuzco fault system from South to North, in the prolongation of the Titicaca lake, from South to North. This is consistent with the analysis described in section *Mapping the displacement across active faults*, and it accredits the Peruvian sliver delimitation proposed by Villegas-Lanza et al., 2016. However, we do not re-

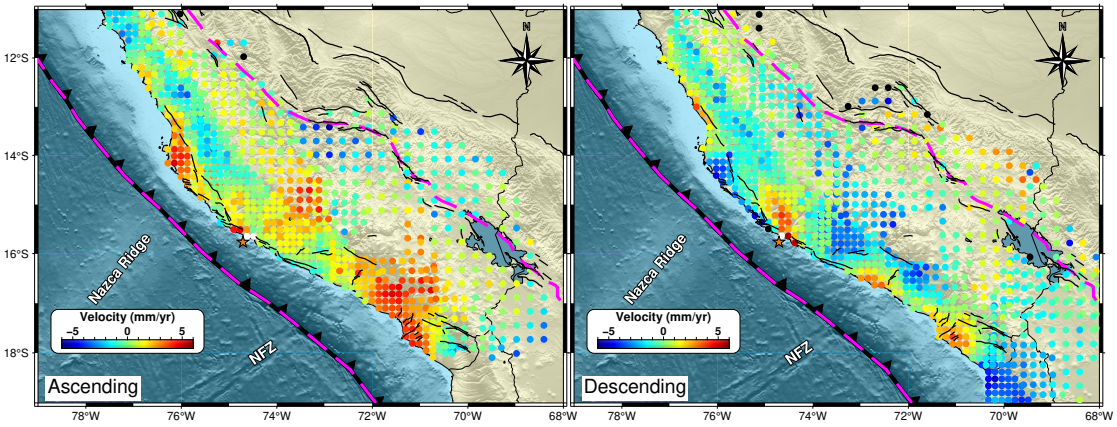

Figure 7.17: Residual velocities in LOS from the inversion of interseismic velocities shown on Figure 7.16, for ascending (left) and descending (right) tracks. Major faults from Styron and Pagani, 2020 are depicted by black lines. The boundaries of the Peruvian Sliver from Villegas-Lanza et al., 2016 are depicted by magenta dashed lines. The epicenter of the 2018 Acari earthquake is reported from the ISC seismic catalog (Bondár and Storchak, 2011) as an orange star.

cover the 5 mm/yr of Southeastward displacement proposed by Villegas-Lanza et al., 2016. This sliver velocity was estimated from the residuals of an interseismic coupling model in a fully elastic half-space, which may have led the authors to overestimate the sliver velocity by not accounting for viscoelasticity, as highlighted by S. Li et al., 2015 in North Chile. It is also possible that the deformation in the upper plate is more diffused, instead of a rigid block motion, like suggested by Yáñez-Cuadra et al., 2022. In addition, the estimate from Villegas-Lanza et al., 2016 was performed from GNSS sites distributed mostly in North and Central Peru, while our analysis is focused on South Peru. Only 10 GNSS sites were located between the Nazca Ridge and the Arica bend in Villegas-Lanza et al., 2016, while we now benefit from about 100 GNSS sites on the same area, in addition to the InSAR data.

6 Conclusions

We publish the first mapping at the scale of the Central Andes from InSAR time series (2015-2021), thanks to the FLATSIM service (FormaTerre, 2020). We referenced the InSAR mean velocity maps using the dense GNSS network now available in Central Andes, notably in South Peru (Villegas-Lanza et al., 2025) and North Chile (Socquet et al., 2023), allowing large-scale tectonic applications of the InSAR acquisitions. The referenced InSAR mean velocity maps have been decomposed into maps of mean East and vertical velocities, providing a significant improvement in spatial resolution compared

to the existing GNSS-based velocities (1-km resolution vs. tens of km), especially on the vertical component for which reliable GNSS measurements are often lacking (Itoh et al., 2019).

A portfolio of geophysical processes is presented, for which InSAR time series bring a significant added value: volcanic deformation (Sabancaya and Casiri volcanoes), landslides (Huanca-Sancos), coseismic (2018 Mw7.1 Acari and 2016 Mw6.2 Lampa earthquakes) and postseismic (2014 Mw8.1 Iquique earthquake) deformation, interseismic locking, or assessment of the displacement accommodated by crustal faults (the Cuzco fault system and the Cordillera Blanca). Although our analysis of the Huanca-Sancos sliding remains simple, we hope that these first-published observations will be pursued by more in-depth analysis of this landslide. We focused our study on tectonic applications, for which the spatial resolution provided by InSAR is of great interest to investigate the partitioning of the deformation in the upper plate. In this purpose, we quantified the East and vertical displacements across the Cuzco fault system (up to 3 mm/yr and 2 mm/yr on the East and vertical components respectively) and the Cordillera Blanca (up to 1.5 mm/yr and 3 mm/yr on the East and vertical components respectively), which have been proposed by Villegas-Lanza et al., 2016 to delimitate the Peruvian sliver. Primary (3-4 mm/yr) and secondary (2 mm/yr) zones of uplift are observed in Peru and Chile, at about 130 and 250 km from the trench respectively. The secondary zone of uplift is associated with high topography, suggesting partial interseismic plastic deformation of the upper plate. Also, the secondary uplift zone in Peru is primarily observed in the flat-slab region and tapered with the transition to dipping-slab.

In addition, joint inversions of interseismic velocities measured by GNSS and InSAR refined the interseismic coupling model in Central to South Peru, notably in the area North of the Nazca Ridge where the GNSS network is sparser. The sensitivity of InSAR to vertical displacements is especially interesting to better locate the interseismic coupling along dip. The resulting interseismic coupling is raised by about 50% on the segment in front of Lima (11°S to 13°S), and by about 30% in the vicinity of the NFZ. The analysis of the residuals of the interseismic coupling model, and the observed velocity offsets across the Cuzco fault system and the Cordillera Blanca, corroborate the existence of the Peruvian Sliver proposed by Villegas-Lanza et al., 2016. It attests of a partitioning of the deformation at the Cuzco fault system through a left-lateral strike-slip mechanism, in addition of a normal mechanism reported by Benavente et al., 2018. The lack of observation on the North component is however a limitation to assess the displacement across crustal faults, for which GNSS sites on each side of the Cuzco and Cordillera Blanca faults could raise the remaining ambiguities.

While this study was more focused on South Peru rather than North Chile, it would be of great interest to include the InSAR mean velocity maps over North Chile in an inversion of interseismic velocities at the scale of the Central Andes. For this purpose,

some additional work is required in order to have a viscoelastic model of the subduction including the North Chile segment, which has been affected by the 2014 Mw8.1 Iquique earthquake. A unified interseismic coupling model also raises the question of the Andean sliver (Métois et al., 2016), and of the accommodation of the deformation at the Arica bend (Arriagada et al., 2008). An incremental update of the InSAR time series with more recent years would also provide information on the evolution of the postseismic deformation following the 2014 Iquique and 2001 Arequipa earthquakes.

Chapter 8

Conclusions and outlook

One of the main objectives of this PhD thesis was to publish updated interseismic coupling models of the Central to Southern Peru subduction. The models released in Lovery et al., 2024 take advantage of the long-term efforts to densify the GNSS network in Central Andes since the 1990's (Bevis et al., 2001; Kendrick et al., 1999; Khazaradze and Klotz, 2003; Klotz et al., 1999; Métois et al., 2016; Norabuena et al., 1998; Socquet et al., 2023; Villegas-Lanza et al., 2025; Villegas-Lanza et al., 2016). From interseismic velocities computed at 73 GNSS sites, we propose an interseismic coupling model of the South Peru subduction (12°S to 20°S) with an unprecedented resolution. This model is highly heterogeneous, with locked asperities offshore of Lima (12°S), Atico (16°S), and Ilo (17.5°S) cities. Low coupling is observed where the Nazca Ridge is subducting, which is consistent with a rate-strengthening behavior (Kaneko et al., 2010). Indeed, the Nazca Ridge has been reported as a strong seismic barrier, stopping the along-strike rupture propagation of large earthquakes such as the 2007 Mw8.0 Pisco (Remy et al., 2016; Sladen et al., 2010; Tavera and Bernal, 2008), the 1996 Mw7.7 Nazca (Swenson and Beck, 1999; Tavera and Buforn, 2001; Tavera et al., 2006), or the 1942 Mw8.2 (S. L. Beck and Ruff, 1989; Dorbath et al., 1990; Sennson and Beck, 1996) earthquakes. We also observe a lowered coupling where the Nazca Fracture Zone is subducting, which has been reported as slowing-down the rupture propagation of the 2001 Mw8.4 Arequipa earthquake (Robinson et al., 2006). This area of lower coupling is overlapping the rupture area of the Arequipa earthquake (Giovanni et al., 2002; Tavera et al., 2002), so we suspected that it could be related to the postseismic displacement following the Arequipa earthquake (Hergert and Heidbach, 2006; Perfettini et al., 2005; Sun et al., 2018). From the proposed interseismic coupling model, we performed a moment budget analysis following a methodology similar to Avouac, 2015 and Chlieh et al., 2021. Taking advantage of the information provided by geodetic data on the energy accumulated through interseismic loading, balanced with the energy released by earthquakes reported in the seismic catalogs, we discussed the maximum magnitude earthquake

that the South Peru segment could host. Depending on the seismic catalogs used for this analysis and the considered fraction of transient slip released by afterslip and SSE during the cycle, we found that this segment could host a maximum magnitude earthquake ranging between 8.4 and 9.0, with an associated recurrence time of about 100 and 900 years respectively. The largest earthquake reported in the instrumental seismic catalogs (i.e., recorded by seismometers) on this segment is the 2001 Mw8.4 Arequipa earthquake, however the 1868 earthquake that ruptured most of the South Peru segment from the Nazca Ridge to the Arica bend may had a magnitude between 8.5 and 8.9 (S. L. Beck and Ruff, 1989; Carvajal et al., 2025; Dorbath et al., 1990; Villegas-Lanza et al., 2016). The high coupling observed offshore of Lima and Pisco, on the Central Peru segment, indicates that this segment could also host a large earthquake, however the sparser GNSS network North of the Nazca Ridge restrained us from performing a moment budget analysis on this segment. The Central Peru segment, from the Mendaña Fracture Zone to the Nazca Ridge, is expected to have rupture on most of its length during the 1746 M~8.6 earthquake (S. L. Beck and Nishenko, 1990; Jimenez et al., 2013). The wide range of maximum earthquake magnitude we propose for the South Peru segment is accounting for the various uncertainty factors that can affect this type of analysis, the two major ones being the b-value of the considered seismic catalogs (which ranges from 0.7 to 1.0 with the four seismic catalogs we considered) and the rate α of seismic events over all transient events (estimated between 30 and 80% in South Peru). The identification and quantification of postseismic displacements and slow-slip events (identified in South Peru by Jara et al., 2024) is therefore fundamental to refine the earthquake potential assessment. In addition, to assessing interseismic coupling and earthquake potential, Lovery et al., 2024 also provide an afterslip model for the 2014 Mw8.1 Iquique earthquake from the analysis of long GNSS time series (up to 8 years after the earthquake). This model is however not accounting for the viscoelastic relaxation of the asthenosphere, which has been reported as the main driver of long-term (several decades) postseismic displacement following great megathrust earthquakes (Barbot and Fialko, 2010; Cresseaux, 2024; Hoffmann et al., 2018; Hu et al., 2004; Klein et al., 2016; S. Li et al., 2017; S. Li et al., 2018; Pollitz, 1997; Sun et al., 2018; K. Wang et al., 2007).

A second objective of this thesis was therefore to study the aspects related to the viscoelastic relaxation of the asthenosphere, in order to better model postseismic and interseismic phases of the seismic cycle. In Lovery et al., 2025, we were interested in modeling the postseismic displacements following the 2001 Mw8.4 Arequipa earthquake. By revisiting legacy survey GNSS data, in addition to the thirty-year time series of the continuous GNSS station in Arequipa, we have been able to capture the evolution of surface velocities across South Peru within the 23 years following the Arequipa earthquake. By comparing them with the pre-earthquake velocities, we observe a velocity decrease of about 15% in the horizontal velocity in Arequipa. To model the

viscoelastic relaxation, we developed a 3-D Finite Element Method (FEM) model of the subduction zone in South Peru with an elastic lithosphere (30 and 40-km thick on the continental and oceanic sides respectively) laying over a viscoelastic lithosphere. Fitting the data required a bi-viscous Burgers rheology in the asthenosphere with a Maxwell viscosity $\eta_M = 9 \cdot 10^{18}$ Pa·s and a Kelvin viscosity $\eta_M = 5 \cdot 10^{18}$ Pa·s in the continental domain. We chose to add an elastic cold-nose in our model down to a 85-km depth, following the findings from Gao, Tilmann, et al., 2021; Luo and Wang, 2021; Sobolev and Muldashev, 2017; Sun and Wang, 2015; Wada and Wang, 2009. Adding the cold-nose improved the fit to the data, notably on the vertical component since it controls the location of uplift. In addition to assessing the postseismic displacements associated with the Arequipa earthquake, this study defined an adequate structure and rheology for South Peru. Thereby, we computed viscoelastic Green's functions using the assessed rheology, in order to have a full viscoelastic interseismic coupling model. The results show a shallower interseismic coupling distribution and a better fit to the GNSS velocities in the back-arc, as reported by S. Li et al., 2015 and S. Li et al., 2020. This has important implications for assessing tsunami potential, as a shallow rupture has a higher risk of generating a tsunami (Bilek and Lay, 2002; Carvajal et al., 2022; Polet and Kanamori, 2000). After correcting for the postseismic displacement associated with the Arequipa earthquake, the coupling and the moment deficit rate are raised by 9% on the South Peru segment, and up to 24% in the vicinity of the Arequipa rupture, which is something that needs to be considered for assessing the earthquake potential. It appears that the decrease of coupling where the Nazca Fracture Zone is subducting is a persistent feature of the interseismic coupling models, although it is less pronounced after correcting for postseismic displacement. This result is interesting since we would expect a high coupling where the Arequipa earthquake ruptured, however it is likely that the rupture nucleated West of the NFZ where the epicenter from the ISC catalog is located (Bondár and Storchak, 2011) and propagated East of the Nazca Ridge where the locking is strong. Another intriguing observation of this study is the evolution of the vertical displacement in Arequipa, for which we were not able to fit the long-term subsidence with out model. It could potentially be related to the volcanic activity at the Sabancaya volcano (Boixart et al., 2020; Machacca et al., 2023; MacQueen et al., 2020; Torres et al., 2025) generating a crown of subsidence surrounding the inflating area, as observed on other volcanoes by Chaussard, 2016 and Shreve et al., 2021. Indeed, we observe this kind of pattern on the InSAR mean velocity maps on the 2015-2021 period.

In addition to the FEM modeling aspects and the exploitation of the extensive GNSS dataset, a large part of the PhD was dedicated to the use of InSAR acquisitions on the 2015-2021 period, processed in the frame of the FLATSIM Central Andes project (FormaTerre, 2020), for large-scale tectonic applications in Central Andes. We first worked on modeling the long-wavelength signals that affect the InSAR time series, notably the ocean tide loading (OTL), solid earth tides (SET), and ionospheric phase

delay using global models of total electronic content (TEC). Although we did not retain this approach for referencing the InSAR mean velocity maps, since we performed the referencing using GNSS velocities, the results of the OTL and SET modeling on Central Andes have been included in the article from Marconato et al., 2025. These corrections reduce the high-frequency noise in the InSAR ramp (i.e., linear gradient in range and azimuth directions) time series, and improve the consistency in the time evolution of GNSS and InSAR ramps, suggesting a more GNSS-independent referencing of InSAR acquisitions.

After referencing the InSAR mean velocity maps using GNSS, we decomposed the line-of-sight signal into East and vertical components. These products have a significant added value compared to existing GNSS time series in Central Andes since it provides a fine spatial resolution over a large area of 900,000 km^2. The mapping of the vertical velocity is especially interesting as it is often poorly constrained by GNSS (notably at survey sites), allowing to better constrain the along-dip localization of interseismic locking and providing a proxy on the structure of the subduction zone such as the localization of the cold-nose edge. By performing joint inversions of interseismic velocities measured by GNSS and InSAR, we refined the interseismic coupling model in South Peru. The degree of locking is then raised by about 50% on the segment offshore of Lima (11°S to 13°S) compared to a model based on GNSS only, and by about 30% in the vicinity of the Arequipa earthquake rupture. In addition, the InSAR data was extremely relevant to quantify the displacement across crustal faults in Peru. The analysis at the Cuzco fault system and the Cordillera Blanca attest of several millimeters of horizontal and vertical displacement across these crustal structures. These observations are fundamental to assess the partitioning of the deformation in the upper plate, between a block motion accommodated at crustal faults and internal deformation (Jolivet et al., 2020; S. Li et al., 2015; Yáñez-Cuadra et al., 2022). It is in this way the first direct geodetic observation of the Peruvian Sliver proposed by Villegas-Lanza et al., 2016, delimited by the Cuzco fault system and the Cordillera Blanca. Primary and secondary zones of uplift are observed in Peru and Chile, at about 130 and 250 km from the trench respectively. The secondary zone of uplift is associated with high topography, suggesting partial interseismic plastic deformation of the upper plate. Also, the secondary uplift zone in Peru is primarily observed in the flat-slab region and tapered with the transition to dipping-slab. Despite all the benefits from InSAR, we see that a dense and well-maintained GNSS network is fundamental for several reasons: we still need GNSS to reference InSAR acquisitions, GNSS provides displacements on the three components (East, North, Up) without geometrical assumptions, the temporal resolution is better (daily measurements or better vs. measurements every six to twelve days for Sentinel-1), some areas are difficult to map with InSAR (e.g., vegetation, snow, sand...), the signal is more stable in time, and we can have continuous measurements for several decades (which is not guaranteed by satellite missions).

In the following of this work, the next milestone would be to extend the interseismic coupling model to Northern Chile. It requires some additional work in order to have viscoelastic Green's functions for North Chile, accounting for an adequate structure and rheology of this area that has been affected by the 2014 Mw8.1 Iquique earthquake. Explorations in this direction have been done by Cresseaux, 2024, S. Li et al., 2015, Hoffmann et al., 2018, Boulze et al., 2022, and Boulze et al., 2025, with different approaches. The question of the sliver is also fundamental in North Chile, where a rigid Andean sliver has been introduced by Brooks et al., 2003, applied for interseismic models by Chlieh et al., 2011; Métois et al., 2013; Métois et al., 2016; Métois et al., 2014, and challenged by Klein et al., 2018; S. Li et al., 2015; Yáñez-Cuadra et al., 2022. In addition, a unified model of interseismic coupling for Central Andes has to account for the rotation in the surface displacement (Arriagada et al., 2008; Métois et al., 2016) that occurs at the Arica bend, for which substantial internal deformation needs to be accommodated. A comparison with dense seismic catalogs (Chalumeau et al., 2025) would also be of great interest, since it can provide information both on the frictional regime of the interface, the slab bending, or the distribution of slip on crustal faults. Additional refinements in the structure and rheology of the subduction may also be introduced, such as a low-viscosity layer at the boundary between the lithosphere and the asthenosphere (Sun et al., 2024), low-viscosity zones in the vicinity of volcanic structures (Manea and Gurnis, 2007; Yamasaki and Kobayashi, 2018), or adding lateral variations of the cold-nose edge depth (Dhar et al., 2023). However, increasing the complexity of the models is only meaningful if enough data are available to constrain the parameters. A solution would be to model the postseismic displacements associated with other megathrust earthquakes on the Peru-Chile subduction, such as the 2007 Mw8.0 Pisco, or the 2007 Mw7.7 Tocopilla earthquakes.

References

Aagaard, B. T., Knepley, M. G., & Williams, C. A. (2013):
A domain decomposition approach to implementing fault slip in finite-element models of quasi-static and dynamic crustal deformation. *Journal of Geophysical Research: Solid Earth*, *118*(6), 3059–3079. https://doi.org/10.1002/jgrb.50217

Aagaard, B., Knepley, M., & Williams, C. (2019):
Geodynamics/pylith v2.2.2. https://doi.org/10.5281/zenodo.3269486

Aguilera, F., Apaza, F., Del Carpio, J., Grosse, P., Jiménez, N., Ureta, G., Inostroza, M., Báez, W., Layana, S., Gonzalez, C., Rivera, M., Ortega, M., Gonzalez, R., & Iriarte, R. (2022):
Advances in scientific understanding of the Central Volcanic Zone of the Andes: A review of contributing factors. *Bulletin of Volcanology*, *84*(3), 22. https://doi.org/10.1007/s00445-022-01526-y

Aguirre, E., Benavente, C., Audin, L., Wimpenny, S., Baize, S., Rosell, L., Delgado, F., García, B., & Palomino, A. (2021):
Earthquake surface ruptures on the altiplano and geomorphological evidence of normal faulting in the December 2016 (Mw 6.1) Parina earthquake, Peru. *Journal of South American Earth Sciences*, *106*, 103098. https://doi.org/10.1016/j.jsames.2020.103098

Albino, F., Gremion, S., Pinel, V., Bouygues, P., Peltier, A., Beauducel, F., Froger, J.-L., & Santoso, A. B. (2025):
Benefits of GNSS Local Observations Compared to Global Weather-Based Models for InSAR Tropospheric Corrections Over Tropical Volcanoes: Case Studies of Piton De La Fournaise and Merapi. *Journal of Geophysical Research: Solid Earth*, *130*(4), e2024JB028898. https://doi.org/10.1029/2024JB028898
e2024JB028898 2024JB028898

Allègre, C. J., Le Mouel, J. L., & Provost, A. (1982):
Scaling rules in rock fracture and possible implications for earthquake prediction [Publisher: Nature Publishing Group]. *Nature*, *297*(5861), 47–49. https://doi.org/10.1038/297047a0

Altamimi, Z., Rebischung, P., Métivier, L., & Collilieux, X. (2016):
ITRF2014: A new release of the International Terrestrial Reference Frame modeling nonlinear station motions. *Journal of Geophysical Research: Solid Earth*, *121*(8), 6109–6131. https://doi.org/10.1002/2016JB013098

Alvarez-Vargas, J., Calisto, I., Faccenna, C., Cifuentes-Lobos, R., Cortés-Aranda, J., & Araya, R. (2025):
Megathrust earthquake characterization along the central Chile Gap: Exploring Historical Earthquakes Using the Stochastic Logic Tree Approach.

Amstutz, A. (1955):
Structures alpines; subductions successives dans l'ossola. *Comptes Rendus Hebdomadaires des Seances de l'Academie des Sciences*, *241*(15), 967–969.

Antayhua, Y., Velarde, L., Vargas, K., Tavera, H., & Villegas, J. C. (2021):
Actividad sismica en el entorno de la falla pacollo y volcanes purupuruni-casiri (2020–2021). *Informe Técnico, Instituto Geofísico del Perú*, (010-2021).

Aoki, Y., & Kreemer, C. (2024):
Gnss monitoring of the terrestrial environment: Earthquakes, volcanoes and climate change. *Elsevier*.

Armijo, R., Rauld, R., Thiele, R., Vargas, G., Campos, J., Lacassin, R., & Kausel, E. (2010):
The West Andean Thrust, the San Ramón Fault, and the seismic hazard for Santiago, Chile. *Tectonics*, *29*(2). https://doi.org/10.1029/2008TC002427

Arriagada, C., Roperch, P., Mpodozis, C., & Cobbold, P. R. (2008):
Paleogene building of the Bolivian Orocline: Tectonic restoration of the central Andes in 2-D map view. *Tectonics*, *27*(6). https://doi.org/10.1029/2008TC002269

Augier, A. (2011):
Etude de l'éruption d'avril 2007 du Piton de la Fournaise (île de la Réunion) à partir de données d'interférométrie RADAR et GPS, développement et application de procédures de modélisation (These de doctorat). Clermont-Ferrand 2. Retrieved August 8, 2025, from https://theses.fr/2011CLF22209

Avouac, J.-P. (2015):
From Geodetic Imaging of Seismic and Aseismic Fault Slip to Dynamic Modeling of the Seismic Cycle. *Annual Review of Earth and Planetary Sciences*, *43*(1), 233–271. https://doi.org/10.1146/annurev-earth-060614-105302

Báez, J. C., Leyton, F., Troncoso, C., Del Campo, F., Bevis, M., Vigny, C., Moreno, M., Simons, M., Kendrick, E., Parra, H., & Blume, F. (2018):
The Chilean GNSS Network: Current Status and Progress toward Early Warning Applications. *Seismological Research Letters*, *89*(4), 1546–1554. https://doi.org/10.1785/0220180011

Baize, S., Audin, L., Alvarado, A., Jomard, H., Bablon, M., Champenois, J., Espin, P., Samaniego, P., Quidelleur, X., & Le Pennec, J.-L. (2020):
Active Tectonics and Earthquake Geology Along the Pallatanga Fault, Central Andes of Ecuador [Publisher: Frontiers]. *Frontiers in Earth Science*, *8*. https://doi.org/10.3389/feart.2020.00193

Barbot, S. (2018):
Asthenosphere Flow Modulated by Megathrust Earthquake Cycles. *Geophysical Research Letters*, *45*(12), 6018–6031. https://doi.org/10.1029/2018GL078197

Barbot, S., & Fialko, Y. (2010):
A unified continuum representation of post-seismic relaxation mechanisms: Semi-analytic models of afterslip, poroelastic rebound and viscoelastic flow. *Geophysical Journal International*, *182*(3), 1124–1140. https://doi.org/10.1111/j.1365-246X.2010.04678.x

Barrientos, S. E., & Ward, S. N. (1990):
The 1960 Chile earthquake: Inversion for slip distribution from surface deformation. *Geophysical Journal International*, *103*(3), 589–598. https://doi.org/10.1111/j.1365-246X.1990.tb05673.x

Bassett, D., & Watts, A. B. (2015):
Gravity anomalies, crustal structure, and seismicity at subduction zones: 2. Interrelationships between fore-arc structure and seismogenic behavior. *Geochemistry, Geophysics, Geosystems*, *16*(5), 1541–1576. https://doi.org/10.1002/2014GC005685

Bausilio, G., Khalili, M. A., Virelli, M., & Di Martire, D. (2024):
Italian COSMO-SkyMed atlas: R-Index and the percentage of measurability of movement. *GIScience & Remote Sensing*, *61*(1), 2312705. https://doi.org/10.1080/15481603.2024.2312705

Beck, M. E. (1998):
On the mechanism of crustal block rotations in the central Andes. *Tectonophysics*, *299*(1), 75–92. https://doi.org/10.1016/S0040-1951(98)00199-1

Beck, M. E. (2004):
The Central Andean rotation pattern: Another look. *Geophysical Journal International*, *157*(3), 1348–1358. https://doi.org/10.1111/j.1365-246X.2004.02266.x

Beck, S. L., & Nishenko, S. P. (1990):
Variations in the mode of great earthquake rupture along the Central Peru Subduction Zone. *Geophysical Research Letters*, *17*(11), 1969–1972. https://doi.org/10.1029/GL017i011p01969

Beck, S. L., & Ruff, L. J. (1989):
Great earthquakes and subduction along the Peru trench. *Physics of the Earth and Planetary Interiors*, *57*(3), 199–224. https://doi.org/10.1016/0031-9201(89)90112-X

Béjar-Pizarro, M., Carrizo, D., Socquet, A., Armijo, R., Barrientos, S., Bondoux, F., Bonvalot, S., Campos, J., Comte, D., de Chabalier, J. B., Charade, O., Delorme, A., Gabalda, G., Galetzka, J., Genrich, J., Nercessian, A., Olcay, M., Ortega, F., Ortega, I., … Vigny, C. (2010):
Asperities and barriers on the seismogenic zone in North Chile: State-of-the-art after the 2007 Mw 7.7 Tocopilla earthquake inferred by GPS and InSAR data. *Geophysical Journal International*, *183*(1), 390–406. https://doi.org/10.1111/j.1365-246X.2010.04748.x

Béjar-Pizarro, M., Socquet, A., Armijo, R., Carrizo, D., Genrich, J., & Simons, M. (2013):
Andean structural control on interseismic coupling in the North Chile subduction zone [Number: 6 Publisher: Nature Publishing Group]. *Nature Geoscience*, *6*(6), 462–467. https://doi.org/10.1038/ngeo1802

Benavente, C., Delgado, G., Fernandez, B., Aguirre, E., & Audin, L. (2018):
Neotectónica, evolución del relieve y peligro sísmico en la región arequipa-[boletín c 64]. *Instituto Geológico, Minero y Metalúrgico-INGEMMET*.

Bertiger, W., Bar-Sever, Y., Dorsey, A., Haines, B., Harvey, N., Hemberger, D., Heflin, M., Lu, W., Miller, M., Moore, A. W., Murphy, D., Ries, P., Romans, L., Sibois, A., Sibthorpe, A., Szilagyi, B., Vallisneri, M., & Willis, P. (2020):
GipsyX/RTGx, a new tool set for space geodetic operations and research. *Advances in Space Research*, *66*(3), 469–489. https://doi.org/10.1016/j.asr.2020.04.015

Beuchert, M. J., & Podladchikov, Y. Y. (2010):
Viscoelastic mantle convection and lithospheric stresses. *Geophysical Journal International*, *183*(1), 35–63. https://doi.org/10.1111/j.1365-246X.2010.04708.x

Bevis, M., & Brown, A. (2014):
Trajectory models and reference frames for crustal motion geodesy. *Journal of Geodesy*, *88*(3), 283–311. https://doi.org/10.1007/s00190-013-0685-5

Bevis, M., Kendrick, E., Smalley Jr., R., Brooks, B., Allmendinger, R., & Isacks, B. (2001):
On the strength of interplate coupling and the rate of back arc convergence in the central Andes: An analysis of the interseismic velocity field. *Geochemistry, Geophysics, Geosystems*, *2*(11). https://doi.org/10.1029/2001GC000198

Bevis, M., Kendrick, E. C., Smalley, R., Herring, T., Godoy, J., & Galban, F. (2000):
Crustal motion north and south of the Arica deflection: Comparing recent geodetic results from the central Andes. *Geochemistry, Geophysics, Geosystems*, *1*(12), 1999GC000011. https://doi.org/10.1029/1999GC000011

Biggs, J., Anantrasirichai, N., Albino, F., Lazecky, M., & Maghsoudi, Y. (2022):
Large-scale demonstration of machine learning for the detection of volcanic deformation in Sentinel-1 satellite imagery. *Bulletin of Volcanology*, *84*(12), 100. https://doi.org/10.1007/s00445-022-01608-x

Bilek, S. L., & Lay, T. (2002):
Tsunami earthquakes possibly widespread manifestations of frictional conditional stability. *Geophysical Research Letters*, *29*(14), 18–1–18–4. https://doi.org/10.1029/2002GL015215

Bird, P. (2003):
An updated digital model of plate boundaries. *Geochemistry, Geophysics, Geosystems*, *4*(3). https://doi.org/10.1029/2001GC000252

Blewitt, G., Hammond, W. C., & Kreemer, C. (2018):
Harnessing the GPS Data Explosion for Interdisciplinary Science. Retrieved July 24, 2025, from https://eos.org/science-updates/harnessing-the-gps-data-explosion-for-interdisciplinary-science

Blewitt, G., Kreemer, C., Hammond, W. C., & Gazeaux, J. (2016):
MIDAS robust trend estimator for accurate GPS station velocities without step detection. *Journal of Geophysical Research: Solid Earth*, *121*(3), 2054–2068. https://doi.org/10.1002/2015JB012552

Boehm, J., Werl, B., & Schuh, H. (2006):
Troposphere mapping functions for GPS and very long baseline interferometry from European Centre for Medium-Range Weather Forecasts operational analysis data. *Journal of Geophysical Research: Solid Earth*, *111*(B2). https://doi.org/10.1029/2005JB003629

Boixart, G., Cruz, L. F., Miranda Cruz, R., Euillades, P. A., Euillades, L. D., & Battaglia, M. (2020):
Source Model for Sabancaya Volcano Constrained by DInSAR and GNSS Surface Deformation Observation [Number: 11 Publisher: Multidisciplinary Digital Publishing Institute]. *Remote Sensing*, *12*(11), 1852. https://doi.org/10.3390/rs12111852

Bondár, I., & Storchak, D. (2011):
Improved location procedures at the International Seismological Centre. *Geophysical Journal International*, *186*(3), 1220–1244. https://doi.org/10.1111/j.1365-246X.2011.05107.x

Boudin, F., Bernard, P., Meneses, G., Vigny, C., Olcay, M., Tassara, C., Boy, J. P., Aissaoui, E., Métois, M., Satriano, C., Esnoult, M.-F., Nercessian, A., Vallée, M., Vilotte, J.-P., & Brunet, C. (2022):
Slow slip events precursory to the 2014 Iquique Earthquake, revisited with long-base tilt and GPS records. *Geophysical Journal International*, *228*(3), 2092–2121. https://doi.org/10.1093/gji/ggab425

Boulze, H., Fleitout, L., Klein, E., & Vigny, C. (2022):
Post-seismic motion after 3 Chilean megathrust earthquakes: A clue for a linear asthenospheric viscosity. *Geophysical Journal International*, *231*(3), 1471–1478. https://doi.org/10.1093/gji/ggac255

Boulze, H., Garaud, J.-D., Klein, E., Fleitout, L., Vigny, C., & Chiaruttini, V. (2025):
A 3D finite-element mesh for modeling large-scale surface deformation induced by subduction megathrust earthquakes: Application to Chile. *Seismica*, *4*(2). https://doi.org/10.26443/seismica.v4i2.1544

Brooks, B. A., Bevis, M., Smalley Jr., R., Kendrick, E., Manceda, R., Lauría, E., Maturana, R., & Araujo, M. (2003):
Crustal motion in the Southern Andes (26°–36°S): Do the Andes behave like a microplate? *Geochemistry, Geophysics, Geosystems*, *4*(10). https://doi.org/10.1029/2003GC000505

Brooks, B. A., Bevis, M., Whipple, K., Ramon Arrowsmith, J., Foster, J., Zapata, T., Kendrick, E., Minaya, E., Echalar, A., Blanco, M., Euillades, P., Sandoval, M., & Smalley, R. J. (2011):
Orogenic-wedge deformation and potential for great earthquakes in the central Andean backarc [Publisher: Nature Publishing Group]. *Nature Geoscience*, *4*(6), 380–383. https://doi.org/10.1038/ngeo1143

Burgers, J. M. (1935):
Mechanical considerations-model systems-phenomenological theories of relaxation and of viscosity. *First report on viscosity and plasticity*, *1*.

Bürgmann, R., Kogan, M. G., Steblov, G. M., Hilley, G., Levin, V. E., & Apel, E. (2005):
Interseismic coupling and asperity distribution along the Kamchatka subduction zone. *Journal of Geophysical Research: Solid Earth*, *110*(B7). https://doi.org/10.1029/2005JB003648

Byerlee, J. D., & Brace, W. F. (1968):
Stick slip, stable sliding, and earthquakes—Effect of rock type, pressure, strain rate, and stiffness. *Journal of Geophysical Research (1896-1977)*, *73*(18), 6031–6037. https://doi.org/10.1029/JB073i018p06031

Campos, J., Hatzfeld, D., Madariaga, R., Lopez, G., Kausel, E., Zollo, A., Iannacone, G., Fromm, R., Barrientos, S., & Lyon-Caen, H. (2002):
A seismological study of the 1835 seismic gap in south-central Chile. *Physics of the Earth and Planetary Interiors*, *132*(1), 177–195. https://doi.org/10.1016/S0031-9201(02)00051-1

Carvajal, M., Gubler, A., Davies, G., Wang, K., Sun, T., & Catalán, P. A. (2025):
Large Size of Two 19th-Century Chile-Peru Earthquakes Inferred From Trans-Pacific Tsunami Records. *Geophysical Research Letters*, *52*(12), e2024GL113849. https://doi.org/10.1029/2024GL113849
e2024GL113849 2024GL113849

Carvajal, M., Sun, T., Wang, K., Luo, H., & Zhu, Y. (2022):
Evaluating the Tsunamigenic Potential of Buried Versus Trench-Breaching Megathrust Slip. *Journal of Geophysical Research: Solid Earth*, *127*(8), e2021JB023722. https://doi.org/10.1029/2021JB023722
e2021JB023722 2021JB023722

Chalumeau, C., Sanchez-Reyes, H., Münchmeyer, J., Langlais, M., Villegas-Lanza, J. C., Gonzales, A., Norabuena, E., Tavera, H., & Socquet, A. (2025):
From flat to steep subduction: The south peru margin imaged by a new high-density seismic catalog. *Geophysical Journal International [submitted]*.

Chanard, K., Fleitout, L., Calais, E., Barbot, S., & Avouac, J.-P. (2018):
Constraints on Transient Viscoelastic Rheology of the Asthenosphere From Seasonal Deformation. *Geophysical Research Letters*, *45*(5), 2328–2338. https://doi.org/10.1002/2017GL076451

Chaussard, E. (2016):
Subsidence in the Parícutin lava field: Causes and implications for interpretation of deformation fields at volcanoes. *Journal of Volcanology and Geothermal Research*, *320*, 1–11. https://doi.org/10.1016/j.jvolgeores.2016.04.009

Chlieh, M., Avouac, J. P., Sieh, K., Natawidjaja, D. H., & Galetzka, J. (2008):
Heterogeneous coupling of the Sumatran megathrust constrained by geodetic and paleogeodetic measurements. *Journal of Geophysical Research: Solid Earth*, *113*(B5). https://doi.org/10.1029/2007JB004981

Chlieh, M., Beauval, C., Yepes, H., Marinière, J., Saillard, M., & Audin, L. (2021):
Seismic and Aseismic Cycle of the Ecuador–Colombia Subduction Zone [Publisher: Frontiers]. *Frontiers in Earth Science*, *9*. https://doi.org/10.3389/feart.2021.701720

Chlieh, M., De Chabalier, J. B., Ruegg, J. C., Armijo, R., Dmowska, R., Campos, J., & Feigl, K. L. (2004):
Crustal deformation and fault slip during the seismic cycle in the North Chile subduction zone, from GPS and InSAR observations. *Geophysical Journal International*, *158*(2), 695–711. https://doi.org/10.1111/j.1365-246X.2004.02326.x

Chlieh, M., Avouac, J.-P., Hjorleifsdottir, V., Song, T.-R. A., Ji, C., Sieh, K., Sladen, A., Hebert, H., Prawirodirdjo, L., Bock, Y., & Galetzka, J. (2007):
Coseismic Slip and Afterslip of the Great Mw 9.15 Sumatra–Andaman Earthquake of 2004. *Bulletin of the Seismological Society of America*, *97*(1A), S152–S173. https://doi.org/10.1785/0120050631

Chlieh, M., Perfettini, H., Tavera, H., Avouac, J.-P., Remy, D., Nocquet, J.-M., Rolandone, F., Bondoux, F., Gabalda, G., & Bonvalot, S. (2011):

Interseismic coupling and seismic potential along the Central Andes subduction zone. *Journal of Geophysical Research: Solid Earth*, *116*(B12). https://doi.org/10.1029/2010JB008166

Cohen, S. C. (1979):
Postseismic surface deformations due to lithospheric and asthenospheric viscoelasticity. *Geophysical Research Letters*, *6*(3), 129–131. https://doi.org/10.1029/GL006i003p00129

Cohen, S. C., & Kramer, M. J. (1984):
Crustal deformation, the earthquake cycle, and models of viscoelastic flow in the asthenosphere. *Geophysical Journal International*, *78*(3), 735–750. https://doi.org/10.1111/j.1365-246X.1984.tb05068.x

Cohen-Tannoudji, C., Diu, B., & Laloë, F. (2018):
Mécanique quantique - tome 1.

Comte, D., & Pardo, M. (1991):
Reappraisal of great historical earthquakes in the northern Chile and southern Peru seismic gaps. *Natural Hazards*, *4*(1), 23–44. https://doi.org/10.1007/BF00126557

Conroy, P., van Diepen, S. A. N., Van Asselen, S., Erkens, G., van Leijen, F. J., & Hanssen, R. F. (2022):
Probabilistic Estimation of InSAR Displacement Phase Guided by Contextual Information and Artificial Intelligence. *IEEE Transactions on Geoscience and Remote Sensing*, *60*, 1–11. https://doi.org/10.1109/TGRS.2022.3203872

Cortés-Aranda, J., González, R., Fernández, V., Astudillo, L., Miller, M., Molina, D., & Oviedo, A. (2021):
Neotectonic evidence for Late Quaternary reverse faulting in the northern Chile outer forearc (22.5°S-23°S): Implications for seismic hazard. *Journal of South American Earth Sciences*, *109*, 103219. https://doi.org/10.1016/j.jsames.2021.103219

Coudurier-Curveur, A., Tapponnier, P., Okal, E., Van der Woerd, J., Kali, E., Choudhury, S., Baruah, S., Etchebes, M., & Karakaş, Ç. (2020):
A composite rupture model for the great 1950 Assam earthquake across the cusp of the East Himalayan Syntaxis. *Earth and Planetary Science Letters*, *531*, 115928. https://doi.org/10.1016/j.epsl.2019.115928

Crawford, O., Al-Attar, D., Tromp, J., Mitrovica, J. X., Austermann, J., & Lau, H. C. P. (2018):
Quantifying the sensitivity of post-glacial sea level change to laterally varying viscosity. *Geophysical Journal International*, *214*(2), 1324–1363. https://doi.org/10.1093/gji/ggy184

Cresseaux, J. (2024):
Large-scale interactions during sequence of large subduction earthquakes in south america (PhD thesis). Université Grenoble Alpes.

Currie, C. A., Hyndman, R. D., Wang, K., & Kostoglodov, V. (2002):
Thermal models of the Mexico subduction zone: Implications for the megathrust seismogenic zone. *Journal of Geophysical Research: Solid Earth*, *107*(B12), ETG 15–1–ETG 15–13. https://doi.org/10.1029/2001JB000886

De Zan, F., & Monti Guarnieri, A. (2006):
TOPSAR: Terrain Observation by Progressive Scans. *IEEE Transactions on Geoscience and Remote Sensing*, *44*(9), 2352–2360. https://doi.org/10.1109/TGRS.2006.873853

Delouis, B., Monfret, T., Dorbath, L., Pardo, M., Rivera, L., Comte, D., Haessler, H., Caminade, J., Ponce, L., Kausel, E., & Cisternas, A. (1997):
The Mw = 8.0 Antofagasta (northern Chile) earthquake of 30 July 1995: A precursor to the end of the large 1877 gap. *Bulletin of the Seismological Society of America*, *87*(2), 427–445. https://doi.org/10.1785/BSSA0870020427

Delouis, B., Pardo, M., Legrand, D., & Monfret, T. (2009):
The Mw 7.7 Tocopilla Earthquake of 14 November 2007 at the Southern Edge of the Northern

Chile Seismic Gap: Rupture in the Deep Part of the Coupled Plate Interface. *Bulletin of the Seismological Society of America*, *99*(1), 87–94. https://doi.org/10.1785/0120080192

DeMets, C., Gordon, R. G., & Argus, D. F. (2010):
Geologically current plate motions. *Geophysical Journal International*, *181*(1), 1–80. https://doi.org/10.1111/j.1365-246X.2009.04491.x

Devlin, K. R., & Lohman, R. B. (2025):
Evaluation of Vegetation Bias in InSAR Time Series for Agricultural Areas Within the San Joaquin Valley, CA. *Earth and Space Science*, *12*(6), e2024EA004062. https://doi.org/10.1029/2024EA004062
e2024EA004062 2024EA004062

Dewey, J. F., & Lamb, S. H. (1992):
Active tectonics of the Andes. *Tectonophysics*, *205*(1), 79–95. https://doi.org/10.1016/0040-1951(92)90419-7

Dhar, S., Muto, J., Ohta, Y., & Iinuma, T. (2023):
Heterogeneous rheology of Japan subduction zone revealed by postseismic deformation of the 2011 Tohoku-oki earthquake. *Progress in Earth and Planetary Science*, *10*(1), 9. https://doi.org/10.1186/s40645-023-00539-1

Dieterich, J. H. (1972):
Time-dependent friction in rocks. *Journal of Geophysical Research (1896-1977)*, *77*(20), 3690–3697. https://doi.org/10.1029/JB077i020p03690

Dieterich, J. H. (1978):
Time-dependent friction and the mechanics of stick-slip. *pure and applied geophysics*, *116*(4), 790–806. https://doi.org/10.1007/BF00876539

Ding, X.-l., Li, Z.-w., Zhu, J.-j., Feng, G.-c., & Long, J.-p. (2008):
Atmospheric Effects on InSAR Measurements and Their Mitigation [Publisher: Molecular Diversity Preservation International]. *Sensors*, *8*(9), 5426–5448. https://doi.org/10.3390/s8095426

Doin, M. P., & Fleitout, L. (1996):
Thermal evolution of the oceanic lithosphere: An alternative view. *Earth and Planetary Science Letters*, *142*(1), 121–136. https://doi.org/10.1016/0012-821X(96)00082-9

Doin, M. .-P., Lasserre, C., Peltzer, G., Cavalié, O., & Doubre, C. (2009):
Corrections of stratified tropospheric delays in SAR interferometry: Validation with global atmospheric models. *Journal of Applied Geophysics*, *69*(1), 35–50. https://doi.org/10.1016/j.jappgeo.2009.03.010

Doin, M.-P., Cheiab, A., & Thollard, F. (2023):
Strategy Used for Phase Unwrapping in the NSBAS MT-InSAR Chain [ISSN: 2153-7003]. *IGARSS 2023 - 2023 IEEE International Geoscience and Remote Sensing Symposium*, 8210–8213. https://doi.org/10.1109/IGARSS52108.2023.10283158

Doin, M.-P., Guillaso, S., Jolivet, R., Lasserre, C., Lodge, F., Ducret, G., & Grandin, R. (2011):
Presentation of the small baseline NSBAS processing chain on a case example: The Etna deformation monitoring from 2003 to 2010 using Envisat data. *Proceedings of the Fringe symposium*, 3434–3437.

Dorbath, L., Cisternas, A., & Dorbath, C. (1990):
Assessment of the size of large and great historical earthquakes in Peru. *Bulletin of the Seismological Society of America*, *80*(3), 551–576. https://doi.org/10.1785/BSSA0800030551

Duputel, Z., Jiang, J., Jolivet, R., Simons, M., Rivera, L., Ampuero, J.-P., Riel, B., Owen, S. E., Moore, A. W., Samsonov, S. V., Ortega Culaciati, F., & Minson, S. E. (2015):
The Iquique earthquake sequence of April 2014: Bayesian modeling accounting for prediction uncertainty. *Geophysical Research Letters*, *42*(19), 7949–7957. https://doi.org/10.1002/2015GL065402

Duretz, T., de Borst, R., & Yamato, P. (2021):
Modeling Lithospheric Deformation Using a Compressible Visco-Elasto-Viscoplastic Rheology and the Effective Viscosity Approach. *Geochemistry, Geophysics, Geosystems*, *22*(8), e2021GC009675. https://doi.org/10.1029/2021GC009675
e2021GC009675 2021GC009675

Dziewonski, A. M., Chou, T.-A., & Woodhouse, J. H. (1981):
Determination of earthquake source parameters from waveform data for studies of global and regional seismicity. *Journal of Geophysical Research: Solid Earth*, *86*(B4), 2825–2852. https://doi.org/10.1029/JB086iB04p02825

Dziewonski, A. M., & Anderson, D. L. (1981):
Preliminary reference Earth model. *Physics of the Earth and Planetary Interiors*, *25*(4), 297–356. https://doi.org/10.1016/0031-9201(81)90046-7

Eberle, B., Santi, P., & Meza, P. (2024):
Quantitative analysis of changing hazard exposure due to community growth in the Arequipa Region of Peru [ISSN: 2693-5015]. https://doi.org/10.21203/rs.3.rs-3990372/v1

Eddington, A. S. (1928):
The nature of the physical world. New York, The Macmillan Company; Cambridge, Eng., The University Press. Retrieved August 29, 2025, from http://archive.org/details/natureofphysical00eddi

Ehlers, T. A., & Poulsen, C. J. (2009):
Influence of Andean uplift on climate and paleoaltimetry estimates. *Earth and Planetary Science Letters*, *281*(3), 238–248. https://doi.org/10.1016/j.epsl.2009.02.026

Einstein, A. (1905):
Zur Elektrodynamik bewegter Körper. *Annalen der Physik*, *322*(10), 891–921. https://doi.org/10.1002/andp.19053221004

Einstein, A. (1915):
Die feldgleichungen der gravitation. *Sitzungsberichte der Königlich Preußischen Akademie der Wissenschaften*, 844–847.

Ekström, G., Nettles, M., & Dziewoński, A. M. (2012):
The global CMT project 2004–2010: Centroid-moment tensors for 13,017 earthquakes. *Physics of the Earth and Planetary Interiors*, *200-201*, 1–9. https://doi.org/10.1016/j.pepi.2012.04.002

Fialko, Y. (2004):
Evidence of fluid-filled upper crust from observations of postseismic deformation due to the 1992 Mw7.3 Landers earthquake. *Journal of Geophysical Research: Solid Earth*, *109*(B8). https://doi.org/10.1029/2004JB002985

Fialko, Y., Sandwell, D., Simons, M., & Rosen, P. (2005):
Three-dimensional deformation caused by the Bam, Iran, earthquake and the origin of shallow slip deficit [Publisher: Nature Publishing Group]. *Nature*, *435*(7040), 295–299. https://doi.org/10.1038/nature03425

Florsch, N., Revil, A., & Camerlynck, C. (2014):
Inversion of generalized relaxation time distributions with optimized damping parameter. *Journal of Applied Geophysics*, *109*, 119–132. https://doi.org/10.1016/j.jappgeo.2014.07.013

FormaTerre. (2020):
Flatsim data products.

Foster, J., & Bevis, M. (2014):
Pisagua Megathrust Bolivia RAPID Response GPS Network. https://doi.org/10.7283/T5DJ5D0X

Frey, O., Werner, C. L., Wegmuller, U., Wiesmann, A., Henke, D., & Magnard, C. (2013):
A car-borne SAR and InSAR experiment [ISSN: 2153-7003]. *2013 IEEE International Geoscience and Remote Sensing Symposium - IGARSS*, 93–96. https://doi.org/10.1109/IGARSS.2013.6721100

Gaete, A., Walter, T. R., Bredemeyer, S., Zimmer, M., Kujawa, C., Franco Marin, L., San Martin, J., & Bucarey Parra, C. (2020):
Processes culminating in the 2015 phreatic explosion at Lascar volcano, Chile, evidenced by multiparametric data [Publisher: Copernicus GmbH]. *Natural Hazards and Earth System Sciences*, *20*(2), 377–397. https://doi.org/10.5194/nhess-20-377-2020

Gagnon, K., Chadwell, C. D., & Norabuena, E. (2005):
Measuring the onset of locking in the Peru–Chile trench with GPS and acoustic measurements [Number: 7030 Publisher: Nature Publishing Group]. *Nature*, *434*(7030), 205–208. https://doi.org/10.1038/nature03412

Gao, Y., Tilmann, F., van Herwaarden, D.-P., Thrastarson, S., Fichtner, A., Heit, B., Yuan, X., & Schurr, B. (2021):
Full Waveform Inversion Beneath the Central Andes: Insight Into the Dehydration of the Nazca Slab and Delamination of the Back-Arc Lithosphere. *Journal of Geophysical Research: Solid Earth*, *126*(7), e2021JB021984. https://doi.org/10.1029/2021JB021984
e2021JB021984 2021JB021984

Gao, Y., Yuan, X., Heit, B., Tilmann, F., van Herwaarden, D.-P., Thrastarson, S., Fichtner, A., & Schurr, B. (2021):
Impact of the Juan Fernandez Ridge on the Pampean Flat Subduction Inferred From Full Waveform Inversion. *Geophysical Research Letters*, *48*(21), e2021GL095509. https://doi.org/10.1029/2021GL095509
e2021GL095509 2021GL095509

García, B., Guevara-Pillaca, C. J., Unsworth, M., Pereyra, P., Benavente, C., Combey, A., Palacios, D., Palomino, A., Ponce, R., Rosell, L., & Muñoz, A. (2025):
Locating active faults in the Cusco Valley using magnetotelluric and radon gas data. *Tectonophysics*, *898*, 230639. https://doi.org/10.1016/j.tecto.2025.230639

Garzione, C. N., Hoke, G. D., Libarkin, J. C., Withers, S., MacFadden, B., Eiler, J., Ghosh, P., & Mulch, A. (2008):
Rise of the Andes [Publisher: American Association for the Advancement of Science]. *Science*, *320*(5881), 1304–1307. https://doi.org/10.1126/science.1148615

Giambiagi, L., Tassara, A., Echaurren, A., Julve, J., Quiroga, R., Barrionuevo, M., Liu, S., Echeverría, I., Mardónez, D., Suriano, J., Mescua, J., Lossada, A. C., Spagnotto, S., Bertoa, M., & Lothari, L. (2022):
Crustal anatomy and evolution of a subduction-related orogenic system: Insights from the Southern Central Andes (22-35°S). *Earth-Science Reviews*, *232*, 104138. https://doi.org/10.1016/j.earscirev.2022.104138

Giovanni, M. K., Beck, S. L., & Wagner, L. (2002):
The June 23, 2001 Peru earthquake and the southern Peru subduction zone. *Geophysical Research Letters*, *29*(21), 14–1–14–4. https://doi.org/10.1029/2002GL015774

Goldstein, R. V., Gorodtsov, V. A., Lisovenko, D. S., & Volkov, M. A. (2014):
Negative Poisson's ratio for cubic crystals and nano/microtubes. *Physical Mesomechanics*, *17*(2), 97–115. https://doi.org/10.1134/S1029959914020027

González L., G., Dunai, T., Carrizo, D., & Allmendinger, R. (2006):
Young displacements on the Atacama Fault System, northern Chile from field observations and cosmogenic 21Ne concentrations. *Tectonics*, *25*(3). https://doi.org/10.1029/2005TC001846

González-Alfaro, J., Vargas, G., Ortlieb, L., González, G., Ruiz, S., Báez, J. C., Mandeng-Yogo, M., Caquineau, S., Álvarez, G., del Campo, F., & del Río, I. (2018):
Abrupt increase in the coastal uplift and earthquake rate since ~40 ka at the northern Chile seismic gap in the Central Andes. *Earth and Planetary Science Letters*, *502*, 32–45. https://doi.org/10.1016/j.epsl.2018.08.043

Grandin, R., Socquet, A., Binet, R., Klinger, Y., Jacques, E., De Chabalier, J.-B., King, G., Lasserre, C., Tait, S., Tapponnier, P., et al. (2009):
September 2005 manda hararo-dabbahu rifting event, afar (ethiopia): Constraints provided by geodetic data. *Journal of Geophysical Research: Solid Earth*, *114*(B8).

Grandin, R. (2015):
Interferometric Processing of SLC Sentinel-1 TOPS Data. https://doi.org/10.5270/Fringe2015.pp116

Grant Ludwig, L. (2015):
4.21 - Paleoseismology. In G. Schubert (Ed.), *Treatise on Geophysics (Second Edition)* (pp. 559–579). Elsevier. https://doi.org/10.1016/B978-0-444-53802-4.00088-9

Gutenberg, B. (1926):
Über die Ausbreitung des Schalles in der Atmosphäre. *Naturwissenschaften*, *14*(16), 338–342. https://doi.org/10.1007/BF01506968

Gutenberg, B., & Richter, C. (1949):
Seismicity of the earth associated phenomena, [OCLC: 1323229850]. Princeton University Press.

Gutscher, M.-A., Spakman, W., Bijwaard, H., & Engdahl, E. R. (2000):
Geodynamics of flat subduction: Seismicity and tomographic constraints from the Andean margin. *Tectonics*, *19*(5), 814–833. https://doi.org/10.1029/1999TC001152

Gutscher, M.-A., Westbrook, G. K., Marcaillou, B., Graindorge, D., Gailler, A., Pichot, T., & Maury, R. C. (2013):
How wide is the seismogenic zone of the Lesser Antilles forearc? *Bulletin de la Société Géologique de France*, *184*(1-2), 47–59. https://doi.org/10.2113/gssgfbull.184.1-2.47

Hashima, A., & Sato, T. (2017):
A megathrust earthquake cycle model for Northeast Japan: Bridging the mismatch between geological uplift and geodetic subsidence. *Earth, Planets and Space*, *69*(1), 23. https://doi.org/10.1186/s40623-017-0606-6

Hashimoto, M., Enomoto, M., & Fukushima, Y. (2010):
Coseismic Deformation from the 2008 Wenchuan, China, Earthquake Derived from ALOS/PALSAR Images. *Tectonophysics*, *491*(1), 59–71. https://doi.org/10.1016/j.tecto.2009.08.034

Hayes, G. P., Moore, G. L., Portner, D. E., Hearne, M., Flamme, H., Furtney, M., & Smoczyk, G. M. (2018):
Slab2, a comprehensive subduction zone geometry model [Publisher: American Association for the Advancement of Science]. *Science*, *362*(6410), 58–61. https://doi.org/10.1126/science.aat4723

Hergert, T., & Heidbach, O. (2006):
New insights into the mechanism of postseismic stress relaxation exemplified by the 23 June 2001 Mw = 8.4 earthquake in southern Peru. *Geophysical Research Letters*, *33*(2). https://doi.org/10.1029/2005GL024858

Hersbach, H., Bell, B., Berrisford, P., Hirahara, S., Horányi, A., Muñoz-Sabater, J., Nicolas, J., Peubey, C., Radu, R., Schepers, D., Simmons, A., Soci, C., Abdalla, S., Abellan, X., Balsamo, G., Bechtold, P., Biavati, G., Bidlot, J., Bonavita, M., … Thépaut, J.-N. (2020):
The ERA5 global reanalysis. *Quarterly Journal of the Royal Meteorological Society*, *146*(730), 1999–2049. https://doi.org/10.1002/qj.3803

Hirose, H., Hirahara, K., Kimata, F., Fujii, N., & Miyazaki, S. (1999):
A slow thrust slip event following the two 1996 Hyuganada Earthquakes beneath the Bungo Channel, southwest Japan. *Geophysical Research Letters*, *26*(21), 3237–3240. https://doi.org/10.1029/1999GL010999

Hoffmann, F., Metzger, S., Moreno, M., Deng, Z., Sippl, C., Ortega-Culaciati, F., & Oncken, O. (2018):
Characterizing Afterslip and Ground Displacement Rate Increase Following the 2014 Iquique-

Pisagua Mw 8.1 Earthquake, Northern Chile. *Journal of Geophysical Research: Solid Earth*, *123*(5), 4171–4192. https://doi.org/10.1002/2017JB014970

Hooper, A., Pietrzak, J., Simons, W., Cui, H., Riva, R., Naeije, M., Terwisscha van Scheltinga, A., Schrama, E., Stelling, G., & Socquet, A. (2013):
Importance of horizontal seafloor motion on tsunami height for the 2011 Mw=9.0 Tohoku-Oki earthquake. *Earth and Planetary Science Letters*, *361*, 469–479. https://doi.org/10.1016/j.epsl.2012.11.013

Hu, Y., Wang, K., He, J., Klotz, J., & Khazaradze, G. (2004):
Three-dimensional viscoelastic finite element model for postseismic deformation of the great 1960 Chile earthquake. *Journal of Geophysical Research: Solid Earth*, *109*(B12). https://doi.org/10.1029/2004JB003163

Hubbert, M. K. (1937):
Theory of scale models as applied to the study of geologic structures. *GSA Bulletin*, *48*(10), 1459–1520. https://doi.org/10.1130/GSAB-48-1459

Hubbert, M. K. (1945):
Strength of the Earth1. *AAPG Bulletin*, *29*(11), 1630–1653. https://doi.org/10.1306/3D9337A4-16B1-11D7-8645000102C1865D

Hyndman, R. D., Yamano, M., & Oleskevich, D. A. (1997):
The seismogenic zone of subduction thrust faults. *Island Arc*, *6*(3), 244–260. https://doi.org/10.1111/j.1440-1738.1997.tb00175.x

Ida, Y. (1975):
Analysis of stick-slip and earthquake mechanism. *Physics of the Earth and Planetary Interiors*, *11*(2), 147–156. https://doi.org/10.1016/0031-9201(75)90008-4

Isacks, B. L. (1988):
Uplift of the Central Andean Plateau and bending of the Bolivian Orocline. *Journal of Geophysical Research: Solid Earth*, *93*(B4), 3211–3231. https://doi.org/10.1029/JB093iB04p03211

Ishigaki, A., Higashi, H., Sakamoto, T., & Shibahara, S. (2013):
The Great East-Japan Earthquake and Devastating Tsunami: An Update and Lessons from the Past Great Earthquakes in Japan since 1923. *The Tohoku Journal of Experimental Medicine*, *229*(4), 287–299. https://doi.org/10.1620/tjem.229.287

Itoh, Y., Socquet, A., & Radiguet, M. (2023):
Largest Aftershock Nucleation Driven by Afterslip During the 2014 Iquique Sequence. *Geophysical Research Letters*, *50*(24), e2023GL104852. https://doi.org/10.1029/2023GL104852 e2023GL104852 2023GL104852

Itoh, Y., Wang, K., Nishimura, T., & He, J. (2019):
Compliant Volcanic Arc and Backarc Crust in Southern Kurile Suggested by Interseismic Geodetic Deformation. *Geophysical Research Letters*, *46*(21), 11790–11798. https://doi.org/10.1029/2019GL084656

Jaillard, E., & Soler, P. (1996):
Cretaceous to early Paleogene tectonic evolution of the northern Central Andes (0–18°S) and its relations to geodynamics. *Tectonophysics*, *259*(1), 41–53. https://doi.org/10.1016/0040-1951(95)00107-7

Jara, J., Jolivet, R., Socquet, A., Comte, D., & Norabuena, E. (2024):
Detection of slow slip events along the southern Peru - northern Chile subduction zone [Publisher: McGill]. *Seismica*, *3*(1), 17567–17579. https://doi.org/10.26443/seismica.v3i1.980

Jara, J., Sánchez-Reyes, H., Socquet, A., Cotton, F., Virieux, J., Maksymowicz, A., Díaz-Mojica, J., Walpersdorf, A., Ruiz, J., Cotte, N., & Norabuena, E. (2018):
Kinematic study of Iquique 2014 Mw 8.1 earthquake: Understanding the segmentation of the

seismogenic zone. *Earth and Planetary Science Letters*, *503*, 131–143. https://doi.org/10.1016/j.epsl.2018.09.025

Jarrin, P., Nocquet, J.-M., Rolandone, F., Mora-Páez, H., Mothes, P., & Cisneros, D. (2023): Current motion and deformation of the Nazca Plate: New constraints from GPS measurements. *Geophysical Journal International*, *232*(2), 842–863. https://doi.org/10.1093/gji/ggac353

Jiang, W., & Li, Z. (2023): Estimation of the finite fault source model for the 2018 Mw7.1 Acari, Peru earthquake using a hybrid simulation prediction approach. *Soil Dynamics and Earthquake Engineering*, *164*, 107613. https://doi.org/10.1016/j.soildyn.2022.107613

Jimenez, C., Moggiano, N., Mas, E., Adriano, B., Koshimura, S., Fujii, Y., & Yanagisawa, H. (2013): Seismic Source of 1746 Callao Earthquake from Tsunami Numerical Modeling. *Journal of Disaster Research*, *8*(2), 266–273. https://doi.org/10.20965/jdr.2013.p0266

Jolivet, R., Grandin, R., Lasserre, C., Doin, M.-P., & Peltzer, G. (2011): Systematic InSAR tropospheric phase delay corrections from global meteorological reanalysis data. *Geophysical Research Letters*, *38*(17). https://doi.org/10.1029/2011GL048757

Jolivet, R., & Simons, M. (2018): A Multipixel Time Series Analysis Method Accounting for Ground Motion, Atmospheric Noise, and Orbital Errors. *Geophysical Research Letters*, *45*(4), 1814–1824. https://doi.org/10.1002/2017GL076533

Jolivet, R., Simons, M., Duputel, Z., Olive, J.-A., Bhat, H. S., & Bletery, Q. (2020): Interseismic Loading of Subduction Megathrust Drives Long-Term Uplift in Northern Chile. *Geophysical Research Letters*, *47*(8), e2019GL085377. https://doi.org/10.1029/2019GL085377 e2019GL085377 10.1029/2019GL085377

Jolivet, R., Agram, P. S., Lin, N. Y., Simons, M., Doin, M.-P., Peltzer, G., & Li, Z. (2014): Improving InSAR geodesy using Global Atmospheric Models. *Journal of Geophysical Research: Solid Earth*, *119*(3), 2324–2341. https://doi.org/10.1002/2013JB010588

Joughin, L., & Winebrenner, D. (1994): Effective number of looks for a multilook interferometric phase distribution. *Proceedings of IGARSS '94 - 1994 IEEE International Geoscience and Remote Sensing Symposium*, *4*, 2276–2278 vol.4. https://doi.org/10.1109/IGARSS.1994.399712

Kanamori, H. (2003): 72 - Earthquake Prediction: An Overview. In W. H. K. Lee, H. Kanamori, P. C. Jennings, & C. Kisslinger (Eds.), *International Geophysics* (pp. 1205–1216). Academic Press. https://doi.org/10.1016/S0074-6142(03)80186-9

Kanaya, T., & Hirth, G. (2018): Brittle to Semibrittle Transition in Quartz Sandstone: Energetics. *Journal of Geophysical Research: Solid Earth*, *123*(1), 84–106. https://doi.org/10.1002/2017JB014682

Kaneko, Y., Avouac, J.-P., & Lapusta, N. (2010): Towards inferring earthquake patterns from geodetic observations of interseismic coupling [Number: 5 Publisher: Nature Publishing Group]. *Nature Geoscience*, *3*(5), 363–369. https://doi.org/10.1038/ngeo843

Karami, E., Shami, S., Maghsoudi, Y., Ranjgar, B., & Azadnejad, S. (2025): Investigating the InSAR Phase Bias in the SBAS Algorithm and Its Effect on Different Landcovers. *IEEE Access*, *13*, 82514–82526. https://doi.org/10.1109/ACCESS.2025.3568144

Karato, S.-i. (2012): On the origin of the asthenosphere. *Earth and Planetary Science Letters*, *321-322*, 95–103. https://doi.org/10.1016/j.epsl.2012.01.001

Kendrick, E., Bevis, M., Smalley, R. F., Cifuentes, O., & Galban, F. (1999):
Current rates of convergence across the central Andes : Estimates from continuous GPS observations. *Geophysical Research Letters*, *26*(5), 541–544. https://doi.org/10.1029/1999GL900040

Kendrick, E., Bevis, M., Smalley, R., Brooks, B., Vargas, R. B., Lauría, E., & Fortes, L. P. S. (2003):
The Nazca–South America Euler vector and its rate of change. *Journal of South American Earth Sciences*, *16*(2), 125–131. https://doi.org/10.1016/S0895-9811(03)00028-2

Kendrick, E., Bevis, M., Smalley Jr., R., & Brooks, B. (2001):
An integrated crustal velocity field for the central Andes. *Geochemistry, Geophysics, Geosystems*, *2*(11). https://doi.org/10.1029/2001GC000191

Khazaradze, G., & Klotz, J. (2003):
Short- and long-term effects of GPS measured crustal deformation rates along the south central Andes. *Journal of Geophysical Research: Solid Earth*, *108*(B6). https://doi.org/10.1029/2002JB001879

Klein, E., Fleitout, L., Vigny, C., & Garaud, J. (2016):
Afterslip and viscoelastic relaxation model inferred from the large-scale post-seismic deformation following the 2010 Mw 8.8 Maule earthquake (Chile). *Geophysical Journal International*, *205*(3), 1455–1472. https://doi.org/10.1093/gji/ggw086

Klein, E., Métois, M., Meneses, G., Vigny, C., & Delorme, A. (2018):
Bridging the gap between North and Central Chile: Insight from new GPS data on coupling complexities and the Andean sliver motion. *Geophysical Journal International*, *213*(3), 1924–1933. https://doi.org/10.1093/gji/ggy094

Klein, E., Vigny, C., Fleitout, L., Grandin, R., Jolivet, R., Rivera, E., & Métois, M. (2017):
A comprehensive analysis of the Illapel 2015 Mw8.3 earthquake from GPS and InSAR data. *Earth and Planetary Science Letters*, *469*, 123–134. https://doi.org/10.1016/j.epsl.2017.04.010

Klinger, Y. (2022):
Paleoseismology. *The Seismic Cycle* (pp. 267–286). John Wiley & Sons, Ltd. https://doi.org/10.1002/9781394173709.ch11

Klotz, J., Angermann, D., Michel, G. W., Porth, R., Reigber, C., Reinking, J., Viramonte, J., Perdomo, R., Rios, V. H., Barrientos, S., Barriga, R., & Cifuentes, O. (1999):
GPS-derived Deformation of the Central Andes Including the 1995 Antofagasta Mw = 8.0 Earthquake. *Pure appl. geophys.*, *154*.

Klotz, J., Khazaradze, G., Angermann, D., Reigber, C., Perdomo, R., & Cifuentes, O. (2001):
Earthquake cycle dominates contemporary crustal deformation in Central and Southern Andes. *Earth and Planetary Science Letters*, *193*(3), 437–446. https://doi.org/10.1016/S0012-821X(01)00532-5

Knupp, P. M. (2001):
Hexahedral and Tetrahedral Mesh Untangling. *Engineering with Computers*, *17*(3), 261–268. https://doi.org/10.1007/s003660170006

Kohlhase, A., Feigl, K., & Massonnet, D. (2003):
Applying differential InSAR to orbital dynamics: A new approach for estimating ERS trajectories. *Journal of Geodesy*, *77*(9), 493–502. https://doi.org/10.1007/s00190-003-0336-3

Kohlstedt, D., & Hansen, L. (2015):
Constitutive Equations, Rheological Behavior, and Viscosity of Rocks. *Treatise on Geophysics* (pp. 441–472). Elsevier. https://doi.org/10.1016/B978-0-444-53802-4.00042-7

Konca, A. O., Avouac, J.-P., Sladen, A., Meltzner, A. J., Sieh, K., Fang, P., Li, Z., Galetzka, J., Genrich, J., Chlieh, M., Natawidjaja, D. H., Bock, Y., Fielding, E. J., Ji, C., & Helmberger, D. V. (2008):
Partial rupture of a locked patch of the Sumatra megathrust during the 2007 earthquake se-

quence [Number: 7222 Publisher: Nature Publishing Group]. *Nature*, *456*(7222), 631–635. https://doi.org/10.1038/nature07572

Kosari, E., Metzger, S., Navarro-Sanchez, V., Oncken, O., Schurr, B., & Rosenau, M. (2024): Interseismic deformation fingerprints on the hyperarid coastal landscape in North Chilean subduction [Publisher: EarthArXiv]. Retrieved October 1, 2025, from https://eartharxiv.org/repository/view/7853/

Kositsky, A. P., & Avouac, J.-P. (2010): Inverting geodetic time series with a principal component analysis-based inversion method. *Journal of Geophysical Research: Solid Earth*, *115*(B3). https://doi.org/10.1029/2009JB006535

Kreemer, C., Blewitt, G., & Klein, E. C. (2014): A geodetic plate motion and Global Strain Rate Model. *Geochemistry, Geophysics, Geosystems*, *15*(10), 3849–3889. https://doi.org/10.1002/2014GC005407

Lambert, V., & Barbot, S. (2016): Contribution of viscoelastic flow in earthquake cycles within the lithosphere-asthenosphere system. *Geophysical Research Letters*, *43*(19), 10, 142–10, 154. https://doi.org/10.1002/2016GL070345

Lanari, R., Berardino, P., Bonano, M., Casu, F., Manconi, A., Manunta, M., Manzo, M., Pepe, A., Pepe, S., Sansosti, E., Solaro, G., Tizzani, P., & Zeni, G. (2010): Surface displacements associated with the L'Aquila 2009 Mw 6.3 earthquake (central Italy): New evidence from SBAS-DInSAR time series analysis. *Geophysical Research Letters*, *37*(20). https://doi.org/10.1029/2010GL044780

Landau, L. D., & Lifshitz, E. M. (2013): *Fluid Mechanics: Landau and Lifshitz: Course of Theoretical Physics, Volume 6*. Elsevier.

Lay, T., Kanamori, H., Ammon, C. J., Koper, K. D., Hutko, A. R., Ye, L., Yue, H., & Rushing, T. M. (2012): Depth-varying rupture properties of subduction zone megathrust faults. *Journal of Geophysical Research: Solid Earth*, *117*(B4). https://doi.org/10.1029/2011JB009133

Le Breton, E., Dauteuil, O., & Biessy, G. (2010): Post-glacial rebound of Iceland during the Holocene [Publisher: The Geological Society of London]. *Journal of the Geological Society*, *167*(2), 417–432. https://doi.org/10.1144/0016-76492008-126

Lemrabet, L., Doin, M.-P., Lasserre, C., & Durand, P. (2023): Referencing of Continental-Scale InSAR-Derived Velocity Fields: Case Study of the Eastern Tibetan Plateau. *Journal of Geophysical Research: Solid Earth*, *128*(7), e2022JB026251. https://doi.org/10.1029/2022JB026251
e2022JB026251 2022JB026251

León, T., Vargas, G., Salazar, D., Goff, J., Guendon, J. L., Andrade, P., & Alvarez, G. (2019): Geo-archaeological records of large Holocene tsunamis along the hyperarid coastal Atacama Desert in the major northern Chile seismic gap. *Quaternary Science Reviews*, *220*, 335–358. https://doi.org/10.1016/j.quascirev.2019.07.038

Li, S., & Chen, L. (2024): Revisiting interseismic deformation in Nankai: Focusing on slip-deficit accumulation in the ETS zone and comparison with Cascadia. *Earth, Planets and Space*, *76*(1), 108. https://doi.org/10.1186/s40623-024-02054-z

Li, S., Fukuda, J., & Oncken, O. (2020): Geodetic Evidence of Time-Dependent Viscoelastic Interseismic Deformation Driven by Megathrust Locking in the Southwest Japan Subduction Zone. *Geophysical Research Letters*, *47*(4), e2019GL085551. https://doi.org/10.1029/2019GL085551
e2019GL085551 2019GL085551

Li, S., Moreno, M., Bedford, J., Rosenau, M., Heidbach, O., Melnick, D., & Oncken, O. (2017):
Postseismic uplift of the Andes following the 2010 Maule earthquake: Implications for mantle rheology. *Geophysical Research Letters*, *44*(4), 1768–1776. https://doi.org/10.1002/2016GL071995

Li, S., Moreno, M., Bedford, J., Rosenau, M., & Oncken, O. (2015):
Revisiting viscoelastic effects on interseismic deformation and locking degree: A case study of the Peru-North Chile subduction zone. *Journal of Geophysical Research: Solid Earth*, *120*(6), 4522–4538. https://doi.org/10.1002/2015JB011903

Li, S., Wang, K., Wang, Y., Jiang, Y., & Dosso, S. E. (2018):
Geodetically Inferred Locking State of the Cascadia Megathrust Based on a Viscoelastic Earth Model. *Journal of Geophysical Research: Solid Earth*, *123*(9), 8056–8072. https://doi.org/10.1029/2018JB015620

Liao, W.-T., Tseng, K.-H., Lee, I.-T., Liibusk, A., Lee, J.-C., Liu, J.-Y., Chang, C.-P., & Lin, Y.-C. (2020):
Sentinel-1 interferometry with ionospheric correction from global and local TEC maps for land displacement detection in Taiwan. *Advances in Space Research*, *65*(5), 1447–1465. https://doi.org/10.1016/j.asr.2019.11.041

Lorito, S., Romano, F., Atzori, S., Tong, X., Avallone, A., McCloskey, J., Cocco, M., Boschi, E., & Piatanesi, A. (2011):
Limited overlap between the seismic gap and coseismic slip of the great 2010 Chile earthquake [Publisher: Nature Publishing Group]. *Nature Geoscience*, *4*(3), 173–177. https://doi.org/10.1038/ngeo1073

Loveless, J. P., & Meade, B. J. (2011):
Spatial correlation of interseismic coupling and coseismic rupture extent of the 2011 MW = 9.0 Tohoku-oki earthquake. *Geophysical Research Letters*, *38*(17). https://doi.org/10.1029/2011GL048561

Lovery, B., Chlieh, M., Norabuena, E., Villegas-Lanza, J. C., Radiguet, M., Cotte, N., Tsapong-Tsague, A., Quiroz, W., Sierra Farfán, C., Simons, M., Nocquet, J. M., Tavera, H., & Socquet, A. (2024):
Heterogeneous Locking and Earthquake Potential on the South Peru Megathrust From Dense GNSS Network. *Journal of Geophysical Research: Solid Earth*, *129*(2), e2023JB027114. https://doi.org/10.1029/2023JB027114
e2023JB027114 2023JB027114

Lovery, B., Radiguet, M., Chlieh, M., Norabuena, E., Villegas-Lanza, J. C., Cresseaux, J., Ragon, T., Tsapong-Tsague, A., Tavera, H., & Socquet, A. (2025):
Viscoelastic Relaxation Following the 2001 Mw 8.4 Arequipa Earthquake and Its Impact on the Interseismic Coupling of the South Peru Megathrust. *Geophysical Research Letters*, *52*(12), e2024GL113879. https://doi.org/10.1029/2024GL113879
e2024GL113879 2024GL113879

Luo, H., & Wang, K. (2021):
Postseismic geodetic signature of cold forearc mantle in subduction zones [Number: 2 Publisher: Nature Publishing Group]. *Nature Geoscience*, *14*(2), 104–109. https://doi.org/10.1038/s41561-020-00679-9

Luo, H., Wang, K., Feng, L., & Hill, E. M. (2025):
Interseismic secondary zone of subsidence during earthquake cycles in subduction zones [Publisher: Nature Publishing Group]. *Nature Geoscience*, 1–7. https://doi.org/10.1038/s41561-025-01778-1

Lyard, F. H., Allain, D. J., Cancet, M., Carrère, L., & Picot, N. (2021):
FES2014 global ocean tide atlas: Design and performance [Publisher: Copernicus GmbH]. *Ocean Science*, *17*(3), 615–649. https://doi.org/10.5194/os-17-615-2021

Machacca, R., Lesage, P., Tavera, H., Pesicek, J. D., Caudron, C., Torres, J. L., Puma, N., Vargas, K., Lazarte, I., Rivera, M., & Burgisser, A. (2023):
The 2013–2020 seismic activity at Sabancaya Volcano (Peru): Long lasting unrest and eruption. *Journal of Volcanology and Geothermal Research*, *435*, 107767. https://doi.org/10.1016/j.jvolgeores.2023.107767

MacQueen, P., Delgado, F., Reath, K., Pritchard, M. E., Bagnardi, M., Milillo, P., Lundgren, P., Macedo, O., Aguilar, V., Ortega, M., Anccasi, R., Lazarte Zerpa, I. A., & Miranda, R. (2020):
Volcano-Tectonic Interactions at Sabancaya Volcano, Peru: Eruptions, Magmatic Inflation, Moderate Earthquakes, and Fault Creep. *Journal of Geophysical Research: Solid Earth*, *125*(5), e2019JB019281. https://doi.org/10.1029/2019JB019281
e2019JB019281 10.1029/2019JB019281

Maldonado, V., Contreras, M., & Melnick, D. (2021):
A comprehensive database of active and potentially-active continental faults in Chile at 1:25,000 scale [Publisher: Nature Publishing Group]. *Scientific Data*, *8*(1), 20. https://doi.org/10.1038/s41597-021-00802-4

Manaker, D. M., Calais, E., Freed, A. M., Ali, S. T., Przybylski, P., Mattioli, G., Jansma, P., Prépetit, C., & De Chabalier, J. B. (2008):
Interseismic Plate coupling and strain partitioning in the Northeastern Caribbean. *Geophysical Journal International*, *174*(3), 889–903. https://doi.org/10.1111/j.1365-246X.2008.03819.x

Manea, V., & Gurnis, M. (2007):
Subduction zone evolution and low viscosity wedges and channels. *Earth and Planetary Science Letters*, *264*(1), 22–45. https://doi.org/10.1016/j.epsl.2007.08.030

Marconato, L., Audin, L., Doin, M.-P., Nocquet, J.-M., Jarrin, P., Rolandone, F., Harrichhausen, N., Mothes, P., Mora-Páez, H., & Cisneros, D. (2024):
Internal deformation of the North Andean Sliver in Ecuador and southern Colombia observed by InSAR. *Geophysical Journal International*, *239*(3), 1557–1575. https://doi.org/10.1093/gji/ggae338

Marconato, L., Doin, M.-P., Lovery, B., Rolland, L., & Durand, P. (2025):
Long-wavelength ionospheric compensation of insar time-series based on global ionosphere maps. *Geophysical Research Letters [submitted]*.

Marill, L., Marsan, D., Socquet, A., Radiguet, M., Cotte, N., & Rousset, B. (2021):
Fourteen-Year Acceleration Along the Japan Trench. *Journal of Geophysical Research: Solid Earth*, *126*(11), e2020JB021226. https://doi.org/10.1029/2020JB021226
e2020JB021226 2020JB021226

Marone, C. J., Scholtz, C. H., & Bilham, R. (1991):
On the mechanics of earthquake afterslip. *Journal of Geophysical Research: Solid Earth*, *96*(B5), 8441–8452. https://doi.org/10.1029/91JB00275

Matsu'ura, T. (2015):
Late Quaternary uplift rate inferred from marine terraces, Muroto Peninsula, southwest Japan: Forearc deformation in an oblique subduction zone. *Geomorphology*, *234*, 133–150. https://doi.org/10.1016/j.geomorph.2015.01.012

Matsu'ura, T., Kimura, H., Komatsubara, J., Goto, N., Yanagida, M., Ichikawa, K., & Furusawa, A. (2014):
Late Quaternary uplift rate inferred from marine terraces, Shimokita Peninsula, northeastern Japan: A preliminary investigation of the buried shoreline angle. *Geomorphology*, *209*, 1–17. https://doi.org/10.1016/j.geomorph.2013.11.013

Maxwell, J. C. (1861):
On physical lines of force. *The London, Edinburgh, and Dublin Philosophical Magazine and Journal of Science*, *21*(141), 338–348.
Maxwell, J. C. (1867):
IV. On the dynamical theory of gases [Publisher: Royal Society]. *Philosophical Transactions of the Royal Society of London*, *157*, 49–88. https://doi.org/10.1098/rstl.1867.0004
McCann, W. R., Nishenko, S. P., Sykes, L. R., & Krause, J. (1979):
Seismic gaps and plate tectonics: Seismic potential for major boundaries. *pure and applied geophysics*, *117*(6), 1082–1147. https://doi.org/10.1007/BF00876211
McKenzie, D., Jackson, J., & Priestley, K. (2005):
Thermal structure of oceanic and continental lithosphere. *Earth and Planetary Science Letters*, *233*(3), 337–349. https://doi.org/10.1016/j.epsl.2005.02.005
Meade, B. J. (2007):
Algorithms for the calculation of exact displacements, strains, and stresses for triangular dislocation elements in a uniform elastic half space. *Computers & Geosciences*, *33*(8), 1064–1075. https://doi.org/10.1016/j.cageo.2006.12.003
Melnick, D. (2016):
Rise of the central Andean coast by earthquakes straddling the Moho [Publisher: Nature Publishing Group]. *Nature Geoscience*, *9*(5), 401–407. https://doi.org/10.1038/ngeo2683
Meng, L., Ampuero, J.-P., Stock, J., Duputel, Z., Luo, Y., & Tsai, V. C. (2012):
Earthquake in a Maze: Compressional Rupture Branching During the 2012 Mw 8.6 Sumatra Earthquake [Publisher: American Association for the Advancement of Science]. *Science*, *337*(6095), 724–726. https://doi.org/10.1126/science.1224030
Métois, M., Socquet, A., & Vigny, C. (2012):
Interseismic coupling, segmentation and mechanical behavior of the central Chile subduction zone. *Journal of Geophysical Research: Solid Earth*, *117*(B3). https://doi.org/10.1029/2011JB008736
Métois, M., Socquet, A., Vigny, C., Carrizo, D., Peyrat, S., Delorme, A., Maureira, E., Valderas-Bermejo, M.-C., & Ortega, I. (2013):
Revisiting the North Chile seismic gap segmentation using GPS-derived interseismic coupling. *Geophysical Journal International*, *194*(3), 1283–1294. https://doi.org/10.1093/gji/ggt183
Métois, M., Vigny, C., & Socquet, A. (2016):
Interseismic Coupling, Megathrust Earthquakes and Seismic Swarms Along the Chilean Subduction Zone (38°–18°S). *Pure and Applied Geophysics*, *173*(5), 1431–1449. https://doi.org/10.1007/s00024-016-1280-5
Métois, M., Vigny, C., Socquet, A., Delorme, A., Morvan, S., Ortega, I., & Valderas-Bermejo, C.-M. (2014):
GPS-derived interseismic coupling on the subduction and seismic hazards in the Atacama region, Chile. *Geophysical Journal International*, *196*(2), 644–655. https://doi.org/10.1093/gji/ggt418
Metzger, S., Gągała, Ł., Ratschbacher, L., Lazecký, M., Maghsoudi, Y., & Schurr, B. (2021):
Tajik Depression and Greater Pamir Neotectonics From InSAR Rate Maps. *Journal of Geophysical Research: Solid Earth*, *126*(12), e2021JB022775. https://doi.org/10.1029/2021JB022775 e2021JB022775 2021JB022775
Michel, R., Avouac, J.-P., & Taboury, J. (1999):
Measuring ground displacements from SAR amplitude images: Application to the Landers Earthquake. *Geophysical Research Letters*, *26*(7), 875–878. https://doi.org/10.1029/1999GL900138
Michel, S., Gualandi, A., & Avouac, J.-P. (2019):
Interseismic Coupling and Slow Slip Events on the Cascadia Megathrust. *Pure and Applied Geophysics*, *176*(9), 3867–3891. https://doi.org/10.1007/s00024-018-1991-x

Mogi, K. (1979):
Two kinds of seismic gaps. *pure and applied geophysics*, *117*(6), 1172–1186. https://doi.org/10.1007/BF00876213

Mogi, K. (1981):
Seismicity in Western Japan and Long-Term Earthquake Forecasting. *Earthquake Prediction* (pp. 43–51). American Geophysical Union (AGU). https://doi.org/10.1029/ME004p0043

Molina, D., Tassara, A., Abarca, R., Melnick, D., & Madella, A. (2021):
Frictional Segmentation of the Chilean Megathrust From a Multivariate Analysis of Geophysical, Geological, and Geodetic Data. *Journal of Geophysical Research: Solid Earth*, *126*(6), e2020JB020647. https://doi.org/10.1029/2020JB020647
e2020JB020647 2020JB020647

Montagnon, T., Giffard-Roisin, S., Dalla Mura, M., Marchandon, M., Pathier, E., & Hollingsworth, J. (2024):
Sub-Pixel Displacement Estimation With Deep Learning: Application to Optical Satellite Images Containing Sharp Displacements. *Journal of Geophysical Research: Machine Learning and Computation*, *1*(4), e2024JH000174. https://doi.org/10.1029/2024JH000174
e2024JH000174 2024JH000174

Monti-Guarnieri, A., Giudici, D., & Recchia, A. (2017):
Identification of C-Band Radio Frequency Interferences from Sentinel-1 Data. *Remote Sensing*, *9*, 1183. https://doi.org/10.3390/rs9111183

Moreno, M., Melnick, D., Rosenau, M., Bolte, J., Klotz, J., Echtler, H., Baez, J., Bataille, K., Chen, J., Bevis, M., Hase, H., & Oncken, O. (2011):
Heterogeneous plate locking in the South–Central Chile subduction zone: Building up the next great earthquake. *Earth and Planetary Science Letters*, *305*(3), 413–424. https://doi.org/10.1016/j.epsl.2011.03.025

Moreno, M. S., Bolte, J., Klotz, J., & Melnick, D. (2009):
Impact of megathrust geometry on inversion of coseismic slip from geodetic data: Application to the 1960 Chile earthquake. *Geophysical Research Letters*, *36*(16). https://doi.org/10.1029/2009GL039276

Moreno, M., Rosenau, M., & Oncken, O. (2010):
2010 Maule earthquake slip correlates with pre-seismic locking of Andean subduction zone [Number: 7312 Publisher: Nature Publishing Group]. *Nature*, *467*(7312), 198–202. https://doi.org/10.1038/nature09349

Mori, N., Takahashi, T., Yasuda, T., & Yanagisawa, H. (2011):
Survey of 2011 Tohoku earthquake tsunami inundation and run-up. *Geophysical Research Letters*, *38*(7). https://doi.org/10.1029/2011GL049210

Muto, J., Moore, J. D. P., Barbot, S., Iinuma, T., Ohta, Y., & Iwamori, H. (2019):
Coupled afterslip and transient mantle flow after the 2011 Tohoku earthquake [Publisher: American Association for the Advancement of Science]. *Science Advances*, *5*(9), eaaw1164. https://doi.org/10.1126/sciadv.aaw1164

Naumowicz, B., Kowalczyk, K., & Pelc-Mieczkowska, R. (2024):
PPP Solution-Based Model of Absolute Vertical Movements of the Earth's Crust in Poland With Consideration of Geological, Tectonic, Hydrological and Mineral Information. *Earth and Space Science*, *11*(12), e2023EA003268. https://doi.org/10.1029/2023EA003268
e2023EA003268 2023EA003268

Nishenko, S. P. (1991):
Circum-Pacific seismic potential: 1989–1999. *pure and applied geophysics*, *135*(2), 169–259. https://doi.org/10.1007/BF00880240

Nishimura, T. (2014):
Pre-, Co-, and Post-Seismic Deformation of the 2011 Tohoku-Oki Earthquake and its Implication to a Paradox in Short-Term and Long-Term Deformation. *Journal of Disaster Research*, *9*(3), 294–302. https://doi.org/10.20965/jdr.2014.p0294

Nishimura, T., Hirasawa, T., Miyazaki, S., Sagiya, T., Tada, T., Miura, S., & Tanaka, K. (2004):
Temporal change of interplate coupling in northeastern Japan during 1995–2002 estimated from continuous GPS observations. *Geophysical Journal International*, *157*(2), 901–916. https://doi.org/10.1111/j.1365-246X.2004.02159.x

Nocquet, J.-M., Villegas-Lanza, J. C., Chlieh, M., Mothes, P. A., Rolandone, F., Jarrin, P., Cisneros, D., Alvarado, A., Audin, L., Bondoux, F., Martin, X., Font, Y., Régnier, M., Vallée, M., Tran, T., Beauval, C., Maguiña Mendoza, J. M., Martinez, W., Tavera, H., & Yepes, H. (2014):
Motion of continental slivers and creeping subduction in the northern Andes [Number: 4 Publisher: Nature Publishing Group]. *Nature Geoscience*, *7*(4), 287–291. https://doi.org/10.1038/ngeo2099

Norabuena, E., Leffler-Griffin, L., Mao, A., Dixon, T., Stein, S., Sacks, I. S., Ocola, L., & Ellis, M. (1998):
Space Geodetic Observations of Nazca-South America Convergence Across the Central Andes [Publisher: American Association for the Advancement of Science]. *Science*, *279*(5349), 358–362. https://doi.org/10.1126/science.279.5349.358

Ochoa, D., Salas-Gismondi, R., DeVries, T. J., Baby, P., de Muizon, C., Altamirano, A., Barbosa-Espitia, A., Foster, D. A., Quispe, K., Cardich, J., Gutiérrez, D., Perez, A., Valqui, J., Urbina, M., & Carré, M. (2021):
Late Neogene evolution of the Peruvian margin and its ecosystems: A synthesis from the Sacaco record. *International Journal of Earth Sciences*, *110*(3), 995–1025. https://doi.org/10.1007/s00531-021-02003-1

Oleskevich, D. A., Hyndman, R. D., & Wang, K. (1999):
The updip and downdip limits to great subduction earthquakes: Thermal and structural models of Cascadia, south Alaska, SW Japan, and Chile. *Journal of Geophysical Research: Solid Earth*, *104*(B7), 14965–14991. https://doi.org/10.1029/1999JB900060

Ōmori, F. (1894):
On the After-shocks of Earthquakes [Google-Books-ID: HtsPAAAAIAAJ]. The University.

O'Neill, C., Müller, D., & Steinberger, B. (2005):
On the uncertainties in hot spot reconstructions and the significance of moving hot spot reference frames. *Geochemistry, Geophysics, Geosystems*, *6*(4). https://doi.org/10.1029/2004GC000784

Parizzi, A., & Brcic, R. (2011):
Adaptive InSAR Stack Multilooking Exploiting Amplitude Statistics: A Comparison Between Different Techniques and Practical Results. *IEEE Geoscience and Remote Sensing Letters*, *8*(3), 441–445. https://doi.org/10.1109/LGRS.2010.2083631

Park, S.-E., Yamaguchi, Y., & Kim, D.-j. (2013):
Polarimetric SAR remote sensing of the 2011 Tohoku earthquake using ALOS/PALSAR. *Remote Sensing of Environment*, *132*, 212–220. https://doi.org/10.1016/j.rse.2013.01.018

Peacock, S. M. (1996):
Thermal and Petrologic Structure of Subduction Zones. *Subduction* (pp. 119–133). American Geophysical Union (AGU). https://doi.org/10.1029/GM096p0119

Peltzer, G., Rosen, P., Rogez, F., & Hudnut, K. (1996):
Postseismic Rebound in Fault Step-Overs Caused by Pore Fluid Flow [Publisher: American Association for the Advancement of Science]. *Science*, *273*(5279), 1202–1204. https://doi.org/10.1126/science.273.5279.1202

Peña, C., Heidbach, O., Moreno, M., Bedford, J., Ziegler, M., Tassara, A., & Oncken, O. (2020):
Impact of power-law rheology on the viscoelastic relaxation pattern and afterslip distribution following the 2010 Mw 8.8 Maule earthquake. *Earth and Planetary Science Letters*, *542*, 116292. https://doi.org/10.1016/j.epsl.2020.116292

Penniston-Dorland, S. C., Kohn, M. J., & Manning, C. E. (2015):
The global range of subduction zone thermal structures from exhumed blueschists and eclogites: Rocks are hotter than models. *Earth and Planetary Science Letters*, *428*, 243–254. https://doi.org/10.1016/j.epsl.2015.07.031

Perfettini, H., Avouac, J.-P., & Ruegg, J.-C. (2005):
Geodetic displacements and aftershocks following the 2001 Mw = 8.4 Peru earthquake: Implications for the mechanics of the earthquake cycle along subduction zones. *Journal of Geophysical Research: Solid Earth*, *110*(B9). https://doi.org/10.1029/2004JB003522

Perfettini, H., Avouac, J.-P., Tavera, H., Kositsky, A., Nocquet, J.-M., Bondoux, F., Chlieh, M., Sladen, A., Audin, L., Farber, D. L., & Soler, P. (2010):
Seismic and aseismic slip on the Central Peru megathrust [Number: 7294 Publisher: Nature Publishing Group]. *Nature*, *465*(7294), 78–81. https://doi.org/10.1038/nature09062

Philibosian, B., & Meltzner, A. J. (2020):
Segmentation and supercycles: A catalog of earthquake rupture patterns from the Sumatran Sunda Megathrust and other well-studied faults worldwide. *Quaternary Science Reviews*, *241*, 106390. https://doi.org/10.1016/j.quascirev.2020.106390

Phipps Morgan, J., Morgan, W. J., Zhang, Y.-S., & Smith, W. H. F. (1995):
Observational hints for a plume-fed, suboceanic asthenosphere and its role in mantle convection. *Journal of Geophysical Research: Solid Earth*, *100*(B7), 12753–12767. https://doi.org/10.1029/95JB00041

Piñón, D. A., Gómez, D. D., Smalley, R., Jr., Cimbaro, S. R., Lauría, E. A., & Bevis, M. G. (2018):
The History, State, and Future of the Argentine Continuous Satellite Monitoring Network and Its Contributions to Geodesy in Latin America. *Seismological Research Letters*, *89*(2A), 475–482. https://doi.org/10.1785/0220170162

Polet, J., & Kanamori, H. (2000):
Shallow subduction zone earthquakes and their tsunamigenic potential. *Geophysical Journal International*, *142*(3), 684–702. https://doi.org/10.1046/j.1365-246x.2000.00205.x

Pollitz, F. F., McCrory, P., Wilson, D., Svarc, J., Puskas, C., & Smith, R. B. (2010):
Viscoelastic-cycle model of interseismic deformation in the northwestern United States. *Geophysical Journal International*, *181*(2), 665–696. https://doi.org/10.1111/j.1365-246X.2010.04546.x

Pollitz, F. F. (1997):
Gravitational viscoelastic postseismic relaxation on a layered spherical Earth. *Journal of Geophysical Research: Solid Earth*, *102*(B8), 17921–17941. https://doi.org/10.1029/97JB01277

Pollitz, F. F. (2005):
Transient rheology of the upper mantle beneath central Alaska inferred from the crustal velocity field following the 2002 Denali earthquake. *Journal of Geophysical Research: Solid Earth*, *110*(B8). https://doi.org/10.1029/2005JB003672

Pollitz, F. F. (2019):
Lithosphere and shallow asthenosphere rheology from observations of post-earthquake relaxation. *Physics of the Earth and Planetary Interiors*, *293*, 106271. https://doi.org/10.1016/j.pepi.2019.106271

Popescu, R., Anantrasirichai, N., & Biggs, J. (2025):
Unsupervised Anomaly Detection for Volcanic Deformation in InSAR Imagery. *Earth and Space*

Science, *12*(6), e2024EA003892. https://doi.org/10.1029/2024EA003892 e2024EA003892 2024EA003892

Price, E. J., & Sandwell, D. T. (1998):
Small-scale deformations associated with the 1992 Landers, California, earthquake mapped by synthetic aperture radar interferometry phase gradients. *Journal of Geophysical Research: Solid Earth*, *103*(B11), 27001–27016. https://doi.org/10.1029/98JB01821

Pritchard, M. E., Norabuena, E. O., Ji, C., Boroschek, R., Comte, D., Simons, M., Dixon, T. H., & Rosen, P. A. (2007):
Geodetic, teleseismic, and strong motion constraints on slip from recent southern Peru subduction zone earthquakes. *Journal of Geophysical Research: Solid Earth*, *112*(B3). https://doi.org/10.1029/2006JB004294

Rabinowicz, M., Lago, B., & Froidevaux, C. (1980):
Thermal transfer between the continental asthenosphere and the oceanic subducting lithosphere: Its effect on subcontinental convection. *Journal of Geophysical Research: Solid Earth*, *85*(B4), 1839–1853. https://doi.org/10.1029/JB085iB04p01839

Radiguet, M., Cotton, F., Vergnolle, M., Campillo, M., Valette, B., Kostoglodov, V., & Cotte, N. (2011):
Spatial and temporal evolution of a long term slow slip event: The 2006 Guerrero Slow Slip Event. *Geophysical Journal International*, *184*(2), 816–828. https://doi.org/10.1111/j.1365-246X.2010.04866.x

Radiguet, M., Perfettini, H., Cotte, N., Gualandi, A., Valette, B., Kostoglodov, V., Lhomme, T., Walpersdorf, A., Cabral Cano, E., & Campillo, M. (2016):
Triggering of the 2014 Mw7.3 Papanoa earthquake by a slow slip event in Guerrero, Mexico [Number: 11 Publisher: Nature Publishing Group]. *Nature Geoscience*, *9*(11), 829–833. https://doi.org/10.1038/ngeo2817

Ragon, T., & Simons, M. (2023):
A Secondary Zone of Uplift Measured After Megathrust Earthquakes: Caused by Early Downdip Afterslip? *Geophysical Research Letters*, *50*(7), e2022GL101510. https://doi.org/10.1029/2022GL101510 e2022GL101510 2022GL101510

Ramos, V. A., Jordan, T. E., Allmendinger, R. W., Mpodozis, C., Kay, S. M., Cortés, J. M., & Palma, M. (1986):
Paleozoic terranes of the central Argentine-Chilean Andes. *Tectonics*, *5*(6), 855–880. https://doi.org/10.1029/TC005i006p00855

Ramos, V. A., Cristallini, E. O., & Pérez, D. J. (2002):
The Pampean flat-slab of the Central Andes. *Journal of South American Earth Sciences*, *15*(1), 59–78. https://doi.org/10.1016/S0895-9811(02)00006-8

Regard, V., Saillard, M., Martinod, J., Audin, L., Carretier, S., Pedoja, K., Riquelme, R., Paredes, P., & Hérail, G. (2010):
Renewed uplift of the Central Andes Forearc revealed by coastal evolution during the Quaternary. *Earth and Planetary Science Letters*, *297*(1), 199–210. https://doi.org/10.1016/j.epsl.2010.06.020

Reid, H. F. (1910):
The mechanics of the earthquake, the california earthquake of april 18, 1906, report of the state investigation commission. *Carnegie Institution of Washington*, *2*, 16–28.

Remy, D., Perfettini, H., Cotte, N., Avouac, J. P., Chlieh, M., Bondoux, F., Sladen, A., Tavera, H., & Socquet, A. (2016):
Postseismic relocking of the subduction megathrust following the 2007 Pisco, Peru, earthquake. *Journal of Geophysical Research: Solid Earth*, *121*(5), 3978–3995. https://doi.org/10.1002/2015JB012417

Ridzwan, N. S. M., & Yusoff, S. H. M. (2023):
Machine learning for earthquake prediction: A review (2017–2021). *Earth Science Informatics*, *16*(2), 1133–1149. https://doi.org/10.1007/s12145-023-00991-z

Rittman, A. (1951):
Orogénèse et volcanisme. *Archives des Sciences*, *4-5*, 273–314.

Robinson, D. P., Das, S., & Watts, A. B. (2006):
Earthquake Rupture Stalled by a Subducting Fracture Zone [Publisher: American Association for the Advancement of Science]. *Science*, *312*(5777), 1203–1205. https://doi.org/10.1126/science.1125771

Rosen, P. A., Hensley, S., Peltzer, G., & Simons, M. (2004):
Updated repeat orbit interferometry package released. *Eos, Transactions American Geophysical Union*, *85*(5), 47–47. https://doi.org/10.1029/2004EO050004

Rousset, B., Lasserre, C., Cubas, N., Graham, S., Radiguet, M., DeMets, C., Socquet, A., Campillo, M., Kostoglodov, V., Cabral-Cano, E., Cotte, N., & Walpersdorf, A. (2016):
Lateral Variations of Interplate Coupling along the Mexican Subduction Interface: Relationships with Long-Term Morphology and Fault Zone Mechanical Properties. *Pure and Applied Geophysics*, *173*(10), 3467–3486. https://doi.org/10.1007/s00024-015-1215-6

Ruegg, J. C., Rudloff, A., Vigny, C., Madariaga, R., de Chabalier, J. B., Campos, J., Kausel, E., Barrientos, S., & Dimitrov, D. (2009):
Interseismic strain accumulation measured by GPS in the seismic gap between Constitución and Concepción in Chile. *Physics of the Earth and Planetary Interiors*, *175*(1), 78–85. https://doi.org/10.1016/j.pepi.2008.02.015

Ruina, A. (1983):
Slip instability and state variable friction laws. *Journal of Geophysical Research: Solid Earth*, *88*(B12), 10359–10370. https://doi.org/10.1029/JB088iB12p10359

Saillard, M., Audin, L., Rousset, B., Avouac, J.-P., Chlieh, M., Hall, S. R., Husson, L., & Farber, D. L. (2017):
From the seismic cycle to long-term deformation: Linking seismic coupling and Quaternary coastal geomorphology along the Andean megathrust. *Tectonics*, *36*(2), 241–256. https://doi.org/10.1002/2016TC004156

Saillard, M., Hall, S. R., Audin, L., Farber, D. L., Hérail, G., Martinod, J., Regard, V., Finkel, R. C., & Bondoux, F. (2009):
Non-steady long-term uplift rates and Pleistocene marine terrace development along the Andean margin of Chile (31°S) inferred from 10Be dating. *Earth and Planetary Science Letters*, *277*(1), 50–63. https://doi.org/10.1016/j.epsl.2008.09.039

Saillard, M., Hall, S. R., Audin, L., Farber, D. L., Regard, V., & Hérail, G. (2011):
Andean coastal uplift and active tectonics in southern Peru: 10Be surface exposure dating of differentially uplifted marine terrace sequences (San Juan de Marcona, ~ 15.4°S). *Geomorphology*, *128*(3), 178–190. https://doi.org/10.1016/j.geomorph.2011.01.004

Sandwell, D. T., Müller, R. D., Smith, W. H. F., Garcia, E., & Francis, R. (2014):
New global marine gravity model from CryoSat-2 and Jason-1 reveals buried tectonic structure [Publisher: American Association for the Advancement of Science]. *Science*, *346*(6205), 65–67. https://doi.org/10.1126/science.1258213

Satake, K., & Tanioka, Y. (1999):
Sources of Tsunami and Tsunamigenic Earthquakes in Subduction Zones. *pure and applied geophysics*, *154*(3), 467–483. https://doi.org/10.1007/s000240050240

Savage, J. C. (1983):
A dislocation model of strain accumulation and release at a subduction zone. *Journal of Geophysical Research: Solid Earth*, *88*(B6), 4984–4996. https://doi.org/10.1029/JB088iB06p04984

Savage, J. C., & Prescott, W. H. (1978):
Asthenosphere readjustment and the earthquake cycle. *Journal of Geophysical Research: Solid Earth*, *83*(B7), 3369–3376. https://doi.org/10.1029/JB083iB07p03369

Savage, J. C., & Thatcher, W. (1992):
Interseismic deformation at the Nankai Trough, Japan, subduction zone. *Journal of Geophysical Research: Solid Earth*, *97*(B7), 11117–11135. https://doi.org/10.1029/92JB00810

Schellart, W. P. (2011):
A subduction zone reference frame based on slab geometry and subduction partitioning of plate motion and trench migration. *Geophysical Research Letters*, *38*(16). https://doi.org/10.1029/2011GL048197

Schellart, W. (2023):
Subduction Zones: A Short Review. *Dynamics of Plate Tectonics and Mantle Convection* (pp. 321–355). Elsevier. https://doi.org/10.1016/B978-0-323-85733-8.00009-3

Schneider, T., Hu, Y., Gao, X., Dumas, J., Zorin, D., & Panozzo, D. (2022):
A Large-Scale Comparison of Tetrahedral and Hexahedral Elements for Solving Elliptic PDEs with the Finite Element Method. *ACM Transactions on Graphics*, *41*(3), 1–14. https://doi.org/10.1145/3508372

Scholz, C., Molnar, P., & Johnson, T. (1972):
Detailed studies of frictional sliding of granite and implications for the earthquake mechanism. *Journal of Geophysical Research (1896-1977)*, *77*(32), 6392–6406. https://doi.org/10.1029/JB077i032p06392

Scholz, C. H. (1998):
Earthquakes and friction laws [Publisher: Nature Publishing Group]. *Nature*, *391*(6662), 37–42. https://doi.org/10.1038/34097

Scholz, C. H., & Campos, J. (2012):
The seismic coupling of subduction zones revisited. *Journal of Geophysical Research: Solid Earth*, *117*(B5). https://doi.org/10.1029/2011JB009003

Schurr, B., Asch, G., Hainzl, S., Bedford, J., Hoechner, A., Palo, M., Wang, R., Moreno, M., Bartsch, M., Zhang, Y., Oncken, O., Tilmann, F., Dahm, T., Victor, P., Barrientos, S., & Vilotte, J.-P. (2014):
Gradual unlocking of plate boundary controlled initiation of the 2014 Iquique earthquake [Publisher: Nature Publishing Group]. *Nature*, *512*(7514), 299–302. https://doi.org/10.1038/nature13681

Schwartz, S. Y., & Rokosky, J. M. (2007):
Slow slip events and seismic tremor at circum-Pacific subduction zones. *Reviews of Geophysics*, *45*(3). https://doi.org/10.1029/2006RG000208

Segall, P. (2010):
Earthquake and Volcano Deformation [Google-Books-ID: z0xqmAEACAAJ]. Princeton University Press.

Sennson, J. L., & Beck, S. L. (1996):
Historical 1942 Ecuador and 1942 Peru subduction earthquakes and earthquake cycles along Colombia-Ecuador and Peru subduction segments. *pure and applied geophysics*, *146*(1), 67–101. https://doi.org/10.1007/BF00876670

Shi, F., Li, S., & Moreno, M. (2020):
Megathrust Locking and Viscous Mantle Flow Induce Continental Shortening in Central Andes. *Pure and Applied Geophysics*, *177*(6), 2841–2852. https://doi.org/10.1007/s00024-019-02403-0

Shreve, T., Grandin, R., Smittarello, D., Cayol, V., Pinel, V., Boichu, M., & Morishita, Y. (2021):
What Triggers Caldera Ring-Fault Subsidence at Ambrym Volcano? Insights From the 2015 Dike Intrusion and Eruption. *Journal of Geophysical Research: Solid Earth*, *126*(6), e2020JB020277.

https://doi.org/10.1029/2020JB020277
e2020JB020277 2020JB020277

Shrivastava, M. N., González, G., Moreno, M., Soto, H., Schurr, B., Salazar, P., & Báez, J. C. (2019):
Earthquake segmentation in northern Chile correlates with curved plate geometry [Publisher: Nature Publishing Group]. *Scientific Reports*, *9*(1), 4403. https://doi.org/10.1038/s41598-019-40282-6

Sigmundsson, F. (1991):
Post-glacial rebound and asthenosphere viscosity in Iceland. *Geophysical Research Letters*, *18*(6), 1131–1134. https://doi.org/10.1029/91GL01342

Silgado, E. (1978):
Recurrence of tsunamis in the western coast of South America. *Marine Geodesy*, *1*(4), 347–354. https://doi.org/10.1080/01490417809387980

Skakun, S., Roger, J.-C., Vermote, E. F., Masek, J. G., & Justice, C. O. (2017):
Automatic sub-pixel co-registration of Landsat-8 Operational Land Imager and Sentinel-2A Multi-Spectral Instrument images using phase correlation and machine learning based mapping. *International Journal of Digital Earth*, *10*(12), 1253–1269. https://doi.org/10.1080/17538947.2017.1304586

Sladen, A., Tavera, H., Simons, M., Avouac, J. P., Konca, A. O., Perfettini, H., Audin, L., Fielding, E. J., Ortega, F., & Cavagnoud, R. (2010):
Source model of the 2007 Mw 8.0 Pisco, Peru earthquake: Implications for seismogenic behavior of subduction megathrusts. *Journal of Geophysical Research: Solid Earth*, *115*(B2). https://doi.org/10.1029/2009JB006429

Sobolev, S. V., & Muldashev, I. A. (2017):
Modeling Seismic Cycles of Great Megathrust Earthquakes Across the Scales With Focus at Postseismic Phase. *Geochemistry, Geophysics, Geosystems*, *18*(12), 4387–4408. https://doi.org/10.1002/2017GC007230

Socquet, A., Tsapong-Tsague, A., Lovery, B., Janex, G., Metois, M., & Radiguet, M. (2023):
Metadata and GNSS daily position solutions for permanent GNSS stations in South America. https://doi.org/10.17178/GNSS.PRODUCTS.SOUTHAMERICA_GIPSYX.DAILY
SeriesInformation These datasets include station metadata and GNSS daily solutions for over 700 GNSS stations in South America.

Socquet, A., Hollingsworth, J., Pathier, E., & Bouchon, M. (2019):
Evidence of supershear during the 2018 magnitude 7.5 palu earthquake from space geodesy. *Nature Geoscience*, *12*(3), 192–199.

Socquet, A., Valdes, J. P., Jara, J., Cotton, F., Walpersdorf, A., Cotte, N., Specht, S., Ortega-Culaciati, F., Carrizo, D., & Norabuena, E. (2017):
An 8 month slow slip event triggers progressive nucleation of the 2014 Chile megathrust. *Geophysical Research Letters*, *44*(9), 4046–4053. https://doi.org/10.1002/2017GL073023

Song, T.-R. A., & Simons, M. (2003):
Large Trench-Parallel Gravity Variations Predict Seismogenic Behavior in Subduction Zones [Publisher: American Association for the Advancement of Science]. *Science*, *301*(5633), 630–633. https://doi.org/10.1126/science.1085557

Sornette, D., & Sammis, C. G. (1995):
Complex Critical Exponents from Renormalization Group Theory of Earthquakes: Implications for Earthquake Predictions [Publisher: EDP Sciences]. *Journal de Physique I*, *5*(5), 607–619. https://doi.org/10.1051/jp1:1995154

Soudarin, L., & Crétaux, J.-F. (2006):
A model of present-day tectonic plate motions from 12 years of DORIS measurements. *Journal of Geodesy*, *80*(8), 609–624. https://doi.org/10.1007/s00190-006-0090-4

Steinberger, B., & Becker, T. W. (2018):
A comparison of lithospheric thickness models. *Tectonophysics*, *746*, 325–338. https://doi.org/10.1016/j.tecto.2016.08.001

Stesky, R. M., Brace, W. F., Riley, D. K., & Robin, P. .-Y. F. (1974):
Friction in faulted rock at high temperature and pressure. *Tectonophysics*, *23*(1), 177–203. https://doi.org/10.1016/0040-1951(74)90119-X

Styron, R., & Pagani, M. (2020):
The GEM Global Active Faults Database [Publisher: SAGE Publications Ltd STM]. *Earthquake Spectra*, *36*(1_suppl), 160–180. https://doi.org/10.1177/8755293020944182

Sun, T., & Wang, K. (2015):
Viscoelastic relaxation following subduction earthquakes and its effects on afterslip determination. *Journal of Geophysical Research: Solid Earth*, *120*(2), 1329–1344. https://doi.org/10.1002/2014JB011707

Sun, T., Wang, K., & He, J. (2018):
Crustal Deformation Following Great Subduction Earthquakes Controlled by Earthquake Size and Mantle Rheology. *Journal of Geophysical Research: Solid Earth*, *123*(6), 5323–5345. https://doi.org/10.1029/2017JB015242

Sun, T., Wang, K., & He, J. (2024):
Geodetic signature of a weak Lithosphere-Asthenosphere Boundary in postseismic deformation of large subduction earthquakes. *Earth and Planetary Science Letters*, *630*, 118619. https://doi.org/10.1016/j.epsl.2024.118619

Suwa, Y., Miura, S., Hasegawa, A., Sato, T., & Tachibana, K. (2006):
Interplate coupling beneath NE Japan inferred from three-dimensional displacement field. *Journal of Geophysical Research: Solid Earth*, *111*(B4). https://doi.org/10.1029/2004JB003203

Swenson, J. L., & Beck, S. L. (1999):
Source Characteristics of the 12 November 1996 Mw 7.7 Peru Subduction Zone Earthquake. *pure and applied geophysics*, *154*(3), 731–751. https://doi.org/10.1007/s000240050250

Syracuse, E. M., van Keken, P. E., & Abers, G. A. (2010):
The global range of subduction zone thermal models. *Physics of the Earth and Planetary Interiors*, *183*(1), 73–90. https://doi.org/10.1016/j.pepi.2010.02.004

Tarantola, A. (2005):
Inverse Problem Theory and Methods for Model Parameter Estimation [Google-Books-ID: jKeHEWtzdKgC]. SIAM.

Tarantola, A., & Valette, B. (1982):
Generalized nonlinear inverse problems solved using the least squares criterion. *Reviews of Geophysics*, *20*(2), 219–232. https://doi.org/10.1029/RG020i002p00219

Tassara, A., & Echaurren, A. (2012):
Anatomy of the Andean subduction zone: Three-dimensional density model upgraded and compared against global-scale models. *Geophysical Journal International*, *189*(1), 161–168. https://doi.org/10.1111/j.1365-246X.2012.05397.x

Tassara, A., Götze, H.-J., Schmidt, S., & Hackney, R. (2006):
Three-dimensional density model of the Nazca plate and the Andean continental margin. *Journal of Geophysical Research: Solid Earth*, *111*(B9). https://doi.org/10.1029/2005JB003976

Tavera, H., & Buforn, E. (2001):
Source mechanism of earthquakes in Peru. *Journal of Seismology*, *5*(4), 519–540. https://doi.org/10.1023/A:1012027430555

Tavera, H., Buforn, E., Bernal, I., Antayhua, Y., & Vilacapoma, L. (2002):
The Arequipa (Peru) earthquake of June 23, 2001. *Journal of Seismology*, *6*(2), 279–283. https://doi.org/10.1023/A:1015698621075

Tavera, H., & Bernal, I. (2008):
The Pisco (Peru) Earthquake of 15 August 2007. *Seismological Research Letters*, *79*(4), 510–515. https://doi.org/10.1785/gssrl.79.4.510

Tavera, H., Fernández, E., Bernal, I., Antayhua, Y., Agüero, C., Rodríguez, H. S. S., Vilcapoma, L., Zamudio, Y., Portugal, D., Inza, A., Carpio, J., Ccallo, F., & Valdivia, I. (2006):
The Southern Region of Peru Earthquake of June 23rd, 2001. *Journal of Seismology*, *10*(2), 171–195. https://doi.org/10.1007/s10950-006-9014-2

Tavera, H., Fernández, E., & Cuya Crispin, Á. A. (2016):
Sismo de lampa del 1 de diciembre del 2016 (6.0 ml)(puno): Aspectos sismológicos.

Tesauro, M., Audet, P., Kaban, M. K., & Cloetingh, S. (2012):
The effective elastic thickness of the continental lithosphere: Comparison between rheological and inverse approaches. *Geochemistry, Geophysics, Geosystems*, *13*(9). https://doi.org/10.1029/2012GC004162

Teunissen, P., & Montenbruck, O. (2017):
Springer Handbook of Global Navigation Satellite Systems. Springer.

Thollard, F., Clesse, D., Doin, M.-P., Donadieu, J., Durand, P., Grandin, R., Lasserre, C., Laurent, C., Deschamps-Ostanciaux, E., Pathier, E., Pointal, E., Proy, C., & Specht, B. (2021):
FLATSIM: The ForM@Ter LArge-Scale Multi-Temporal Sentinel-1 InterferoMetry Service [Number: 18 Publisher: Multidisciplinary Digital Publishing Institute]. *Remote Sensing*, *13*(18), 3734. https://doi.org/10.3390/rs13183734

Thomson, W. (1865):
IV. On the elasticity and viscosity of metals [Publisher: Royal Society]. *Proceedings of the Royal Society of London*, *14*, 289–297. https://doi.org/10.1098/rspl.1865.0052

Tissandier, R., Nocquet, J.-M., Klein, E., Vigny, C., Ojeda, J., & Ruiz, S. (2023):
Afterslip of the Mw 8.3 2015 Illapel Earthquake Imaged Through a Time-Dependent Inversion of Continuous and Survey GNSS Data. *Journal of Geophysical Research: Solid Earth*, *128*(2), e2022JB024778. https://doi.org/10.1029/2022JB024778
e2022JB024778 2022JB024778

Torres, J.-L., Byrdina, S., Romero-Beltran, G., Garambois, S., Rivera, M., Burgisser, A., Antayhua, Y., Machacca, R., Milla, M., Tavera, H., Hering, P., & Rath, V. (2025):
Magma storage below Sabancaya volcano (Southern Peru) imaged by broad band magnetotellurics. https://doi.org/10.22541/essoar.174413843.30570228/v1

Tozer, B., Sandwell, D. T., Smith, W. H. F., Olson, C., Beale, J. R., & Wessel, P. (2019):
Global Bathymetry and Topography at 15 Arc Sec: SRTM15+. *Earth and Space Science*, *6*(10), 1847–1864. https://doi.org/10.1029/2019EA000658

Tse, S. T., & Rice, J. R. (1986):
Crustal earthquake instability in relation to the depth variation of frictional slip properties. *Journal of Geophysical Research: Solid Earth*, *91*(B9), 9452–9472. https://doi.org/10.1029/JB091iB09p09452

Uchida, N., & Bürgmann, R. (2021):
A Decade of Lessons Learned from the 2011 Tohoku-Oki Earthquake. *Reviews of Geophysics*, *59*(2), e2020RG000713. https://doi.org/10.1029/2020RG000713
e2020RG000713 2020RG000713

Vallée, M., Xie, Y., Grandin, R., Villegas-Lanza, J. C., Nocquet, J.-M., Vaca, S., Meng, L., Ampuero, J. P., Mothes, P., Jarrin, P., Sierra Farfán, C., & Rolandone, F. (2023):
Self-reactivated rupture during the 2019 $Mw = 8$ northern Peru intraslab earthquake. *Earth and Planetary Science Letters*, *601*, 117886. https://doi.org/10.1016/j.epsl.2022.117886

Van Dinther, Y., Gerya, T. V., Dalguer, L. A., Mai, P. M., Morra, G., & Giardini, D. (2013):
The seismic cycle at subduction thrusts: Insights from seismo-thermo-mechanical models. *Journal of Geophysical Research: Solid Earth*, *118*(12), 6183–6202. https://doi.org/10.1002/2013JB010380

van Dinther, Y., Preiswerk, L. E., & Gerya, T. V. (2019):
A Secondary Zone of Uplift Due to Megathrust Earthquakes. *Pure and Applied Geophysics*, *176*(9), 4043–4068. https://doi.org/10.1007/s00024-019-02250-z

van Keken, P. E., & Wilson, C. R. (2023):
An introductory review of the thermal structure of subduction zones: III—Comparison between models and observations. *Progress in Earth and Planetary Science*, *10*(1), 57. https://doi.org/10.1186/s40645-023-00589-5

Vargas-Alva, K. A., & Villegas-Lanza, J. C. (2021):
Deformación de la corteza asociada con sismicidad en el entorno de los volcanes Purupuruni y Casiri.

Vidal, M., Jarrin, P., Rolland, L., Nocquet, J.-M., Vergnolle, M., & Sakic, P. (2024):
Cost-Efficient Multi-GNSS Station with Real-Time Transmission for Geodynamics Applications [Number: 6 Publisher: Multidisciplinary Digital Publishing Institute]. *Remote Sensing*, *16*(6), 991. https://doi.org/10.3390/rs16060991

Vigny, C., Rudloff, A., Ruegg, J.-C., Madariaga, R., Campos, J., & Alvarez, M. (2009):
Upper plate deformation measured by GPS in the Coquimbo Gap, Chile. *Physics of the Earth and Planetary Interiors*, *175*(1), 86–95. https://doi.org/10.1016/j.pepi.2008.02.013

Villegas-Lanza, J. C., Chalumeau, C., Lovery, B., Sánchez-Reyes, H., Radiguet, M., Chlieh, M., & Socquet, A. (2025):
Patterns of interplate locking, microseismicity and oceanic plate structure in the southern peru subduction zone. *In prep.*

Villegas-Lanza, J. C., Chlieh, M., Cavalié, O., Tavera, H., Baby, P., Chire-Chira, J., & Nocquet, J.-M. (2016):
Active tectonics of Peru: Heterogeneous interseismic coupling along the Nazca megathrust, rigid motion of the Peruvian Sliver, and Subandean shortening accommodation. *Journal of Geophysical Research: Solid Earth*, *121*(10), 7371–7394. https://doi.org/10.1002/2016JB013080

Voigt, W. (1890):
Ueber innere Reibung fester Körper, insbesondere der Metalle. *Annalen der Physik*, *283*(12), 671–693. https://doi.org/10.1002/andp.18922831210

Völker, D., Grevemeyer, I., Stipp, M., Wang, K., & He, J. (2011):
Thermal control of the seismogenic zone of southern central Chile. *Journal of Geophysical Research: Solid Earth*, *116*(B10). https://doi.org/10.1029/2011JB008247

von Huene, R., Corvalán, J., Flueh, E. R., Hinz, K., Korstgard, J., Ranero, C. R., & Weinrebe, W. (1997):
Tectonic control of the subducting Juan Fernández Ridge on the Andean margin near Valparaiso, Chile. *Tectonics*, *16*(3), 474–488. https://doi.org/10.1029/96TC03703

Wada, I., & Wang, K. (2009):
Common depth of slab-mantle decoupling: Reconciling diversity and uniformity of subduction zones. *Geochemistry, Geophysics, Geosystems*, *10*(10). https://doi.org/10.1029/2009GC002570

Wada, I., Wang, K., He, J., & Hyndman, R. D. (2008):
Weakening of the subduction interface and its effects on surface heat flow, slab dehydration, and mantle wedge serpentinization. *Journal of Geophysical Research: Solid Earth*, *113*(B4). https://doi.org/10.1029/2007JB005190

Wallace, L. M., Fagereng, Å., & Ellis, S. (2012):
Upper plate tectonic stress state may influence interseismic coupling on subduction megathrusts. *Geology*, *40*(10), 895–898. https://doi.org/10.1130/G33373.1

Wang, D., Elliott, J. R., Zheng, G., Wright, T. J., Watson, A. R., & McGrath, J. D. (2024):
Deciphering interseismic strain accumulation and its termination on the central-eastern Altyn Tagh fault from high-resolution velocity fields. *Earth and Planetary Science Letters*, *644*, 118919. https://doi.org/10.1016/j.epsl.2024.118919

Wang, K., He, J., Dragert, H., & James, T. S. (2001):
Three-dimensional viscoelastic interseismic deformation model for the Cascadia subduction zone. *Earth, Planets and Space*, *53*(4), 295–306. https://doi.org/10.1186/BF03352386

Wang, K., Hu, Y., Bevis, M., Kendrick, E., Smalley Jr., R., Vargas, R. B., & Lauría, E. (2007):
Crustal motion in the zone of the 1960 Chile earthquake: Detangling earthquake-cycle deformation and forearc-sliver translation. *Geochemistry, Geophysics, Geosystems*, *8*(10). https://doi.org/10.1029/2007GC001721

Wang, K., Hu, Y., & He, J. (2012):
Deformation cycles of subduction earthquakes in a viscoelastic Earth [Publisher: Nature Publishing Group]. *Nature*, *484*(7394), 327–332. https://doi.org/10.1038/nature11032

Wegener, A. (1912):
Die Entstehung der Kontinente. *Geologische Rundschau*, *3*(4), 276–292. https://doi.org/10.1007/BF02202896

Wiechert, E. (1893):
Gesetze der elastischen Nachwirkung für constante Temperatur. *Annalen der Physik*, *286*(11), 546–570. https://doi.org/10.1002/andp.18932861110

Willemann, R. J., & Storchak, D. A. (2001):
Data Collection at the International Seismological Centre. *Seismological Research Letters*, *72*(4), 440–453. https://doi.org/10.1785/gssrl.72.4.440

Woods, M. T., & Okal, E. A. (1994):
The structure of the Nazca ridge and Sala y Gomez seamount chain from the dispersion of Rayleigh waves. *Geophysical Journal International*, *117*(1), 205–222. https://doi.org/10.1111/j.1365-246X.1994.tb03313.x

Xiwei, X., Wenjun, K., Tao, W., Xianbing, Z., Yuzhuo, L., Yuxuan, Z., Jizhen, Z., Kang, L., Qixin, W., Jia, C., & Junjie, R. (2025):
The Mw7.7 Myanmar earthquake: A continental longest surface-rupturing supershear cascading event [Publisher: Nature Publishing Group]. *npj Natural Hazards*, *2*(1), 73. https://doi.org/10.1038/s44304-025-00125-z

Xu, G., Xu, C., Wen, Y., & Yin, Z. (2019):
Coseismic and Postseismic Deformation of the 2016 MW 6.2 Lampa Earthquake, Southern Peru, Constrained by Interferometric Synthetic Aperture Radar. *Journal of Geophysical Research: Solid Earth*, *124*(4), 4250–4272. https://doi.org/10.1029/2018JB016572

Xu, H., & Wang, T. (2025):
A Network-Based Phase-Gradient Stacking Method for Resolving Long-Wavelength Deformation From Low-Coherence SAR Interferograms. *Journal of Geophysical Research: Solid Earth*, *130*(4), e2024JB030026. https://doi.org/10.1029/2024JB030026
e2024JB030026 2024JB030026

Yamanaka, Y., & Kikuchi, M. (2004):
Asperity map along the subduction zone in northeastern Japan inferred from regional seismic data. *Journal of Geophysical Research: Solid Earth*, *109*(B7). https://doi.org/10.1029/2003JB002683

Yamasaki, T., & Kobayashi, T. (2018):
Imaging a low viscosity zone beneath the Kutcharo caldera, eastern Hokkaido, Japan, using geodetic data. *Earth and Planetary Science Letters*, *504*, 1–12. https://doi.org/10.1016/j.epsl.2018.09.038

Yáñez-Cuadra, V., Ortega-Culaciati, F., Moreno, M., Tassara, A., Krumm-Nualart, N., Ruiz, J., Maksymowicz, A., Manea, M., Manea, V. C., Geng, J., & Benavente, R. (2022):
Interplate Coupling and Seismic Potential in the Atacama Seismic Gap (Chile): Dismissing a Rigid Andean Sliver. *Geophysical Research Letters*, *49*(11), e2022GL098257. https://doi.org/10.1029/2022GL098257
e2022GL098257 2022GL098257

Yokota, Y., Ishikawa, T., Watanabe, S.-i., Tashiro, T., & Asada, A. (2016):
Seafloor geodetic constraints on interplate coupling of the Nankai Trough megathrust zone [Publisher: Nature Publishing Group]. *Nature*, *534*(7607), 374–377. https://doi.org/10.1038/nature17632

Yunjun, Z., Fattahi, H., Pi, X., Rosen, P., Simons, M., Agram, P., & Aoki, Y. (2022):
Range Geolocation Accuracy of C-/L-Band SAR and its Implications for Operational Stack Coregistration [Conference Name: IEEE Transactions on Geoscience and Remote Sensing]. *IEEE Transactions on Geoscience and Remote Sensing*, *60*, 1–19. https://doi.org/10.1109/TGRS.2022.3168509

Zerathe, S., Lacroix, P., Jongmans, D., Marino, J., Taipe, E., Wathelet, M., Pari, W., Smoll, L. F., Norabuena, E., Guillier, B., & Tatard, L. (2016):
Morphology, structure and kinematics of a rainfall controlled slow-moving Andean landslide, Peru. *Earth Surface Processes and Landforms*, *41*(11), 1477–1493. https://doi.org/10.1002/esp.3913

Zhang, B., Zhu, W., Ding, X., Wang, C., Wu, S., & Zhang, Q. (2022):
A review of methods for mitigating ionospheric artifacts in differential SAR interferometry. *Geodesy and Geodynamics*, *13*(2), 160–169. https://doi.org/10.1016/j.geog.2021.12.001

Zhang, Z., Lou, Y., Zhang, W., Wang, H., Zhou, Y., & Bai, J. (2022):
Assessment of ERA-Interim and ERA5 reanalysis data on atmospheric corrections for InSAR. *International Journal of Applied Earth Observation and Geoinformation*, *111*, 102822. https://doi.org/10.1016/j.jag.2022.102822

List of Figures

1.1 Basic seismotectonic context in Central Andes. Major earthquake ruptures (M≥ 8) since 1868 along the Peru-Chile trench (M. E. Beck, 1998; S. L. Beck and Ruff, 1989; Dorbath et al., 1990; Silgado, 1978; Villegas-Lanza et al., 2016) are reported by white (historical) or orange (recent, 1995 or later) ellipses. Volcanoes are reported in red, and major oceanic features in white. Slab contours are depicted by black dashed lines from the Slab2 model every 20 km (Hayes et al., 2018). The Andes are wider in the vicinity of the Arica bend (500 km or more), in the dipping slab area, while they are thinner (about 300 km in the Nazca region) in the flat slab area. 9

2.1 Schematic view of an ocean-continent subduction (from the United States Geological Survey). This illustration is representative of the Peru-Chile subduction, however readers should be aware that the shape of the subducting slab or the width of the mountain range can differ. Also, not all subductions have a volcanic arc. 11

2.2 All Mw≥ 8.5 earthquakes in the world since 1900. Out of 17 events, 16 nucleated at a subduction. Plates boundaries from Bird, 2003 are reported by black lines. 12

2.3 Main tectonic plates, with their boundaries: subductions, incipient subductions, and collisions (modified from W. Schellart, 2023). Geodetic plate motion model from Kreemer et al., 2014 are reported by black vectors. Trench-normal subducting plate velocities v_{SP} are reported by dark blue vectors, while trench velocities v_T are reported by light blue vectors. The velocities are expressed in the Indo-Atlantic reference frame from O'Neill et al., 2005. 12

2.4 Schematic view of the seismic cycle for a single recurring earthquake, neglecting slow slip events and other earthquakes. The surface displacements on the overriding plate in a given direction plate are expressed along time, while an exaggerated view of the plate deformation is shown at several phases of the cycle. 13

2.5 More realistic view of the seismic cycle, with earthquakes of various magnitudes and slow slip events (SSE). The surface displacements on the overriding plate in a given direction plate are expressed along time. 15

2.6 Schematic view of a subduction segment with zero coupling (left) or non-zero coupling (right). When $\chi_i = 0$ there is no friction between the two plates and no deformation is observed, while when $\chi_i > 0$ we observe a progressive deformation of the overriding plate over time. . . 16

2.7 Figure from Métois et al., 2016 showing heterogeneous coupling on the Chile subduction. LCZ stands for *low coupling zone*. The histogram on panel *A* depicts the rate of Mw>3 earthquakes from the CSN seismic catalog during the interseismic period. Yellow stars indicate swarm-like sequences. Diamonds indicate significant intraplate earthquakes. Panel *B* is showing the variations of coupling, averaged along-dip, and the slip distributions for the Maule, Iquique, and Illapel earthquakes. Finally, panel *C* is showing the coupling distribution with the rupture areas of the Maule, Iquique, and Illapel earthquakes. Note that some areas, highlighted by white rectangles, lack resolution. Overall, coupling is varying significantly along strike and along dip. We observe lowered coupling where some oceanic features are subducting: the Iquique, the Mejillones, the Baranquilla, and the San Antonio ridges. Seismic ruptures overlap quite well with highly locked patches. 17

2.8 Figure from Villegas-Lanza et al., 2016 showing the thermal structure of the Peruvian megathrust. On the map is reported the age of the seafloor ranging from 20 to 55 Ma. In this study, the locking is mostly located between the isotherms 100°C and 300°C. 19

2.9 Figure from Avouac, 2015 illustrating the moment budget assessment using the interseismic coupling χ_i. 20

2.10 Figure from Dziewonski and Anderson, 1981 showing seismic P-wave (V_P) and S-wave (V_S) velocities according to depth. Both V_P and V_S are increasing with depth in the mantle (down to about 3,000 km), except in the low velocity zone (lower mantle, about 30 to 250 km). Then, V_P is dropping when crossing the core-mantle boundary (about 3,000 km) and V_S disappears since there is no shear in a liquid like the outer core. 23

2.11 Figure from Wada and Wang, 2009 illustrating a typical oceanic-continental subduction. The stagnant forearc, a.k.a. *cold nose*, is indicated in purple. The volcanic arc is located atop the melting point at a depth of about 100 km on the interface. Episodic slip and tremors have been observed in Cascadia and Nankai around the area indicated by the green circle. 24

2.12 Figure from Luo and Wang, 2021 illustrating the thermal (a) and rheological (b) structures of subduction zones. The cold nose is elastic, as well as the continental and oceanic lithospheres, while the continental and oceanic asthenosphere are viscoelastic (Burgers rheology). 25

2.13 Figure from Luo and Wang, 2021 showing 2-D models of postseismic deformation to emphasis the importance of the cold nose. On panel (a) are shown vertical (solid lines) and horizontal (dashed lines) postseismic displacements at five years. A model without cold nose is shown in black, a model with higher viscosity in blue, and a model with an elastic cold nose in red. The elastic cold nose is required to generate uplift atop the cold nose edge. The structure with the elastic cold nose is reported on panel (b). On panel (c) are reported the three models of panel (a) on the area delimited by dashed lines on panel (b). Panel (d) shows the effect of the cold nose edge depth on the uplift. 26

2.14 Figure from Punjab Engineering College illustrating stick-slip behavior. 27

2.15 Figure from Lay et al., 2012 indicating the four rupture domains they define (A, B, C, and D) on a megathrust. Note that it is here scaled for the subduction Northeast of Honshu. 30

2.16 Figure from Lay et al., 2012 showing a 3-D representation of the A,B,C, and D rupture domains. Areas of unstable frictional behavior are drawn in dark gray and labeled as *seismic*, while *aseismic* regions are in white. Medium gray indicate regions that exhibit stable sliding, except when adjacent seismic patch rupture. Slow-slip events and seismic tremors can happen in domain D. 31

2.17 Linear elasticity on a strain vs. stress diagram when applying an axial compressive force F on an object. 32

2.18 Linear elasticity on a strain vs. stress diagram when applying a shear force F on an object. 33

2.19 Strain vs. stress diagram when applying an axial compressive force F on an object. First, the object deforms elastically, but past a certain threshold known as the yield point, it enters the plastic deformation regime. Permanent deformation is acquired in the plastic regime, meaning that the object will not return to its initial shape after releasing the stress. 34

2.20 Maxwell, Kelvin-Voigt, and Burgers viscoelastic models. By attaching a Maxwell fluid to a Kevin-Voigt solid, we form a Burgers body. 36

2.21 Stress and strain evolution along time during creep or relaxation, for Maxwell, Kelvin-Voigt, and Burgers viscoelastic models. 37

2.22 *Left:* Major earthquake ruptures (M≥ 7.5) since 1868 along the Peru-Chile trench (M. E. Beck, 1998; S. L. Beck and Ruff, 1989; Dorbath et al., 1990; Silgado, 1978; Villegas-Lanza et al., 2016). Volcanoes are reported in red, major cities in black, and major oceanic features in white. Slab contours are depicted by gray dashed lines from the Slab2 model every 20 km (Hayes et al., 2018). *Right:* Thrust seismicity from gCMT (Dziewonski and Anderson, 1981; Ekström et al., 2012) since 1976, down to 100 km deep, and color-coded by depth. The magnitude of completeness is about 5.2. Plotting thrust events only should be more representative of the plate interface seismicity than plotting all mechanisms, however not all events are on the interface. The seismicity tends to be higher where large earthquakes happened during the observation period because of the aftershock and foreshocks sequences, this is clearly observed for the 2014 Mw8.1 Iquique earthquake. Still, two gaps of seismicity are observed in Chile: one from 21°S to 23°S, and one from 34.5°S to 35.5°S. In Peru, less seismicity is observed in the Northern part. 40

2.23 Figure from Armijo et al., 2010 showing the topography and the main tectonic features at two profiles: one in Northern Chile at 20°S (profile A), and one in Central Chile close at the latitude of Santiago (33°S, profile B). Profile A corresponds to an area where the Andes are very wide compared to profile B. Triassic and pre-Triassic continental basement are colored in brown, post-Triassic basins in yellow, and oceanic crust in blue on the profiles. 44

2.24 Main continental slivers used in geodetic studies over the Peru-Chile trench, with their respective velocities relative to South America: North Andean sliver (NAS, orange) from Nocquet et al., 2014, Western (magenta) and Eastern (green) Peruvian slivers (PS) from Villegas-Lanza et al., 2016, and Andean sliver (royal blue) from Métois et al., 2016. Main active faults are reported as red lines from the GEM Active Faults Database (Styron and Pagani, 2020) and the Chilean Database of Active Faults (Maldonado et al., 2021). The Eastern boundaries of the Eastern PS and Andean sliver are following the East Andean thrust-belt. Note that the Peruvian slivers were defined in a study focused on Peru, while the Andean sliver was defined for Chile, so their South and North boundaries respectively are defined arbitrary. When considering the whole Central Andes, none of these solutions are fully satisfying. . . . 45

2.25 Figures from Norabuena et al., 1998 showing the GNSS network they used (left) with the crustal deformation model they proposed (right). . 47

2.26 Figures from Gagnon et al., 2005 showing the location of the seafloor geodesy arrays (left) and the various surface deformation models they propose with various locking depths. There data required shallow locking close to the trench. 48

2.27 Figure from Chlieh et al., 2011 showing their interseismic coupling model for Central-South Peru and North Chile, with 4 mm/yr of Subandean shortening. The coupling is very high and almost uniform on the Chilean segment, while it is highly heterogeneous in Peru, with low coupling where the Nazca ridge and NFZ are subducting. However, it should be noted that the data are significantly sparser in Peru. 49

2.28 Figure from Nocquet et al., 2014 showing the coupling distribution in Northern Peru. The model on panel *a* shows full creeping from 3°S to 10°S, while the model on panel *c* shows shallow coupling close to the trench. This difference results from the different slip priors in the inversion: creeping slip prior (zero coupling) for panel *a* and locked slip prior for panel c. The slip prior has an impact in the areas with poor resolution, notably close to the trench because of the remoteness of the GNSS sites (no offshore GNSS). Finally, panel *b* shows the same model as panel *a* with some coseismic ruptures, including the 1960 Mw7.6 and 1996 Mw7.5 tsunami earthquakes in North Peru (blue contours). 51

2.29 Figure from Villegas-Lanza et al., 2016 showing their coupling distribution from the inversion of over 100 GNSS sites in Peru, with a two-plate model. Residuals from the inversion are depicted by the blue arrows, and are also reported on the rose. They are relatively high and most of them are oriented in the South-East quarter. 52

2.30 Figure from Villegas-Lanza et al., 2016 showing the coupling distribution with the three-plate model (panel *a*), accounting for a sliver motion. The observed and predicted interseismic GNSS displacements are displayed as black and green vectors respectively. The residuals on the rose are now uniformly distributed in direction, and most of them are below 2 mm/yr. On panel *b* is shown the predicted displacement of the sliver. 53

2.31 Figure from Villegas-Lanza et al., 2016 indicating the continental slivers involved in the partitioning of the deformation on the Peruvian margin: the North Andean Sliver (NAS) from Nocquet et al., 2014, the Peruvian Sliver (PS), and the Eastern Cordillera - Subandean region. Velocities are expressed in the SSA reference frame, in mm/yr. 54

2.32 Figure modified from Chlieh et al., 2004 showing the fit of the interseismic model to the GNSS and InSAR data. On the left panel, dotted lines indicate the 35 (boundary between full locking and the transition zone) and 55 (boundary between the transition zone and the creeping zone) km isodepth contours. On the right panel the fit to InSAR and GNSS data along a profile at 22°S. 55

2.33 Figure from Métois et al., 2014 showing their observed interseismic velocities (black vectors) on a map, along with two previously published datasets (CAP in orange and SAGA in blue), in the SSA reference frame. The Eastern boundary of the Andean sliver is indicated by the black dotted line. Six profiles are plotted (panels *a* to *f*) to show the agreement between the GNSS velocities (dots) and the deformation model with a two-plate (black line) or three-plate model (orange line). The three-plate model fits better the sites in the far range, although it is more difficult to state for the Northern profiles due to the sparsity of the data. 57

2.34 Figure from Métois et al., 2014 reporting the observed vertical GNSS velocities. Subsidence is indicated in blue while uplift is in red. cGNSS stations are surrounded by a black contour. Three profiles (a, b, c) are shown with the two-plate model in black and the three-plate model in red. The authors argue that the three-plate model fits better the vertical displacements, which is somewhat questionable. Actually, only the near range sites on profile *a* and the and the sites of profile *b* appear to be better fit but with still a significant misfit. 58

2.35 Figure from Métois et al., 2014 showing the interseismic coupling distributions for a two-plate (a) or a three-plate (c) model, with their associated residuals on panels (b) and (d) respectively. Areas with low resolution are indicated in gray. Overall, most of the residuals appear to be lowered by adding the third plate, as well as the average coupling. 59

2.36 Figure from Métois et al., 2016 showing the horizontal interseismic velocities in the SSA reference frame. Data processed by the authors (in black) are complemented with other velocity fields (CAP, SAGA, and Brooks et al., 2011) for a total of 396 sites. Note that a major gap remains in the Taltal area. 60

2.37 Figure from Métois et al., 2016 showing heterogeneous coupling on the Chile subduction. The histogram on panel *A* depicts the rate of Mw>3 earthquakes from the CSN seismic catalog during the interseismic period. Yellow stars indicate swarm-like sequences. Diamonds indicate significant intraplate earthquakes. Panel *B* is showing the variations of coupling, averaged along-dip, and the slip distributions for the Maule, Iquique, and Illapel earthquakes. Finally, panel *C* is showing the coupling distribution with the rupture areas of the Maule, Iquique, and Illapel earthquakes. Note that some areas, highlighted by white rectangles, lack resolution. Overall, coupling is varying significantly along strike and along dip. We observe lowered coupling where some oceanic features are subducting: the Iquique, the Mejillones, the Baranquilla, and the San Antonio ridges. Seismic ruptures overlap quite well with highly locked patches. 61

2.38 Figure from Klein et al., 2018 showing their best coupling model (c), with along strike variations (b) when integrated down to 30 (red), 40 (dark red), or 60 (black) km. We observe a low-coupling anomaly where the Salas & Gomez ridge is subducting. Major earthquake ruptures are reported on panel (d). Variations of coupling along deep averaged on two segments are reported on panel (a). It shows that on the Northern segment (red) the depth of maximum locking is about 20 km, while it is about 30 km on the Southern segment. 62

2.39 Figure from Yáñez-Cuadra et al., 2022 showing their interseismic coupling distribution (a) with its along-strike variations (b) integrated between 0 and 40 km (blue) or between 40 and 70 km (orange). Panel (c) shows posterior coupling correction lengths. Panel (d) shows the modeled surface velocities for their interseismic coupling model and panel (e) the regional motion model. Finally, panel (f) shows the residuals. . . 64

2.40 Figure from Jolivet et al., 2020 showing the coupling distribution they obtained by inverting interseismic GNSS velocities from Métois et al., 2016 and Envisat InSAR time series. The colored discs indicate the holocene uplift rates from Melnick, 2016. 65

2.41 Figure modified from M. Moreno et al., 2011 showing on panel *a* the GNSS velocities in the SSA reference frame. On panel *b* is shown the structure of the FEM model they use, with the Young's modulus E, the Poisson's ratio ν, and the viscosity η (for viscoelastic blocks only). Four blocks are defined: slab and continental crust (elastic), oceanic and continental mantle (viscoelastic). 67

2.42 Figure modified from M. Moreno et al., 2011 showing on panels *a* to *d* the coupling distributions for a range of uniform continental mantle viscosity from 2 to $5{\cdot}10^{19}$ Pa·s. We observe that the more viscous is the rheology, the smaller is the coupling because of the smaller postseismic displacements to correct. On panel *e* is shown their best model of coupling, with a viscosity ranging from $3{\cdot}10^{19}$ Pa·s in the South to $4{\cdot}10^{19}$ Pa·s in the North. On panel *f* is plotted the tradeoff curve for the smoothing parameter. 68

2.43 Figure modified from S. Li et al., 2015 showing the structure of their FEM subduction model (a). They shaped their model from the slab contours and continental moho. The meshing is shown on panel (b), with finer cells close to the slab and upper surface. Four blocks are defined (c): elastic oceanic and continental plates, and viscoelastic oceanic and continental mantles. 69

2.44 Figure from S. Li et al., 2015 illustrating the viscoelastic effects on the horizontal (a) and vertical (b) surface deformation. The elastic and viscoelastic interseismic models are depicted by the blue and red lines respectively, while the green line shows the difference between the two and so the viscoelastic effects. Larger horizontal displacements, especially in the inland region are observed with viscoelastic rheology. The subsidence and uplift peaks are also larger with viscoelasticity, and a second zone of subsidence as well as a second zone of uplift in the far-field appear. 70

2.45 Figure from S. Li et al., 2015 showing a comparison of the misfit curves from forward elastic (blue) and viscoelastic (red) models, on all the sites (a) or restricted to the back-arc (b). The WRMS misfit values are computed from the horizontal GNSS observations. We observe that the misfit is lowered by introducing viscoelasticity, especially in the back-arc. In addition, the optimal locking depth is lowered from about 55 to 42 km. 71

2.46 Figure modified from S. Li et al., 2015 showing the slip distribution and interseismic coupling distributions they obtained with an elastic (a, c) or viscoelastic (b, d) model. Observed and modeled horizontal velocities are depicted by the red and blue vectors respectively on panels (a) and (c). Residuals are indicated by the black vectors on panels (b) and (d). We observe a shallower locking depth, as well as lowered residuals with viscoelasticity. 72

3.1 Measuring Earth surface displacements with GNSS on the overriding plate at a subduction zone (modified from K. Wang et al., 2012). 74

3.2 Figure from the CNES showing the basic acquisition scheme of DORIS. Transmitters on the ground are communicating with receivers onboard of satellites. A control center is continuously monitoring the network. 75

3.3 Application of InSAR to measure ground deformation (Modified from B. Zhang et al., 2022). An electromagnetic wave is sent toward the ground by the radar equipment onboard of the satellite, and the back-scattered signal is received. By measuring the phase shift between successive passes, one can compute the displacement in the line-of-sight. For Sentinel-1 satellites, the wavelength is 5.55 cm and the swath width is 250 km. 76

3.4 Figure from Xiwei et al., 2025 showing Sentinel-2 optical acquisitions before (a) and after (b) the 2025 Mw7.7 Myanmar earthquake. By pixel tracking they measured an horizontal offset of more than 4 meters, that can easily be seen on the road profiles. Note the difference in colors between the two acquisitions, probably due to different weather conditions. 77

3.5 Figure from Boudin et al., 2022 showing a long-base hydraulic tiltmeter installed in a mine in North Chile. Two water leveling sensors are monitoring the fluid transfer along the 38-meter long tube. 78

3.6 Illustration of the triangulation principle used to locate a GNSS receiver in space: the travel time, and so the distance, between each satellite and the receiver is computed. The intersection of the three circles gives the receiver location (from Teunissen and Montenbruck, 2017). 80

3.7 Linearly polarized electromagnetic wave propagating along the z-axis. The electric field E (blue) is oriented along the x-axis, while the magnetic field B (red) is oriented along the y-axis. 81

3.8 Main sources of error for static GNSS measurements: satellites orbits error, receiver and satellite clock errors, ionospheric delay, tropospheric delay, multi-paths error due to indirect reflected paths, and phase center error on the antenna's solenoid depending on the incidence angle. . 83

3.9 GNSS network used in this PhD thesis. The coordinates and measurement periods of every GNSS sites are reported in the annexes of this manuscript (Tables 9.1 to 9.11). 85

3.10 GNSS and seismic sites serviced during the field operations in Fall 2024. The low-cost cGNSS have been installed to replace some survey sites. . 86

3.11 Typical setup for a cGNSS station. Here is shown a low-cost one with Septentrio mosaic-X5 GNSS receivers and ArduSimple antennas (setup similar to Vidal et al., 2024), but other cGNSS station use a similar setup, apart from more advanced antennas and receivers. The GNSS receiver is installed in a metallic case, sheltering it from the external elements (rain, sun, wind, dust...). The equipment is powered by a 12-volt lead-acid battery that is charged during the day by a solar panel. A power inverter converts the direct current from the solar panel and the battery to alternative current. The GNSS antenna is installed a few meters from the case in order to mitigate multi-paths errors. The cGNSS sites have the antenna screwed into the ground with a metallic rod. 87

3.12 The ATIC cGNSS station installed close to the Atico city (between Chala and Camaná), installed by Caltech and now operated by IGP. Note that the antenna is equipped with a radome to mitigate wear and tear. 88

3.13 Typical setup for a sGNSS site. Compared to a cGNSS site, there is no solar panel and the case is made of plastic in order to be lighter to carry. This site has a screw pitch were we can screw the antenna with a metallic rod. 89

3.14 The three ways of installing the antenna for a sGNSS site: metallic rod with screw pitch, bipod, and tripod. If the site is already equipped with a screw pitch in the ground, one just have to screw the antenna with a metallic rod in the screw pitch. Otherwise, if there is just a marker, it is necessary to use either a bipod or a tripod to center and level the antenna above the marker. The bipod or tripod is then secured with some stones. 90

3.15 Differential GNSS (D-GNSS) vs. Precise Point Positioning (PPP). With the D-GNSS method, the stations are processed by batch. The various paths between multiple satellites and multiples receivers (here the paths 1a, 1b, 2a, and 2b) are used to cancel the satellite and receiver clocks errors. Each station of the network is referenced relative to reference stations. For PPP, we use correction tables provided by analysis centers to correct for the errors. Each station is processed independently and get an absolute location. 91

3.16 Illustration from UCLA of the Doppler effect: an electromagnetic wave transmitted from a receding object has its wavelength increased, while it is reduced to an approaching object. This effect can be observed on stars: the receding stars are *red-shifted*, while the approaching ones are *blue-shifted*. 94

3.17 *Ascending* and *descending* orbits geometries for the Sentinel-1 SAR satellites. The travel direction is indicated by the red arrow, while the blue arrow corresponds to the line-of-sight (LOS) vector. Sentinel-1 is a *right-looking* satellite while some others are *left-looking*, and some even have the capability to look in both directions (like ALOS-2). Sentinel-1 orbits are tilted by about 8 degrees from the North-South axis. 96

3.18 Acquisition geometry for the Sentinel-1 SAR satellites. The flight direction is indicated by the red arrow, while the line-of-sight (LOS) vector is indicated in blue. The look angle for Sentinel-1 in IW mode (most common acquisition mode, used in this PhD) is varying from 29° in near range to 46° in far range. 97

3.19 Figure from NASA showing the principle of synthetic aperture: it relies on the displacement of the satellite to measure successive backscattered pulses, increasing the antenna aperture. 98

3.20 Chirp radar signal in time (left) and frequency (right) domains. 98

3.21 Amplitude (left) and phase (right) information of one subswath of a Sentinel-1 acquisition over the Ridgecrest area (California) on 2019-07-16, in radar geometry (processed with NSBAS). The amplitude image allows to see some patterns in the terrain geometry, while the phase information without interferometry is useless. 100

3.22 Non-exhaustive chronology of the main SAR satellites launched since the 1990's. Several constellations are still operating today, in 2025, so we reported the estimated operational periods from their respective operators. Note that NISAR is the only SAR satellite with dual-frequency capability (L-band and S-band) but it is going to operate primary with the L-band equipment. 101

3.23 Artistic depiction from the ESA Medialab of a Sentinel-1 satellite acquiring over the Earth. The radar antenna is 12.3 m by 82 cm large and is acquiring on the right of the satellite in its travel direction. Note that the acquisition mode on the illustration just switched from *interferometric wide swath* (IW) mode to *wave* (WV) mode. 104

3.24 Figure from ESA showing the four acquisition modes of Sentinel-1: *stripmap* (SM), *interferometric wide swath* (IW), *extra-wide swath* (EW), and *wave* (WV). The main operational mode over continents is IW, that was used for all the SAR acquisitions used in this PhD thesis. 105

3.25 Figure modified from Monti-Guarnieri et al., 2017 showing the TOPSAR acquisition technology used by Sentinel-1 in IW and EW modes. The swath is divided into three subswaths along the range direction, and bursts are acquired cyclically, forward and backward, over the three subswaths. Bursts are about 4 km, with enough overlap to reconstitute the image smoothly. 106

3.26 Thanks to interferometry, the phase information of Figure 3.26 at epoch 2019-07-16 can now be used with the phase information from another epoch 2019-07-04 to compute an interferogram, showing the differential phase between the two epochs. This interferogram is projected in terrain geometry, on two subswaths. We observe close-set fringes in the middle, caused by the coseismic ground displacement associated with the Mw7.1 Ridgecrest earthquake that happened on 2019-07-05. . 107

3.27 Geometric distortions that can occur with SAR acquisitions: foreshortening (left), layover (middle), and shadow (right). 109

3.28 Figure from Bausilio et al., 2024 showing foreshortening, layover, and shadow effects on a SAR COSMO-SkyMed acquisition. 109

3.29 Figure modified from Yunjun et al., 2022 showing the annual median of vertical TEC (vTEC) in 2014 which corresponds to a solar maximum (a, b), and in 2019 which corresponds to a solar minimum (c, d). They are reported for 6 am (a, c) and 6 pm (b, d) solar times. It shows that vTEC is maximized at a solar maximum, and at 6 pm compared to 6 am. In addition, vTEC is significantly higher in the equatorial region (about three times higher in Ecuador than in France). 111

3.30 Figure modified from B. Zhang et al., 2022 showing an example of ionospheric artifacts on an InSAR interferogram. 112

3.31 Figure from Jolivet et al., 2011 illustrating tropospheric delay on an interferogram. (a) Wrapped interferogram from ENVISAT acquisitions over Himalaya, in radar geometry. (b) Tropospheric correction computed from the ERA-I global atmospheric model. The black crosses indicate the ERA-I grid nodes. (c) Interferogram corrected from the tropospheric contribution. (d) SRTM digital elevation model. (e) Observations (top, black dots), tropospheric ERA-I predictions (middle, red dots), and residuals after tropospheric correction (bottom, gray dots) for local phase-elevation ratios. The dashed line shows zero mean phase-elevation ratio. We observe that the residuals are distributed close to the dashed line, meaning that they removed most of the elevation-correlated tropospheric signal. (f) Observed (x-axis) vs. predicted from the ERA-I model (y-axis) phase-elevation ratios. The red dashed line indicates the unit correlation. We observe a relatively significant correlation (coefficient of 0.67). 113

3.32 Footprints for the ascending (left) and descending (right) Sentinel-1 tracks processed in the frame of the FLATSIM Central Andes project. . 114

3.33 Temporal coherence, from 0 (no coherence) to 1 (perfect coherence). Most of the area westward of the Cordillera show a good coherence because of low vegetation. 116

3.34 Mean velocity maps (2015-2021) in the line-of-sight (LOS) from FLATSIM, prior to any post-processing. Displacements are expressed positive when going away from the satellite. 117

3.35 The typical NSBAS workflow, from the SAFE products to geocoded interferograms. 119

3.36 Figure modified from Augier, 2011 describing the process of unwrapping interferograms. The idea is to recover the actual displacement between the two acquisitions by summing the phase cycles. Unwrapping is performed progressively from a starting point with a high coherence. 120

3.37 Interferogram network for the FLATSIM Central Andes A018NORD track. Each acquisitions (blue dots) are reported according to their respective epoch (x-axis) and perpendicular baseline (y-axis). Interferograms (black lines) are computed from acquisition pairs on short and long temporal baselines. 121

3.38 Figure from Thollard et al., 2021 showing the processing steps in NSBAS for computing filtered atmospheric-corrected unwrapped interferograms: computing interferograms from two SLC acquisitions, multilooking, computing atmospheric phase screen (APS) from the ECMWF ERA5 global model, unwrapping, filtering, and computing the spatial coherence. 122

3.39 Figure from Thollard et al., 2021 illustrating the time series products. Interferograms with various temporal baselines are inverted into displacement time series, and some auxiliary products are provided: maps of the number of interferograms per pixel, root mean square, and temporal coherence. Then, mean velocity maps are computed through pixel-wise linear regression of the time series cube. 123

3.40 Figure from Radiguet et al., 2016 showing *L-curves* used to select the damping parameter (left). The data misfit (χ^2 and the associated average Euclidean norm of the slip vectors for each value of the damping parameter σ_m. The selected value, encircled in black, is chosen in the hollow part of the curve where the absolute value of the second derivative is the highest. On the right is shown the misfit in function of the selected convergence angle, they simply select the value for which the misfit is the lowest. 126

3.41 Diagonal values of the resolution matrix R (left) and restitution (right) on the slab, for the final interseismic model shown in Chapter 4. Whereas the diagonal elements of R inform us about how much the slip of a specific patch is accurately mapped on this patch by the program, the restitution informs us if this slip has been correctly projected onto other patches. We observe distinctly an edge effect near the 60-km iso-depth where the patches have a higher restitution because of the slip confinement, since the displacements on the stations more inland are mainly accommodated by these deep patches. 127

3.42 3-D FEM model of the subduction zone in Southern Peru and Northern Chile. The slab is shaped by the Slab2 contours (Hayes et al., 2018), while bathymetry and topography come from SRTM15+ (Tozer et al., 2019). The mesh is 2,000 by 2,000-km wide and 1,000-km deep, using tetrahedral geometry. The cells are 5-km large close to the fault and the GNSS stations (white dots), and up to 100-km large at the external boundaries. 130

3.43 Generalized Maxwell with three Maxwell elements, characterized by their respective shear modulus μ and viscosity η, and a spring in parallel. 131

3.44 A Burgers body in the Kelvin (left) and Maxwell (right) formalisms, each spring and damper is characterized by their shear modulus μ or their viscosity η respectively. Note that the values of shear modulus and viscosity are not the same in the Kelvin and Maxwell formalisms (e.g., $\mu_{1M} \neq \mu_{1K}$). 132

7.1 Footprints for the ascending (left) and descending (right) Sentinel-1 tracks processed in the framework of the FLATSIM Andes project. On the left panel are reported the GNSS sites as blue triangles (Socquet et al., 2023), the slab contours every 20 km as gray dashed lines (Hayes et al., 2018), and the main earthquakes affecting the area. The slip distributions for the 2001 Arequipa and 2014 Iquique earthquakes are reported from Lovery et al., 2024, from Béjar-Pizarro et al., 2010 for the 2007 Tocopilla earthquakes, and from Chlieh et al., 2011 for the 1995 Antofagasta earthquake. The epicenters of the 2016 Lampa and 2018 Acari earthquakes are reported from the ISC seismic catalog (Bondár and Storchak, 2011). On the right panel are reported the Holocene volcanoes in red, the major cities as black dots, and the main active faults as solid dark burgundy lines from the GEM Active Faults Database (Styron and Pagani, 2020) and the Chilean Database of Active Faults (Maldonado et al., 2021). 315

7.2 Temporal coherence, from 0 (lost coherence) to 1 (perfect coherence) for ascending (left) and descending (right) tracks. Most of the area westward of the Cordillera shows a good coherence because of low vegetation, while we lose the coherence in the Subandean regions. . . . 318

7.3 InSAR mean velocity maps on the 2015-2021 period in the line-of-sight (LOS) after referencing from GNSS for ascending (left) and descending (right) tracks. Positive velocities (blueish colors) indicate an elongation of the satellite to ground distance, while negative velocities (reddish colors) indicate a shortening. Average GNSS velocities on the same period are displayed by red vectors, while the projections into LOS are reported within black circles. One-meter slip contours for the 2007 Pisco, 2001 Arequipa, and 2014 Iquique earthquakes are reported as solid black lines from North to South. The epicenter of the 2018 Acari earthquake is indicated by the orange star. 320

7.4 East (left) and up (right) InSAR mean velocity maps on the 2015-2021 period after decomposition. Average East (left) and Up (right) GNSS velocities on the same period are reported within black circles. One-meter slip contours for the 2007 Pisco, 2001 Arequipa, and 2014 Iquique earthquakes are reported as solid black lines from North to South. The epicenter of the 2018 Acari earthquake is indicated by the orange star. . 321

7.5 Cross-sections (a, b, c, d, e, f, g, h) along the Peru subduction, on the InSAR mean East (left) and Up (right) velocities. InSAR data within 100-km wide boxes are displayed as light blue dots on the cross-sections, with the median and quarters indicated by thick and thin solid blue lines respectively. The average GNSS velocities and associated uncertainties projected in LOS are in red. The topography is indicated by the light gray line. 326

7.6 Cross-sections (a, b, c, d, e, f, g, h) along the Chile subduction, on the InSAR mean East (left) and Up (right) velocities. InSAR data within 100-km wide boxes are displayed as light blue dots on the cross-sections, with the median and quarters indicated by thick and thin solid blue lines respectively. The average GNSS velocities and associated uncertainties projected in LOS are in red. The topography is indicated by the light gray line. 327

7.7 Cross-sections (a, b, c, d, e, f) across the main Cuzco fault, on the InSAR mean East (left) and Up (right) velocities. InSAR data within 50-km wide boxes are displayed as light blue dots on the cross-sections, with the median and quarters indicated by thick and thin solid blue lines respectively. The topography is indicated by the light gray line, the fault locations (Styron and Pagani, 2020) by vertical dark gray lines, and the average GNSS velocities by the red dots. On some profiles (a, b, c, d) an arctangent model of East displacement on the Cuzco fault is displayed as a dashed black line. The corresponding locking depth D and the velocity shift A across the fault are reported next to the profile. 330

7.8 Cross-sections (a, b, c, d, e, f) across the Cordillera Blanca, on the InSAR East (left) and Up (right) velocity maps. InSAR data within 50-km wide boxes are displayed as light blue dots on the cross-sections, with the median and quarters indicated by thick and thin solid blue lines respectively. The topography is indicated by the light gray line, the fault locations (Styron and Pagani, 2020) by vertical dark gray lines. 331

7.9 Referenced InSAR mean velocity map in LOS on the 2015-2021 period, for descending tracks in South Peru. The reddish pattern close to the coast indicates significant displacement toward the satellite, mostly related to the interseismic locking near the coast. We also observe the coseismic (and maybe some postseismic) displacements associated to the Mw6.2 Lampa crustal earthquake (December 1 2016) and to the Mw7.1 Acari subduction earthquake (January 14 2018) (c), as displayed by a clear offset in the time series at the dates of the earthquakes. The sustained inflation of the Sabancaya volcano (d) is also very noticeable, as well as the abrupt inflation of the Casiri volcano starting in 2020 (e). We observe a sliding at the Huanca-Sancos city (a) affected by several transient displacements. The slip distribution for the 2001 Mw8.4 Arequipa earthquake is reported from Lovery et al., 2024 by 1-meter black contours. The epicenter of the 2018 Acari earthquake is reported from the ISC seismic catalog (Bondár and Storchak, 2011). Main active faults from the GEM Active Faults Database (Styron and Pagani, 2020) are reported as solid black lines. Slab contours (gray dashed lines) are reported every 20-km depth, from the Slab2 model (Hayes et al., 2018). InSAR time series (averaged on 4 pixels) at the corresponding locations indicated by the red crosses are reported as insets for the various events. 333

7.10 *Top:* Mean velocity maps in LOS for the ascending A120 (left) and descending D098 (right) tracks, zoomed on Huanca-Sancos. The AY03 GNSS station is located in the city. *Bottom:* InSAR displacement time series in LOS for the ascending A120 (red) and descending D098 (green) tracks at two locations: point 1 (left) is located at the position of the AY03 GNSS station in the Huanca-Sancos city center, while point 2 is located on the Eastern flank of the valley across the river. The GNSS time series at AY03, projected in LOS for the A120 and D098 geometries, are reported in blue and cyan respectively. 336

7.11 InSAR mean velocity maps on the 2015-2021 period in LOS, referenced and corrected from the 2001 Mw8.4 Arequipa and 2014 Mw8.1 Iquique earthquakes postseismic displacements, and from the 2018 Mw7.1 Acari earthquake coseismic step. GNSS velocities on the same period are reported within black circles. 338

7.12 Variation of reduced chi-square in function of the tectonic angle, defined anti-clockwise from the East vector. We retain an angle of 17 degrees, for which the reduced chi-square is the lowest (highlighted in red). 339

7.13 Adjustment of the damping factor σ_m for various correlation lengths λ. The Manhattan distance (L1 norm) and the associated reduced chi-square are reported on the x and y axis respectively. We retained the parameters λ = 20 km and $log_{10}(\sigma_m)$ = -1.1, highlighted in red. 340
7.14 Variation of reduced chi-square in function of the relative weight of GNSS vs. InSAR. We retained a weighting of 60% for GNSS, for which the total misfit is the lowest (highlighted in red). 340
7.15 Interseismic coupling distribution from our inversion of GNSS-only interseismic velocities. Slab contours (dashed lines) are reported every 20-km depth, from the Slab2 model (Hayes et al., 2018). The approximate rupture area of the 2001 Mw8.4 Arequipa is reported from Lovery et al., 2024, while the 2007 Mw8.0 Pisco earthquake rupture is reported from Chlieh et al., 2011. Observed and modeled interseismic velocities are reported by red and blue vectors respectively. 341
7.16 Interseismic coupling distribution from joint inversion of GNSS and InSAR interseismic velocities. Slab contours (dashed lines) are reported every 20-km depth, from the Slab2 model (Hayes et al., 2018). The approximate ruptures of the 2001 Mw8.4 Arequipa and 2007 Mw8.0 Pisco earthquakes are reported from Lovery et al., 2024 and Chlieh et al., 2011 respectively. LOS velocities at InSAR discretized sites are reported by the *jet* colormap for data, model, and residual. Horizontal velocities at GNSS sites are reported by black vectors for data, model, and residual. The epicenter of the 2018 Acari earthquake is reported from the ISC seismic catalog (Bondár and Storchak, 2011) as an orange star. 342
7.17 Residual velocities in LOS from the inversion of interseismic velocities shown on Figure 7.16, for ascending (left) and descending (right) tracks. Major faults from Styron and Pagani, 2020 are depicted by black lines. The boundaries of the Peruvian Sliver from Villegas-Lanza et al., 2016 are depicted by magenta dashed lines. The epicenter of the 2018 Acari earthquake is reported from the ISC seismic catalog (Bondár and Storchak, 2011) as an orange star. 345

Chapter 9

Annexes

Table 9.1: Measurements at survey GNSS sites. In the fifth column are indicated all measured years for each site, with the number of days recorded between parentheses.

Site	Long.	Lat.	Alt. (m)	Measurements
AMOQ	-71.55	-17.25	224	2012(3),2013(4),2015(3),2016(1),2018(5),2022(5)
ANTE	-71.05	-17.47	1363	2013(3),2015(4),2018(4),2022(3),2024(3)
AQUC	-72.44	-16.52	1045	2012(3),2015(2),2018(3),2022(5),2024(4)
AUCA	-73.97	-14.27	3329	2019(3)
AUQS	-75.81	-13.69	613	2019(4),2022(8),2024(5)
AYRO	-69.88	-17.75	4466	1994(5),1996(4),1999(6),2001(6),2014(2)
BAJO	-70.35	-16.95	5142	1994(5),1996(4),1999(5),2001(7),2012(3),2014(2)
BASU	-74.02	-16.0	46	2012(4),2013(7),2015(6),2018(4),2022(3)
CALA	-73.27	-16.32	881	2012(3),2013(4),2015(6),2018(4),2022(5),2024(3)
CAMI	-70.84	-17.68	482	2012(2),2013(3),2014(3),2015(1),2016(5),2018(4),2022(4),2024(4)
CANA	-73.93	-13.99	3653	1994(4),1996(4)
CATA	-72.04	-17.02	85	2012(4),2013(3),2016(4),2018(7),2022(4)
CERI	-70.64	-15.69	4191	2012(3),2015(4),2018(5),2022(4),2024(3)
CHIL	-70.44	-16.7	4496	2012(3),2014(5),2018(7),2022(4),2024(4)
CHVA	-73.85	-14.97	3691	2019(4),2022(3),2025(4)
CLEM	-71.17	-17.28	1526	2012(3),2013(3),2015(4),2016(3),2018(4),2022(3),2024(4)
CLLA	-73.92	-14.48	4193	2019(4),2022(3),2025(5)
CMOR	-70.66	-18.05	223	1994(5),1996(4),1999(4),2001(10),2009(4),2012(3),2014(2),2015(2),2016(3),2018(4),2022(4),2024(3)
COLL	-69.08	-16.6	3974	2012(3),2014(3),2015(1),2018(5),2022(5),2024(4)
COMA	-68.44	-17.04	4161	1994(5),1996(3),1999(3),2001(4)
COND	-69.68	-16.57	4210	2012(3),2014(2),2015(3)
CRMA	-72.3	-16.47	1309	2012(4),2013(4),2015(1),2018(3),2022(4),2024(4)
CRVL	-73.43	-15.76	2620	2012(2),2013(3),2015(6),2018(4),2022(3)
CRVU	-73.56	-15.48	3514	2019(3),2022(5),2024(3)
GORD	-72.68	-16.64	323	2012(3),2015(3),2018(2),2022(5),2024(4)
GUER	-72.01	-16.81	1294	2012(3),2013(3),2015(3),2016(4),2018(4),2022(4),2024(4)
HLLH	-74.71	-14.84	2399	2019(4),2022(4),2025(6)
HUAN	-75.21	-12.13	3381	1994(5),1996(6)
INCU	-73.57	-15.24	3340	2019(4),2022(2),2024(2)
INHU	-73.75	-15.25	3342	2019(4),2022(2),2025(3)
ISLC	-75.24	-13.24	4565	2019(2),2022(7),2025(4)
JAGU	-72.86	-16.52	224	1994(5),1996(4),1999(5),2001(9),2009(4),2012(3),2018(4)
JULI	-69.44	-16.2	4158	2012(4),2014(2),2015(4),2022(5),2024(4)
LAGN	-74.45	-14.47	4280	2019(3),2022(10),2025(7)
LLAC	-75.07	-13.91	4028	2019(4),2022(7),2025(4)
LMPA	-70.35	-15.33	4006	1994(5),1996(4),1999(6),2001(6)
MACU	-70.4	-14.08	4442	1994(4),1996(3),1999(5),2001(6)
MADG	-71.83	-15.6	3348	2001(9),2012(2),2015(3),2018(4),2022(4),2024(4)
NEYO	-73.75	-14.65	4551	2019(4),2022(4),2025(5)
NZ01	-75.54	-13.82	1247	2018(3),2019(4),2022(6),2025(4)
NZ02	-75.2	-13.54	4428	2018(2),2019(4),2022(7),2025(4)
NZ03	-75.22	-14.06	3331	2018(4),2019(4),2022(7),2025(4)
NZ04	-75.95	-14.38	656	2018(5),2019(4),2022(3)
NZ05	-76.15	-14.21	161	2018(4),2019(4),2022(3),2024(3)
NZ06	-75.58	-14.18	556	2018(4),2019(4),2022(9),2024(2)
NZ07	-75.51	-14.5	402	2018(4),2019(4),2022(7)
NZ08	-75.33	-14.72	235	2018(3),2019(4),2022(4),2024(2)
NZ09	-74.97	-14.58	1339	2018(4),2019(4),2022(3)
NZ10	-75.5	-14.94	49	2018(4),2019(4),2022(4),2024(4)
NZ11	-74.74	-14.67	3002	2018(3),2019(4),2022(4),2025(3)
NZ12	-75.18	-14.97	775	2018(8),2019(1)
NZ13	-74.67	-15.62	124	2018(4),2019(3),2022(3)
NZ14	-74.93	-15.25	751	2018(5),2019(4),2022(3)
NZ15	-74.85	-15.57	46	2018(5),2019(4),2022(3),2024(3)
NZ16	-75.37	-15.15	114	2018(5),2019(4),2022(2),2025(8)
NZ17	-74.47	-15.09	889	2018(4),2019(4),2022(14),2025(4)
NZ18	-74.75	-15.36	663	2018(4),2019(4),2022(3),2025(9)
NZ19	-73.9	-16.11	46	2018(5),2019(4),2022(4),2024(4)
NZ20	-73.57	-15.9	1278	2018(5),2019(3),2022(4),2024(3)
NZ21	-73.52	-16.25	513	2018(4),2019(4),2022(7),2024(4)
NZ22	-73.16	-16.04	542	2018(4),2019(4),2022(8),2024(8)
NZ23	-74.15	-15.68	826	2018(1),2019(1),2022(3),2025(3)
NZ24	-73.92	-15.54	2576	2018(4),2019(4),2022(3),2024(2)
PARA	-76.36	-13.87	150	1994(5),1996(5)
PARQ	-70.02	-17.61	3810	2012(3),2014(2),2015(4),2016(4)
PDRG	-74.32	-14.33	4314	2019(3),2022(5),2025(7)
PILP	-74.96	-13.37	4159	2019(3),2022(6),2025(1)
PNAS	-68.49	-16.23	4030	1994(5),1996(4),1999(4),2001(4)

Site	Long.	Lat.	Alt. (m)	Measurements
POCO	-71.37	-17.43	198	1994(5),1996(4),2001(7),2009(4),2012(3),2014(2),2015(3),2016(2),2018(4),2022(5),2024(3)
PUCA	-74.89	-14.26	3603	2019(4),2022(7),2024(4)
PUKI	-71.09	-16.65	3413	2018(5),2022(4),2024(4)
PULT	-74.66	-14.1	4258	2019(4),2022(4)
PUNO	-69.98	-15.86	3900	2012(3),2014(4),2015(4),2018(6),2022(4),2024(4)
QUER	-72.49	-16.16	585	2012(3),2013(4),2015(3),2018(4),2022(6),2024(5)
QUIL	-76.44	-12.95	546	1994(5),1996(4)
REPA	-71.78	-16.53	1753	2012(4),2013(3)
SCRI	-77.02	-12.04	370	1994(4)
SHPU	-74.09	-14.62	3821	2019(4),2022(3),2025(2)
SIGN	-71.55	-16.49	2771	2001(16)
SJUN	-70.86	-16.97	3221	2012(5),2015(4),2016(7),2018(7),2022(5),2024(5)
TACA	-71.04	-17.88	69	2012(4),2013(4),2015(3),2016(3),2018(4),2022(4),2024(4)
TACN	-71.55	-17.25	223	2012(9)
TAMB	-71.56	-17.07	904	2012(2),2013(3),2015(4),2016(4),2022(4),2024(7)
TANC	-74.45	-15.75	196	1994(5),1996(5),1999(3),2001(8),2009(4),2012(4),2013(7),2015(2),2018(4),2022(3),2024(3)
TOMA	-70.54	-17.83	478	2022(3),2024(4)
TOMS	-70.54	-17.83	478	2014(5),2015(4),2022(3)
TUPA	-69.7	-17.0	4173	2012(3),2014(5),2015(3),2018(5),2022(4),2024(4)
UBIN	-71.15	-16.33	4432	2012(2),2015(5),2018(4),2022(5),2024(4)
UNJB	-70.25	-18.02	582	2014(8),2016(3),2018(5),2022(4),2024(4)
ZAMA	-75.62	-14.66	251	1994(5),2009(4)

Table 9.2: Measurements at continuous GNSS sites of the Chilean CSN network.

Site	Long.	Lat.	Alt. (m)	Start	Stop	Epochs
ADAT	-70.75	-27.24	356	2013.693	2014.022	121
AEDA	-70.18	-20.55	90	2003.934	2020.115	4140
AGUI	-71.72	-38.72	2168	2015.975	2016.169	72
ANGO	-72.69	-37.8	94	2013.0	2020.855	2682
ANTC	-71.53	-37.34	746	2013.005	2024.997	1284
ARCO	-73.23	-37.21	28	2014.701	2016.617	210
ARJF	-78.84	-33.63	410	2013.701	2021.337	1565
ATJN	-70.14	-19.3	1598	2005.819	2024.956	6393
BAVE	-70.77	-34.17	514	2016.615	2017.912	421
BING	-70.86	-27.13	48	2018.682	2024.997	2091
BN01	-70.15	-20.22	46	2011.411	2017.997	2334
BN02	-70.41	-23.67	55	2011.0	2023.427	4123
BN03	-70.33	-27.37	418	2011.545	2023.427	3290
BN05	-71.62	-33.04	94	2011.0	2023.427	4482
BN07	-71.66	-35.43	132	2014.0	2022.997	1409
BTON	-71.49	-30.26	43	2007.0	2024.997	5138
CALN	-70.54	-33.4	897	2018.466	2024.997	2360
CAVH	-71.01	-37.85	1680	2015.975	2016.186	73
CBAA	-68.45	-22.75	3515	2006.748	2024.997	5940
CBQC	-72.8	-36.15	36	2015.085	2016.0	68
CCSN	-70.66	-33.46	563	2016.413	2024.997	962
CDLC	-69.76	-22.19	1998	2007.825	2024.997	5082
CERN	-70.93	-32.56	599	2010.175	2016.852	1492
CGTC	-70.07	-20.18	1239	2009.638	2024.713	4847
CGUA	-69.59	-25.16	2538	2013.699	2020.172	1605
CHDA	-70.61	-33.99	668	2015.827	2024.216	2585
CHEN	-70.52	-33.43	806	2018.444	2024.997	2357
CHLA	-71.38	-36.88	2669	2015.975	2016.008	13
CHM2	-69.19	-19.67	3784	2013.274	2015.37	656
CHMZ	-69.19	-19.67	3784	2007.537	2015.37	2050
CHTC	-71.72	-37.11	836	2015.975	2016.199	77
CHYT	-70.34	-18.37	63	2014.31	2024.997	3714
CIFU	-70.65	-25.65	36	2016.891	2024.997	2436
CJNT	-67.76	-23.03	5074	2005.734	2024.803	5052
CLL1	-72.08	-36.6	154	2013.0	2024.997	4184
CLLA	-69.36	-20.95	1555	2008.582	2024.997	5356
CMB2	-71.0	-31.2	1176	2021.614	2024.997	1120
CMBA	-71.0	-31.19	963	2007.348	2021.614	4157
CMPN	-70.69	-29.03	2416	2019.052	2019.614	1
CMRC	-70.33	-18.61	886	2018.488	2023.767	1918
CNBA	-71.46	-31.4	317	2006.888	2024.997	6197
COLC	-68.64	-19.28	3761	2007.833	2016.317	2777
COLL	-68.65	-20.83	3899	2004.399	2005.951	444
CONS	-72.41	-35.33	40	2004.301	2024.997	7096
COPH	-71.16	-37.84	2474	2015.975	2016.186	73
CRIS	-70.39	-24.17	1909	2014.392	2024.997	3374
CRSC	-70.08	-20.92	1518	2005.858	2024.997	6218
CRUZ	-71.8	-38.71	1756	2015.975	2016.169	65
CRZL	-71.41	-29.1	135	2008.872	2024.997	4860
CTLR	-70.1	-21.96	2282	2007.529	2018.337	2362
CTPC	-71.3	-32.56	105	2015.767	2024.997	3330
CURI	-71.23	-34.98	279	2010.184	2013.63	646
DGF1	-70.66	-33.46	581	2003.997	2024.997	7040
ELOA	-70.06	-21.42	46	2018.584	2024.997	2317
EMAT	-71.66	-31.15	47	2007.342	2024.809	5117
FBAQ	-69.76	-20.13	1099	2003.808	2024.333	3742
FMCO	-70.69	-26.58	52	2017.951	2024.997	2359
GTA1	-70.18	-20.57	108	2016.249	2024.997	3061
HLN2	-71.93	-35.01	76	2013.773	2024.997	3418
HLNE	-71.93	-35.01	76	2013.773	2016.492	619
HLPN	-73.19	-36.75	71	2015.693	2024.997	2986
HMBS	-69.89	-20.28	1210	2007.238	2024.566	3048
HSCO	-71.23	-28.46	44	2017.737	2024.997	2632
IACR	-70.33	-18.48	46	2013.093	2024.997	4095
ILOC	-72.18	-34.95	28	2010.186	2024.997	4809
IMCH	-73.89	-38.41	44	2013.647	2022.786	3008
INCA	-69.91	-26.75	1639	2017.86	2024.997	1028
IQQE	-70.13	-20.27	39	2013.011	2024.997	1350
JRGN	-70.57	-23.29	328	2005.726	2024.997	6580

Site	Long.	Lat.	Alt. (m)	Start	Stop	Epochs
JUNT	-70.09	-29.98	2141	2007.951	2024.866	5670
LAVE	-71.65	-38.7	1126	2015.975	2016.169	65
LDMP	-70.56	-36.01	2393	2014.074	2016.172	757
LEMU	-72.0	-34.39	46	2010.181	2015.948	1975
LHOR	-71.3	-29.58	201	2016.885	2024.997	2472
LLCH	-71.08	-28.19	248	2014.101	2024.997	3472
LME2	-70.2	-33.85	1517	2019.852	2024.997	1716
LMEL	-70.2	-33.83	1911	2012.281	2014.808	924
LNQM	-71.36	-38.46	941	2013.0	2024.997	3999
LSCH	-71.25	-29.91	79	2006.888	2024.997	6372
LVIL	-71.51	-31.91	29	2003.57	2024.997	5976
MAUL	-70.82	-35.81	1185	2003.973	2020.727	5386
MCLA	-70.25	-22.75	1033	2005.838	2024.997	6378
MCTE	-73.39	-37.82	101	2015.0	2016.617	97
MHID	-71.17	-37.89	2060	2015.975	2016.186	73
MICA	-69.83	-21.71	1676	2008.085	2012.219	1435
MLZS	-71.12	-37.84	2152	2015.975	2016.186	73
MNMI	-69.6	-19.13	2352	2007.282	2024.997	4721
MOTN	-71.75	-38.68	1997	2015.975	2016.169	65
MRCG	-69.13	-26.84	3983	2014.093	2023.616	3402
NAVI	-71.82	-33.95	146	2010.186	2024.997	4699
NRVL	-72.09	-35.54	228	2016.615	2016.997	2
NUBL	-71.35	-36.85	2355	2015.975	2016.199	77
OVLL	-71.2	-30.6	249	2004.317	2022.137	5195
PA30	-70.09	-20.77	681	2010.819	2024.842	412
PA70	-69.79	-20.75	1232	2014.274	2015.907	580
PAI2	-71.65	-38.87	1094	2015.975	2016.169	65
PAIL	-71.65	-38.87	959	2015.978	2016.025	11
PAPO	-70.5	-25.11	45	2019.679	2024.904	1799
PATH	-70.15	-20.82	873	2016.842	2024.997	2361
PAZU	-70.6	-26.15	377	2013.701	2024.997	4068
PB01	-69.49	-21.04	965	2007.899	2025.11	4497
PB02	-69.89	-21.32	1116	2007.899	2025.162	3519
PB03	-69.75	-22.05	1539	2007.899	2025.162	3188
PB04	-70.15	-22.34	1613	2007.899	2018.29	3245
PB05	-70.2	-22.85	1199	2007.896	2021.551	3020
PB06	-69.57	-22.71	1484	2009.767	2024.361	3618
PB07	-69.89	-21.73	1618	2009.841	2018.29	2592
PB08	-69.16	-20.14	3060	2009.805	2025.159	3799
PB09	-69.24	-21.79	1584	2014.348	2025.162	1991
PB11	-69.66	-19.76	1395	2013.364	2021.468	2136
PB19	-69.3	-23.9	2436	2020.268	2024.997	1067
PCAL	-68.93	-22.46	2300	2003.912	2010.093	343
PCCL	-70.11	-18.46	1144	2005.8	2024.956	6419
PCHA	-69.43	-19.87	1683	2005.501	2018.392	3434
PCLM	-72.0	-34.38	37	2015.762	2018.986	1062
PCMU	-71.96	-34.5	150	2015.307	2024.997	3367
PCVA	-71.62	-30.27	139	2018.178	2020.306	533
PECL	-73.65	-37.69	100	2014.638	2024.997	3403
PEDR	-70.69	-30.84	970	2007.151	2024.997	4958
PELL	-72.61	-35.83	103	2010.186	2024.997	4340
PFRJ	-71.64	-30.67	207	2007.0	2024.997	5971
PICB	-69.33	-20.49	1376	2003.499	2007.844	1224
PICC	-69.33	-20.49	1363	2009.899	2024.997	3869
PLAJ	-72.7	-37.25	79	2010.205	2012.022	659
PLVP	-73.59	-37.15	59	2014.019	2024.997	3166
PMEJ	-70.45	-23.1	49	2003.91	2024.997	6542
PORT	-70.13	-32.84	2926	2002.945	2024.997	6116
PRNL	-70.38	-24.6	2546	2014.49	2019.153	1090
PSGA	-70.12	-19.6	1003	2007.238	2024.997	5077
PTCL	-71.37	-17.7	99	2007.921	2018.03	2738
PTRE	-69.57	-18.19	3608	2005.811	2024.997	6096
PTZL	-71.37	-36.86	2802	2016.071	2016.997	42
PUEL	-70.46	-36.05	2419	2014.0	2016.172	784
PUNA	-67.74	-23.39	4830	2015.647	2016.186	143
PVCA	-71.62	-30.27	139	2016.066	2024.997	2584
QLAP	-72.13	-36.08	182	2010.189	2024.997	4244
QSCO	-71.7	-33.39	31	2018.37	2024.997	2331
QTAY	-71.7	-33.19	40	2016.038	2024.997	2890
QUEB	-67.74	-23.32	4420	2015.647	2016.186	142
RADO	-68.93	-22.08	3254	2007.934	2024.997	6011

Site	Long.	Lat.	Alt. (m)	Start	Stop	Epochs
RCSD	-71.61	-33.65	92	2008.79	2024.997	5548
ROB1	-71.02	-32.98	2209	2016.046	2024.997	3156
ROBL	-71.02	-32.98	2230	2008.825	2014.712	1649
SAAV	-73.38	-38.79	100	2015.485	2024.997	2883
SALF	-70.29	-33.74	1228	2019.011	2024.997	2081
SBLL	-70.78	-34.79	899	2015.033	2024.997	3568
SHLA	-71.38	-36.88	2669	2015.0	2016.199	98
SILL	-70.74	-29.25	2351	2008.448	2024.997	5464
SJAV	-71.73	-35.6	119	2003.323	2024.997	6397
SLM1	-70.97	-32.04	2382	2018.874	2024.997	1878
SLMC	-70.96	-31.78	548	2003.573	2018.192	4728
SMAR	-70.54	-33.27	1452	2018.479	2024.997	2097
SPAT	-68.18	-22.95	2433	2015.416	2024.997	3113
SRGD	-69.35	-22.87	1899	2006.868	2024.997	5753
SURI	-69.14	-18.85	4329	2017.06	2024.997	2079
TAMR	-70.23	-27.59	719	2013.693	2024.997	2962
TCPL	-70.19	-22.09	68	2006.241	2007.997	353
TEST	-70.66	-33.46	556	2018.351	2023.836	13
TLGT	-70.99	-33.78	1349	2014.89	2024.883	3385
TLT2	-70.48	-25.39	70	2021.74	2024.997	1182
TMCO	-72.61	-38.76	137	2013.0	2024.997	3519
TOLO	-70.81	-30.17	2230	2005.356	2024.997	5091
TRPD	-71.65	-33.02	62	2016.609	2024.997	3043
TRST	-70.27	-28.84	1266	2014.112	2024.997	3823
TTAL	-70.43	-25.42	1091	2014.381	2019.562	1775
UAIB	-70.51	-33.49	1080	2015.46	2024.904	3250
UAPE	-70.14	-20.24	56	2000.0	2024.672	8284
UCNF	-70.41	-23.68	73	2005.323	2016.486	3097
UDAT	-70.35	-27.36	405	2014.756	2024.997	3472
UDEC	-72.34	-37.47	178	2013.0	2024.997	4238
UTAR	-70.3	-18.49	88	2003.926	2024.997	6774
VALL	-70.76	-28.57	412	2008.448	2024.997	4917
VALN	-71.64	-33.03	119	2005.356	2023.773	6438
VITA	-72.86	-36.42	35	2010.192	2024.997	4513
VLZL	-69.96	-23.12	1555	2006.734	2024.997	5228
VNEV	-70.25	-33.35	3098	2003.019	2023.482	6544
VZCH	-70.51	-33.6	814	2018.542	2024.828	2235
ZAPA	-71.47	-32.55	35	2010.181	2024.997	4421

Table 9.3: Measurements at continuous GNSS sites of the DEEPtrigger Chile network.

Site	Long.	Lat.	Alt. (m)	Start	Stop	Epochs
AN02	-70.56	-26.59	343	2020.716	2024.552	1316
AN03	-70.35	-26.82	1063	2020.738	2024.552	1375
AN04	-69.77	-27.12	1535	2020.74	2024.552	1141
AN05	-70.91	-27.39	170	2020.743	2024.563	1255
AN06	-71.06	-28.97	602	2020.746	2024.5	1349
AN07	-70.45	-27.97	880	2021.274	2024.546	1178
AN08	-71.02	-27.67	66	2021.079	2024.563	879
AN10	-70.33	-26.52	1016	2021.066	2024.552	1214
AN13	-70.04	-26.31	1086	2021.178	2024.549	1138
AN14	-70.19	-25.3	1612	2021.395	2024.552	515
AN15	-69.22	-25.35	3961	2021.068	2024.56	890
AN19	-69.59	-25.17	2556	2021.255	2024.56	742
AN20	-70.49	-25.41	37	2021.392	2024.508	333
BN01	-70.15	-20.22	46	2011.411	2016.607	1834
BN81	-70.15	-20.21	49	2022.014	2022.608	348
BN91	-70.15	-20.21	46	2018.34	2021.97	1220
COBA	-69.59	-24.82	2542	2021.17	2021.97	82
FNKE	-69.87	-25.84	1806	2021.392	2021.97	215
ICHA	-71.57	-29.03	74	2021.074	2021.97	121
IDMA	-71.53	-29.23	37	2021.071	2021.97	111
INCA	-69.91	-26.75	1639	2021.074	2023.997	535
IST1	-71.42	-28.82	36	2021.063	2025.099	1300
IST2	-71.26	-29.35	328	2021.055	2025.099	1478
IST3	-70.74	-26.79	217	2021.041	2025.107	1318
IST4	-71.01	-28.69	976	2021.066	2025.099	1474
IST5	-70.56	-27.18	698	2021.03	2025.107	1490
IST6	-70.21	-27.14	1481	2021.033	2025.107	1489
IST7	-70.14	-27.8	974	2021.06	2025.104	1372
IST8	-70.83	-27.95	407	2021.038	2025.101	1485
IST9	-71.01	-29.66	717	2021.068	2025.096	1472
MFLA	-69.98	-28.12	1504	2021.299	2024.56	1173
URUS	-67.11	-17.95	3767	2009.668	2022.844	2758

Table 9.4: Measurements at continuous GNSS sites of the Copiapo Chile network.

Site	Long.	Lat.	Alt. (m)	Start	Stop	Epochs
BAR2	-70.79	-27.6	291	2019.195	2020.749	569
COP5	-70.02	-27.27	970	2019.216	2020.749	561
LCHO	-71.26	-29.28	227	2019.184	2020.749	518
MMOR	-70.64	-26.87	452	2019.214	2020.749	562
PCHO	-71.46	-29.25	59	2019.162	2020.749	579
TOT5	-70.34	-27.95	1134	2019.197	2020.749	568
TTRL	-71.06	-27.88	323	2019.197	2020.749	471

Table 9.5: Measurements at continuous GNSS sites of the IGP/ISTerre Peru network.

Site	Long.	Lat.	Alt. (m)	Start	Stop	Epochs
ATIC	-73.7	-16.23	54	2010.745	2022.8	3758
CBRO	-71.79	-17.0	1073	2007.912	2022.918	4229
CHIN	-76.39	-13.63	35	2007.655	2009.121	376
CHRA	-72.93	-16.52	66	2011.063	2022.384	3120
DANC	-70.25	-17.26	3565	2011.37	2022.137	3810
ENAP	-76.29	-13.81	39	2007.658	2011.348	1160
GLRV	-74.4	-14.67	3991	2010.751	2022.247	2903
GUAD	-75.79	-14.0	741	2007.658	2022.918	5087
JUAN	-75.97	-13.42	539	2007.66	2009.405	410
LAGU	-76.27	-14.15	74	2007.649	2022.915	4631
LOMI	-75.85	-14.71	35	2011.901	2022.921	3949
LYAR	-70.57	-18.13	352	2007.811	2022.937	5213
MUSE	-76.27	-13.87	33	2007.674	2007.937	57
NZCA	-74.96	-14.86	578	2010.762	2022.932	4044
PALC	-69.96	-17.78	3047	2011.367	2022.69	3877
PMCA	-70.91	-17.95	40	2011.37	2021.403	3024
PTCL	-71.37	-17.7	99	2018.0	2022.063	765
PTIN	-74.31	-15.84	58	2011.381	2022.795	3480
QCA2	-72.43	-16.72	121	2016.0	2022.644	1768
QUCA	-72.43	-16.72	121	2011.378	2022.318	1814
SJUA	-75.19	-15.36	50	2011.058	2022.926	4260
SLRZ	-77.21	-12.08	46	2009.797	2011.781	690
SMRG	-75.2	-14.44	490	2011.921	2022.668	3838
TORA	-70.85	-17.08	2269	2011.373	2015.468	1328
TQPL	-70.64	-17.3	2738	2009.699	2022.918	4326
TRTA	-70.04	-17.48	3202	2009.312	2020.038	3451

Table 9.6: Measurements at continuous GNSS sites of the DEEPtrigger Peru network.

Site	Long.	Lat.	Alt. (m)	Start	Stop	Epochs
ANMA	-75.35	-13.94	2251	2021.907	2025.46	1298
CAZL	-76.47	-13.02	34	2009.849	2025.477	2598
CHIA	-76.13	-13.28	388	2021.923	2025.458	1270
COYN	-75.36	-14.77	272	2021.918	2025.46	1295
CRVP	-73.37	-15.76	1880	2021.91	2025.466	1300
NZ04	-75.95	-14.38	657	2024.913	2025.458	200
OCUC	-75.68	-14.33	502	2021.904	2025.307	1244
PARA	-76.33	-13.83	238	2021.901	2025.458	1300
PLCA	-74.23	-15.22	1085	2021.912	2025.463	1298

Table 9.7: Measurements at continuous GNSS sites of the Peruvian IGN network.

Site	Long.	Lat.	Alt. (m)	Start	Stop	Epochs
AM01	-77.87	-6.24	2320	2010.373	2018.997	2884
AM02	-78.53	-5.64	450	2010.663	2015.956	1368
AM03	-78.53	-5.64	450	2015.959	2018.997	1111
AN01	-77.53	-9.53	3098	2010.249	2017.704	2638
AN02	-78.53	-9.13	39	2009.899	2018.997	2586
AN03	-78.04	-8.47	3370	2010.444	2018.997	2376
AN04	-77.54	-9.51	3170	2017.707	2018.997	472
AP01	-72.88	-13.64	2419	2010.548	2023.189	4080
AQ01	-71.51	-16.42	2455	2010.671	2023.189	4386
AQ02	-72.02	-17.03	65	2009.847	2021.712	3751
AQ03	-72.49	-16.08	662	2011.263	2023.189	3788
AQ04	-73.62	-16.23	68	2017.0	2023.189	1963
AQ05	-71.77	-15.62	3408	2017.622	2018.997	503
AQ06	-72.9	-15.21	2725	2017.633	2018.997	190
AY01	-74.23	-13.16	2800	2009.833	2023.189	4559
AY02	-73.78	-15.02	3224	2010.499	2023.189	3539
AY03	-74.33	-13.92	3468	2017.0	2018.997	730
CJ01	-78.51	-7.15	2731	2009.94	2018.997	2758
CS01	-71.96	-13.52	3410	2010.551	2023.189	3877
CS02	-72.08	-14.45	3712	2009.934	2023.189	3277
CS03	-73.83	-12.52	640	2010.162	2023.189	3609
CZ01	-71.96	-13.52	3410	2010.636	2012.566	218
GEO2	-71.53	-16.41	2375	2017.0	2018.997	727
GNC1	-77.02	-12.1	160	2010.326	2010.997	30
HC01	-76.24	-9.93	1928	2010.493	2014.805	1110
HC02	-74.97	-9.38	243	2013.0	2018.997	1560
HC03	-76.24	-9.93	1928	2014.805	2018.997	1505
HV01	-74.97	-12.79	3721	2010.622	2023.189	3656
IC01	-75.73	-14.08	442	2009.833	2023.189	4411
IC03	-74.94	-14.83	631	2010.408	2018.997	2659
IC04	-76.2	-13.71	49	2009.97	2018.997	2497
ILO1	-71.34	-17.63	44	2010.323	2010.997	45
ISTK	-77.05	-12.08	129	2008.456	2010.575	767
JGRC	-78.81	-5.7	777	2017.34	2017.575	241
JU01	-75.21	-12.06	3301	2011.759	2023.189	3332
JU03	-75.33	-11.06	830	2017.0	2018.997	724
LB01	-79.87	-6.78	43	2009.888	2018.997	2189
LB02	-79.75	-5.99	184	2017.721	2018.997	364
LI01	-77.02	-12.1	158	2008.664	2023.189	4994
LI02	-77.17	-11.77	34	2010.263	2018.997	2525
LI03	-76.76	-11.97	699	2010.23	2018.997	2505
LI04	-76.8	-12.48	41	2010.0	2023.189	4444
LI05	-77.78	-10.7	109	2011.285	2018.997	2440
LIJP	-77.01	-12.09	190	2017.0	2017.997	365
LL01	-79.04	-8.1	56	2010.518	2016.831	2023
LL02	-79.04	-8.1	56	2013.0	2018.997	2119
MD01	-69.19	-12.59	233	2010.534	2018.997	2329
MQ01	-70.92	-17.19	1510	2009.915	2018.641	2456
MQ02	-71.34	-17.63	44	2010.323	2023.189	4152
PA01	-76.25	-10.67	4392	2010.482	2018.997	2697
PI01	-80.63	-5.18	52	2010.0	2018.997	2911
PI02	-79.45	-5.24	1969	2010.173	2016.131	1609
PI04	-79.45	-5.24	1969	2017.0	2018.997	726
PI07	-80.82	-5.56	36	2017.712	2018.997	381
PU01	-70.43	-14.07	4384	2010.318	2015.222	684
PU02	-70.18	-15.51	3881	2010.34	2023.189	4229
PU03	-69.09	-16.24	3888	2013.622	2023.189	2411
PU04	-70.43	-14.07	4384	2015.225	2018.997	1337
SED1	-76.98	-12.03	270	2017.0	2018.997	720
SM01	-76.99	-6.02	885	2011.296	2018.997	2710
SM02	-76.73	-7.18	296	2010.745	2018.997	2825
SM03	-76.53	-8.19	514	2017.0	2018.997	562
TC01	-70.26	-18.0	605	2010.055	2023.189	4545
UC01	-74.53	-8.38	183	2010.625	2018.997	2309

Table 9.8: Measurements at continuous GNSS sites of the Brazilian network.

Site	Long.	Lat.	Alt. (m)	Start	Stop	Epochs
CRUZ	-72.67	-7.61	236	2012.429	2024.585	3847
RIOB	-67.8	-9.97	173	2010.0	2025.608	5447
ROGM	-65.33	-10.78	158	2010.0	2020.585	3740

Table 9.9: Measurements at continuous GNSS sites of the Ramsac Argentina network.

Site	Long.	Lat.	Alt. (m)	Start	Stop	Epochs
25MA	-67.72	-37.77	374	2013.37	2025.663	4331
ABRA	-65.7	-22.72	3530	2013.89	2025.663	2632
ALUM	-66.6	-27.32	2737	2008.79	2025.663	4331
CATA	-65.77	-28.47	547	2008.724	2025.663	6072
CFAG	-68.23	-31.6	703	1999.0	2025.663	6668
CHMA	-70.28	-37.37	876	2015.301	2023.849	2696
CSJ1	-68.43	-31.98	580	2009.729	2025.663	4767
CSLO	-69.3	-31.78	2639	2005.786	2025.663	6296
DINO	-67.84	-30.16	1423	2012.738	2025.627	4402
ETSJ	-68.82	-32.89	758	2018.197	2020.907	928
GRLS	-68.32	-31.61	604	2010.0	2025.315	1636
JBAL	-65.62	-27.58	409	2009.441	2025.663	5637
JCHL	-68.75	-30.24	1206	2015.658	2025.099	3394
LARJ	-66.85	-29.41	536	2015.496	2025.663	3610
LHCL	-65.6	-38.0	405	1996.678	2025.663	7134
LNQM	-71.36	-38.46	941	2015.474	2025.005	2879
MA01	-68.06	-38.95	323	2009.564	2025.049	2405
MGUE	-69.4	-35.78	1554	2012.904	2025.356	3917
MZAC	-68.88	-32.9	860	2004.418	2025.663	7179
MZAE	-68.15	-33.25	636	2007.452	2025.663	5407
MZAL	-68.6	-32.72	636	2013.326	2025.663	3462
MZAN	-68.88	-32.89	863	2004.249	2004.661	65
MZAR	-68.47	-33.2	700	2015.17	2025.663	2240
MZAS	-68.33	-34.61	729	2007.37	2010.811	1229
MZAU	-69.12	-33.74	1057	2011.71	2025.663	3303
MZGA	-67.7	-34.98	504	2014.408	2025.63	3695
MZRF	-68.33	-34.61	730	2016.954	2025.663	2527
MZSR	-68.33	-34.62	731	2010.918	2016.831	1492
NEQN	-68.06	-38.95	349	2018.849	2025.663	2473
NUGA	-65.26	-35.11	332	2014.51	2023.052	2345
OAFA	-68.62	-31.51	727	2015.915	2025.66	2933
PEDR	-70.69	-30.84	970	2018.104	2021.263	601
PORT	-70.13	-32.84	2926	2022.167	2024.978	331
RODE	-69.13	-30.21	1636	2015.803	2025.663	3391
SAIS	-66.94	-36.23	339	2016.508	2025.663	2245
SANT	-70.67	-33.15	723	2009.436	2025.614	4105
SL01	-66.31	-33.16	865	2009.737	2025.663	5326
TAVA	-65.71	-26.85	2037	2013.523	2025.663	4374
TGTA	-67.57	-28.07	1242	2019.674	2025.663	2055
TILC	-65.4	-23.58	2518	2012.964	2025.663	4211
TRN1	-65.28	-26.23	816	2020.918	2025.663	1668
TRNC	-65.28	-26.23	816	2013.145	2020.063	2480
TRST	-70.27	-28.84	1266	2018.123	2021.263	896
TUCU	-65.23	-26.84	485	1999.0	2025.663	8499
UNSA	-65.41	-24.73	1258	2000.003	2025.658	7964
UNSJ	-68.58	-31.54	709	2007.175	2025.663	6682
ZPLA	-70.07	-38.91	1047	2015.307	2025.663	3279

Table 9.10: Measurements at continuous GNSS sites of the Unavco network.

Site	Long.	Lat.	Alt. (m)	Start	Stop	Epochs
ACPM	-70.54	-33.45	725	2010.008	2015.474	857
AMDE	-67.63	-20.24	3716	2014.581	2017.959	1047
ANGO	-72.69	-37.8	93	2010.326	2016.235	1681
ARCO	-73.23	-37.21	28	2010.471	2016.249	1792
AREG	-71.49	-16.47	2489	2015.0	2022.444	2689
AREV	-71.49	-16.47	2489	2010.17	2017.693	2060
ATIC	-73.7	-16.23	55	2012.0	2015.0	1097
BCOR	-68.43	-17.18	4023	2014.537	2016.522	726
BDEC	-68.6	-19.27	3733	2014.578	2016.525	712
BDJC	-67.43	-19.13	3809	2014.808	2017.959	1070
BLOV	-68.25	-19.85	3736	2014.578	2018.463	1049
BMWS	-67.97	-21.06	3727	2014.584	2016.525	640
BNOE	-68.41	-17.84	3945	2014.562	2016.484	702
BRDQ	-67.68	-18.35	3808	2014.573	2016.484	572
BTNT	-69.32	-17.48	4021	2014.559	2016.525	654
BWSZ	-68.26	-18.79	3773	2014.578	2016.525	712
CAUQ	-72.34	-35.97	157	2010.238	2016.73	2270
CBAA	-68.45	-22.75	3515	2006.748	2015.005	3010
CBQC	-72.8	-36.15	36	2010.351	2016.249	1645
CBRO	-72.4	-37.04	146	2010.334	2016.254	1705
CDLC	-69.76	-22.19	1998	2006.759	2015.455	2999
CFAG	-68.23	-31.6	703	2010.666	2010.455	50
CGSJ	-69.42	-31.37	1461	2015.852	2019.37	1286
CGTC	-70.07	-20.18	1239	2009.638	2015.997	2207
CHML	-70.15	-37.36	1251	2010.249	2016.183	2153
CHMZ	-69.19	-19.67	3784	2007.537	2015.37	2395
CHRA	-72.93	-16.52	66	2012.0	2014.992	777
CJNT	-67.76	-23.03	5074	2005.83	2015.997	3200
CLL1	-72.08	-36.6	154	2010.197	2016.235	2005
CLLA	-69.36	-20.95	1555	2008.582	2014.997	2142
CMPN	-70.69	-29.03	2416	2010.0	2016.107	2185
COLO	-67.8	-22.17	4377	2010.279	2022.893	4128
CONT	-73.03	-36.84	173	2010.666	2014.723	1442
CONZ	-73.03	-36.84	181	2010.666	2015.26	1673
COPO	-70.34	-27.38	479	2010.666	2015.589	1551
CRBR	-71.79	-17.0	1073	2012.0	2014.301	842
CRNL	-73.15	-37.03	26	2010.332	2012.077	203
CRRL	-68.35	-36.15	1226	2010.205	2016.186	1824
CRSC	-70.08	-20.92	1518	2005.858	2014.997	3305
CSPS	-69.64	-31.21	2420	2015.855	2019.378	604
CSQM	-66.39	-23.43	3707	2014.512	2019.386	1781
CTLR	-70.1	-21.96	2282	2007.529	2014.781	2151
CUVI	-71.13	-33.35	261	2010.381	2016.238	1678
DUAO	-72.15	-34.87	27	2010.227	2013.715	976
ELA2	-69.81	-35.18	1868	2010.222	2017.06	1691
ESCA	-71.06	-37.89	1731	2010.258	2014.781	957
GAS1	-69.59	-36.21	1385	2010.167	2013.605	1197
GOLG	-65.76	-24.69	2381	2009.833	2015.151	1943
HLNE	-71.74	-35.0	65	2010.236	2016.243	2073
JRGN	-70.57	-23.29	328	2005.844	2015.455	3359
LAJA	-71.38	-37.39	1438	2010.0	2016.257	2145
LCEN	-68.6	-25.33	4271	2010.847	2018.362	2662
LLST	-68.52	-25.17	5272	2010.847	2015.611	1098
LMHS	-70.75	-37.02	1270	2010.249	2019.068	1984
LNDS	-70.58	-32.84	884	2010.0	2016.238	1907
LNQM	-71.36	-38.46	941	2010.0	2016.238	2048
LNRS	-71.63	-35.85	167	2010.222	2016.224	1360
LTUE	-71.73	-34.1	286	2010.356	2012.571	758
LVRA	-66.31	-22.52	4279	2014.515	2019.389	1781
LYAR	-70.57	-18.13	352	2012.0	2014.97	1086
MCLA	-70.25	-22.75	1033	2005.838	2015.455	3422
MELP	-71.15	-33.68	214	2010.46	2015.764	1700
MGUE	-69.4	-35.78	1554	2012.601	2020.26	2791
NIHU	-72.4	-36.39	113	2010.238	2016.73	2263
NRVL	-72.09	-35.54	228	2010.222	2016.243	1672
PANE	-71.2	-35.72	456	2010.227	2015.762	545
PCCL	-70.11	-18.46	1144	2005.8	2015.005	3153
PCLM	-72.0	-34.38	37	2010.244	2017.701	2632
PECL	-73.65	-37.69	100	2010.395	2015.63	802

Site	Long.	Lat.	Alt. (m)	Start	Stop	Epochs
PHDP	-67.13	-36.03	355	2010.436	2013.605	680
PLLN	-72.51	-35.49	70	2010.197	2011.863	224
PLVP	-73.59	-37.15	59	2010.211	2016.24	890
PMQE	-71.63	-34.55	189	2010.236	2015.759	1196
PTCL	-71.37	-17.7	99	2012.0	2014.992	959
PTPC	-72.0	-34.13	106	2010.249	2011.455	441
PWRO	-69.21	-38.42	492	2010.43	2023.658	3011
QUET	-67.34	-22.2	4271	2010.285	2011.192	332
RANC	-71.57	-36.55	466	2010.216	2016.205	1397
RDCM	-69.08	-30.95	3180	2015.863	2019.367	937
RDEO	-66.77	-18.9	3776	2014.586	2018.395	1391
RDLP	-69.71	-31.93	1984	2015.868	2019.334	685
RGAO	-69.38	-34.25	2342	2010.211	2015.468	1920
SALC	-66.32	-24.21	3842	2010.427	2015.151	1726
SANP	-71.48	-33.87	191	2010.359	2016.268	2059
SCTC	-66.05	-21.95	3877	2014.501	2019.389	1461
SOCM	-68.3	-24.45	3970	2011.701	2022.997	3749
SOLD	-73.14	-36.7	107	2010.205	2011.956	624
SRGD	-69.35	-22.87	1899	2006.868	2015.005	2971
SRSA	-65.95	-24.45	3154	2010.178	2015.151	1816
TLCR	-71.67	-35.41	113	2010.288	2011.014	254
TMCO	-72.61	-38.76	137	2010.381	2015.805	1898
TOCA	-69.44	-30.66	2619	2015.858	2019.37	911
TQPL	-70.64	-17.3	2738	2012.0	2014.992	1009
TRGN	-72.67	-38.24	279	2010.326	2016.257	1486
TRTA	-70.04	-17.48	3202	2012.0	2014.992	995
TUZG	-66.52	-24.03	4339	2009.841	2015.153	1135
UDEC	-72.34	-37.47	178	2010.0	2018.937	3242
UNSA	-65.41	-24.73	1258	2010.666	2018.956	2902
UTUR	-67.21	-22.24	5184	2010.285	2020.577	3755
VALP	-71.63	-33.03	31	2010.666	2015.57	1254
VLDR	-69.48	-30.17	2888	2015.866	2019.37	234
VLZL	-69.96	-23.12	1555	2006.734	2014.962	2741
YANI	-73.66	-37.36	52	2010.208	2012.071	247
YAVC	-65.47	-22.12	3613	2014.499	2019.389	1787

Table 9.11: Measurements at continuous GNSS sites of the IGS network.

Site	Long.	Lat.	Alt. (m)	Start	Stop	Epochs
ANTC	-71.53	-37.34	746	2002.496	2025.674	6589
AREQ	-71.49	-16.47	2489	1994.082	2025.674	10779
CONZ	-73.03	-36.84	181	2002.438	2015.26	4581
COPO	-70.34	-27.38	479	2002.496	2015.592	4170
IQQE	-70.13	-20.27	39	2002.496	2025.671	6446
MGUE	-69.4	-35.78	1554	2012.601	2025.674	4769
SANT	-70.67	-33.15	723	2000.0	2025.674	8429
UNSA	-65.41	-24.73	1258	2000.0	2025.674	8887